



# PROCEEDINGS OF THE FOURTH INTERNATIONAL SYMPOSIUM ON THE INTERACTION OF NON- NUCLEAR MUNITIONS WITH STRUCTURES (VOL I)

L.C. CLOUSTON

APPLIED RESEARCH ASSOCIATES, INC.  
TYNDALL AFB FL 32403-6001

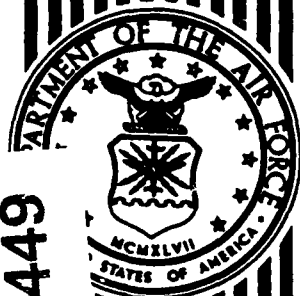
APRIL 1989

FINAL REPORT

APRIL 1989 — APRIL 1989

DTIC  
ELECTE  
MAY 30 1990  
S 3 D D

APPROVED FOR PUBLIC RELEASE: DISTRIBUTION UNLIMITED



AD-A222 449



90 05 29 110

AIR FORCE ENGINEERING & SERVICES CENTER  
ENGINEERING & SERVICES LABORATORY  
TYNDALL AIR FORCE BASE, FLORIDA 32403

NOTICE

PLEASE DO NOT REQUEST COPIES OF THIS REPORT FROM  
HQ AFESC/RD (ENGINEERING AND SERVICES LABORATORY).  
ADDITIONAL COPIES MAY BE PURCHASED FROM:

NATIONAL TECHNICAL INFORMATION SERVICE  
5285 PORT ROYAL ROAD  
SPRINGFIELD, VIRGINIA 22161

FEDERAL GOVERNMENT AGENCIES AND THEIR CONTRACTORS  
REGISTERED WITH DEFENSE TECHNICAL INFORMATION CENTER  
SHOULD DIRECT REQUESTS FOR COPIES OF THIS REPORT TO:

DEFENSE TECHNICAL INFORMATION CENTER  
CAMERON STATION  
ALEXANDRIA, VIRGINIA 22314

## REPORT DOCUMENTATION PAGE

Form Approved  
OMB No. 0704-0188

|   |   |  |   |                                     |                          |
|---|---|--|---|-------------------------------------|--------------------------|
| 1a. REPORT SECURITY CLASSIFICATION<br>Unclassified  |   |  | 1b. RESTRICTIVE MARKINGS  |                                     |                          |
| 2a. SECURITY CLASSIFICATION AUTHORITY   |   |  | 3. DISTRIBUTION / AVAILABILITY OF REPORT<br>Distribution Unlimited<br>Approved for public release   |                                     |                          |
| 2b. DECLASSIFICATION / DOWNGRADING SCHEDULE   |   |  | 5. MONITORING ORGANIZATION REPORT NUMBER(S)   |                                     |                          |
| 4. PERFORMING ORGANIZATION REPORT NUMBER(S)<br>ESL-TR-89-21   |   |  | 7a. NAME OF MONITORING ORGANIZATION<br>Air Force Engineering and Services Center  |                                     |                          |
| 6a. NAME OF PERFORMING ORGANIZATION<br>Applied Research Associates,<br>Inc  | 6b. OFFICE SYMBOL<br>(if applicable)<br>ARA                                       | 7b. ADDRESS (City, State, and ZIP Code)<br>HQ AFESC/RDCS<br>Tyndall AFB, FL 32403-6001 |   |                                     |                          |
| 6c. ADDRESS (City, State, and ZIP Code)<br>Tyndall AFB, FL 32403-5000   | 9. PROCUREMENT INSTRUMENT IDENTIFICATION NUMBER<br>F08635-88-C-0067, Subtask 2.03 |  |   |                                     |                          |
| 8a. NAME OF FUNDING / SPONSORING ORGANIZATION   | 8b. OFFICE SYMBOL<br>(if applicable)  | 10. SOURCE OF FUNDING NUMBERS  |   |                                     |                          |
| 8c. ADDRESS (City, State, and ZIP Code)   |   | PROGRAM<br>ELEMENT NO.<br>62206F   | PROJECT<br>NO.<br>2673  | TASK<br>NO.                         | WORK UNIT<br>ACCESSION N |
| 11. TITLE (Include Security Classification)<br>Proceedings of the Fourth International Symposium on the Interaction of Non-nuclear Munitions with Structures (Volume 1) (Unclassified)  |   |  |   |                                     |                          |
| 12. PERSONAL AUTHOR(S)<br>Administered by Lily C. Clouston, University of Florida Graduate Engineering Center, Eglin  |   |  |   |                                     |                          |
| 13a. TYPE OF REPORT<br>Final  | 13b. TIME COVERED<br>FROM 89-04 TO 89-04  | 14. DATE OF REPORT (Year, Month, Day)<br>April 17-21, 1989                             |   | 15. PAGE COUNT<br>414               |                          |
| 16. SUPPLEMENTARY NOTATION<br>Volume 1 of symposium proceedings; Volume 2 being consolidated now.   |   |  |   |                                     |                          |
| 17. COSATI CODES  |   |  | 18. SUBJECT TERMS (Continue on reverse if necessary and identify by block number)   |                                     |                          |
| FIELD   | GROUP   | SUB-GROUP  | International symposium; Blast effects, Fragmentation, Non-nuclear munitions, Equipment, Impact, Penetration, Structures, Material behavior, Failure analysis, Scale modeling. (held) |                                     |                          |
|   |   |  |   |                                     |                          |
| 19. ABSTRACT (Continue on reverse if necessary and identify by block number)<br>This report contains proceedings of unclassified presentations at the symposium. The presentations covered the following broad topic areas: material behavior, constitutive equations (soil, concrete, metal, rock), blast-structure interaction (near field, far field, soil, air), structural response (blast effects, kinetic energy, above and below ground), failure analysis of components and systems, impact and penetration, scale modeling technique design and construction details, equipment features (blast doors, blast valves, shock isolation), and fragmentation effects and air blast-fragment synergism. <i>Keywords:</i> |   |  |   |                                     |                          |
| 20. DISTRIBUTION / AVAILABILITY OF ABSTRACT<br><input checked="" type="checkbox"/> UNCLASSIFIED/UNLIMITED <input type="checkbox"/> SAME AS RPT. <input type="checkbox"/> DTIC USERS   |   |  | 21. ABSTRACT SECURITY CLASSIFICATION<br>Unclassified  |                                     |                          |
| 22a. NAME OF RESPONSIBLE INDIVIDUAL<br>Capt Diane B. Miller   |   |  | 22b. TELEPHONE (Include Area Code)<br>(904)-283-3728  | 22c. OFFICE SYMBOL<br>HQ AFESC/RDCS |                          |

## PREFACE

This report is Volume One of the Proceedings of the Fourth International Symposium on the Interaction of Non-Nuclear Munitions with Structures, held at the Edgewater Beach Resort, Panama City Beach, Florida from 17 through 21 April 1989 with a worldwide audience in attendance. The symposium was sponsored by the Air Force Engineering and Services Center, Engineering and Services Laboratory, Tyndall AFB, Florida, and endorsed by the American Society of Civil Engineers' Structural Division.

The symposium was coordinated by Applied Research Associates, Inc. (ARA), Tyndall AFB, Florida, under USAF Contract F08635-88-C-0067, Subtask 2.03, and administered by the University of Florida Graduate Engineering Center, Eglin AFB, Florida, under subcontract to ARA. Mrs Lily C. Clouston was the University of Florida's Symposium Administrator; Dr Douglas H. Merkle was ARA's Symposium Coordinator and Proceedings Editor; and Captain Diane B. Miller was the Engineering and Services Laboratory's Symposium Project Officer.

These symposium proceedings are being published in the format in which presented and distributed to participants because of their potential interest to the worldwide scientific and engineering community. Proceedings are being published in two volumes.

This report has been reviewed by the Public Affairs Office and is releasable to the National Technical Information Service (NTIS). At NTIS, it will be available to the general public, including foreign nations.

This technical report has been reviewed and is approved for publication.

*Diane B. Miller*

DIANE B. MILLER, Capt, USAF  
Project Officer

*Robert J. Majka*

ROBERT J. MAJKA, Lt Col, USAF  
Chief, Engineering Research  
Division

*James M. Underwood*  
JAMES M. UNDERWOOD, LT CEC USN  
Acting Chief, Airbase Structures and  
Weapon Effects Branch

*Frank P. Gallagher III*  
FRANK P. GALLAGHER III, Colonel, USA  
Director, Engineering and  
Services Laboratory



**Proceedings  
of the  
Fourth International Symposium  
on the  
Interaction of Non-nuclear Munitions  
with Structures  
(volume 1)**

**Panama City Beach, Florida  
April 17-21, 1989**

**90 05 29 110**

# **Proceedings** **of the** **Fourth International Symposium** **on the** **Interaction of Non-nuclear Munitions** **with Structures** **(volume 1)**



|                    |                                     |
|--------------------|-------------------------------------|
| Accession For      |                                     |
| NTIS CRA&I         | <input checked="" type="checkbox"/> |
| DTIC TAB           | <input type="checkbox"/>            |
| Unannounced        | <input type="checkbox"/>            |
| Justification      |                                     |
| By                 |                                     |
| Distribution /     |                                     |
| Availability Codes |                                     |
| Dist               | Avail and/or Special                |
| AH                 |                                     |

**Panama City Beach, Florida**  
**April 17-21, 1989**

This document is Volume One of the Proceedings of the Fourth International Symposium on the Interaction of Non-Nuclear Munitions with Structures, held at the Edgewater Beach Resort, Panama City Beach, Florida from 17 through 21 April 1989. The symposium was sponsored by the Air Force Engineering and Services Center, Engineering and Services Laboratory, Tyndall AFB, Florida, and endorsed by the American Society of Civil Engineers' Structural Division.

The symposium was coordinated by Applied Research Associates, Inc. (ARA), Tyndall AFB, Florida, under USAF Contract F08635-88-C-0067, Subtask 2.03, and administered by the University of Florida Graduate Engineering Center, Eglin AFB, Florida, under subcontract to ARA. Mrs. Lily C. Clouston was the University of Florida's Symposium Administrator; Dr. Douglas H. Merkle was ARA's Symposium Coordinator and Proceedings Editor; and Captain Diane B. Miller was the Engineering and Services Laboratory's Symposium Project Officer.

All manuscripts in this document authored by United States authors have been approved for public release.

# TABLE OF CONTENTS

|  |    |  |    |
|--|----|--|----|
| ENGINEERING IN THE FIELD OF PROTECTIVE STRUCTURE DESIGN<br>Gerald Ast, Sigma Karlsruhe Engineers, WEST GERMANY   | 1  | EVALUATION OF TRANSMITTED STRESS ACROSS A SEMI-RIGID BOUNDARY CONDITION FOR A MODEL RUNWAY SLAB<br>Bengt E. Vretblad, Royal Swedish Fortification Administration, and Mark Amend, Directorate of Engineering Analysis        | 50 |
| PROGRESS IN BLAST-RESISTANT STRUCTURES RESEARCH<br>Chen Zhao-yuan and Wang Shuang-jin<br>Tsinghua University, Beijing, CHINA   | 4  | PENETRATION OF PROJECTILES INTO FINITE THICK REINFORCED CONCRETE TARGETS<br>Hermann Pahl, NATO Headquarters, BELGIUM   | 55 |
| DESIGN OF ROCK TUNNELS IN ROCK: DAMAGE ESTIMATES AND ENGINEERING COUNTERMEASURES<br>Arnon Rozen, BNE-Beitkha, ISRAEL   | 10 | CONCRETE PENETRATION - ARE ALL PENETRATION FORMULAS CREATED EQUAL AND CAN THEY BE USED EQUALLY?<br>Bengt E. Vretblad, Royal Swedish Fortification Administration, SWEDEN, and Phillip T. Nash, Southwest Research Institute  | 61 |
| PROMIX, A COMPUTER CODE FOR CALCULATING BUILDING DAMAGE FROM INTERNAL EXPLOSIONS<br>Rickard Forsen and Torbjorn Jonasson, Swedish Defence Research Establishment, SWEDEN                     | 15 | INVESTIGATION OF EXPLOSIVELY FORMED PROJECTILES IMPACTING CONCRETE<br>M. J. Worswick, D. J. Mackay, A. McQuilkin, C. A. Weickert, T. Storrie and S. Mowers, Defence Research Establishment Suffield, CANADA                  | 67 |
| FAR-FIELD EFFECTS ON STRUCTURES FROM A HIGH-EXPLOSIVE DETONATION<br>Paul W. Graham, Gayle E. Albritton and James B. Cheek, U.S. Army Engineer Waterways Experiment Station                   | 21 | SMALL ARMS PENETRATION OF CONCRETE<br>M. J. Iremonger, Royal Military College of Science, K. J. Claber, Military Works Force, UNITED KINGDOM, and K. Q. Ho, Housing and Development Board, SINGAPORE                         | 74 |
| EXTERNAL SHOCK MITIGATION FOR BURIED STRUCTURES<br>Henry S. McDevitt, Jr., U.S. Army Engineer Waterways Experiment Station   | 26 | USE OF ROCK/POLYMER COMPOSITES AS PROTECTIVE MATERIALS<br>William F. Anderson, Alan J. Watson and Andrew J. Gallagher, University of Sheffield, UNITED KINGDOM   | 80 |
| THE RESPONSE OF AN AIRCRAFT SHELTER TO A BURIED EXPLOSION 3D COUPLED SIMULATION<br>W. Pfrang, W. Bergerhoff and H. J. Schittke<br>Industrieanlagen-Betriebsgesellschaft mbH WEST GERMANY     | 32 | RICOCHET AND SHALLOW PENETRATION OF BOMBS IMPACTING ON HARD LAYERS<br>D. Favarger, Defence Technology and Procurement Agency, SWITZERLAND and P. Eyer, M. Koller, Glauser, Studer, Stussi, Consulting Engineers, SWITZERLAND | 86 |
| BLAST LOADING FROM ARRAYS OF PARALLEL LINE CHARGES<br>Quentin A. Baker, Wilfred E. Baker and Kathy H. Spivey, Wilfred Baker Engineering, and Edward D. Esparza, Southwest Research Institute | 40 | PENETRATION TESTS WITH SCALED AP AND MK-BOMB MODELS IN LAYERED STRUCTURES<br>Helga Langheim and A. J. Stilp, Ernst-Mach-Institut, WEST GERMANY   | 92 |
| SCALE MODEL TESTS TO DETERMINE BLAST PARAMETERS IN TUNNELS AND EXPANSION ROOMS FROM HE-CHARGES IN THE TUNNEL ENTRANCE<br>G. Scheklinski-Gluck, Ernst-Mach-Institut, WEST GERMANY             | 45 |  |    |

|  |     |  |     |
|--|-----|--|-----|
| NUMERICAL METHOD TO PREDICT PROJECTILE PENETRATION<br>Larry A. Schoof, Frank A. Maestas, Applied Research Associates, Inc., and<br>C. Wayne Young, Sandia National Laboratories                                  | 98  | A NEW BLAST METHOD FOR CONCRETE BRIDGES<br>D. Kraus, Universitat der Bundeswehr Munchen, WEST GERMANY  | 157 |
| MULTIPLE HITS: A NEW THREAT TO CONSIDER?<br>H. J. Hader, E. Basler & Partners, SWITZERLAND   | 104 | FINITE ELEMENT ANALYSIS OF CIVIL DEFENSE SHELTER SUBJECTED TO BLAST LOAD<br>Jonas Palm, Royal Swedish Fortifications Administration, SWEDEN  | 161 |
| PROTECTIVE LAYERS FOR MULTIPLE HITS AND PENETRATORS REQUIREMENTS AND CHANCES<br>Werner Heierli and Max Gloor, Heierli Consulting Engineers, Inc. SWITZERLAND   | 109 | THE NORMAL MODE TECHNIQUE: APPLICATIONS FOR THE ANALYSIS OF TRANSIENT LOADED STRUCTURES<br>W. P. M. Mercx, Prins Maurits Laboratory TNO, THE NETHERLANDS   | 167 |
| IMPLICATIONS OF CENTRIFUGE PENETRATION TESTS FOR USE OF YOUNG'S EQUATION<br>Teresa Taylor, University of Missouri-Columbia/Kansas City, and<br>Richard J. Fragaszy, Washington State University                  | 114 | ENGINEERING - QUANTITY/DISTANCE ANALYSIS OF AMMUNITION AND EXPLOSIVES OPERATIONS<br>David Kossover, Norval Dobbs, Ammann & Whitney, Consulting Engineers, and<br>Joseph Caltagirone, U.S. Army Armament Research, Development and Engineering Center | 173 |
| THE BombCAD ZONE OF INVOLVEMENT (ZOI) MODEL-- A MACRO MODEL FOR ASSESSING STRUCTURAL DAMAGE FROM HIGH EXPLOSIVE DETONATIONS<br>Ronald J. Massa, LORRON CORPORATION, and John W. Howard, Everett I. Brown Company | 119 | FRAGMENT AND DEBRIS HAZARD EVALUATION--A NEED FOR NEW Q-D CRITERIA FOR DOE FACILITIES<br>Patricia Moseley Bowles, Southwest Research Institute   | 179 |
| STRESS WAVE PROPAGATION IN THICK SLABS SUBJECTED TO BLAST OR IMPULSIVE LOADS<br>J. Ballmann, Technical University Aachen, and K. S. Kim, W. Nachtsheim, ITAM Consultants, WEST GERMANY                           | 126 | INTERACTION OF DEFORMATION AND SHOCK RESPONSE FOR BURIED STRUCTURES SUBJECT TO EXPLOSIONS<br>Eve Hinman, Weidlinger Associates   | 184 |
| BURIED PROTECTIVE STRUCTURES SUBJECTED TO SURFACE IMPACT LOADING-- AN EXPERIMENTAL STUDY<br>Michael C. R. Davies, University of Wales College of Cardiff, UNITED KINGDOM   | 132 | TEST PROGRAM FOR DETERMINATION OF REFLECTED PRESSURES IN ACCEPTOR BAYS<br>Darrell D. Barker and Steven L. Young, Mason & Hanger - Silas Mason Co., Inc.  | 190 |
| NUMERICAL SIMULATIONS OF REINFORCED STRUCTURE RESPONSE SUBJECTED TO HIGH EXPLOSIVE DETONATION<br>J. M. Terrier and J. F. X. Boisseau, SNPE Centre de Recherche du Bouchet, FRANCE                                | 137 | A MODIFIED TIMOSHENKO BEAM APPROACH FOR THE ANALYSIS OF REINFORCED CONCRETE STRUCTURES UNDER IMPULSIVE LOADS<br>A. Assadi-Lamouki, AEC Engineers, and T. Krauthammer, University of Minnesota  | 196 |
| LARGE PLASTIC DEFORMATION OF STEEL PLATES AT IMPULSIVE BLAST LOAD<br>Gerhard H. Guerke, Ernst-Mach-Institut, WEST GERMANY  | 145 | A COMBINED SYMBOLIC-NUMERIC PROCESS FOR STRUCTURAL ASSESSMENT WITHIN A LARGE SCALE DECISION SUPPORT SYSTEM FOR POST ATTACK ENVIRONMENTS<br>Theodor Krauthammer, Walter Schimdt, and Raman Muralidharan, University of Minnesota                      | 202 |
| THE IMPORTANCE OF DYNAMIC REACTIONS IN THE DESIGN OF EXPLOSIVELY LOADED FLEXURAL MEMBERS<br>Thomas P. Carroll, Center for Blast Resistant Design   | 154 | STOCHASTIC METHODS FOR PROTECTIVE STRUCTURES DESIGN<br>Timothy J. Ross, University of New Mexico, and Shyh-Yuan Kung, Intelligent Systems Integration, Inc.  | 208 |

|  |     |   |     |
|--|-----|---|-----|
| FUZZY PROBABILITY ANALYSIS OF<br>BASEMENT TYPE SHELTERS<br>X. L. Liu and C. M. Liu, Tsinghua<br>University, CHINA  | 214 | LARGE SIZE PROTECTIVE DOOR - PART II:<br>BEHAVIOR UNDER DYNAMIC LOADING<br>D. Russwurm, Federal Armed Forces Office<br>for Studies and Exercises  | 275 |
| TWO-POUND HIGH EXPLOSIVE TEST FIRE<br>CHAMBER DESIGN, CONSTRUCTION AND<br>TESTING<br>Steven L. Young and Darrell D. Barker,<br>Mason & Hanger - Silas Mason Co., Inc.                                  | 219 | RESPONSE OF A BLAST VALVE TO SHOCK<br>WAVES OF DIFFERENT DURATION<br>J. Hasler and H. H. Oppliger, LUWA Ltd.,<br>SWITZERLAND  | 278 |
| THE DESIGN OF UNDERGROUND MASS<br>TRANSIT STRUCTURES TO RESIST CON-<br>VENTIONAL WEAPON EFFECTS<br>C. A. Mills, WS Atkins & Partners, UNITED<br>KINGDOM  | 224 | RATE EFFECT ON MIXED-MODE FRACTURE<br>OF CONCRETE<br>S. P. Shah, Northwestern University  | 283 |
| DESIGN, DEVELOPMENT AND TESTING<br>OF A HARDENED UNDERGROUND TRANS-<br>PORTABLE COMPOSITE HYPERBOLIC<br>PARABOLOID (HUTCH) SHELTER<br>T. F. Moriarty and P. von Buelow, The<br>University of Tennessee | 230 | STRAIN RATE EFFECT ON STRESS-STRAIN<br>RELATIONSHIPS OF CONCRETE<br>Hiroshi Yamaguchi and Kazuo Fujimoto,<br>Japan Defense Agency, JAPAN, and<br>Setsuro Nomura, Science University of Tokyo,<br>JAPAN  | 290 |
| PRACTICAL EXPERIENCE IN THE DESIGN<br>AND CONSTRUCTION OF RAPID ERECTABLE<br>PRE-ENGINEERED HARDENED STRUCTURES<br>Micaela and Reuben Eytan, Eytan Building<br>Design Ltd., ISRAEL                     | 236 | DYNAMIC TESTING OF CONCRETE WITH THE<br>SPLIT HOPKINSON PRESSURE BAR<br>Lawrence E. Malvern, David A. Jenkins,<br>Tianxi Tang, and Jyh-Cherng Gong,<br>University of Florida  | 296 |
| TESTS PERFORMED ON THE ASP CON-<br>STRUCTION SYSTEM<br>Yaakov Yerushalmi, The ASP Group  | 242 | HIGH STRAIN RATE EFFECTS ON TENSILE<br>STRENGTH OF CONCRETE<br>C. Allen Ross, S. T. Kuennen and W. S.<br>Strickland, HQ AF Engineering and Ser-<br>vices Center   | 302 |
| EARTHQUAKE DAMAGE REPAIR TECHNOLOGY<br>APPLIED TO BLAST DAMAGED STRUCTURES<br>Phillip T. Nash, Southwest Research Institute,<br>and James O. Jirsa and Amador Teran, The<br>University of Texas        | 246 | INELASTIC ANALYSIS OF THE DYNAMIC<br>SPLIT CYLINDER TEST<br>Joseph W. Tedesco and Robert M. Brunair,<br>Auburn University, and<br>C. Allen Ross, A.F. Engineering and Ser-<br>vices Center  | 309 |
| ANALYSIS AND DESIGN RECOMMENDATIONS<br>FOR THE HAYMAN IGLOO CONVENTIONAL<br>WEAPONS STORAGE FACILITY<br>Captain Darell J. Lawver, United States Air<br>Force Academy                                   | 254 | WEAPONS TESTS ON A SIFCON DEFENSIVE<br>FIGHTING POSITION<br>Bruce Schneider, New Mexico Engineering<br>Research Institute, University of New Mexico   | 315 |
| DESIGN AND CONSTRUCTION OF THE SEMI-<br>HARD TR-1 AIRCRAFT SHELTER<br>Frank Theos, Headquarters, United States<br>Air Forces in Europe   | 260 | IMPACT RESISTANCE AND MECHANICAL<br>PERFORMANCE OF KEVLAR FIBER REIN-<br>FORCED CEMENT COMPOSITES<br>Parviz Soroushian, Michigan State University,<br>Ziad Bayasi, Bradley University, and<br>Paul G. Riewald, E. I. DuPont De Nemours<br>& Co., Inc. | 321 |
| NON-PROPAGATING ONE POUND HIGH<br>EXPLOSIVE STORAGE CABINETS<br>Phillip D. Stewart, Steven L. Young and<br>A. G. Papp, Risk Management Department,<br>Pantex Plant                                     | 266 | SATURATED SAND LIQUEFACTION UNDER<br>EXPLOSIVE LOADING<br>Hassen A. Hassen and Wayne A. Charlie,<br>Colorado State University   | 327 |
| LARGE SIZE PROTECTIVE DOOR - PART I:<br>STRUCTURAL DETAILS<br>K-L. Fricke, Engineering Office, Konstruktiv,<br>WEST GERMANY  | 272 | HIGH AMPLITUDE STRESS WAVE PROPAGA-<br>TION IN MOIST SAND<br>Steven J. Pierce and Wayne A. Charlie,<br>Colorado State University, and<br>C. Allen Ross, HQ AF Engineering and Ser-<br>vices Center  | 331 |

|  |     |  |     |
|--|-----|--|-----|
| STRUCTURAL RESPONSE IN IMPACT<br>TENSILE TESTS ON CONCRETE<br>J. Weerheijm, Prins Maurits Laboratory,<br>THE NETHERLANDS, and<br>H. W. Reinhardt, Darmstadt University<br>of Technology, WEST GERMANY                          | 336 | CRATERING BY BURIED CHARGES IN WET<br>MEDIA: COMPARISON OF CENTRIFUGE<br>AND FIELD EVENTS<br>Edward S. Gaffney, Ktech Corporation,<br>Conrad W. Felice, 485th Civ. Eng. Sq.<br>(USAFE) and<br>R. Scott Steedman, Cambridge University,<br>UNITED KINGDOM | 402 |
| CRITERIA USED FOR THE PARTIAL SUB-<br>STITUTION OF STEELBARS BY STEEL<br>FIBERS IN PROTECTIVE CONCRETE<br>STRUCTURES<br>Major Guido Charles Georges Naeyaert,<br>Ministry of Defence, BELGIUM                                  | 341 |  |     |
| STRAIN-DEPENDENT CAP MODEL FOR<br>FITTING MILL YARD TEST BED SOIL<br>BEHAVIOR<br>George Y. Baladi, Air Force Weapons<br>Laboratory/NTE   | 348 |  |     |
| STRESS STRAIN BEHAVIOR OF SANDS -<br>A MICROSTRUCTURAL APPROACH<br>Ching S. Chang and Anil Misra, University<br>of Massachusetts   | 354 |  |     |
| A GENERAL STRESS-STRAIN MODEL FOR<br>GRANULAR SOILS<br>Kingsley Harrop-Williams, The BDM Corp.   | 360 |  |     |
| CONSTITUTIVE MODELLING OF CONCRETE<br>Dusan Krajcinovic, University of Illinois at<br>Chicago  | 365 |  |     |
| EMPIRICAL STUDY ON THE EFFECTS OF<br>SHOCK LOADS ON AIRCRAFT SHELTER<br>EQUIPMENT COMPONENTS AND ASSOCIATED<br>MOUNTING ELEMENTS<br>Hans-Georg Mett, Federal Armed Forces<br>Office for Studies and Exercises, WEST<br>GERMANY | 372 |  |     |
| SMALL-SCALE MODEL TESTING FOR<br>DYNAMICALLY LOADED BURIED STRUCTURES<br>Hung-Liang Chen, Surendra P. Shah and<br>Leon M. Keer, Northwestern University  | 378 |  |     |
| EXPLOSIVE TESTS ON MODEL CONCRETE<br>BRIDGE ELEMENTS<br>Brian Hobbs, Alan J. Watson and Stuart<br>J. Wright, University of Sheffield, UNITED<br>KINGDOM  | 384 |  |     |
| LABORATORY SIMULATION OF GROUND<br>SHOCK LOADING<br>F. Y. Sorrell, North Carolina State<br>University  | 391 |  |     |
| GRAVITY EFFECTS IN SMALL-SCALE<br>STRUCTURAL MODELING<br>Tony F. Zahrah and Douglas H. Merkle,<br>Applied Research Associates, Inc.  | 396 |  |     |

# AUTHOR INDEX

- Albritton, J. E., 21  
 Amend, M., 50  
 Anderson, W. F., 80  
 Assadi-Lamouki, A., 196  
 Ast, G., 1  
 Baker, Q. A., 40  
 Baker, W. E., 40  
 Baladi, G. Y., 348  
 Ballmann, J., 126  
 Barker, D. D., 190, 219  
 Bayasi, Z., 321  
 Bergerhoff, W., 32  
 Boisseau, J. F. X., 137  
 Bowles, P. M., 179  
 Brunair, R. M., 309  
 Caltagirone, J., 173  
 Carroll, T. P., 154  
 Chang, C. S., 354  
 Charlie, W. A., 327, 331  
 Cheek, J. B., 21  
 Chen, H-L., 378  
 Chen, Z-Y., 4  
 Claber, K. J., 74  
 Davies, M. C. R., 132  
 Dobbs, N., 173  
 Esparza, E. D., 40  
 Eyer, P., 86  
 Eytan, M., 236  
 Eytan, R., 236  
 Favarger, D., 86  
 Felice, C. W., 402  
 Forsen, R., 15  
 Fragaszy, R. J., 114  
 Fricke, K-L., 272  
 Fujimoto, K., 290  
 Gaffney, E. S., 402  
 Gallagher, A. J., 80  
 Gloor, M., 109  
 Gong, J-C., 296  
 Graham, P. W., 21  
 Guerke, G. J., 145  
 Hader, H. J., 104  
 Harrop-Williams, K., 360  
 Hasler, J., 278  
 Hassen, H. A., 327  
 Heierli, W., 109  
 Hinman, E., 184  
 Ho, K. Q., 74  
 Hobbs, B., 384  
 Howard, J. W., 119  
 Iremonger, M. J., 74  
 Jenkins, D. A., 266  
 Jirsa, J. O., 246  
 Jonasson, T., 15  
 Keer, L. M., 378  
 Kim, K. S., 126  
 Koller, M., 86  
 Kossover, D., 173  
 Krajcinovic, D., 365  
 Kraus, D., 157  
 Krauthammer, T., 196, 202  
 Kuennen, S. T., 302  
 Kung, S-Y., 208  
 Langheim, H., 92  
 Lawver, D. J., 254  
 Liu, C. M., 214  
 Liu, X. L., 214  
 Mackay, D. J., 67  
 Maestas, F. A., 98  
 Malvern, L. E., 296  
 Massa, R. J., 119  
 McDevitt, H. S., Jr., 26  
 McQuilkin, A., 67  
 Mercx, W. P. M., 167  
 Merkle, D. H., 396  
 Mett, H-G., 372  
 Mills, C. A., 224  
 Misra, A., 354  
 Moriarty, T. F., 230  
 Mowers, S., 67  
 Muralidharan, R., 202  
 Nachtsheim, W., 126  
 Naeyaert, G. C. G., 341  
 Nash, P. T., 61, 246  
 Nomura, S., 290  
 Oppliger, H. H., 278  
 Pahl, H., 55  
 Palm, J., 161  
 Papp, A. G., 266  
 Pfrang, W., 32  
 Pierce, S. J., 331  
 Reinhardt, H. W., 336  
 Riewald, P. G., 321  
 Ross, C. A., 302, 309, 331  
 Ross, T. J., 208  
 Rozen, A., 10  
 Russwurm, D., 275  
 Scheklinski-Gluck, G., 45  
 Schimdt, W., 202  
 Schittke, H. J., 32  
 Schneider, B., 315  
 Schoof, L. A., 98  
 Shah, S. P., 283, 378  
 Soroushian, P., 321  
 Sorrell, F. Y., 391  
 Spivey, K. H., 40  
 Steedman, R. S., 402  
 Stewart, P. D., 266  
 Stilp, A. J., 92  
 Storrie, T., 67  
 Strickland, W. S., 302  
 Tang, T., 296  
 Taylor, T., 114  
 Tedesco, J. W., 309  
 Teran, A., 246  
 Terrier, J. M., 137  
 Theos, F., 260  
 von Buelow, P., 230  
 Vretblad, B. E., 50, 61  
 Wang, S-J., 4  
 Watson, A. J., 80, 384  
 Weerheijm, J., 336  
 Weickert, C. A., 67  
 Worswick, M. J., 67  
 Wright, S. J., 384  
 Yamaguchi, H., 290  
 Yerushalmi, Yaakov, 242  
 Young, C. W., 98  
 Young, S. L., 190, 219, 266  
 Zahrah, T. F., 396



## ENGINEERING IN THE FIELD OF PROTECTIVE STRUCTURE DESIGN

Gerald Ast

Sigma Karlsruhe Engineers, D-7500 Karlsruhe

This report is based on experiences derived from structural design tasks the author's firm was involved in. In particular a major airbase exposed to an exceptional threat will be referred to. To meet the specific requirements of the structural design of the aircraft shelters and other protective buildings of this project, a more advanced approach than commonly used was necessary. Special care was taken of the realistic prediction and proof of resistance against weapon effects, such as impact and explosion. The final proof of resistance against weapon effects was given by a combined procedure of physical testing and computer simulation. To illustrate this procedure, a film will be presented.

Passive protection measures have a key role to play in the defence system. They come into use when all other components have failed to prevent an enemy incursion.

Assessing the probability of such a case and its severity is the task of military specialists. From this results the definition of the requirements for protection against specific types of hit, which is in the following described as the military engineers' contribution to the field of protective design. The civil engineers' contribution is to provide sheltered space in which survivability during an attack can be guaranteed.

The top priority in ensuring survivability is to protect personnel from injury and to maintain acceptable living conditions until the danger has passed. Further on all the equipment which is necessary to allow reactive defence must be protected.

In order both to protect, by means of structural hardening, and to provide acceptable living conditions, by means of installing appropriate environmental systems, the design engineer must apply a multidisciplinary approach. He has to handle all the knowledge and expertise of weapon effects, structures and materials, and of environmental systems. The relationships of all the technologies involved and the input of knowledge necessary can be illustrated by means of fig. 1.

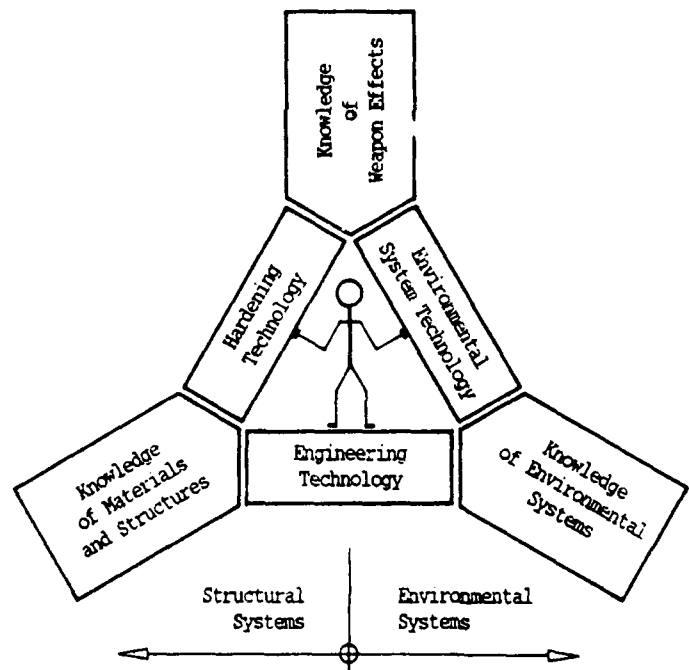


Fig. 1: Components of protective structure design

Through this approach the engineer can bring into action each of these technologies most effectively and thus achieve the best possible protection in the most economic way.

Taking the area of structural systems, different approaches can be adopted to cope with the task, which will be described as the "traditional" approach as opposed to the "advanced" approach. In the traditional approach the civil engineer anticipates detailed design load assumptions as input for a quasi-static procedure of structural design. These load assumptions must be defined by military engineers. The advantage of this approach is that the civil engineer who has complete charge of the design can use resources and tools he has close at hand in his daily work. The requirements of military engineers can be fulfilled by using formulas and tables of handbooks and standards. The traditional approach meets the requirements of many tasks in the field of protective building design.

But in this presentation an example will be given where this approach failed to provide a satisfactory solution. For a major military airbase exposed to an exceptional threat an effective and economic solution for the design of aircraft shelters and the protective buildings was to be found.

According to the military requirements, especially the aircraft shelters had to resist a direct hit of a 2000 lb aircraft bomb. The basic concept of protection for these structures functions on the principle that attacking bombs are caused to detonate at a predetermined distance from the inner shelter structure by means of a burster shield. When the burster shield successfully fulfils this requirement, the inner structure has only to withstand the shock wave and blast effects which result from the detonation of a HE-charge on top of the burster shield; see fig. 2.

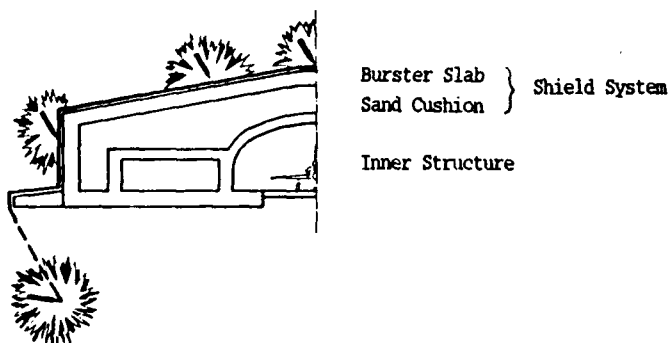


Fig. 2: Illustration of a special concept of protection

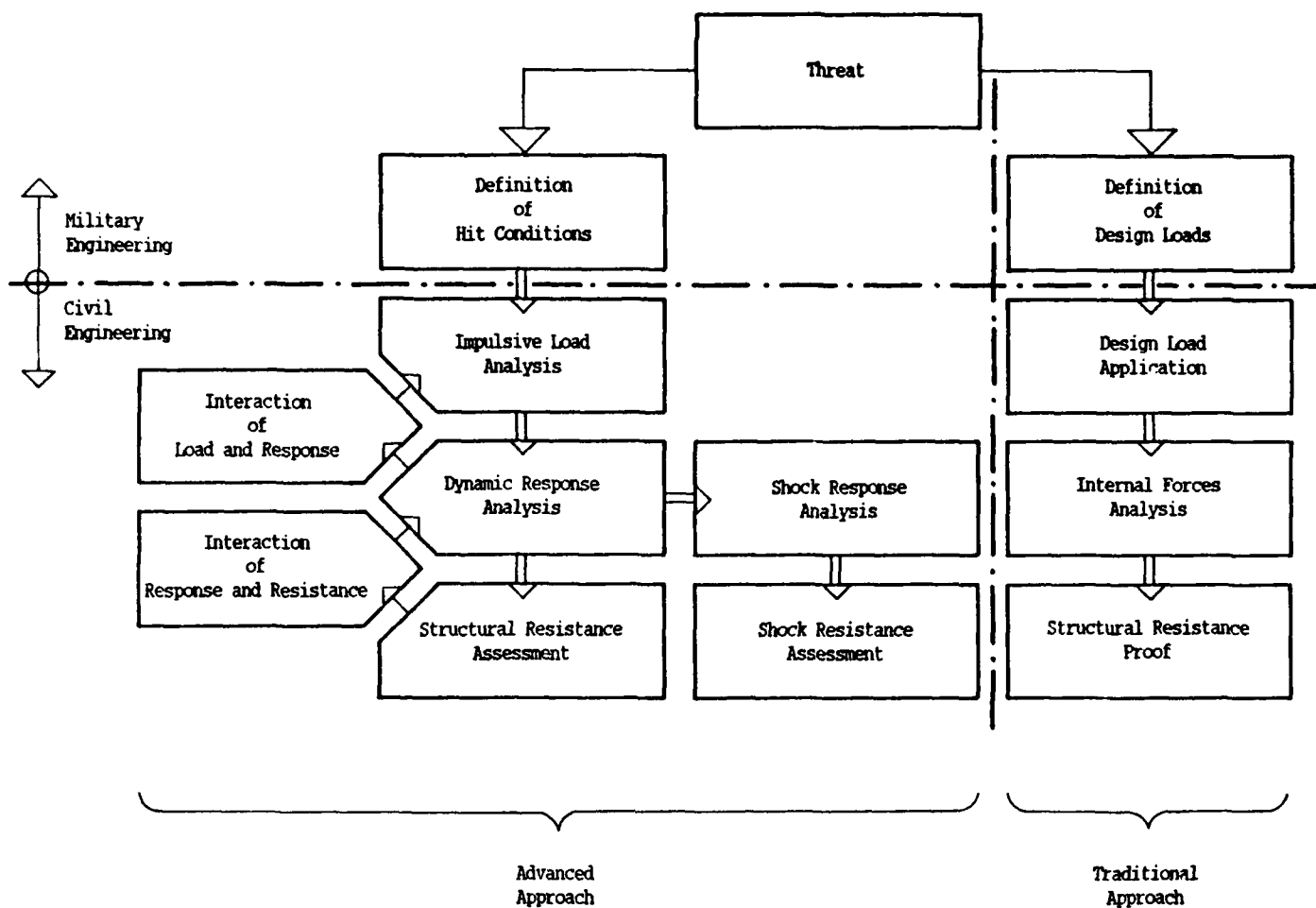
In a more advanced approach the civil engineer in this project took as his starting point data recorded from actual weapon effects, such as impact, explosion or heat. Through comprehensive analysis of the structural behaviour in response to these weapon effects, he obtained all the information he needed to assess how far the structure would be able to absorb the energy from a hit and to assess to what extent the equipment would be affected by shock. The engineering approach which was applied to cope with the intrinsic complexity of the task is schematically shown in fig. 3.

To meet satisfactorily all requirements such as proof of resistance against weapon effects as well as against prevailing loads, assessment of shock influences on equipment, economic foundation of the exceptional loads on an unsuitable ground, an advanced engineering technology had to be applied. Only in this way was it possible to exploit to the full the protective potential of the applied structural concept so that the best possible protection could be provided for a reasonable outlay in the range of the given brief. Finally the client had to be convinced that in spite of economic solutions the degree of protection sought really was achieved. For the approval procedure the predictions made analytically by structural engineers were therefore confronted in a careful study with the results of physical tests of weapon effects.

But the tests were not only executed to provide the final proof of effectiveness close to reality, they were also evaluated to prove and refine the design techniques which were applied as a means of creative problem solving in response to the inherent difficulties of the task. So it was possible to create additional knowledge of how to evolve new concepts designed to exploit to the full the mechanical properties of materials in the field of protective structure design.

Such concepts must be designed to minimize the transmission of hit energy to the structure and to optimize the structural capability to absorb the transmitted energy most effectively by transformation into strain and friction.

To illustrate the test procedure and the test results a film will now be presented.



**Fig 3:** Steps in the engineering approach of protective structure design

# PROGRESS IN BLAST-RESISTANT STRUCTURES RESEARCH

Chen Zhao-yuan, Wang Shuang-jin

Department of Civil Engineering  
Tsinghua University, Beijing, China

## Abstract

Research on structural members and materials for blast-resistant structures is described and a variety of results are given, which include the dynamic behavior of materials under rapid strain rates, the resistance function of reinforced concrete members under impulsive loads, shear strength for uniform-loaded beams and indirect loaded beams, the effect of post-yield shear failure on ductility, and the use of high-strength materials and composite structural members. Besides, experimental studies on soil-structure interaction in the field and laboratory are also briefly discussed.

Significant progress has been made in research on blast-resistant structures during the last two decades in China. In this paper, some research activities directed toward the improvement of design methods for blast-resistant structures, which have been undertaken in the Tsinghua University, are presented.

## 1. Behavior of structural materials

Structural materials and members are subjected to rapid rate of deformation under blast loading, the time interval to reach yield  $t_y$ , or to reach ultimate strength  $t_m$ , is usually in the order of several to tens milliseconds depending on the natural period of the structure, the load-time history, and the ratio of the maximum dynamic displacement to the yield displacement.

A systematic experimental research was performed on the dynamic behavior of different structural materials under rapid strain rates. The materials tested include sixteen types of reinforcing steel with yield strength from 240 to 700 MPa, ordinary and high-strength concrete with cube strength up to 100 MPa, steel-fiber concrete, polymer-impregnated concrete, reinforced plastics, and timber. For each type of steel, bars with different diameters and from different producing plants were selected. More than one hundred test items were completed, and for each test item, specimens cut from the identical rebar or fabricated from the same batch of concrete mix were divided

into groups loaded with different constant strain rates on the specially designed pneumatic-hydraulic machines.

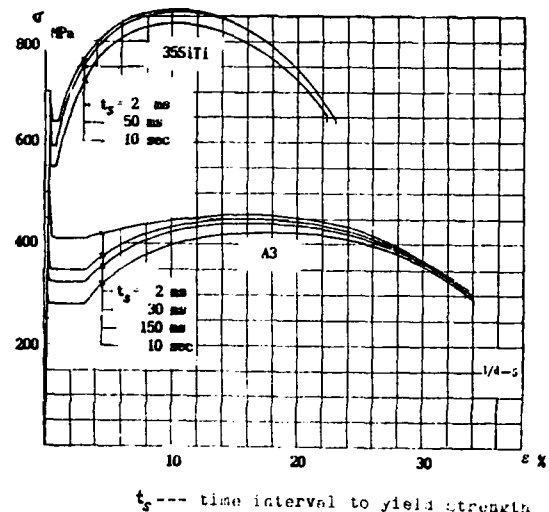


Fig.1 Stress-strain curves of steel

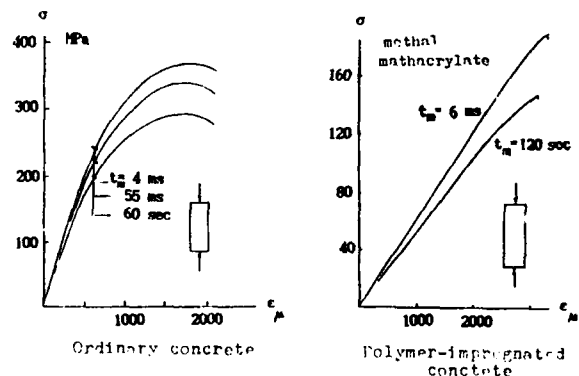


Fig.2 Stress-strain curves of concrete

The general trend of the material behavior under rapid strain rate (with  $t_y$  or  $t_m$  not less than milliseconds) is well known, that is, an increase in strength and little change in deformation parameters. Fig.1 and 2 are typical stress-strain curves for steel and concrete derived from the tests, in which A3 is a common used type of low-carbon structural steel and 35 SiTi is a type of

low-alloy steel. Fig.3 shows the dynamic increase factors for yield strength of steel and for ultimate strength of other materials.

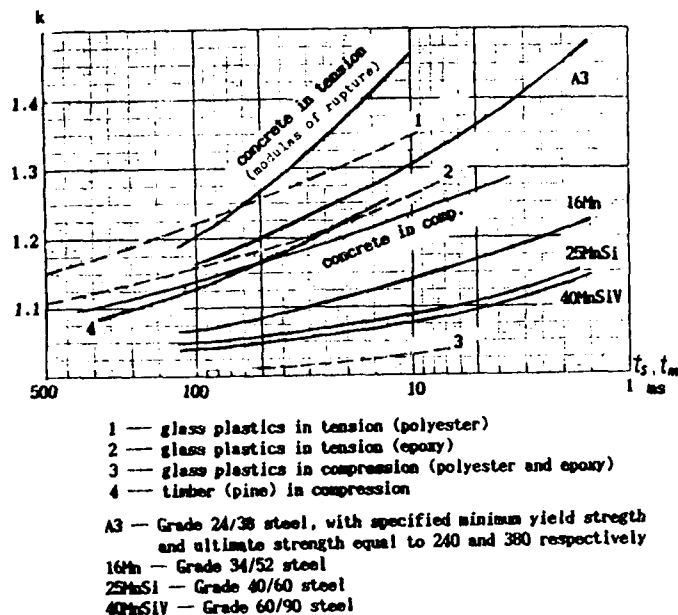


Fig.3 Dynamic increase factor

It is worth notice the following results:

a) The dynamic increase factor for yield strength of steel is sensitive to the original static strength, a lower grade steel has a larger dynamic increase factor, but no appreciable difference was observed for compressive strength of various kinds of concrete. The dynamic increase factor in Fig.3 for concrete in compression is also effective to high-strength concrete and steel-fiber concrete.

b) Even for a given type of steel, bars with lower static yield strength usually tend to have a higher increase of strength under rapid strain rate. Therefore, the variation of steel strength tends to decrease with the increase of strain rate. But it is not the case for concrete.

c) The dynamic increase factor for yield strength of steel in tension is about the same as in compression, while for concrete, it is much larger in tension than in compression. However, the effect of age on concrete strength in compression is more significant than in tension.

d) The existence of initial static stress (up to 75% static yield strength for steel and 25% static compressive strength for concrete) is proved to have no effect on the magnitude of dynamic strength.

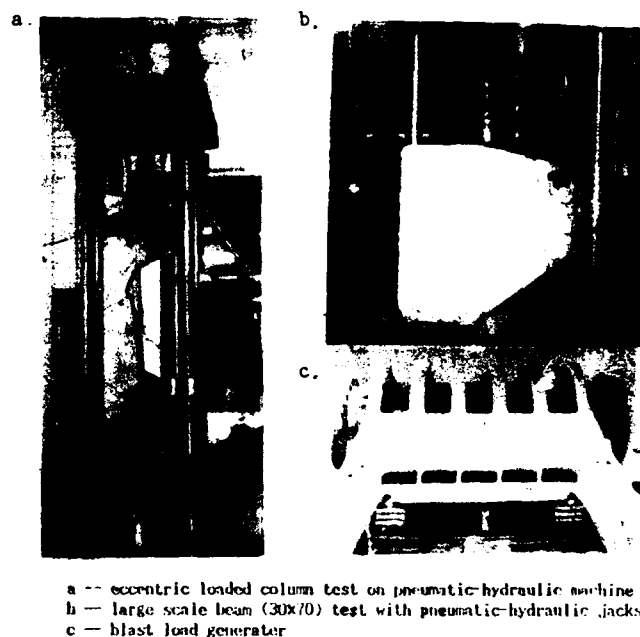
e) The failure modes of specimens kept unchanged in all test items except for the splitting tensile test of ordinary concrete. The failure surface, that passed through the boundary between gravels and cement paste in static loading, changed to cutting across the gravels under rapid strain rate. The dynamic increase factor for splitting

tensile strength is about 50% higher than that of flexural tensile strength (modulus of rupture) obtained from the bending test. It is believed that the result from the splitting test is not adequate for dynamic design.

The dynamic increase factor curves in Fig.3 represent the average values of test results and can be served as a basis for specifying the dynamic strength of materials under impulsive loading. However, there are other facts such as the variance of strength, the ductile performance, the age effect, the discrepancy of deforming process between the actual dynamic responses and rapid loading tests with constant strain rates, that should be considered in selecting an appropriate value of dynamic strength. Apparently, it is preferable to specify a less conservative design value for steel rather than for concrete.

## 2. Dynamic behavior of reinforced concrete members

In order to determine the dynamic behavior of reinforced concrete members, a total number of fifty four beams and fifty three columns were tested on the pneumatic-hydraulic rapid loading machines (Fig.4 - a,b). Most of beams were reinforced in



a -- eccentric loaded column test on pneumatic-hydraulic machine  
b -- large scale beam (30x70) test with pneumatic-hydraulic jacks  
c -- blast load generator

Fig.4 Loading facilities

tension with steel ratio from 0.1 to 1.55%. Ordinary concrete with cube strength 30-42 MPa and steel bars with yield strength 275-710 MPa were used. Three types of loading generated by the pneumatic-hydraulic machines were adopted: 1-- static loading with constant rate of deflection up to failure; 2-- rapid loading with constant rate of deflection up to failure, in which the time interval to yield was about 50 milliseconds; 3-- rapid loading, in which a predetermined load corresponding to 85-95% of dynamic strength was quickly applied in 50 milliseconds and then unloading slowly. All beams were simply supported and two-point loaded. Generally,

one out of 2-3 identical specimens in each group was loaded statically for comparison with the others under rapid loading. The feature of the rapid loading method is no appreciable inertia force created in the test and hence the dynamic resistance of specimens can be determined statically with sufficient accuracy.

In addition to the rapid loading tests, another twelve beams were tested in a blast load generator (Fig.4-c). The uniform distributed pressure acting on the top surface of the specimens was generated by detonation of primicords. Each beam was experienced three subsequent dynamic loadings with different peak pressure which caused the elastic response at first and then the elasto-plastic responses. With the measured load-time history and the resistance function based on the rapid loading test results, a numerical intergration method was used to calculate the dynamic deflection which was compared with the measured values.

The main conclusions from these tests are summarized as follows:

a) The dynamic resistance of reinforced concrete members can be predicted accurately provided the material behavior under rapid strain rate is taken into account. The shape of the dynamic resistance-deflection curve is similar to the static case.

b) The ductility ratio of reinforced concrete members, as well as the ultimate compressive strain of concrete in reinforced concrete beams, remain unchanged under rapid rate of deformation as compared with the static loading. Shown in Fig.5 is the ratio of the ultimate deflection to the yield deflection for simply supported flexural members.

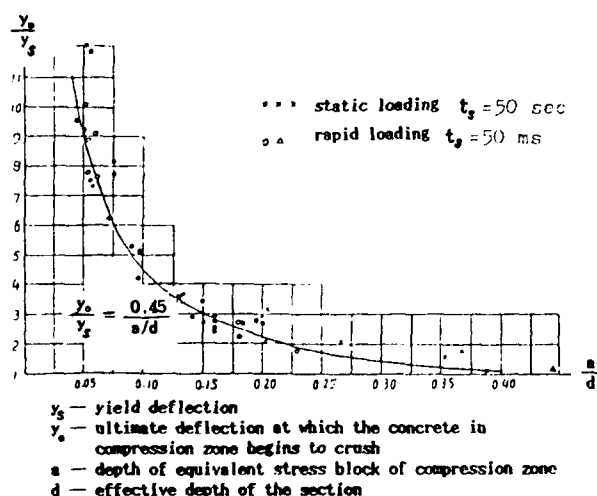


Fig.5 Ductility ratio

c) Reinforced concrete beams with very low steel ratio ( $\rho < 0.2\%$ ) would collapse suddenly by the fracture of tension steel, the dynamic resistance function is substantially different from that of ordinary under-reinforced beams. Therefore, a higher minimum steel ratio should be provided for beams subjected to impulsive loads.

d) If a load with its peak value near to the dynamic ultimate resistance is quickly applied to a reinforced concrete column, a delayed failure may take place as the load decays slowly. But no delayed yield phenomenon has been observed in the beam tests and this is perhaps due to the existence of an upper yield point of steel.

e) The equivalent damping ratio under explosive loading might be as high as 0.15-0.20 in elastic response for beams with maximum dynamic stress up to 400-600 MPa in reinforcing bars. The natural period of beam also varies with stress level and may be doubled at high stress level as the stiffness of beam section seriously decreased. The dynamic loading capacity in flexure is greatly underestimated if the damping effect and the stress hardening of steel are neglected.

Studies on dynamic behavior of structural members and materials as mentioned above have been described in detail in references [1] and [2].

### 3. Shear problems

It is of great importance to avoid a brittle shear failure under impulsive loading. Some research projects related to the shear resistance of blast-resistant structures have been done and are briefly described here.

a) Shear strength under rapid rate of deformation.

Sixteen reinforced concrete beams were tested with half of them subjected to rapid loading and others at static speed for comparison. All beams had a same section and a same steel ratio of 1.05%. High-strength steel bars were used to enhance the flexural capacity and forced specimens to fail in shear. Different modes of shear failure were observed, and as discussed above, the failure modes were independent of rapid strain rate. It is found that the dynamic increase for shear strength depends on the mode of shear failure as seen in Tab.1.

Dynamic increase for shear strength  
( $t_m = 50$  ms)

Tab.1

| a/d | $\rho_v$ % | Failure mode     |                   |                      |
|-----|------------|------------------|-------------------|----------------------|
|     |            | Diagonal tension | shear compression | Diagonal compression |
| 3   | 0          | 40%              |                   |                      |
| 3   | 0.12       |                  | 22%               |                      |
| 1.9 | 0          |                  | 23%               |                      |
| 1.9 | 0.12       |                  |                   | 15%                  |

Note: 1. a/d-- shear span to depth ratio  
2.  $\rho_v$  -- stirrups steel ratio  
3. All beams were simply-supported and one point loaded

b) Shear strength of beams with low tension steel ratio

Flexural members in blast-resistant structures usually have low steel ratio. It is well known that

the shear strength decreases with the reduction of longitudinal tension steel, but few tests have been conducted on beams with low steel content.

An experimental study on simply supported beams reinforced with extra high-strength bars ( $f_y = 1490$  MPa) was undertaken to find the influence of steel ratio on the shear capacity. All variables for test beams were kept constant except for the content of longitudinal steel. As shown in Fig.6, the ultimate shear strength tends to be independent of tension steel ratio if the latter is less than 0.8%. This phenomenon is contradictory to common views [3], there are other test data [4] however, that reflect the same trend if the ultimate shear strength is concerned. It should be noted that the shear strength defined in this paper is referred to the nominal strength at failure load rather than the diagonal cracking load.

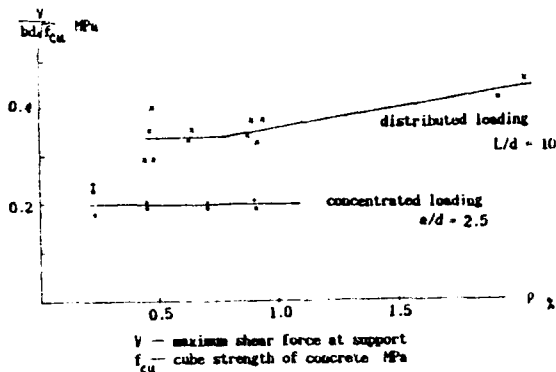


Fig.6 Relation between ultimate shear strength and tension steel ratio (with no web reinforcement)

#### c) Shear strength under uniform loading

The influence of the end restrained moment on the shear capacity of reinforced concrete members without web reinforcement is sometimes important for slabs design in blast-resistant structures. Fig.7 shows test results of eighteen restrained beams under uniform loading. All specimens had a section of  $20 \times 30$  cm and a tension steel ratio of 0.6% with extra high-strength bars. No web reinforcement was provided in the tested span. The nominal ultimate shear strength at support varies with the ratio of negative end-moment to positive midspan moment  $M/M_n = n$ . The relation between the shear strength and the moment ratio  $n$  is not in a monotonic manner for a given span to depth ratio, and there exists a peak

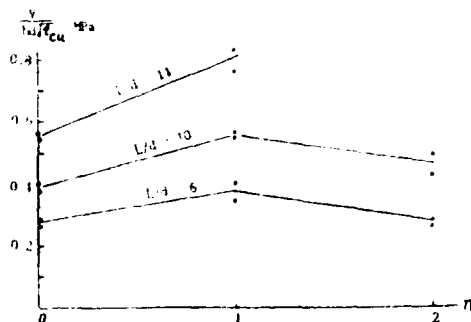


Fig.7 Relation between ultimate strength and moment ratio

strength approximately at  $n=1+0.8(14-L/d)$ . For beams with moment ratio less than this critical value, the inclined failure surface would be located at the positive moment region in the span.

#### d) Shear strength of indirect loaded beams

Indirect loaded beams with slabs at bottom surface have the advantage of larger clearance for interior rooms in buried structures. In order to determine the shear behavior of indirect loaded beams under uniform load, twenty eight beams were tested with indirect load at the bottom flange (Fig.8). The main parameters varied in this investigation were the stirrups steel ratio ( $\rho_v = 0.17-0.89\%$ ), the span to depth ratio ( $L/d = 5.2-10.2$ ), and the ratio of end restrained moment to mid-span moment ( $n = 0, 1, 2$ ).

The shear capacity of indirect loaded beams under uniform loading is much weaker than that of direct loaded. As contrasted to ordinary beams, the shear strength of indirect loaded beams decreases drastically with the reduction of span to depth ratio (Fig.9), and is nearly independent of moment ratio  $n$ . The vertical tensile stress in indirect loaded beams makes the inclined failure surface less steep and stretch to the mid-span. It is found that the following empirical formula for shear strength is in good agreement with the test data of indirect uniform loaded beams:

$$\frac{V}{bd} = 0.16 \left(1 + 0.1 \frac{L}{d}\right) \sqrt{f_c} + \rho_v f_{vy}$$

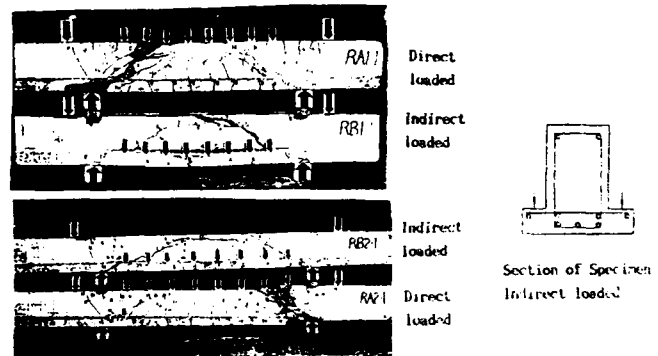


Fig.8 Indirect and direct loaded beams

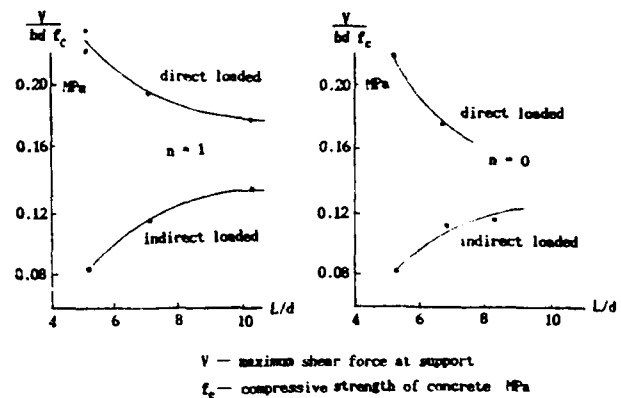


Fig.9 Relation between ultimate shear strength and span to depth ratio ( $\rho_v = 0.17\%$ ,  $f_c = 25 - 30$  MPa)

where  $V/bd$  is the nominal ultimate shear strength and  $V$  is the maximum shear at support,  $L/d$  is the span to depth ratio,  $\rho_v$  is the stirrups ratio,  $f_{vy}$  and  $f_c$  are the yield strength of stirrup steel and the compressive strength of concrete in MPa, respectively. In addition, a minimum stirrups ratio should be provided to carry the whole indirect load and to limit the horizontal cracks between the web and bottom flange. However, for indirect loaded beam with short span to depth ratio, its shear strength is always less than that of direct loaded even if the additional stirrups are given.

#### e) Post-yield shear failure

Most of blast-resistant structures are designed to work in the plastic range, so it is important to reveal the behavior of post-yield shear failure which occurs at the plastic hinge region near supports in continuous beams or frames. Post-yield shear failure is the result of progressive yielding of tension steel that reduces the shear-compression area of concrete as well as the aggregate interlock action and the dowel action along the inclined crack. The ductility of flexural members may be limited by a premature post-yield shear failure.

A large number of restrained and continuous beams have been tested in Tsinghua University to evaluate the effect of post-yield shear failure under uniform static loading. The indication is that the ductility of post-yield shear failure mainly depends on the tension steel index  $\omega$  and the ratio  $V/V_s$ , where  $\omega = \rho_f f_c$ ,  $V$ =acting shear force,  $V_s$ =shear capacity prior to yielding of tension steel. For beams with low tension steel ratio and no web reinforcement, in which the sum of steel index ( $\omega_e + \omega_m$ ) at fixed-end and midspan less than 0.15, no post-yield shear failure was observed and all specimens with different span to depth ratio ( $L/d=6,10,14$ ) experienced extremely large plastic deformation in flexure. For beams with no web reinforcement and  $(\omega_e + \omega_m) = 0.2-0.25$ , all were yielded at fixed end and many of them finally collapsed due to post-yield shear failure, in the latter case, the maximum compressive strain of concrete was less than the ultimate strain. It seems that the post-yield shear failure might not cause serious trouble to light reinforced members such as slabs with no web reinforcement, especially the ultimate strain of concrete in slabs would be greatly enhanced by the effect of transverse confinement. For beams with web reinforcement subjected to large shear force, most of them were collapsed in post-yield shear failure and the ultimate rotation of plastic hinge was more or less restricted. It should be mentioned that the recommended ductility ratio in some design manuals is based on the test results of simply supported beams, care should be taken for beams with negative end moment and large shear force. In this case, it is reasonable to use a less ductility ratio.

### 4. Use of high-strength materials and composite structural members

#### a) High-strength reinforcing steel

Use of high-strength steel bars in blast-

resistant structures has been proved successful and cost effective. It is recommended to use grade 50/80 steel with a minimum specified strength 500 MPa owing to its weldability and acceptable ultimate elongation (not less than 15%). As shown by the test results, beams reinforced with high-strength bars might have excellent ductile behavior and are not inferior to the comparative beams with ordinary steel bars if both of these beams are equal in steel index. For structures designed to resist a definite magnitude of explosion and especially when the large plastic deformation is not allowed for serviceability limit states, the use of non-prestressed high-strength bars is the most suitable. The residual tension crack width of concrete in all tested beams has found to be only 0.05-0.1 mm after rapid rate of deformation although the elastic tensile stress in steel bars has once reached a high level of 500-600 MPa.

#### b) Reinforced concrete composite slabs

Reinforced concrete composite slabs has been used for the roof of underground shelters in recent years. These slabs are composed of two parts, a bottom layer of precast slab and a top layer of cast-in-situ concrete, with no vertical reinforcement across the joint interface. The top surface of the precast slab is finished with natural roughness. To verify the applicability of composite slabs, a total number of fifty beam-type specimens with different span to depth ratios, different tension steel contents, and different supporting conditions, were tested under static loading, rapid loading, and explosive loading. As shown in the test, the composite specimens behaved just like the comparative integral ones provided the tension steel ratio in these members was not so high. In certain cases, local horizontal cracks at the joint interface might appear within the central part of the span (Fig.10), these cracks should be prevented although which did no harm to the ductility and maximum resistance for composite members under uniform loads. The first appeared horizontal crack along the interface was usually located at approximately one third span length away from the support, where the vertical stress was maximum in tension as indicated by the finite element analysis. Placement of shear keys at that location was proved the most effective to strengthen the shear capacity against horizontal cracks. A design method has been recommended for composite slabs based on experimental and theoretical analysis.

#### c) Steel confined concrete members

The concrete filled steel tubular columns has its advantage of high capacity accompanied with excellent ductile behavior, and is very effective to resist explosive loads. In a research project

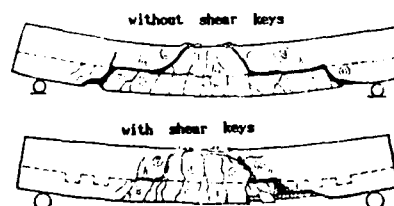


Fig.10 Composite specimens



carried in the Tsinghua University, forty two concrete filled steel tubular columns were tested in an attempt to provide information on dynamic behavior under rapid deformation. Shown in Fig.11 is the resistance curve in axial loading where  $\epsilon_l$  and  $\epsilon_c$  are longitudinal and circumferential strain respectively. It is concluded that there is no need to consider a delayed failure for concrete filled tubular columns, and the effect of slenderness on strength can also be neglected under dynamic loading for axially-loaded columns with the effective length less than 10 times diameter.

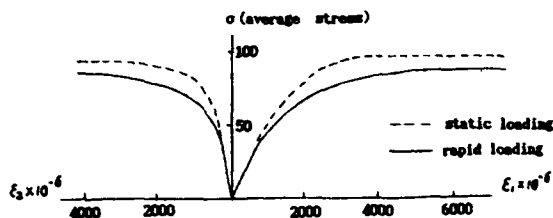


Fig.11 Typical stress and strain curve of concrete filled steel tubular column

Another type of composite members that has been investigated is the steel-plate concrete (Fig.14). Between two thick steel plates, close-spaced tie rods were placed with two ends inserted into the holes in plates and welded together to make a skeleton, then filled with high-strength concrete. The confined effect on concrete as a function of steel contents and rod spacing was studied with tests of axially and eccentrically loaded specimens, and numerically analyzed. Fig.15 shows a loading test of composite arch that was made of such a steel-plate concrete.



Fig.12 Steel-plate confined concrete arch

## 5. Soil-structure interaction

One dimensional study on soil-structure interaction has been performed with the help of plane wave generator (Fig.13). Based on the loading tests on soil columns and soil-mass-spring systems, we now have a better understanding of soil-structure interaction in one-dimensional environment. The testing tube, in which the soil specimens are placed, is an assembly of alloy aluminum rings with rubber cushion rings between each two of them, so the tube wall can deform freely in the longitudinal direction to eliminate the friction force on the specimen. Tests on soil columns with a height of 7 meters have shown, that the peak reflected pressure measured on the bottom plate varied from 0.9 to 2.6 times the surface peak pressure in different dry sands and loesses, and the rise time to peak reflected pressure might be equal to one tenth to more than ten times as large as that of the surface pressure.

A field loading technique something like FOAM HEST [5] has also been used for testing shallow-buried structures in sand and loess. The explosion cavity shown in Fig.14 was assembled by steel frames. It was found that the transverse rarefaction effect was not evident, and the roof pressure was mainly dominated by the one-dimensional wave effect provided the deflection of the roof was small. On the other hand, the pressure on the base slab varied not only with the velocity as indicated in one-dimensional wave theory but also with the displacement. Theoretical analysis of soil-structure interaction has been done in parallel with the experimental investigation, leading to a more realistic loading pattern for design of buried structures.

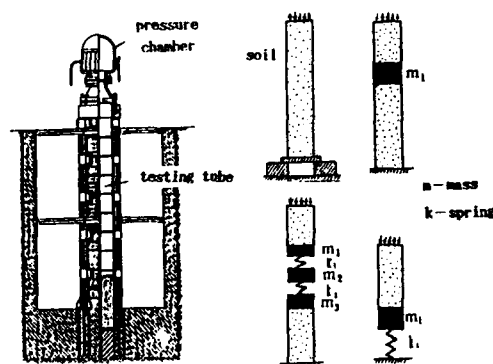


Fig.13 Plane wave generator and specimens for test

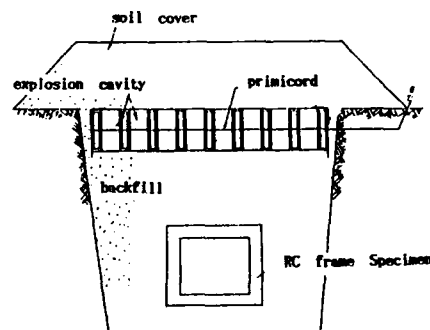


Fig.14 A field loading technique for shallow-buried structures

## References

1. Chen Zhao-yuan, et al, Behavior of reinforced concrete structural members subjected to impulsive loads (in Chinese), 1986, Tsinghua University Press
2. Chen Zhou-yuan, Dynamic behavior of structural materials (in Chinese), 1972, Research report of Civil Engineering Department, Tsinghua University
3. Batchelor B. and Kwun M., Proc.ASCE St.5, 1981
4. Rajagapalan, K.S. and Ferguson, P.M., Jour.ACI Aug., 1968
5. Kiger, S.A. and Gatchell, J.V., Vulnerability of shallow-buried flat-roof structures, AEWES, SL-80-7, Sept. 1980

## DESIGN OF ROCK TUNNELS IN ROCK: DAMAGE ESTIMATES AND ENGINEERING COUNTERMEASURES

Arnon Rozen, BNE-Beitkha, Kfar Jona B, 40 300, ISRAEL

### ABSTRACT

The paper summarized the design process of a shallow rock tunnel against conventional air bombings; prediction of type and degree of damage as a function of the scaled depth and rock mass quality, estimate of weight and speed of impacting rock debris and selection of adequate protective liners using standard rock reinforcement measures.

The present work stems from the "old", 1965, Technical Manual series TM 5-857 1 to 5 of the US Army Engineers, which was based on tests carried out by ERA during the 50s. This data is being adapted to the new support systems that were introduced by the tunnelling industry during the last 20 years (shotcrete, reinforced shotcrete, rock bolts etc.) and to a variety of softer sedimentary rock media (Marly chalk, Chalk and soft Limestone).

### BACKGROUND.

Military tunnels were used for many years. Their main uses were defensive as part of fortresses, strongholds and other prepared systems of defence. During the First World War tunnels were used also as a weapon of offence trying to mine under the trenches of the enemy.

During the Second World War tunnels and underground caverns were used to protect crucial installations, ranging from sheltering a garrison as in Gibraltar, to command posts and even complete large factories as in Germany. During the last forty years, when the protection from nuclear weapons became a dominant factor in military consideration, many underground chambers were designed and used for command posts, shelters, aircraft hangars, submarine pens and fuel storage installations. The Scandinavian and Swiss experience became quite legendary.

In the 1983-85 war in Lebanon the Palestinian terrorists used shallow and medium-depth tunnels as personnel shelters, vehicles shelters and ammunition storage

in order to achieve a higher degree of protection against conventional (non-nuclear) air raids by the Israel Defence Forces. Similar use of shallow tunnels and natural caves was observed in other parts of the world.

As a result, there is a need to present a fresh and updated systematic approach to the design of protected rock tunnels, especially at shallow depths which are relevant for conventional wars.

### DAMAGE PREDICTION.

The present approach to the definition of damage pattern in underground rock tunnels was developed and described by Engineering Research Associates based on comprehensive testing program during the early 50's (Ref. 1, 2 & 3). This approach was adapted by the US Army Engineers into their Engineering Manuals and Technical Manuals (Ref. 4 & 5).

Four damage zones were identified:

Zone 1= Total destruction indicated by a complete breakthrough from the surface to the tunnel level.

Zone 2= Heavy damage, characterized by continuous spalling over the tunnel periphery closest to the detonation, with damaged area of 30% to 80% of the original tunnel area, many fractures forming in the solid rock and rock spalls flying at very high velocities.

Zone 3= Moderate damage, with continuous spalling over the tunnel periphery closest to the detonation, but the damage pattern highly influenced by the natural geological discontinuities or planes of weakness within the rock. The spalls are smaller and with relatively lower velocities.

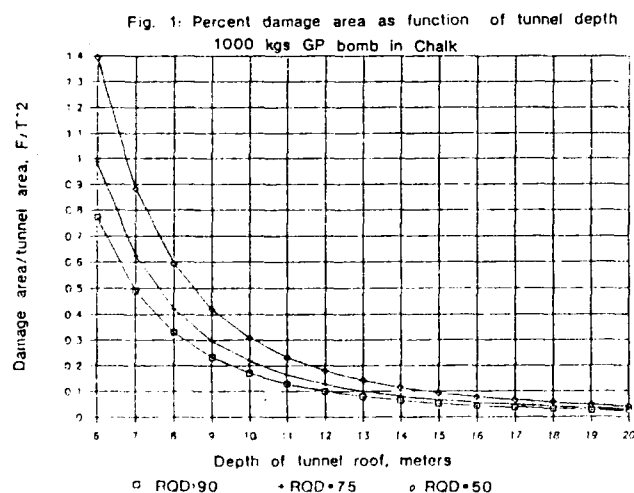
Zone 4= Light damage, indicating very light, discontinuous damage which probably results from dislodging previously loosened

material or pieces of jointed rock. The geologic structure determines to a large extent the size and shape of the fractured pieces. The rock spalls fall at very low velocities or merely drop to the floor.

The damage is, therefore, defined by the amount, size and velocity of the falling and flying rock, and the design should be aimed at absorbing the energy imparted by the series of impacts. It is not expected to solve the problems associated with Zone 1 as the amount of rock debris dislodging at very high speed causes an extreme loading condition.

The damage prediction is based on both  $T/W^{1/3}$  or the scaled charge to tunnel distance and, to a lesser extent,  $D/W^{1/3}$  or the scaled tunnel diameter. The relationship between the fractured or damaged rock area (volume of dislodged rock per unit length of tunnel) and the scaled tunnel distance was given in Ref. 5 in a log-log graphical solution irrespective of the rock type, although it is known that the tests were conducted in granite, hard limestone and hard sandstone. The available test data are, therefore, limited to hard and very hard rocks.

Figure 1 presents  $F/T^2$  (damaged area to tunnel area ratio) as caused by 1000 kg GP bombs (542 kgs of TNT equivalent) in chalk, chalky limestone and soft limestone formations. The data, averaged for the range of soft limestone and chalk, was crudely correlated to the in-situ rock mass quality by using the RQD correction factor suggested in reference 6.



The data as measured in "very good" rock, with  $RQD > 90$ , is given in fig. 1 and fits into equation (1):

$$(1) F/T^2 = 0.3119 \times (D/W^{1/3})^{(-2.9598)}$$

Where: F= Area of damaged rock, meter  
T= Equivalent tunnel diameter, meter  
D= Charge to tunnel distance, meter  
W= Explosive charge, TNT equivalent, kilogram

#### INFLUENCE OF ROCK MASS.

When the rock mass is highly jointed, the rock mass behavior is influenced by the characteristics of the joints, or other discontinuities, which may overshadow the characteristics of the intact rock within the rock mass. The RQD as a measure of Rock Quality Designation was suggested by Deere (Ref. 8) and adapted into several rock classification methods which are currently being used for tunnel design (Ref. 9).

Due to the importance of the natural planes of weakness and their influence on the damage pattern in Zone 3, it was essential that due consideration should be given to them. Based on test data (Ref. 7), used also in Ref. 6, a correction factor was suggested as presented in equation (2):

$$(2) CF = (100/RQD)^{0.85}$$

Where: CF = Rock quality correction factor.  
RQD= Rock Quality designation

The use of this correction factor should be limited to cases in which  $RQD > 50$  as discussed in Ref. 6, but this is hardly a limitation because rock tunnels with  $RQD < 50$  are expected to be heavily supported by pattern rockbolting, usually fully resin or cement grouted, and reinforced shotcrete. This liner is able to partially absorb, or if properly upgraded, even to hold the spalls' impacts.

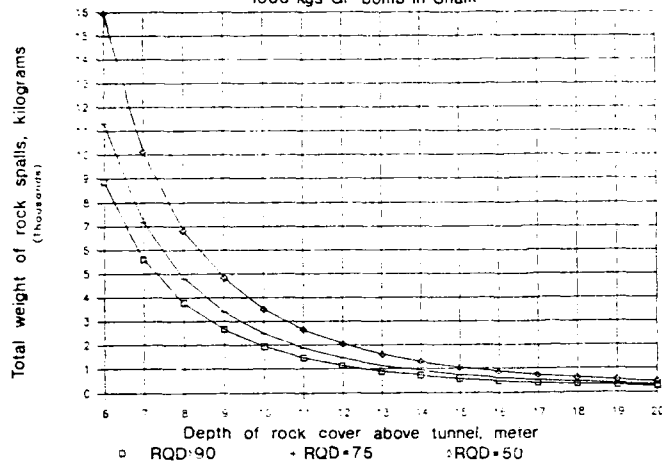
#### ROCK LOAD PREDICTION.

The total weight of flying rock spalls was calculated based on the rock unit weight and is presented in fig. 2 for three values of RQD. The estimates of rock weight were based on the correction factor suggested in equation (2) and were found to fit the measured spalls, even though some scatter was observed.

For design purposes, the impacts which the tunnel liner receives should be considered as successive impacts. Ref. 5 suggests that the first impacts are derived from small spalls at high velocities, and the last impacts are derived from large rock spalls at relatively low velocities.

The fraction of the total energy per impact recommended for design purpose in ref. 5 was given as:

Fig. 2 Total weight of rock spalls  
1000 kgs GP bomb in Chalk



Light damage - Zone 4: 1/2  
Medium damage - Zone 3: 1/5  
Heavy damage - Zone 1: 1/10

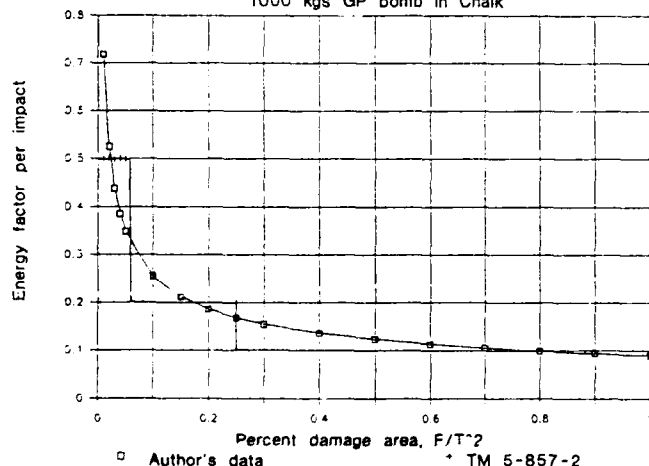
Due to the continuous pattern of spalling and rock damage, as observed along the tunnel floor, a smoother curve is required in order to describe the above fraction of energy per impact. The original suggestion of three distinct levels for the three different zones simply did not fit the observed pattern of damage. The suggested function in equation (3) seems to fit the observed facts although this is somewhat subjective judgement due to difficulties in detailed measurements:

$$(3) EF = 0.0245 * (F/T^2)^{-0.7045}$$

Where: EF = Fraction of total energy factor

Fig. 3 presents a comparison between the fraction of total energy per impact as recommended for design by Ref. 5 and the smoother relationship suggested in equation (3) herein and used in the calculations.

Fig. 3: Energy factor per impact vs. damage area  
1000 kgs GP bomb in Chalk



The spalls' velocities were measured in the field by ERA and given by the USAE (Ref. 2) as expected velocity range per damage zone:

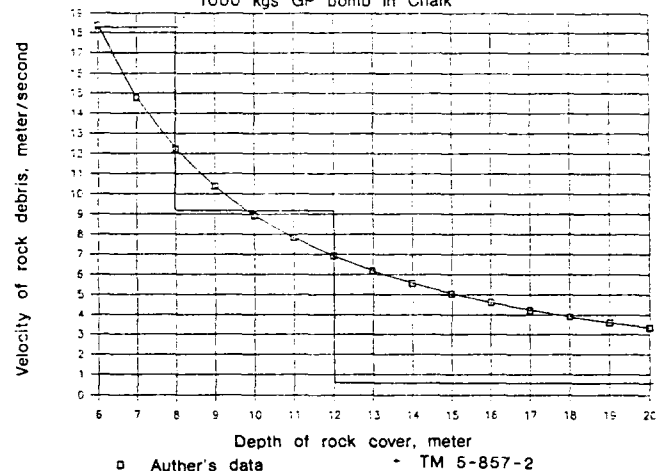
Light damage-Zone 4 : 0-2 fps, 0-0.6 m/sec  
Medium damage-Zone 3: 2-30 fps, 0.6-9 m/sec  
Heavy damage-Zone 2 : 30-60 fps, 9-18 m/sec

Once more, it became clear that the damage pattern as observed should be described using a smooth function for the spalls' velocities and not by "step function" as derived from reference 5. The suggested relationship, presented in fig. 4, fits to the original ERA data, was compatible with the measured velocities although some scatter was observed in certain cases, especially in the soft, unjointed Chalk:

$$(4) V = 11.92 * (D/W^{1/3})^{-1.41}$$

Where: V = Spall velocity, meter/sec

Fig. 4: Velocity of rock spalls vs. distance  
1000 kgs GP bomb in Chalk



The energy of the impacting spalls was calculated as suggested by Ref. 3 & 4 and the thickness of the shotcrete liner was estimated based on a factor of absorption found experimentally.

$$(5) E0 = (1/2) * M * V^2 = (1/2) * (W/g) * V^2$$

Where: E0 = Total energy,  
W = Weight of rock spalls, kgs/ meter of tunnel length  
M = Mass of spalls, kgs-sec^2/meter of tunnel length  
g = Acceleration of gravity, 9.81 m/sec^2

The final Design Impact was estimated based on the fraction of energy per impact:

$$(6) E = EF * E0$$

Where: E = Design energy per impact per meter of tunnel length

## LINER EVALUATION.

The basic solution suggested in Ref. 4 & 5 was a cast-in-place reinforced concrete liner with a layer of granular shock absorbing material. While this solution seems adequate for very high degree of protection, such as the one required against nuclear blasts, it is over conservative and expensive when dealing with protection against conventional bombing.

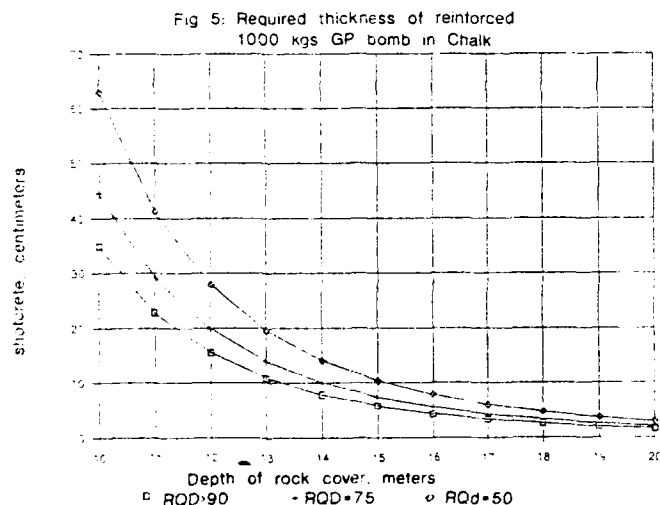
Furthermore, the present standard type of rock support (one should call it rock reinforcement) used to assure static stability from geotechnical considerations is based on combination of rock bolts and shotcrete. It is therefore useful to apply the same support system to assure the dynamic stability under the impacts of the rock spalls.

The thickness of the shotcrete, reinforced with standard welded mesh (usually with 5 millimeters bars at 15 centimeters "eyes"), was calculated based on:

$$(7) t = E / (6.42 \sqrt{L})$$

Where:  $t$  = Thickness of shotcrete reinforced with welded mesh, centimeters  
 $L$  = Length of active part of the liner, meters.

The active part of the tunnel liner,  $L$ , is usually the upper half of the perimeter for a circular tunnel; or the length of the roof for a rectangular tunnel. Fig. 5 presents the calculated thickness for the different values of RQD.



There is a reason to believe that steel fiber shotcrete can replace certain amount of the reinforcing mesh, but the available data are still inconclusive. Additional tests must be performed under controlled conditions to better evaluate the capability of the steel-fibre shotcrete.

The rock bolts should be fully grouted, either with resin or cement, and with embedded, active, length longer by at least 60 centimeters than the expected depth of the damage area, but preferably a length equal to one third of the bolt's length as determined from geotechnical analysis. This means that at shallow depth, such as near the portal, the length of the rock bolts will be longer than the one used for the same span at deeper depth.

The use of expansion type bolts, or bolts that are not fully-grouted is discouraged in cases involving the dynamic loadings of the type discussed herein.

## SUMMARY.

The design of shallow rock tunnels against conventional air bombing is re-evaluated using the "old" Engineering Manuals of the US Army Corps of Engineers, adapted to new types of rock reinforcement, and to softer, weaker sedimentary rocks.

The design method is simple, easy to follow and results in a safe and stable tunnel. Additional tests may improve the evaluation of liner thickness for unreinforced plain shotcrete, or unreinforced steel-fibre shotcrete.

New empirical-numerical expressions replaced the present log-log graphical solutions, easing the solution by using standard PC software. The use of spreadsheet programs such as the LOTUS 123 permit a quick sensitivity analysis for various parameters such as: scaled tunnel diameter, scaled charge to tunnel distance, scaled depth etc.

Calculation of the debris weight per unit length of the tunnel and the use of correction factors for the four "standard" damage zones leads to an estimate of the impact load and its kinetic energy.

Although many parameters are yet to be analyzed the suggested equations improve the design process and offer a wider range of empirical data.

## REFERENCES.

1. Engineering Research Associates, 1953, "Underground Explosion Test Program", Final Report - Rock, U.S. Army Corps of Engineers, Sacramento District
2. Engineering Research Associates, 1952, "Underground Explosion Test Program - Granite and Limestone, US Army Corps of Engineers, Sacramento District
3. Engineering Research Associates, 1953, "Underground Explosion Test Program - sandstone", US Army Corps of Engineers, Sacramento District

4. U.S. Army Engineers, 1965, "Design of Underground Installations in rock - Penetration and explosion Effects", TM 5-857-4. Formerly EM 1110-345-434 dated 1961.

5. U.S. Army Engineers, 1965, "The Design of Underground Installations in Rock Tunnels and Linings", TM 5-857-2. Formerly EM 1110-345-432.

6. Johnson W. J. and Rozen A., 1988, "Underground Storage in Unlined Rock Tunnels: Rock Mechanics Considerations in Estimating Damage Levels", 23rd DoD Explosive Safety Seminar, Atlanta, GA., August 9-11.

7. Rozen A., 1983, Unpublished data.

8. Deere D. U., 1963, "Technical Description of Rock Cores for Engineering Purposes", Felsmechanik und Ingenieurgeologie, Vol. 1, No. 1, 16-22,

9. Bieniawski Z. T., 1979, "Tunnel Design by Rock Mass Classifications", USAE-Waterways Experiment Station, Tech. Rep. GL-79-19, NTIS AD-A076 540.

PROMIX.  
A Computer Code for Calculating  
Building Damage from Internal Explosions.

Rickard Forsén & Torbjörn Jonasson

Swedish Defence Research Establishment (FOA)  
Weapons Technology Department  
FOA Grindsjön, P.O.Box 551, S-147 25 Tumba, Sweden

ABSTRACT.

The computer program PROMIX is an efficient tool in computing the expected effects of explosions in a multi-room structure.

PROMIX calculates the gas pressure due to the explosion as well as the pressure increases and decreases in each room due to leakage. Also calculated are the movements caused by the pressure on the surrounding walls and joist system.

PROMIX takes in consideration such factors as the composition of the explosive as well as five different types of fracture modes for walls and joist systems.

INTRODUCTION.

A confined or partially confined explosion in a building may cause severe damage to the building and to the inhabitants if the explosion originates from for example an aerial bomb, an artillery shell or a terrorist high explosive charge.

The pressure from a confined explosion is characterized by an initial shock wave followed by multiple reflections. Typically for the confined explosion is the gas pressure which often will remain even after the dissipation of the reflected shock waves.

The gas pressure is often of long duration and thus causing a high impulse density and if the walls of the confinement are not strong enough to withstand the pressure they will accelerate and the movement will create successive increase of volume and openings in the confinement. The high pressure in the confinement where the explosion has taken place of course will leak out through openings to other rooms and to the open air.

For purpose of estimating the damage from confined explosions to buildings or to estimate the amount of high explosive detonated in accidents or acts of explosion sabotage a computer program, PROMIX, has been evaluated.

THEORY.

A high explosive charge detonating inside a confinement will create two different types of pressure acting on the walls, a dynamic pressure from the initial shock waves and a quasi-static gas pressure from hot reaction products (Fig. 1). The amplitude of the quasi-static gas pressure depends on the specific energy and the weight of the high explosive and the volume of the confinement.

If there are any openings between the confinement and the adjacent rooms or to the open air there will be a pressure leakage. This will decrease the pressure in the confinement and increase the pressure in adjacent rooms. If the pressure is high enough it may cause windows to break and surrounding walls to crack or possibly break apart thus creating new venting openings. By the repetition of this process in adjacent rooms a whole building might be affected by an explosion.

The movement of a wall is affected by its resistance, mass, inserting and the mode of failure (Fig. 2). The resistance is affected by the fastening of the wall. For a reinforced concrete wall for instance the amount of reinforcement and its location are important parameters.

The mode of failure for a wall is affected by such things as the material of the wall and the location of the reinforcement.

Depending on the mode of failure the movement of a wall is governed by either an equilibrium of forces:

$$P \cdot A = m \cdot a + K \quad (1)$$

or by an equilibrium of momentums:

$$P \cdot A \cdot e = \alpha \cdot J + K_m \quad (2)$$

Where  $P$ =pressure (Pa),  $A$ =area of wall ( $m^2$ ),  $m$ =mass of wall (kg),  $K$ =internal force of movement (N),  $e$ =distance between point of balance and axis of rotation(m),  $\alpha$ =angular acceleration ( $rad/s^2$ ),  $J$ =mass-moment of inertia ( $kg \cdot m^2$ ) and  $K_m$ =moment of resistance (Nm).

The duration of the pressure is an important parameter in deciding the effects of an explosion. An initial shock wave with high pressure but with short duration might cause a small deflection while a gas pressure with lower amplitude but with long duration and thus a high impulse density might give a larger deflection. This can be shown with isodamage curves in a pressure-impulse density diagram (Fig. 3). The impulse density is the area under the pressure-time curve. The isodamage curves are formed by such combinations of pressure and impulse density that yield a specified deflection. To gain a larger deflection than for the isodamage curve in question, a characteristic pressure ( $P_c$ ) and a characteristic impulse density ( $I_c$ ) both must be exceeded.

In determination of damage from confined explosions the amplitude and duration of the gas pressure often are more important parameters than the initial shock wave because the initial shock wave often has a very short duration and thus a small impulse density.

#### THE COMPUTER PROGRAM PROMIX.

The computer program PROMIX calculates the effects of an internal explosion in a building with several rooms. PROMIX uses the following algorithm:

1. Read input data.
2. Calculate the gas pressure in the room of the explosion.
3. Calculate the movement of each wall during the time step  $\Delta t$ .
4. Calculate new venting openings and volumes.
5. Calculate new pressures.
6. If overpressure in the room of the explosion  $> 0$  then go to 3.
7. Print the results.

Input data can be divided into four different groups:

1. Data for high explosive properties are weight and mixture.
2. Data for the different rooms are volume, initial pressure and temperature.
3. Data for the different walls and floors are weight, mode of deflection, resistance amplitude and length, inserting and dimensions etc.
4. Data for the venting openings are the areas.

Gas pressure is calculated using a method by Proctor (1972). First the number of moles of air initially in the volume is calculated. One mole of air is assumed to be composed of 0.21 mole  $O_2$  and 0.79 mole  $N_2$ . The number of moles of C, H, O, N and Al in the explosive charge are calculated. The reaction products created are  $H_2O$ ,  $Al_2O_3$ , CO and  $CO_2$ . If there is oxygen enough in the high explosive and in the room air there will be no CO created but complete combustion occurs such that all carbon appears as  $CO_2$ . The heats of formation for the components of air, high explosive and gas products used together with the composition of reaction products give the total energy of the reaction and thus the temperature and pressure.

If the combustion is not complete in the first room and the gases leak into an other room there will be a rise of pressure due to afterburning. This pressure rise is calculated in the same manner as above.

The venting process is assumed to be governed by two equations (Proctor, 1972) one for sonic and one for subsonic flow and the establishment of pressure equilibrium in each volume is assumed to occur instantaneously for each timestep. The movement of walls and floors are calculated using equation (1) or (2). The movement of the walls or the floors during the timestep  $\Delta t$  causes a change of volume and area of venting openings (Fig. 2).

Output data are pressure and impulse density for all the rooms and velocity and movement of all the walls and floors as a function of time.

#### RESULTS OF CALCULATION.

PROMIX has been used to calculate the damage to a multistorey concrete frame residential building caused by the detonation of 125 kg of TNT inside one of the apartments (Fig. 4). The plans of the storey of the detonation and the storey above and the storey beneath have been simplified by omission of non-bearing partition walls (Fig. 4). The input data are shown in Table 1.

The external wall of the confinement where the detonation has taken place will get a maximum velocity of 45 m/s. The internal walls of the confinement which are slightly heavier will get 37 m/s and floors which are even heavier and also with higher resistance will get 34 m/s maximum velocity (Tab. 1). Also the external and internal walls of apartments above and beneath will be slightly removed (Tab. 1).

The gas pressure in the confinement where the detonation has taken place rises momentarily to a maximum of 1878 kPa. In adjacent confinements there will be a slower rise to much lower pressures (Fig. 5).

PROMIX also has been used to calculate the internal pressure and the velocities of the walls for the experimental setup of Figure 6. The maximum velocities are calculated to approximately 34 m/s for the walls and 31 m/s for the floors. The maximum gas pressure is calculated to 2310 kPa and impulse density to 13.7 kPas (Fig. 7).

#### COMPARISON WITH EXPERIMENTS.

In order to estimate the debris launch velocity caused by the detonation of a 250 kg General Purpose Bomb (approximately 50 % charge weight ratio) inside a multistorey concrete frame residential building a test series was made (Forsén, 1989).



A typical apartment in such a building can be divided into sections limited by load bearing concrete walls. The volume of such a section is approximately  $125 \text{ m}^3$ . Thus the loading density (i.e. the weight of the high explosive divided by the volume of such a section) will be approximately  $1 \text{ kg/m}^3$ . In the experiments a much smaller confinement with a volume of  $8 \text{ m}^3$  (Fig. 6) was used but the same loading density was gained using a high explosive charge of  $8.4 \text{ kg}$  Comp B. The scaled venting area in the confinement (i.e. the area of venting openings divided by the volume) was the same as in the full scale building namely  $0.11 \text{ m}^{-1}$ . The thickness ( $0.15 \text{ m}$ ) and reinforcement of walls and floors were almost equal to those of the real building.

The pressure inside the volume was recorded with piezo-electric pressure transducers. The first shock wave is followed by several weaker reflected shocks and then a gas pressure decreasing to zero after approximately  $20 \text{ ms}$  (Fig. 1). The recorded impulse density was approximately  $19 \text{ kPas}$ .

The destruction of the confinement was recorded by high speed cameras and deflection gages on the walls and floors. The maximum velocity of walls is approximately  $40 \text{ m/s}$  and floors (which were slightly stronger reinforced) to approximately  $35 \text{ m/s}$ . The high speed films show that each wall do not break in pieces but shears off along the edges and moves parallel outwards as an unbroken plate.

The velocities of walls and floors in the experiment,  $40$  and  $35 \text{ m/s}$ , are higher than the velocities for the same setup calculated with PROMIX,  $34$  and  $31 \text{ m/s}$ . The impulse density recorded in the experiment,  $19 \text{ kPas}$ , also is higher than the calculated  $13.7 \text{ kPas}$  (Fig. 7). The parameter inserting used in the calculations was chosen to be  $0.3 \text{ m}$  for the floors and three walls and  $0.1 \text{ m}$  for the fourth wall. A higher value of the inserting in the calculations would give higher velocities of walls and floors and also a higher impulse density.

In the test series referred to above the mode of deflection for the walls was found to be Type 1. Other experiments (Forsén, 1987) with lower loading densities and other material of walls have resulted in other modes of deflection such as Type 2 and Type 4.

One of the most difficult parameters to choose is the inserting (Fig. 2). The maximum inserting of for instance an external wall is the thickness of the wall. Different breaking patterns (Fig. 8) may cause a lower value of inserting. Parametric studies of the influence on maximal wall velocity of inserting, resistance and length of resistance of external walls of the multistorey, concrete frame residential building (Fig. 4) have been made (Fig. 9).

A variation of these parameters between zero and twice the ordinary value shows that the inserting is a much more important parameter, at least in this example, than the resistance.

## CONCLUSIONS AND FURTHER DEVELOPMENT.

The computer program PROMIX calculates the effects of an internal explosion in a building with several storeys and rooms.

So far PROMIX has not been verified experimentally to any significant degree. Comparison to a detonation in a single volume structure indicates reasonable accuracy for rough estimations but there is a great need for accurate input data.

Parametric studies have shown the influence of different input data. It is a matter of high concern to determine reasonable values on these input data using practical experiments. A test bench will be built specially for experiments with confined explosions and the parameters used as input data in PROMIX will be studied. The experiments also will form the basis of further development of PROMIX.

The program can be further developed in many different ways such as:

- \* the program calculates the correct mode of failure
- \* more modes of failure
- \* consideration of geometry and location of different rooms in order to deal with the effects of collision between walls for instance.

## REFERENCES.

- |                            |  |
|----------------------------|--|
| Broberg<br>1987            | "TYPHUSKATALOG - Bostäder." (Catalogue of Residential House Types). FOA Report C 20669-2.6, Augusti 1987. (In Swedish.)  |
| Forsén<br>1987             | "INNESLUTEN EXPLOSION II. Belastningsförlopp och verkan på byggnadselement. "(CONFINED EXPLOSION II. Internal Loading Characteristics and Displacement of Walls in a Semiclosed Volume). FOA Report C 20655-2.6, April 1987. (In Swedish.) |
| Forsén<br>1989             | "INITIALVERKAN. Verkan av inneslutna explosioner. "(INITIAL PHASE. Effects of Explosions in Buildings). FOA Report in preparation. (In Swedish.)   |
| Jonasson & Åseborn<br>1988 | "PROMIX. Ett datorprogram som beräknar verkningarna av inneslutna explosioner i byggnader." (PROMIX. A Computer Program that Calculates the Effects of Confined Explosions in Buildings). FOA Report C 20720-2.3, Juni 1988. (In Swedish.) |
| Proctor<br>1972            | "Internal Blast Mechanisms Computer Program." Naval Ordnance Laboratory, NOLTR 72-231, 1972.   |

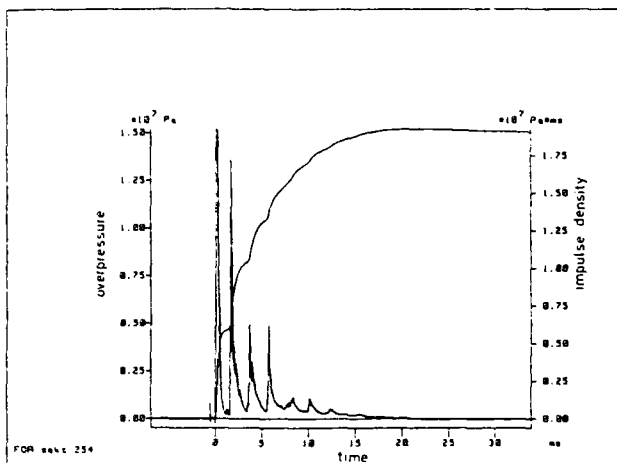


Figure 1. Recorded pressure-time history from an experiment with a high explosive charge of 8.4 kg of Comp B detonating inside an 8 m³ confinement with 0.9 m² venting opening (Forsen, 1989).

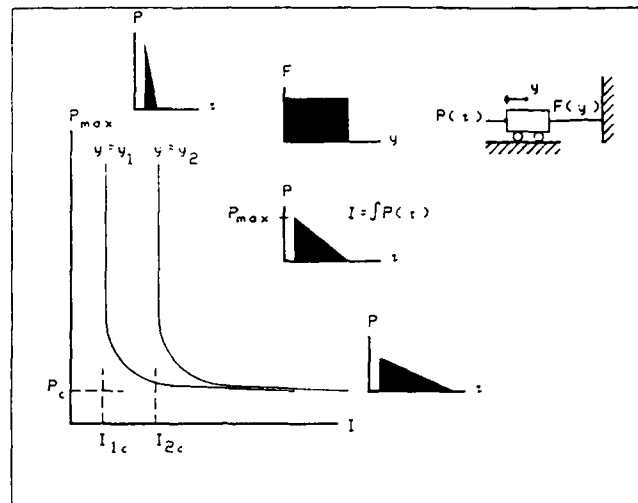


Figure 3. Examples of isodamage curves for a triangular load  $P(t)$  in a pressure-impulse density diagram.

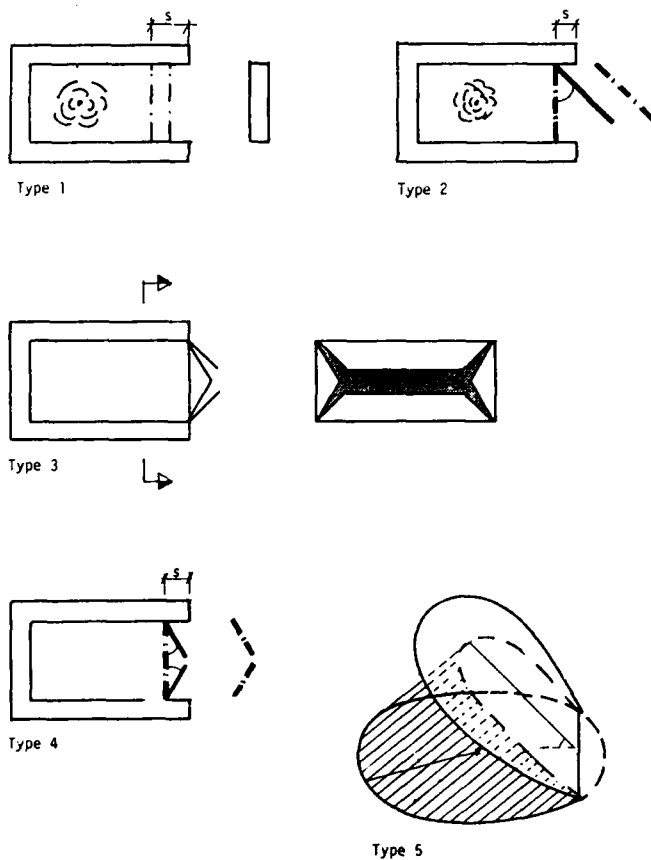


Figure 2. Different modes of failure that can be used in PROMIX. The letter "s" denotes the inserting.

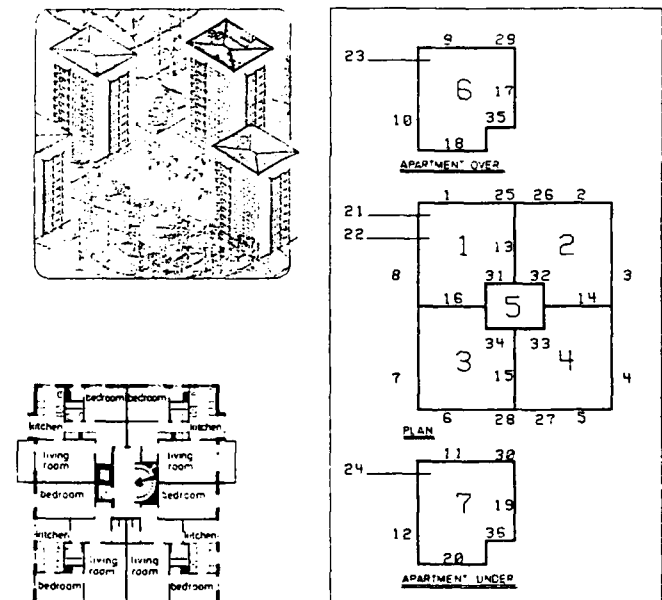


Figure 4. Perspective view of a multistorey concrete frame residential building (Broberg, 1987), with an original plan and a simplified one used in PROMIX. Figures denote confinements, walls, floors and venting openings.

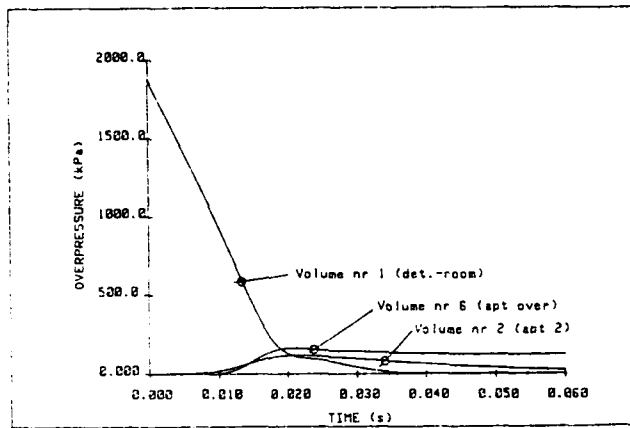


Figure 5. Calculated pressure-time curves inside a building (Fig. 4).

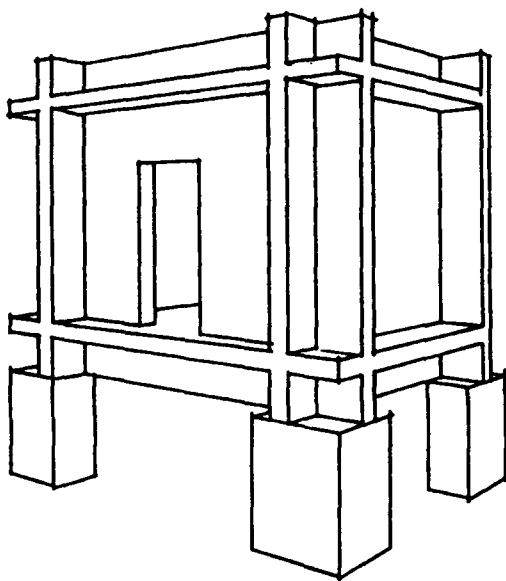


Figure 6. Experimental setup used for the detonation of 8.4 kg of Comp B in an 8 m<sup>3</sup> confinement (Forsen, 1989).

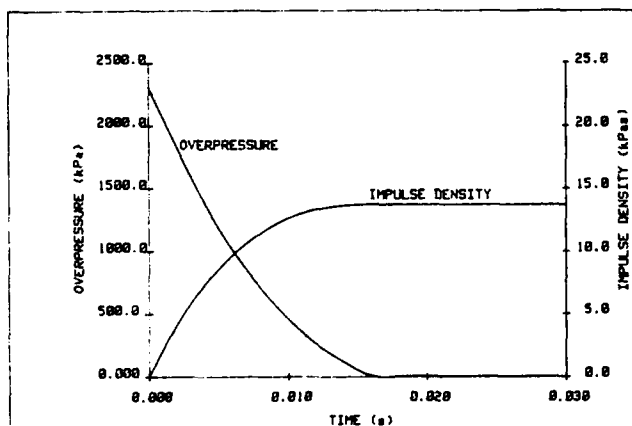


Figure 7. Calculated overpressure and impulse density inside the confinement of Fig. 6.

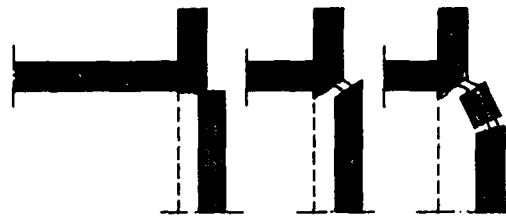


Figure 8. Different breaking patterns might affect the inserting and result in a lower value of this parameter than the theoretical which is the thickness of the wall (see Fig. 2).

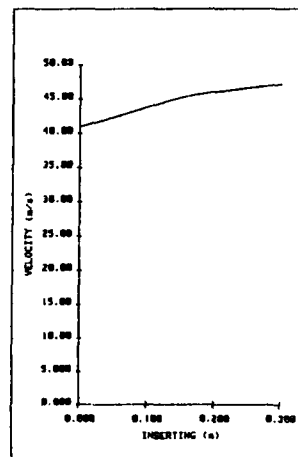
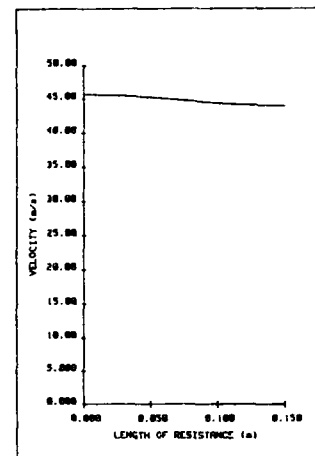
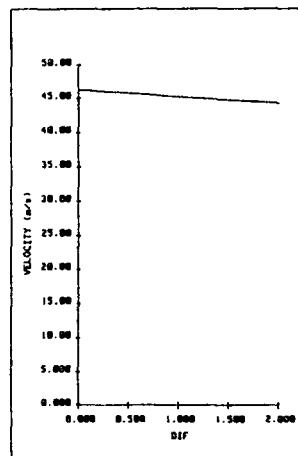


Figure 9. Theoretical parametric studies of the influence on maximal external wall velocity of DIF (Dynamic Increase Factor for the static resistance of the wall), length of resistance and inserting for the external wall of building in Figure 4.

## VOLUMES INPUT DATA:

| NR | DESCRIPTION | VOLUME(m**3) | PRESSURE(kPa) | TEMP(C) |
|----|-------------|--------------|---------------|---------|
| 1  | det.-room   | 150.0        | 100.0         | 20.0    |
| 2  | apt2        | 150.0        | 100.0         | 20.0    |
| 3  | apt3        | 150.0        | 100.0         | 20.0    |
| 4  | apt3        | 150.0        | 100.0         | 20.0    |
| 5  | well        | 40.0         | 100.0         | 20.0    |
| 6  | apt over    | 150.0        | 100.0         | 20.0    |
| 7  | apt under   | 150.0        | 100.0         | 20.0    |
| 8  | OUTSIDE     |              | 100.0         | 20.0    |

## RESULTS:

| MAX OVERPRESSURE(kPa) | MAX IMPULS DENSITY(kPa*s) |
|-----------------------|---------------------------|
| 1878.2                | 19.8                      |
| 118.0                 | 3.6                       |
| 118.0                 | 3.6                       |
| 3.7                   | .1                        |
| 410.5                 | 8.8                       |
| 157.6                 | 6.8                       |
| 157.6                 | 6.8                       |

## VENTING AREAS INPUT DATA:

## INITIAL VENTING AREAS:

| NR | DESCRIPTION | DELIMITS | AREA(m**2) |
|----|-------------|----------|------------|
| 25 | windows     | 1 - 8    | 6.0        |
| 26 | windows     | 2 - 8    | 6.0        |
| 27 | windows     | 4 - 8    | 6.0        |
| 28 | windows     | 3 - 8    | 6.0        |
| 29 | windows     | 6 - 8    | 6.0        |
| 30 | windows     | 7 - 8    | 6.0        |
| 31 | door        | 5 - 1    | 1.5        |
| 32 | door        | 2 - 5    | 1.5        |
| 33 | door        | 5 - 4    | 1.5        |
| 34 | door        | 3 - 5    | 1.5        |
| 35 | door        | 6 - 8    | 1.5        |
| 36 | door        | 7 - 8    | 1.5        |

## TYPE 1. Parallel movement.

| NR | DESCRIPTION | DELIMITS | AREA<br>(m**2) | MAX<br>VENT.AREA<br>(m**2) | CIRCUM-<br>FERENCE<br>(m) | WEIGHT<br>(kg/m**2) | IN-<br>SERTING<br>(m) | RESISTANCE<br>(N) | LENGTH OF<br>RESISTANCE<br>(m) |
|----|-------------|----------|----------------|----------------------------|---------------------------|---------------------|-----------------------|-------------------|--------------------------------|
| 1  | ext. wall   | 1 - 8    | 20.0           | 20.0                       | 21.0                      | 435.0               | .150                  | .21E+07           | .050                           |
| 2  | ext. wall   | 2 - 8    | 20.0           | 20.0                       | 21.0                      | 435.0               | .150                  | .21E+07           | .050                           |
| 3  | ext. wall   | 2 - 8    | 20.0           | 20.0                       | 21.0                      | 435.0               | .150                  | .21E+07           | .050                           |
| 4  | ext. wall   | 4 - 8    | 20.0           | 20.0                       | 21.0                      | 435.0               | .150                  | .21E+07           | .050                           |
| 5  | ext. wall   | 4 - 8    | 20.0           | 20.0                       | 21.0                      | 435.0               | .150                  | .21E+07           | .050                           |
| 6  | ext. wall   | 3 - 8    | 20.0           | 20.0                       | 21.0                      | 435.0               | .150                  | .21E+07           | .050                           |
| 7  | ext. wall   | 3 - 8    | 20.0           | 20.0                       | 21.0                      | 435.0               | .150                  | .21E+07           | .050                           |
| 8  | ext. wall   | 1 - 8    | 20.0           | 20.0                       | 21.0                      | 435.0               | .150                  | .21E+07           | .050                           |
| 9  | ext. wall   | 6 - 8    | 20.0           | 20.0                       | 21.0                      | 435.0               | .150                  | .21E+07           | .050                           |
| 10 | ext. wall   | 6 - 8    | 20.0           | 20.0                       | 21.0                      | 435.0               | .150                  | .21E+07           | .050                           |
| 11 | ext. wall   | 7 - 8    | 20.0           | 20.0                       | 21.0                      | 435.0               | .150                  | .21E+07           | .050                           |
| 12 | ext. wall   | 7 - 8    | 20.0           | 20.0                       | 21.0                      | 435.0               | .150                  | .21E+07           | .050                           |
| 13 | int. wall   | 2 - 1    | 15.0           | 2.5                        | 17.0                      | 480.0               | .100                  | .17E+07           | .050                           |
| 14 | int. wall   | 2 - 4    | 15.0           | 2.5                        | 17.0                      | 480.0               | .100                  | .17E+07           | .050                           |
| 15 | int. wall   | 3 - 4    | 15.0           | 2.5                        | 17.0                      | 480.0               | .100                  | .17E+07           | .050                           |
| 16 | int. wall   | 3 - 1    | 15.0           | 2.5                        | 17.0                      | 480.0               | .100                  | .17E+07           | .050                           |
| 17 | int. wall   | 6 - 8    | 15.0           | 2.5                        | 17.0                      | 480.0               | .100                  | .17E+07           | .050                           |
| 18 | int. wall   | 6 - 8    | 15.0           | 2.5                        | 17.0                      | 480.0               | .100                  | .17E+07           | .050                           |
| 19 | int. wall   | 7 - 8    | 15.0           | 2.5                        | 17.0                      | 480.0               | .100                  | .17E+07           | .050                           |
| 20 | int. wall   | 7 - 8    | 15.0           | 2.5                        | 17.0                      | 480.0               | .100                  | .17E+07           | .050                           |
| 21 | floor       | 6 - 1    | 60.0           | 4.8                        | 32.0                      | 505.0               | .150                  | .10E+08           | .050                           |
| 22 | floor       | 7 - 1    | 60.0           | 4.8                        | 32.0                      | 505.0               | .150                  | .10E+08           | .050                           |
| 23 | floor       | 6 - 8    | 60.0           | 4.8                        | 32.0                      | 505.0               | .150                  | .10E+08           | .050                           |
| 24 | floor       | 7 - 8    | 60.0           | 4.8                        | 32.0                      | 505.0               | .150                  | .10E+08           | .050                           |

## RESULTS:

| MAX VELOCITY<br>(m/s) |
|-----------------------|
| 45.21                 |
| .16                   |
| .16                   |
| .00                   |
| .00                   |
| .16                   |
| .16                   |
| 45.21                 |
| 6.60                  |
| 6.60                  |
| 6.60                  |
| 37.11                 |
| .00                   |
| .00                   |
| 37.11                 |
| 3.38                  |
| 3.38                  |
| 3.38                  |
| 3.38                  |
| 34.39                 |
| 34.39                 |
| .00                   |
| .00                   |

Table 1. PROMIX input data and results for the detonation of 125 kg of TNT inside a multistorey concrete frame residential building.

## FAR-FIELD EFFECTS ON STRUCTURES FROM A HIGH-EXPLOSIVE DETONATION

Paul W. Graham, Gayle E. Albritton, and James B. Cneek

U.S. Army Engineer Waterways Experiment Station  
Structures Laboratory  
Vicksburg, Mississippi 39181-0631

The U. S. Army Engineer Waterways Experiment Station frequently uses explosive charges to generate dynamic test loads. Due to unique geologic requirements, a test was conducted at a site near a large population center. In order to maximize safety to the local community due to blast effects, efforts were made to minimize the impact of the airblast by monitoring the weather. Far-field airblast pressure and ground motion were predicted to determine if the test could be safely conducted within acceptable risks. No posttest damage claims were filed. This paper outlines the calculational and operational procedures used. Included are the procedures used for the explosive detonation, recorded test data, weather watch, airblast and ground-motion calculations with their respective damage criteria, test results, and conclusions.

### INTRODUCTION

High-explosive field tests have been conducted for many years in order to understand the response of structures and soil to airblast and ground shock loading. For both personal safety and legal reasons, it is imperative to know beforehand what the resulting far-field effects are on nearby structures. Such a test was conducted at a remote area on the Fort Knox, KY, Military Reservation, and pretest calculations were made as to the far-field airblast and ground shock effects on houses and commercial buildings located outside of the Reservation (Reference 1). Also, weather forecasting (Reference 2) and airblast and seismic measurements were made at the time of detonation. The high-explosive event was conducted based on weather predictions that would minimize the far-field effects on the densely populated areas surrounding the test site.

The objectives of the far-field effects effort for the test were: (a) to predict maximum far-field airblast and ground shock effects on nearby structures, (b) to record far-field measurements at the structures' locations and compare them with predictions, and (c) to verify use of available solutions in predicting far-field effects.

The far-field effects study was part of a 48-ton high-explosive field event conducted at Fort Knox, KY. Prior to the test, calculations were made to predict the far-field airblast and ground

shock effects on nearby structures to ensure that minimal damage would be incurred. Weather forecasting was made up to shot time to maximize the accuracy of input weather data so that the far-field effects would be minimized. At shot time, measurements of airblast and ground shock were made at six locations, varying from 1.07 to 11.01 miles away. This experimental information was compared to the calculations for verification of the ability in predicting these effects.

### PROCEDURES

#### High-Explosive Detonation

The test environment was generated by detonation of a buried high-explosive charge. Two explosives were used for the charge, which had a total weight of 48 U.S. tons and covered an area approximately 200 feet square. Part of the explosive charge (33 tons of Iremite-60) was placed in polystyrene foam boards for proper spacing, then covered with 4 feet of compacted crushed limestone. The remainder of the charge (15 tons of ammonium nitrate/fuel oil explosive) was buried at a depth of 10 feet in the native soil.

Detonation of the charge was accomplished by using 50-grains-per-foot detonation cord placed throughout the explosives.

#### Recorded Data

Active instrumentation data of the far-field environment were recorded at six locations surrounding the Rodgers Hollow test site as shown in Figure 1. These measurements consisted of both ground motion and airblast overpressure at three locations and maximum noise levels at the other three sites. Locations of these sites were chosen to capture the far-field environment in all critical directions from the test site.

Most critical of the six locations were the nearest house and the towns of Shepherdsville and Radcliff, which were the closest concentrated population and the nearest town in the direction of the predominant winds at test time, respectively. Because these three locations were the primary data collection points, highly reliable and sensitive equipment were used. A microbarograph recorded the airblast overpressure, and a triaxial accelero-

meter canister was used to record the ground motions, with the radial direction from the test site to the principle axis. The nearest house was located at far-field Station 1 (FF1) at a range of 14,430 feet and an azimuth of 35 degrees from the test site. The location of Shepherdsville (FF2) was at a range of 40,780 feet at an azimuth of 70 degrees, and the town of Radcliff (FF5) was the farthest location of all six measurements at a range of 58,130 feet and an azimuth of 220 degrees. Thus, these three locations were to the north, northeast, and southwest.

Measurements at the other three locations were less critical and, therefore, were recorded with handheld sound level meters whose output in decibels was converted to the overpressure equivalent. These locations were the test control area (FF6), which was the closest measurement at a range of 5,650 feet at an azimuth of 180 degrees; the town of Lebanon Junction (FF4) at a range of 53,950 feet at an azimuth of 145 degrees; and the bridge construction site at a range of 26,900 feet at an azimuth of 300 degrees. These locations, therefore, covered the general areas in the south, southeast and northwest directions from the test site, respectively.

#### Weather at Detonation Time

Weather was monitored closely, beginning with a long-range forecast eight days prior to the test and becoming more detailed up to the actual test time. This was required in order to minimize the enhancement (focusing of airblast) on the surrounding population and structures that would lead to possible safety hazards at shot time. Most critical were the populations of Shepherdsville and Louisville to the northeast and north, respectively. Weather conditions were near ideal at test time; light winds from the north northeast at surface to 1,500 feet, with higher altitude winds also from the north at 20 knots. Prior to the test, the surface air temperature was allowed to warm to the daily high to minimize inversion effects. It was recorded at Fort Knox as 73-degrees Fahrenheit.

### PEAK AIRBLAST PRESSURE CALCULATIONS

#### Airblast Calculations

Peak airblast pressure is the parameter used to predict airblast-induced damage to far-field structures. In order to avoid damage, we must have an accurate method to predict peak pressure at various ranges from the blast site. Two types of calculations must be made. One calculation model deals with the complex bending of the sound rays (focusing) by the atmosphere (this will be discussed later). The other model, discussed below, deals with the direct transmission of the pressure pulse in the air.

#### Peak Pressure Standard

As outlined in the ANSI standard (Reference 3), much progress has been made in mathematically modeling the variation of peak pressure with range for a 1-kiloton (kt) nuclear burst in

free air. This far-field airblast data base from nuclear tests is extensive and is used here to calculate the high-explosives effects after correcting the actual weights to the nuclear yield (this is discussed later). That work was initially done on very large, high-speed digital computers. The early problems with numerical instability in the calculations at long ranges were finally resolved, yielding results that agree with the known effects and experimental data. A product of that effort is a closed-form equation that models peak pressure over ranges from 30 to 30 million feet.

#### Scaling Laws and Approximations

By using Sach's scaling laws (Reference 4), the peak pressure produced by a specific nuclear explosion at a given range is obtained from the pressure predicted by the above-mentioned 1-kt model. This is accomplished by using the scaled range,  $\lambda$  (the range (R) divided by the cube root of the weapon yield in kt), as input to the peak-pressure calculating equation.

As mentioned previously, the peak pressure predicted by the 1-kt model is for a free-air burst. Under ideal conditions (point burst and perfect horizontal reflector), the pressure produced by a surface burst will be twice that produced by a free-air burst having the same yield.

Since the power of a nuclear weapon is described in terms of its "TNT equivalent" yield, one is inclined to think the same peak pressure is produced by the detonation of an equal amount of TNT. Such is not the case. For reasons outlined in References 3 and 4, the peak pressure from solid or liquid high-explosive sources is greater than that of a numerically equal nuclear source. The yield scale factor varies with scaled range; but for peak pressures below about 200 psi, the actual TNT charge weight must be doubled before calculating peak pressure with the procedure described above. Thus, for pressures less than 200 psi, the peak pressure from a high-explosive charge is calculated using the nuclear model by increasing the charge weight by a factor of two.

#### Practical Calculations

The peak pressure model may be used in several ways for the many calculations that must be made during the planning and shot day efforts. For low pressure levels, the peak pressure model can be plotted on log-log graph paper for the planned charge weight. This is simple and quick. However, we have found it helpful to have the equation programmed on both personal computers and handheld calculators.

#### Focusing of Sound Waves

On a "perfect day" for blasting, there is no wind and the air temperature decreases as elevation increases (negative thermal gradient). Since the speed of sound in air is proportional to the air temperature, the sound speed will decrease with elevation. In that situation, the lower (in elevation) portion of the blast wave travels

slightly faster than the portion just above it. This effect turns the wave upward and away from the things we want to protect. Consequently, the pressure at distant points on the ground is much less than that predicted by the peak pressure model.

On a not perfect day, which is to say almost all of the time, there are some directions (azimuths) along which the sound of speed will not decrease with elevation. There are two reasons for this. First, there may be warm layers of air over the cooler layers beneath them (positive thermal gradient). Second, the wind speed may increase as elevation increases. In that situation, the effective sound speed (with respect to the ground) is increasing with elevation because the sound is moving in the air at its sonic velocity, but the air is moving too. In both cases, the sound rays will be turned back toward the ground.

In deciding if the weather conditions are acceptable for detonating the explosive, two questions must be answered. How much bending is taking place? Where will the bending rays return to the ground (both azimuth and range)? In the case of minor bending, the pressure at the rays' return point is just a bit higher than predicted. In the worst case of bending, many of the sound rays are bent in such a way that they all return to the same point on the ground. In other words, they are focused (called a caustic). Under those conditions, the peak pressure is seven to eight times the peak predicted by the model. This brings us to the second computational aid, ray tracing.

#### Computational Ray Tracing and Weather Monitoring

If we know in precise detail just what the temperature and wind velocity values are at any point in the air, then ray tracing is a rather simple computer task (provided we have an automated procedure to get the data). But knowing the location of the focus points is only part of the needed information. We also need to know the peak pressure. At the current state of our computational capability, we can only say that the observed peak pressure will be the model pressure multiplied by a factor between one and eight.

Turning to the real-world situation, the best weather information is a velocity and temperature versus elevation profile taken shortly before shot time. Less satisfactory (but often all that is available) are the data taken by the weather people at nearby stations and/or short term forecasts based on computer processing of such data. Ray tracing, based on such a sparsely populated data base, is as much art as it is science. For that reason, the skill of the weather-watch person is the key element in estimating the reliability of the input data and interpreting the significance of the predicted focus points. Our current ray-tracing programs are operational on personal computers with supporting graphics. They are used by the weather-watch personnel at the test site during the critical several hours prior to the scheduled detonation time to estimate the azimuth and range of potential focus points. That information is essen-

tial to making a go or no-go decision when the anticipated peak pressures are near the damage threshold for structural and personal safety.

#### Damage Criteria

Two kinds of window breakage calculations were made for the test. The first calculation, using the peak pressure model, determined that on a day having ideal weather conditions (a negative thermal gradient, no bending of the sound rays) there would be no peak airblast pressure above 0.03 pound per square inch at the nearest house (range of 14,430 feet). This level is the threshold of window cracking. See Figure 2 for airblast comparison of test results from this test and a previous data base (Reference 5) and curves discussed above.

The second computation was made about an hour before test time to see that the focus points would not fall in populated areas. This weather-driven requirement can cause long delays (weeks) during periods of unfavorable weather. Fortunately, such was not the case for this event.

#### GROUND-SHOCK CALCULATIONS

##### The Ground-Shock Model

Peak particle velocity is the ground shock parameter used to set the damage threshold of far-field structures. Models to calculate peak particle velocity at a stated range from a given charge weight are extremely sensitive to the soil characteristics, rock type, location, and the ground-water surface. Consequently, it is extremely difficult to do more than make a rough estimate at a new site (no history of explosive testing and instrumental ground motions). For this test event, we are fortunate in having a long history of explosive events at which the ground motions were recorded at a variety of ranges. In that situation, it is a simple matter of adjusting the scale factor and the exponents of the range and charge weight terms in order to agree with the observed data. The result is either a simple exponential equation in a handheld calculator or a straight line on log-log paper (we use both). See Figure 3 for a plot of the predicted and recorded ground peak velocity versus range used for this test event.

#### Damage Criteria

The ground shock damage threshold for residential structures is generally agreed to be 2.0-inches-per-second peak particle velocity. This is the level at which minor cracking of plaster takes place. To be conservative, we used 1.0 inch per second. Our predictions for the ground motion at the nearest house (range of 14,430 feet) indicated a peak particle velocity of only 0.16 inch per second, well below the damage threshold.

For people, we used the generally accepted level for "unpleasant" ground motion of 0.4 inch per second to set the range at which no person, other than test personnel, would be allowed within during the test.

Our predictions indicated that the ground motion of 0.05 inch per second would develop along Highway 44 north of the site. Because this level is close to the threshold of motion that can initiate rock slides, this section was monitored during the test. No slides developed.

Predictions for the six far-field measurement sites are given in Table 1 for airblast and ground motion.

#### TEST RESULTS

Measured test results at the six far-field sites are given in Table 1 along with the pretest predictions. Ground motion data were recorded near the predicted values as expected for this familiar test site (Figure 3). However, airblast predictions were overly conservative and overpredicted by 20 to 50 times the recorded values (Figure 2). The airblast predictions are for an exposed airburst on flat ground. Since the actual charge was buried and located in wooded and hilly terrain, this greatly restricts airblast propagation. This restriction was not accounted for in the calculations.

No complaints from area residents were filed. Far-field crews described the noise levels as low, and no damage occurred to the areas structures.

#### CONCLUSIONS

Ground motion predictions were very good and agree well with the recorded data. The airblast calculations should account for the buried effect and terrain to reduce the overly conservative predictions. The more realistic values would provide better data on which to base decisions on a shoot/no shoot situation. An airblast prediction should either provide an expected scatter band (confidence interval) or give the upper bound of

the expected values (thus conservative again). If one is to err on far-field calculations, it is much better to miss on the high side (safety side) than to allow unknowns to increase the risk of life and structural safety.

#### ACKNOWLEDGEMENTS

We gratefully acknowledge permission from the Office, Chief of Engineers, to publish this paper.

#### REFERENCES

1. "Environmental Impact Assessment, Rodgers Hollow-Silo Test Program." 1987 (May). Fort Knox, KY, U.S. Army Engineer Waterways Experiment Station, Vicksburg, MS.
2. J. W. Reed. 1988 (May). "Weather Watch and Airblast Predictions," Sandia National Laboratory, Albuquerque, NM.
3. "Estimating Airblast Characteristics for Single Point Explosions in Air, with a Guide to Evaluation of Atmospheric Propagation and Effects." 1983. S2.20-1983, American National Standards Institute, New York, NY.
4. R. G. Sachs. "The Dependence of Blast on Ambient Pressure and Temperature." 1944. BRL Report No. 472, Army Ballistic Research Laboratory, Aberdeen Proving Ground, MD.
5. J. B. Cheek, J. S. Shore, and F. M. Warren. "Mitigation of Far-field Airblast Associated with Explosive Detonations Near Populated Areas." Presented and published at the Twenty-Third Department of Defense Explosives Safety Seminar. 1988. U.S. Army Engineer Waterways Experiment Station, Vicksburg, MS.

Table 1. Far-field predictions with recorded data in parentheses.

| Location           | Range<br>ft | Airblast<br>psi | Ground Motion<br>ips |
|--------------------|-------------|-----------------|----------------------|
| FF1 Nearest House  | 14,430      | 0.105 (0.005)   | 0.177 (0.101)        |
| FF2 Sheperdsville  | 40,780      | 0.031 (0.001)   | 0.018 (0.018)        |
| FF3 Bridge         | 26,900      | 0.051 (0.001)   | ****                 |
| FF4 Lebanon Junct. | 53,950      | 0.023 (0.001)   | ****                 |
| FF5 Radcliff       | 58,130      | 0.021 (0.001)   | 0.008 (0.013)        |
| FF6 Test Control   | 5,650       | 0.327 (0.006)   | ****                 |

\*\*\*\* No ground motion measurements were made, and the airblast was recorded with sound level meters.



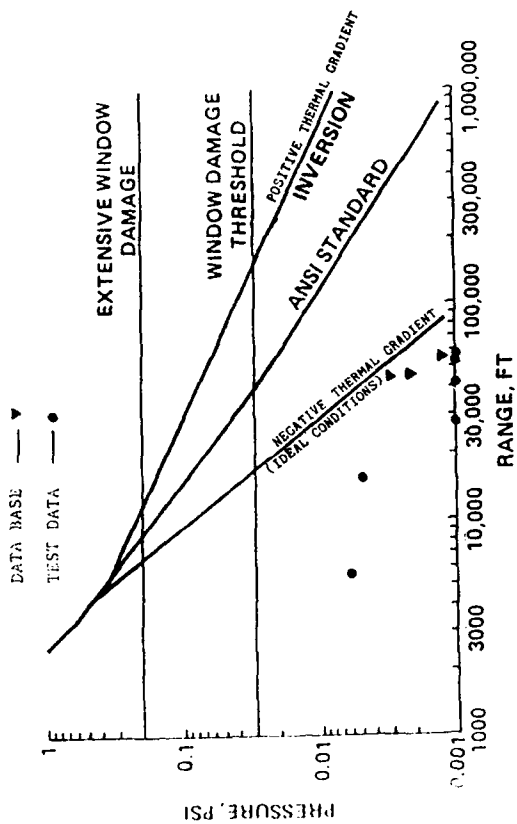


Figure 2. Far-field airblast predictions and results for 50-ton tests.

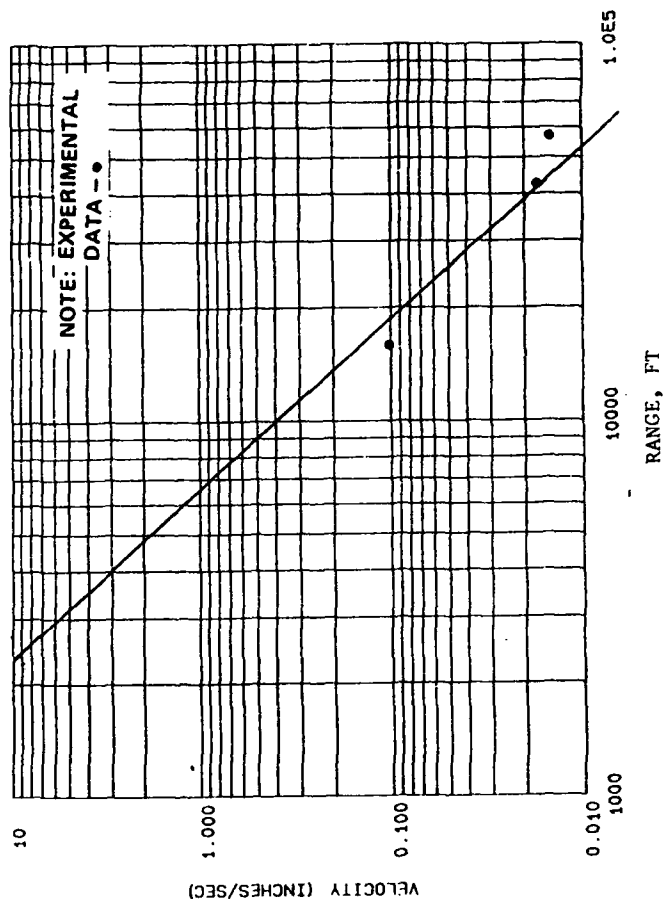


Figure 3. Far-field ground-shock predictions and results for 50-ton tests.

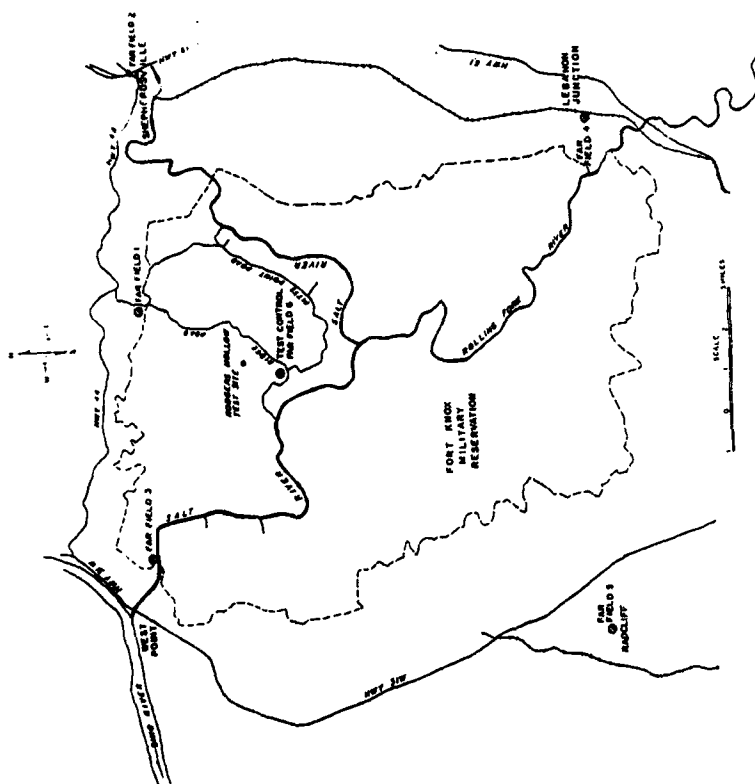


Figure 1. Far-field measurement locations.

## EXTERNAL SHOCK MITIGATION FOR BURIED STRUCTURES

Henry S. McDevitt, Jr.

U.S. Army Engineer Waterways Experiment Station  
Vicksburg, MS 39181-0631

### ABSTRACT

External Shock Mitigation (ESM) is being studied as a possible means of retrofitting existing buried structures to provide additional protection from ground shock. As part of this study, two tests were conducted on four ESM models and a control structure. The test articles were placed at a common distance and subjected to the ground motions created by a buried explosive charge consisting of 2,000 pounds of nitromethane (NM). Adequate instrumentation data were obtained to assess the response of the four ESM models. The assessment relied heavily on direct comparison of horizontal motions measured in the models, with similar measurements in the control structure. From the tests, it was observed that peak accelerations were reduced by a factor of 5 by the ESM. However, the particle velocities and displacements were not significantly affected by the ESM.

### INTRODUCTION

#### Background

The ESM Test Series was initiated to explore various shock mitigation concepts. Expanded polystyrene concrete with fly ash (EPSCFA) was selected as a candidate material from which to fabricate some of the ESM conceptual models. The concepts that were investigated were EPSCFA piles, EPSCFA backpacking, and air-filled excavations exterior to a structure.

The effectiveness of the ESM concepts defined above was assessed by two field tests and analytical analyses. Both tests contained five models as follows: a control structure, EPSCFA piles, EPSCFA backpacking, EPSCFA-filled moat, and an open moat. These models were placed at a common distance and subjected to the ground motions created by a buried explosive charge consisting of 2,000 pounds of NM.

#### Objective and Approach

The primary objective of the test program was to perform simple proof-of-principle tests on four candidate ESM concepts and one control structure. The results were to be used to select one or two of the more promising concepts for further testing at larger scale.

Two tests were conducted on five model structures. In each test, the primary structural loading came from a buried charge of 2,000 pounds of NM. Free-field and structural accelerometers were used to obtain data produced by these tests.

### CONCEPT DESIGN AND FABRICATION

#### Design Philosophy

The four candidate ESM systems fielded in the two tests (EZ-2 and EZ-3) fell under two different design concepts. Three systems (the backpack, filled moat, and soft piles) fell under the concept of energy absorption and rarefaction. In this concept, shock mitigation is achieved by absorption and rarefaction of the shock energy as well as isolation of the structure from motion and shock inputs. To achieve the desired results for the three systems listed above, EPSCFA with a density of 35 pcf was chosen as the candidate material. The fourth system, namely the open moat, relied only on the isolation of the structure from external shock and thus fell under the concept of isolation.

#### Gage Canister Fabrication

The gage canisters for the ESM tests were fabricated as per the design drawing shown in Figure 1. The canisters consisted of nominal 12-inch-diameter schedule 80 steel pipe in 6-foot lengths with wooden inserts in the center.

Four-by-four cedar timbers were glued and bolted together and then planed to form the inserts. A groove in the center of the inserts contained aluminum gage mounts to which accelerometers were installed (Figure 2). The completed inserts (Figure 3) were placed in the steel pipes, and the pipes were filled with epoxy and BI-WAX. These materials served as water proofing and as a shock absorber for the gages.

#### Concept Fabrication

The concepts fielded in the ESM tests are shown in Figure 4. Fabrication of ESM-1 and ESM-2 involved casting 35-pcf EPSCFA into cylindrical forms, which were removed at the test site. The open moat (ESM-3) concept was fabricated by using two 3/16-inch-thick A-36 steel cylindrical

liners. Fabrication of the piles for ESM-4 involved casting 35-pcf EPSCFA into fourteen 8-inch-diameter by 7-foot-long PVC pipes. These pipes were split and removed in the field.

#### EXPERIMENTAL PROCEDURES

##### Test Bed Description and Explosive Source

The test beds for EZ-2 and EZ-3 were located about 200 feet apart. Locations were chosen based on water table requirements. A seismic refraction survey indicated an average water table depth of 6.0 feet for EZ-2 and 5.9 feet for EZ-3.

The direct-induced explosive source for both tests was 2,000 pounds of unsensitized NM. NM is a liquid explosive with an energy release slightly greater than TNT on a mass basis. The NM was placed in a buried, thin-walled, steel, cylindrical tank. A 1.25-pound charge of Composition 4 was used as a central initiation source.

##### Measurements

There were a total of 74 channels of active instrumentation on both tests. Measurements included free-field and structural acceleration. Low-range (2-10 kg) Endevco Model 2264A accelerometers were used to make the required measurements.

##### Field Placement of Models

Test articles were placed in the test bed as shown in Figure 5. Figures 6 through 10 show the filled moat, open moat, backpacked, control, and pile concepts, respectively, after being placed in the test bed. After all concepts and accelerometers were in place, the test bed was graded to the proper elevation.

#### TEST RESULTS

##### Field Observations

The results from both tests were nearly identical. Average crater diameter for the first test was 70.5 feet and 72.7 feet for the second test. None of the nonresponding instrumentation canisters received any damage. The ESM material, EPSCFA 35, that surrounded the ESM-1, ESM-2, and ESM-4 concepts responded in an identical manner. The material was broken into individual pieces and strewn throughout the test areas. There was no visible evidence that any crushing of the material had occurred. Figure 11 shows a posttest view of the ESM-1 model.

##### Data

Gage survivability on EZ-2 was excellent; but only fair on EZ-3. However, the quality and quantity of data produced were sufficient for determination of the motions of the four ESM concepts and the control structures. The assessment of the ESM concepts relies heavily on direct comparison of horizontal motions measured in the concepts, with similar measurements in the control structure. Inspection of the data traces, Figures 12 through 16, provides the following observations.

- Apart from slight timing differences, the control structure velocities and displacements for both tests were virtually the same. This lends confidence in the measurements including the data processing.
- Velocities were noticeably higher for the ESM concepts than for the control structures.
- Displacements were only slightly greater for the ESM concepts than for the control structures.
- Peak accelerations were very effectively mitigated by most of the concepts with values ranging from about 10 to 25 percent of the control structure horizontal acceleration peaks.
- The open moat concept provided considerable delay in arrival of peak velocity and growth of displacement, yet the peak velocity was not attenuated but exceeded the control velocity.

#### CONCLUSIONS

The ESM concepts proved to be effective in reducing accelerations by a factor of about 5. Velocities were slightly higher for the concepts than for the control structures with displacements, being about the same for both.

Crushing of the EPSCFA material was anticipated, but did not occur. The material broke into individual pieces rather than crushing as a single mass.

ESM methods seem to be effective in reducing structural accelerations and may be useful for this purpose. Further study is needed to determine the cost effectiveness of these methods and to determine if a material other than EPSCFA would be more useful.

#### ACKNOWLEDGMENT

The author gratefully acknowledges permission from the Office, Chief of Engineers, to publish this paper.

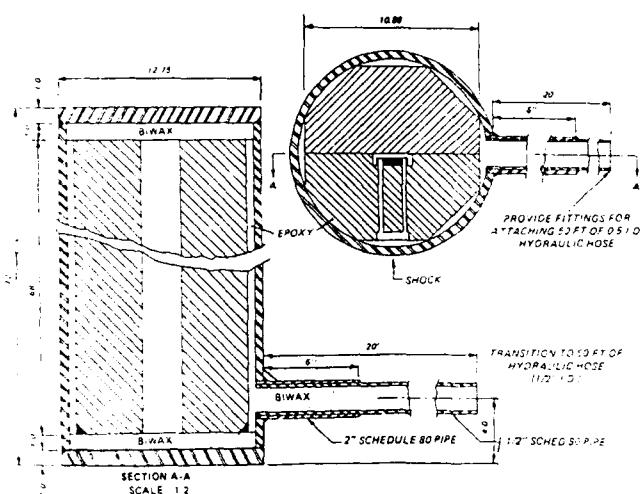


Figure 1. Gage canister design drawing.



Figure 2. Gage mounts with accelerometers in place.

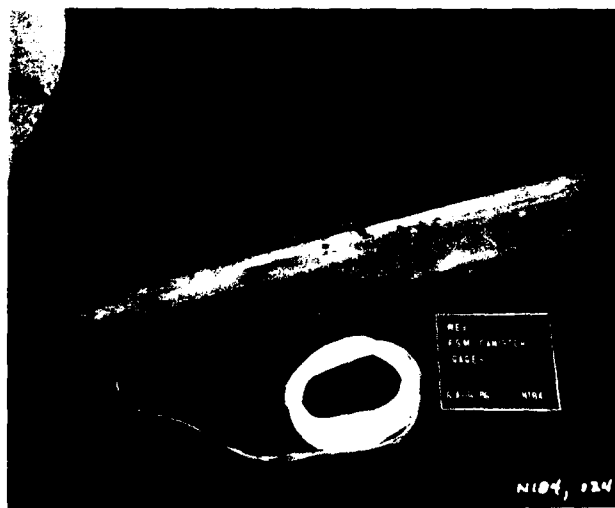


Figure 3. Completed canister insert.

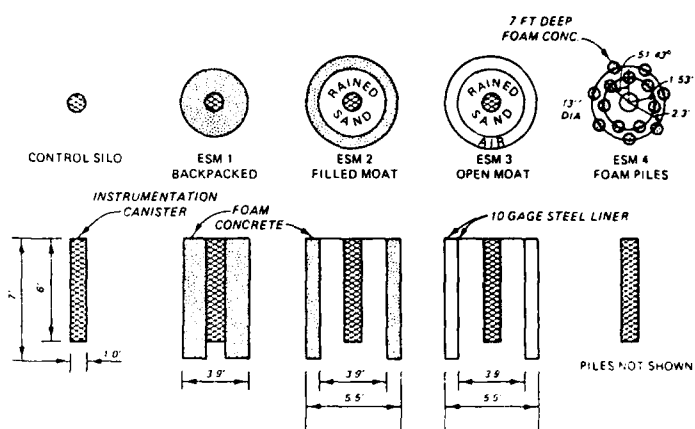


Figure 4. ESM concepts.

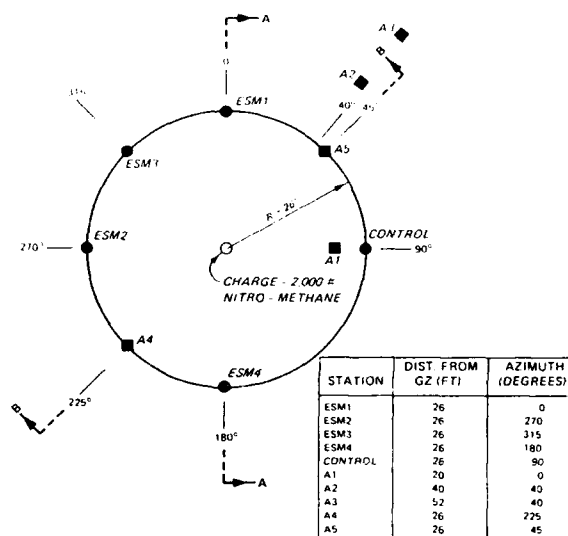


Figure 5. EZ-2 test bed layout.



Figure 6. Filled moat in the test bed.



Figure 7. Open moat after being placed in the test bed.



Figure 8. Completed placement of the backpacked concept.



Figure 9. Completed placement of the control structure.



Figure 10. Completed foam pile concept.



Figure 11. Closeup view of the backpacked concept.

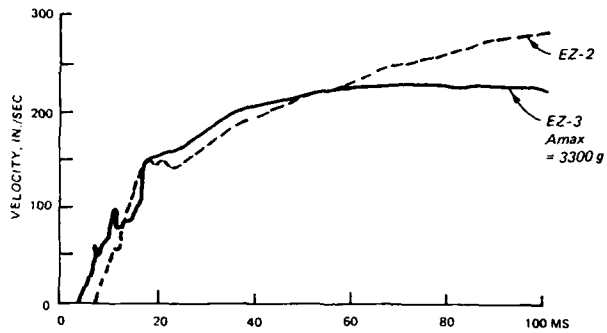
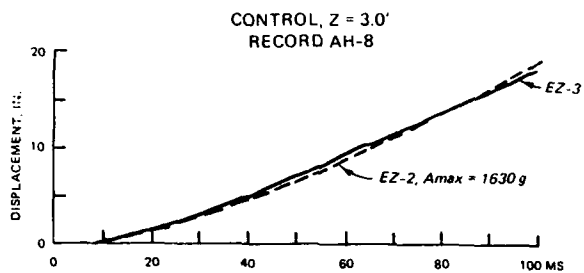


Figure 12. Control structure, Gage AH-8.

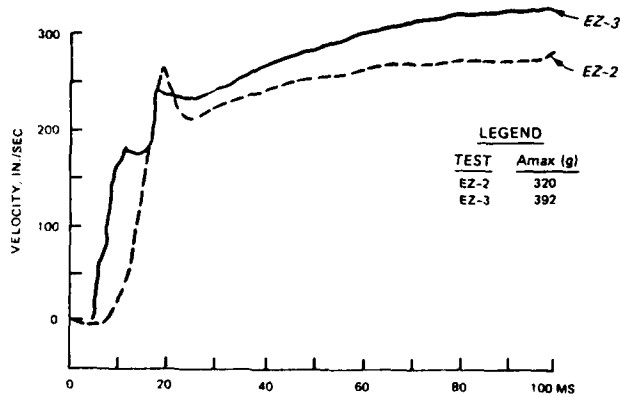
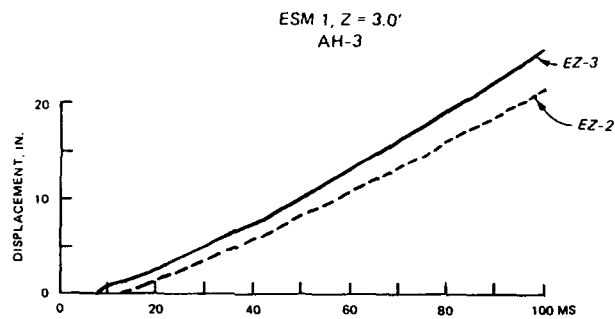


Figure 13. Backpacker concept, Gage AH-3.

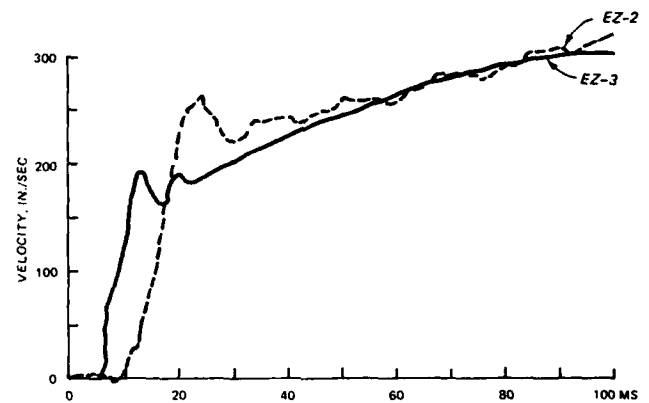
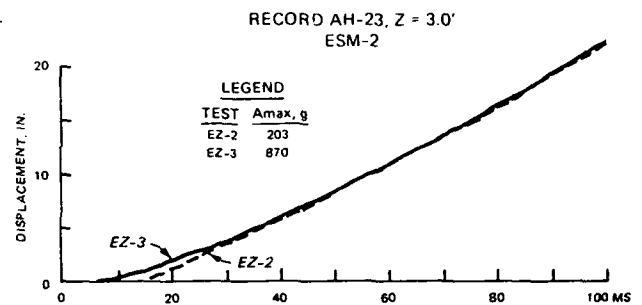


Figure 14. Filled moat concept, Gage AH-23.

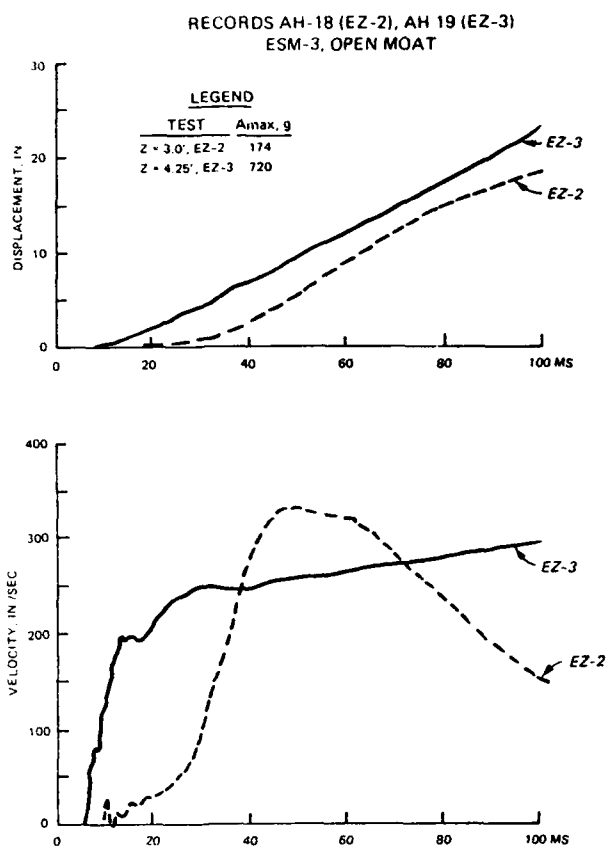


Figure 15. Open moat concept, Gages AH-18 and AH-19.

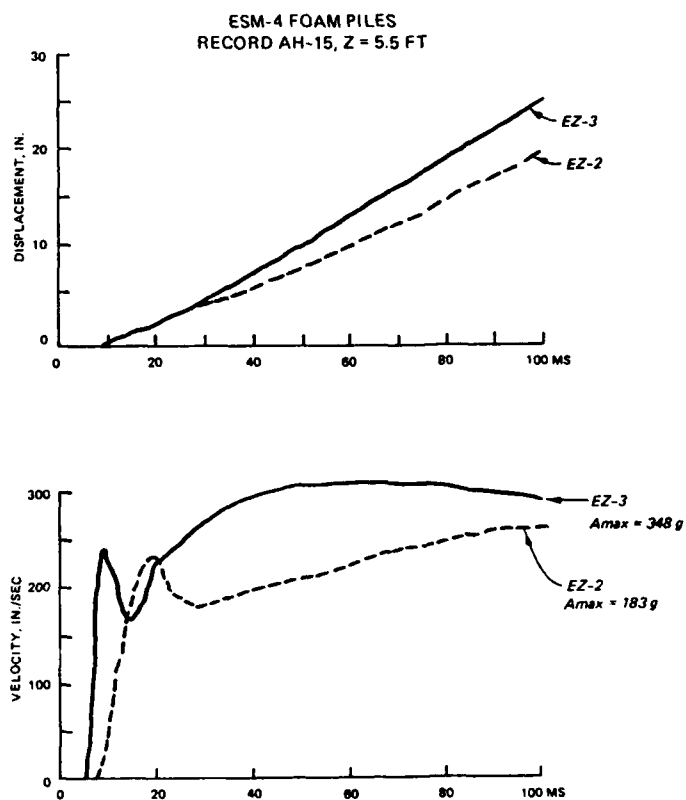


Figure 16. Foam pile concept, Gage AH-15.

# The Response of an Aircraft Shelter to a Buried Explosion 3D Coupled Simulation

W. Pfrang, W. Bergerhoff, H.J. Schittke

Industrieanlagen-Betriebsgesellschaft mbH  
Einsteinstraße 20, D-8012 Ottobrunn, West Germany

## Abstract

This contribution is dealing with the problem of a charge detonating near the foundation of an aircraft shelter after penetrating into the adjacent soil. Following a series of precalculations a load case with three-dimensional explosion geometry is investigated to analyse the essential phenomena of the explosion in soil and the developing soil-structure interaction problem. Results are given in the form of transient flow fields, load history data and structural response characteristics in terms of displacements, distortions and shock response spectra.

## Introduction

The investigation of the detonation of a buried charge below the foundation of a shelter structure has to include very complex dynamic soil-structure interaction phenomena due to the combined effect of explosive shock wave and the expanding motion of the gaseous reactive products. Additionally highly non-linear material stiffness and inertia properties in the structural elements make it necessary to include the local deformation behaviour and its distributed soil reaction effects in the investigation. It is evident that the detailed analysis of a problem of this complexity necessitates the application of sophisticated simulation tools.

Based on extensive experience in the field of explosively induced 3D fluid-structure interaction the coupled code **DYSMAS/ELC** [1,2] is used for the analysis of the problem at hand. To take care of special phenomena arising from this case, several extensions of the internal code models had to be included which will be shortly described below.

## Numerical Models

The code **DYSMAS/ELC** simulates the real-world physical phenomena by integrating the fundamental conservation equations of mass, energy and momentum using state-of-the-art mathematical algorithms. A Eulerian FD-mesh in space/time-fixed coordinates is used for the description of the motion of explosive gases and 3-phase soil components as well as the propagation of the detonative shock wave. The structural behaviour uses a FE-mesh for the investigation of the resulting high-transient deformation of the shelter structure and the assessment of the related stress-strain behaviour under the explosive load distribution in the surrounding soil.

Special care was taken concerning the description of the materials involved with special compound elements, concrete modelled according to **Willam/Warnke** [3], and membrane elements for the consideration of the steel reinforcement structural parts. These elements were modelled using an elastic-plastic description including strain hardening and strain rate dependency. The three-phase soil used a high-dynamic hydrodynamic description for the material components air, water and solid quartz particles with free slip-flow of the respective components. The deviatoric elasto-plastic soil behaviour was modelled according to a non-linear **Coulomb-cone**, with parameters depending on hydrostatic pressure and the local compaction [4].

A special coupling module as part of the code **DYSMAS/ELC** performed the task to transfer the hydrodynamic and deviatoric load information from the soil across the interface to the adjacent structural elements, and, vice-versa, the structural motion information back to the surrounding



soil. To account for separation effects between the structure and the adjacent soil, special care was taken concerning the exchange of energy and momentum depending on the local relative motion. Due to the highly interactive nature of the simulated processes it was necessary to perform this complex task throughout the simulation of the total event within each time step, starting from an initial steady-state distribution of gravity-induced pressure and deviatoric forces.

### Preliminary Studies

Prior to the simulation of the total three-dimensional shelter structure the behaviour of the DYSMAS/ELC code was tested and validated against the results of dedicated experiments [5,6]. These problems described the behaviour of a 4m-diameter circular plate of reinforced concrete, loaded by the detonation of a small charge of TNT buried at a certain distance below the center of the plate (fig.1). The experiments showed that - due to the effect of the explosive load - the concrete plate was thrown to a maximum height of about 50 cm with a large crater forming below.

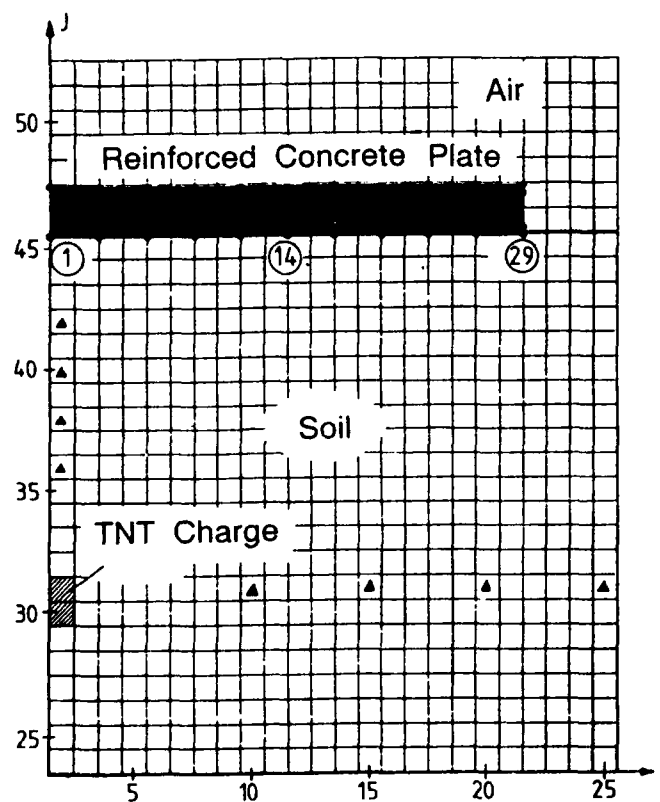


Fig.1 Detonation Geometry

The simulation of the same problem (described in more detail in [7]) showed that the load on the structure consisted of essentially two parts: a first high-amplitude peak of short duration from the detonative shock was followed by a lower-amplitude pressure pulse of much longer duration (fig.2). This latter pulse results from the dynamic pressure forces of the soil material pushed against the structure by the expansion of the explosive gases. The amplitudes of these two load constituents were found to decay very fast with distance from the charge, with propagation velocities dropping far below the 100 m/s value for the larger distances (fig.3).

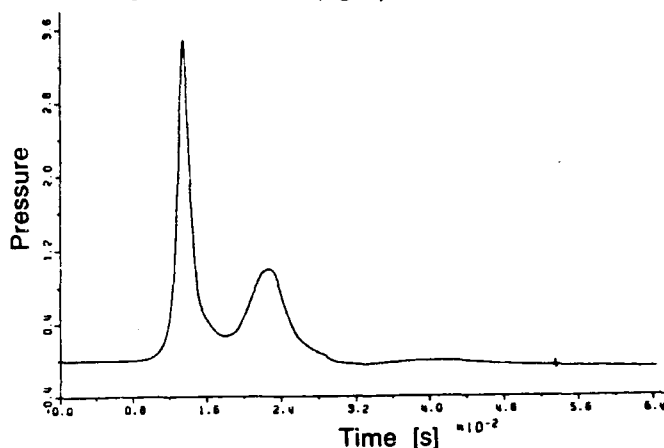


Fig.2 Pressure Load Transient at Plate Center

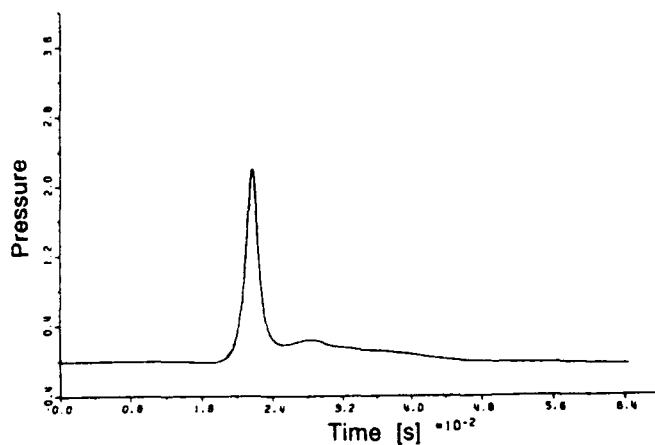
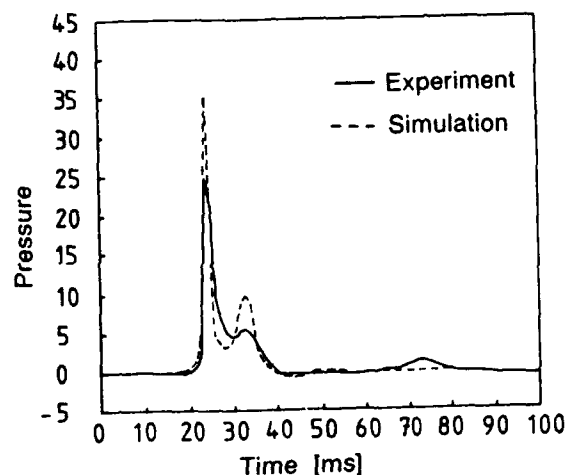


Fig.3 Pressure Load Transient at Intermediate Point

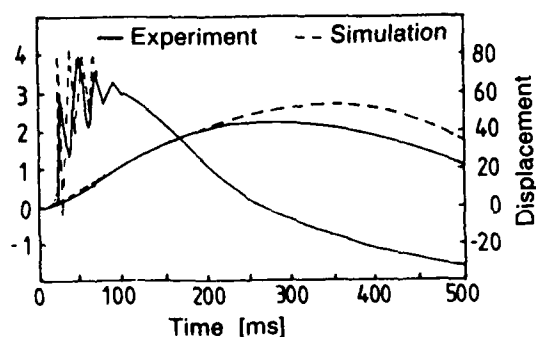
Parallel investigations showed that the dynamic parameters of the load transients as well as their propagation velocities and respective decay rates varied considerably with the soil constitu-

tion, especially in connection with the actual values of porosity and water content [8]. On the other hand the local impulse density was found to be influenced to a much lesser degree by these variations. A soil constitution of 62 % solid particles of quartz, 14 % water and 24 % air, with an internal friction angle of about  $30^\circ$  was found to give an appropriate description of the experimental ambient conditions.

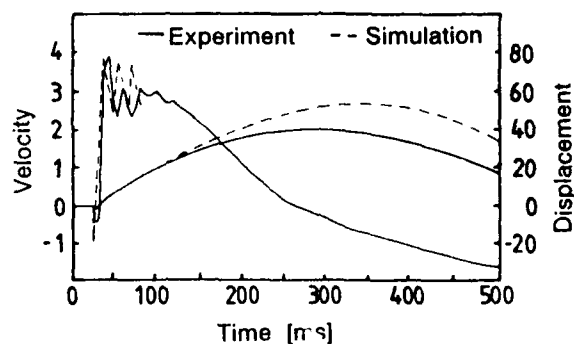
The results of the simulation were highly consistent with the experimental data, showing the same transient load characteristics as visualised in the comparison of pressure transients (fig.4). Additionally the motion of the flying concrete plate is simulated with good accuracy as demonstrated in figs.5 and 6 for two positions on the plate surface.



**Fig.4** Comparison of Pressure Load Transients at Plate Center



**Fig.5** Comparison of Velocities and Displacements at Plate Center



**Fig.6** Comparison of Velocities and Displacements at Circumferential Point

As evident from the velocity transient results of both, simulation and experiment, the soil-structure loading took effect between about 50 and 100 ms. Here the transients show a high degree of qualitative and quantitative agreement up to the point that they show the same velocity oscillation phenomena. After about 150 ms the plate has separated over its total width from the underlying soil. At this point the simulation could be stopped and extrapolated using a free-flight motion behaviour assumption based on the effect of gravity forces, visible also in the experimental results. The residual larger differences in this time-regime can be accounted to neglect of air resistance in the numerical extrapolation, but predominantly to drift effects in the double integrated acceleration measurement data, as evident from the available high-speed camera exposures.

## Shelter Structure Load Simulation

### Preliminary Considerations

The FE-model of the aircraft shelter is shown in fig.7 in an exploded representation. It is designed especially to the case of a buried explosion, while for other load-cases adopted element meshes were used. The shelter construction is made of reinforced concrete with a bottom plate containing tension ties. These ties compensate the horizontal forces from the roof arc by pre-stressing.

The foundations are modelled by 8-node continuum elements. Additionally the reinforcement

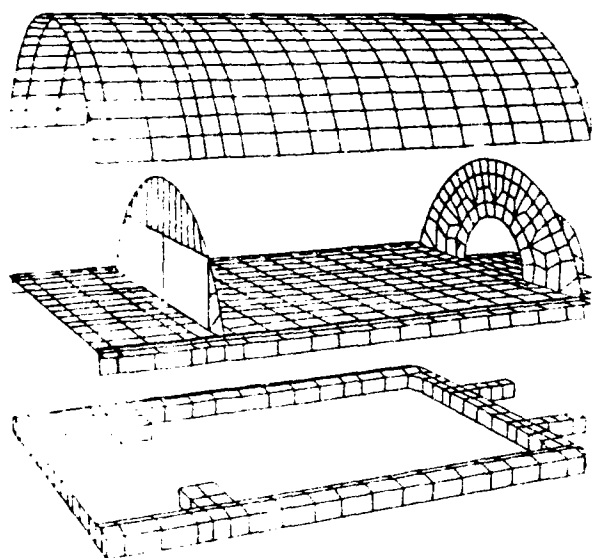


Fig. 7 Finite Element Model of the Aircraft Shelter

consisting of membrane elements is merged to the concrete elements. The bottom plate has only a weak reinforcement on the upper side. The bottom plate as well as the rear wall, the exhaust channel and the roof is modelled by specific compound plate elements where the reinforcements are accounted for by an orthotropic layer formulation. The tension ties mapped by rods are fixed to the foundations on both sides of the arc while they are tied to the nodal points of the bottom plate. During the static prerun tied nodes in lateral direction are released and fixed again after the initial state of prestressing is established. The gate in the front wall is represented by two rigid body elements connected with the reinforced concrete wall on both sides of the building and fastened centrally by a spring element with the properties of the locking device.

Figs. 8 to 10 give an overview of the coupled problem space by three sectional views through the Eulerian grid including the structural interface of the aircraft shelter. The Eulerian grid with a size of about 40000 cells is designed to a total simulation time up to 230 ms and contains the explosive, the air above ground and the three-component soil as described above. In the vicinity of the charge equidistant meshing is used with increasing cell sizes in remote regions.

In this complex numerical investigation two pre-calculations had to be carried out in order to define the initial conditions for the 3D-coupled

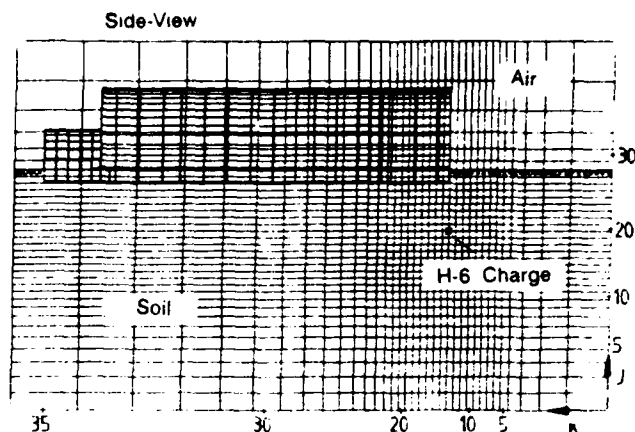


Fig. 8 Coupled Problem Space (Side-View)

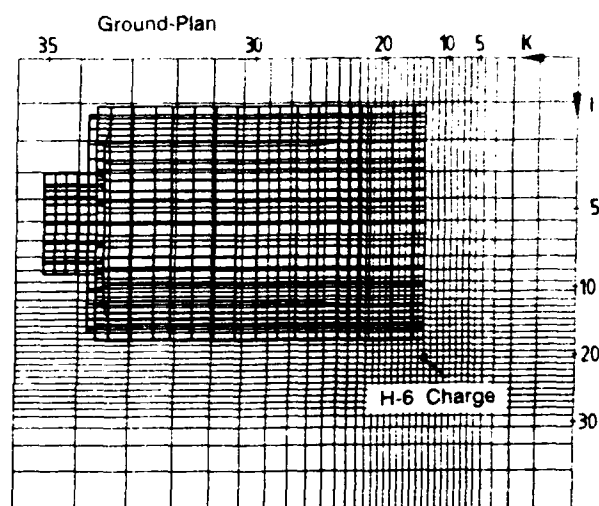


Fig. 9 Coupled Problem Space (Ground Plan)

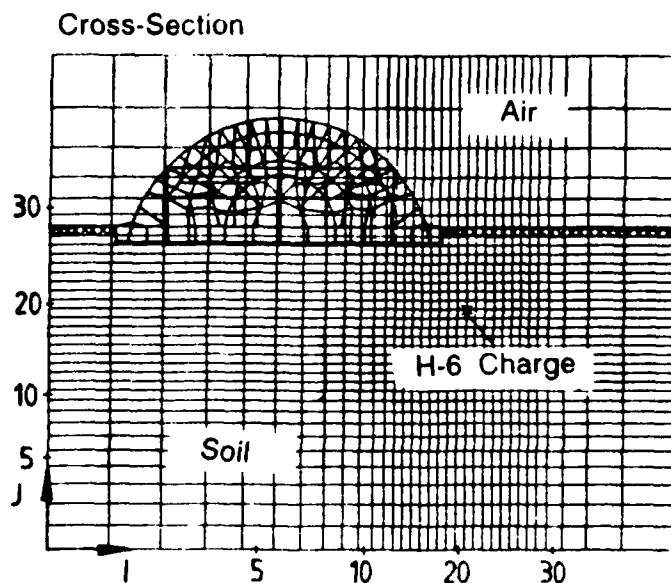


Fig. 10 Coupled Problem Space (Cross Section)

simulation. This included the free-field precalculation of the charge explosion and the propagation of the resulting shock wave through the soil up to the structural interface. In accordance with the actual problem domain this was done using a series of interconnecting rezoned axially symmetric grids of growing sizes. The use of this first decoupled step greatly reduces computing time with the additional effect of giving flow field distributions of higher accuracy compared to starting the whole simulation in the final 3D-grid.

Parallel to these investigations a static prerun was performed to establish the initial prestressed state of the structure under gravitational loads. This second step was carried out using dynamic relaxation methods [9].

### Soil-Structure-Interaction Investigation

Based on the initial state derived from the precalculations described above, a three-dimensional coupled simulation was added to assess the effect of the detonative load on the shelter structure. The shock propagation and the gas bubble expansion are shown by 4 snap-shots of a cross sectional view through the center of the charge showing material contours and velocity vectors in the soil (figs. 11 to 14). At the start of the 3D-coupled simulation at 16.74 ms after ignition the shockwave is almost spherical and the gas bubble already is of remarkable size (fig. 11).

During the further process the material velocities as well as the velocity of the shock front are

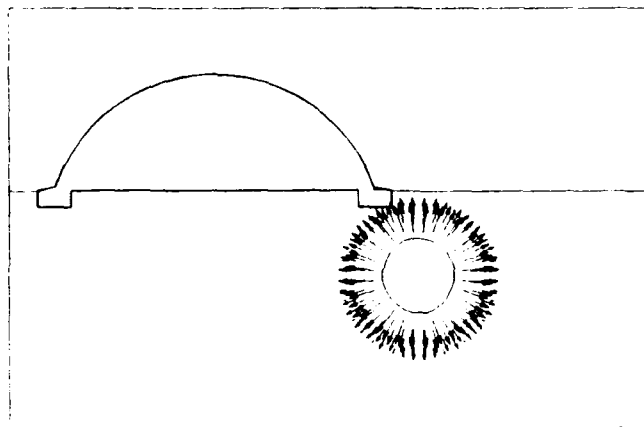


Fig. 11 Soil Velocity Flow Field ( $t = 16.7$  ms)

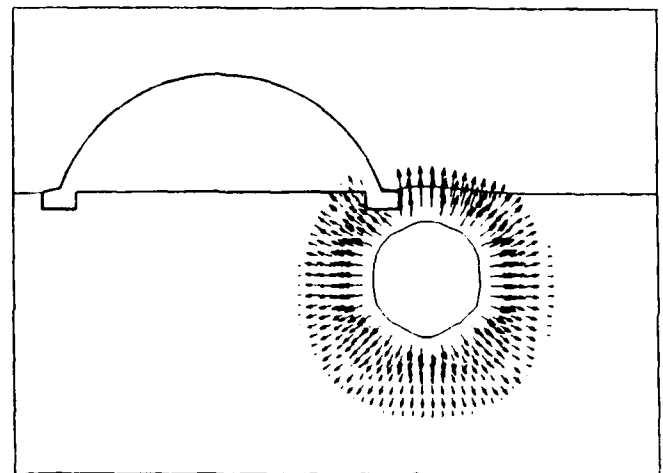


Fig. 12 Soil Velocity Flow Field ( $t = 58.8$  ms)

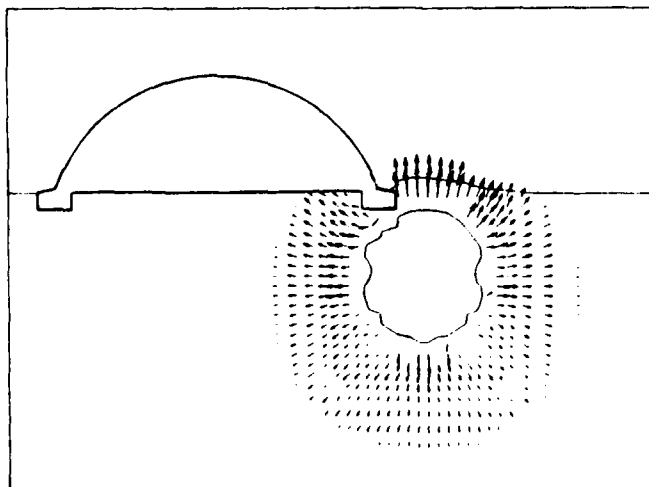


Fig. 13 Soil Velocity Flow Field ( $t = 91.2$  ms)

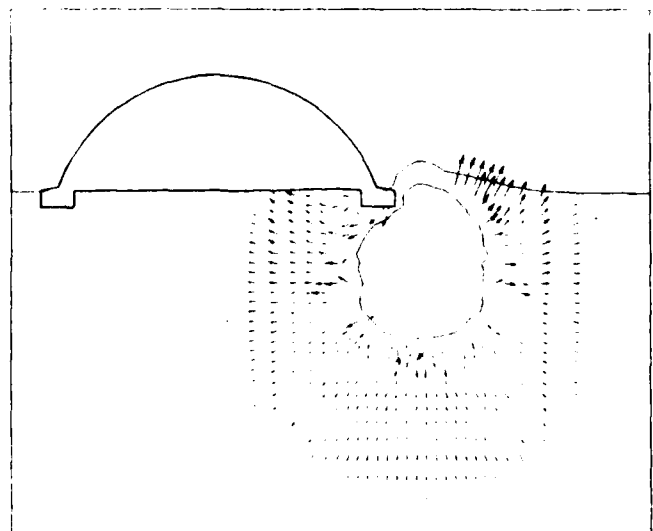


Fig. 14 Soil Velocity Flow Field ( $t = 142.2$  ms)

decreasing considerably caused by dissipation effects in the soil. For the later time points the gas bubble is expanding predominantly in the direction of the free surface pushing up under the foundation and causing increasing surface lift beneath the foundation. The small soil layer on top of the gas bubble is cracking in the further course of time initiating the blow out of the gas. Figs. 15, 16 give two corresponding pressure distributions in similar representation where the effects of energy dissipation due to the friction behaviour of the soil become evident.

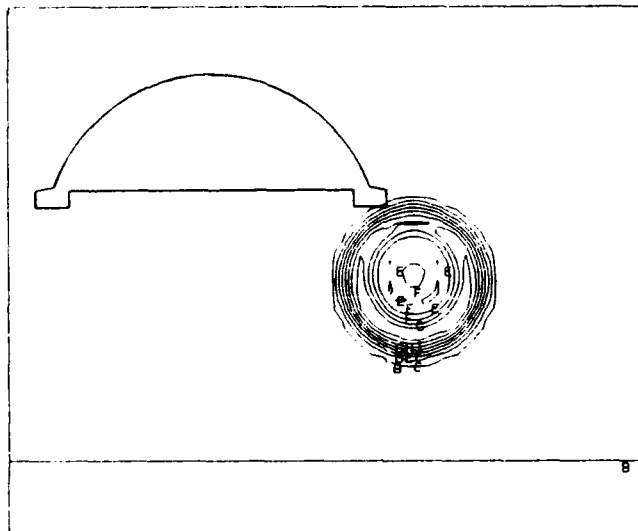


Fig. 15 Soil Pressure Distribution ( $t = 16.7$  ms)

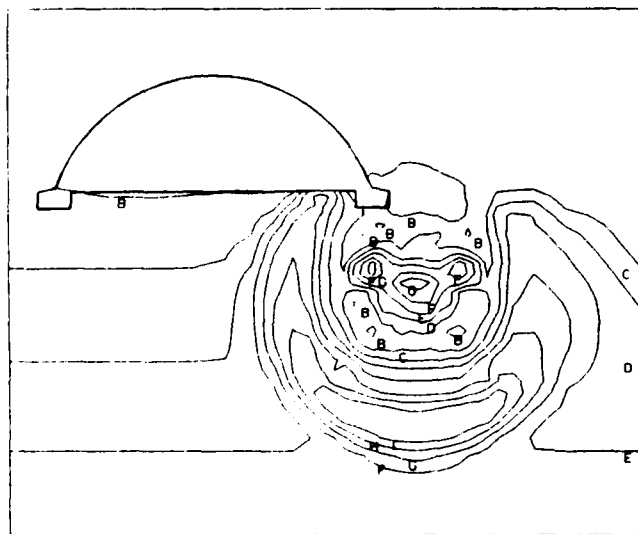


Fig. 16 Soil Pressure Distribution ( $t = 91.2$  ms)

Typical pressure transients at the structural interface are shown in Figs. 17, 18. At the corner of the foundation close to the charge a high pressure peak of short duration is observed, followed by a second pulse resulting from the dynamic interaction. Up to 80 ms a rather low pressure is acting in this region, caused by the expanding gases pushing the soil against the structure. At a nodal point of the bottom plate the shock wave which is diffracted around the foundation arrives at a rather late time with a reduced amplitude and longer duration. Not only the effect of energy loss due to dissipation is responsible for this change, but also the fact that the observed point of the bottom plate is starting to move upwards long before the arrival of the shock wave due to structural shock.

The separation of the bottom plate from the soil in this phase leads to a pressure drop (see Fig. 18) and this gap has to be filled up before the shock wave is able to act on the bottom plate. The second increase in the time range between 110 and 160 ms is caused by the dynamic soil pressure against the bottom plate. From resulting force transients at certain nodal points it is evident that the hydrostatic pressure contribution is clearly prevailing that of the deviatoric stresses in the loading.

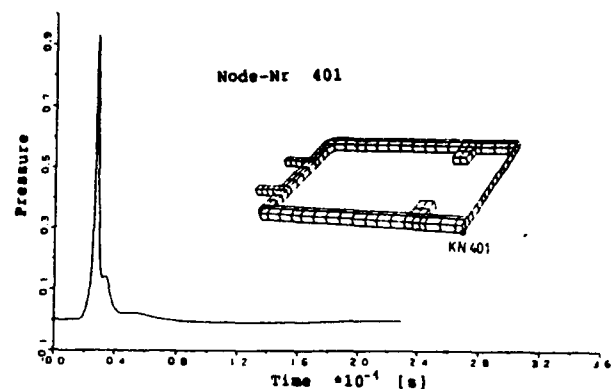


Fig. 17 Interface Pressure at the Foundation

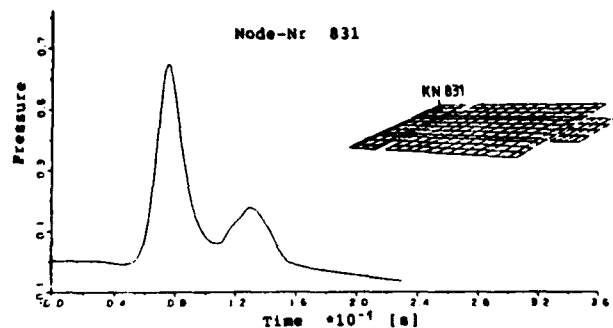


Fig. 18 Interface Pressure at Bottom Plate

In dynamic interaction problems the resulting load transients of the structure usually are closely connected with the corresponding displacement transients. An assembly of displacement curves from nodal points of the foundation and of the bottom plate is shown in fig.19,20. Slight bending occurs along the lateral foundation, but the vertical displacements mainly result from combined rotations of the whole structure around the lateral and the longitudinal axis. Only the closest point with respect to the charge position shows local response on the initial shock wave. In all other locations the ground shock is arriving with a time delay to the structural shock. There is also a slight torsion in the frontal part of the foundation caused by the loading acting first at the outer edge and afterwards moving towards the center of the shelter with decreasing energy and impulse content.

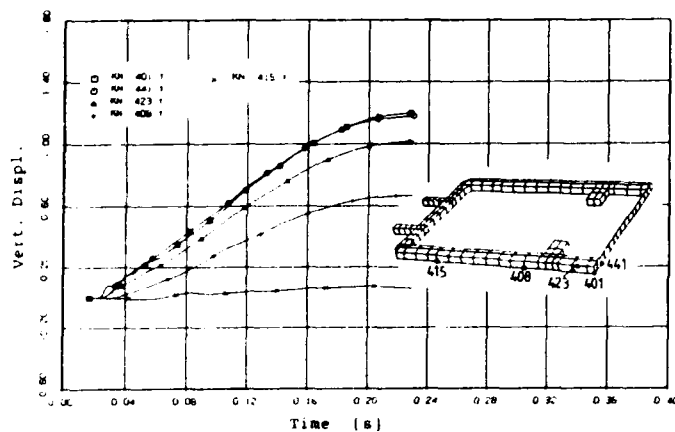


Fig.19 Vertical Displacements at the Foundation

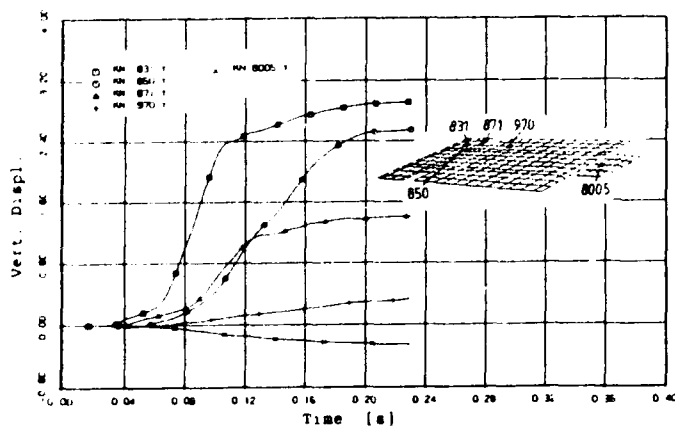


Fig.20 Vertical Displacements at Bottom Plate

The bottom plate is first accelerated by the structural shock and the motion of the foundation. The ground shock wave causes a second steeper increase of the displacements at the flexible

bottom plate in the vicinity of the charge, while the rear end of the shelter is moving downwards by the global rotations. Maximum displacements are reached in all parts after 230 ms. The displacement gradients especially in the region between the lateral foundation in the front of the building and the door foundation are so severe, that plastic flow occurs in the reinforcement and the concrete is damaged by tension failure as evident from fig.21,22, where transients for the **von Mises** equivalent strain and stress for the reinforcement are shown.

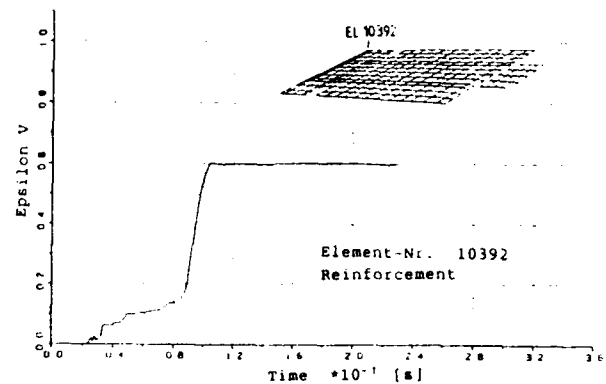


Fig.21 Von Mises Strain Reinforcement of Bottom Plate

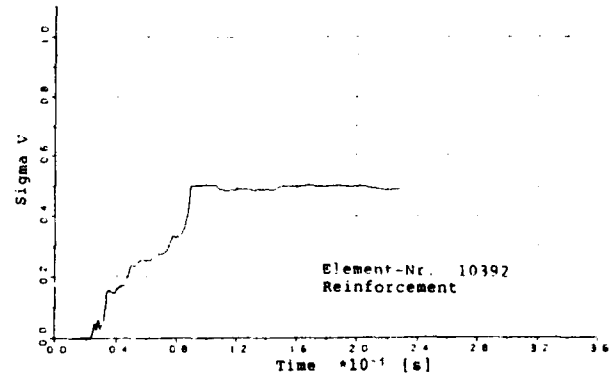
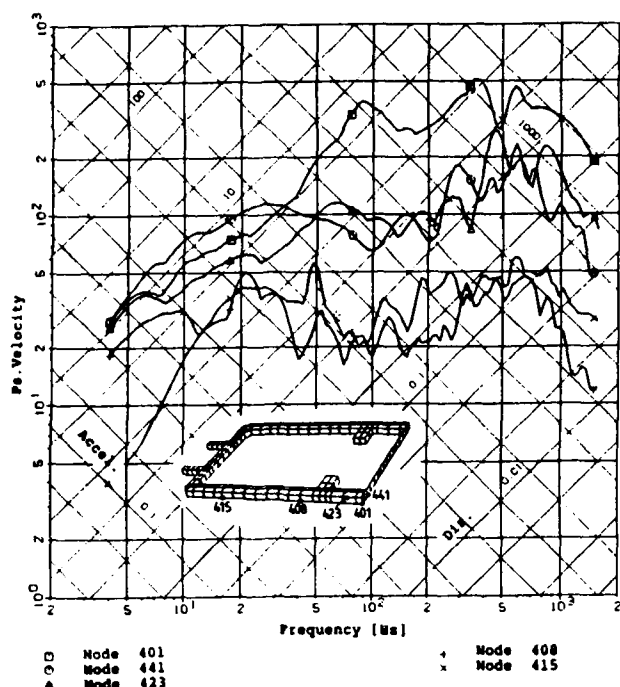
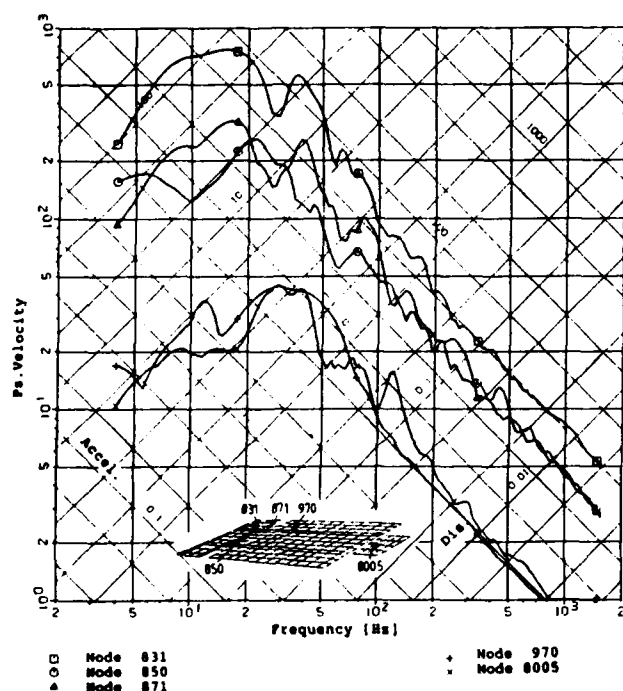


Fig.22 Von Mises Stress Reinforcement of Bottom Plate

Especially in the case of high-dynamic loads as investigated here the shock response behaviour is strongly depending on the location in the structure and the local properties in terms of stiffness and mass. An assembly of shock response spectra (SRS) according to the displacements shown in fig.19,20 is given in fig.23,24. The high and low pass behaviour of the different parts of the structure such as stiff foundations and flexible bottom plate is very distinct. Equipment attached to the stiff parts will be affected predominantly by high accelerations in the high frequen-



**Fig.23 Maximax Shock Response Spectra (Foundation)**



**Fig.24 Maximax Shock Response Spectra (Bottom Plate)**

cy range, while devices mounted on the flexible parts are loaded by high relative displacements at low frequencies. The response levels are decreasing with the distance from the primarily affected location. The valuation of the vulnerability of discrete equipment - fixed or elastically

bedded with respect to the design criteria or damage limits - could be carried out by the SRS.

## Conclusions

Based on the results of numerical simulations as given here the shock response and the structural damage due to a specific load case can be evaluated realistically. Furthermore the derivation of design criteria is possible. Another advantage of numerical investigation is the estimation of secondary damage of the installed equipment, the aircraft, and the operating staff. The shock loading of the equipment can be examined directly using shock response spectra or by adding separate simulations using substructures. In this case the results from the coupled calculation for the total shelter represent realistic excitations.

## Literature

- [1] The Program Family DYSMAS  
B-TF-V197/2, IABG, Munich 1986
- [2] Bergerhoff W., Mohr W., Pfrang W., Scharpf F.  
The Program DYSMAS/ELC and its Application on the Underwater Shock Loading of Vessels  
Proceedings of the First Intercontinental Symposium for Maritime Simulation and Mathematical Modelling  
Munich, June 3-5, 1985 (Springer Verlag)
- [3] Willam K.J., Warnke E.P.  
Constitutive Model for the Triaxial Behaviour of Concrete Structures Subjected to Triaxial Stresses  
Bergamo, 1974
- [4] Schittke H.J.  
Modellierung der hochdynamischen Kompaktierung von Schüttungen im Rahmen von DYSMAS/E-Simulationen  
B-TFV-226, IABG, Munich 1986
- [5] Wösten  
Bodendruck- und Beschleunigungsmessungen beim Anspringen von Flugzeugshelterplatten mit Integration der Signalverläufe  
Meßprotokoll E 91-2, Nr. 123/86, 1986
- [6] Hagsphil  
Auswertung der Meßfilme zur Anspringung Flugzeugshelter  
Meßprotokoll E 91-2, Nr. 75/86, 1986
- [7] Pfrang W., Bergerhoff W., Schittke H.J., Glaser F.  
Die numerische Simulation einer verdämmten Bodendetonation  
Interaktion konventioneller Munition mit Schutzbauten  
Internationales Symposium Mannheim, März 1987
- [8] Krassin D.  
Überprüfung von Flugzeugschutzbauten aus wehrtechnischer Sicht  
B-TF-2050, IABG, Munich 1986
- [9] Cassel A., Hobbs R.  
Dynamic Relaxation  
Proceedings of the Symposium of International Union of Theoretical and Applied Mechanics  
University de Liege, 1971

## BLAST LOADING FROM ARRAYS OF PARALLEL LINE CHARGES

Quentin A. Baker  
Wilfred Baker Engineering

Kathy H. Spivey  
Wilfred Baker Engineering

Dr. Wilfred E. Baker  
Wilfred Baker Engineering

Edward D. Esparza  
Southwest Research Institute

### ABSTRACT

Arrays of parallel line charges were evaluated as a system to defeat land mines. The arrays were designed to distribute the explosive mass over a large surface area, attempting to achieve better area coverage than the MICLIC line charge presently fielded. Experiments were conducted to determine reflected pressure and specific impulse at standoffs from two parallel Primacord<sup>®</sup> charges. Scaling laws were developed for such arrays, and the data were scaled. Trade-offs among charge weight, standoff, and line spacing were analyzed. Mach stem formation was examined. Uniformity of blast loading and peak overpressure between charges were greatly affected by the extent to which a Mach stem had formed when the shock waves reached ground surface. A scaled curve was developed to predict when a Mach stem was fully formed.

### INTRODUCTION

The purpose of this paper is to present experimental data concerning the blast output of a pair of parallel line charges. This information was developed as part of a program for the U.S. Marine Corps to develop an improved system for rapidly clearing a lane through a minefield. The system presently fielded is the MICLIC line charge. It consists of a single rather heavy line charge. The major drawback to MICLIC is that its effectiveness varies with distance from the line charge. This project is attempting to improve effectiveness by using many small line charges, achieving uniform area coverage. In essence, the objective is to more efficiently use the explosive mass of MICLIC by distributing it over a wide area.

A literature search was conducted in preparation for the project, and while a large body of knowledge was available for cord explosives or cylindrical charges, none existed for arrays of parallel line charges. The initial phase of this program, which is the subject of this paper, developed the basic blast output data needed to design a system using an array of parallel line charges.

### SCALING LAWS

A similitude analysis was performed prior to undertaking any experiments with parallel arrays of line charges to assist in the design of the test matrix, to minimize the number of tests, and to predict blast parameters for larger or smaller scale arrays from those tested. Scaling laws of blast phenomena have been widely discussed in literature.<sup>(1,2,3)</sup> Since many aspects of blast wave loading are well known, an abbreviated set of parameters which will suitably describe the testing of explosives arrays will be used. Figure 1 is a schematic of a portion of a line charge array above the ground surface and shows the choice of variables. The line charges have a spacing  $S$  and the array is located at a distance  $R$  above the ground. The parameters  $d$  and  $\theta$  in the figure represent the distance and angle, respectively, from

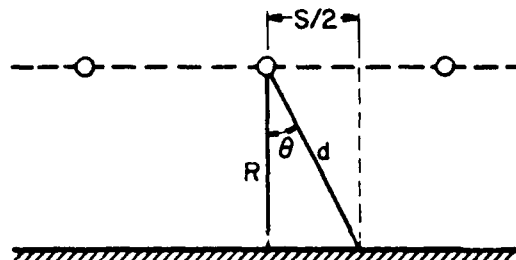


Figure 1. Schematic of a Portion of a Line Charge Array

a detonating cord to the ground midway between the projection of the cords on the ground. The explosive has an energy per unit length  $E_L$ , the cord length is  $L$ , and array width is  $W$ . The blast wave variables are reflected pressure  $P_r$ , reflected specific impulse  $i_r$ , duration  $t_d$ , and time of arrival  $t_a$ . Additional geometric parameters are needed to locate the pressure measurement points on the ground plane. The  $X$  direction is transverse to the array, and the  $Y$  direction is in the direction of detonation propagation. The origin is at a location midway between two parallel cords.  $X$  and  $Y$  are the geometric variables representing distance from the origin. Other parameters are atmospheric variables which will allow dimensionless scaling. The list of physical parameters is summarized in Table 1. Units in the table are dimensions of force  $F$ , length  $L$ , and time  $T$ .

Table 1. Physical Parameters for Line Charge Array

| Symbol     | Parameters                         |
|------------|------------------------------------|
| $\mu_i$    | Cross-sectional shape of explosive |
| $L$        | Length of explosive cords          |
| $P_o$      | Atmospheric pressure               |
| $E_L$      | Energy per length of explosive     |
| $S$        | Spacing between explosive cords    |
| $W$        | Width of array                     |
| $R$        | Height of array above ground       |
| $X$        | Gage location along array          |
| $Y$        | Gage location across array         |
| $\gamma_o$ | Ratio of specific heats in air     |
| $P_r$      | Reflected pressure                 |
| $i_r$      | Reflected specific impulse         |
| $A_o$      | Speed of sound in air              |
| $T_d$      | Duration                           |
| $T_a$      | Time of arrival                    |

The number of dimensionless groups is equal to the number of variables less the number of dimensions, or  $12 (15 - 3 = 12)$   $\pi$  terms. Using the Buckingham Pi Theorem<sup>(2)</sup> it can be shown that one set of  $\pi$  terms are those given in Table 2. The first



$\pi$  term requires that the cross-sectional shape of the explosive remain the same. The next three  $\pi$  terms deal with geometric similarity. That is, if any dimension (L, S, W, or R) is changed, every other array dimension must be changed in the same proportion to preserve the scaling relationship. Note that  $\pi$  terms 2 through 7 each contain only one variable describing array geometry, and that none of these terms contain any of the blast wave variables ( $p_r$ ,  $i_r$ ,  $t_d$ , and  $t_a$ ). These  $\pi$  terms were cast in this manner so they could be used as independent variables when designing the test matrix.  $\pi_8$  merely requires that the experiment be performed in similar gaseous environments and is definitely satisfied in any outdoor experiment.  $\pi_9$  through  $\pi_{12}$  are scaled response terms or air blast loading terms.

Table 2. Dimensionless  $\pi$  Terms for Line Charge Array

| Term   | Description                           |                            |
|--|---------------------------------------|----------------------------|
| $\pi_1 = \mu_1$                              | Similar explosive cross-section shape | Array Geometric Similarity |
| $\pi_2 = (L P_o^{1/2} / E_L^{1/2})$          | Scaled cord length                    |                            |
| $\pi_3 = (S P_o^{1/2} / E_L^{1/2})$          | Scaled cord spacing                   |                            |
| $\pi_4 = (W P_o^{1/2} / E_L^{1/2})$          | Scaled array width                    |                            |
| $\pi_5 = (R P_o^{1/2} / E_L^{1/2})$          | Scaled standoff                       |                            |
| $\pi_6 = (Y P_o^{1/2} / E_L^{1/2})$          | Scaled gage location along array      | Response                   |
| $\pi_7 = (X P_o^{1/2} / E_L^{1/2})$          | Scaled gage location across array     |                            |
| $\pi_8 = \gamma_o$                           | Ratio of specific heats               |                            |
| $\pi_9 = (P_r / P_o)$                        | Scaled reflected overpressure         |                            |
| $\pi_{10} = (i_r A_o / P_o^{1/2} E_L^{1/2})$ | Scaled reflected specific impulse     |                            |
| $\pi_{11} = (T_d A_o P_o^{1/2} / E_L^{1/2})$ | Scaled duration                       |                            |
| $\pi_{12} = (T_a A_o P_o^{1/2} / E_L^{1/2})$ | Scaled arrival time                   |                            |

The next step in the analysis is to decrease the number of parameters if possible. Above, it was shown that  $\pi_8$  is always satisfied, so it is not needed.  $\pi_1$  requires that we use the same explosive cross-sectional shape in model and full scale experiments. Circular cross-section cord explosive was always used, so this term is satisfied. In those cases where we are not concerned with edge effects in the direction of the explosion cord and where the array length is considerably greater than the standoff ( $L \gg R$ ),  $\pi_2$  and  $\pi_6$  are not necessary. The remaining relationships allow us to scale from limited experimental arrays to full scale arrays. The scaled response of an array can be described as a function of the scaled cord spacing ( $\pi_3$ ), scaled standoff ( $\pi_5$ ), and the location between strands on the ground surface ( $\pi_7$ ).

A relationship, which proved most useful in the design of the test matrix, is apparent from the scaled parameters. The arrays can be easily redesigned and their performance predicted whenever the explosive loading ( $E_L$ ) of the line charges is altered. For instance, if  $E_L$  increases by a factor of 4, line charge spacing and standoff increase by a factor of 2. Reflected pressure ( $\pi_9$ ) is unchanged, and reflected specific impulse ( $\pi_{10}$ ), duration ( $\pi_{11}$ ) and time of arrival ( $\pi_{12}$ ) each increase by a factor of 2.

#### TEST SET-UP AND INSTRUMENTATION

The line charge experiments were conducted at the Explosives Range located on the Southwest Research Institute campus. The experimental apparatus consisted of a horizontal, 2-inch thick, 6 x 6-ft square plate used to mount pressure transducers, and a 1-inch thick 3 x 6-ft plate used as the vertical reflecting surface. The horizontal plane was machined to accept up to 15 pressure transducers and to allow various relative positions for the reflecting surface. For each test configuration, ten reflected pressure measurements were made to characterize the blast loading from a single line charge.

Three different sizes of the explosive cord were used: 40, 100, and 400 grains/foot. The strand of explosive cord used on each test was positioned parallel to the horizontal and vertical plates. The explosive cord was suspended from each end by tying short peices of nylon string which in turn were pulled taut and tied to a square metal frame surrounding the experimental

apparatus. The frame was adjustable in the vertical direction to allow for different standoff distances from the line charge to the pressure transducer plate. The explosive cord was initiated at one end with a Reynolds RP-83 explosive bridgewire detonator. Figure 2 is a plan view sketch of the set up for one of the 51 experiments conducted.

The reflected pressure measurements on these tests were made with PCB Piezotronics Model 102A03 transducers. These piezoelectric gages used an acceleration-compensated, quartz sensing element coupled to a miniature source follower within the body of the transducer. They are capable of measuring peak blast pressures up to 20,000 psi with a rise time of one

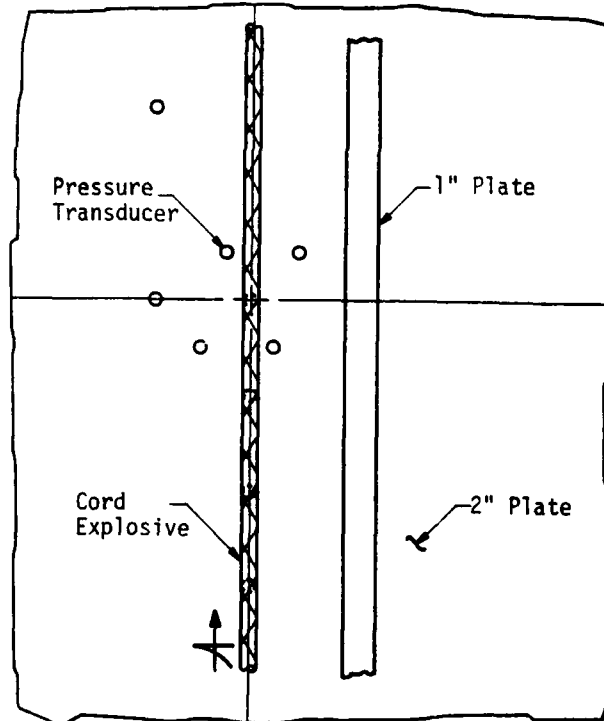


Figure 2. Plan View of Test Set-Up

microsecond. Power and signal amplification (reduction) were provided by PCB Model 494A06 six-channel units. The pressure-time histories were recorded on magnetic tape using an Ampex Model 2230, Wideband II, FM tape recorder at 120 ips. The analog data were digitized and processed in sets of four data channels using two Nicolet Model 2090 transient recorders. The digital data were transferred from the transient recorder to a DEC 11/23 computer. Final data processing and plotting were then

accomplished with a DEC 11/70 computer. The high-frequency response of the entire system was 180 kHz.

## EXPERIMENTAL RESULTS

A total of 51 tests were conducted, each using a single strand of Primacord<sup>®</sup> explosive. The tests simulated a pair of parallel line charges as shown in Figure 3. The test matrix is shown in Table 3. Test conditions ranged from 1.5-inch spacing at a 2-inch standoff using 40-grain/foot Primacord<sup>®</sup> up to a 9-inch spacing at 16-inch standoff using 400-grain/foot Primacord<sup>®</sup>. (All spacings in this paper are simulated line charge spacing, or twice the spacing between the line charge and vertical reflecting plate.) The conditions were selected to cover a broad range of scaled spacings and scaled standoffs. Two tests were run at each combination of spacing and standoff, with four pressure transducers being located directly beneath the line charge during each test. Thus, typically eight data points were available to calculate a mean and standard deviation.

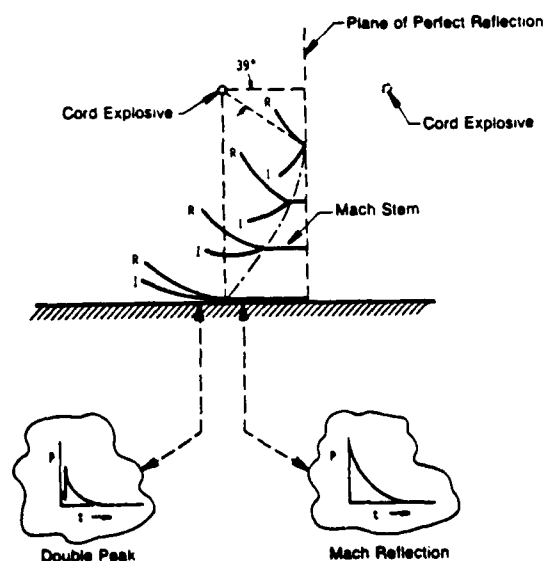


Figure 3. Interaction of Blast Waves from Parallel Line Charges

Table 3. Test Matrix

| $E_1$<br>(gr/ft) | Cord<br>Spacing<br>(in) | Standoffs<br>(in) |
|------------------|-------------------------|-------------------|
| 40               | 1.5                     | 2, 3, 5           |
| 40               | 3.0                     | 5, 7, 10          |
| 100              | 1.5                     | 3, 5, 7           |
| 100              | 3.0                     | 5, 7, 10          |
| 100              | 6.0                     | 5, 8, 12          |
| 400              | 3.0                     | 5, 8, 12          |
| 400              | 6.0                     | 8, 12, 16         |
| 400              | 9.0                     | 8, 12, 16         |

In addition, pressure transducers were positioned perpendicular to the direction of the line charge as shown in Figure 2. Pressure histories from these transducers were used to analyze Mach stem formation. One objective of this study was to define the line charge spacings and standoffs at which the Mach stem had just fully formed on the ground surface directly below the line charge. This was accomplished by looking for pressure histories that exhibited the single peak that is characteristic of a Mach stem as compared to the double peaks for incident and reflected pressure waves, as shown in Figure 3.

Reflected pressure, reflected specific impulse, duration, and time of arrival data were scaled; the mean and standard deviation of each parameter is shown in Figure 4. Separate curves are presented for each parameter for five scaled spacings. Scaling was accomplished according to the relationships presented above.

Reviewing the scaled reflected pressure and specific impulse curves (Figure 4), it can be seen that the curves display some irregularities or "humps" rather than a smooth exponential decay from high to low pressures (impulses). These irregularities are attributed to two factors: Mach stem formation and experiment errors. In most cases, the "hump" in a curve corresponds to the spacing and standoff at which the Mach stem had fully formed on the ground surface directly beneath the line charge. However, experimental error cannot be overlooked. The standard deviation for each point is shown on the graphs. Standard deviation was typically greatest at the smallest scaled spacings and standoffs. The majority of the curves were easily plotted through the means of the data points, but the data could always be improved by increasing the statistical sample size.

The scaled reflected pressure curves indicate that reflected pressure increases very rapidly below scaled standoffs of 0.1. If the curves for the various scaled spacings were plotted together, they would converge to a single line at very low scaled standoffs. This is reasonable since, at small standoffs, the reflected pressure will be a strong function of the incident shock wave (see Figure 3) with little contribution from the reflected wave. Scaled reflected impulse curves demonstrate the same characteristics, except the curve for a scaled spacing of 0.0692. This spacing demonstrates an unusual downturn in impulse at low scaled standoffs. The reason for this downturn is not understood, and more data are needed to clarify the situation.

It is interesting to note that the  $P_r$  and  $i_r$  curves (Figure 4) for the three largest scaled spacings (0.1036, 0.1136, and 0.1382) conform closely to one another. Also, it can be seen that, at these wide cord spacings, pressure and impulse decline more rapidly as a function of standoff than at narrower spacings.

Scaled duration and time of arrival are also presented in Figure 4. The duration data were very repeatable and consistent from one spacing to the next. The time of arrival data were also repeatable and consistent, except at the smallest scaled spacing of 0.0346. The figure for the 0.0346 spacing contains data for 100-grain/foot and 400-grain/foot Primacord<sup>®</sup>. The uppermost data points correspond with the 400-grain/foot. The reason for the poor agreement between these two sets of data could not be ascertained. These  $t_a$  data are the only instance in which differing Primacord<sup>®</sup> sizes did not scale closely.

The scaled spacings and standoffs at which the Mach stem had fully formed on the ground surface directly beneath a line charge are shown in Figure 5. It should be noted that it was frequently difficult to identify whether a Mach stem had formed or not, especially with 40-grain/foot Primacord<sup>®</sup> at the closest spacing. Pressure histories frequently exhibited up to 4 peaks rather than one or two as shown in Figure 3, and many of the pressure histories simply could not be used in this analysis. Nonetheless, reasonably good agreement was obtained among the three sizes of Primacord<sup>®</sup> tested, as shown in Figure 5. The data indicate that standoff height must be increased as line spacing increases for a Mach stem to fully form on the ground surface directly beneath the line charge. The Mach stem will have fully formed at any combination of scaled spacing and standoff that lies on or above the curve in the Figure 5. The position of the Mach stem is important when considering the uniformity of ground pressure loading between line charges; a more uniform loading will be achieved when the Mach stem has fully formed.

The reader should be cautioned that the above results pertain to two parallel line charges. Pressures and impulses are expected to increase under arrays containing larger numbers of parallel line charges at locations that are not subject to edge

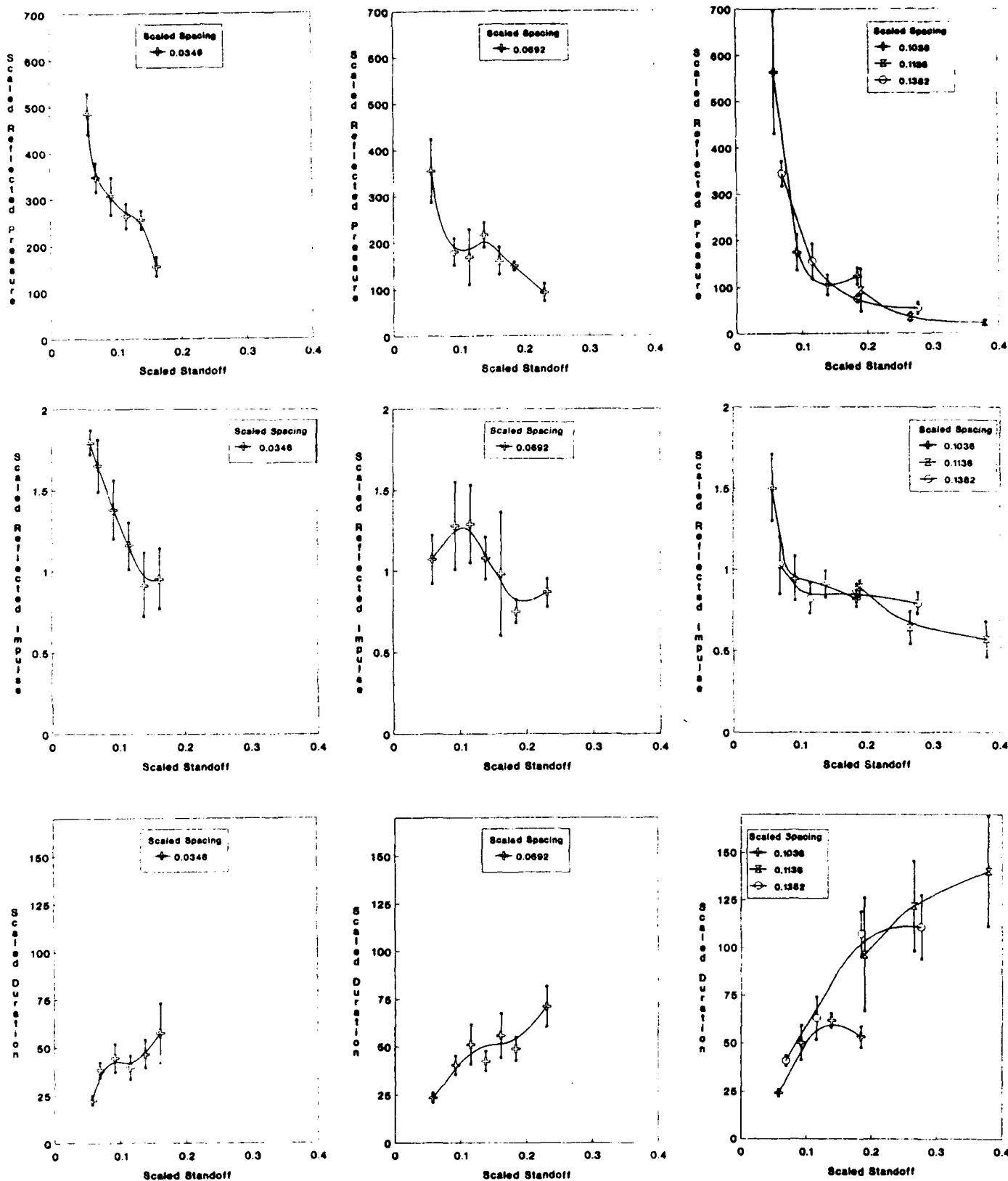


Figure 4. Scaled Blast Curves for Two Parallel Line Charges

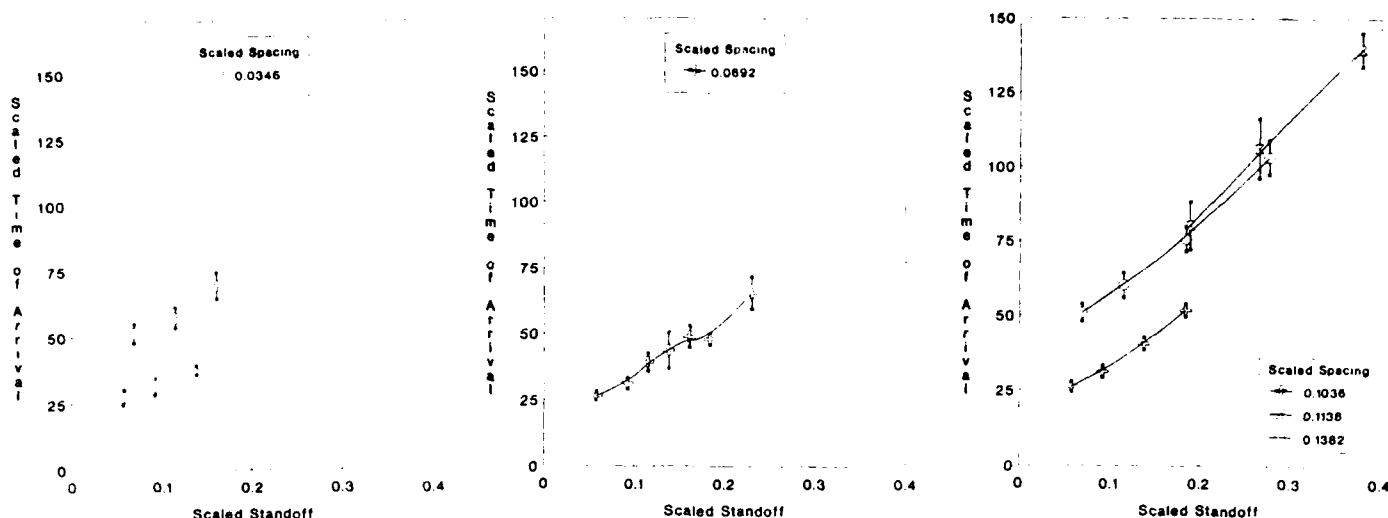


Figure 4. Scaled Blast Curves for Two Parallel Line Charges (Continued)

effects. However, Mach stem formation will not be affected by the number of line charges. Tests are planned to measure pressure under large line charge arrays.

#### ACKNOWLEDGMENTS

The work described in this paper was sponsored by the U.S. Marine Corps and the contract was administered by the Naval Coastal Systems Center (NCSC). The technical monitor at NCSC was Mr. J. Charles Wicke, Jr. The authors wish to thank these agencies for funding this study and permitting the results to be published.

#### REFERENCES

1. Baker, W. E., Explosions in Air, University of Texas Press, Austin, Texas, 1973 (Second printing, Wilfred Baker Engineering, San Antonio, Texas, 1983).
2. Baker, W. E., P. S. Westine, and F. T. Dodge, Similarity Methods in Engineering Dynamics, Hayden Book Company, Inc., Rochelle Park, New Jersey, 1973.
3. Sachs, R. G., "The Dependence of Blast on Ambient Pressure and Temperature," BRL Report No. 466, Aberdeen Proving Ground, Maryland, 1944a.

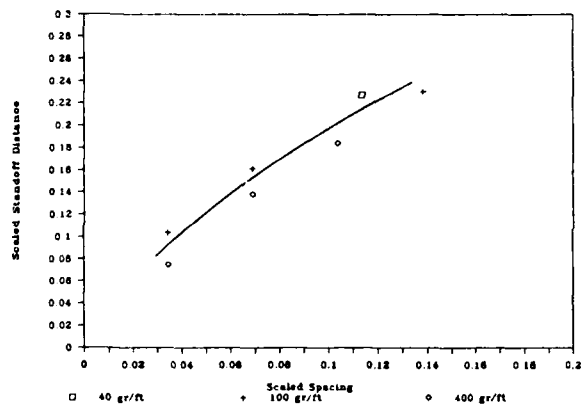


Figure 5. Position of Parallel Line Charges to Fully Form a Mach Stem on the Ground Surface

#### CONCLUSIONS

Reflected pressure, specific impulse, duration, and time of arrival were defined for a wide range of spacings and standoffs using a test apparatus that simulated two parallel line charges. Scaling laws were developed for parallel line charge arrays, and the measured data were presented in the form of scaled curves for greatest utility. The combinations of scaled spacing and standoff at which a Mach stem fully formed on the ground surface beneath parallel line charges was also defined.

# Scale Model Tests to Determine Blast Parameters in Tunnels and Expansion Rooms from HE-charges in the Tunnel Entrance

G. Scheklinski-Glück

Fraunhofer-Institut für Kurzzeitdynamik  
Ernst-Mach-Institut  
Freiburg, Germany

## Abstract

The objective of this report is to present a system of approximation formulae in order to calculate pressure-time histories inside underground tunnel and chamber systems in case of conventional weapon detonation at the entrance. It is necessary to know how a blastwave propagates through tunnels and rooms inside a structure in order to define the loading on blast closures or ventilation systems of an underground shelter.

## 1. Introduction

The formation and propagation of the shocks and the flow field for real structural geometries is quite complex and depends on many parameters. Most of the available data have been obtained through long-duration shock tube tests to simulate nuclear blast at relatively low pressure levels. Only few data are available for short-duration high pressure loads from conventional weapons. Fig. 1 shows the situation.

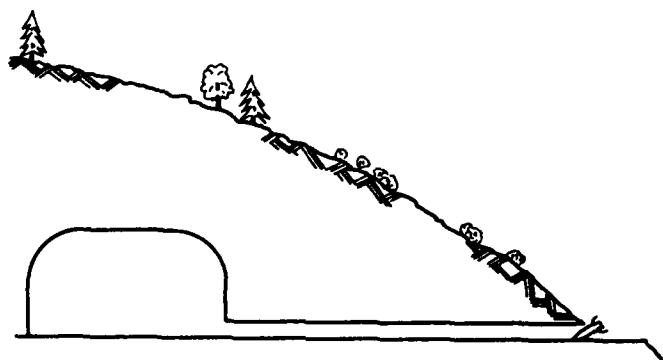


Fig. 1 Situation of an underground shelter.

## 2. The propagation of a blastwave in a tunnel

Small-scale model tests using theoretical and empirical scaling techniques allow many tests with different configurations. A steel tube model of 8.8 cm inner diameter serves as a basis for a great number of tests with different tunnel lengths, area changes and junctions of 90 degrees. The shape of the cross sectional area is circular, square or rectangular. The length of the main as well as the branch tunnel may vary between 10 and 100 times the tunnel diameter. Four different charge masses are used. Attention is directed to avoid choking effects in the model tube.

As a result of the evaluation of the model tests approximation formulae are developed for the blast parameters. An example for the primary incident wave is given in Section 2.1. More formulae, especially for reflected waves from closed or open tunnel end, are listed in Report E 1/88 of the Ernst-Mach-Institut, where a computer program is available.

### 2.1 Approximation formulae for blast parameters in tunnels

#### Definition of Symbols

- $Q$  = charge mass, kg
- $D$  = tunnel diameter, m
- $Z$  =  $Q/D^3$  scaled charge parameter,  $\text{kg/m}^3$
- $L1$  = gage location, distance from tunnel entrance, m
- $L2$  = tunnel length, m
- $X$  =  $L2/D$  scaled tunnel length
- $Y$  =  $L1/D$  scaled distance

#### primary blastwave:

- $TA$  = shockfront arrival time, ms
- $PS$  = peakoverpressure at the shock front, bar
- $IS +$  = side-on blast impulse, bar.ms
- $T+$  = positive duration, ms
- $w$  = shockfront velocity, m/s

### Range of validity

$$\begin{aligned} 10 &< x < 100 \\ 5 &< y < 100 \\ 1 &< z < 100 \end{aligned}$$

### Blast parameters for the incident blastwave

$$\begin{aligned} TA_1 &= 0,36 \cdot D \cdot Z^{-0,14} \cdot Y^{1,42} \cdot Z^{-0,04} & \text{für } \frac{TA_1}{D} < 15, \text{ sonst} \\ TA_2 &= 0,417 \cdot D \cdot Z^{-0,345} \cdot Y^{1,4} \end{aligned} \quad (1)$$

$$\begin{aligned} PS_1 &= 117 \cdot Y^{-1,37} \cdot Z^{0,35} \cdot Y^{0,27} & \text{für } 7,5 \leq Y \leq 25 \\ PS_2 &= 53,1 \cdot Y^{-1,124} \cdot Z^{0,83} & \text{für } 25 \leq Y \leq 100 \end{aligned} \quad (2)$$

$$IS+ = 12,3 \cdot D \cdot Z^{0,81} \quad \text{für } 20 \leq Y \leq 100$$

(in erster Näherung auch für  $7,5 \leq Y \leq 20$ ) (3)

$$T+ = 1,255 \cdot L \cdot Z^{0,09} \quad (4)$$

$$\begin{aligned} W_1 &= 570 \cdot Z^{0,37} \cdot e^{-0,01 \cdot Y} & \text{für } 20 \leq Y \leq 50 \\ W_2 &= 484,3 \cdot Z^{0,4} \cdot e^{-0,01 \cdot Y} & \text{für } 50 \leq Y \leq 100 \end{aligned} \quad (5)$$

### 2.2 Computation of pressure-time histories in tunnels

In order to generate pressure-time histories for the positive phase of the incident blastwave, the Friedlander function

$$p(t) = PS \cdot (1 - t/T+) \cdot e^{-b \cdot t/T+} \quad (6)$$

can be integrated over the positive phase to obtain the impulse  $IS+$ . The decay constant  $b$  is determined from the resulting equation

$$IS+ = \frac{PS \cdot T+}{b} \cdot (1 - \frac{1-e^{-b}}{b}) \quad (7)$$

By inserting the values of  $PS$ ,  $T+$  and  $b$  in equation (6), it is possible to calculate  $p(t)$  at any time  $t$ . An example is shown in Fig. 2.

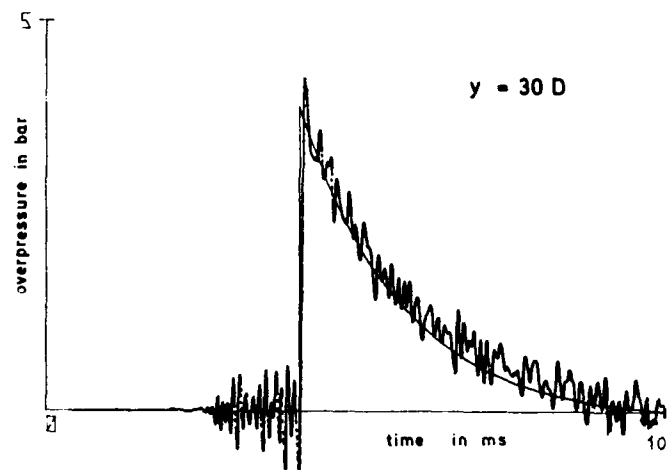


Fig. 2 Calculated and measured pressure-time histories of an incident wave in a straight tunnel.

### 3. Pressure-time histories inside expansion rooms

In a distance of 10 to 100 tunnel diameters, the straight tunnel enters in an expansion chamber. Its form can be a cube or a cuboid. Its volume is  $1000 \text{ m}^3$  for a tunnel cross section of  $10 \text{ m}^2$ . The jump in cross section from tunnel to chamber front side is 1 : 10 for a cubical room. For a cuboid, we have 1 : 5 for a long and flat cuboid, or up to 1 : 20 for a short and high cuboid. Fig. 3 shows steel models of the investigated chambers.

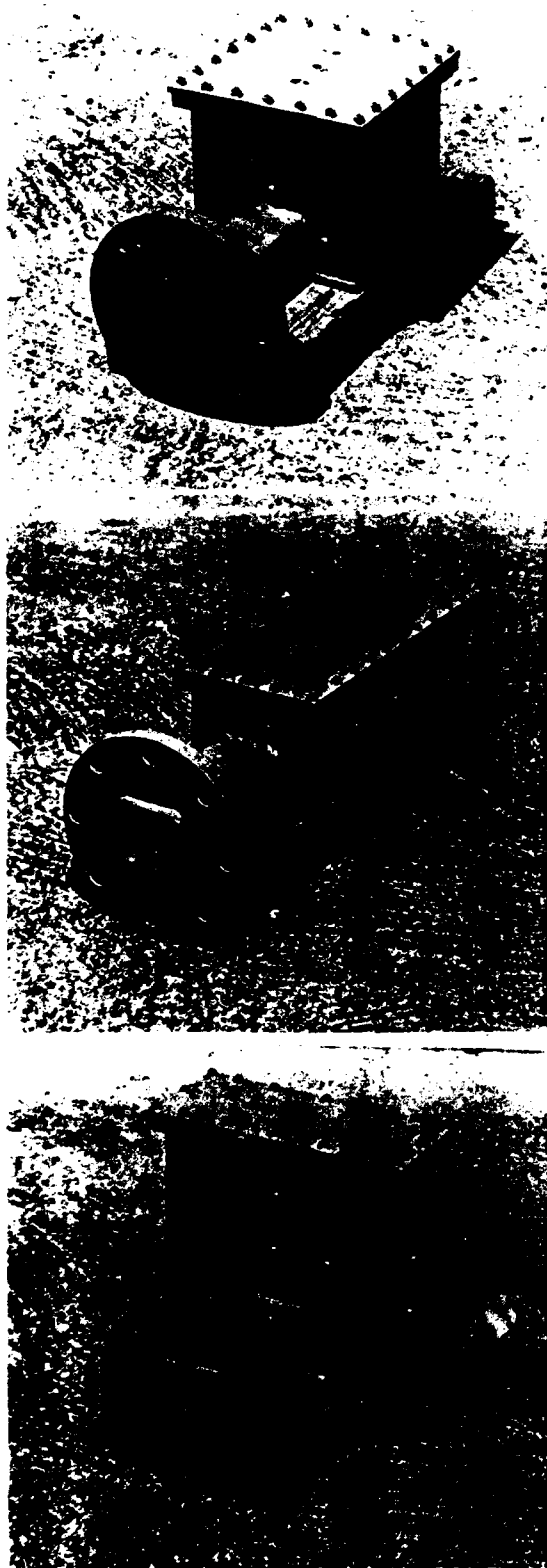


Fig. 3 Steel models of expansion rooms: cube, long and short cuboid with the same volume.

The loading at the chamber walls consists of three phases (Fig. 4):

The first phase is the reflected blast loading consisting of high-pressure, short duration pulses. They are represented by one triangular peak in the reconstruction ("Spike" with overpressure  $P_s$  and time  $T_s$ ). The gas flows into the chamber until the maximum quasistatic pressure  $P_m$  is reached. This second loading phase is approximated by a parabolic curve. During a third phase, the overpressure descends slowly, which is described by an exponential function and depends on the vented area of the room. The total positive duration  $T_{ges}$  is subdivided by 20 % for parabolic and 80 % for Friedlander phase. The total positive impulse is  $I_{ges}$ .

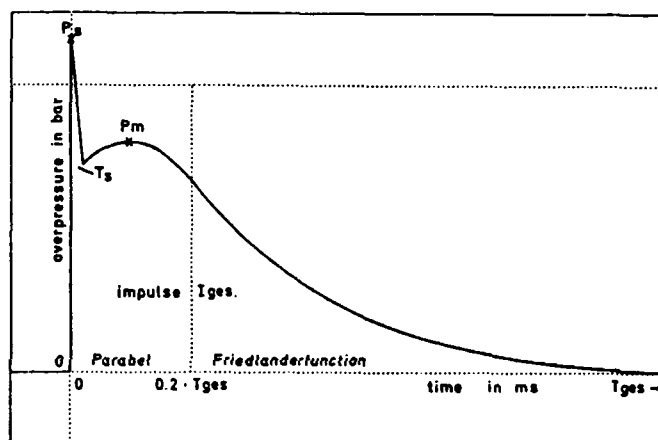


Fig. 4 Principle pressure-time history inside an expansion chamber. Approximation by a parabola and annexed Friedlander function.

### 3.1 Development of approximation formulae for expansion rooms

Fig. 5 shows the maximum pressure  $P_m$  versus scaled charge  $Z = Q/D^3$ .  $Q$  is the charge mass in kg,  $D$  the tunnel diameter. By variation of the tunnel length the pressure at chamber entrance (PSE) is adjusted to PSE = 20 bar, 50 bar, 80 bar and 100 bar. From the four PSE values four parallel straight lines result. Their equation is

$$P_m = A \cdot (Q/D^3)^{0.576}$$

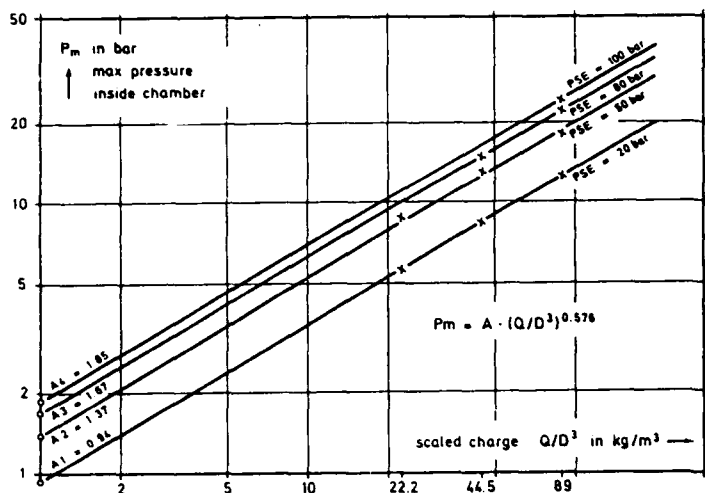


Fig. 5 Development of empirical formula.  
Max. pressure in the chamber versus scaled charge

0.576 is the slope of the lines. The parameter A depends on the entrance-pressure PSE, as is shown in Fig. 6.

$$A = 0.27 \cdot PSE^{0.415}$$

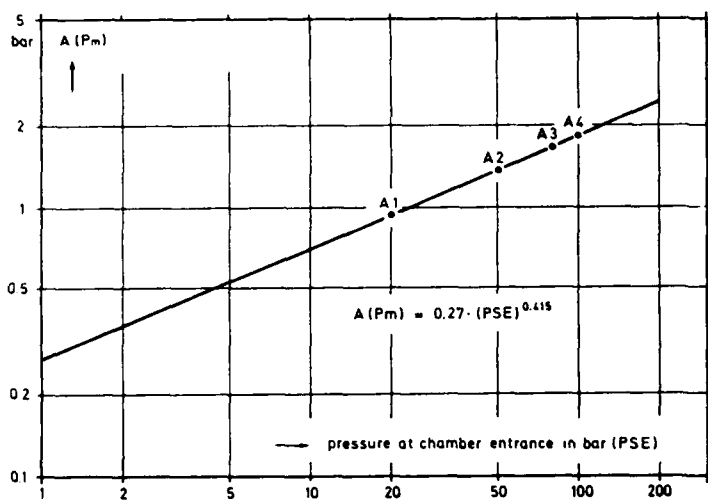


Fig. 6 Development of empirical formula.  
Parameter A versus entrance pressure PSE.

From this follows the approximation formula

$$P_m = 0.27 \cdot PSE^{0.415} \cdot (Q/D^3)^{0.576}$$

The formulae for the other parameters are developed in a similar way.

The result of the evaluation of the model tests with different expansion chambers is as follows: for all locations on the different walls in a chamber, the principle pressure-time history is the same, within the accuracy of the measurements. The worst case of normal reflexion is measured on the back side of the chamber and is described by the "Spike" parameters  $P_s$  and  $T_s$ . The principle blast loading is the same also for different forms of rooms, if the volume is equal.

For chambers with the double volume other formulae are developed. In a current investigation formulae are developed for the triple volume and it is planned to find a formula for any chamber volume independent of the tunnel cross section. Further expansion rooms with a second tunnel on the opposite side are investigated.

### 3.2 Range of validity

For a given diameter  $D$ , the scaled charge  $Q/D^3$  is valid from 1 to 100. The charge  $Q$  is calculated as follows:

Range of validity for charge mass  $Q$  in kg:

| Tunnel cross section in $m^2$ | Diameter $D$ in m | $Q/D^3 = 1$ charge mass $Q$ in kg | $Q/D^3 = 100$ charge mass $Q$ in kg |
|-------------------------------|-------------------|-----------------------------------|-------------------------------------|
| 3                             | 1.95              | from 7.5 kg                       | to 750 kg                           |
| 10                            | 3.57              | from 45 kg                        | to 5 000 kg                         |
| 20                            | 5.05              | from 128 kg                       | to 12 800 kg                        |
| 50                            | 7.98              | from 500 kg                       | to 50 000 kg                        |

As described in Section 3, the chamber volume must be calculated for a cubical room by the jump in cross section from tunnel to chamber front side 1 : 10 and can vary between 1 : 5 and 1 : 20.

### 3.3 Approximation formulae for expansion rooms

Within the range of validity, the following empirical formulae are developed for the investigated forms and volumes of expansion chambers.

$$\begin{aligned} \text{max. pressure } P_m &= 0.27 \cdot PSE^{0.415} \cdot Z^{0.58} & (8) \\ \text{pos. impulse } I_{ges} &= 16.6 \cdot D \cdot PSE^{0.14} \cdot Z^{0.85} & (9) \\ \text{pos. duration } T_{ges} &= 120 \cdot D \cdot PSE^{-0.255} \cdot Z^{0.32} & (10) \end{aligned}$$



For the double volume:

$$P_m = 0.046 \cdot PSE^{0.73} \cdot Z^{0.58} \quad (11)$$

$$I_{ges} = 6 \cdot D \cdot PSE^{0.57} \cdot Z^{0.64} \quad (12)$$

$$T_{ges} = 56 \cdot D \cdot Z^{0.32} \quad (13)$$

For normal reflexion peaks, especially on the back side of the chamber:

$$\text{Spike pressure } P_s = 2.2 \cdot P_m \quad (14)$$

$$\text{Spike time } T_s = 0.03 \cdot T_{ges} \quad (15)$$

### 3.4 Computation of pressure-time histories in expansion rooms

By using formulae (8) to (15) in Section 3.3, the parameters  $P_m$ ,  $I_{ges}$ ,  $T_{ges}$  and  $P_s$  and  $T_s$  can be calculated.

Fig. 7 shows a set of curves with differently bended parabolae through a given maximum pressure  $P_m$ , and annexed Friedlander function with positive duration  $T_{ges}$ . At the connection point P2, both curves have the same slope. The pressure-time history in a shelter can be calculated if it is possible to find out the curve with the impulse  $I_{ges}$  given by equation (9). The selection can be done with a computer program.

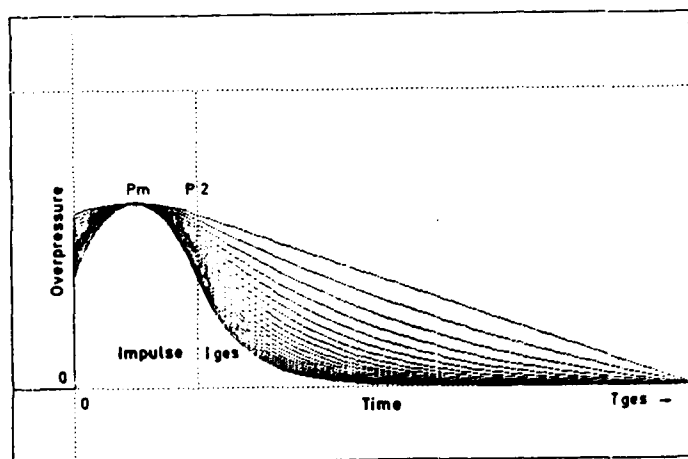


Fig. 7 Set of pressure-time histories inside a chamber. All parabolae are going through max. pressure  $P_m$ . The annexed Friedlander function has the same slope at point P2.

The comparison of computed and measured curves is a quality check on the approximation model consisting of parabola and Friedlander function (Fig. 8).

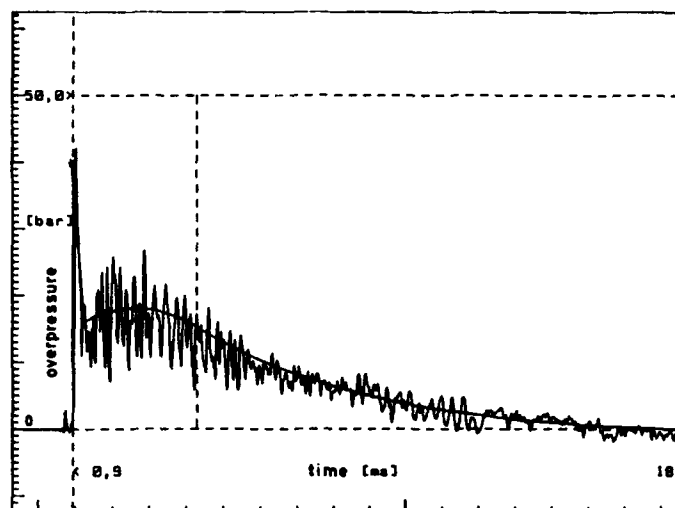


Fig. 8 Typical pressure-time history and smooth curve computed from approximation formulae.

### 3.5 Parameter studies

A basic program is available that allows the construction of pressure time histories at any point in the tunnel and chamber system. The range of validity is given in Section 3.2. Parametric studies can be done with this program in order to learn how the pressure changes with different charges at a certain tunnel arrangement or different chamber volumes (Fig. 9).

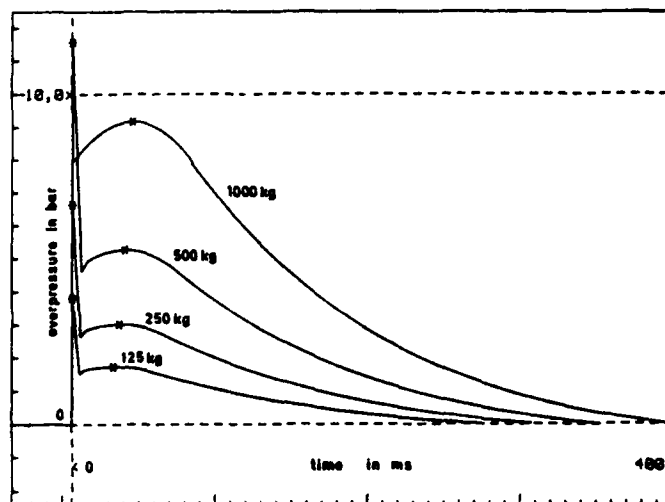


Fig. 9 Parameter study:  
Effect of a bomb size on the pressure-time history inside a 1000 m³ chamber. Tunnel cross section 10 m², tunnel length 20 m.

# Evaluation of Transmitted Stress Across a Semi-Rigid Boundary Condition for a Model Runway Slab

Bengt E Vretblad

Mark Amend

FortF-Royal Swedish Fortification Administration  
Eskilstuna, Sweden

Directorate of Engineering Analysis  
Eglin AFB, Florida

## ABSTRACT

This paper describes an experimental apparatus which is used to measure the transmitted soil stress from a subsurface detonation of high explosives to a slab element on grade. In addition, the relative contribution of mass and stiffness in defining the interface stress history due to soil structure interaction is evaluated. A structural analysis model has been previously proposed, where an artificial viscosity term appears in the equation of motion for the response of a structure being loaded by the transmission of soil stress across a semi-rigid boundary condition. Since this damping effect for any given charge weight and standoff is proportional to the difference in the structural velocity (which varies with the inertial and stiffness characteristics of the structure) and the soil particle velocity (which varies with soil type) a massive but non-ductile structural element such as a runway slab may exhibit quite different damping characteristics from a lighter structural member designed primarily for flexural strength.

## BACKGROUND

The pressure on the walls of a buried structure from a detonated penetrating weapon has significant importance for the fortification engineer.

Tests performed in the early 40ies were reported in /1/. The tests were made with structures that had a very low thickness/span ratio. In short it gives maximum pressure and maximum impulse to be 2.0 and 2.8 times higher respectively, than the corresponding free-field values.

Later tests indicated that due to "arching" effects the design load for structures should in many cases rather be lower than the corresponding free-field values.

At FortF a number of tests have been made that illustrates how the properties of the structure e.g. mass and stiffness influence on the pressure and impulse it will be subjected to from detonating charges. The tests have been reported e.g. in /2/ and /3/.

Computer calculations by Felix Wong reported in /4/ give similar results.

Drake & Rochefort in /5/ give a theoretical model where an artificial viscosity is introduced to account for the structure media interaction (SMI). They also compare the calculations with experimental results.

For the case with detonations under a horizontal slab no similar work - as known to the authors - has been presented.

## INTRODUCTION

Obviously, from previous studies, the structural velocity figures in the SMI effect. Therefore the mass and stiffness of the structure should influence the loading function. In order to study this a mechanical apparatus has been developed which has the capability of varying the mass and stiffness of the system. Since it is desirable to follow an iso-frequency contour when investigating the relative contribution of mass and stiffness to the system response, the system should have approximately the same range of variation in mass and stiffness. Also, since most problems of interest involve loads which are many times larger than the static collapse load, the mechanical stiffness should also possess plasticity. Furthermore, in order to evaluate the artificial viscosity model, knowledge of the free field characteristics of the load are required.

## TEST SETUP

The present apparatus was devised to simulate the structural characteristics at half scale for an unreinforced runway slab, basically according to Fig 1. The system stiffness for the present test series was calculated using yield line theory and an assumption of uniform loading over the whole slab.

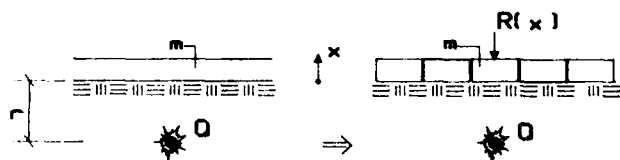


Fig 1 Simulation principle

In order to obtain an element of loading which would simulate a subsurface detonation of explosive against a horizontal slab on grade a steel encased concrete block 25 cm x 25 cm x 15 cm with surrounding confinement was used. The confinement was achieved by means for some of the tests similar, adjacent, concrete blocks and for other tests of a steel plate through which the block element passed, cfr Fig 2. The load path consisted of the block element, a steel axle, and a beam element, see Fig 3. System mass was provided by the concrete block plus system appurtenances such as an in-line force transducer assembly and the steel half cylinder bar stock which transferred load from the axle to the beam. A mass factor of 0.5 was used for the mass of the beam itself. The system stiffness was provided by structural steel tubing with center point loading and simple supports which were movable. Thus a continuum of stiffnesses could be achieved. The load was transmitted from the block to the beam through an axle whose axial stiffness was much higher than the bending stiffness of the beam. A steel beam superstructure was erected to provide and maintain the desired support conditions for the mechanical system as seen in Fig 4.



Fig 2 Concrete block



Fig 3 Measuring components

#### SYSTEM MEASUREMENTS

In order to assure maximum confidence in the measurement process, independent measurements of acceleration, velocity and displacement were made. Simultaneity of a null value of the parent function and maxima of derivative functions qualitatively corroborates the measurement of the system response. A load cell measured the force transmitted from the axle to the beam. A strain gage mounted 7 cm offcenter and outside the region of the plastic hinge of the beam provided useful quantitative information during elastic response and useful qualitative (strain remained constant during rotation of plastic hinge) information even during plastic response. An inductive coil measured the displacement of the beam. Velocity was measured using a differential transformer. Free-field pressure measurements were made using a piezo-electric transducer mounted in the face of a plexiglass-cube.

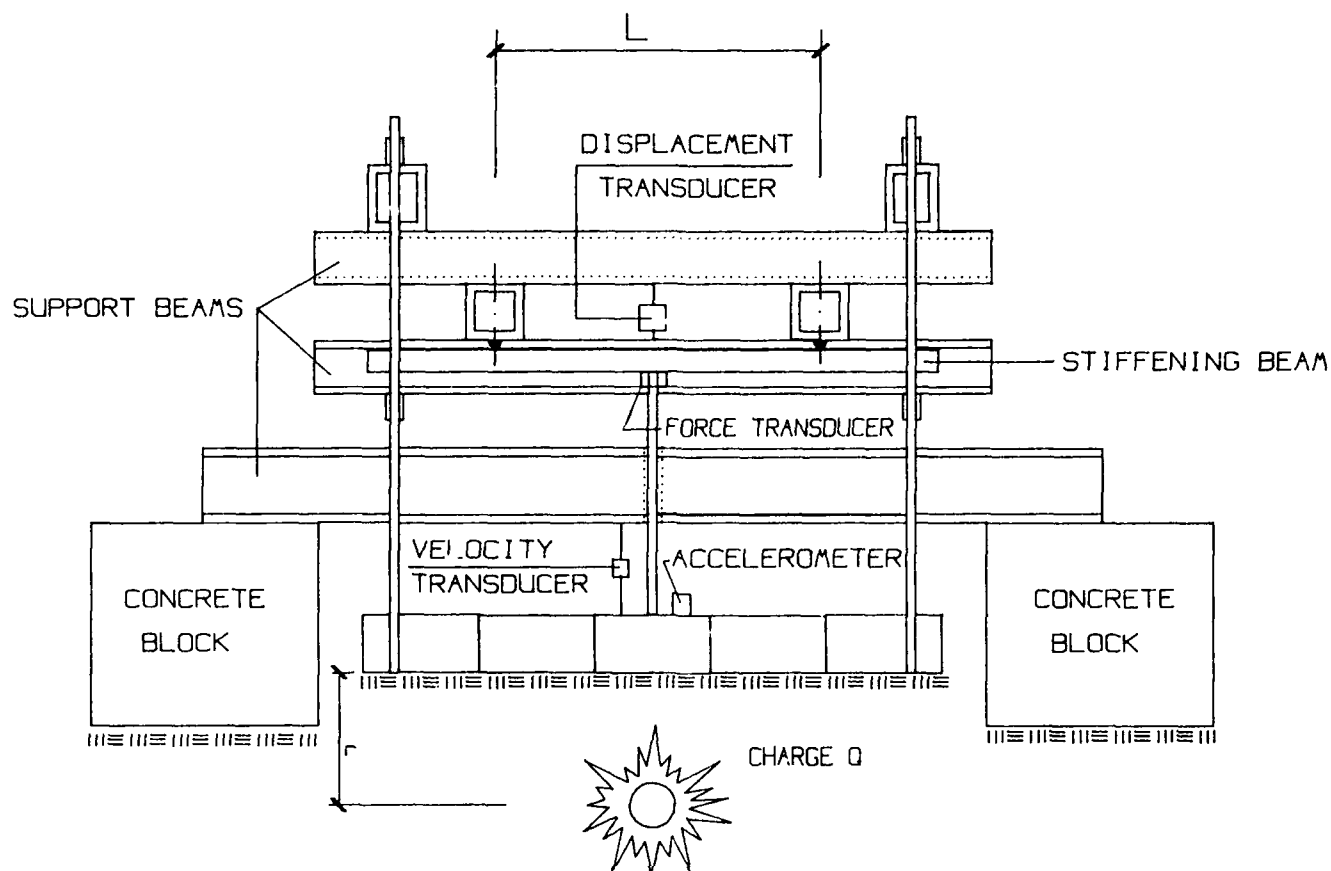


Fig 4 Testing apparatus

#### TEST EXECUTION

Calibration and initial system checkout was accomplished with a 50 g charge weight of spherical TNT at a standoff distance of 0.5 m. This loading allowed the response to remain in the elastic region. The scaled standoff distance is  $1.36 \text{ m/kg}^{1/3}$ . Shorter values of the scaled standoff distance well in the plastic region for this system, however, are of interest. The stiffness for the half-scale unreinforced slab of thickness 15 cm and width 3 m is  $1.57 \text{ MN/m}$  for an elemental area of  $0.0625 \text{ m}^2$ . The total system mass in the minimal configuration was 40.47 kg.

The system's natural frequency was evaluated by clamping the block axle assembly to the beam and allowing the system to go into free vibration after a small explosive loading applied to the block. The measured value of 32 msec for the period of vibration agreed very closely to the theoretical value indicating the assumption of the mass factor for the beam was valid. The elastic limit displacement for the model runway

slab should be 3.1 mm. The stiffness of the apparatus matched the model runway; however, the elastic limit was exceeded. It would be possible to match both stiffness and elastic limit by selecting a beam with a different section modulus, but since the initial purpose of this study was to determine the loading function rather than system response, and since it was not possible with the beam selection available to match both stiffness and plasticity characteristics it was decided to match stiffness since its influence comes into play in determining structural velocity first. In order to first evaluate the calculational model for the SMI effect it was decided to use a loading where the response would remain elastic. The charge weight was 100 g at a stand-off distance of 0.5 m making the scaled standoff distance  $1.07 \text{ m/kg}^{1/3}$ . Table 1 lists the beam stiffness and mass as well as the explosive loading characteristics for the tests. One test was performed to verify the response of the system where a constant plastic resistance is achieved. Fig 5 shows the plastic deformation which was residual in the beam element.

TABLE 1 Test data

| Shot | Charge weight (g) | Standoff distance (m) | Beam length (m) | Beam stiffness (MN/m) | System mass (kg) | Remarks  |
|------|-------------------|-----------------------|-----------------|-----------------------|------------------|--|
| 1    | 50                | 0.50                  | 1.00            | 3.05                  | 40.5             | System check out<br>Plastic response<br>Frequency analysis |
| 2    | 50                | 0.50                  | 1.00            | 3.05                  | 40.5             |  |
| 4    | 175               | 0.50                  | 1.00            | 3.05                  | 40.5             |  |
| 6    |                   |                       | 1.00            | 3.05                  |                  |  |
| 7    | 100               | 0.50                  | 0.75            | 7.23                  | 40.5             |  |
| 8    | 100               | 0.50                  | 0.75            | 7.23                  | 40.5             |  |
| 9    | 100               | 0.50                  | 0.75            | 7.23                  | 62.5             |  |
| 10   | 100               | 0.50                  | 1.25            | 1.57                  | 62.5             |  |
| 12   | 100               | 0.50                  | 1.25            | 1.57                  | 40.5             |  |

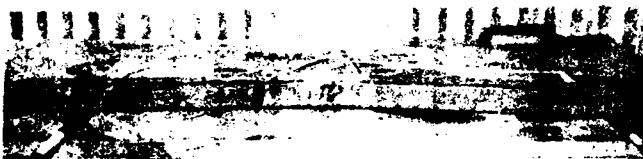


Fig 5 Residual deformation in beam element past test

## MATHEMATICAL MODEL

The differential equation for the apparatus response which includes a differential velocity model for soil structure interaction effect is given by

$$m(\ddot{x} + g) + R(x) = (2\sigma_{ff} - \rho c \dot{x}) \cdot A \quad (1)$$

where  $m$  = system equivalent mass

$R(x)$  = reactive force

$\sigma_{ff}$  = free-field soil stress

$x, \dot{x}, \ddot{x}$  = displacement, velocity and acceleration, cfr Fig 6.

$A$  = loaded area

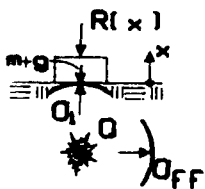


Fig 6 Notations

For the interface stress,  $\sigma_i$ , we have

$$\sigma_i = 2\sigma_{ff} - \rho \cdot c \cdot \dot{x} + mg/A \quad (2)$$

## DISCUSSION OF RESULTS

The influence of mass and stiffness in determining peak interface stress values in the first and second peaks respectively was observed as in the previous work /2/ and /3/. When the system possessed comparatively low mass the first peak was smaller than when the higher mass was used. Likewise, the second peak in the interface stress record showed correlation to the stiffness characteristics of the system. A higher stiffness resulted in a higher peak interface stress. The measured and calculated pressures for shot # 8 are shown in figure 7.

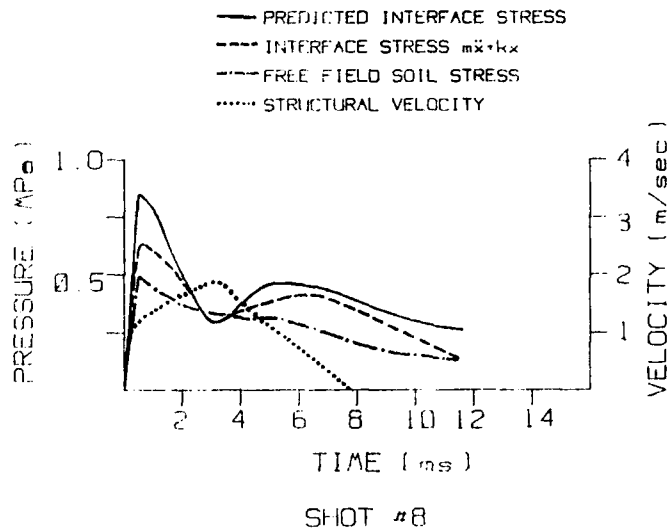


Fig 7 Results from shot number 8

It is of interest to study the time required for the interface stress to decay to the free field stress. The reflected pulse apparently decays more rapidly for the heavier structure. The average decay time for the 40.5 kg structure was 3-3.5 msec while the decay time for the heavier 62.5 kg structure was only 1.5 msec.

Although the tests so far have been rather limited, apparently a soil structure effect exists which is velocity influenced. In general, the interface stress reduces to the free field stress and then approaches zero as the structural velocity increases to twice the free field particle velocity. However, the attenuation does not persist even when the structural velocity remains at or above the value where attenuation is most pronounced. Since the acoustic impedance has a value greater than what corresponds to the critical damping for the system this is hard to account for using a viscous damping model.

## CONCLUSIONS/RECOMMENDATIONS

Neither the tests nor the evaluations have yet been finalized. The concept of measuring the response of a simplified mechanical system undergoing a soil mediated loading has, though, proven useful in evaluating a mathematical soil structure interaction model. In order to correlate system response future investigations will follow iso-frequency contours and non-dimensional time of response will be compared.

## REFERENCES

- /1/ Effects of Impact and Explosion. -Summary Technical Report of the National Defense Research Committee. Washington, D.C., 1946.
- /2/ Hultgren, S., Verkan av underjordsexplosioner i sand mot deformerbara väggar. (Effects of buried charges in sand against deformable walls.) Omgång II. Fortifikationsförvaltningen, Forskningsbyrå C-rapport nr 200, Mårsta, 1980. (IN SWEDISH)
- /3/ Vretblad, B., Response of Structures to Detonations in Sand. The Interaction of Non-Nuclear Munitions with Structures, U.S. Air Force Academy, Colorado, 1983.
- /4/ Dynamics of Structures. Proceeding of the sessions at Structures Congress '87. ASCE, New York, 1987.
- /5/ Drake, J.L. & Rochefort, M.A., Response of Buried Structural Walls to Earth Penetrating Conventional Weapons. Proc. Structures Congress '87. ASCE, New York, 1987.

# PENETRATION OF PROJECTILES INTO FINITE THICK REINFORCED CONCRETE TARGETS

Hermann Pahl

NATO Headquarters, Brussels

## Abstract

Handbook formulae allow the prediction of maximum penetration into infinite thick reinforced concrete targets. It can be shown that additional penetration will occur when the target is of finite thickness. The target can be considered a halfspace if the calculated maximum penetration is less than 50% of the target thickness. Perforation will occur if the calculated maximum penetration is at least 63% of the target thickness.

## Foreword

At the end of the 19th Century engineers began to use concrete for the construction of protective structures. In 1904-1905 during the siege of Port Arthur in the Russo-Japanese War this new construction material was tested under battle conditions. Fighting positions and barracks of Port Arthur were designed against hits of 15 cm artillery shells. A thickness of 91 cm was used (Reference (1)). The adequacy of the design was demonstrated during the siege when multiple hits of 15 cm artillery shells caused only minor damage. Due to the relatively small impact angle even hits of the Japanese 28 cm shells achieved little effect. However, one shell obviously hit the target almost normal to the surface and perforated the arch; General Kontradtchenko, together with his staff, were killed. The design engineer was subsequently court-martialled. This is just one example that demonstrates that designing military structures is and always has been an extremely risky and dangerous profession.

## Introduction

Protective structures are designed against the combined effects of penetration and detonation. In the worst case - taking the defenders point of view - the detonation of the charge of a shell or bomb occurs after maximum penetration of the projectile into the target has been achieved. The degree of damage created by the detonation depends on the position of the shell inside the target at the moment the detonation occurs. The test results given below demonstrate this.

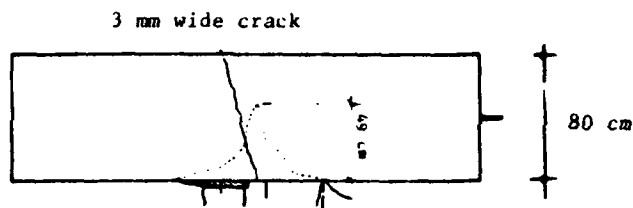


Figure 1: Damage created by a 105 mm artillery shell penetrating a reinforced concrete target  
(Penetration effects only)

The tip of the nose had reached a penetration depth of  $x = 0.61 \times$  target thickness. The follow-on detonation created little damage to the target, see Figure 2 (Reference (2)).

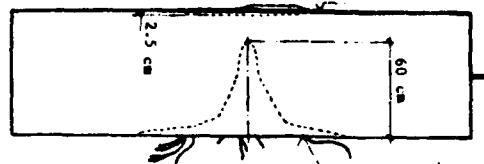


Figure 2: Damage created by the detonating charge of the shell

In another test of the same serial a penetration depth of 0.75 times the target thickness was measured. The follow-on detonation of the charge created a breakthrough; see Figure 3.

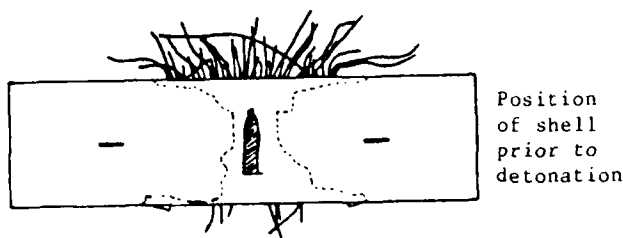


Figure 3: Damage created by the detonating charge

#### Penetration into infinite thick targets

Handbooks for the design of protective structures, see for example Reference (4), give formulae for maximum penetration into infinite thick reinforced concrete targets as well as for the perforation limits. However, a clear definition of when a material behaves as though its thickness was "infinite" is needed together with estimates concerning the additional penetration depth if a structure is to be classified as being of "finite" thickness.

##### (a) US Army Corps of Engineer's Formula

By using this formula it can be shown that the maximum penetration into infinite thick reinforced concrete structures will be overpredicted for big caliber projectiles and underpredicted for small caliber projectiles.

$$x = \frac{282.7 W V^{1.5}}{1.785 d (fc')^{0.5}} + 0.5 d \quad (1)$$

The following figures based on actual and predicted penetrations show this very clearly.

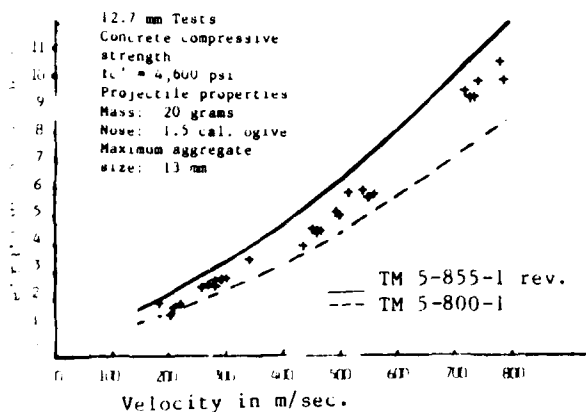


Figure 4: Penetration of 12.7 mm rounds into infinite thick reinforced concrete targets

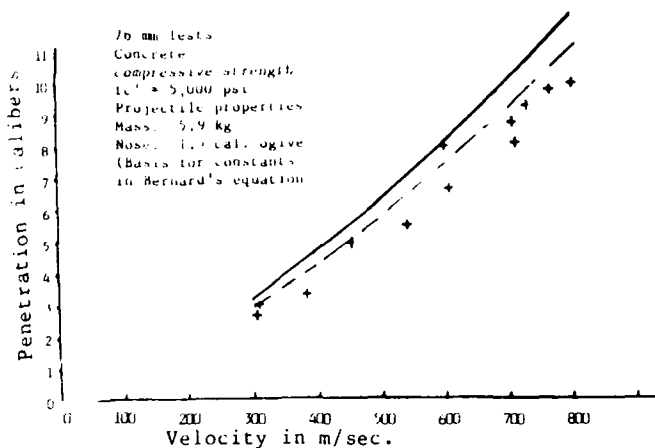


Figure 5: Penetration of 76 mm shells into infinite thick reinforced concrete targets (Reference (3))

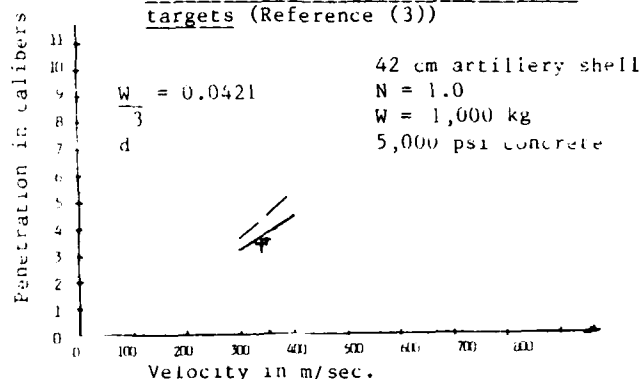


Figure 6: Penetration of 42 cm artillery shells into infinite thick reinforced concrete targets

##### (b) US Army Corps of Engineer's Formula revised

To predict more accurately the effects of penetration into finite thick targets, formula (1) has been slightly modified by the author:

$$x = \frac{400 \times W \times V^{1.5}}{2 \times d (fc')^{0.5}} \times \frac{N G}{0.5} + 0.75 d$$

where

x = maximum penetration into infinite thick reinforced concrete targets, in inches

W = weight of projectile in pounds

V = impact velocity in 1,000 ft/sec.

N = nose shape factor

d = diameter of shell in inches

fc' = compressive strength in psi

$$G = \left( \frac{d}{g \cdot 1.35} \right)^{0.5} \leq 1$$

g = gravel size

The maximum penetration into infinite thick reinforced concrete targets represents an upper limit to all available test data.



## Penetration into finite thick targets

### (a) The problem

The penetration of a projectile into a finite thick target can, in a simplified way, be broken down into the following phases:

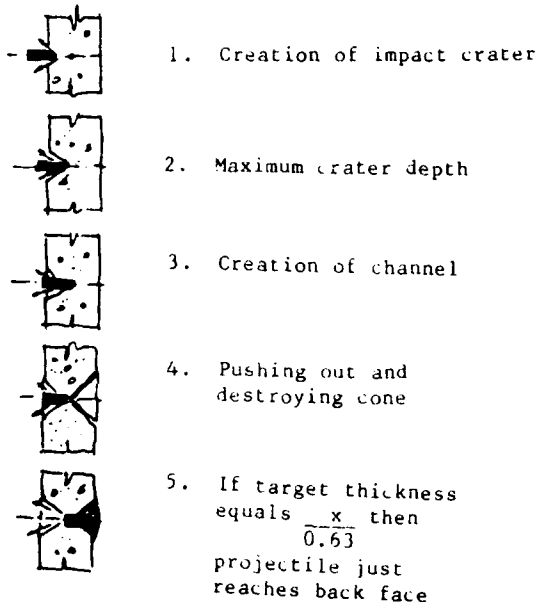


Figure 7: Phases of the penetration/perforation process

The pushing out of the cone at the back side of the target leads to a dramatic drop in target resistance and is responsible for the additional penetration depths which are typical for finite thick targets.

The pushing out of a cone is shown in the next figure. The rear face of a reinforced concrete target after being hit by a model MK 83 bomb ( $\lambda = 4.5$ ) with an impact velocity of  $v = 250$  m/sec. is shown. The test series was conducted by the Ernst-Mach-Institut at Freiburg, Reference (5).

### (b) Test results

The test results given below demonstrate that if sections are built only to meet the minimum requirement a small increase of impact velocity above the assumed level leads to catastrophic results.



Figure 8: Rear side of a reinforced concrete target after being hit by a model MK 83 bomb. The pushed out cone can clearly be identified. Ernst-Mach-Institut test

|                                       |       |       |
|---------------------------------------|-------|-------|
| Impact velocity in m/sec:             |       |       |
| 315                                   | 374   | 341   |
| Concrete compressive strength in psi: |       |       |
| 4,600                                 | 4,600 | 3,800 |

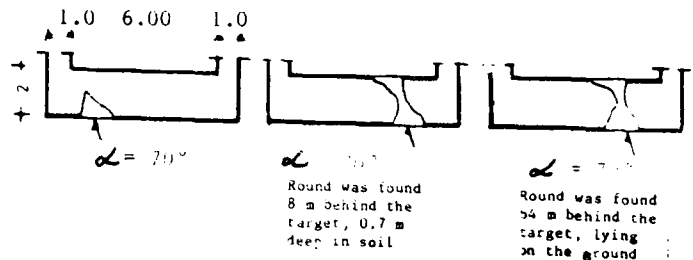


Figure 9: Artillery shells of 30.5 cm caliber (386 kg) fired against 2 m thick reinforced concrete targets, (Reference (6))

The following figures show )  
 results of penetration )  
 tests for a range of ) Where calibers  
 calibers. Note that ) range from  
 perforation occurs when ) 38 cm to 5 cm  
 the predicted penetration )  
 depth exceeds 63% of the )  
 target thickness, )  
 reference (7). )

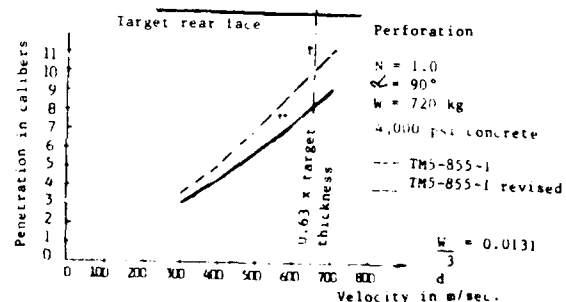


Figure 10: 38 cm shells fired into 5 m thick reinforced concrete targets

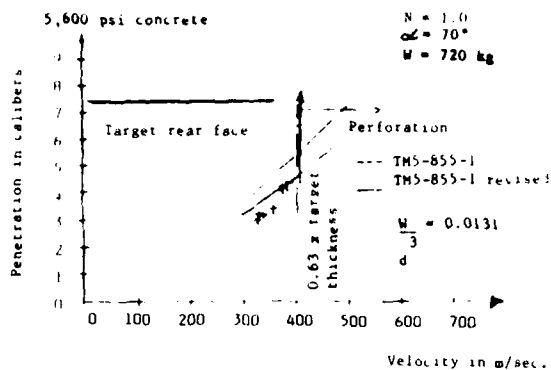


Figure 11: 38 cm artillery shells fired into 2.5 m thick reinforced concrete targets

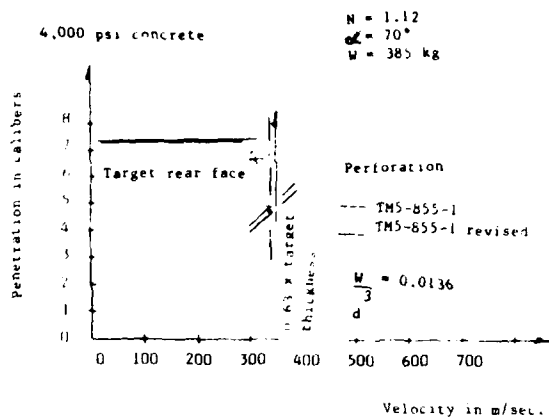


Figure 12: 30.5 cm artillery shells fired into 2 m thick reinforced concrete targets

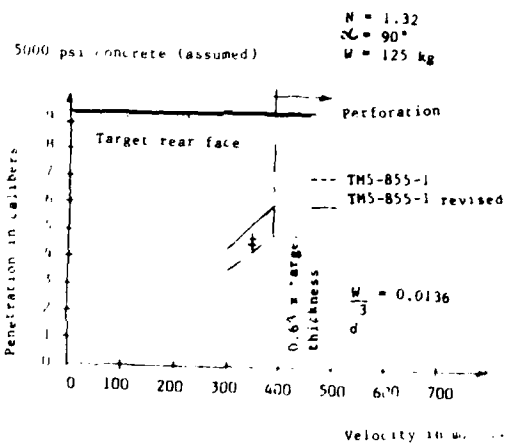


Figure 13: 21 cm artillery shells fired into 2.0 m thick reinforced concrete targets

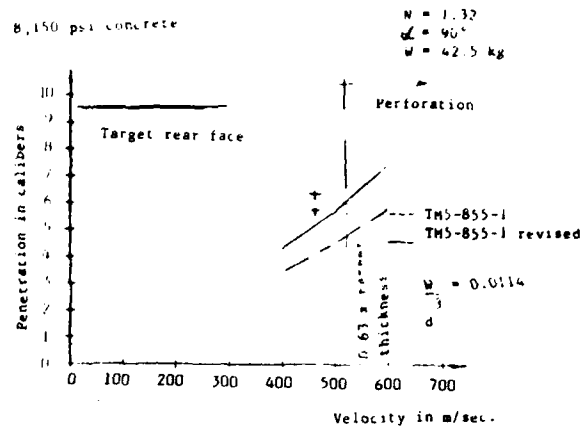


Figure 14: 15.5 cm artillery shells fired into 1.5 m thick reinforced concrete

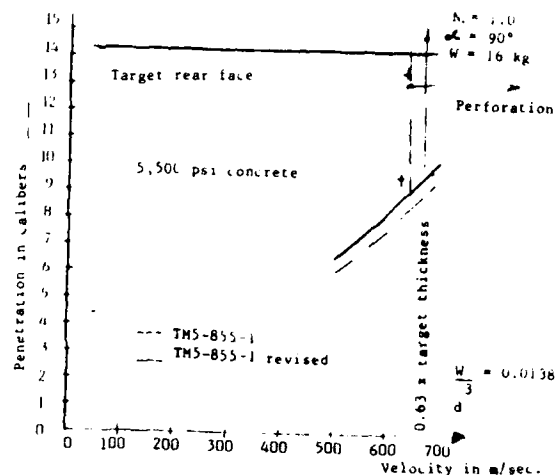


Figure 15: 10.5 cm artillery shells fired into 1.5 m thick reinforced concrete targets

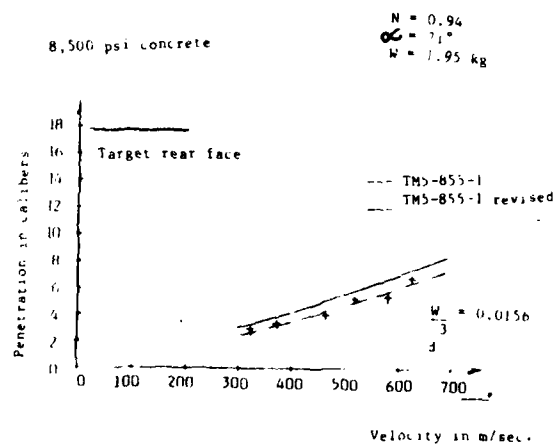


Figure 16: 5 cm anti-tank shells fired into 0.8 m thick reinforced concrete targets

(c) Evaluation of test results

(i) Calibers varying between 42 cm and 10.5 cm

All existing test data are represented in Figure 16.

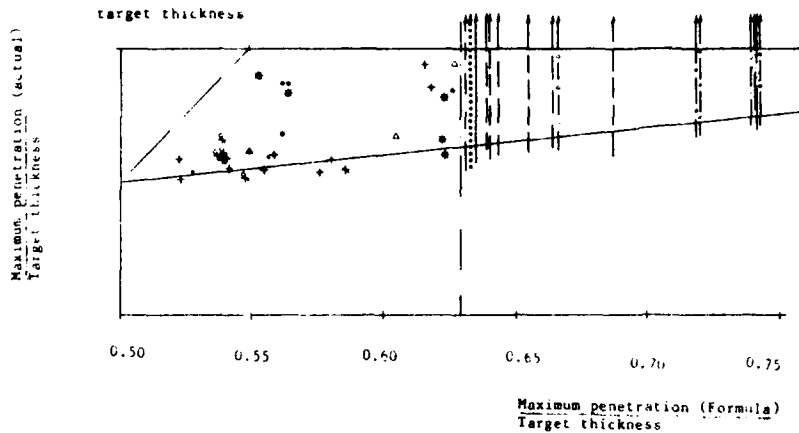


Figure 17: Penetration of projectiles ranging from 42 cm to 10.5 cm into finite thick reinforced concrete targets (References (6) and (7))

The results can be summarised as follows:

Maximum penetration expressed as % of target thickness

- 0 - 50% The target can be considered infinitely thick.
- 50% - 55% The actual penetration is greater than the formula predicts. An upper bound for the additional penetration is given by the use of an increase factor of 1.0 at 50% target penetration and 1.818 at 55% target penetration.
- 55% - 63% The test data scatter and are found between the predicted value for penetration into a half space and the rear face of the target. From the defender's point of view it might be necessary to assume that the point of the nose reaches the rear face of the target.
- 63% The point of the nose reaches the rear face.
- 63% Perforation occurs.

(ii) Test series conducted at MEPPEN in 1971-1973

The results of a test series conducted at Meppen, where only one type of weapon was used, which were fired into targets of equal thickness, however, of different

compressive strength is given below. All shells were fired with the same velocity. Due to classification restrictions the thickness of the target, the caliber of the shell, and the impact velocity are not given. Even so, it can be clearly seen, that the same result as described under (i) was achieved, as described reference (8).

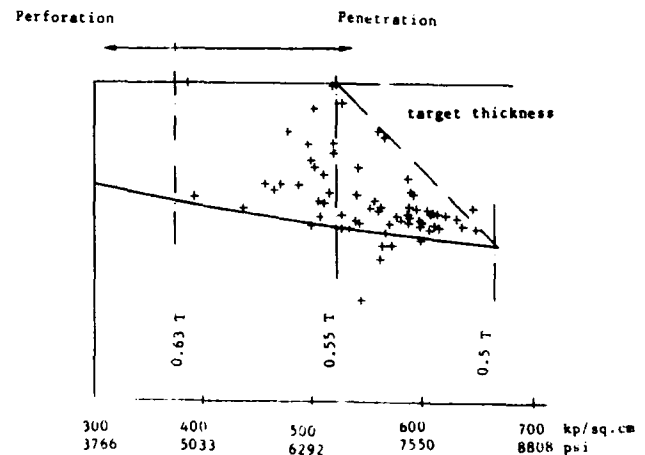


Figure 18: Penetration of projectiles into reinforced concrete targets (MEPPEN test series)

## Actual Data

To give an example of what has happened under battlefield conditions, results are presented from experience from WW I. The most famous French fortification was Fort DOUAUMONT at VERDUN. French engineers had designed this fortification so well that it was able to withstand the effects of no less than 120,000 hits by artillery shells of all calibers up to 42 cm. "The concrete won," wrote Maneger, the former artillery commander of the fortifications around VERDUN.

A few examples are given below.

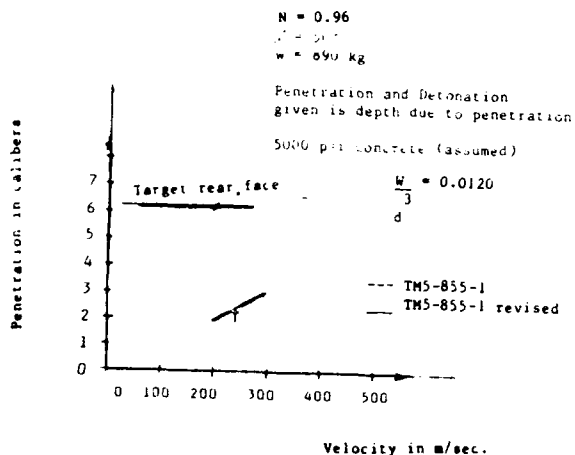


Figure 19: 42 cm artillery shell fired into 1.54 m thick reinforced concrete arch at Fort DOUAUMONT - 1916

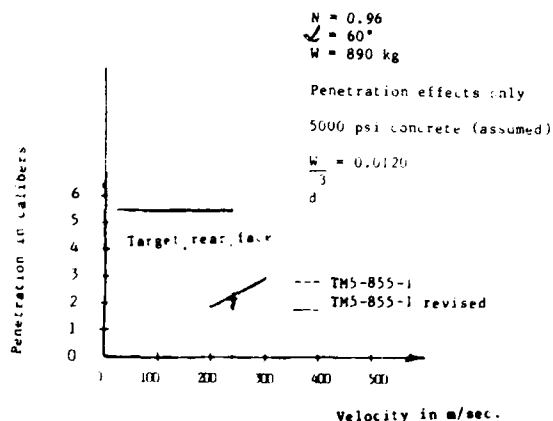


Figure 20: 42 cm artillery shell fired into 1.75 m thick reinforced concrete arch at Fort DOUAUMONT - 1916

## Summary

Evaluation of test results demonstrates that formulas which predict the maximum penetration into reinforced concrete targets are only valid if the target thickness is at least twice the penetration depth. If the maximum penetration is 63% of the target thickness perforation will occur. Between the 50% and the 63% marks the test data scatter and only upper and lower bound values can be given.

## References

- (1) Speth, Beton im Festungsbau und sein Verhalten gegen Geschosswirkung, Beton und Eisen, 37.Jahrgang, Heft 15
- (2) Stahlfaserbeton, II. Teilbericht, Oberjettenberg, 1978
- (3) Fundamentals of Protective Design for Conventional Weapons, July 1984, Department of the Army, US Army Corps of Engineers, Washington DC
- (4) Confield, Clater, Development of a scaling law and techniques to investigate penetration in concrete, 1966, US Naval Weapons Laboratory, Dahlgren, Virginia
- (5) Ernst-Mach Institut, Freiburg, Communication with Dr. Stulp, Mrs. Langheim, Mr. Huelsewig
- (6) Versuchsserie ALTENWALDE, Militararchiv Freiburg
- (7) Papers of Heereswaffenamt, Probably Mr. Speth's collection
- (8) Communication with Mr. Hans Heine, Meppen

# CONCRETE PENETRATION - ARE ALL PENETRATION FORMULAS CREATED EQUAL AND CAN THEY BE USED EQUALLY?

Bengt E. Vretblad  
FortF - Royal Swedish Fortification Administration  
Eskiltuna, Sweden

and

Phillip T. Nash  
Southwest Research Institute  
San Antonio, Texas

## ABSTRACT

The purpose of this paper is to describe physics involved in concrete penetration, compare different equations for projectile penetration with an existing data base, and discuss the spread in the data and the consequences in using the formulas for the needs of the artillerist in the field, for projectile design or for fortification design. Comparisons include actual penetration depths from tests and nondimensional formulations of the impact conditions and results.

The concrete penetration equations are shown to describe only a portion of possible impact conditions. In general, most of the equations provide about the same degree of precision in predicting penetration depths within their respective domain of application. However, for extrapolation outside of these conditions care should be taken so that governing physical constraints are not exceeded. One penetration equation is adapted for either offensive or defensive design and differences in the corresponding penetration depths are shown to be significant. Significant differences in equation predictions illustrate the importance of considering the objectives when choosing the formulation.

## BACKGROUND

Penetration formulas were originally developed based upon the physics controlling the conditions to be modeled. Later, the experimental data base grew to make possible improving these formulas and developing new ones. The development of the newer formulas, to a degree, relied more heavily on the statistics provided by the data base than the inherent physics. A major concern is that the formulas were changed to improve the precision of the relationships rather than to provide an adequate tool for the projectile designer desiring to guarantee penetration or the fortification engineer whose main objective is to prevent penetration. Relying on the statistics of the relationships rather than the physics involved can lead to errors when extrapolating beyond the limits of the data base.

The history of projectile penetration formulas dates back with the history of artillery. As early as in 1742 Benjamin Robins made an analytic, quantitative, estimation of the depth of penetration based on a constant resistant force during the penetration [1]. The formula was elaborated by Leonard Euler in 1745, [2]. The depth of penetration,  $x$  was found as:

$$x = \frac{M V^2}{2R} \quad (1)$$

where:  $V$  - velocity  
 $M$  - projectile mass  
 $R$  - resistant force.

\* Consistent parameter units are required unless otherwise specified

Equation (1) is based upon the physical consideration that the projectile undergoes little or no deformation while the impact stresses generated greatly exceed the failure strengths of the target material.

In 1829 J. V. Poncelet published [3] and introduced the sectional pressure as one relevant parameter for the calculation of penetration. Poncelet's formula for penetration can be written as:

$$x = K \frac{M}{A} N \log (a + b V^2) \quad (2)$$

where:  $A$  - cross sectional area of the projectile  
 $N$  - factor accounting for nose shape  
 $K$  - overall constant  
 $a, b$  - constants depending on the crushing properties and the inertial effects for the target material respectively.

The introduction of empirically derived constants into penetration formulas allowed for increases in the precision of formula predictions with better penetration test data. As the evaluation of Poncelet's formula was not very straight forward it was modified by Petry, [4], to be written in the form:

$$x = \frac{KM}{d^2} f(V) \quad (3)$$

where:  $d$  - diameter of projectile  
 $f(V)$  - a function of the velocity

Petry's formula was considered an improvement of Poncelet's equation and included an extensive regression effort to solve for the empirically derived constants.

From the turn of the century concrete has been a major material for protective structures. Therefore, the calculation of penetration into concrete is of high importance. The formulas for penetration mentioned subsequently all refer to concrete.

During and after the World War II comprehensive tests were performed and added substantially to the data base. As a result of these tests other penetration formulas were developed. Beth, [5], [6], [7], performed series of tests in different scales that led him to the formula:

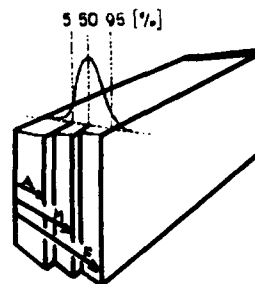
$$x = N \left\{ \sqrt{\frac{KMV^{1.5}}{f_c d^{1.75}}} + 0.5d \right\} \quad (4)$$

where:  $f_c$  - compressive strength of concrete

Other formulas are named after the Corps of Engineers (based upon Beth's work), [8], Bernard, [9], a British formula, [10], Halder and Miller, [11], Hughes, [12], National Defense Research Committee (NDRC), [11], Sandia (Young), [10], Tolch and Bushkovitch, [13], and the FortF formula, [14]. Some formulas give a wider spectrum of scatter than others, [10]. Not even for carefully planned and executed tests can scatter be prevented. Complete descriptions of each of these formulas will not be presented in this paper for the sake of brevity. Descriptions are available from the listed references.

This raises the question of what purpose a penetration formula should serve: (1) should it give a best fit to an existing set of test data; (2) should it be a tool for the projectile designer to give a high probability of killing the target or (3) should it serve the purpose of the fortification engineer giving a high probability of structural survivability?

Measured data compared with calculated values according to [14] are given in Figure 1. The figure shows the thicknesses for 95 percent chance of penetration and 95 percent chance of survivability with reference to the mean value. The two values differ with a factor of 2.2! Obviously, the choice of a correct formula can be very cost-effective, but the use of the formula correctly is likewise important!



A = thickness that 5% of projectiles will penetrate  
M = " " 50% " " " "  
F = " " 92% " " " "

For the case in the test  $F = 2.2 A$   
(Note: The penetration values refer to thick targets where perforation does not occur. Regarding perforation in similar comparisons will change the numbers to some extent but not the overall principle.)

Figure 1.

## PHYSICS OF PENETRATION

The penetration is largely dependent on the properties of the projectile, the properties of the target and the velocity.

The impact conditions can be characterized in different ways. One approach outlined in [16] results in nine discrete impact regimes identified by the relationship of the impact generated pressures to the strengths of the projectile and target materials. For all problems that can be related to one of these regimes similar solution techniques fit for problems with similar geometries. "It is the nature of research that the problems studied are those of greatest immediate relevance or those most easily understood", [16]. This holds true also for impact mechanics.

|                             | $\frac{P}{\sigma_p} \ll 1$ | $\frac{P}{\sigma_p} \sim 1$ | $\frac{P}{\sigma_p} \gg 1$ |
|-----------------------------|----------------------------|-----------------------------|----------------------------|
| $\frac{P}{\sigma_t} \ll 1$  | (1, 1)                     | (1, 2)                      | (1, 3)                     |
| $\frac{P}{\sigma_p} \sim 1$ | (2, 1)                     | (2, 2)                      | (2, 3)                     |
| $\frac{P}{\sigma_p} \gg 1$  | (3, 1)                     | (3, 2)                      | (3, 3)                     |

where  $P$  - Impact Pressures  
 $\sigma_p$  - Projectile Strength  
 $\sigma_t$  - Target Strength

Figure 2. Matrix of Impact Regimes

For the corner boxes in Figure 2 the analytical procedures are more straight forward, e.g.  $\sigma_t \ll P \ll \sigma_p$  [Regime (1,3)] which is applicable for low or intermediate velocity impacts in soft materials. For the non-corner boxes the solutions get more complicated as strength effects, large displacements and failure mechanisms must be recognized. Generally, the solutions to problems in these cases have usually been semi-empirical or empirical.

Bombs and artillery shells penetrating into concrete usually fall into Regime (1,2) meaning that the impact stresses are lower than the failure stresses of the bomb cases yet higher than the ultimate stresses for the target material. However, for high impact velocities, which are relevant for some new high velocity penetrators the Regime (2,3) will be applicable since impact stresses are nearer the failure stresses of the bomb case.

The penetration formula of Equation (1) results from considering the kinetic energy at impact equal to the work of the (constant) reactive force during the penetration. This simple approach has been used as the basis for a number of concrete penetration prediction methods developed in steps to account for more complicated conditions. Poncelet's contribution was to account for not a constant but varying reactive force decreasing with increased penetration. Other refinements included accounting for the geometry of the projectile and better definitions of material resistances. For example, projectiles with ogive noses have better penetration capabilities than projectiles with blunt noses. This led to the introduction of a nose factor. Petry's formulation of his penetration equation contains the projectile diameter raised to the exponent -2.0. Beth's careful studies brought him to use the corresponding exponent -1.78. The reason for this difference can be found in the fact that for the same velocity and the same M/A ratio projectiles with bigger diameter have a tendency to penetrate deeper than those with smaller diameters. The curing of concrete takes time - more time for a thicker specimen and therefore a small scale test specimen will be better cured than a full scale one and the results on scaling up can be erroneous.

Most of the penetration formulas set the penetration proportional to the velocity raised to an exponent,  $x$ . For the different formulas given above  $x$  varies between 1.0 and 2.0. Obviously this has a significant importance in particular when it comes to extrapolations to higher velocities. Bergman found when developing the FortF formula, [14], that test data did not support such a simplification. Rather, the exponent,  $x$ , should be a function of scaled penetration,  $x/d$ . Empirical data is therefore necessary to better define parameters in the penetration formulas and increase their precision.

However, two points should be remembered when using empirical information to develop or

refine penetration formulas:

- (1) Empirically derived formulas are accurate only for the conditions from which they were derived (i.e. methods develop for impact Regime (1,2) might not apply to impact conditions within Regime (2,3))
- (2) The formulas should serve the user (i.e. projectile designer or fortification engineer).

These two points will be illustrated by presenting an existing data base in nondimensional form, comparing several concrete penetration formulas with the nondimensional data base, and then comparing predictions from the equations with the data.

### CONCRETE PENETRATION DATA

Dimensionless ratios can be obtained from the parameters which describe the impact of a projectile against a concrete target using the pi theorem. Pi terms generally can be categorized as nondimensional parameters, self-similar geometries, densities, strengths and response terms. For concrete penetration, two response terms were chosen for comparisons:

$$\pi_1 = \frac{\rho^{1/2} V}{f'_c}$$

$$\pi_2 = \frac{\rho A x}{M}$$

where:

- $\rho$  - concrete density
- $V$  - impact velocity
- $f'_c$  - concrete strength
- $A$  - bomb frontal area
- $M$  - bomb mass
- $x$  - penetration depth

Concrete penetration data was derived from several sources for comparing penetration formulas. The primary source of data was a compilation of test results from [5]. Other records were available at Southwest Research Institute from testing of scaled penetrators into massive concrete targets. Items from the semi-infinite target data base are plotted in Figure 3 using the two response pi terms. Test data were for weapons ranging in weight from one to several hundred pounds. Variations probably result from inherent scatter and finer differences in details of the target or penetrator such as aggregate size, bomb nose shape, etc. However, an important observation is the increase in data variation with an increase in the value of  $\pi_1$ . The ratio  $\pi_1$  can be interpreted as the ratio of stress at the projectile/target interface to the failure stress of the target material. For lower velocities (lower values of  $\pi_1$ ) the interface stresses are

well below the failure stress of the projectile material. As the velocity increases the interface stresses increase until they eventually equal or exceed failure stresses in the bomb case and case deformations result. This transition between impact regimes has been observed with similar scatter by other researchers investigating soil penetration [17] and heavy metal penetrators against concrete [18]. Figure 3 does not specifically denote the transition between impact regimes, but simply shows the tendency for change. Because concrete penetration formulas or equation constants are usually empirically derived for specific impact regimes, caution should be used in general application of the formulas to other impact regimes. Unfortunately, no great attempt has been taken to accurately define limits of the various impact regimes.

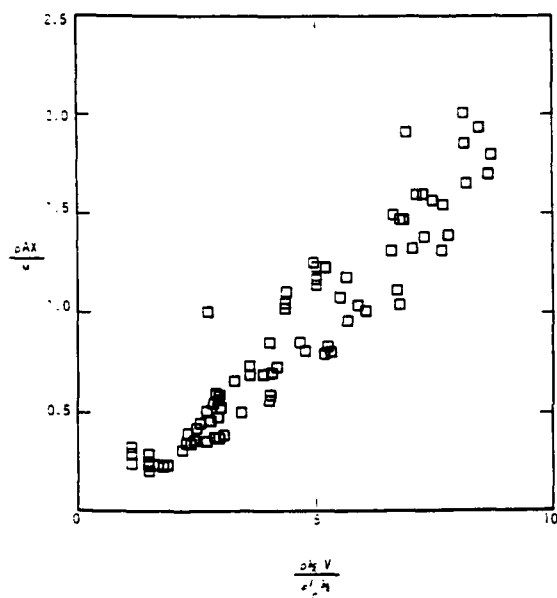


Figure 3. Concrete Penetration Data  
-Nondimensional Form

An interesting comparison was suggested by Westine [10]. Several familiar formulas for predicting concrete penetration were developed in terms of  $\pi_1$  and  $\pi_2$  by using typical values of bomb/concrete target descriptions and impact conditions and compared with the nondimensional data of Figure 3. The results are shown in Figure 4 for three equations: (1) Army Corps of Engineers (COE), (2) Hughes, and (3) Modified Petry. The COE equation falls within the scatter over the entire data base although it appears greater accuracy would be seen for the lower velocities. The Hughes equation would seem to overpredict penetration at the lower velocities and underpredict at the higher velocities. The Modified Petry equation falls within the scatter at lower velocities while greatly underpredicting at higher velocities. These comparisons are not presented to recommend nondimensional forms of penetration equations because they cannot account

for finer details of specific impact conditions. However, the comparisons do illustrate that concrete penetration equations cannot be arbitrarily applied over all ranges of impact conditions.

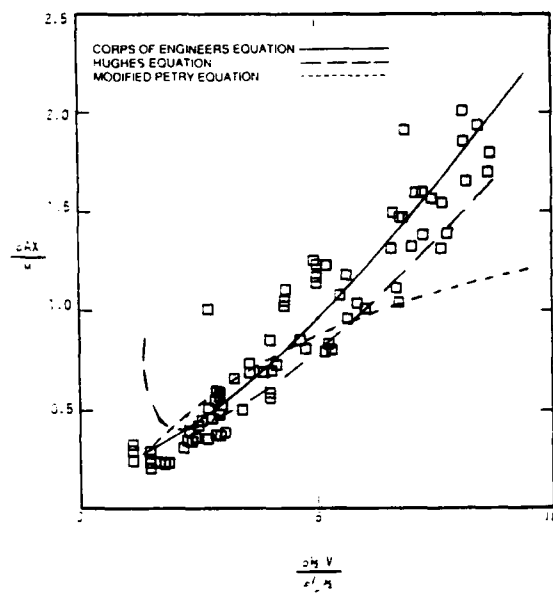


Figure 4. Comparison of Non-Dimensional  
Equations and Data

A comparison of several of the concrete penetration formulas will illustrate the difficulty in developing more precise equations and the need for adapting the formulas as tools for either projectile designers or fortification engineers. Concrete penetration formulas were compared with the available data base by defining prediction error as the difference between calculated and measured penetration depth. The error was expressed as percentage of error through the following relationship:

Error =

$$\frac{(\text{Calculated depth} - \text{Measured depth})}{\text{Measured depth}} \times 100\% \quad (5)$$

With this definition, an error of 100 percent indicates that the equation predicted a depth of penetration twice as large as what was actually obtained in the test. An error of -50 percent indicates that the equation predicted that the projectile would travel only half as far as it actually did in the test. A summary of depth of penetration prediction errors is shown in Figure 5 for several formulas. The important observation from Figure 5 is that although there is some difference in the relative accuracies of the various equations, both overpredictions and underpredictions are evidence for each equation. This means that the equations have no inherent conservatism for either the projectile designer or the fortification designer. The designer is therefore left to use his own judgement for factors of safety and trusting the accuracy of the equation can result in great error. A more



logical approach would be to develop forms of the concrete penetration equations based upon the designers perspective and confidence levels derived from the data base.

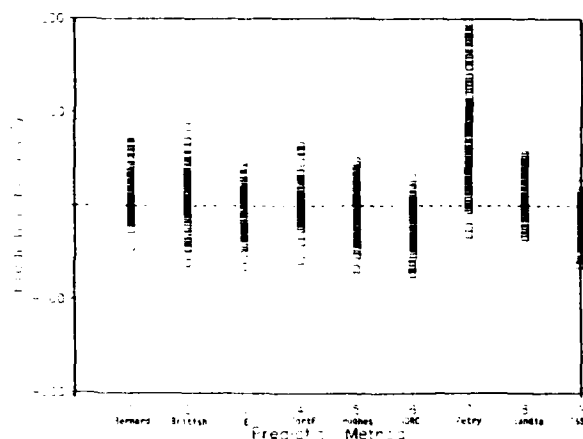


Figure 5. Depth of Penetration Prediction Errors

### CONCLUSIONS

Obviously, not all penetration formulas are created equal nor do they give equal results. Most formulas are semi-empirical in nature and are based on a certain set of data. It is to be expected that a formula based on one particular set of data should fit impact regimes of that data set. However, extrapolation of results from one impact regime to another must give proper regard to the physics involved and penetration formulas must be matched with their proper impact regime.

The spread in data is considerable for all known formulas. The question then becomes not only to choose the right formula but use it correctly. This includes being aware of the purpose of the calculation whether it be to design a successful projectile or survivable fortification. It has been shown that a design based upon a 95 percent chance of penetration and a design based upon a 95 percent chance of survival can lead to differences in concrete thickness more than a factor of 2.2.

### ACKNOWLEDGMENTS

The authors express their thanks to Sandia National Laboratories and the Air Force Armament Laboratory for supporting previous efforts from which many of the observations reported were taken. We wish also to thank the Royal Swedish Fortification Administration and Southwest Research Institute for their support during the preparation of this paper.

### REFERENCES

1. Robins, B., *New Principles of Gunnery*, London, 1742.
2. Euler, L., Note in the translation of [1] into German, Berlin, 1745.

3. Poncelet, J. V., *Cours de Mecanique Industrielle*, 1829.
4. Cranz, C., *Aussere Ballistik*, Berlin, 1925.
5. Beth, R. A., Stipe, G. J., *Penetration and Explosion Tests on Concrete Slabs*, Interim Report to the Chief of Engineers United States Army by the Committee on Passive Protection Against Bombing, Washington, D. C., January, 1943.
6. Beth, R. A., *Concrete Penetration*, NDRC Report No. A-319, OSRD Report No. 4856.
7. Beth, R. A., *Effect of Concrete Properties on Penetration Resistance*, Interim Report No. 27 National Research Council Committee on Fortification Design, July, 1944.
8. *Protective Design, Fundamentals of Protective Design (Non-Nuclear)*, Department of the Army Technical Manual TM-855-1, July 1965.
9. Bernard, R. S., *Empirical Analysis of Projectile Penetration in Rock*, U. S. Army Waterways Experiment Station Paper AEWES-MP-S-77-16.
10. Nash, P. T., et al, *Concrete Penetration Data Base and Evaluation of Predictive Equations*, Southwest Research Institute, Final Report, Project 06-8691, April, 1986.
11. Halder, A. and Miller, F. J., *Penetration Depth in Concrete for Nondeformable Missiles*, Nuclear Engineering and Design, Vol. 71, pp. 79-88, 1982.
12. Hughes, G., *Hard Missile Impact on Reinforced Concrete*, Nuclear Engineering and Design, Vol. 77, pp. 23-35, 1984.
13. Tolch, N. A. and Bushkovitch, A. V., *Penetration and Crater Volume in Various Kinds of Rocks as Dependent on Caliber, Mass, Striking Velocity of Projectile*, BRL Report No. 641, October, 1947.
14. *Fortifikationshandbok del 1*, MSB, Stockholm, 1987. (In Swedish)
15. Vretblad, B., *Penetration of Projectiles in Concrete According to FortH 1*, FortF/F Report C4:88, Eskilstuna, 1988.
16. Wilbeck, J. C., *Classification of Impact Regimes*, SwRI Project No. 06-9304, Final Report, San Antonio, Texas, 1985.
17. Stilp, A. J., et al, *Penetration of Fragments into Sand*, Proceedings of Second Symposium on the Interaction of Non-Nuclear Munitions with Structures, Panama City Beach, Florida, April 15-18, 1985, pp. 333-337.

18. Stilp, A. J., Langheim, H. and Schilling, H., Eindringverhalten von KE-Penetratoren in Betonziele, Internationales Symposium Interaktion Konventioneller Munition mit Schutzbauten, Band I, Mannheim, 09-13 Maerz, 1987, page 203.

# Investigation of Explosively Formed Projectiles Impacting Concrete

M.J. Worswick, D.J. Mackay, A. McQuilkin, C.A. Weickert, T. Storrie, S. Mowers

Defence Research Establishment Suffield  
Ralston, Alberta, Canada, T0J 2N0

## Abstract

The use of explosively formed projectiles (EFPs) for remote-standoff demolition of pre-stressed concrete bridge beams is investigated. Results from a field trial series in which commercial EFPs were fired into pre-stressed concrete beams are presented, along with a number of supporting finite element simulations of the EFP formation and penetration into the beam. The EFP was effective in breaching up to 1 m of concrete at a standoff distance of 12 m. The reinforcing cables cut, however, were limited to those located directly in the path of the EFP. Good agreement was obtained between the numerical simulations and experiment.

## 1 Introduction

Bridge demolition is a primary counter-mobility method used by military engineers. Methods used in bridge demolition typically involve the use of direct contact high explosives or linear shaped charge devices for cutting steel bridge beams and massive bulk charges for top attack of concrete bridge decks. While these techniques have proven effective, some question exists concerning the most rapid and effective methods for explosive demolition of modern bridge designs with massive reinforced and tensioned precast concrete beams.

Of particular interest in the current study is the demolition of modern pre-stressed concrete bridge beams which are composites of concrete with interior pre- or post-tensioned cables. The cables are tensioned in order to place the concrete in a state of axial compression thus improving the load-carrying capacity of the beam.

One approach to the demolition of such beams involves the use of large high explosive charges designed to destroy a large section of concrete along the length of the beam. While such a charge would not cut all of the cables within the beam, simply-supported beams would collapse under the dead load of the beam due to an inability to support compressive bending stresses. However, it is questionable whether continuously-supported beams would collapse since the uncut cables could support the dead weight of the section cut and straightforward bridging operations could repair the bridge for use by military vehicles. Thus it would be desirable to develop demolition devices for cutting the interior tensioned cables in addition to destroying the concrete.

A second issue arises in all military engineering demolition requirements, namely the desire to obtain reliable remote-standoff devices to replace existing direct-attachment devices. Remote-standoff demolition devices can be set up and fired remotely from the target, saving considerable time and resources and reducing the exposure of personnel involved in the setup.

One device that has been suggested for use in remote-standoff demolition of pre-stressed concrete beams is the explosively formed projectile (EFP). EFPs consist of high explosive-backed, dish-shaped metallic liners which form into high velocity projectiles during detonation of the explosive. These devices can be used in remote-standoff applications

since the projectiles will fly considerable distances and can be aimed accurately at a range of up to 100 m if properly designed. In view of these attributes, a preliminary study was undertaken at the Defence Research Establishment Suffield (DRES) to determine the effectiveness of EFPs in demolishing pre-stressed concrete beams.

A series of field trials were undertaken in which commercially available EFPs were fired against pre-stressed concrete beams. Three criteria were selected for assessing the damage inflicted by the EFP on the beams studied:

1. the number of pre-stressed cables cut by the EFP;
2. the extent to which the concrete surrounding the target point is destroyed or breached due to impact of the EFP;
3. the accuracy of the EFP device studied under remote-standoff conditions.

To complement the experiments, numerical simulations of the EFP liner collapse, projectile formation and penetration of the beam were undertaken using the 1986 release of the finite element code EPIC-2 [1]. The purpose of these calculations was to obtain a more detailed picture of the penetration process and to evaluate the predictive capability of the EPIC-2 code for problems involving penetration of reinforced concrete.

## 2 Experimental Details

Experimental firings of the EFPs against the pre-stressed concrete beams were performed at the DRES experimental proving ground. The EFP used in this study was the CIL "power cone" used in the mining industry. Figure 1 shows a cross-sectional view of the EFP used. The liner was made of copper, with an outer diameter of 28 cm, and the casing was mild steel. The explosive loading was 13.5 kg of pentolite.

Figure 2 shows a flash X-ray radiograph of the liner taken 2000  $\mu$ sec after firing of the charge. The figure shows that the liner breaks into

| Trial Number | Attack Orientation | Standoff Distance (m) | Vertical Offset† ( $\delta$ ) (cm) | Length of Breach (cm) |
|--------------|--------------------|-----------------------|------------------------------------|-----------------------|
| 203-2        | Bottom             | 0.9                   | na                                 | 75                    |
| 203-3        | Side               | 5.2                   | 5.1                                | 66                    |
| 203-4        | Side               | 0.9                   | 0.0                                | 0                     |
| 203-5        | Side               | 9.1                   | 8.9                                | 102                   |
| 203-6        | Side               | 12.2                  | 5.1                                | 75                    |

† See Figure 5.

Table 1: Attack orientations and standoff distances.

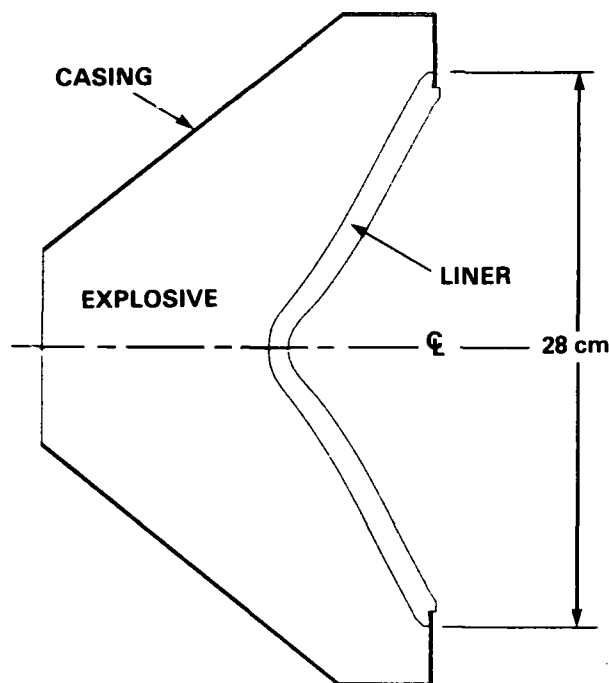


Figure 1: Cross-section of CIL "power cone" EFP showing liner profile and explosive loading.

two primary fragments and several smaller fragments. The velocities of the lead and follower primary fragments are 1.5 and 1.16 km/sec, respectively, in a direction from right to left in Figure 2. Three EFPs were fired at the DRES flash X-ray site and all of the liners formed two fragments similar to those shown in Figure 2.

The beams used in this study were 14 m in length and simply-supported. Their cross-sectional view, showing the pre-stress cable pattern, is shown in Figure 3. The beams were 61 cm in depth and 89 cm in width while the reinforcing cables were 12.7 mm in diameter. Additional steel reinforcing (not shown) was located running along the beam width and depth to support secondary bending stresses and running axially under the upper surface of the beam. Using impact hammer tests, the concrete strength was estimated to be 34 MPa. Measurements of the cable strength were not performed.

Two attack orientations were tested, side attack and bottom attack, as shown in Figure 3. The bottom attack orientation represents a typical method for remote-standoff demolition of bridges. The EFPs used for side attack were either aimed directly at or slightly above the bottom row of cables. Table 1 summarizes the various attack orientations and standoff distances considered and, for the side attack trials, the vertical offset ( $\delta$ ) of the EFP trajectory relative to the bottom row of cables.

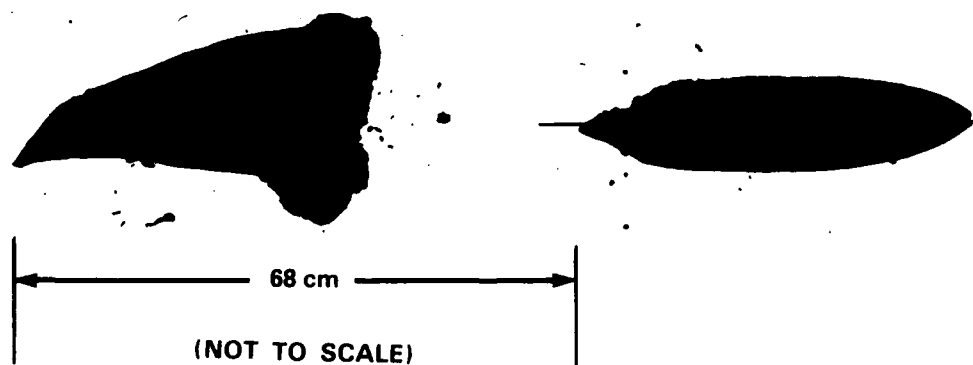


Figure 2: Radiograph showing EFP fragments at 2000  $\mu$ sec.

One additional trial was performed (203-7) using two DREStructor linear shaped charges fired against the bottom of a beam. The DREStructor [2], developed at DRES, has a mild steel liner and is driven by a 10 kg load of trigran explosive immersed in water. This device was used to compare the performance of the axisymmetric EFP with a more conventional demolition "cutting charge".

In another trial (203-1), the EFP was fired into a monolithic concrete cylinder, 119 cm in diameter and 183 cm in length. The cylinder was encased in a steel pipe 123 cm in diameter with a 12.7 mm wall thickness. The purpose of this trial was to determine the penetration of the EFP into concrete without any steel reinforcement. The standoff for this trial was 0.9 m.

### 3 Experimental Results

The results of trial 203-1, in which the EFP was fired into the monolithic block of concrete, were quite impressive in terms of the penetration capability of the EFP. The EFP fully penetrated the 183 cm length of concrete with a hole diameter of roughly 10 cm. There were also radial cracks running from the hole out to the periphery of the concrete cylinder, indicating that the concrete block would have been shattered without the containment of the steel cylinder. There was also a longitudinal crack through the wall of the steel cylinder, running 2/3 of its length.

Thus the total penetration capability of the EFP was not established by this trial, although a lower bound penetration depth of 183 cm was impressive.

The results of the trials in which the EFP was fired against the prestressed beams are discussed in terms of the cables cut, the extent of concrete breached by the EFP and the accuracy of the EFP at distances up to 12 m.

#### 3.1 Bottom Attack

Bottom attack (trial 203-2) resulted in complete penetration and collapse of the beam. The entire beam cross-section of concrete was breached for a length of approximately 75 cm. Figure 4 shows the cable pattern; the cable locations crossed out were completely cut while the circled locations were partially cut. The pattern of cables cut shows that the EFP passed through the beam vertically, cutting all of the cables along the beam centre-line and completely or partially cutting the next column of cables spaced 5.1 cm from the central cables. It is worth noting that the EFP also completely penetrated four 5.1 cm thick mild steel plates which were stacked on top of the beam to limit the vertical flight of the emerging fragments.

#### 3.2 Side Attack

The pattern of cables cut from the side attack orientations are summarized pictorially in Figure 5. In the short standoff trial (203-2), the

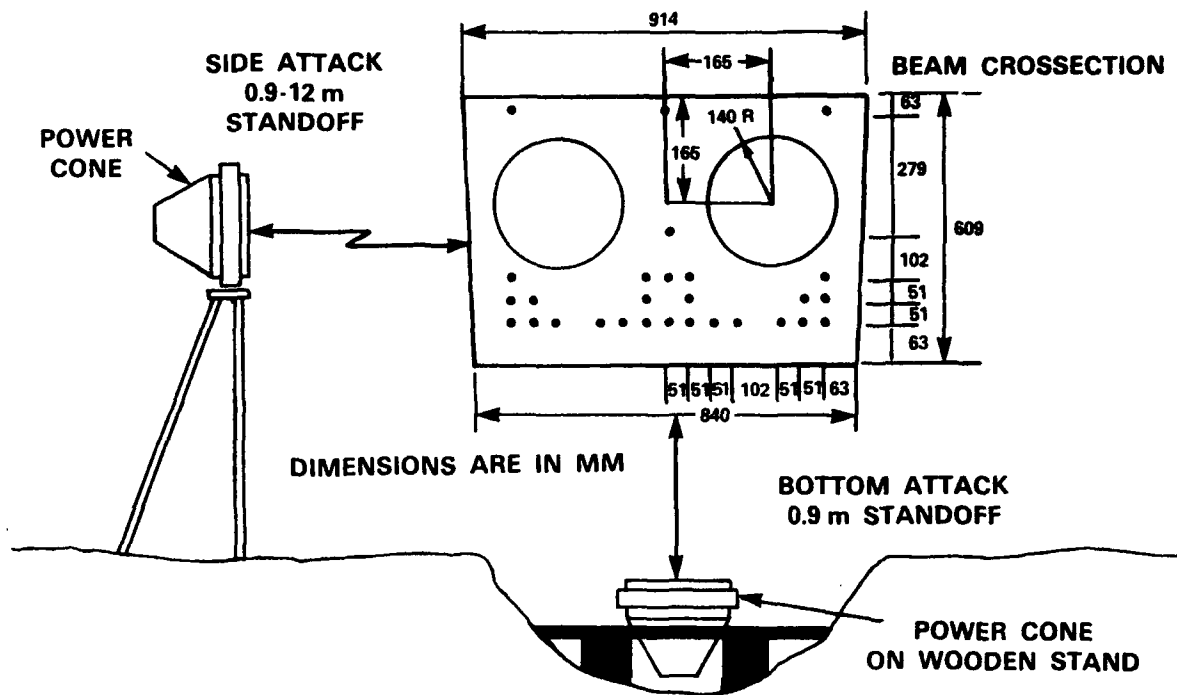


Figure 3: Cross-section of pre-stressed concrete beam used in study.

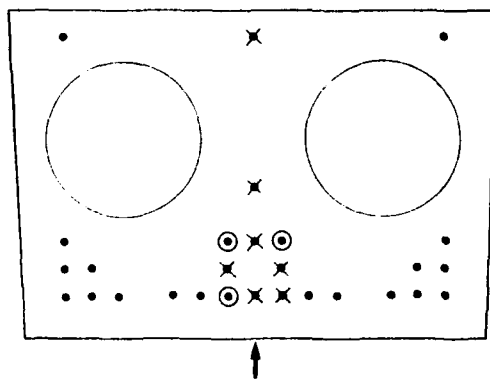


Figure 4: Damage to cables: Bottom attack, 0.9 m standoff.

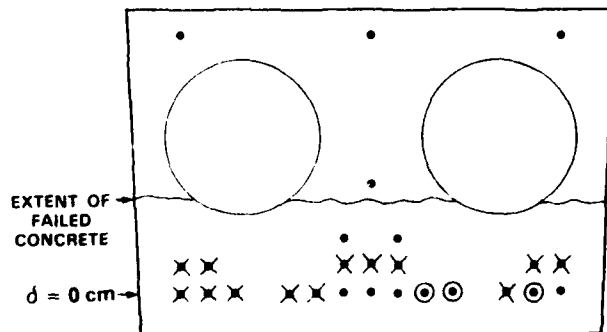
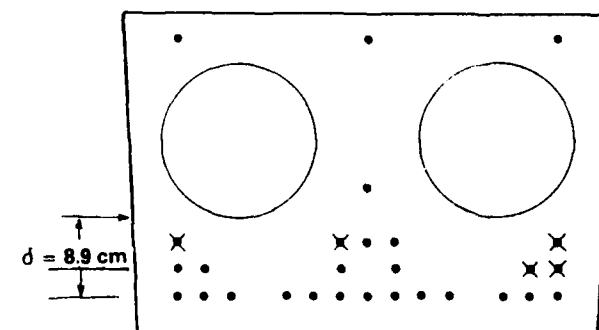
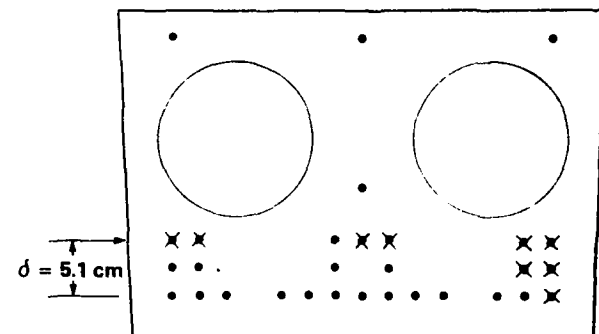
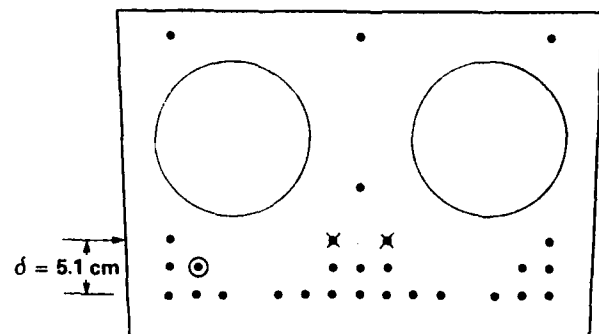


Figure 5: Damage to cables: Side attack



EFP was aimed directly along the line of the lower layer of cables and left only four cables of the bottom twenty uncut (Figure 5a). On exiting this beam, the EFP entered an adjacent beam (not shown), spaced 100 mm from the first beam, cutting 10 more cables prior to exiting via the bottom face of the second beam.

The longer standoff trials, in which the EFP was aimed above the bottom row of cables resulted in fewer cables being cut. Those cables that were cut were in the second and third rows, indicating that the EFP entered the beams close to the intended trajectories shown in Figure 5.

With the exception of trial 203-4, in which the EFP was aimed closest to the bottom of the beam, the entire cross-section of the concrete was shattered resulting in collapse of the beam. The actual lengths of concrete breached are summarized in Table 1 and the depth of concrete destroyed in trial 203-4 is indicated in Figure 5a by a wavy line.

Examination of Table 1 reveals that the extent of concrete destroyed was increased when the EFP impacted the beam nearer its middle (increased  $\delta$ ). The results also demonstrated that simply cutting the tensile reinforcing cables was insufficient to cause collapse of the beams. The trial which resulted in the greatest number of cables being cut did not cause the beam to collapse because the concrete cross-section was not fully breached. The concrete remaining lay in the upper, compressively-loaded region of the beam (Figure 5a) and prevented the formation of a hinge.

### 3.3 Linear Shaped Charge Results

The DREstructor linear shaped charges placed across the bottom of the beam completely severed the beam. The cutting action of the shaped charge liner left only the top three cables uncut, as seen in Figure 6, and the concrete was destroyed for a length of 150 cm. Comparison of the results using the axisymmetric EFP and the linear shaped charge clearly demonstrates the wider cutting action of the shaped charge. Note however that the performance of the EFP did not degrade significantly with increased standoff in the range 1-12 m whereas the shaped charge device must be attached directly to the target.

## 4 Numerical Simulation of EFP Formation and Impact

In order to better understand the mechanics of the liner formation and penetration processes, numerical simulations were performed using the finite element code EPIC-2.

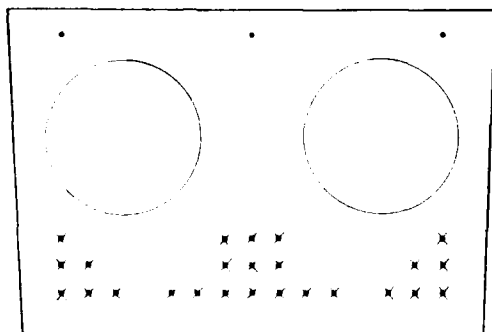


Figure 6: Damage to cables: DREstructor linear shaped charge.

Figure 7 shows the finite element mesh used to model the EFP liner, explosive and casing. The mesh is shown in the initial configuration prior to detonation and the explosive initiation point is shown in the figure. The model was axisymmetric about the z-axis, permitting reduction of the problem to two-dimensions.

Standard EPIC library properties were used to describe the constitutive response of the liner components. The liner, explosive and casing materials were copper, pentolite and mild steel, respectively. The in-

terface between the various materials were described numerically using "slide lines" which permit sliding and separation of adjacent surfaces but prevent the materials from overlapping. Description of the finite element equations of motion and the material models used in EPIC is given in [3-6].

The liner formation and collapse was modelled for a period of 250  $\mu\text{sec}$ . The explosive and casing elements were dropped from the calculations after 75  $\mu\text{sec}$  at which point the majority of the work done on the liner by the explosive is complete.

No attempt was made to model the detailed ductile fracture processes that caused the liner break up seen in Figure 2. Instead, formation of the two main fragments was modelled by manually failing a line of elements within the liner 75  $\mu\text{sec}$  after detonation. Figure 8 shows the predicted liner shape 0.1  $\mu\text{sec}$  after manually failing the liner elements. The fracture path shown was selected in order to match the observed shape of the two primary fragments. The predicted fragment profiles at 250  $\mu\text{sec}$ , shown in Figure 9, agreed relatively well with the actual profiles in Figure 2, supporting the choice of the assumed fracture path.

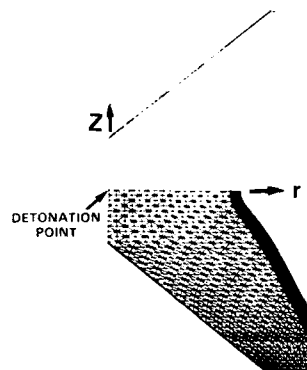


Figure 7: Finite element mesh used to simulate EFP formation.

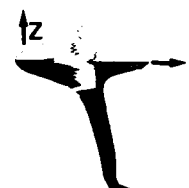


Figure 8: Predicted EFP profile at 75.1  $\mu\text{sec}$  (0.1  $\mu\text{sec}$  after failure).



Figure 9: Predicted fragment profiles at 250  $\mu\text{sec}$ .

Rather than continuing the simulations of the EFP liner collapse and fracture to consider impact with the targets, it was decided to build new models based on the known fragment profiles shown in Figure 2. Figure 10 shows the finite element meshes used to model the impact of the two primary fragments with the concrete targets. These meshes were developed using digitized profiles of the fragments in Figure 2 which were altered slightly to allow axisymmetric modelling of the problem.

Both the monolithic concrete and bridge beam targets were modelled using varying degrees of simplification. Figure 11 shows the axisymmetric finite element mesh used to model the concrete cylinder in trial 203-1. The cylinder was encased in mild steel and a slide line was introduced along the concrete and steel interface.

The finite element mesh used to model the pre-stressed bridge beam is shown in Figure 12. The model was assumed to be axisymmetric; thus the actual target modelled was a concrete cylinder containing steel reinforcing hoops. In this manner, the tensile reinforcement of the cables would be "seen" in carrying tensile hoop stresses within the cylinder during impact of the fragments and in the erosive effect of the hard steel cables on the copper fragments. The reinforcing cables were modelled as solid UNS 4340 steel.

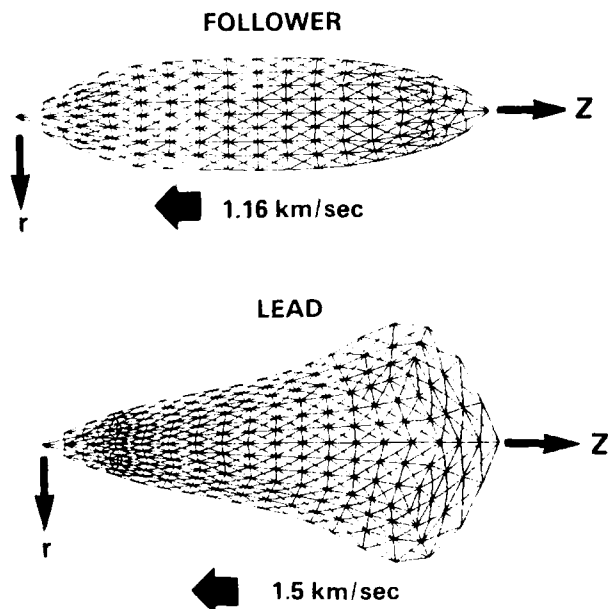


Figure 10: Finite element meshes of lead and follower fragments (meshes mirrored about z-axis).

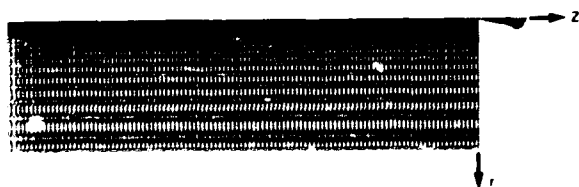


Figure 11: Finite element mesh used to model monolithic concrete target (outline mirrored about z-axis).

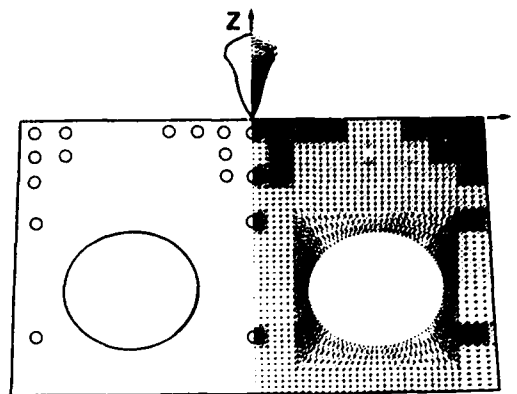


Figure 12: Finite element mesh used to model pre-stressed beam target (outline mirrored about z-axis).

The lead and follower fragments impacted the target along its axis at velocities of 1.5 and 1.16 km/sec, respectively. The interfaces between the fragments and target were modelled using the "eroding interface" algorithm in EPIC-2 which models the progressive failure of the fragments and target at their interface. The complex failure processes leading to erosion of the fragments and cratering of the target were not considered; instead, the elements along the interface were assumed to fail (and were dropped from the calculation) once the strain within an element exceeded a user-specified value. Detailed description of the eroding interface algorithm used in this study is given in [6].

The erosion strain used for the copper fragments was set at 1.5 as suggested by Stecher and Johnson [6]. The effect of the concrete erosion strain on penetration was studied parametrically using three different concrete erosion strains: 0.2, 0.4, 0.6. Calculations were performed in which the lead projectile impacted the monolithic concrete target at a velocity of 1.5 km/sec.

Figure 13 compares the predicted crater profiles 2000  $\mu$ sec after the impact of the lead fragment for the three values of erosion strain considered. In each case, the fragment has been completely eroded. The figure shows that the crater size increased with decreased erosion strain, as expected. Inspection of the results also revealed that the projectile failed more rapidly when the concrete erosion strain was increased.

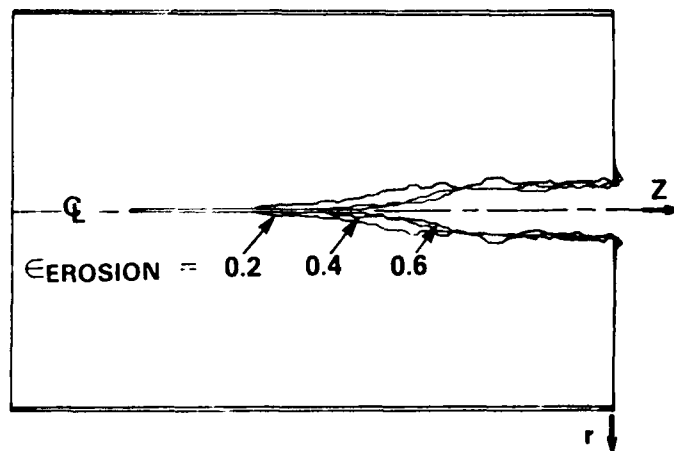


Figure 13: Predicted crater profiles in unreinforced concrete at 2000  $\mu$ sec due to lead fragment only.

Note that a long, narrow hole extends below the main crater along the cylinder centre-line. This hole was due to a deficiency in the eroding interface algorithm. As elements fail within the projectile and target, they are dropped from the calculation and no longer carry any stress. However, the nodes and nodal-lumped masses associated with the failed elements remain active and continue to exert pressure on the crater surface. Consequently erosion of the concrete continues long after the projectile elements have been completely eroded due to the action of the remaining projectile nodes. This residual erosion is most active along the axis where the nodes are constrained in the radial direction and "stack up" at the crater centre-line.

This residual erosion also led to premature failure of the follower fragment in simulations considering both fragments. Figure 14 shows the predicted fragment and crater profiles 1000  $\mu\text{sec}$  after impact of the lead fragment, assuming a concrete erosion strain of 0.2. The figure shows that the follower fragment is extensively eroded by the nodes from the failed concrete elements prior to reaching the bottom of the crater. While some erosion of the follower fragment would be expected due to debris within the crater, it was felt that the treatment of the eroded nodes in the current eroding interface algorithm was incorrect. Attempts to model impact of both fragments were subsequently abandoned. Modifications to the EPIC-2 eroding interface algorithm which would permit the eroded nodes to "flow around" the follower fragment are under consideration but were beyond the scope of the current paper.

The residual erosion problem with the EPIC-2 eroding interface algorithm rendered the multiple fragment simulations inaccurate. Consequently it was decided to simulate the attack of the EFP on the reinforced concrete target using only the lead fragment. This approach is reasonable because the crater depths in Figure 13 were well in excess of the depth of the beam. It was expected that the lead fragment would be adequate to completely penetrate the beam.

The concrete erosion strain used in this simulation was 0.2, the lowest of the three values considered in the parametric study. This value was selected since it produced a predicted lead fragment penetration of just over 50% of the unreinforced target (Figure 13) and it was known experimentally that the combined lead and follower fragments fully penetrated the target. The concrete erosion strain of 0.2 adopted was considerably less than the value of 1.5 used by Johnson *et al.* [7] in similar studies.

The predicted fragment and crater profiles 750  $\mu\text{sec}$  after impact are shown in Figure 15. The fragment is heavily eroded; however, the crater has just broken through the target back face showing that the lead fragment was sufficient to fully penetrate the beam. It is assumed that the follower fragment would pass cleanly through the beam.

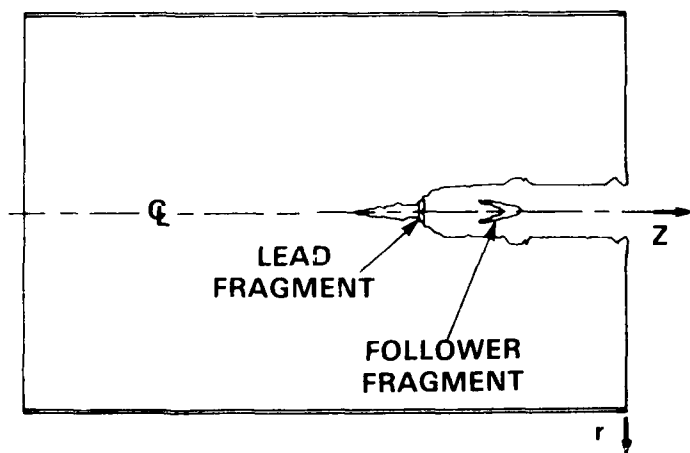


Figure 14: Multiple fragment simulation at 1000  $\mu\text{sec}$  showing premature erosion of follower fragment

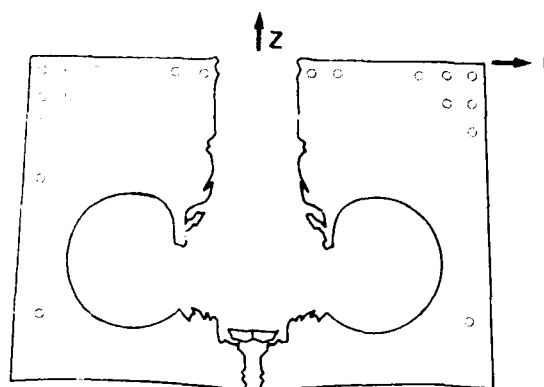


Figure 15: Predicted fragment and crater profiles in reinforced target at 750  $\mu\text{sec}$ .

Examination of the reinforcing cable pattern in Figure 15 shows that the cables not located in the path of the fragment were left intact. Only the centre cable and cables located 5.1 mm from the centre of the beam were eroded by the projectile, in excellent agreement with the measured pattern of cut and damaged cables from the corresponding trial (Figure 4).

## 5 Discussion

The experiments have demonstrated that EFPs are effective in breaching concrete beams. However, there exists a finite radius, roughly equal to the fragment radius, within which reinforcing cables are cut. Cables outside of this radius are not damaged due to the inability of the rather brittle concrete to transmit sufficient energy into the cables. In contrast, the linear cutting action of the DREstructor severed all of the cables embedded to a depth of 17 cm within the beam. The more extensive damage produced by the DREstructor suggests that linear EFPs, similar in concept to linear shaped charges but producing a solid fragment rather than a jet, might provide a compromise between standoff distance and cutting "radius". Alternatively, an in-line array of axisymmetric EFP's might create a linear cut while maintaining good penetration and standoff. Such a concept could be optimized with respect to explosive loading and EFP spacing.

A number of numerical difficulties were identified with the eroding interface algorithm in EPIC-2. Improved treatment of the nodes released during erosion is necessary to allow these nodes to flow out around the fragment during penetration. Such an improved capability would be useful for studies of tandem EFPs which also produce two projectiles. Further development of models of ductile fracture is also necessary to permit more meaningful predictions of liner breakup.

## 6 Conclusions

1. Explosively formed projectiles are effective at breaching large cross-sections of reinforced concrete at standoff distances of 12 m.
2. Based on the pattern of cables cut within the beam, the EFP studied was accurate to within 10 cm at the standoff distances considered.
3. There was a finite radius of damage, equal to the fragment radius, around which the reinforcing cables were undamaged.
4. Lagrangian finite element simulations show promise in predicting deep penetration of projectiles into composite materials. Further development of material failure models and improved interface algorithms would be of value in reducing the level of empiricism necessary in current calculational techniques.



## 7 Acknowledgement

The authors thank Mr. G. Briosi for his advice, assistance and encouragement during the course of this study.

## References

- [1] Johnson, G.R. and Stryk, R.A., *User Instructions for the EPIC-2 Code*, Honeywell Inc. Edina, MN, AFATL-TR-86-51, 1986.
- [2] Briosi, G.K. and Schmitke, R.T., *Development of a Low-Cost Linear Shaped Charge for Structural Demolition*, Suffield Report 416, Defence Research Establishment Suffield, September, 1985.
- [3] Johnson, G.R., Recent Developments and Analyses Associated with the EPIC-2 and EPIC-3 Codes, *Advances in Aerospace and Structures and Materials*, ed. Wang, S.S. and Renton, W.J., AD-01, ASME, 1981.
- [4] Johnson, G.R., Dynamic Analysis of Explosive-Metal Interaction in Three Dimensions, *Journal of Applied Mechanics*, ASME, **103**, March, 1981.
- [5] Stecher, F.P. and Johnson, G.R., Lagrangian Computations for Projectile Penetration into Thick Plates, *proc. 1984 International Computers in Engineering Conference*, Las Vegas, NV, August, 1984.
- [6] Johnson, G.R. and Cook, W.H., A Constitutive Model and Data for Metals Subjected to Various Strains, Strain Rates, Temperatures and Pressures, *Engineering Fracture Mechanics*, **21**, no. 1, 1985.
- [7] Johnson, G.R., Stryk, R.A. and Nixon, M.E., *Two- and Three-dimensional Computational Approaches for Steel Projectiles Impacting Concrete Targets*, presented at the Post-SMIRT Seminar on Impact, Lausanne, Switzerland, August, 1987.

## SMALL ARMS PENETRATION OF CONCRETE

Dr M J Iremonger<sup>1</sup>  
Major K J Claber, RE<sup>2</sup>  
Mr K Q Ho<sup>3</sup>

<sup>1</sup>Royal Military College of Science, Shrivenham UK

<sup>2</sup>Military Works Force, Beeston, Nottingham, UK

<sup>3</sup>Housing and Development Board, Singapore

### ABSTRACT

Experiments are described which quantify the penetration of concrete by 5.56 mm NATO SS109 and 7.62 mm NATO SS77 bullets. The effects of varying concrete strength and aggregate size and type are considered. Tests showed that both rounds give similar first shot penetration inversely proportional to the tensile strength of concrete target. Penetration was reduced by using harder aggregate and increased by using smaller aggregate. The application to these rounds of formulae which predict single shot penetration are considered. The analytical predictions give a wide range of values. The SS77 round was modelled by a representation of the whole bullet. The SS109 round was modelled by just its hardened steel core. Experiments on the multi-hit breaching of concrete by these rounds are described and their relative effectiveness is assessed.

### 1. INTRODUCTION

Experiments were conducted to quantify the small arms protective capability of concrete and to study the effects of varying the material characteristics. The consequences of varying concrete strength and aggregate size and type are considered in this paper.

Much work has been done on the prediction of ballistic penetration. Kennedy (1976), Siiter (1980) and Brown (1986) survey a number of theoretical and empirical formulae. Most are based on rigid homogeneous penetrators. There is a comparative lack of reliable data on real small arms bullets which are inhomogeneous in nature. This paper considers two small arms bullets, a 7.62mm calibre lead core ball round (NATO SS77) and a 5.56mm round with a core of hardened steel and lead (NATO SS109). The paper discusses the application to these rounds of a range of predictive formulae.

In practice the single shot penetration of concrete by small arms fire is less important than the accumulated breakthrough caused by multiple hits or burst fire. The relative effectiveness for wall breaching of the 5.56mm and 7.62mm rounds described above is also discussed.

### 2. EXPERIMENTAL PROGRAMME

#### 2.1 Ammunition

Details of the two ammunition natures are as follows:

**NATO SS109 5.56 mm x 45 mm.** As shown in Fig 1 the core comprises an air gap in front of a flat-tipped hardened steel core weighing 0.495 grams and of minimum hardness 600 HV (Vickers). The rear part of the core is a 90% lead/10% antimony alloy. The core is encased in a gilding metal (90% copper 10% zinc) envelope. The total bullet mass is 4.00 gram.

**NATO SS77 7.62 x 51 mm.** The complete core is made of 90% lead/10% antimony as shown in Fig 1. The envelope is gilding metal. The total bullet mass is 9.33 gram.

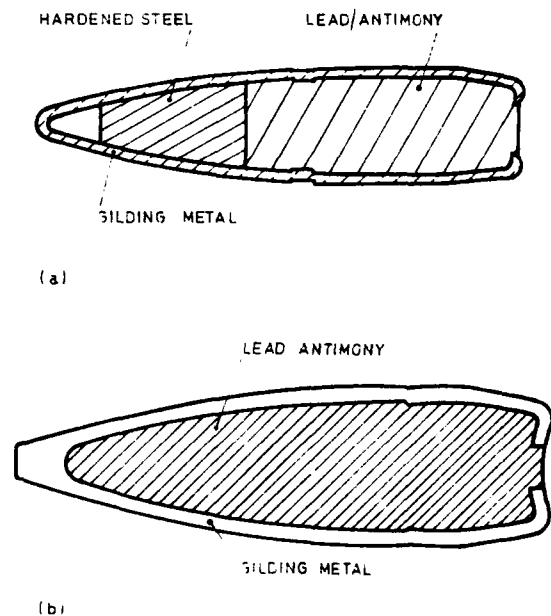


FIG. 1: 5.56mm SS109 (a) and  
7.62mm SS77 (b) bullets

## 2.2 Concrete Targets

The concrete was mixed to give nominal grades (compressive strength in MPa) 15, 30, 45 and 60. Ordinary Portland cement and a 5mm down fine limestone aggregate was used in all the targets.

Three types of coarse aggregate were used

- 20mm - 5mm river valley limestone rock gravel
- 20mm - 5mm angular flint based gravel
- 10mm down river valley limestone rock gravel

The targets were made as 400mm x 400mm square panels with thicknesses ranging from 30 mm to 150mm.

Compressive strengths were derived from tests on 100mm cube specimens. A 4% reduction factor was applied to give values representative of preferred standard 150mm cubes (see Neville (1981)). A further correction factor was applied to give a compressive strength value representative of that determined from a standard 6 inch diameter x 12 inch long cylindrical specimen as used in the USA. Tests using the latter test piece more closely approach the ideal case of uniaxial compression because they are less affected by end restraints than with cube specimens. The ratio of cylinder strength over cube strength  $r$  is less than unity. The current British Standard gives a ratio  $r$  of 0.87 for all the cubes tested. Neville (1981) however shows that  $r$  depends on the concrete strength and quotes a relationship by L'Hermite:

$$r = 0.76 + 0.2 \log_{10} (f_{cu}/2840)$$

Where  $f_{cu}$  is the cube strength in psi. The nature of the aggregate may also affect this ratio.

Tensile splitting strengths were obtained from the cylindrical specimens. A 2% reduction factor was applied to account for their being smaller than the preferred standard. The values obtained are consistent with the common assumption that concrete tensile strength is proportional to the square root of the compressive strength (Neville (1981) and Nawy (1985)).

Typical data for the 150 mm thick targets made with 20 mm - 5 mm coarse limestone aggregate are shown in Table 1.

| Nominal Grade                                | 15    | 30    | 45    | 60    |
|--|-------|-------|-------|-------|
| Average Density<br>$w$ (Kg/m <sup>3</sup> )  | 2219  | 2250  | 2315  | 2321  |
| Corrected Cube<br>$f_{cu}$ (MPa) Strength    | 29.10 | 47.65 | 62.90 | 67.05 |
| L'Hermite Ratio                              | 0.79  | 0.84  | 0.86  | 0.87  |
| Equivalent Cylinder<br>$f'_c$ (MPa) Strength | 23.00 | 40.05 | 54.10 | 58.35 |
| Corrected Tensile<br>$f_t$ (MPa) Strength    | 2.90  | 3.40  | 3.75  | 4.10  |

Table 1: Corrected Concrete Strength Data

Values of the modulus of elasticity ( $E_c$ ), shear strength ( $V_c$ ) and bulk modulus ( $K_c$ ) were obtained by calculation. These properties are needed only for predictions using the Recht formula and can be derived from values of compressive strength and density, (Ho (1988)).

## 2.3 Firing Trials

The firing trials were conducted in an indoor range at RMCS. The general arrangement is shown in Fig 2. The sky screens enabled velocities to be determined before and, when appropriate, after impact with the target. At the short range of 10.5 m obliquity was negligible. Some tests through witness cards showed that the yaw caused by lack of spin stabilisation at such a short range was also small.

The targets were clamped into a four section steel frame with tightening bolts and nuts to provide nominal edge restraint and compression. This restraint prevented failure due to gross cracking, particularly after multiple hits.

The SS109 ammunition was fired from a standard UK Ministry of Defence (MOD) issue 5.56 mm SA 80 Individual Weapon (IW). The SS77 rounds were fired from a standard MOD issue 7.62 mm L2A1 Self-Loading Rifle (SLR).

A total of 84 SS 109 and 60 SS 77 rounds were fired into the 48 concrete target panels during the ballistics tests, 3 rounds for each target. The projectile velocities before impact and after perforation were measured for each shot by the photo-electric sky screens at the range. After each shot, the target was examined for damage. The penetration depth and the front spall and/or rear scab crater sizes were measured and recorded. For crater size, the widest and the narrowest diameters of each crater were noted. For scabbing, the depth of scab was also recorded.

A separate series of trials was held to assess the multiple hit breakthrough of both SS109 and SS77 rounds against concrete of a single nominal strength. These targets had a mean compressive cube strength of 30.7 MPa and a density of 2261 kg/m<sup>3</sup>. Each target was cast with a hoop steel wire mesh around the inside of the target to give a central 300 mm square unreinforced area. Eight concrete targets of each thickness were fired at as follows:

- Two targets were engaged by 5.56 mm SS109 ammunition with all rounds aimed at the same point of impact.
- Two targets were engaged by 5.56 mm SS109 ammunition, with rounds deliberately aimed into a 132 mm diameter circle representing the dispersed group expected of an infantryman using an IW at 70 m range.
- Two targets were engaged by 7.62 mm NATO Ball ammunition with all rounds aimed at the same point of impact.
- Two targets were engaged by 7.62 mm NATO Ball ammunition, with all rounds deliberately aimed into a 200 mm diameter circle representing the dispersed group expected of an infantryman using an SLR at 70 m range.

The 'typical' group sizes used in the trial were obtained by firing each weapon in turn at a paper target mounted at 25 m and then extrapolating the group size obtained to give figures for 70 m. Targets were examined between shots (or each 4-5 shots in the dispersed trials) and a record made of the bullet velocity, the damage caused in terms of crater size, penetration and cracking to each face, and the fall of shot in the case of the dispersed trials.

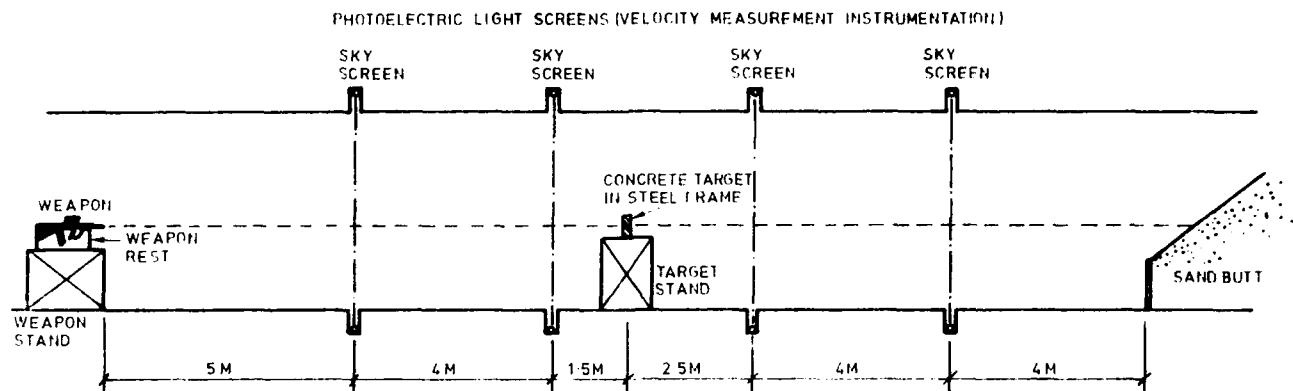


FIG. 2 : Small Arms experimental range at RMCS

### 3. ANALYTICAL PREDICTIONS

A number of formulae have been developed to predict the ballistic penetration of missiles into concrete. The following formulae were considered:

- a) The ACE Formulae (1946)
- b) The Modified NDRC Formulae (1972)
- c) The Petry Formula (1910)
- d) The Modified Petry Formulae (1950)
- e) The Modified BRL Formulae (1973)
- f) The Ammann and Whitney Formula (1963)
- g) The Bechtel Scabbing Formula (1976)
- h) The CEA-EDF Perforation Formula (1977)
- i) The Kar Formulae (1978)
- j) The Whiffen Formulae (1978)
- k) The Healey and Weissman Formulae (1974)
- l) The Recht Formulae (1963).

Descriptions of these formulae have been given by Brown (1986) and Ho (1988).

Almost all the formulae on penetration relate the total penetration depth ( $x$ ) to the inverse of the square root of the concrete compressive strength ( $f'_c$ ), or to the inverse of the concrete tensile strength as in the case of the Recht Formulae. This is consistent with both the British and American codes which stipulate that the tensile strength of concrete is directly proportional to the square root of its compressive strength, Nawy (1985) and Neville (1981). The exceptions to this trend are the Petry Formula which provides a coefficient ( $K_p$ ) dependent on the reinforcing rather than concrete strength, the Modified Petry Formulae in which the coefficient ( $K_p$ ) is a function of the concrete compressive strength ( $f'_c$ ) based on a graphical relationship, and the CEA-EDF Formula which uses the power value of  $(3/8)$  for the concrete strength ( $f'_c$ ) rather than 0.5 (ie square root).

A wide variation is also noted in the relationship between the total penetration depth ( $x$ ) and the striking velocity ( $V$ ). In the formulae, the total penetration depth ( $x$ ) is directly proportional to some power of the striking velocity ( $V$ ). This power value ranges from 0.5 to 1.8, and in the case of the Whiffen Formula it is again a function of the concrete strength ( $f'_c$ ). These differences are due mainly to the empirical origins of the formulae (except for the Recht Formulae), in that most of them were derived from regression analyses to fit their respective experimental test data. They, thus, also suffer from limitations in the range of their available test data.

The formulae apply to impacts against massive and except in a local sense, non-deformable concrete targets. Calculations of limit thicknesses for scabbing and perforation are derived from the penetration depth.

Only the original Petry Formula explicitly takes into account the reinforcing in the concrete target. As for the size of aggregate used in the concrete target, only the Kar Formulae and the Whiffen Formula provide an explicit term for it. None of the formulae, however, takes into consideration the effects of different types or strengths of the aggregate.

The formulae are based on non-deforming projectiles. As the envelope of an armour-piercing round becomes stripped on impact, the US Army Technical Manual TM5-855-1 (1985) suggests that the AP core alone be considered for estimates of penetration. For jacketed lead ball (usually lead/antimony alloy) ammunition which deforms completely against concrete, it noted that the penetration is normally 50% (or less) that for the corresponding AP ammunition. This approach is supported by Healey and Weissman (1974).

### 4. DISCUSSION

#### 4.1 Experimental Results

##### Bullet Behaviour

The mean striking velocity of the SS 109 bullet was measured at 923.63 m/s with a standard deviation of 10.22 m/s. Upon impact with the concrete target, at the early stage of penetration, the gilding metal jacket was stripped off the core. Traces of the jacket were found in only a few cases, around the penetration path in the initial 15-20 mm from the target front (impact) face. More often, there was no trace of it. It was probably disintegrated by friction with the concrete and then mixed into the pulverised concrete material around the penetration path. The hardened steel front core portion, however, had remained virtually undeformed when recovered from the target. In some cases, the lead alloy rear core portion was also found in contact with or very close to the steel core portion, but it had suffered severe deformation and some disintegration. It had apparently stayed with the steel core portion travelling along the penetration path. It was also seen that the core had deviated substantially from its initial line of impact as it penetrated the concrete mass before coming to rest. The final orientation of the core was often tilted far from the presumed striking direction normal to the target face.

The mean striking velocity of the SS 77 bullet was measured at 799.29 m/s with a standard deviation of 7.01 m/s. The bullet behaviour upon impact was very different from that of the SS 109. With a larger calibre, it made a broader penetration hole. When recovered from the target, the gilding metal jacket and the lead alloy core were found to be generally intact, though severely deformed. Some jacket material could have stripped off during penetration, but this was not detected.

As shown in Fig 3 the two rounds had similar single shot penetration capability. The effect of multiple hits is discussed in section 4.3.

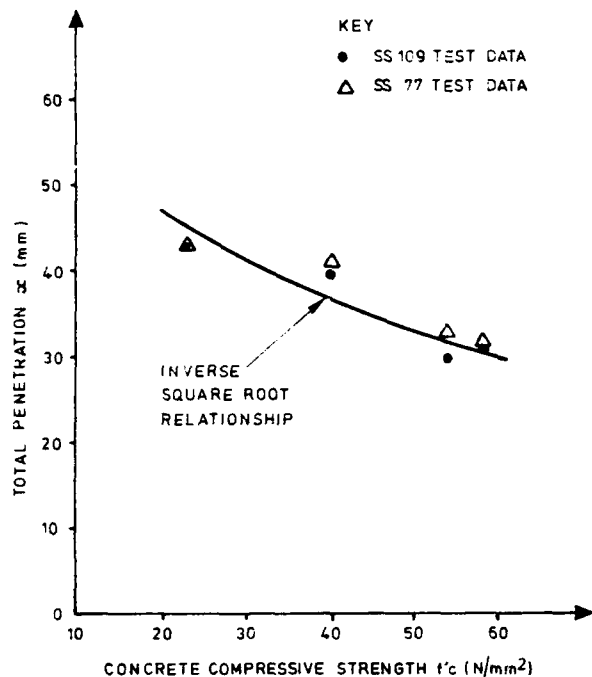


FIG. 3 Single shot penetration of 20mm-5mm limestone coarse aggregate targets

#### Concrete Strength

The single shot penetration depth decreases with concrete compressive strength as shown in Fig 3. The results give a reasonable fit to an inverse square root relationship between penetration depth and compressive strength. This result is consistent with many of the predictive formulae (see later) and indicates also that the penetration depth is approximately directly proportional to the concrete tensile strength (see section 2.2).

#### Aggregate Type

The effects of aggregate type on penetration is illustrated in Table 4. Only SS 109 ammunition was investigated.

The stronger flint aggregate reduced penetration. The aggregate remained intact and partially embedded in the concrete or was completely dislodged with the spall material. There was no aggregate fracture as occurred with the limestone aggregate of similar size.

The use of small (10 mm down) limestone aggregate caused increased penetration. Fracture of this aggregate was less than its larger counterpart because of its reduced size. The craters were generally smoother.

It was observed generally that crater size increased with concrete strength.

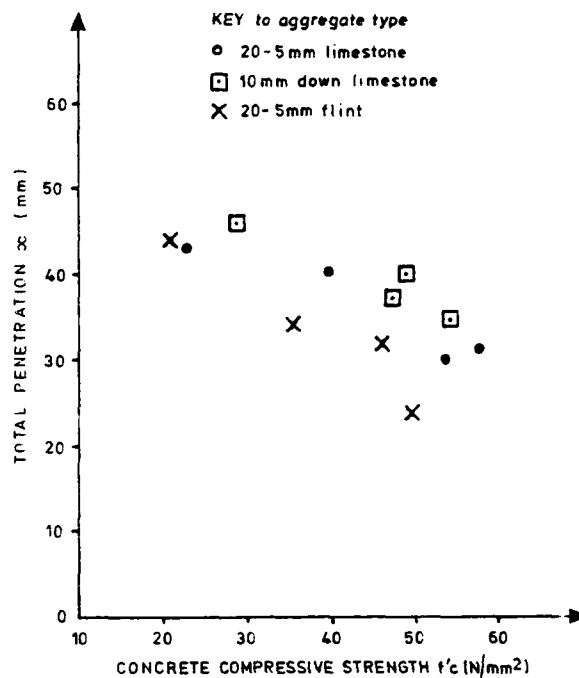


FIG. 4 Single shot penetration of SS109 rounds against 150mm concrete targets.

#### Perforation and Scabbing Thickness

The tests on 30 mm, 50 mm, 75 mm, 100 mm and 150 mm thick concrete targets containing 20 mm - 5 mm coarse limestone aggregate enabled estimates to be made of the perforation and scabbing limit thicknesses. Values were between 50 mm and 100 mm. They reduced as the concrete strength increased. Though, by definition, the scabbing limit thickness exceeds that for perforation the excess was sometimes only marginal. The limit thicknesses using SS77 ammunition were greater than those for the SS109 rounds despite their similar single shot penetration depths.

The areal size of front face spalling increased with target thickness up to about 100 mm after which it generally remained constant or even reduced. The size also increased with concrete strength. Diameters varied from about 65 mm to 150 mm for SS109 ammunition. Where rear face scabbing occurred its size was larger than the front crater. The SS77 rounds caused larger crater sizes.

#### 4.2 Comparison with Theory

The analytical formulae listed in section 3 were used to predict the single shot penetrations of thick (150 mm) targets.

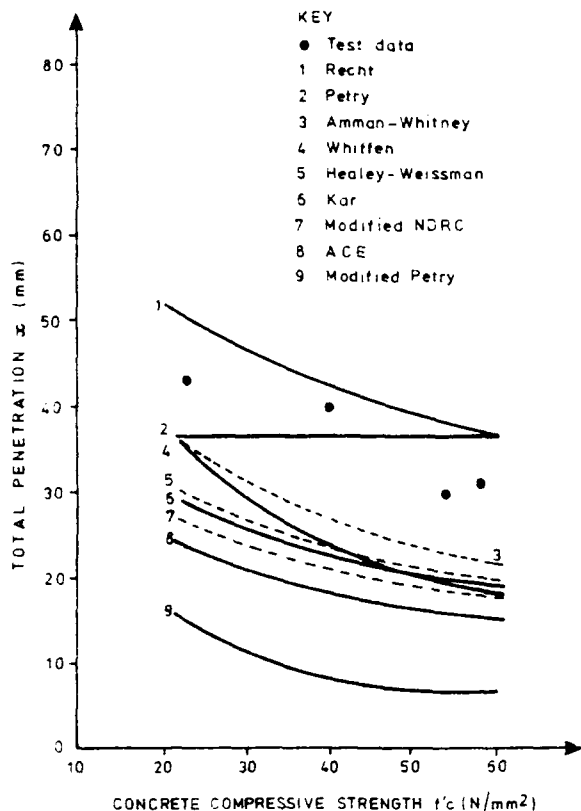


FIG. 5 Predicted and actual single shot penetration for 20mm-5mm Cerney coarse aggregate targets impacted by 5.56mm SS109 ammunition.

#### SS109 Ammunition

The comparisons shown in Fig 5 for a range of formulae are based on the 5.56 mm SS109 rounds being modelled only in terms of its 0.495 gram steel core. This is assumed to have a diameter of 3.774 mm, the maximum diameter of the actual core.

There is a wide variation between the predictions. The spread of predicted values would not be radically altered by changing the penetrator characteristics. All except the Petry formulae take concrete strength into account and model its variation quite accurately. Ironically the Petry formula gives the best absolute prediction of single shot penetration.

Of the other formulae, all but that of Recht underestimate the penetration. It was observed (see Section 4.1) that a plug of lead/antimony of equal diameter to that of the rear of the steel often remained in contact with it during penetration, its mass being of the same order as that of the steel. It may therefore be sensible to increase the mass of the projectile whilst maintaining its cross-section. The penetration depth is directly proportional to projectile mass in all the formulae. Values of constant correction factors which would lead to the formulae producing accurate predictions of penetration depth (with or without added mass) can be inferred from Fig 5.

The Recht equation contains many more projectile and target parameters than the other formulae which give scope for varying the predicted penetration. There is a particular uncertainty about the choice of dynamic friction coefficient. The value of 0.33 was used for the predictions shown in Fig 5 was supported by some simple static experiments. A lower value gives greater penetration. Increasing the mass of the projectile as discussed above would increase the error.

#### SS77 Ammunition

The gilding metal jacket of the 7.62 mm SS77 round is harder than its lead alloy core and would be expected to contribute to its penetrative capability. The bullet was modelled as a homogeneous material with a density and elastic modulus taken as an average of those of the gilding metal, lead and antimony in proportion to their relative proportions by weight. To account for lead deformability a penetrability coefficient of 0.5 was used with all the formulae as discussed in Section 3.

Fig 6 shows the predicted single shot penetrations against concrete targets with 20 mm - 5 mm coarse limestone aggregate. Several formulae give good predictions across the whole range of concrete strength.

The Recht predictions based on a 16° half angle conical nose cylindrical projectile gave grossly excessive penetrations.

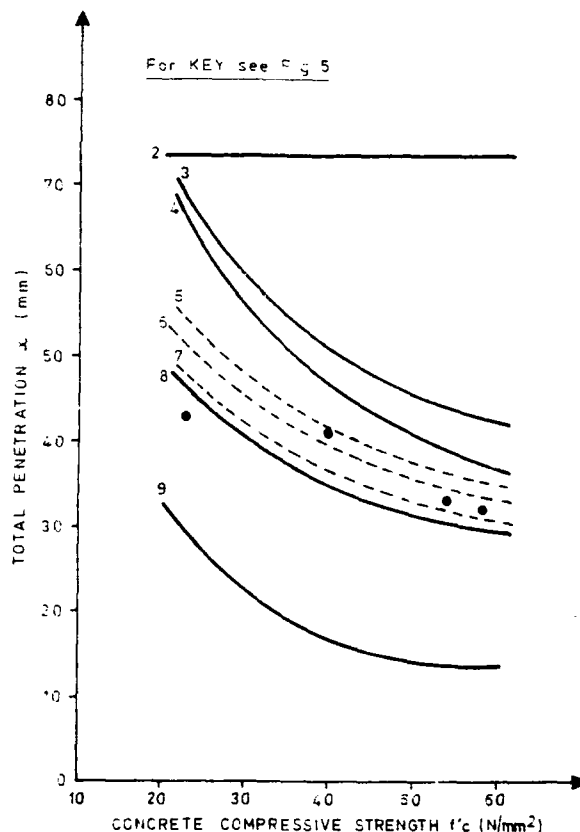


Fig. 6 Predicted and actual single shot penetration for 20mm-5mm Cerney coarse aggregate targets impacted by 7.62mm SS77 ammunition.

### Variations in Aggregate Type and Size

None of the formulae take any account of aggregate type and strength. As shown in Fig 4 however the presence of stronger aggregate does inhibit penetration. This reduction does mean that the errors in predicting penetration are reduced for all the formulae except that of Recht.

Only the Whiffen formula explicitly takes the size of aggregate into account. The typical 8% increase in penetration into the concrete containing 10 mm down coarse limestone aggregate compared with to concrete 20 mm - 5 mm aggregate were accurately modelled by this formula.

### 4.3 Multiple Hits

Fig 7 shows the number of rounds required to perforate concrete targets of various thicknesses. The consistent data refer to repeated hits on the same impact point, whereas the dispersed data represent a typical grouping at 70 m range (section 2.3).

These limited tests indicate that SS77 ammunition is between 1.1 and 1.6 times as effective as SS109 ammunition on a bullet for bullet basis. However as the complete rounds are twice as heavy, the SS77 ammunition is 1.25 to 1.8 times less effective on a weight for weight basis. Significantly less kinetic energy is required to achieve perforation using the SS109 bullet. A limited examination of the effect of burst fire showed a significant reduction in rounds required to achieve perforation. More work is required to quantify this effect.

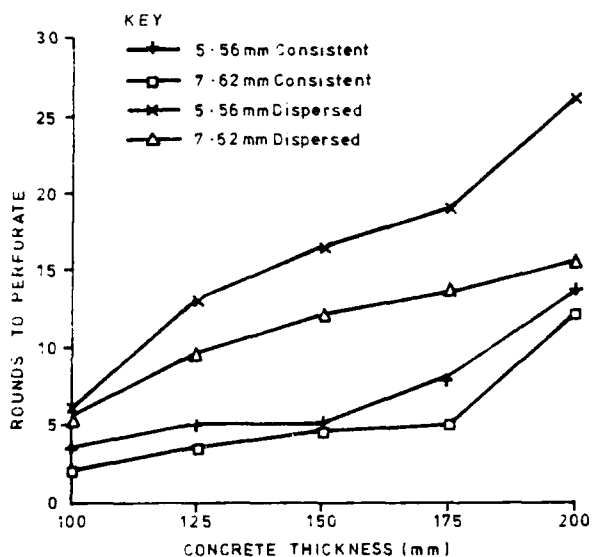


FIG. 7 Multiple hit perforation

### 5. CONCLUSIONS

This study has shown that the 5.56 mm SS109 and the 7.62 SS77 rounds give similar first shot penetration inversely proportional to the tensile strength of a concrete target. A flint based coarse aggregate reduced penetration by about 14% compared with an equivalent size limestone aggregate. Halving the size of the limestone aggregate increased penetration by about 10%. Multiple hit perforation studies showed that SS109 ammunition is less effective than SS77 on a round for round basis but more effective on a weight for weight basis.

Analytical predictions of first shot penetration depth gave a wide range of values. Modelling the SS109 round by just its hardened steel core gave poor correlation with practice except with the Recht and Petry formulae. Improved predictions with other formulae can be made if a penetrator with increased mass is considered (to reflect the presence of some lead core behind the steel). The SS77 round was modelled with some success by a representation of the whole bullet and by using a penetration coefficient of 0.5 to reflect its deformability.

### 6. ACKNOWLEDGEMENTS

The authors wish to acknowledge the work of three Royal Engineer Officers: Maj P A H Poole, Capt R C Hendicott and Capt J W R Thorn who conducted the multiple hit studies. This work has been carried out with the support of Procurement Exec., Ministry of Defence.

### 7. REFERENCES

- Brown, S J (1986). Energy Release Protection for Pressurised Systems, Part II. Review of Studies Into Impact/Terminal Ballistics. ASME Applied Mechanics Review, vol 39 No 2, Feb.
- Healey, J J and Weissman, S (1974). Primary Fragment Characteristics and Impact Effects in Protective Design. Minutes of 16th Explosives Safety Seminar, Vol II. US Dept of Defence Explosives Safety Board, Sep.
- Ho, KQ (1988) Effects of Concrete Properties on the Protective Capability of Concrete Targets in withstanding Small Arms Fire No 2 Blast Course USc Thesis, RMCS Shrivenham UK.
- Kennedy, R P (1976). A Review of Procedures for the Analysis and Design of Concrete Structures to Resist Missile Impact Effects. Nuclear Engineering and Design, No 37.
- Nawy, E G (1985). Reinforced Concrete - A Fundamental Approach. Prentice-Hall.
- Neville, A M (1981). Properties of Concrete. 3rd Edition. Pitman.
- Sliter, G E (1980). Assessment of Empirical Concrete Impact Formulas. ASCE Journal of the Structural Division, Vol 106, May.
- US Army Technical Manual TM 5-1300 (1969). Structures to Resist the Effects of Accidental Explosions. US Dept of the Army, Jun.
- US Army Technical Manual TM 5-855-1 (1985). Fundamentals of Protective Design for Conventional Weapons. US Dept of the Army, Nov.

## USE OF ROCK/POLYMER COMPOSITES AS PROTECTIVE MATERIALS

William F. Anderson, Alan J. Watson, Andrew J. Gallagher

Department of Civil and Structural Engineering  
University of Sheffield, U.K.

### ABSTRACT

A rock/polymer composite has been produced which uses the water present in damp aggregate to effect a cure of a single component polyurethane to overcome the 'blowing reaction' which normally occurs when polyurethanes cure in the presence of water. The resultant composite, which achieves full strength in about an hour, is capable of defeating 0.5" armour piercing rounds with little loss of integrity. It is proposed as a cost effective alternative to armoured plate when low rise protective structures are required quickly.

### INTRODUCTION

There is often a need to rapidly construct small defensive structures or upgrade the defensive capabilities of existing structures. Although armour plate is suitable for this purpose, it is expensive and may not be readily available. Concrete can use local aggregates but may require a considerable cure time to reach full strength, and its brittleness leads to rapid deterioration when attacked.

Work reported by Anderson et al. (1) indicated the potential of rock aggregate bound together by a matrix of sand filler and polymer to defeat small arms fire and explosive attack. A number of different polymers and rock aggregates were investigated and the resultant composites optimised in terms of cost effectiveness and penetration resistance using a statistical method known as response surface theory (2). Best performances were found using two part polyurethane and recommendations were given for thickness of composite to defeat single impact of a 7.62 mm armour piercing (AP) round.

There was, however, a potential problem with the composites for large scale field use. The chemical reaction during curing of polyurethanes is such that carbon dioxide gas is produced if water is

present. All the laboratory studies had used dried aggregate, but this may not be feasible for field use. The carbon dioxide produced during casting with damp aggregate causes foaming of the composite matrix, with a consequent loss of strength and possible loss of structural integrity.

In recent years the use of polymers in the construction industry, mainly as repair materials, has increased considerably and developments have also taken place in polymer technology. A further study of rock/polymer composites has therefore been carried out in an attempt to produce a material which reaches full strength within 1 - 2 hours, does not deteriorate significantly when impacted, is capable of site production using damp aggregate and will defeat a defined threat.

### POLYMER ASSESSMENT

A wide range of polymers is now used to produce polymer impregnated concretes and polymer concretes. These include epoxy resins, unsaturated polymer resins, acrylics, furan polymers and polyurethanes. Preliminary tests indicated that epoxy resins and polyurethanes would be the most suitable for producing a rapid curing, non-brittle, energy absorbing composite, but the initial impact tests showed that resistance of high cost epoxy resin based composites was no better than that of low cost polyurethane based composites. The main testing was therefore confined to the latter.

Polyurethanes are polymeric materials containing methane groups produced by the reaction of a polyol with an isocyanate. If water is present two major reactions occur. The water and isocyanate react to form a urea and carbon dioxide. This is known as a "blowing reaction" due to the carbon dioxide trying to escape and forming bubbles in the polymer. The other major reaction generates polymer growth by the reaction of other hydrogen compounds



with isocyanate to form urethanes. This is known as the "gelling reaction" since it causes chain growth to develop soft polymer segments as well as cross linking for rapid molecular weight increase.

There are available many different types of polyol and several types of isocyanate. By selection of the right combination, materials can be produced which are soft or hard, flexible or rigid, but still retain toughness and durability. If, in additives to this wide choice of chemical combinations, the large number of possible additives is considered, then the range of end products becomes very extensive.

The products may be classified into three groups.

- I) two component resin systems based on hydroxyl polymers and reactive isocyanates,
- II) single component moisture cure polyurethanes which are available as reactive resins which can be applied as very tough coatings and which depend upon the presence of atmospheric moisture to promote cross linking,
- III) polyurethane coatings in paints and varnishes in which the urethane components are fully reacted during the manufacture of the paint binder.

The best polymer in the original study (1) was a two part polyurethane of type (I). In the current study attempts were made to overcome the blowing reaction during cure of this type of polymer due to water present in damp aggregate. Some specimens were cast with a blend of polymer designed to give a much harder than required end product, so that after deterioration due to the blowing reaction the cured composite would satisfy the end product specification. Impact tests showed that this did partially overcome the weakening effects of the aggregate moisture, but penetration resistance was still considerably worse than composites cast with dry aggregate.

Some series of tests were carried out incorporating varying amounts of rapid hardening cement in the mix to try to soak up aggregate moisture before the isocyanate/water reaction started. This also met with limited success.

Tests reported by Czarnecki (3) indicated optimum moisture absorption should be achieved by including 0.25% aluminium silicate by aggregate weight in the composite mix. By premixing the aluminium silicate with the aggregate and leaving it for an hour before adding the polymer, the blowing reaction was eliminated but the

cure time was so short that the composite was impossible to cast and compact properly.

Because of the difficulties in casting two part polyurethanes with damp aggregate, it was decided to attempt to use single component moisture cure polyurethanes and initiate the gelling reaction using aggregate moisture rather than atmospheric moisture as in their normal usage as thin coatings.

Preliminary tests showed that curing could be affected by the aggregate moisture, but some foaming still occurred due to the blowing reaction. However, refinement of the composite production technique eliminated this problem.

### MAIN TEST SERIES

#### Aggregates and Mix Proportions

Most of the main series tests were carried out using 20 mm single size basalt aggregate and zone II or zone III sand, specifications for which are given in British Standard 882: Pt 2: 1973 (4). The aggregate stockpile was found to have an average moisture content of 4% and the sand was air dry and stored under cover.

The optimum mix by weight for the two component polyurethane used by Anderson et al (1) was 59% gravel, 31.2% sand and 9.8% polymer. In this study a mix of 60% gravel, 30% sand and 10% polymer by weight was used for all main series tests. This is fairly typical of polymer concretes.

#### Specimen Preparation

The batched fine and coarse aggregates were mixed for 20 seconds in a 0.9 metre diameter pan mixer, then the one part polymer was added and the composite mixed for a further 2 minutes. The mix was then shovelled into oiled moulds, compacted and left to foam. When foaming reached a peak the composite started to spread over the edges of the mould. If at this stage it was scraped back into the mould and punctured to allow the gas to escape, it settled down and could be recompacted before it had hardened. Compaction was carried out using a vibrating hammer with a 100 mm x 140 mm plate attachment. The composite could be demoulded an hour after casting had begun.

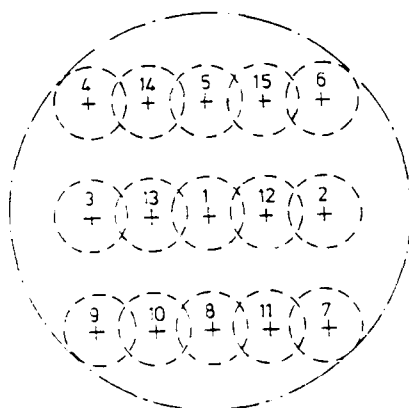
Test specimens of varying size were used. For the early tests in the main series blocks 300 mm square x 900 mm long were cast and cut to the required test thickness. As the main test programme progressed, most specimens were prepared as 450 mm square slabs of nominal thickness 125 mm and three slabs stuck together using pure polymer as an adhesive

to give the required specimen thickness.

#### Impact Test Procedure:

The specimens were impacted centrally by 0.5" armour piercing (AP) rounds of mass 45.8 gm and velocity approximately 880 m/s. Both single shots and bursts of up to 10 rounds were fired using a remotely triggered automatic weapon which was rigidly fixed in a gun mounting and frame bolted to the indoor range floor.

For single shot tests and multiple shot tests the target specimens were held in place by elastic straps to a rigid frame bolted to the range floor. Range length from the front end of the weapon barrel to the rear face of the target was 18.0 metres. In the multiple shot tests the target was moved 20 mm between each shot so that the impact points resembled a group impact around the target centre. The sequence of shots to give a 70 mm grouping is shown in Figure 1. If the target had not been perforated when all fifteen impact positions had been used, all further shots were aimed at the central impact point.



Vertical spacing = 20 mm  
Horizontal spacing = 10 mm

Figure 1 Sequence of shots to give 70 mm diameter grouping.

During tests when bursts were being fired from the fixed automatic weapon, the targets were left free standing on the target frame. It was hoped that each impact might cause slight movement of the target and thus simulate the spread of shots that would result from a burst fired from a hand held weapon.

#### Test Results

Initially tests were carried out to find the thickness of composite required to defeat a single 0.5 inch A.P round. The results are given in Table 1. A 250 mm thick block was perforated by a single round so five 300mm nominal

thickness targets were impacted. All retained the single shot, so a thinner target (265 mm) was again tried. As with the 250 mm target this was perforated so further tests were carried on 300 mm nominal thickness specimens. Some were subject to multiple round attack, moving the target between each impact. A total of thirteen tests was carried out on targets with nominal thickness 300 mm and in only two were the targets defeated by a single shot.

A series of five targets nominally 330 mm thick was then tested. In each case bullets were fired down the same central impact hole until perforation occurred. Two targets were defeated by the second bullets and three targets by the third bullets. The results of multiple shot tests are plotted in Figure 2.

In all of the tests in this series no target thicker than 310 mm was defeated by a single 0.5" AP round.

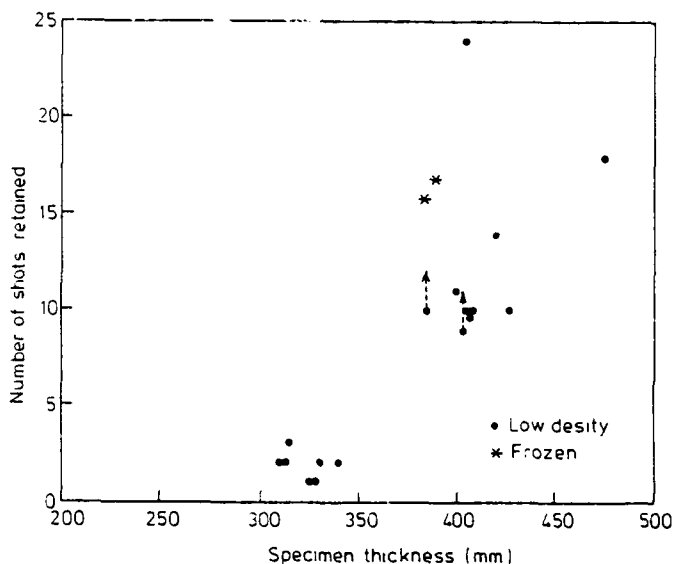


Figure 2 Plot of number of shots retained against specimen thickness.

Further series of tests were carried out to find a thickness of target which would withstand at least ten shots fired either as separate impacts, bursts or a combination of single shots and bursts. Results are summarised in Table 2 and plotted in Figure 2. From this it will be seen that all specimens greater than 400 mm thick (i.e. 3 x 125 mm nominal thickness slabs stuck together) satisfied the 'ten shot resistance' specification.

Since construction of defensive structures may be required at any time of the year, the composite should be suitable for low temperature production and use. With moisture curing polymers, as long as

| Specimen No | Type of Test | Shots Fired | Target Thickness (mm) | Density Mg/m <sup>3</sup> | Shots Retained |
|-------------|--------------|-------------|-----------------------|---------------------------|----------------|
| 35A         | Single       | 1           | 250                   | 2.13                      | No             |
| 35B         | Single       | 1           | 300                   | 1.90                      | Yes            |
| 35C         | Single       | 1           | 295                   | 1.90                      | Yes            |
| 35D         | Single       | 1           | 315                   | 2.22                      | Yes            |
| 36A         | Single       | 1           | 310                   | 1.81                      | Yes            |
| 36B         | Single       | 1           | 307                   | 1.93                      | Yes            |
| 37A         | Single       | 1           | 265                   | 2.06                      | No             |
| 37B         | Single       | 1           | 310                   | 2.26                      | Yes            |
| 37C         | Multiple     | 4           | 315                   | 1.91                      | 3              |
| 37D         | Multiple     | 3           | 310                   | 1.91                      | 2              |
| 38A         | Single       | 1           | 310                   | 2.08                      | Yes            |
| 38B         | Single       | 1           | 315                   | 2.12                      | Yes            |
| 38C         | Single       | 1           | 305                   | 2.05                      | No             |
| 38D         | Single       | 1           | 308                   | 1.98                      | No             |
| 39A         | Multiple     | 2           | 326                   | 1.98                      | 1              |
| 39B         | Multiple     | 3           | 340                   | 1.80                      | 2              |
| 39C         | Multiple     | 3           | 310                   | 2.03                      | 2              |
| 40C         | Multiple     | 2           | 324                   | 1.70                      | 1              |
| 40B         | Multiple     | 3           | 330                   | 1.79                      | 2              |
| 40C         | Single       | 1           | 301                   | 1.90                      | Yes            |

**TABLE 1 SUMMARY OF 0.5" PENETRATION TEST RESULTS - TESTS TO FIND THICKNESS TO DEFEAT SINGLE SHOT**

| Specimen No | Type of Test | Shots Fired  | Target Thickness mm | Density (Mg/m <sup>3</sup> ) | Shots Retained |
|-------------|--------------|--------------|---------------------|------------------------------|----------------|
| 36C         | Multiple     | 19           | 476                 | 1.88                         | 18             |
| 41          | Multiple     | 11           | 405                 | 1.89                         | 10             |
| 42          | Multiple     | 15           | 420                 | 2.00                         | 14             |
| 43          | Multiple     | 11           | 427                 | 1.87                         | 10             |
| 44          | Multiple     | 10           | 408                 | 1.98                         | 10             |
| 45          | Multiple     | 11           | 400                 | 2.02                         | 11             |
| 46          | Bursts       | 4x3 rounds   | 403                 | 2.03                         | 9+             |
| 47          | Bursts       | 2x5 rounds   | 405                 | 2.00                         | 24             |
|             | + Multiple   | +14          |                     |                              |                |
| 48          | Bursts       | 1x10 rounds  | 385                 | 2.04                         | 10+            |
|             |              | + 1x3 rounds |                     |                              |                |
| 49          | Bursts       | 1x10 rounds  | 405                 | 2.01                         | 10             |
|             |              | + 1x3 rounds |                     |                              |                |
| 51 (Frozen) | Multiple     | 17           | 390                 | 2.09                         | 17             |
| 52 (Frozen) | Bursts       | 4x3 rounds   | 384                 | 2.08                         | 16             |
|             | + Multiple   |              |                     |                              |                |

**TABLE 2 SUMMARY OF 0.5" PENETRATION TEST RESULTS - TESTS TO FIND THICKNESS TO DEFEAT MULTIPLE SHOTS AND BURSTS**

moisture is available for the required chemical changes to occur, curing will take place and the end product will be unchanged. The impact resistance at low temperatures was assessed by leaving specimens in a freezer for four days prior to carrying out the impact tests. The average temperature of the specimens when tested was lower than  $-10^{\circ}\text{C}$ . The results are given in Table 2, and shown in Figure 2, and suggest a slightly better performance than specimens impacted at ambient temperature. These frozen specimens were not as brittle as was anticipated. No noticeable shattering or cracking occurred, and the bullet entry holes were not noticeably different from those in specimens tested at ambient temperature.

### DISCUSSION

When a target is impacted by a projectile damage may be defined in terms of an impact crater, a projectile burrow, and if the target is defeated, or defeat imminent, a back face bulging or scabbing.

A major advantage of this polymer/rock composite is that impact face crater damage is minimal when compared to that of concrete where the impact face crater results not only from the crushing during impact, but also from tensile failure due to the stress waves reflected from the rear face of the target. The elastic nature of the composite is such that little, if any, tensile failure spalling occurs, most of the damage being the result of particle crushing and cavity expansion in the area of impact.

For single 0.5" A.P. round impact the front face crater dimensions ranged from 30 - 90 mm with an average diameter just under 50 mm i.e. less than four times the bullet diameter. Multiple impact using the 70 mm diameter grouping shown in Figure 1 resulted in a maximum crater dimension of 90 mm. Maximum spall dimension when targets were impacted by bursts was 120 mm, the nominal impact area being 70 mm diameter. The low level of damage at the impact face under all these levels of attack means that the integrity of the composite is maintained, even when it is subjected to repeated fire, as shown in Figure 3.

Sectioning of specimens after testing indicated that the projectile burrow was initially relatively straight. In specimen 36C which had been impacted by eighteen rounds on a 70 mm area, the burrow was approximately 45 mm diameter stretching about 260mm beyond a 40 mm deep impact crater. This suggests that with multiple shots the bullets are channelled



Figure 3 Impact crater (80 mm x 77 mm) after attack by eleven single shots on a 70 mm group pattern.

towards existing burrows. As reported by Anderson et al (1) projectile penetration into composite materials is quite complicated. In the current tests it was often difficult to trace the final portions of bullet path as the burrows in the composite closed back on themselves, but a high proportion of cores were found with their noses pointing towards the front of the target suggesting that either the bullets had deviated, going through a U-turn, or they had been destabilised, rotated and completed their penetration in a reversed orientation. The fact that some cores with reversed orientation were found nearer to the impact face than the end of the projectile burrow, and some radial distance away from it, suggests that severe path deviation rather than projectile rotation has occurred.

The nature of the composite was such that rear face scabbing of targets was not severe. Rear face damage often manifested itself as bulging before defeat of the target occurred. In some cases bulging was apparent well before perforation occurred, indicating that although the target was damaged it still maintained the ability to defeat further attack.

For the composite to be a viable proposition for field use it has to use locally available aggregates, be capable of production using relatively unsophisticated plant and semi-skilled labour, be structurally sound and be cost effective.

A limited series of multiple shot tests on specimens prepared with 20 mm rounded river gravel gave similar results to the basalt tests. The study reported by Anderson et al (1) indicated that

penetration resistance was influenced by aggregate hardness and if softer aggregates than basalt or river gravel are used it may be necessary to increase the thickness of composite to defeat a defined threat.

In this study a production method has been developed which allows the problems associated with the use of polyurethanes and damp aggregate to be overcome. However, if there is too much moisture present during mixing a rapid chemical reaction occurs and the cure time is too short for effective casting of composites. If the aggregate is too dry, cure periods are very long. For any specified aggregate moisture content the speed of reaction will depend on two factors. The higher the temperature, the faster the reaction will occur, but perhaps of more importance is that speed of reaction depends on how readily available the moisture is. Aggregates vary in their water absorption capacities and two aggregates may have the same water content when found by oven drying, but one may contain more of the water within its particle pore spaces than on the particle surface than the other. It is therefore impossible to specify an ideal water content or range of water contents for the aggregate, although water contents up to 5% have been successfully used in this study. For the aggregate water content to be acceptable, the blowing reaction should start in the period between 2 and 10 minutes after mixing and the composite will be workable for between 10 and 30 minutes. Composite specimens can be demoulded after an hour, at which time they have almost achieved full strength.

It is proposed that the composite is precast as blocks 450 mm x 225mm x 150 mm, having a mass of about 30 kg so that blocks can be used in a number of configurations to give a total wall thickness of 450 mm, which on the basis of the tests carried out would be sufficient to defeat a 10 round burst of automatic fire.

The density of good quality 150 mm trial cubes compacted by hand tamping with a metal rod can be used as a quality control in the large scale production of the composite. All large units should have a minimum density of 90% of the average density of the trial cubes. If this criterion had been applied in the current project, only one of the main test series specimens would have failed it. This specimen is indicated in Figure 2.

Compression tests on 200 mm high x 100 mm diameter specimens of composite gave a compressive strength of 1.6N/mm<sup>2</sup> and elastic modulus of 100N/mm<sup>2</sup>. Although the compressive strength is only about 10% of

that of an average construction quality concrete, the composite is suitable for construction of, or cladding onto, low rise defensive structures. A cost comparison with similar armour plated structures showed it to be an economical alternative.

### CONCLUSIONS

1. Single component moisture cure polyurethanes can be used to rapidly produce cost effective rock/polymer composites for defensive structures.
2. The thickness of composite necessary to defeat a single 0.5" AP round is about 310 mm.
3. The thickness of composite necessary to defeat ten rounds of 0.5" AP fire, either as multiple shots or a burst within a 70 mm grouping, is 400 mm.
4. Impact damage to the polyurethane composites is much less than with concrete, and deterioration with repeated impact is low.

### ACKNOWLEDGEMENTS

This work has been carried out with the support of the Procurement Executive, Ministry of Defence (RARDE, Christchurch).

### REFERENCES

1. ANDERSON, W.F., WATSON, A.J., JOHNSON, M.R. and McNEIL, G.M. 'Rock/elastomer composites as impact resistant materials'. Proc Symposium on the Interaction of Non-nuclear Munitions with Structures. Colorado, 1983, Vol 1, pp 85-90.
2. ANDERSON, W.F., WATSON, A.J., JOHNSON, M.R. and McNEIL, G.M. 'Optimisation of rock/polymer composites to resist projectile penetration'. Materials and Structures, Vol 16, 1983, No 95, pp 343-352.
3. CZARNECKI, L. Epoxide compositions with a moisture containing mineral filler. Polimery - Tworzywa Wielkocząsteczkowe, 25, 1980, Nos 6/7, pp 249-252.
4. BRITISH STANDARDS INSTITUTION B.S. 882 Specifications for aggregates from natural sources for concrete, Part 2., 1973.

## RICOCHET AND SHALLOW PENETRATION OF BOMBS IMPACTING ON HARD LAYERS

D. Favarger  
Defence Technology and  
Procurement Agency (DTPA)  
CH-3602 Thun, Switzerland

P. Eyer, M. Koller  
GSS, Glauser, Studer, Stüssi,  
Consulting Engineers  
CH-8032 Zurich, Switzerland

Full scale tests showed that hard layers give a very good protection against bombs even at high impact angle. Optimizing hard layers in full scale testing is not feasible with reasonable costs. Therefore we use a simple physical model of impact to compute shallow penetration of spheres as well as their velocity and direction after hit. Because the target damage of a ricocheting or a capsizing bomb is similar, we simplify the geometry of the projectile to a sphere of the same weight. The calculations correspond well with experimental data with steel spheres impacting in aluminium plates. Computed crater patterns are in agreement with the full scale tests. The model allows limited sensitivity analyses concerning target material and gives some possibilities to understand which material properties prevent penetration and enhance ricocheting. It will be extended for cylindrical projectiles.

### Introduction

Because the lack of available information about the interaction between aerial bombs and rock rubble layers the Swiss DTPA has performed several full scale tests since 1984. Full scale tests unfortunately don't practically allow no parametrical studies. Therefore we solve the equations of movement for projectiles similar to bombs and analyse their impact behaviour in different models. The aim of that research program is to enhance properties of overlays which cause the ricocheting of impacting projectiles.

### Full scale tests

In 1984 we dropped a dozen inert GP bombs at an impact angle of about  $55^\circ$  (relatively to the normal) on a sand filled rock overlay. The bombs penetrated without noticeable deformations. If they would have been live, their confined explosion would have damaged

severely the underground structure. For the next test in 1985 the holes between the boulders were filled with grout to reduce penetration. The inert bombs, dropped at the same angle as before, were ricocheting or tumbling on the hard layer and caused only shallow cratering.

In 1987 we dropped various bombs at a higher impact angle ( $33^\circ$  to the normal in the average) on rock rubble layers of different thicknesses. The GP bombs ricocheted far from the target and were severely bumped and bended by the impact. Most SAP bombs penetrated.

The models described below are yet too simple to account entirely for the observed impact behaviour of the bombs, but give already realistic results.

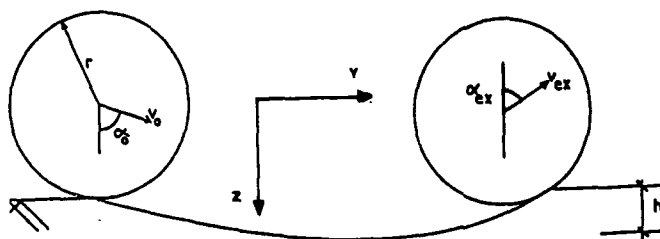


Fig. 1. Impact parameters.

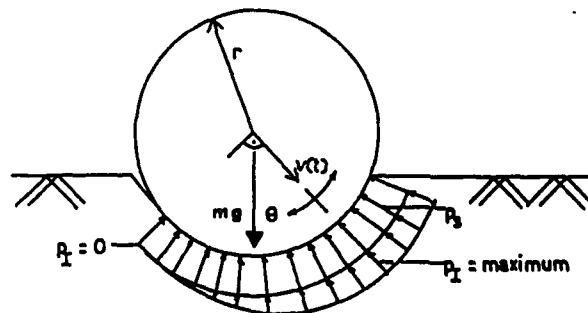


Fig. 2. Acting forces.

## Ricochetting Sphere (1)

In the simplest model we integrate the movement equations for impacting spheres with crude assumptions about the target material. We had first to check if such a model could give reasonable impact data. The homogenous aluminium target has the following specifications:

density  $\rho = 2700 \text{ kg/m}^3$   
 yield strength  $Y = 386 \text{ MPa}$   
 Young's modulus  $E = 72000 \text{ MPa}$

We consider rigid (steel) spheres as projectiles to simplify the geometry and reduce the degrees of freedom of the model (Fig. 1) with the parameters defined below:

weight  $m = 1.044 \text{ g}$  and  
 dimension  $r = 0.3175 \text{ cm}$

impact velocity  $V_0$   
 impact angle  $\alpha_0$   
 penetration speed  $V(t)$   
 penetration angle  $\alpha(t)$   
 penetration or crater depth  $h$   
 exit velocity  $V_e$   
 exit angle  $\alpha_e$

Within the speed range of bombs and artillery shells, the impact resistance due to inertia and to material strength (Fig. 2) are of the same order of magnitude. The calculation of these forces is based on the spherical cavity expansion theory as in (2), but neglecting in a first approach compressibility effects and strain hardening (Fig. 2). We use the following expressions

$P_i = 2 V_0^2 / 3$  for the dynamic pressure and  
 $P_s = 2 (1 + \ln 2E / 3Y) / 3$  for the normal

compressive stress. The gravity force is taken in consideration.

For an impact angle  $\alpha_0 = 60^\circ$  the computed exit velocity  $V_e$  and angle  $\alpha_e$  correspond very well with the experimental results of (3) (Fig. 3). The difference between calculated and experimental crater depth  $h$  is typical for a semi-empirical penetration theory like the one described in (2) and is quite acceptable. The comparison between theoretical and measured impact parameters for  $\alpha_0 = 45^\circ$  (Fig. 4) shows a fair agreement. The analysis of the differences is not obvious. In the model, the low theoretical exit speed above 600 m/s impact velocity is consistent with high exit angle but we would rather expect a lower kinetic energy loss and higher theoretical crater depth. The tendency of the theory to underestimate the penetration depth with increasing impact velocity, as it is mentioned in (2), may explain this feature.

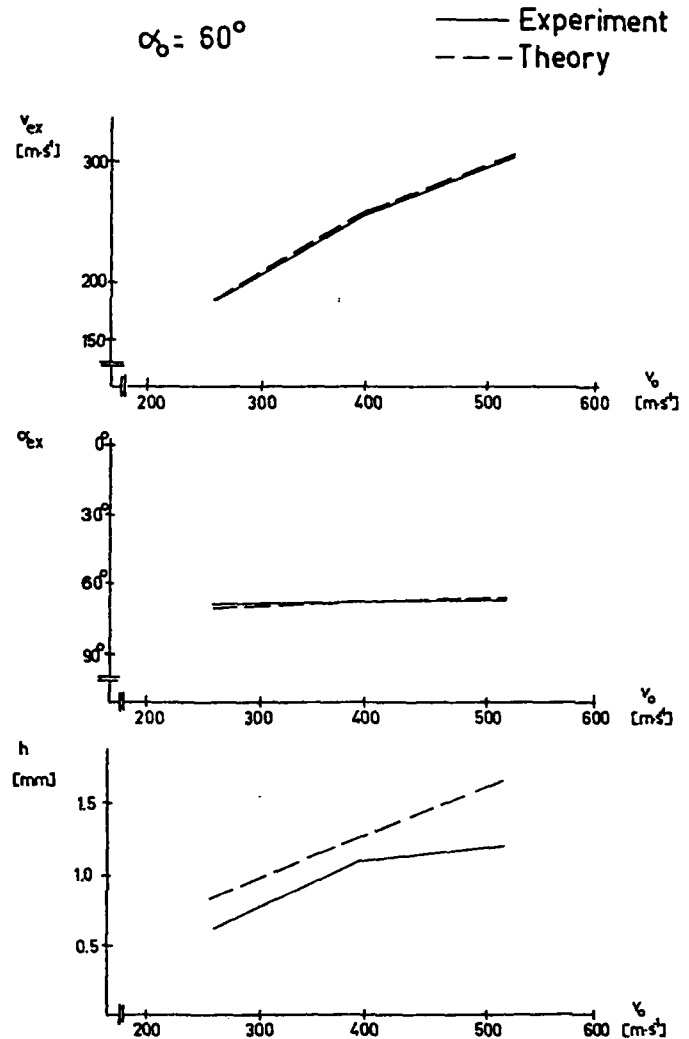


Fig. 3. Comparison between model and experiment.

The exit parameters ( $V_e$ ,  $\alpha_e$  and  $h$ ) show only low sensitivity to the Young's modulus and to the density of the target. The maximum penetration depends in first approximation on  $(Y)^{-1/2}$  and is fairly proportionnal to  $V_0$  as it was already mentioned in (5) and (6).

Since the horizontal component of the stress vector  $P_{sy}$  is overestimated near the target surface, we consider that it has some value between zero and  $P_s$  and set in the upper layer

$$P_{sy} = P_{sz} / 2 \text{ (see Fig. 5)}$$

where  $P_{sz}$  is the vertical component of  $P_s$ . This modification improves appreciably the calculated values of the exit velocity (Fig. 4) above 600 m/s impact velocity.

We considered also a rigid sphere weighing 450 kg with 30 cm diameter and 240 m/s initial velocity to simulate bomb impacts on concrete overlays with following specifications:

density  $\rho = 2400 \text{ kg/m}^3$   
 yield strength  $Y = 35 \text{ MPa}$   
 Young's modulus  $E = 22500 \text{ MPa}$

The observed crater dimensions and patterns in the full scale tests scatter much more for the deeper than for the lower (Fig. 6) impact angle. Although it is only possible to define an average and not a typical observed crater in the case of deeper impact angle, the computed pattern seems quite realistic. But the penetration depth and the crater dimensions in concrete given by the theory are likely twice too small.

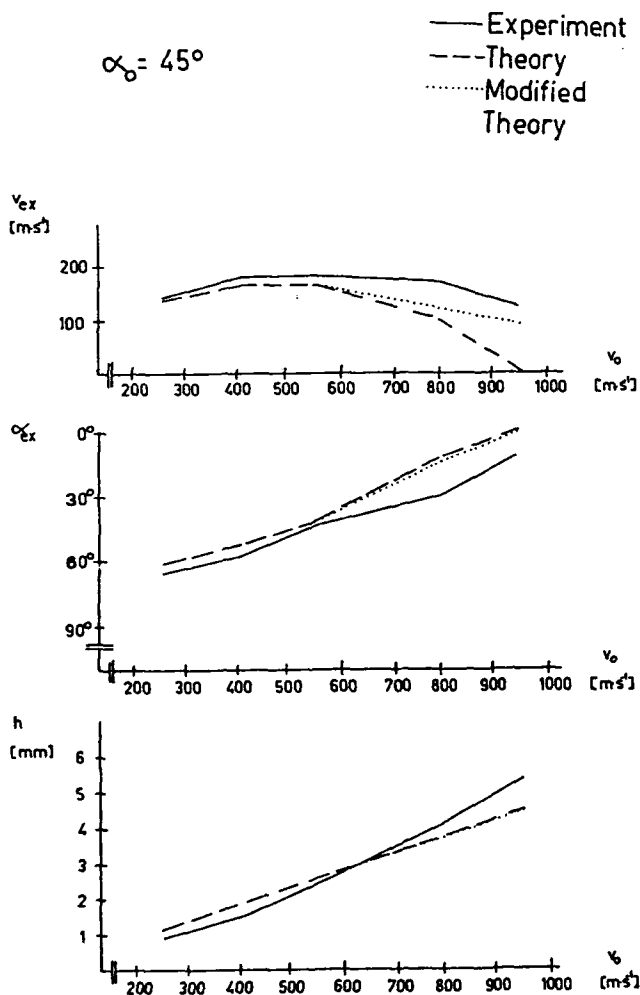


Fig. 4. Comparison between model and experiment.

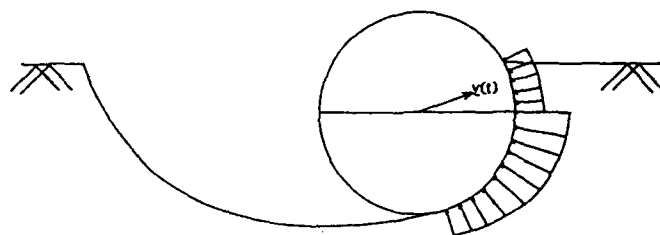


Fig. 5. Modified stress distribution.

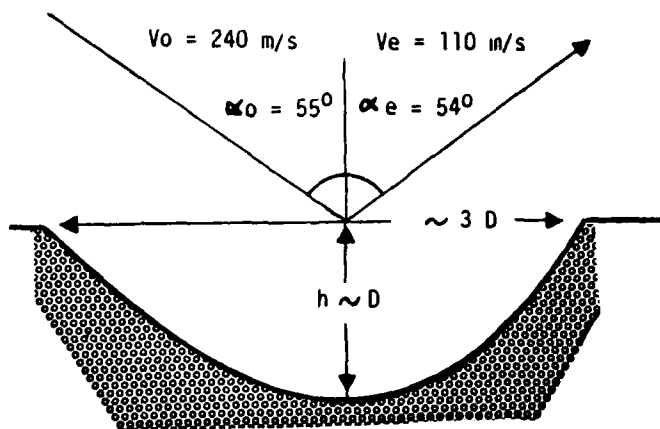


Fig. 6. Computed crater patterns in concrete.

#### Parallelepipedic bombs

A bomb impacting on a hard layer in a 2-dimensional plane has one degree of freedom more than a sphere. We assume that it can rotate with the speed  $\omega$  around a horizontal axis passing through the c.g. (Fig. 7). If we consider cylindrical rigid bombs with a flat front, the penetration velocity on the nose and the crushing velocity on the case side vary linearly with the distance to the c.g. This rotation speed component must be added to the c.g. velocity. In such a case, it is possible to integrate the expressions for  $P_s$  and  $P_r$  analytically to determine the force and the torque acting on the bomb. Now, after the nose has caused a crater, it can happen, for instance, that the aft part of the bomb touches the rear crater edge. The momentum given to the bomb by such or similar contacts with the target is much easier to compute in a plane than in a curved geometry. Therefore, we consider parallelepipedic bombs with following specifications:

weight  $m = 450 \text{ kg}$   
 caliber  $D = 2r = 0.35 \text{ m}$   
 length  $l = 1.7 \text{ m}$



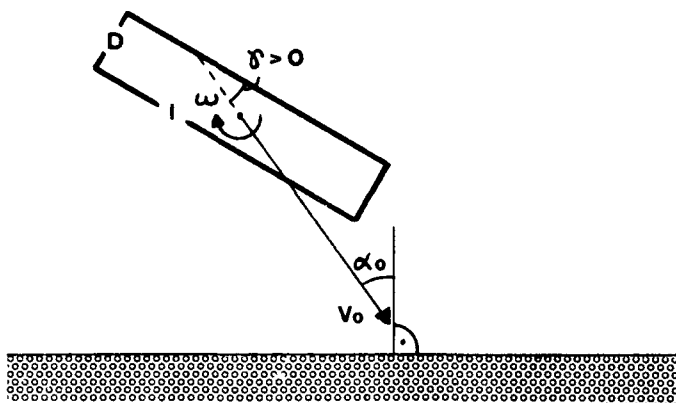


Fig. 7. Impact parameters of the cylindrical bomb

c.g. position: same as the geometric center of the parallelepiped. They are falling on a concrete overlay (see specifications above). As in the model of the ricocheting sphere, in the upper layer of the target, we use various assumptions about  $P_{sy} = k \cdot P_{sz}$ , where  $k < 1$ . The verification of the energy conservation throughout the computation revealed to be a powerful tool to check the accuracy of the results.

#### A) Flat impact angle $\alpha_0 = 55^\circ$

In the model, the impact behaviour of the bomb depends strongly on the yaw angle  $\gamma$ . We can determine three ranges of  $\gamma$  with well defined motion types (Fig. 8). Beyond the penetration limits we have either capsizing or ricocheting too, but the motions are too slow to be achieved after the bomb have been stopped. During the full scale tests no bomb penetrated in the rock rubble layer with grout filled interstices. The observations and films of motion show the bombs tumbling after impact. Although they confirm roughly the model calculations, we see (Fig. 8 a), that capsizing needs a yaw angle less than  $-2^\circ$ . The real value of  $\gamma$  for unguided bombs may not very often fill this condition, because the aerodynamic lift on the fin tail would give more likely a positive yaw angle.

To simulate inhomogeneities in the hard overlay, we consider a bomb hitting asymmetrically a rock boulder with a yield strength six times higher than concrete strength. We assume first, that the lower third of the front section is penetrating in such a boulder, that the higher penetration drag acts during the whole motion in the target. The two upper third of the front section are encountering only concrete. Thus, the range of penetration becomes smaller than for the homogenous target and the values which define the different type of motion are

clearly shifted with about  $+3^\circ$  on the  $\gamma$ -axis (Fig. 8 b). As expected, we see that a hard layer acting immediately after the first contact of the bomb enhance the tendency to capsize.

If the upper third of the front section is penetrating in the rock, the yaw angles which are limiting the three types of motion in the Fig. 7 are slightly ( $-1/2^\circ$ ) moved left towards lower values of  $\gamma$ . The result can be expected because the force and torque changes corresponding to the inhomogeneous overlay are occurring late. It would be wrong to conclude that inhomogeneities induce ricocheting. The limits of  $\gamma$  for penetration in an homogenous rock layer (Fig. 8 c) differ only slightly from the ones indicated in the Fig. 8 b. This means that hardness and not inhomogeneity is the important parameter. If we increase the slenderness ratio  $l/D$  from about 5 to 10, the bomb penetrate much more reliably (Fig. 8 d). If we reduce the  $l/D$  ratio from about 5 to 2.5, the bomb capsizes at impact up to  $+15^\circ$  yaw angle or more.

#### B) Deeper impact angle $\alpha_0 = 35^\circ$

As Fig. 8 e) shows, unguided bombs with relatively small yaw angle should generally penetrate into the target. During the full scale tests, the bombs with deeper impact angle were guided by Payeway II units. We could see on the films and with naked eye how the digital fin control was turning the bomb axis while falling. Thus, yaw angle up to  $\pm 10^\circ$  at impact could be quite realistic. The SAP bombs penetrated up to 3 calibers and stay with angles sometimes deeper, sometimes flatter than the trajectory angle.

Because of the strong inhomogeneity of the rock rubble layer and, may be, because of the yaw angle scattering, the craters have showed quite different patterns.

The case of the GP bombs impacting the hard overlay were considerably buckling. This may explain why they did not penetrate but were tumbling or ricocheting away. In a further model development, we shall study the impact of bombs made of two rigid parts held by a hinge with a rigid ideal plastic characteristic corresponding to the yield bending strength of the GP bombs.

As it was already pointed out above, the penetration depth and crater dimensions are about twice too small, but the different computed shapes correspond nearly with the observed ones.

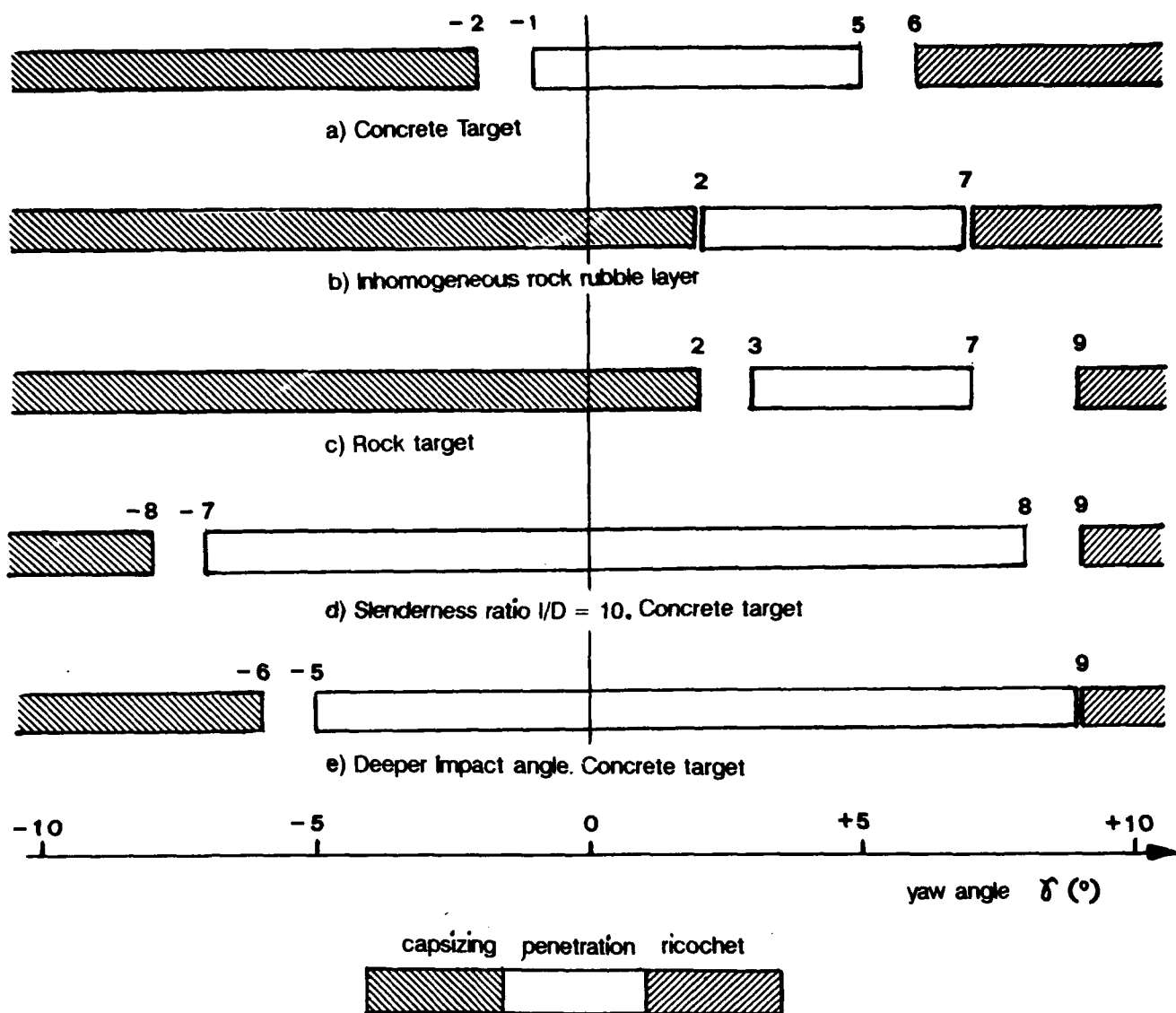


Fig. 8. Bomb behaviour as function of the yaw angle for different impact parameters

#### Summary

The full scale tests were no scientific experiment and allow only more qualitative than quantitative comparison with the model results. We need more experimental data, for instance about the impact of cylindrical small caliber projectiles on aluminium plates, to check the model more exactly. The penetration theory have to be improved too, but should keep its formalism to take in account the different strengthes parallelly and normally to the target. In spite of its lacks, the model pointed out the most important parameters inducing capsizing or ricochetting of bombs like projectile slenderness and yaw angle, as well as target hardness.

## References

- (1) Studer J.A. and Koller M. Ricochetting: Computational Models. Workshop on Penetration of Warheads into Hardened Structures. Design of Burster Slabs/Rock Rubble Overlays. Stockholm. May 1988.
- (2) Bernard R.S. Development of a projectile penetration theory, US Army Engineer Waterways Experiment Station, Vicksburg, Mississippi. Technical Report S-75-9-1. September 1975.
- (3) Zook J., Slack W., Izdebski B. Ricochet and Penetration of Steel Spheres Impacting Aluminium Targets. US Army A.R.D.C., B.R.L. Aberdeen Proving Ground, Maryland. Report ARBRL-MR-03243. February 1983.
- (4) Bernard R.S. Empirical analysis of projectile penetration in rock. U.S. Army Engineer Waterways Experiment Station, Vicksburg, Miss., Technical Report S-77-16, November 1977.
- (5) Gyllenspetz I.M. Equations for Determining Fragment Penetration and Perforation Against Metals. National Defense Research Institute (FOA). Stockholm. Shock and Vibration Bulletin. Nr. 50. September 1980.

## Penetration Tests with Scaled AP and MK-Bomb Models in Layered Structures

Helga Langheim and A. J. Stilp

Fraunhofer-Institut für Kurzezeitdynamik  
Ernst-Mach-Institut, Freiburg i. Br.

### Abstract

A series of impact tests was carried out with 1 : 4 and 1 : 5.8 scaled inert AP and MK-bomb models against homogeneous and layered structures of concrete and sand targets. The subscale tests were performed to reduce the number of full-scale tests, to check the influence of several test parameters and the validity of scaled test results. The impact tests were carried out in the EMI proving ground impact range. The projectiles were launched from a 100 mm cal. smooth bore gun with sabots fabricated from hard styrofoam and polyethelene. In the test program, the following parameters were varied: type of projectiles, AP 2000 and MK84 scaled bomb models, the angle of incidence, 0° and 30° Nato, the target structure, reinforced concrete slab and layered structures of concrete and sand, and the impact velocity from 135 m/s to 240 m/s. The experimental results indicated a good agreement with the full-scale test.

### Objectives and Approach

The objective of these tests was the determination of the limit velocity of two bomb types to perforate concrete slabs with given thicknesses and reinforcements. Well-known empirical or semiempirical formulae are not applicable because they are not valid for highly deformable projectiles.

In previous test programs performed at the ERNST-MACH-Institut the penetration behavior of deformable and undeformable projectiles and the protection behavior of reinforced concrete slabs, steel fibre reinforced concrete slabs and of rock/rubble burster layers have been studied.

Many of these tests have been performed as subscale tests. They serve for preparation of full-scale tests and to perform parameter studies. Full-scale tests with large concrete slabs are expensive and time-consuming.

Previous investigations, e.g. Canfield/Clator [1], show that results from subscale tests agree with data from full-scale tests, if the model scale factor is not too big (not more than 1 : 10) and if the scaling laws

are carefully applied. All parameters which influence the penetration process must be transformed in accordance with the CRANZ similarity law. The model should not only show geometrical similarity in all details with the original, it must also consist of the same material (Replica-model) with the same dynamic material properties. This demands equal material density, equal strength, elongation etc. for subscale and full-scale tests. Impact velocity and impact angle must be identical for subscale as well as for full-scale tests. Only under these conditions prototype and model will show comparable damage.

### Facility Description and Experimental Set-up

The impact tests were carried out at the ERNST-MACH-Institut proving ground impact range (Figure 1). This range consists of a launcher system (three different types of energy reservoirs) and a concrete impact bunker with dimensions of 5 x 4 x 4 m, with a wall thickness of 75 cm. Target sizes of up to 2 x 2 x 2 m can be handled in this target bunker. In the space between launcher and impact bunker (10 m) blast tanks, velocity measurement station and sabot catcher tank are installed. The range is a completely closed system connected to efficient vacuum and exhaust systems.

The bombs were launched from a 100 mm cal. smooth bore gun with sabots fabricated from hard styrofoam and polyethelene. The sabot segments which encase the projectile during the acceleration in the launch tube are aerodynamically separated from the projectile in the blast tank and they are stopped by a steel catcher plate with a central hole. Flow visualization and velocity measurement of the projectile after separation are obtained by means of two stereo-shadowgraph systems with point light sources. The point spark light sources are triggered by two HeNe-laser light barriers. The velocities are calculated from distance measurements read on films and times recorded by an electronic counter. The accuracy of the velocity measurement is in the order of 2 %.

The projectiles hit the targets in the 50 m<sup>3</sup> impact chamber. The concrete slabs are freely suspended; the angle of incidence can be varied by rotating the target suspension. In order to simulate larger dimensions the slabs were fitted into a massive steel frame.

The test set up of the layered structure is shown in Figure 2, it is a cross-section of an aircraft shelter. The burster shield system consists of a reinforced concrete slab on the front side, supported by a layer of compacted dry sand and a rear concrete slab with steel liner, all tied together by prestressed steel rods.

### Test Parameters

In the test program the following parameters were varied: type of bomb, angle of incidence, impact velocity, target structure. The two bomb types are shown in Figure 3 with original and subscale dimensions. For the GP-bomb MK84 a model scale 1 : 5.8 was chosen because the launch tube has a diameter of 100 mm. The AP 2000 bomb has a scale factor 1 : 4.5. Only the main dimensions of the bombs are scaled exactly, details such as fins, fuses, support elements etc. have been ignored. The bomb-models are filled with a resin quartz powder mixture having roughly the same mechanical properties as the explosive filler composition B. The model bombs were fabricated from steel, with the same material properties as the original bombs.

The tests have been performed under two angles of incidence: 0° and 30° NATO, the impact velocity varied between 135 and 240 m/s.

The lateral dimensions of the target slabs and the thickness as well as the spacing of the reinforcing bars were scaled 1 : 4 and 1 : 5.8, respectively. Only the diameter of the reinforcing bars and the aggregate size were scaled 1 : 4 in order to use available materials (cement and aggregates), which reduced costs. Test cubes made from the same material as the model slabs had compressive strength of about 42 N/mm<sup>2</sup> (equivalent to cylinder compressive strength of 5200 lb/in<sup>2</sup>). The geometrical dimensions of the unsupported model slabs simulate original slab dimensions of 3.6 x 3.6 m with thicknesses of 1.55 and 2.00 m. The supported (layered) targets (Figure 2) simulate lateral dimensions of 7 x 6 m and thicknesses for the front concrete slabs of 1.55 m, for the sand layer of 3 m and for the rear concrete slab of 0.9 m.

### Test Results and Interpretation

#### MK84 Bombs Against Concrete Slabs

10 impact tests were performed with MK84 model bombs against concrete slabs with 2 different thicknesses (26.7 and 34.4 cm, corresponding to original thicknesses of 1.55 and 2.00 m); i.e. model scale 1 : 5.8. Normal impact with a velocity of

180 m/s on the thinner slab resulted in armor complete, the bomb remained in the slab. With the same velocity the bomb penetrated into the thicker slab only 99 cm, without causing scabbing on the rear. At an impact velocity of 200 m/s the bomb perforated the thinner plates, the thicker plates showed scabbing on the rear side. The bomb showed no visual deformation.

The deformation behavior of MK84 bombs and the damage profile of the impacted slabs is dramatically changed when the bombs impact at a 30° angle. Figure 4 shows that the direction of the bomb is changed considerably. At an impact velocity of 184 m/s the bomb ricochets totally. The indicated penetration depths were the vertically measured maximum depths of the resulting spallation craters.

Figure 5 shows the model bombs after penetration. Some bombs were broken into 2 or 3 pieces.

#### AP 2000 Bombs Against Concrete Slabs

Two impact tests with the AP 2000 bomb at 0° impact angle with velocities 135 and 168 m/s showed only penetration into the slabs. On the rear side only cracks and beginning scabbing were visible.

Figure 6 shows the penetration trajectories of the bombs impacting at 30°. At an impact velocity of 153 m/s the bomb ricochets totally. In this case as well as at velocities up to 200 m/s the rear sides of the slabs showed only small cracks and no scabbing. An increase of the impact velocities of up to 240 m/s leads to complete perforation of the plate. In all cases the AP 2000 bombs showed no deformation. Their behavior under the conditions of these tests were like a rigid, undeformable missile: no energy reduction is caused by plastic deformation of the bomb.

#### AP 2000 Bombs Against Layered Structures

A series of 5 tests was performed involving layered structures shown in Figure 2 with AP 2000 bomb models at 30° incidence in the velocity range from 190 to 230 m/s. No perforation occurred.

Figure 7 shows the penetration trajectories of this test series. At the rear face of the front slab only small cracks are observed at an impact velocity of 213 m/s. At a velocity of 230 m/s the beginning of scabbing is visible, as shown in Figure 8.

A bomb projectile having a slightly higher impact velocity of 240 m/s against an unlayered slab led to perforation with a considerable exit energy of the bomb. A strong confinement is obtained by a bonding of front slab, sand layer and rear slab. Thus early scabbing on the rear face can be prevented.

### Comparison of the Model-scale and Full-scale Tests

A MK84 bomb in original size was shot against the prototype of a layered structure of an aircraft shelter, as shown in Figure 2. Impact conditions were exactly the same as in the model test: velocity 190 m/s, angle of incidence 30° NATO. The original bomb ricocheted from the front concrete slab and no scabbing on the slab's rear face occurred.

The correspondence between model (1 : 5.8) and prototype test was excellent. Figure 9 shows the front faces of both slabs after the tests. Table 1 shows the results from the model test, in comparison with calculated results for a corresponding full-scale impact and finally with the results from the full-scale test.

These data show that model tests deliver correct results, if the scaling laws are strictly applied.

| Crater dimensions       | model scale<br>test (1:5,8) | calculated<br>1:1 | full scale<br>test |
|-------------------------|-----------------------------|-------------------|--------------------|
| max. depth (m)          | 0,08                        | 0,46              | 0,4                |
| max. length (m)         | 0,24                        | 1,39              | 1,5                |
| max. width (m)          | 0,44                        | 2,54              | 2,6                |
| max. aggregate size (m) | 0,008                       |                   | 0,032              |

Table 1 : Comparison of the 1:5,8 model scale test and full scale test

### References

- [ 1 ] Canfield, J.A., Clator, I.G., Development of a Scaling Law and Techniques to Investigate Penetration in Concrete, U. S. Naval Weapons Laboratory, Dahlgren, Virginia NWL-Report No. 2057, Aug. 1966.
- [ 2 ] Stilp. A.J., The New EMI Terminal Ballistics and Hypervelocity Impact Range, ERNST-MACH-Institut, Bericht 2/87, Aug. 1987

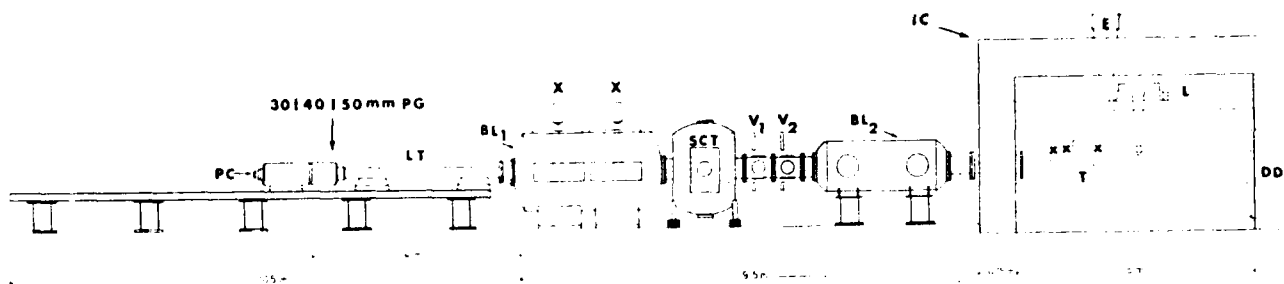


Figure 1 Schematic drawing of the range

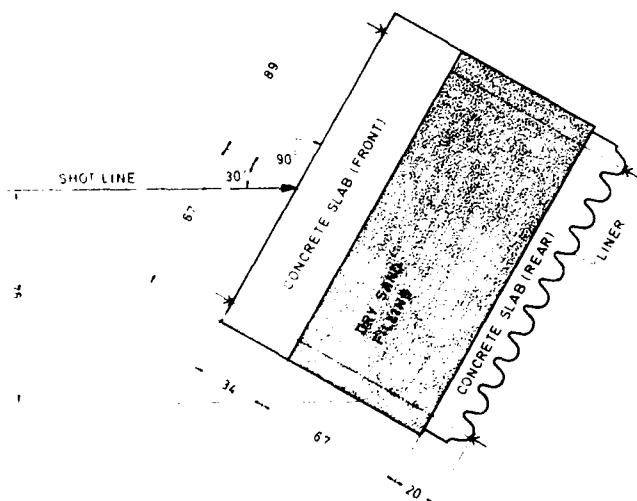


Figure 2 Test set up of the model scale layered structure

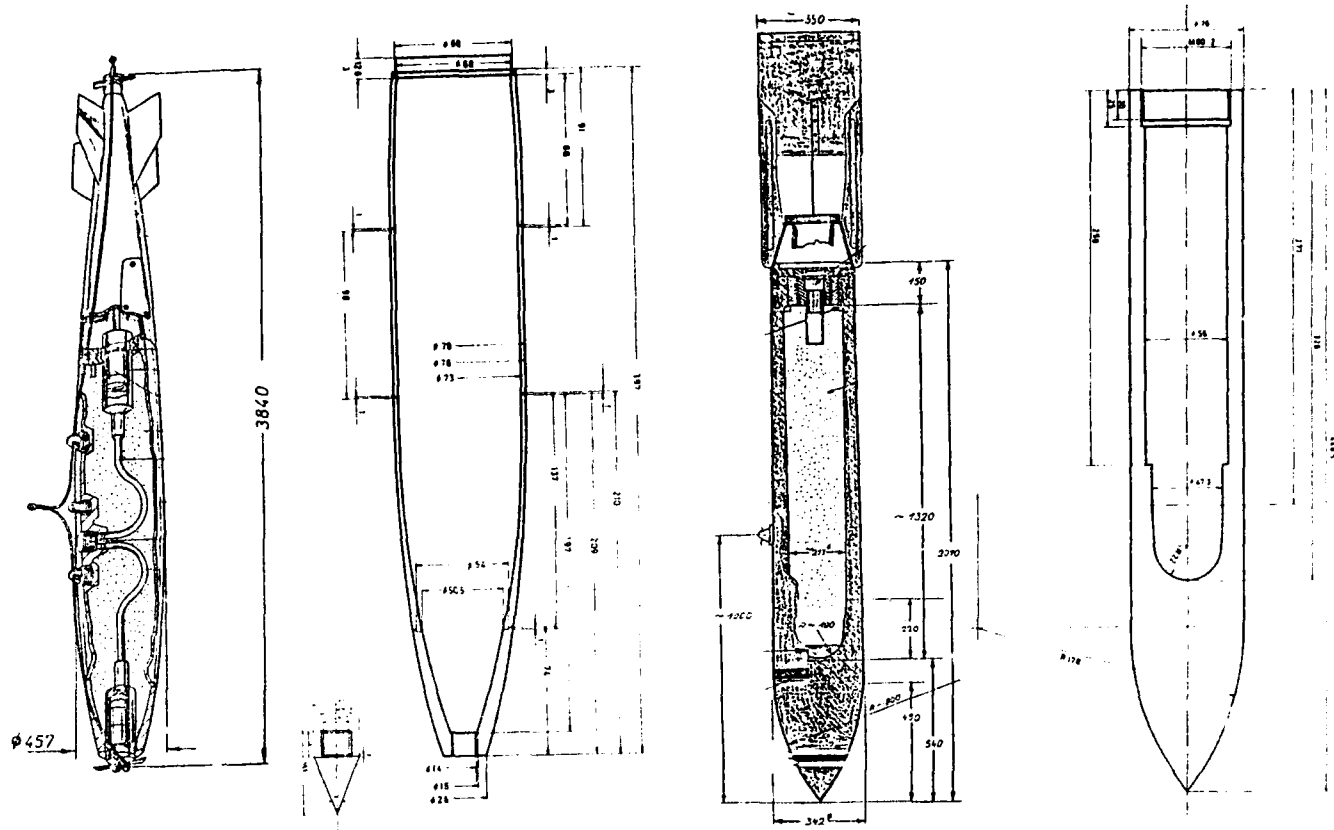


Figure 3 Full scale MK 84 bomb and 1 : 5.8 scale model bomb and full scale AP 2000 bomb and 1 : 4.5 scale model bomb

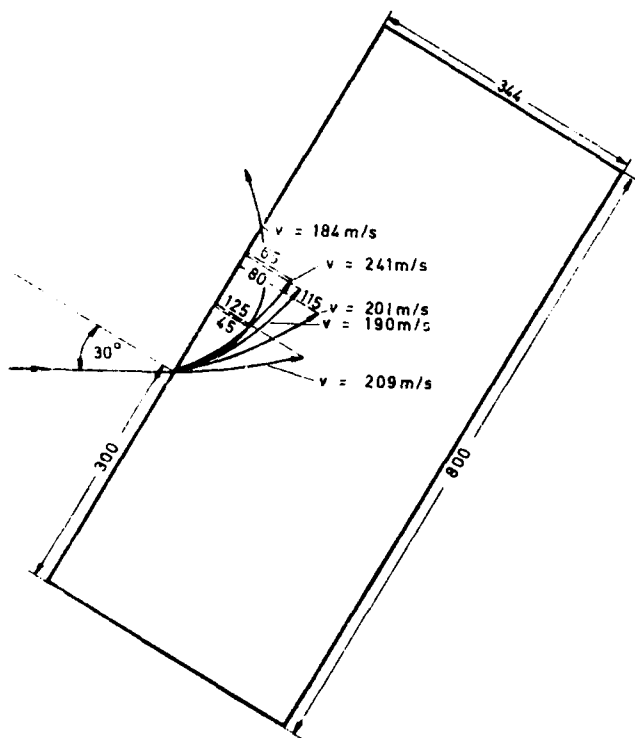


Figure 4 MK 84 bomb model trajectories

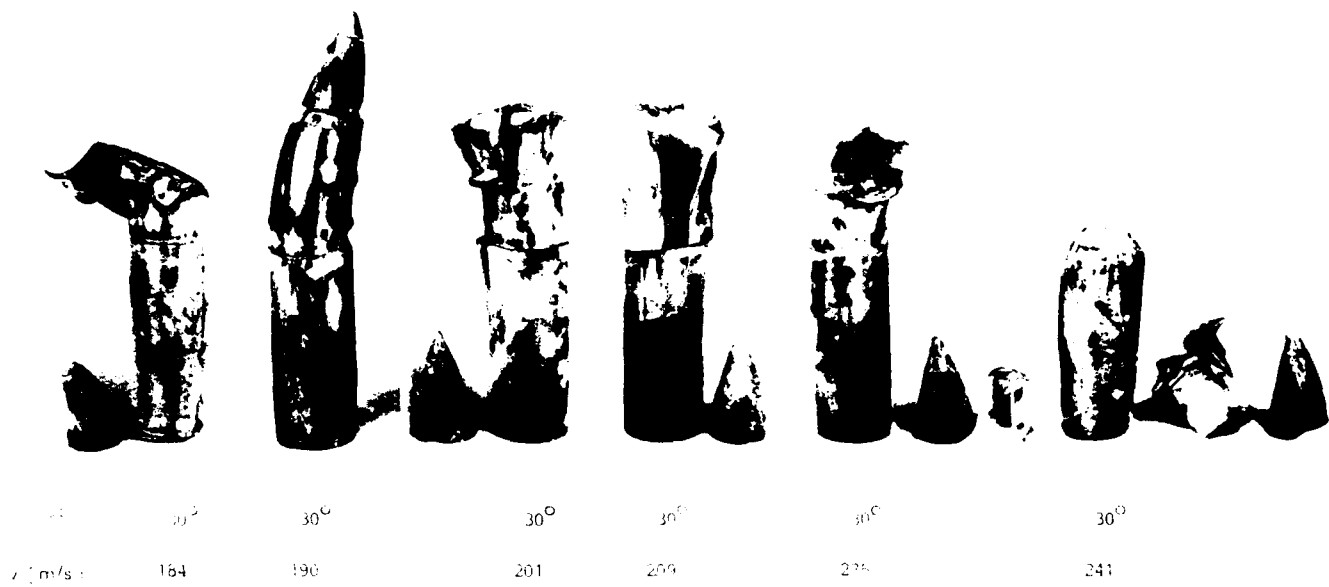


Figure 5 MK 84 bomb models after penetration into model concrete slabs

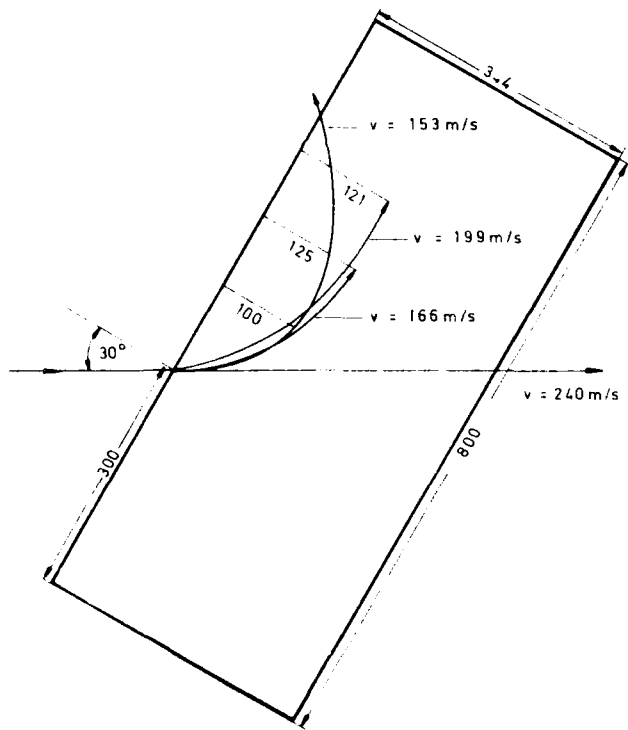


Figure 6 MK 84 bomb model trajectories

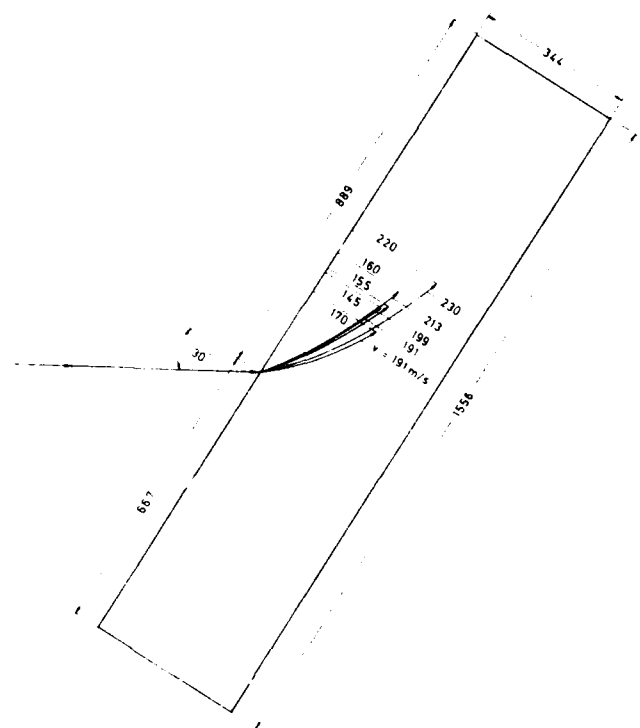


Figure 7 AP 2000 bomb model trajectories - Layered structures



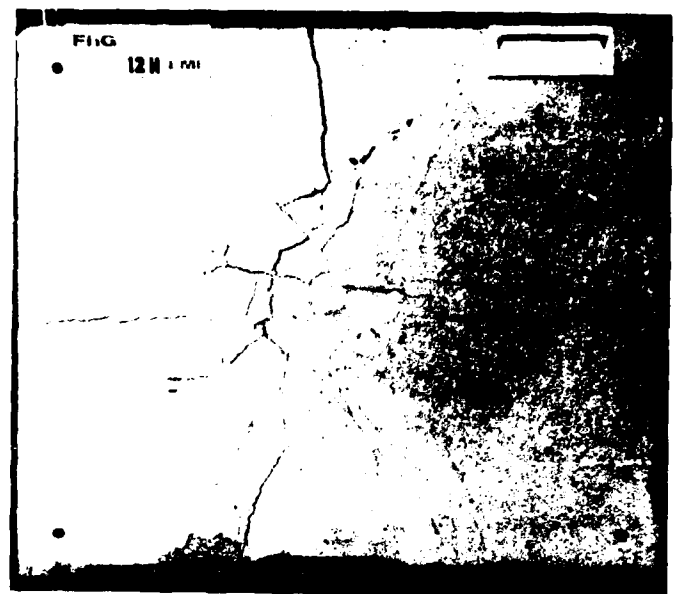
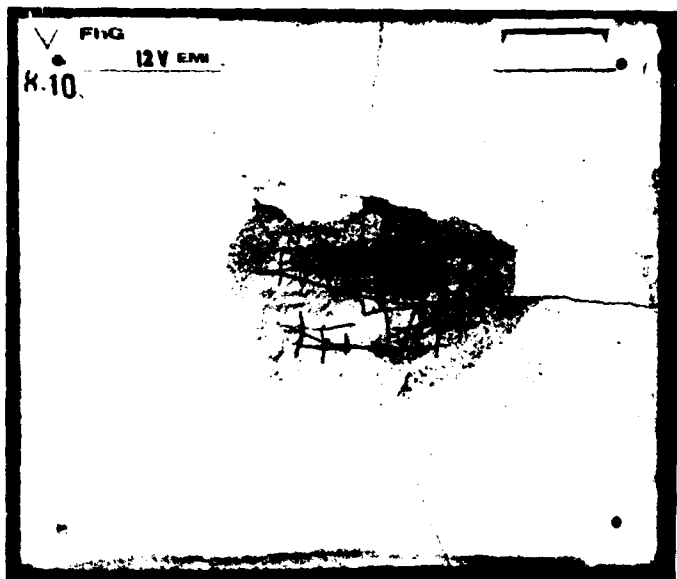
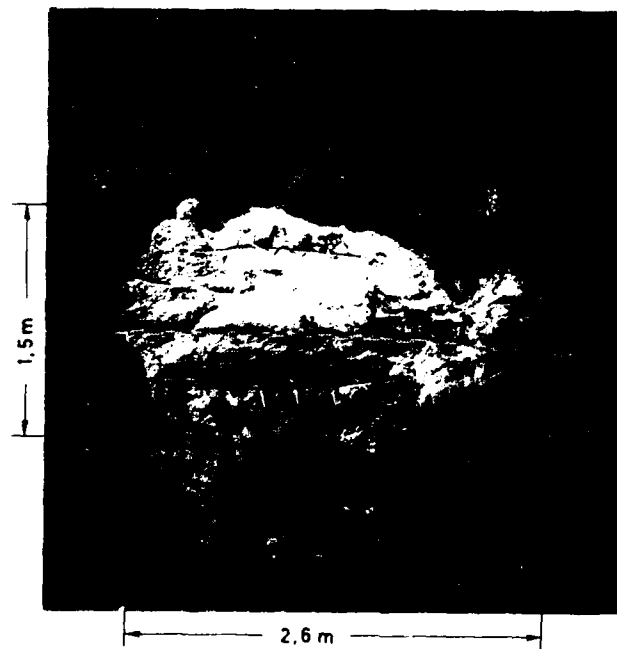
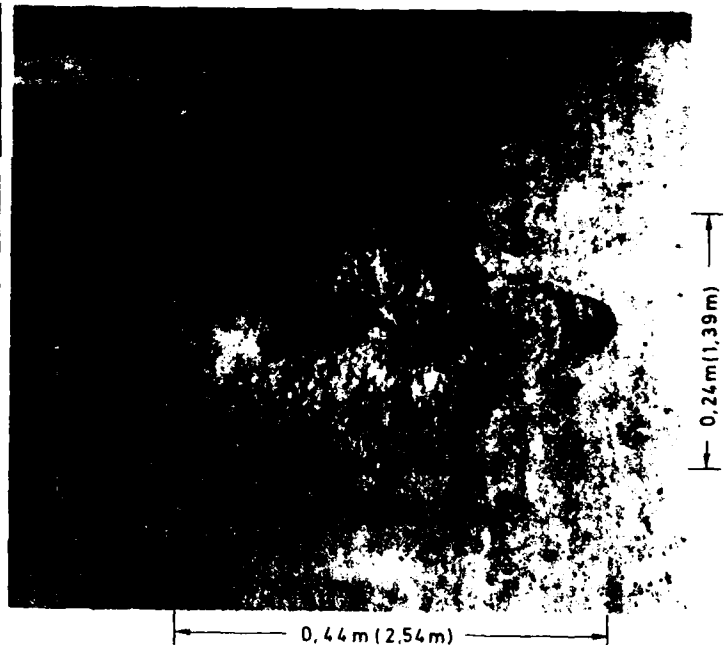


Figure 8 Model concrete target after penetration of AP 2000 bomb model ( $\theta = 30^\circ$ ;  $v = 230$  m/s;  $p = 22$  cm) - front and rear faces of the slab - Layered structure



Full scale test  
 $p = 40$  cm



1 : 5.8 model scale test  
 $p = 8.0$  cm  
corresponding full scale 46.4 cm

Figure 9 Front faces of the concrete slabs after penetration of MK 84 bomb,  $\theta = 30^\circ$ ,  $v = 190$  m/s

# NUMERICAL METHOD TO PREDICT PROJECTILE PENETRATION

Larry A. Schoof, Frank A. Maestas, and C. Wayne Young\*

Applied Research Associates, Inc., Albuquerque, NM

\*Sandia National Laboratories, Albuquerque, NM

## **ABSTRACT**

The Simplified Analytical Model of Penetration with Lateral Loading (SAMPLL) computer code developed at Sandia National Laboratories has been modified to allow additional penetration capabilities. The new capabilities include the ability to model penetration by other than cylindrical penetrators (flares, tapers, and boattails) and the ability to calculate penetration/perforation of multiple layers of different materials. Additionally, updated soil and rock empirical equations have been added to the model. A broader range of problems can now be modeled more accurately with the modified SAMPLL.

## **INTRODUCTION**

The SAMPLL code has been in use for five years. The algorithms used in the code are generally empirical in nature and are based on an extensive experimental data base. The current version of the code accounts for lateral loads due to angle of attack and impact angle, cratering and spallation of the target, layered targets, multiple slab targets, penetrator damage or failure, and allows complex penetrator shapes. This paper will give a brief description of the SAMPLL code and give several examples of how the code can be applied.

## **SAMPLL BACKGROUND**

As a technology, earth penetration by projectiles has been studied and reported for over 300 years, but the focus of the studies has changed. Prior to World War II, earth penetration was studied from the perspective of how to build a protective cover against shells, with no specific effort to improve the penetration characteristics of the weapons. During

World War II, the Germans began to design weapons specifically for earth penetration, and the British conducted a significant research program to better understand concrete penetration. After the war, the United States began to study the penetration characteristics of its conventional bombs, but it was not until 1960 when Sandia National Laboratory (SNL) began its terradynamics program that earth penetration evolved as a scientific discipline.

Current penetrators are designed to carry payloads including conventional explosives, nuclear weapons, and complex sensor systems. The analytical tools required to make the necessary calculations have to be continually improved to keep pace with the complexity of the earth penetrator applications. The simplified techniques and codes such as SAMPLL are not expected to eliminate the need for the three-dimensional finite element and finite difference numerical codes, but are necessary to economically perform the large number of calculations required for some parametric studies.

The SAMPLL code was developed to calculate the lateral loading due to impact angle and angle of attack. Before SAMPLL, there were empirical equations developed to calculate the depth of penetration into natural earth materials and concrete (ref 1, 2, 3, 4). The empirical equations were a fit to data acquired over 28 years of full-scale penetration testing into natural earth targets. Most of the more significant data are included in a data base management system at SNL (ref 5).

The SAMPLL code was first written in 1982 and published in 1984 (ref 6). SAMPLL has been used (and verified) extensively on a number of development programs both in the DOE and DOD. It has been continually improved as the need arises to account for different phenomenology. Even as more test data become available, it has not been necessary to

make significant changes to the code to better fit the data.

## **SAMPLLL CAPABILITIES**

SAMPLLL is a two-dimensional empirical code developed to predict the penetration and failure of large projectiles impacting hard materials (i.e., concrete, rock, cemented soils, and ice/frozen soil). The newest version of the code allows for multiple layered targets of different materials by accounting for impedance mismatches at layer interfaces. This phenomenon causes projectiles to tend toward layers with lower relative penetrability.

Another recently added feature is the ability to input penetrators of general shapes (flares, tapers, and boattails). The code compares the flare angle with the instantaneous angle of attack to determine if the penetrator is in contact with the target media and then uses this information in calculating the lateral loads.

SAMPLLL is not applicable in all situations. Currently it does not account for separation of the projectile body from the target material and thus does not accurately predict motion through soft soils (due to the soil wake phenomenon). Also, results are suspect if a target layer thickness is less than the penetrator nose length.

## **SAMPLLL ALGORITHMS**

Two basic premises form the foundation of the SAMPLLL code: (1) an average rigid body axial deceleration is computed from Young's penetration depth equations (ref 7), and (2) penetrator axial and lateral loads are both a function of the target material "resistance" and thus are proportional as shown below:

$$\frac{F_l}{A_s} = f\left(\frac{F_a}{A_f}\right)$$

where

$F_l$  = lateral force

$A_s$  = side-projected area

$F_a$  = axial force

$A_f$  = frontal-projected area

The required inputs for SAMPLLL are descriptions of the penetrator (weight, length, nose shape, diameter, and the yield stress), the target (each layer's thickness, material type, and penetrability number), and the impact conditions (velocity, trajectory angle, and angle of attack). The code then utilizes a time-stepping algorithm and determines the rigid body motion of the penetrator at each step due to the axial and lateral loads. The axial load is calculated from Young's depth equations (ref x) as follows:

$$D = f\left(S, N, \frac{W}{A_f}, V\right)$$

$$a = \frac{V^2}{2D}$$

$$F_a = ma = \frac{mV^2}{2D}$$

where

$D$  = depth of penetration

$S$  = material penetrability number

$N$  = nose performance coefficient

$W$  = penetrator weight

$A_f$  = frontal-projected area of the penetrator

$V$  = velocity

$a$  = rigid body deceleration

$F_a$  = axial force

$m$  = penetrator mass

The lateral forces are calculated at discrete elements ( $\gamma_i$ , see Figure 1) along the length of the penetrator as a function of the axial force, trajectory angle, angle of attack, and proximity to layer interfaces (to account for target stress reliefs). This is shown below:

$$F_{li} = f(A_{si}, F_a, A_f, pn, en, \phi, \alpha, \epsilon, \epsilon')$$

where

$F_{li}$  = lateral force on the  $i$ th element

$A_{si}$  = side-projected area of the  $i$ th element

$F_a$  = axial force

$A_f$  = frontal-projected area

$pn$  = distance to lower layer interface, perpendicular to penetrator axis

$en$  = distance to upper layer interface, perpendicular to penetrator axis

$\phi$  = penetrator angle (see Figure 1)

$\alpha$  = angle of attack

$\epsilon$  = vertical distance to upper layer interface  
 $\epsilon'$  = vertical distance to lower layer interface

At each time step, the translational motion of the penetrator is calculated using the axial force and sum of the lateral forces. The rotational motion (angular acceleration) is computed from the lateral forces in the following manner:

$$\tau = \sum_{i=1}^n (F_{li})(l_i)$$

$$\ddot{\phi} = \frac{\tau}{moi}$$

where

$\tau$  = torque

$F_{li}$  = lateral force on the  $i$ th element

$l_i$  = distance from  $i$ th element to the penetrator

center of gravity

$\ddot{\phi}$  = angular acceleration

$moi$  = mass moment of inertia

The output of the code includes time histories of penetrator position ( $x$  and  $z$  location), orientation (trajectory angle and angle of attack), and motion (axial, lateral, and rotational velocities and accelerations), as well as an estimate of penetrator failure based on "excess impulse" (amount of stress above the yield stress multiplied by time). Figures 2, 3, and 4 graphically depict the output of a typical SAMPLL run. Figure 2 shows the position and orientation of a projectile as it penetrates a one-foot thick concrete slab. The lateral accelerations at the penetrator nose, tail, and center of gravity are shown in Figure 3. The stress vs. time plot in Figure 4 represents the stresses at the penetrator center of gravity and another (user selected) point. The stress at these points are calculated as a combination of axial and bending stresses and give an indication of weapon failure.

## **SAMPLLL APPLICATIONS**

SAMPLLL has been used in both development and analysis applications. Weapon developers have performed parametric studies with SAMPLL to optimize specific weapon characteristics. As an analysis tool, SAMPLL was used to determine the trajectory of a weapon through a target in the vulnerability assessment computer code SLAVE3D. ARA developed SLAVE3D as a fast-running statistical code to accurately model damage to a structure and its contents given an attack.

Tables of results from the SAMPLL code for various weapons were developed which included the change in the trajectory angle, angle of attack, and velocity for a weapon passing through concrete. These data were analyzed and pertinent aspects plotted. Figures 5 and 6 illustrate typical plots for change in the trajectory angle and angle of attack versus impact angle of attack. These plots illustrate a linear relationship that exists between changes in trajectory angles and impact angles of attack for the range where the weapon survives penetration. Similar plots were developed for other combinations of the following critical parameters: initial velocity, initial trajectory angle, and concrete thickness. Each of these relationships is extremely dependent upon the weapon, medium, and terminal delivery parameters. Thus, SAMPLL calculations were run for representative impact conditions and input into a data structure in SLAVE3D. The code interpolates between the values in the data structure in determining changes in angle of attack and trajectory angle, given specific impact conditions.

SLAVE3D utilizes SAMPLL results to predict the change in the trajectory of a weapon as it travels through a target. Because SLAVE3D is a three-dimensional code, the SAMPLL results must be transformed to three dimensions. This is accomplished by sampling for the initial angle of attack and trajectory angle. The attack conditions are defined in terms of means and standard deviations. Given the sampled initial angle of attack ( $AOA_i$ ), a projected radius,  $R$ , is determined by:

$$R = \frac{L}{2} \tan(AOA_i)$$

where  $L$  is the weapon length. This procedure assumes that the angle of attack is likely to occur anywhere along the circumference of a circle with radius  $R$ . The exact location on that circumference is determined by uniform sampling techniques. This sampled location provides an in-plane and out-of-plane angle of attack. These values are then used to determine the in-plane and out-of-plane change in angle of attack and trajectory angle for weapons traveling through concrete. The out-of-plane change in trajectory is determined using an initial trajectory angle of  $90^\circ$ .

Associated with trajectory are two other important phenomena: weapon survivability and penetration. In addition to determining trajectory changes and ricochet, SLAVE3D also determines

weapon survivability at each concrete surface and examines the weapon's ability to penetrate the full extent along the path through a medium. Weapon survivability is determined in much the same manner as trajectory changes. SAMPLL results for various weapon-delivery-medium conditions were evaluated, algorithms developed, and incorporated into SLAVE3D.

For use in evaluating runway damage due to penetrating weapons, ARA has proposed to develop a statistical analysis tool that includes an accurate penetration algorithm and a simplified damage algorithm so that parametric studies can be performed. The resulting model will be a Monte Carlo-based code that will integrate SAMPLL with a simple breach algorithm developed by ARA.

### **CONCLUSIONS**

SAMPLL is a powerful development and analysis tool which can be used to predict penetration/perforation and failure of projectiles impacting hard surfaces. It can be applied in target vulnerability analysis, weapon design, weapon effectiveness studies, and numerous other areas of conventional weapons effects.

### **RECOMMENDATIONS FOR FUTURE WORK**

The applicability of SAMPLL should be expanded to include penetration into soft media (i.e., soil). This would entail a study of the soil wave phenomenon and approximating it sufficiently to be appropriate for an empirical model.

### **ACKNOWLEDGMENTS**

The most significant contributions others have made towards improving the SAMPLL code have come from the users of SAMPLL. The authors express gratitude to the Air Force Armament Laboratory (AFATL/SAA), Sandia National Laboratories, Lockheed, and NASA for funding, support, and suggestions received during the development and application of SAMPLL in numerous projects.

### **REFERENCES**

1. Young, C.W., The Development of Empirical Equations for Predicting Depth of an Earth Penetrating Projectile, SC-DR-67-60, Sandia National Laboratories, Albuquerque, NM, May 1967.
2. Young, C.W., Depth Predictions for Earth Penetrating Projectiles, Journal of Soil Mech Found SM3, May 1969.
3. Young, C.W., Empirical Equations for Predicting Penetration Performance in Layered Earth Materials for Complex Penetrator Configurations, SC-DR-72-0523, Sandia National Laboratories, Albuquerque, NM, Dec 1972.
4. Young, C.W., Penetration of Sea Ice by Air-Dropped Projectiles, SLA-74-0022, Sandia National Laboratories, Albuquerque, NM, Mar 1974.
5. Christiansen, B.K., Twenty-Five Years of Penetration Records at Sandia National Laboratories: PENTOB, A Relational Database, Sandia National Laboratories, Albuquerque, NM, to be published Mar 1989.
6. Young, C.W., and Young, E.R., Simplified Analytical Model of Penetration With Lateral Loading, SAND84-1635, Sandia National Laboratories, Albuquerque, NM, May 1985.
7. Young, C.W., Equations for Predicting Earth Penetration by Projectiles: An Update, SAND88-0013, Sandia National Laboratories, Albuquerque, NM, July 1988.

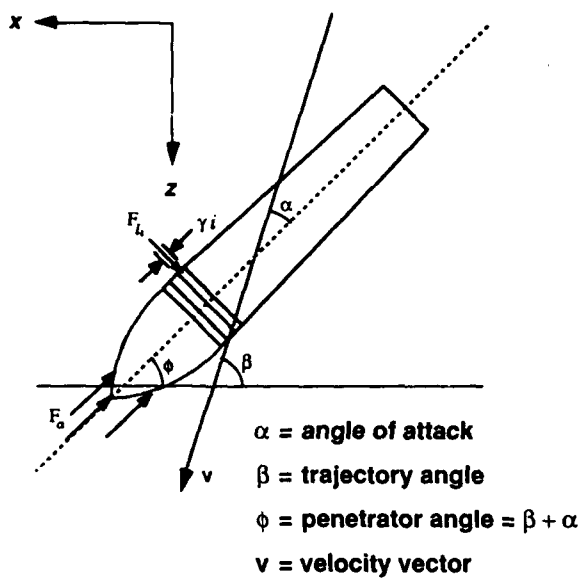


Figure 1. SAMPLL Conventions.

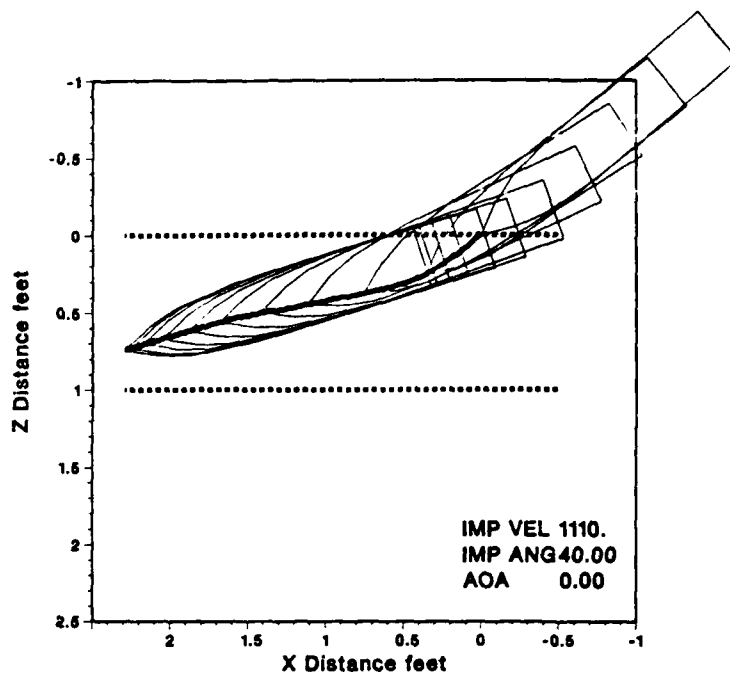


Figure 2. Penetration Simulation.

Figure 3. Lateral Acceleration vs. Time.

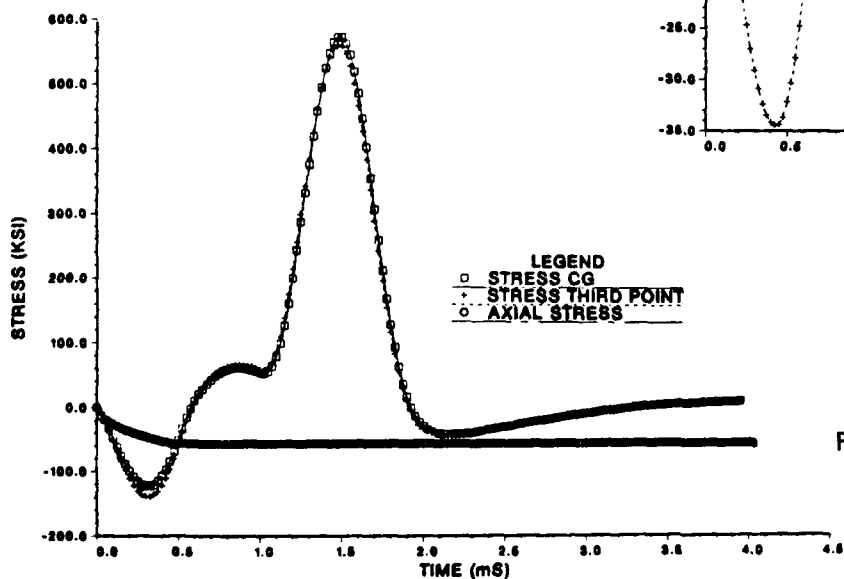
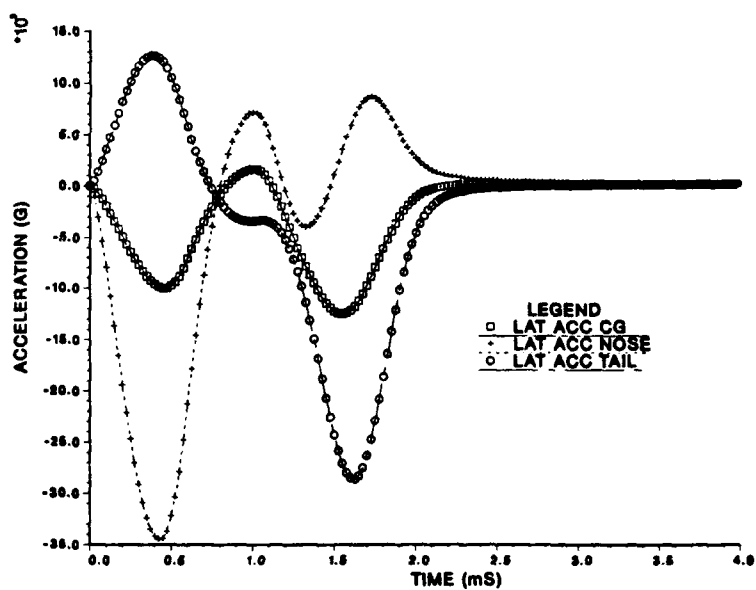


Figure 4. Stress vs. Time.

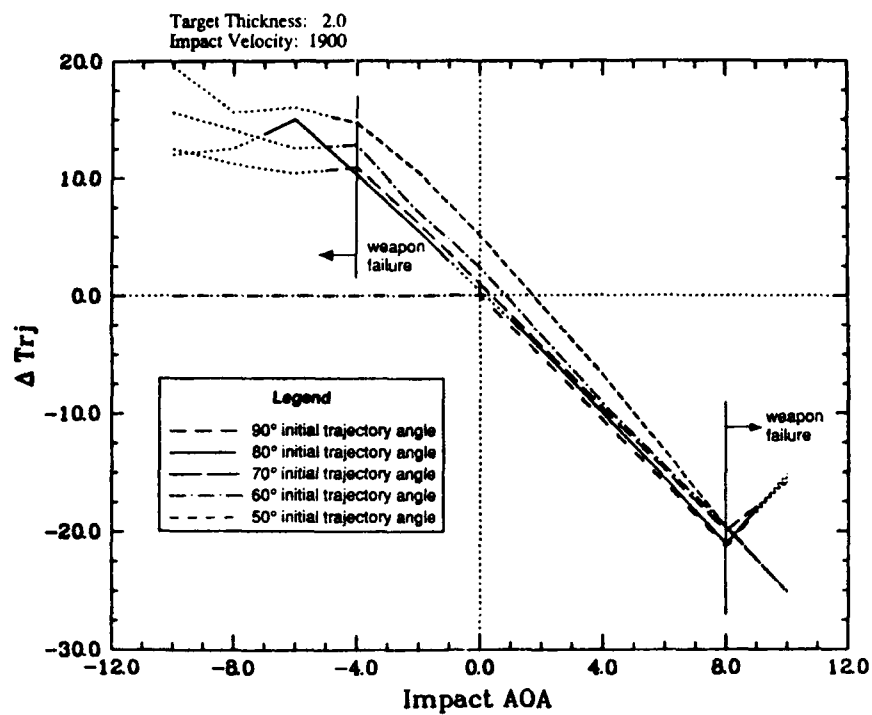


Figure 5. Change in Trajectory Angle.

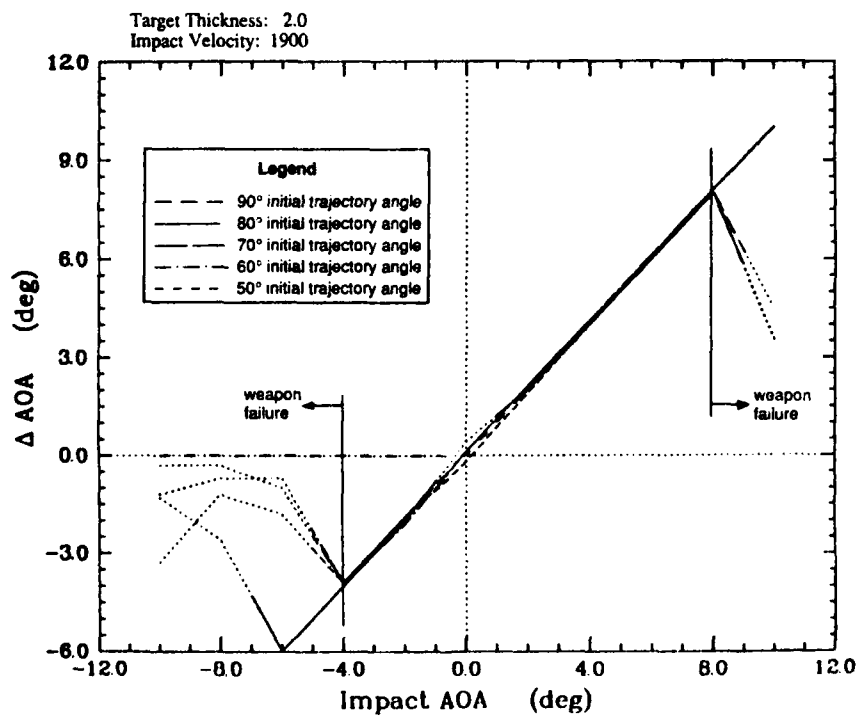


Figure 6. Change in Angle of Attack.

## MULTIPLE HITS: A NEW THREAT TO CONSIDER?

H.J. Hader

E. Basler & Partners, Consulting Engineers  
CH-8702 Zollikon-Zürich, Switzerland

### ABSTRACT

During the past two decades, precision-guided weapons have changed the course of conventional weapons significantly. In this paper, changes in the design of important protective structures as a result of the improved precision of smart bombs are discussed.

The accuracy of smart air-to-ground weapons not only increases the probability of direct hits, but also affects terminal ballistic parameters which may enhance effects of weapons. In particular, craters of different bombs may overlap increasing penetration drastically.

A simple model for estimating the cumulative effect of multiple hits is presented. Using this model, practical variations in the design and cost of protective reinforced concrete structures are shown for a range of air-to-ground weapons.

### 1. INTRODUCTION

For important defence installations a high level of protection against non-nuclear weapons is one of the major protective requirements. Air-to-ground attacks represent a major threat to such structures.

Since the number of air-to-ground weapons equipped with a precision guidance system has increased rapidly in recent years, their threat has to be considered for an also growing number of installations.

The precision of guided air-to-ground weapons leads to a high probability of direct hits. Large weapons such as heavy guided bombs may produce craters large enough that further weapons might hit the same crater.

The powerful effect of concentrated fire with multiple hits on a hard target has been demonstrated, e.g., when the Iraqi nuclear reactor Tammuz 1 at El-Tuwaitha was destroyed by a series of video-guided bombs <sup>1)</sup>.

The best protection against such attacks can be achieved with installations built into rock, but this type of protection is not always feasible. Therefore, we face the difficulty of adequately designing buried protective structures.

However, no data is available yet for the design of protective structures taking into account multiple hits of heavy precision-guided bombs. In order to get an idea of the cumulative effect of consecutive hits, a simple model has been created. This model provides an estimate of the most probable total crater depth. It is based on the known effects of single hits as well as the number and probable distribution of multiple hits.

---

1) TIME, June 22, 1981, pp. 24-40



## 2. GUIDANCE PARAMETERS RELEVANT FOR MULTIPLE HITS

The deviation of a precision-guided weapon from a target depends on different technical as well as human parameters. For the probable scatter of multiple hits it is important to distinguish between

1. possible errors in recognizing the target and aiming, and
2. the technical error of the weapon guidance system resulting in a scatter around a selected target point.

The first of these points is mainly affected by intelligence, camouflage, target location etc., which are not discussed in this paper. Once a target point has been selected and the necessary launch criteria are fulfilled, advanced guidance systems will guide the weapon with a system-inherent precision to the target point. The scatter relative to the theoretical target point is characterized by the so-called (circular error probable (CEP), i.e. the radius of a circle including 50 % of all hits.

Current guidance systems based on laser or video guidance achieve CEPs of about 2 m, whereby the size of the weapon is not relevant.

This scatter is very small compared to the size of most protective structures.

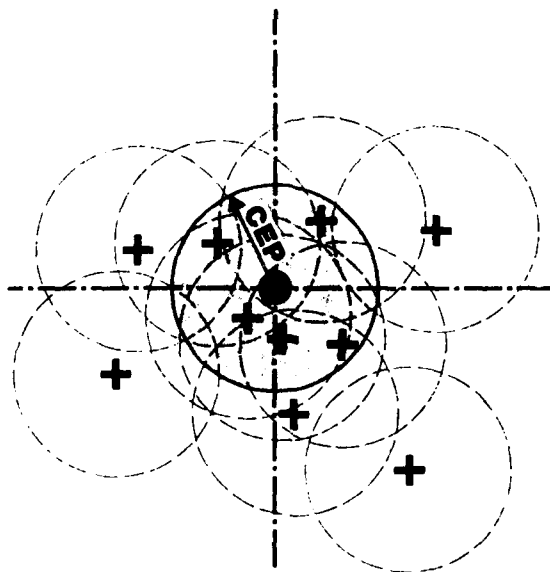


Figure 1: Expected statistical deviation of a number of guided bombs from their common aiming point.

Figure 1 shows a realistic example of the expected deviation of a number of guided bombs around their common aiming point.

The scatter of a series of consecutive weapons may be enlarged by various nuisance effects. With a target point marked by a stationary laser, an increase in the time interval between consecutive bombs dropped does not reduce accuracy. But an airborne laser might slowly move over the target, thereby stretching the CEP of multiple hits depending on the time interval between the release of the weapons. Furthermore, dust and smoke from a first hit may disturb the guidance of following weapons.

However, it seems feasible to overcome such problems, e.g. by suitable timing, target recognizers using excentrical markers, etc. For all further considerations it is assumed that multiple hits with a CEP comparable to that of a single hit may be achieved also in an actual air-to-ground attack.

## 3. COMBINED EFFECT OF MULTIPLE HITS

For a single hit, the maximum depth of destruction, by penetration and detonation of a weapon, is decisive, whereas the crater diameter is of secondary interest. In the question of multiple hits, the crater diameter and the extent of the surrounding crushed zone are also significant.

The penetration of a bomb striking a crater produced by a previous weapon is obviously increased due to (see Fig. 2):

- the open path from the former surface down to the apparent crater surface:
- very limited resistance of loose debris material.
- significantly reduced resistance on the path through the crushed zone.

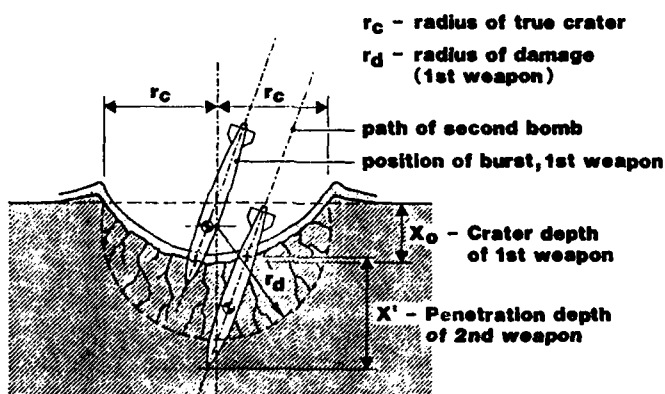


Figure 2: Penetration of a bomb in a crater of a previous weapon.

The enhanced penetration will lead to a higher degree of confinement and, thus, to larger crater dimensions.

Without having usable experimental data on combined effects of multiple hits, we have assumed a linear superposition of overlapping craters as a first approach. The shape of the crater is approximated by a parabolic function. After the first hit we assume, for all further hits with the same type of weapon, an increased crater depth of 1.5 times that of the first hit.

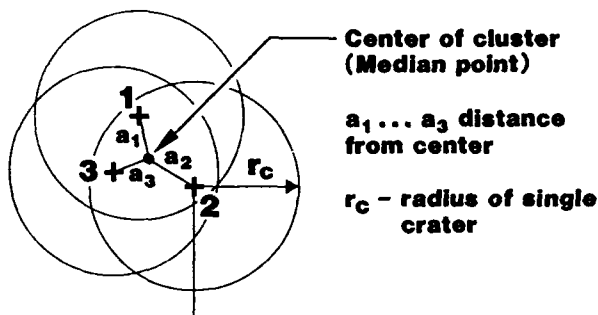


Figure 3: Bomb hits with centers in the junction of their craters.

For  $m$  hits with centers in the junction of their craters (Fig. 3), the cumulative crater depth can be estimated as follows:

$$\frac{x}{x_0} = 1.5 \left( m - \frac{a_1^2 + a_2^2 + \dots + a_m^2}{r_c^2} \right) - 0.5 \cdot \left( 1 - \frac{a_1^2}{r_c^2} \right) \quad (1)$$

- $x$  : depth of combined craters
- $x_0$  : depth of initial single crater
- $m$  : number of hits with centers in the junction of their craters
- $a$  : distance of each hit from the center of cluster
- $r_c$  : true radius of single crater

In this approach, the contribution of each overlapping crater to the crater depth in the median point of all hits is calculated. It may be used mainly for craters in concrete and solid rock, whereby the effects of the finite thickness are not taken into account. For combined craters deeper than about four times  $x_0$ , a reduced penetration due to large amounts of debris within the combined crater may be expected.

#### 4. MOST PROBABLE DEPTH OF CUMULATED CRATERS

The probability of overlapping multiple hits is a function of the number of weapons dropped, the CEP and the size of the crater. This function is somewhat complicated by the fact that we have to consider statistical distributions.

Assuming a normal distribution of hits around a common target point, we get a two-dimensional Gaussian probability distribution as shown in Figure 4. Since it is most likely to get cumulative effects in the center of the group of hits, we may estimate the portion of overlapping hits as follows:

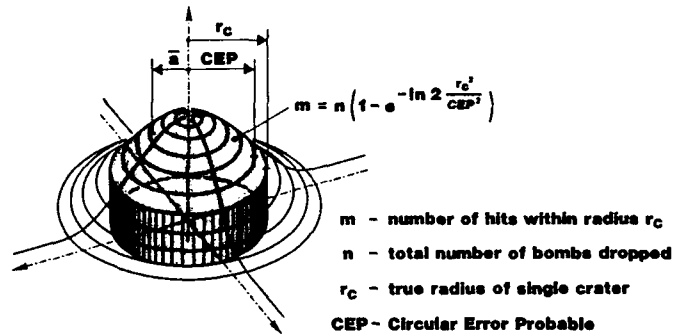


Figure 4: Probable portion of hits within radius  $r_c$  from cluster center.

$$m = n \left[ 1 - \exp \left( - \ln 2 \frac{r_c^2}{\text{CEP}^2} \right) \right] \quad (2)$$

- $m$  : number of hits within radius  $r_c$  from center of clusters
- $n$  : total number of bombs dropped
- $r_c$  : true radius of a single crater
- CEP: Circular Error Probable

In addition to the hits within the radius  $r_c$ , craters from other hits outside this range may overlap as well. However, this limited contribution to the overall probability of multiple hits is neglected in this approach.

In order to determine the cumulative crater depth by Eq. (1), the median distance of hits within the range of  $r = 0$  to  $r = r_c$  has to be estimated. Assuming the center of the cluster at  $r = 0$ ,  $\bar{a}$  can be calculated as follows (see Fig. 4):

$$\bar{a} = \left\{ - \frac{\text{CEP}^2}{\ln 2} \cdot \ln \left[ \frac{1}{2} \left( 1 + e^{-\ln 2 \frac{r_c^2}{\text{CEP}^2}} \right) \right] \right\}^{1/2} \quad (3)$$

Having defined the median distance of  $m$  hits as  $\bar{a}$ , we may rewrite Eq. (1):

$$\frac{x}{x_0} = (1.5 m - 0.5) \cdot \left[ 1 - \left( \frac{\bar{a}}{r_c} \right)^2 \right] \quad (4)$$

$x/x_0$  represents the statistically expected ratio of cumulative versus initial crater depth. In Figure 5 this function is plotted for craters half the size to twice the size of their CEP ( $0.5 < r_c/CEP < 2.0$ ).

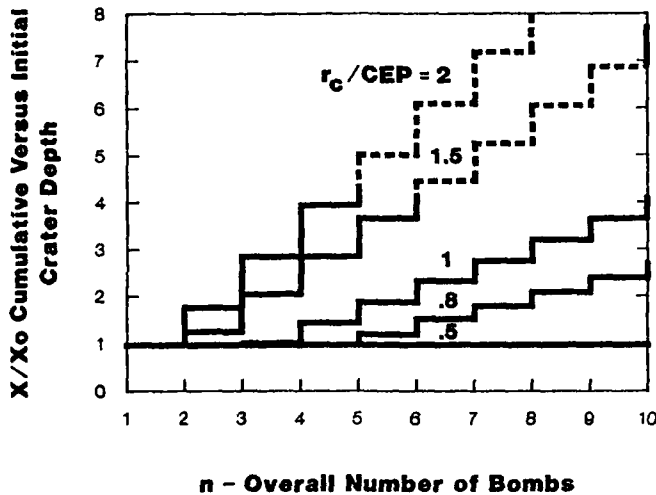


Figure 5: Statistically expected ratio of cumulative versus initial crater depth as a function of the number of bombs, crater radius and CEP.

As can be seen in Fig. 5, no enhanced crater depth should be expected from up to 10 bombs if their crater radius is less than half their CEP ( $r_c/CEP < 0.5$ ).

Perhaps most interesting is the step function for weapons producing craters with the same radius as their CEP ( $r_c/CEP = 1$ ). This case corresponds, e.g., to common laser-guided 1000-kg SAP-bombs which produce craters with radii of about 2.5 m in concrete layers and have an assumed CEP of 2.5 m. This means 50 % of all bombs are expected to strike within the CEP with their craters overlapping the target point.

For example, from a total of four bombs two will most probably overlap partially, producing an enhanced crater depth of about 1.5 times that of a single crater. For a number of 8 hits, we get a cumulative crater depth which is more than 3 times the initial depth.

The results for  $r_c/CEP = 1.5$  and 2.0 demonstrate, as extremes, the powerful effect of multiple hits in combination with large calibers and high precision. If precision is improved by a factor two, the number of weapons required for a given crater depth is reduced by a factor of three. This means the payload of weapons required for a given mission would also be reduced by that factor.

For values  $x/x_0 > 4$  the curves have been dashed since the limiting effect of large amounts of debris in combined craters has not been considered in this approach.

## 5. CONSEQUENCES FOR PROTECTIVE STRUCTURES

For important military structures which are to withstand air-to-ground attacks, various types of burster layers and slabs are used. In order to demonstrate consequences of the possible threats from multiple hits in terms of cost, a simple reinforced concrete structure is looked at.

In Figure 6, four different protection levels are compared. Levels 1 and 2 include single hits by bombs of the 250-kg respectively 1000-kg class. Levels 3 and 4 correspond to multiple hits from a total of 4 respectively 8 1000-kg SAP bombs. The CEP is assumed approximately equal to the crater size. This range of weapons is by far not complete. But it also covers a number of other air-to-ground bombs and missiles not discussed here.

The thickness of protective structural elements includes allowances for standard deviation of data and the high-slenderness of bombs. Cost estimates are based on a buried two-storey installation with a floor area of  $2 \times 5000 \text{ m}^2$ . Basic costs for this installation including building and technical supply installations, but no protection against direct hits, have been estimated at 20 million SFrs..

The extra cost for protection against single and multiple direct bomb hits show a significant increase for each level. Since funds for military installations are short everywhere, the question whether or not such enhanced threats must be considered becomes very important.

In this context, it has to be kept in mind that

- an air-to-ground attack is typically carried out by more than one aircraft, each aircraft carrying several bombs, and
- not only new bombs, but also most of the existing bombs may be equipped with guidance units at limited cost.

Due to the rapidly growing number of guided bombs, less important structures may also become a target for such weapons. However, the cost of adequate protection will require careful selection.

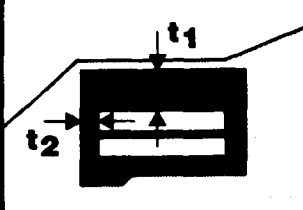
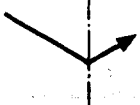

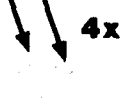
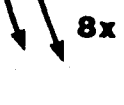
|   |   |   |   |   |
|---|---|---|---|---|
|  | <b>1</b><br><b>GP 250 kg</b><br> | <b>2</b><br><b>SAP 1000 kg</b><br> | <b>3</b><br><b>SAP 1000 kg</b><br> | <b>4</b><br><b>SAP 1000 kg</b><br> |
| <b>Impact velocity</b>  | <b>&lt;250 m/s</b>  | <b>&lt;400 m/s</b>  | <b>&lt;400 m/s</b>  | <b>&lt;400 m/s</b>  |
| <b>Angle of obliquity</b>   | <b>&gt;60°</b>  | <b>20°</b>  | <b>20°</b>  | <b>20°</b>  |
| <b>Precision</b>  | <b><math>r_c/CEP &lt; 0.5</math></b><br>→ single hit  | <b><math>r_c/CEP &lt; 0.5</math></b><br>→ single hit  | <b><math>r_c/CEP \sim 1</math></b><br>→ multiple hit  | <b><math>r_c/CEP \sim 1</math></b><br>→ multiple hit  |
| <b>Slab</b>   | <b>1.6 m</b>  | <b>3.2 m</b>  | <b>4.3 m</b>  | <b>7.5 m</b>  |
| <b>Wall</b>   | <b>2.2 m</b>  | <b>3.5 m</b>  | <b>3.5 m</b>  | <b>3.5 m</b>  |
| <b>Cost for extra protection per m<sup>2</sup> net area</b>                       | <b>1000 sFr.</b>  | <b>2200 sFr.</b>  | <b>2600 sFr.</b>  | <b>3600 sFr.</b>  |
| <b>in % of project</b>  | <b>25 %</b>   | <b>55 %</b>   | <b>65 %</b>   | <b>90 %</b>   |

Figure 6: Approximate dimensions and extra costs for protection of r.c. structure for different protection levels.

## 6. CONCLUSIONS

For important installations required to withstand direct bomb hits, it is imperative to take into account the possibility of multiple hits. The use of precision-guidance can drastically increase the effective fighting capacity of an aircraft.

The cumulative effects of overlapping multiple hits can already be achieved with existing technology. Thus, it could turn out to be more efficient to use multiple bombs against very hard targets rather than as a single large special weapon.

This trend requires new solutions for the protection of important buried installations. Examples demonstrate that even small changes in the assumed threat may lead to considerable extra cost.

Data for predicting the interaction of consecutive hits with structures is still rather crude and deserves further investigation. Above all, the penetration of weapons into the crushed zone below craters in rock and reinforced concrete will have to be investigated in detail.

Furthermore, all parameters affecting the crater width and limiting the removal of protective slabs are to be considered. Testing will become more difficult since the penetration and detonation effects may not be separated completely.

Above all, for an adequate design of protective installations against future threats including multiple hits, the procurement of better data is absolutely necessary.

## Acknowledgement:

The author thanks his colleagues J.P. Halbritter and M. Kruse for their kind support in the preparation of this paper.

Protective Layers for Multiple Hits and Penetrators  
Requirements and chances

Werner Heierli and Max Gloor

Heierli Consulting Engineers Inc.  
CH-8033 Zurich, Switzerland

Abstract

Modern guidance systems allow to achieve direct hits on important targets. With regard to economics, it has to be anticipated that modern bombs will differ from the "old iron bombs": For hardened facilities, penetrator bombs (or multiple hits by SAP bombs) will be used. Cost considerations show that facilities protected by thick layers of unreinforced concrete and mined facilities in rock will be the answer to the threat. Geologic conditions play a major role in the expense due to the problems of side- and under-shooting.

1. Introduction

History shows us, over a long time, an uninterrupted need for protected facilities. Even countries whose strategy primarily relies on mobile forces cannot dispense with hardened structures housing important functions like C<sub>3</sub>I<sup>1)</sup>, logistics or counterattack facilities.

This paper deals with the protection of important military and other facilities against direct hits by conventional weapons.

The aspect of protective layers only is treated here, not the problem of entrances, doors, air intakes, embrasures, communication lines and other connections to the outside.

2. Threat

In the nuclear field, the threat has developed, over the past 25 years, from large yield but inaccurate weapon systems to accurate, much smaller, highly specialized, low collateral damage systems.

In the conventional field, the Second World War has seen the so-called "old-iron-bombs" used in large numbers to score one or a few direct hits on important facilities. Nowadays, attacks against such facilities would be performed with very few but accurate weapons. If we roughly compare the economics of the earlier and the modern types of attack, we can see the following three characteristics:

- The number of sorties to achieve a direct hit has been greatly reduced, but the cost per sortie - which also includes the cost of the aircraft multiplied by the probability of its loss - has increased manyfold.
- The cost for the guidance system has increased.
- The cost for one bomb may have remained more or less constant, but due to the drastic decrease in numbers, the cost of all bombs used to score one or a few direct hits has greatly diminished.

Since "economics" is the name of the game - both for attack and defence/hardening - the following trends become evident:

- The cost of aircraft, due to the expense for survivability in a modern air defense environment, will probably increase rather than decrease.
- The cost of guidance systems will presumably stay constant and possibly decrease, due to the fast expanding world market for electronics in general and for guidance systems in particular, and due to the participation of the Newly Industrialized Countries in this special market. - The cost for standoff delivery may stay more or less constant.

1) Command, Control, Communications, Intelligence

- The cost per bomb (or missile warhead) will remain the same if the "old iron bomb technology" is used, or increase if modern warheads are developed. Still, overall costs for all bombs to be procured for a given task will decrease compared to the Second World War.

In comparison, the cost per sortie will be the largest part, the cost of the guidance (and standoff delivery) system may remain roughly constant and the cost of the necessary bombs - even of sophisticated bombs - will probably be the smallest part of the total cost.

The conclusions which are or will be drawn from these economic considerations are doubtlessly the following:

- To primarily minimize the number of sorties - or, if surface-to-surface missiles are included - the number of weapon carriers. This also means that the unit weight per effective hit should be minimized and the number of independently targeted warheads maximized.
- To further improve guidance systems, especially those using target coordinates.
- To maximize the effectiveness of each bomb or missile warhead, which means that:
  - . The guidance system should not only provide the highest possible direct hit probability under many different conditions of attack, but also an angle of attack close to perpendicular on the protective layer.
  - . The terminal velocity should be high, e.g. by using terminal acceleration (booster).
  - . The bomb or missile should be optimized, in order to achieve penetration into the hardened facility and to have the warhead charge detonate in the facility, whereby blast damage as well as carbon monoxide contamination (which is often unduly disregarded) would create assured large damage or total loss.

From these considerations it appears that the threat to important and protected facilities, in a relatively near future, can be characterized as follows:

- Important targets will be exposed to direct hits, possibly even to hits on small selected spots.
- The modern bombs or warheads will be highly effective penetrating weapons, with impact velocities of 250 - 400 m/s without booster (and 400 - 600 m/s and more with boosters), and with impact angles close to optimum. The bomb weights will be in the order of 500 - 1000 kg (and probably reach 2000 kg or more) with about 90% of the weight in metal (high strength alloys such as special steel, tungsten carbide or depleted uranium) and only 10% of explosives at the tail end.

- "Old iron bombs" may still be used, as long as there are plenty of targets that do not justify the use of better weapons; however, the merciless laws of economics will not allow their employment for well hardened targets. Multiple hits using normal SAP bombs, as described in the paper by H. Hader, may well be an alternative for the very near future, or for special cases like targets with uncemented layers of rock which can be blasted away by a first bomb in order to expose the facility to the next warhead. But it is believed that - in the future - targets will be destroyed by one warhead (per point of attack), not by two ore more. Long penetration projectiles can be viewed as a succession of short bombs, ore attached to the other, with the last bomb carrying the charge.

### 3. Protective layers

#### 3.1. Materials considerations

In view of the threat forecast, modern warheads should ideally not be allowed to penetrate into the protective layer at all, i.e. ricochet. Ricochets, however, can be produced at shallow angles of attack only. Modern guidance systems allow bombs to come in at an angle not far from perpendicular - except for certain special cases. High strength warheads at high terminal velocities do not ricochet, unless impacting at very shallow angles.

For economic reasons, it is clear that the warhead material will always be considerably superior in strength to the protective layer material. The warhead has a mass which is probably four or five orders of magnitude less than the mass of a specific protective layer. The hardening engineer, therefore, cannot "win the race" by using a protective material into which modern bombs cannot penetrate, or just a little. This may only be achieved for GP bombs or some "soft" SAP bombs, but not for suitable SAP bombs or penetrators.

The "strongest" material to be used in a protective layer may be armor steel or normal steel. The cost of (armor) steel, however, probably excludes its general use for protected facilities with the exception of small areas, like doors or embrasures. It should be borne in mind that steel armor, apart from the cost of procurement, requires a considerable additional expense for joining the plates together and for fastening them to the structure. The cost of (normal) steel plates may be in the order of 800 \$ for a thickness of 0.1 m (or 8'000 \$ for 1 m) per m<sup>2</sup>, which is about 80 times that of unreinforced concrete. - To give an idea of the thickness required for armor steel, it may be mentioned that, in 1943, the battleship "Roma" was sunk by one AP bomb of the type PC 1400 perforating 150 mm of armor steel and fully detonating inside the ship afterwards<sup>1)</sup>. (There was no concrete under the armor plate, of course, but the bomb was an "old iron bomb".)

1) Marquardt, Die Planung und Entwicklung von Bomben für die deutsche Luftwaffe (1925-1945) p.69/248

The second material in line would be a kind of rock masonry, made from very large blocks cut out from solid bedrock. Such blocks could be about 2 m x 2 m x 2 m or 20 tons (just about one block per truck). The mass of a block would certainly be many times the mass of any bomb. The jointing and fastening problems would be minor, thanks to the large inertia and the interlocking of the huge blocks. Ref (2) shows penetration depths of PC 1400 bombs about 1 m into solid granite bedrock (not layers of blocks). This means that, while blocks of rock will certainly reduce the required thickness of protective layers, they do not avoid substantial penetration into them. In view of the price of rock masonry, which we estimate to be about 800 US\$ per m<sup>3</sup>, compared to about 100 US\$ per m<sup>3</sup> of unreinforced concrete, layers of large blocks are probably uneconomical except for certain special applications where weight or space are governing factors, or where the above cost assumptions do not apply.

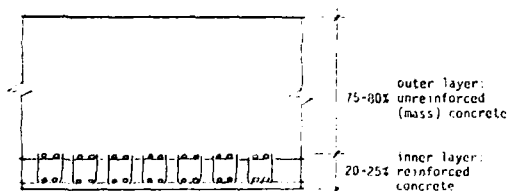
The third material to be investigated would be layers of very heavily reinforced concrete. It is known that "normal" percentages of reinforcement do not appreciably reduce bomb penetration or cratering effects. Very large percentages could do so. It is believed that a possible solution could be to install used rails in the outer layers of the concrete. No data on the design of this type are available to the authors. It is thought, however, that such highly reinforced concrete layers may be effective against some SAP bombs, but probably not against harder projectiles like AP bombs or penetrators, since these would, upon penetration, just push the reinforcement aside into the concrete or blow the concrete through the interspaces between the reinforcement bars or rails. Again, it is probable that economy will prohibit the use of this scheme on a large scale. - The next chapter will deal with the application of concrete.

### 3.2. Mass concrete

Apart from in-situ rock in mined protective facilities, mass concrete is probably the most economical material to protect against penetration (and explosion). This statement may have to be checked in important practical applications, by comparing the above mentioned alternatives to concrete.

The order of magnitude of thickness necessary to protect important facilities against direct hits of bombs or missiles is roughly 4 - 10 m. It is therefore logical to distinguish (Fig. 1)

Fig. 1: Roof Slab section



(2) Marquardt, see above, p. 49/217

- a thick outer layer, essentially unreinforced, designed to stop the projectile, and
- an inner layer, reinforced, which prevents damage effects of detonations or of the penetrator head at the shelter side of the layer.

This latter, inner layer may be comparatively thin, some 1 - 2 m or 20 to 25% of the entire thickness. In the case of arched inside faces, the thickness of this layer may be even considerably smaller. Interestingly, (3) shows, that the protective thickness necessary for tallboy bombs (5.2 ton bombs of the Allied in the Second World War) was considerably smaller for arched or vaulted inside faces, as the literature excerpt at the end of the paper shows (appendix). Vaults, therefore, should be considered wherever possible; they were even standard for First World War fortifications (often unreinforced).

The major volume of concrete, 80% or more, is the unreinforced mass concrete of the outer layer. Since - as already stated - economics is one of the prime laws governing defense preparations, it pays to investigate the various possibilities for economic procurement and placement of mass concrete. Civilian uses, especially in dams and roads/yards, have helped develop the concept of "Roller Compacted Concrete" or RCC (4). RCC is a no-slump concrete whose water content is not such that it can be vibrated by an internal vibrator, but which is at "Proctor Optimum" like that of a gravelly base course of a road. RCC is spread by bulldozers and compacted by vibratory rollers. The following are the main differences between "normal" concrete and RCC:

- Lower water content, meaning higher strength and less shrinkage at the same cement dosage.
- Higher rates of placement, fully mechanized.
- Bigger maximum aggregate size, if suitable mixing equipment is available, meaning less cement for the same strength.

The use of RCC should be considered at an early stage, since the design and the details may be different in this case from the case of normal concrete application.

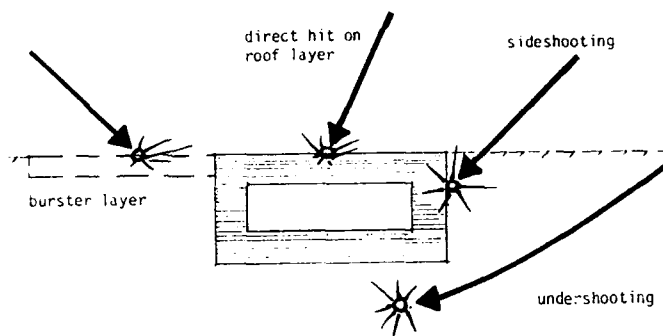
(3) Constructions Spéciales, by Roland Hautefeuille, 1985 (18, rue de Pré au Clercs, 75007 Paris)

(4) American Concrete Institute, Detroit, (ACI), ACI Materials Journal, Sept-Oct 1988, Roller Compacted Concrete, pp. 400-477

### 3.3. Taking advantage of geology

In the absence of rock, a shelter for an important facility will not only have to be protected against direct hits on the roof slab, but also against bombs aimed at the sides or the floor slab. It is proposed to term such hits against the sides as "side shooting", analogous to "undershooting" (for the floor).

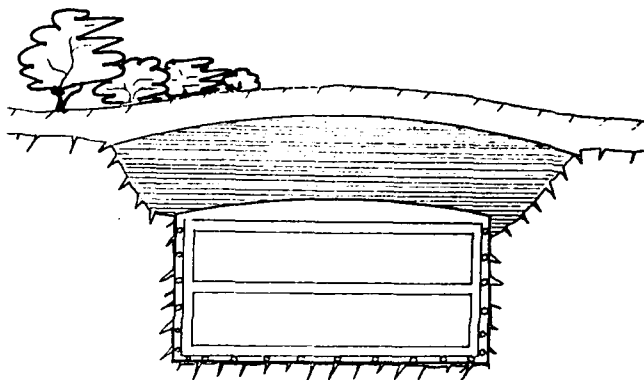
Fig. 2: Direct hits on protected facility



Side- and undershooting are no less probable for facilities of the type shown than direct hits aimed at the roof slab, unless proper countermeasures are taken. If a direct hit against the roof slab can be achieved, it can also be achieved against the side walls or the floor slab, in the manner shown in fig. 2. It should even be noted that side- and undershooting allow the use of GP or SAP bombs which easily penetrate into considerable layers of soil or even rock muck. The detonation of their charges occur fully tamped, which means a factor of 7 in efficiency (charge-wise) compared to an explosion in free air. Calculations for massive shelters have shown that not only the necessary concrete thicknesses become very large, but also that the shock caused by the explosion can easily be so high as to jeopardize humans in the shelter. This leads to extensive countermeasures to avoid side- and undershooting, such as burster layers covering the area outside the structure (in RCC, preferably). These burster layers or other measures, due to the large area to cover, can become very expensive.

For this reason, it is highly desirable to use the help of bedrock if such sites can be found at all. If bedrock is close to the surface, very economic designs will result, such as shown in figure 3, for the case of competent bedrock.

Fig. 3: Protected facility in rock (cut-and-cover)



It is easily seen that the volume of concrete is far less in figure 3 than in figure 2, only due to the presence of shallow bedrock. The excavation in rock, using modern scraping or mining (blasting) techniques, is relatively unexpensive. The lower the bedrock, the less the share it can take of the burden of protection. But even placing shelters just on rock will considerably reduce the volume of concrete, as shown in figure 4. Often, it may be more economic to found a shelter on rock - even if this leads to a deeper structure - than to have to resort to other precautions against undershooting.

Fig. 4: Protected facility on rock

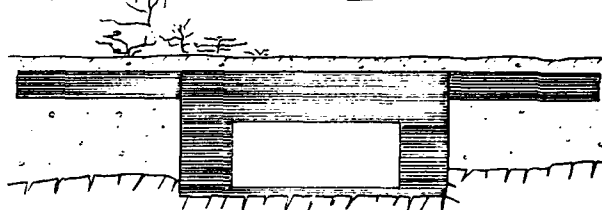


Fig. 5 shows a protected facility on rock, above-ground. This is an alternative worthwhile to investigate, since the cost of excavation is small and the side walls are not exposed to tamped explosions (but to penetrating bombs). It should be mentioned that most of the large German Civil Defense shelters in World War II were of this type ("Hochbunker"), not belowground.

The purpose of this chapter is to show that there is a continuous transition from a "rock facility" to a "non-rock facility". Facilities completely in rock - using horizontal or vertical (shaft) access - will very often be the best choice. But if a mined facility is not feasible, good use may still be made of the rock for avoiding the often neglected, but highly dangerous threats of side- and undershooting. Undershooting, by the way, was also a preferred way of bomb-attacking naval vessels. Special anti-ricochett warheads were developed to "penetrate into the water". The philosophy - to produce a tamped explosion - was exactly the same.



Fig. 5: Protected facility on rock (above ground)



#### 4. Summary and conclusions

In the future, important protected facilities will face the threat of direct hits, including side- and undershooting. Due to the cost of the attacking aircraft or of the carrier missile, and of the guiding system, it is uneconomical to use "old iron bombs" against the top protective layers, unless the facility has a low degree of protection. The threat of the future will be the penetration bomb or missile warhead, which will be able to overcome considerable thicknesses of concrete due to:

- a high L/D ratio,
- a sturdy weapon design with a high strength alloy body carrying only a small charge at the tail end, and
- a "void fuze" for detonation of this charge in the facility, causing maximum damage and widespread CO-contamination inside the shelter.

The strength of the projectile and the suitable angle of impact deny the defender the possibility of using protective materials that will produce ricochets, deform or break up the bomb or damage the fuze. The strength of protection layers will always be much inferior to the strength of the penetrator alloy.

In cases where good rock is available, rock cavities with horizontal or shaft access are often the best solution. Where this is not the case, mass concrete seems to be the most economic answer. Modern methods of economic concreting like Roller Compacted Concrete allow good quality concrete at a considerably reduced price. Side- or undershooting by GP or SAP bombs with considerable explosive charges have to be avoided by suitable burster layers or diaphragm walls or, more economically - if bedrock is shallow - by placing the facility on or into the rock formation.

Appendix from Ref. (3)

Required concrete thicknesses to withstand the "Tallboy (M)" bomb

| Type of roof slab/vault      | Span<br>m (!) | Thickness in m                 |                      |
|------------------------------|---------------|--------------------------------|----------------------|
|                              |               | For to-<br>tal pro-<br>tection | For slight<br>damage |
| horizontal (plane) slab < 12 |               | 7.50                           | 6.50                 |
| horizontal (plane) slab > 25 |               | 7.20                           | 6.20                 |
| vault (arched) > 60          |               | 6.75                           | 5.75                 |
| vault (arched) > 90          |               | 6.50                           | 5.50                 |
| dome (cupola) > 60           |               | 6.50                           | 5.50                 |
| dome (cupola) > 100          |               | 6.00                           | 5.00                 |

## Implications of Centrifuge Penetration Tests for Use of Young's Equation

Teresa Taylor<sup>1</sup> and Richard J. Fragasz<sup>2</sup>

<sup>1</sup>Asst. Prof., Civil Eng., University of Missouri-Columbia/Kansas City

<sup>2</sup>Asst. Prof. & Head, Geotechnical and Transportation Eng. Section,  
Dept. of Civil & Environmental Eng., Washington State University

### ABSTRACT

Results from 1-g penetration tests and from centrifuge penetration tests performed at higher g levels were compared to depth predictions from Young's empirical equation. The penetration tests were conducted in carefully prepared sand targets, which allowed better analysis of the relationship between penetration depth and target properties than has been typical in development of existing empirical equations. Based on the test results, which were well bracketed by the bounds predicted by Young's equation, penetration depth was determined to be a function of the soil type and density. A dimensionless term was developed which included absolute and relative soil densities and allowed a single function to be defined for a given soil type. In addition, an arbitrary mass scaling factor used in Young's equation was eliminated in the power law depth prediction equations developed in this research.

### INTRODUCTION

Many penetration equations have been developed since research first began on the subject in the 18th century. Perhaps the most widely used equation today is Young's equation, developed during the 1960's and 70's. Young used the data from large-scale penetration tests to develop his empirical relationship, discussed in detail below. Like many formulas based on empirical methods, there is considerable scatter in the data base used by Young, and his method can lead to considerable error in predicting penetration depth. One of the main difficulties in the use of Young's equation is the need to select a soil penetrability index based only on a qualitative description of the soil of interest, and on experience in using the equation.

The authors have recently completed a series of centrifuge penetration tests in which spherical projectiles were shot into uniform deposits of granular soil. Because of the size of the experiments, very tight control on the density and uniformity of the target soil was possible. The results of these tests clearly show the validity of centrifuge modeling of penetration into granular material, and add significantly to the data base on penetration in sands. Based on these tests, several observations were made with respect to Young's

equation which suggest that significant improvement might be made in its accuracy. A brief description of the testing program and general test results are presented in this paper, followed by the specific applications of the results to the use of Young's equation.

### YOUNG'S EQUATION

The results of over 500 large-scale penetration tests conducted by the Sandia Corporation have been analyzed by Young (1967, 1969, 1970, 1972, 1978). His best-fit empirical relationship for these data has been expressed both in the form of a nomogram or ballistic phase diagram (Colp, 1968; Melzer, 1970), and in equation form. For velocities less than 61 m/s, his equation is:

$$P = 2KSN(W/A)^{0.5} \ln(2V^2 \times 10^{-4}) \quad (1)$$

where

P = penetration depth (cm)  
K = mass scaling factor (dimensionless, used only for masses less than 27kg)  
S = soil constant (dimensionless)  
N = nose shape factor (dimensionless)  
W = projectile mass (kg)  
A = projectile cross-sectional area (m<sup>2</sup>)  
V = velocity (m/s)

For velocities greater than or equal to 61 m/s:

$$P = 0.117KSN(W/A)^{0.5}(V-30.5) \quad (2)$$

Values for the dimensionless terms were determined by replicating tests holding all parameters constant except the dimensionless term of interest.

There are several aspects of the use of Young's equation which are questionable. First, the equation is not dimensionally correct. This leads to the assumption that potentially important parameters may be missing. Second, in order to compensate for reduced penetration depths observed for small projectile masses, Young uses the mass scaling factor, K, for projectiles less than approximately 27 kg. There is no theoretical basis for use of the mass scaling factor (Young, 1969); therefore, its required inclusion reinforces the concern that the equation does not account for all necessary parameters.

A third concern is the exponent used with the mass to area ratio term. Young initially used a linear correlation to describe the relationship between penetration depth and projectile mass to area ratio (Young, 1967). To provide better correlation with additional large-scale test data that became available, this linear relationship was subsequently revised and a mass to area ratio exponent of 0.5 was introduced. Because of the differences in target material between the initial test data used to justify a linear relationship and subsequent data which led to a power relationship, it is possible that the actual relationship between mass to area ratio and penetration depth varies with target material properties.

Finally, the selection of the soil penetrability index,  $S$ , is very qualitative. No actual material properties such as density, strength or stiffness are used, and information on water table is not incorporated. The only guidelines are a brief written description of a limited number of soil types with a range of  $S$  values for each. The lack of certainty involved in both the establishment and selection of the appropriate  $S$  value for a given soil is generally recognized as the most significant drawback to the use of Young's equation (Young, 1969; True, 1975; Aitken, et al., 1976).

The values suggested by Young for  $S$  range from 1 for frozen clay or silt, to 50 for very soft clays and loose sandy topsoil. According to Young (1969) and Halada (1975), appropriate selection of this constant requires experience in earth penetration. This limitation was also pointed out by Aitkin et al. (1976), along with the disadvantage that penetration tests are needed in all target materials of interest to determine the proper  $S$  values.

With accurate selection of  $S$ , the equation is claimed to provide penetration depth predictions within  $\pm 20\%$  of actual depths obtained in full-scale tests (Colp, 1968; Young, 1969). A pretest depth prediction reported by Hadala (1975) found a 27% error in maximum penetration prediction. True (1975) determined that Young's equation typically underpredicted for soft soils, based on his investigations for saturated silts and clays. True attributed this apparent discrepancy to the fact that most of the penetration test data on which Young's equation is based were collected from tests conducted in relatively hard soils and rocks.

#### DESCRIPTION OF CENTRIFUGE TESTS

A series of approximately 80 centrifuge model tests were conducted during 1987 and 1988 using the centrifuge facility at the Air Force Engineering and Services Center, Tyndall Air Force Base. An additional 60 1-g tests were also conducted for comparison purposes. The major objective of the testing program was to determine if centrifuge modeling is an appropriate testing technique for projectile penetration in granular soils. A dimensional analysis conducted before the centrifuge testing began showed that gravity should be scaled, due to the self-weight dependency of soil strength. However, the dimensional analysis could not be used to determine the relative importance of scaling gravity compared to other test parameters.

The target material was clean quartz sand (either commercially obtained Ottawa sand or local beach sand) with various gradations. A small series of tests was performed on a mixture of Ottawa and ASTM sands. The sand sample was prepared by pluviating the dry sand into a 457 mm (18 inch) diameter aluminum bucket. The pluviating process and equipment, described by Taylor et al., 1988, produced uniform, reproducible samples with maximum density variation within and between samples of  $0.01 \text{ Mg/m}^3$ . Both very loose and very dense samples were produced.

Spherical brass projectiles were fired into the soil at velocities of approximately 300 m/s, using a Thompson Contender pistol. The projectile diameters were 56.9, 7.82, 9.09, and 10.92 mm, corresponding to 22, 30, 38 and 44 caliber. Penetration depth was measured to  $\pm 1$  mm and reproducibility of the data was excellent. Further details of the testing program are given by Taylor (1988).

#### SUMMARY OF GENERAL TEST RESULTS

Analysis of the centrifuge and 1-g test data resulted in the following general conclusions:

- 1) Reproducible projectile penetration tests can be conducted at elevated g-level in a centrifuge.
- 2) Projectile penetration into clean, dry sand at elevated g-level is significantly less than at one gravity, all other test parameters held constant.
- 3) Soil density significantly influences penetration depth in clean, dry sands.
- 4) Modeling-of-models test results support the hypothesis that centrifuge tests can be used to predict full-scale penetration behavior.

#### COMPARISON OF TEST RESULTS TO PREDICTIONS USING YOUNG'S EQUATION

The 1-g and centrifuge test results from this study provide important data relevant to each of the problems related to Young's equation that were previously discussed. The centrifuge test results fall within the range of penetration depths predicted by Young's equation using the range of  $S$  values applicable for most sands ( $S = 2$  to 8). This can be seen in Fig. 1., which is a plot of all centrifuge test data from this study along with the predicted values based on Young's equation for  $S = 2$  and  $S = 8$ . However, closer examination of Fig. 1 shows that the penetration depths for each soil type are increasing at a faster rate than the two curves showing Young's equation predictions. This implies an exponent for the mass to area ratio larger than 0.5. Another way to illustrate this is to examine the back calculated  $S$  values (for a single soil target) required to make the equation prediction equal the measured penetration depth. Since the target material is the same for each test, one would expect only random variation about a mean value. However, in Fig. 2, it can be seen that there is a definite increase in  $S$  with increasing mass to area

ratio. In other words, in order to make the test data fit Young's equation, the S value would have to be a function of the projectile size, an unlikely situation.

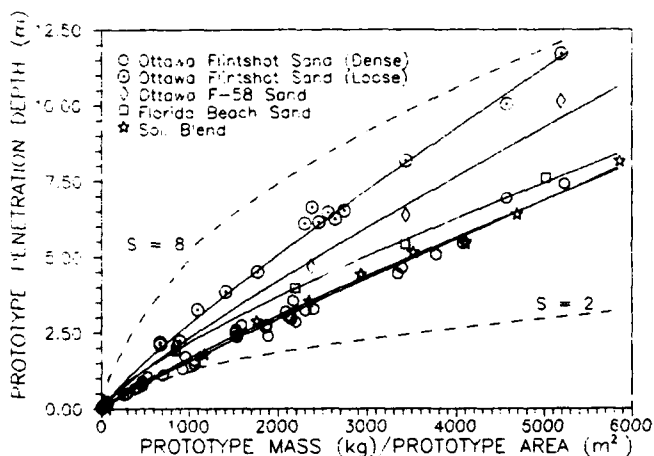


Fig. 1 Prototype Mass to Area ratio vs. Prototype Penetration Depth, with Young's equation results superimposed

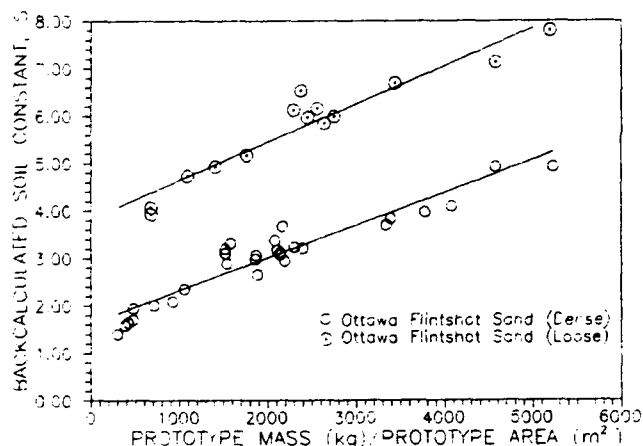


Fig. 2 Prototype Mass to Area ratio vs. Backcalculated S values from Young's equation, for Ottawa Flintshot sand

To investigate these questions of exponent and S value, a regression analysis was performed on each data set. Figs. 3 and 4 present the results for dense Ottawa Flintshot sand. The best fit equation for these test data is:

$$P = 0.00282 (M/A)^{0.915} \quad (3)$$

where P is the prototype penetration depth in meters. The correlation coefficient for this equation is 0.998. It is significant to note that both 1-g and centrifuge test data fit this equation with remarkable accuracy and without the use of a mass scaling factor! Very good fit to a power equation is

also found for loose Ottawa Flintshot sand. In this case, however, the coefficient and exponents on the M/A term are 0.00634 and 0.880, respectively. The correlation coefficient for these data is 0.998.

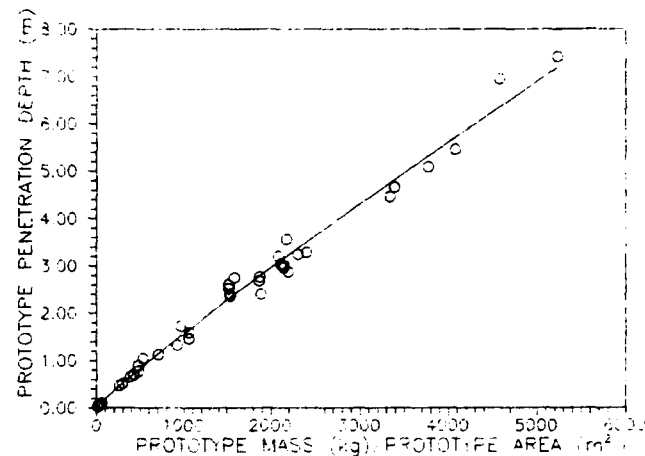


Fig. 3 1-g and Centrifuge Test Results for Prototype Mass to Area Ratio vs. Prototype Penetration Depth, Ottawa Flintshot Sand (Dense)

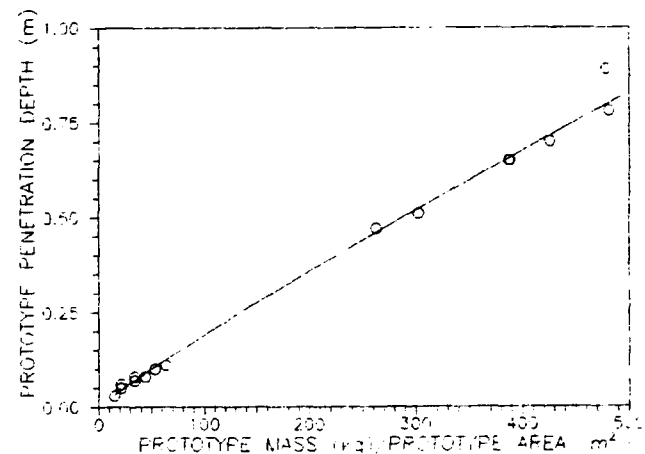


Fig. 4 Exploded View, Low g Test Results for Prototype Mass to Area Ratio vs. Prototype Penetration Depth, Ottawa Flintshot Sand (Dense)

The coefficient and exponent for all soils for which sufficient tests were conducted to determine them are presented in Table 1, on the following page.

Since the velocity and nose shape factor for each test are constant, the S value can be backcalculated from the coefficient on the M/A term. For dense Ottawa Flintshot sand, the S value is 0.137. In Fig. 5, the backcalculated S value for each individual test in dense Ottawa sand is shown plotted against M/A. Very little variation is seen, as expected, considering the care taken to make each soil target the same density. Based on the above discussion, it is evident that the exponent on the mass to area ratio is a function of soil type and soil density. This added complication is not

Table 1. Power equation parameters and correlation coefficients for 1-g and centrifuge test results.

| Soil Type(1) | Soil Density (Mg/m <sup>3</sup> ) | a(2)    | b(2)  | r(3)  |
|--------------|-----------------------------------|---------|-------|-------|
| FL           | 1.83                              | 0.00282 | 0.915 | 0.998 |
| FL           | 1.62                              | 0.00634 | 0.880 | 0.998 |
| F58          | 1.64                              | 0.00611 | 0.860 | 0.997 |
| MX           | 1.94                              | 0.00372 | 0.883 | 0.996 |
| BS           | 1.60                              | 0.01072 | 0.768 | 0.999 |

- (1) FL = Ottawa Flintshot sand; F58 = Ottawa F58 sand; MX = Soil blend (Ottawa and ASTM sands); BS = Florida beach sand  
 (2) a and b are the coefficient and exponent, respectively, in the power equation of the form  $P = a(M/A)^b$   
 (3) correlation coefficient

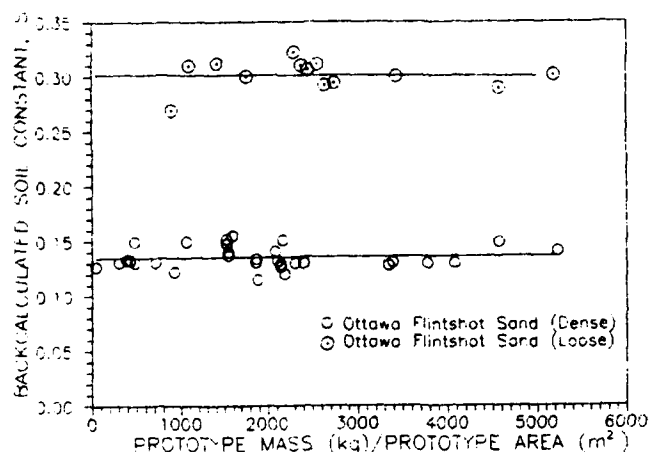


Fig. 5 Prototype Mass to Area Ratio vs. Backcalculated S value from Power Fit Equations for Ottawa Flintshot Sand

likely to be seen as an improvement over Young's equation, even though the mass scaling factor has been eliminated. However, significant improvement can easily be made, without sacrificing simplicity, by replacing the mass to area ratio by the dimensionless parameter,  $\pi_{Dr}$ :

$$\pi_{Dr} = (M_p g) / (A_p \rho_t v^2 D_r^{0.5}) \quad (4)$$

where  $M_p$  and  $A_p$  are the mass and area of the projectile,  $\rho_t$  is the total density of the soil,  $v$  is the projectile velocity, and  $D_r$  is the relative density of the soil (a measure of the soil density in relation to its minimum and maximum values). The value of 0.5 on the exponent for the relative density provides the best fit to the data as determined by statistical analyses. Figs. 6 and 7 present the best fit power curve to all penetration tests conducted in Ottawa sands in terms of  $\pi_{Dr}$  and prototype penetration depth. Again, both 1-g and centrifuge data fit the curve well without the

necessity of a mass scaling factor. The equation for the power curve is:

$$P = 21.427(\pi_{Dr})^{0.894} \quad (5)$$

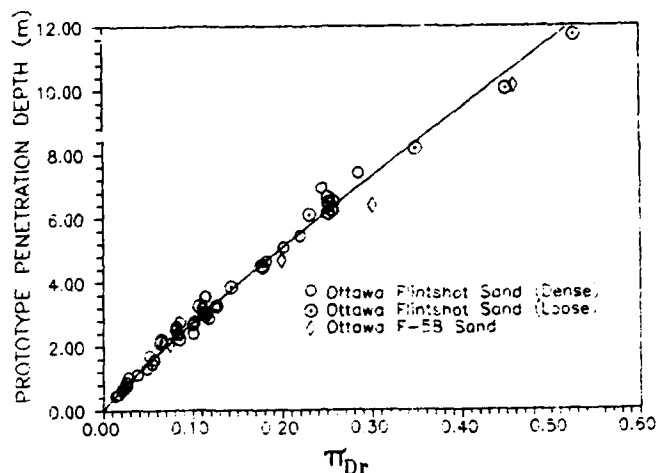


Fig. 6  $\pi_{Dr}$  vs. Prototype Penetration Depth for Ottawa Sands

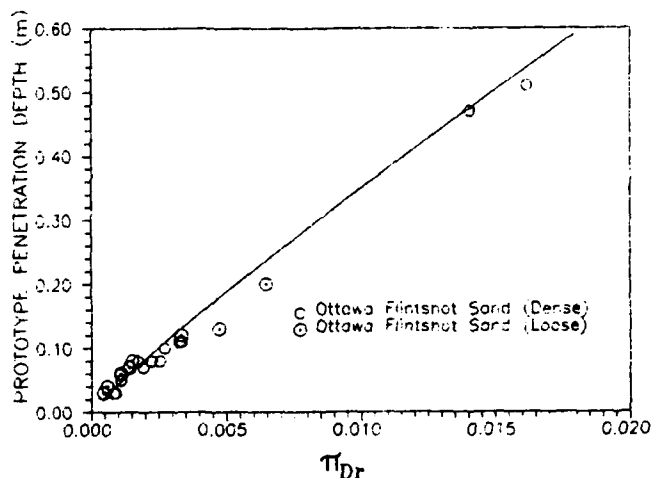


Fig. 7 Exploded View, Low g Test Results for  $\pi_{Dr}$  vs. Prototype Penetration Depth for Ottawa Sands

The correlation coefficient for Equation 5 is 0.996. By bringing the absolute and relative densities of the soil into the equation through use of  $\pi_{Dr}$ , the nature of the soil target is rationally quantified, in terms of easily measured or estimated engineering properties.

More tests are required before it can be determined if the penetration depth into any granular target can be represented by a single equation. It is likely that additional soil parameters will be required before this is possible. A measure of grain size distribution, grain shape and soil particle crushability are likely candidates. However, the work to date has shown that material

properties of the target soil can and should be included in depth of penetration calculations.

## SUMMARY AND CONCLUSIONS

Data from 1-g and centrifuge model tests of projectile penetration in granular soils have been compared to predictions based on Young's equation. The data were found to fit within the bounds predicted by Young's equation using reasonable values for the soil penetrability index. However, for each soil target, the relationship between penetration and projectile mass to area ratio differed from that assumed by Young. The exponent for the  $M/A$  term was found to be larger than 0.5 for all cases and a function of the soil type and density. No mass scaling factor was required and a very high correlation coefficient was obtained.

Analysis of the data for all tests in Ottawa sands showed that use of a dimensionless term, which includes absolute and relative soil densities rather than just  $M/A$ , leads to a single power equation which fits the data very well. It appears possible that with one or more additional terms describing the soil target, a single equation may be developed which can be used to predict penetration in any granular soil with considerably more accuracy than Young's equation in its present form.

## ACKNOWLEDGEMENTS

Research sponsored by the Air Force Engineering and Services Center (AFESC), United States Air Force, under Contract F08635-86-K-0279. The United States Government is authorized to reproduce and distribute reprints for governmental purposes notwithstanding any copyright notation hereon.

The authors would also like to acknowledge the assistance with this research provided by the technical monitor, Lt. Steven T. Kuennen, by AFESC personnel Sgt. Frank Doerle, Sgt. Scott Kortum and William Naylor, and by Michael Meyer.

## REFERENCES

Aitken, G. W., Swinzow, G. K., and Farrell, D. R., "Projectile and Fragment Penetration in Soil and Frozen Soil," Cold Regions Research and Engineering Lab, Hanover, New Hampshire, 1976, 14 pp.

Colp, J. L., "Terradynamics: A Study of Projectile Penetration of Natural Earth Materials," Report No. SC-DR-68-215, Sandia Laboratory, Albuquerque, New Mexico, June 1968, 61 pp.

Hadala, P. F., "Evaluation of Empirical and Analytical Procedures Used for Predicting the Rigid Body Motion of an Earth Penetrator," Report No. AEWES-MISC-PAPER-S-75-15, U.S. Army Engineering Waterways Experiment Station, Vicksburg, Mississippi, June, 1975, 81 pp.

Melzer, I. K. J., "Soil Exploration from the Air," *Journal of the Indian National Society of Soil Mechanics and Foundation Engineering*, Vol. 9, No. 4, October, 1970, pp 363-369.

Taylor, T., "Centrifuge Modeling of Projectile Penetration in Granular Soils," Ph.D. dissertation, Washington State University, August, 1988, 157 pp.

True, D. G., "Penetration of Projectiles Into Seafloor Soils," Final Report No. CEL-TR-822, Navy Civil Engineering Lab, Port Hueneme, California, May, 1975, 63 pp.

Young, C. W., "The Development of Empirical Equations for Predicting Depth of an Earth-Penetrating Projectile," Report No. SC-DR-67-60, Sandia Laboratory, Albuquerque, New Mexico, May, 1967, 41 pp.

Young, C. W., "Depth Prediction for Earth-Penetrating Projectiles," *Journal of the Soil Mechanics and Foundations Division*, ASCE, Vol. 95, No. SM3, May, 1969, pp. 803-817.

Young, C. W., "The Terradynamic Development of a Low-Velocity Earth Penetrating Projectile," Report No. SC-DR-70-302, Sandia Laboratory, Albuquerque, New Mexico, July, 1970, 102 pp.

Young, C. W., "Empirical Equations for Predicting Penetration Performance in Layered Earth Materials for Complex Penetrator Configurations," Report No. SC-DR-720523, Sandia Laboratory, Albuquerque, New Mexico, December, 1972, 65 pp.

Young, C. W., "A Review of Full Scale Terradynamic Testing," Report No. SAND78-1767c, Sandia Laboratory, Albuquerque, New Mexico, 1978, 6 pp.

THE BombCAD ZONE OF INVOLVEMENT (ZOI) MODEL-- A MACRO MODEL  
FOR ASSESSING STRUCTURAL DAMAGE FROM HIGH EXPLOSIVE DETONATIONS

by

Dr. Ronald J. Massa  
LORRON CORPORATION  
44 Mall Road  
Burlington, Massachusetts 01803

and

Mr. John W. Howard  
Everett I. Brown Company  
950 N. Meridian Street  
Indianapolis, Indiana 46204

ABSTRACT

This paper describes the composition and use of a macro model for assessing damage to diverse structures resulting from specific high explosive detonations within or near the structure. The model is referred to as the BombCAD Zone of Involvement (ZOI) model. The ZOI model is used by BombCAD to analyze the vulnerability of specific facilities to bomb attack, and through the use of computer-aided-design (CAD) features of BombCAD, to assist in the design of siting, screening and hardening/softening aspects of comprehensive bomb defense programs. The ZOI model depicts the approximate three-dimensional volume of the structure which is impacted by a specific bomb detonation, on the highly detailed architectural CAD model of the intact structure. Conceptual and analytic limitations of the ZOI model are discussed. Field verification of the ZOI through post-incident analysis is described.

BACKGROUND

A BombCAD vulnerability analysis begins with the definition of a hypothetical bomb threat to a specific facility. The analysis involves the four (4) major elements shown in Figure 1. The bomb threat is defined by specifying a TNT-equivalent charge weight, a bomb location (in three-dimensional coordinates) and the characteristics of the bomb "case."<sup>1</sup> All of the parameters of the threat can be easily changed to simulate a variety of bomb attack scenarios.

The BombCAD facility model (ELEMENT #2) depicts the facility (and site) features in an architectural CAD format and groups each of the structural components of a facility in one of two categories -- incidental structure or primary structure. Incidental structure includes any or all

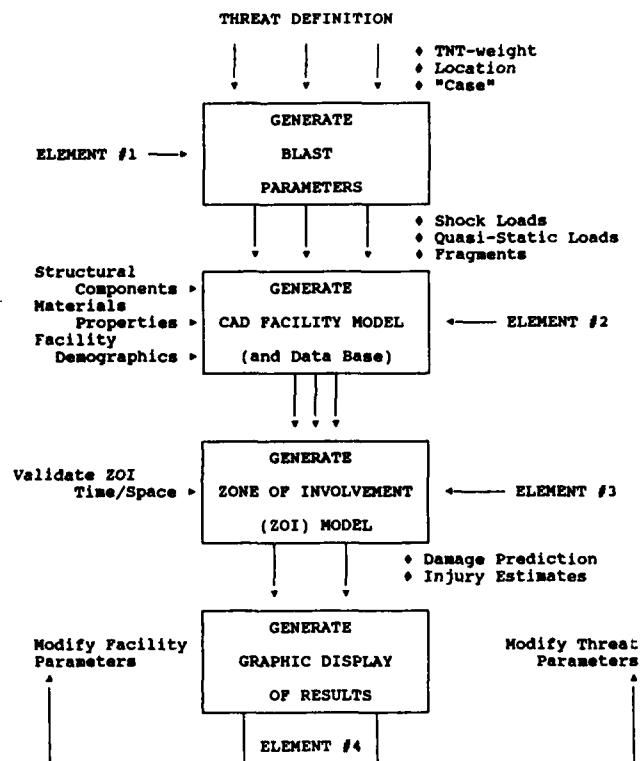


Figure 1  
SCHEMATIC BombCAD VULNERABILITY ANALYSIS

of the structural components which can be removed from the facility without collapse or deformation of the primary structure. Windows, doors, interior partitions and mechanical equipment are examples of incidental structural elements. The primary structure includes all of the structural elements which either bear or contain loads. Beams, columns, load bearing walls and stiffening slabs are examples of primary structural components. The facility model also includes non-graphic data bases such as materials properties and

facility demographics.

The ZOI model (ELEMENT #3) provides a straightforward -- though approximate -- technique for interpreting the damage potential of basic blast wave parameters as they impact structural elements. The blast wave parameters which are generated by BombCAD (ELEMENT #1) for use with the ZOI model include shock loads such as peak positive overpressure, positive phase duration and time-of-arrival and (for internal explosions) gas pressure or quasi-static loads.

The architectural CAD data base includes not only the location and orientation of the incidental and primary structural elements of the facility but damage "thresholds" as well. These thresholds are generally stored in the form of p-T (overpressure-duration) diagrams for each material and/or construction technique. Of course, the theoretical understanding and test confirmation which is required to accurately express such damage thresholds is not available for many -- if not most -- structural components. The ZOI model has limited -- but nonetheless, significant -- capability to deal with this situation.

The ZOI model compares the predicted blast wave load, expressed in p-T terms, with the damage threshold of each structural element stored in the CAD data base and, through a sequence of calculations, directly predicts the "failure" or "survival" of each incidental structural component. Failure is regarded as a binary phenomenon -- the incidental structural component is either left intact or totally "vaporized." The model continues to compute until a specific three-dimensional volume is either (1) entirely enclosed by incidental structural elements which are predicted to remain intact or, (2) all of the volume boundaries are either predicted to remain intact or are vented to the outside. In this manner the ZOI model defines the three-dimensional volume within a structure or facility which is impacted by (or involved in) a specific bomb blast.

In addition, once an incidental structural component -- such as a window pane -- is predicted to fail, secondary fragments (glass shards, in the case of a shattered window) are considered in subsequent blast wave effects calculations (made by ELEMENT #1) in the directions in which such fragments are propelled.

An important test of the validity of this zone of involvement concept is to ascertain that additional, unpredicted damage does not occur through secondary effects such as structural collapse and/or pro-

gressive collapse. Therefore, the ZOI model also compiles the approximate dynamic loads on the primary structural elements, within and around the ZOI, identified in the architectural/structural information maintained in the CAD system data base. These loads are generally studied by a structural engineer to determine the likelihood of such secondary damage ("Validate ZOI [in] Time/Space"). Where secondary damage is not likely, the ZOI model provides an effective engineering approximation to the structural damage which results from a bomb blast. Through other computations, estimates of the likely human injury within the zone of involvement are developed.

The final element of the BombCAD analysis, ELEMENT #4, generates a graphic display of predicted damage and injury overlaid on a two- or three-dimensional rendition of the intact facility. This graphic display includes block legends which contain details of the consequences of the hypothetical attack such as "Estimated Cost to Repair," "Estimated Number Injured" and "Estimated Fatalities." From these graphic presentations of results, the architect/engineer, security professional or facility owner can modify either the facility or the threat to mitigate the consequences of potential attack scenarios. This process significantly enhances the design and evaluation of siting, screening and hardening/softening aspects of comprehensive bomb defense programs for a specific facility.

The remainder of this paper presents details, including limitations, of the structural modeling, blast parameter and blast effects estimation and field verification related to the ZOI approach within BombCAD.

#### THE ZONE OF INVOLVEMENT (ZOI) MODEL -- A SUMMARY

The zone of involvement (ZOI) model used by BombCAD is, in fact, a simple series of rules used by the computer (1) to calculate blast wave parameters at points where the outgoing shock front encounters structural features and, (2) to predict the failure or survival of the structural features which are encountered. These rules include provisions for handling both bomb blasts within the structure and blasts external to the structure.

These analysis rules -- and, hence, the ZOI model itself -- embody a sequence of approximations which systematically and deliberately bypass the complex problems of blast wave interactions with structural components encountered when one tries to determine the precise blast loads which induce individual failure mechanisms.



While solving these problems is unquestionably important to the development of a complete understanding of shock loads on structural components, such detailed solutions are frequently unnecessary to achieve the primary objective of the ZOI model, i.e. realistically, but conservatively, approximating the three dimensional volume of a facility involved or impacted by a specific bomb detonation.

The underlying ZOI concept is quite simple; the numbers associated with bomb blast loads enhance the validity of this simple concept in a substantial majority of cases of practical interest.

Consider two identical unit cubic volumes (dimensions 1x1x1) which share a party wall. See Figure 2. A bomb (represented by a little diamond in Figure 2) is exploded somewhere within the right cube. The key question is, "What does an observer somewhere within the left cube experience?"

Simple logic tells us that the experience of the observer in the left cube is strongly dependent on the fate of the party wall. If the party wall remains intact, the observer is likely to experience only a "what was that?" reaction. If the party wall fails in any one of a number of ways, the observer will experience a more significant effect and will become "involved" in the blast. Hence, the left cube will be drawn into the zone of involvement of the blast detonated in the right cube.

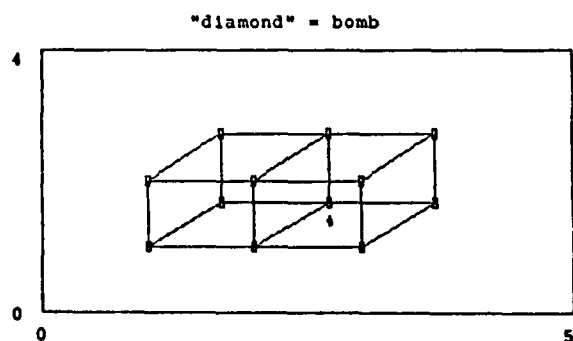


Figure 2  
BASIC ZOI CONCEPT

Now let's look at the failure mechanisms that the party wall might experience as a result of the blast. The wall could be (1) breached, (2) cracked, rotated or twisted, (3) spall fragments from the left face. In all three cases the observer in the left volume is placed at risk from the blast. In most bomb security scenarios, this conclusion is more important than discovery of the failure mechanism and the

precise size and location of bomb which precipitates the failure.

In virtually all security applications, the aggressor has some flexibility with respect to both bomb size and location. Therefore, even if we could easily determine the precise details of the wall failure, we rarely can pin down the attack well enough to effectively use this detailed information.

Of course, the precise environment faced by the observer in the left cube, will depend on the specific failure mechanism and the specific blast load which causes the failure. The ZOI model greatly simplifies this environment by (1) assuming that if the incidental structural component is predicted to fail, it vaporizes, (2) treating the shock wave load in the left hand space as it would be if the wall had not been present, and (3) representing the wall's original presence by adding an additional threat -- a mass of fragments propelled in the shock wave propagation direction by the incident blast wave -- in the left cube.

When necessary, the ZOI model can approximately adjust for the energy absorbed by the wall in failing and for the total kinetic energy assumed by wall fragments as they are propelled.

Now let's examine some numbers associated with a typical bomb blast wave emanating from a 20 lb (TNT-equivalent weight) charge. The peak positive reflected overpressure is depicted on a typical blast parameter scaling chart as described by BAKER<sup>2</sup> and others<sup>3</sup> in Figure 3. The actual chart shown in the figure was generated using the BombCAD computational routines adapted from the 'SECUREPLAN' BOMB UTILITY<sup>4</sup>. The chart indicates (with small rectangles) the high overpressure extreme, H, (experienced at 1 foot from the blast) and the low overpressure extreme, L, (experienced at 100 feet from the blast). The magnitude of the blast load over a range of 1 to 100 feet (1:100) varies by more than 10000:1!<sup>5</sup>

Thus, the shock loads imposed on structural elements can vary by several orders of magnitude for relatively small charges (20 lbs) over relatively modest distances from a security/facility perspective (1 to 100 feet).

Now let's turn our attention to the estimation of structural damage. Refer again to Figure 3. The small diamonds and connecting lines delineate a 10:1 range of shock load (from 10 to 100 psi) and a corresponding 2.5:1 (from 14.8 to 6) range of scaled distance. Let us assume that this 10:1 range represents (1) the uncer-

tainty associated with our understanding of the behavior of a structural component when impacted by a blast wave, (2) the aggregate of inaccuracy associated with blast wave parameter estimation, or (3) a combination of both.

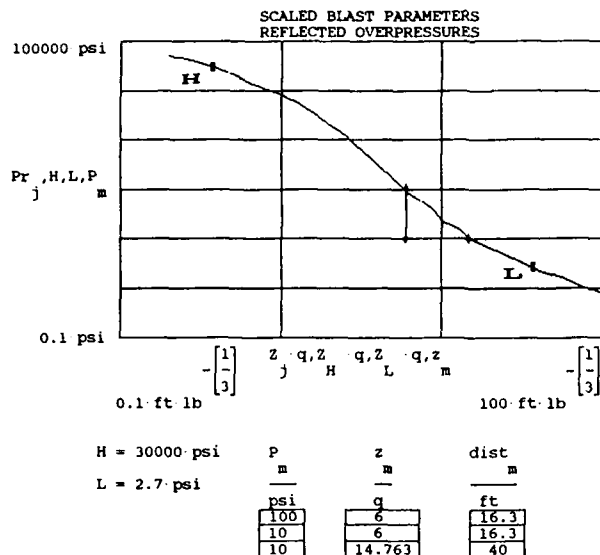


Figure 3  
PEAK POSITIVE REFLECTED OVERPRESSURE  
-- A TYPICAL SCALING CHART --

Along the horizontal axis, the 10:1 uncertainty in overpressure maps into a scaled distance variation of 16.3 to 40 feet for a 20 pound charge. Thus, in the roughly 100 foot region of interest around the bomb, we would have no doubt about the fate of a structural component closer than 16 feet (it fails) or further than 40 feet (it survives) -- even in the face of a 10:1 computation error or material behavior uncertainty!

Consider the sketches in Figure 4. The analysis is significantly encumbered by a 10:1 uncertainty in either material performance or blast wave estimation. Fortunately, this severe potential error only obscures our ability to accurately predict the fate of a specific structural component in the distance range from 16 to 40 feet -- 24% of the distance range of interest. The BombCAD analysis technique permits us to easily calculate the zone of involvement using the best case approximation in (b) or the worst case approximation in (c). Because of the number of different materials, the different distances and angles from the blast, the complex geometries of many structures and the fact that practical uncertainties are often significantly less than 10:1, the variation in ZOI is frequently very small.

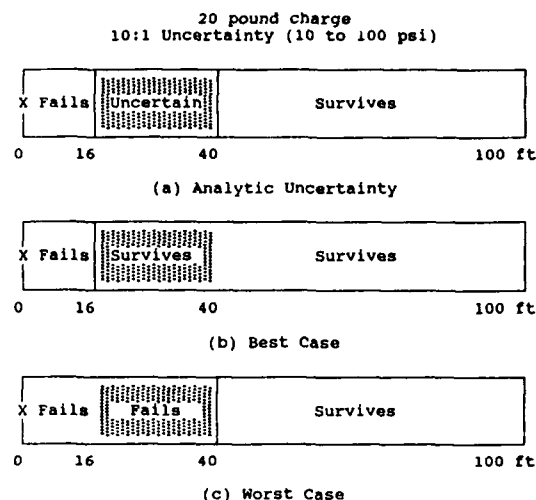


Figure 4  
ZOI UNCERTAINTY

Table I shows typical analytic uncertainties based on a more modest 2:1 materials/computation uncertainty (10 psi to 5 psi) for explosive charges of different weight. Note that magnitude of uncertainty is also a function of where in the overpressure spectrum the center of the uncertainty range lies.

TABLE I  
TYPICAL ZOI UNCERTAINTIES

For a 2:1 (5 psi to 10 psi)  
material/computation uncertainty

| Bomb Size | Typical Distance Uncertainty |
|-----------|------------------------------|
| 1 lb      | +/- 4.5 feet                 |
| 10 lb     | +/- 10 feet                  |
| 100 lb    | +/- 21 feet                  |
| 1000 lb   | +/- 45 feet                  |

Specifics of the BombCAD computation process and the ZOI model composition are discussed in the sections which follow.

## STRUCTURAL MODELING

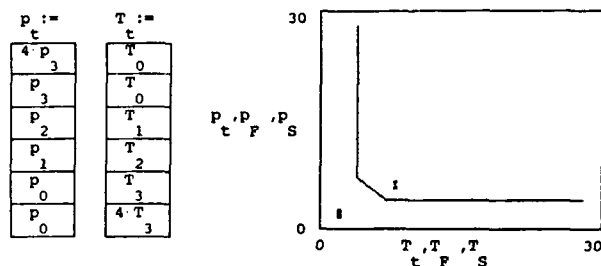
The architectural CAD element of the BombCAD system models the facility, including external site features such as topography. As this model is developed, the CAD operator separates all structural components into two groups -- incidental structure and primary structure. As each component<sup>6</sup> is inserted into the model, it is tagged with its group designation and non-graphic data which describes its composition and "strength."

Primary structural components are typically tagged with their static design loads. BombCAD presently computes the dynamic load parameters (direction of application, reflected overpressure and positive phase

duration) experienced by the component. These are graphically tagged to the component for analysis by a structural engineer to assess the likelihood of structural collapse or progressive collapse which would invalidate the ZOI analysis.

Incidental structural components are typically tagged with a p-T representation of their anticipated failure/survival boundary under blast load. Figure 5 depicts a representative case. The load point marked "X" represents a load for which the component would be predicted to fail; the rectangle represents a load for which the component would be predicted to survive.

A major limitation of the BombCAD analysis technique -- and many other analysis efforts -- is the unavailability of materials performance data for blast environments. However, BombCAD, when used in post-incident analysis, can provide meaningful dynamic performance estimates.



The table above defines the material property ---  $p = f(T)$  -- representing the blast dynamic failure threshold.

... where  $T := 2 - \frac{1}{p}$

Figure 5  
REPRESENTING BLAST RESISTANCE OF  
INCIDENTAL STRUCTURAL COMPONENTS

Window and architectural glass are major components in the construction of modern buildings. They are extremely vulnerable to failure in a blast environment and frequently shatter, resulting in a secondary fragment load which can be very damaging -- both to construction materials and persons.

BombCAD uses a proprietary shatter/breakage model, adapted from Mainstone<sup>7</sup> which directly predicts the failure of glass panes as a function of estimated peak positive reflected overpressure, pane geometry and glass type (including, annealed, heat strengthened and laminated glass panes).

None of the analyses presently used in BombCAD develop negative phase loads. All use the triangular wave approximation for peak positive overpressure. Shock loads reflected from other objects in the envi-

ronment are not considered.

## BLAST PARAMETER ESTIMATION

A number of blast wave parameters are estimated to drive the ZOI model. The techniques used to make these parameter estimates are briefly described below.

All blast wave parameters are corrected for site altitude (air density using a standard atmospheric model). Computations can be made in either US or metric units or combinations as desired.

Basic explosives scaling laws and charts are used<sup>2,3</sup> to generate three (3) fundamental blast wave parameters -- (1) peak positive incident overpressure ( $P_s$ ), (2) peak positive incident impulse ( $i_s$ ), and (3) peak positive reflected impulse ( $i_r$ ). Peak positive incident overpressure is related to a scaled distance,  $Z$ , as shown below.

$$P_a := f1(\text{site\_altitude}) \quad (1)$$

$$Z := \frac{R}{\left[ \frac{a \cdot t \cdot W}{k} \right]^{\frac{1}{3}}} \quad (2)$$

$$P_s := f2(Z, P_a) \quad (3)$$

$$Pr := 2 + \left[ 6 \cdot \frac{\frac{P_s}{P_a}}{7 + \left[ \frac{P_s}{P_a} \right]} \right] \cdot P_s \quad (4)$$

where ...

$a$  = air/ground burst parameter

$R$  = observation distance of interest

$t$  = relative strength coefficient for various explosives

$W$  = physical charge weight

$Z$  = scaled distance

$P_a$  = ambient air pressure

The function,  $f2$ , through which  $P_s$  is related to  $Z$  is a direct linear interpolation between 22 points in a table of data points read directly from scaling charts. The maximum discrepancy in this simple process is about 11% with zero discrepancy at the 22 data points and an "average" discrepancy well within 5%. A similar technique is used to estimate the incident and reflected impulses,  $i_s$  and  $i_r$ .

The function in equation (4) is directly adapted from Doering and Burkhardt<sup>8</sup> and many others. It assumes that air remains a perfect gas mixture at all overpressures. It provides valid results up to free-stream overpressures ( $P_s$ ) of about 100 psi. Above this value, a correction based on Brode<sup>9</sup> can be applied if desired.

For internal (poorly vented) blasts, quasi-static and/or gas pressure loads are calculated<sup>10</sup> and displayed. The architectural CAD model facilitates the calculation of ZOI surface areas and volumes to support the quasi-static load estimates -- quasi-static pressure, total gas impulse and blowdown interval.

Figure 6 depicts the SITE PLAN view of a typical BombCAD facility model. The cross-

hatched area, greatly magnified to reveal a small portion of the data available in the CAD model, is presented in Figure 7. It shows typical blast effects data within the ZOI related to a 20 lb bomb located at the radial pattern origin. (1) Overpressure/impulse shock loads on an interior wall surface. (2) Shock loads on the ceiling. (3) A quasi-static load data block. (4) Predicted incidental structural component failure (an interior wall shown dotted).

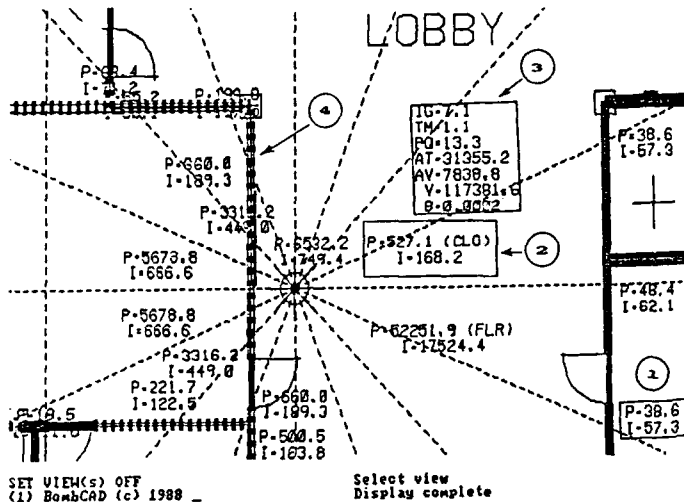


Figure 6  
TYPICAL FACILITY MODEL  
-- SITE PLAN VIEW --

#### ADDITIONAL BLAST EFFECTS

In addition to estimation of the effects of bomb blasts on structures, BombCAD's ZOI model also facilitates the estimation of potential human injuries due to a specific bomb blast. This is accomplished by estimating free stream overpressure, Ps, and impulse, Is, loads within various sub-zones of the ZOI and comparing these loads with various published injury thresholds. If facility demographic data is available for the same sub-zones, BombCAD will estimate the number of injuries and fatalities likely to result from a specific bomb blast.

Three injury/fatality mechanisms are considered, (1) hearing damage, (2) lung collapse, and (3) whole body translation. Analysis techniques and threshold data are adapted from the cited references as follows. Hearing damage analysis uses damage criteria published by Hirsh (1968)<sup>11</sup>, Ross *et al* (1967)<sup>12</sup> and White (1968)<sup>13</sup>, and generally follows the analysis approach taken by Baker *et al*<sup>2</sup>. The lung collapse analysis used in BombCAD follows Baker *et al*<sup>2</sup> based on survivability data from Bowen *et al* (1968)<sup>14</sup> and White (1971)<sup>15</sup>. The analysis of whole body translation and injury is attributed to

Baker *et al* (1983)<sup>2</sup> based on data and techniques published by White (1971)<sup>15</sup>.

#### FIELD VERIFICATION THROUGH POST INCIDENT ANALYSIS

The validity of the ZOI model in predicting damage and injury from hypothetical bomb attacks can only be effectively assessed through a comparison of its predictions vis-a-vis the observed consequences of an actual bomb attack on a real facility.

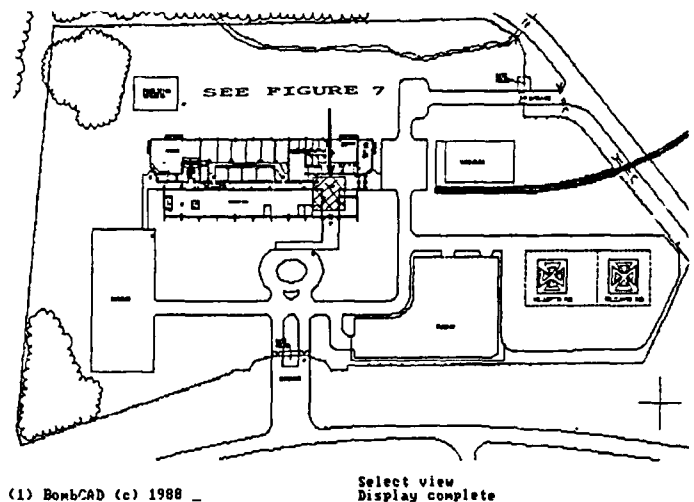


Figure 7  
TYPICAL BLAST PARAMETERS IN THE ZOI

How closely does this technique -- based on the ZOI model -- predict the actual damage which occurs when a real facility is subjected to a real bomb attack?

This question can be answered in a definitive manner through exercise of one of the major applications of BombCAD -- post-incident analysis. Various versions of BombCAD have been used, since 1986, in analyzing actual terrorist bomb attacks on several facilities in South America. It is worthwhile to describe these analyses and the role they have played in both the development and validation of BombCAD's ZOI model.

The first step in a post-incident analysis involves reconstructing the attack scenario. Bomb size, location, type and case must be established first. A number of techniques can be used in conjunction with BombCAD to do this. A good estimate of bomb location and a crude estimate of size can be made using the bomb crater location and dimensions. A similar crude estimate of size can be used in car bomb attacks by observation of the car wreckage. A car bomb "rule of thumb" gives a broad range of charge sizes. If it still looks like a car -- less than 10 kg. If the car body is unrecognizable, but the wheels/axles and engine are all attached -- less than 20

kg. Engine block stripped, wheels and axles separated -- greater than 20 kg. BombCAD can also exercise its car bomb model to make a closer estimate through data provided from the distances major auto components are propelled.

The best approach comes from noting the location and fate of window panes of the same size and type directly exposed to the blast wave but at greatly different distances. This technique offers the added advantage of providing a good measure of the free-stream blastwave itself.

Once, the attack is defined the attack ZOI and surrounding regions are modeled through field inspection or photographs. Damage to specific incidental structural components is noted in a manner consistent with the ZOI model assumptions. BombCAD is run and its damage predictions are compared with the noted damage using the estimated blast resistance properties of the damaged and undamaged components. Even initial results are usually close for glass and some masonry materials.

The estimated blast resistance of frequently employed structural components is then varied to achieve the "best fit". If these modifications produce a consistent result, the analysis is successful -- not only on explaining the incident but in adding to our understanding of blast resistant properties of certain materials.

The analysis of six actual terrorist bombing incidents in South America provided substantial corroboration of ZOI damage predictions.

#### REFERENCES

- (1) The bomb case characteristics are used to estimate the extent to which a bomb case absorbs the charge energy and/or contributes primary fragments to the blast threat. Four types of cases, with different fragment/absorption characteristics, are routinely used -- the person, a satchel, a generic case and a vehicle.
- (2) Baker, W.E., P. A. Cox, et al, Explosion Hazards and Evaluation, Elsevier Scientific Publishing Company, New York, 1983.
- (3) Kingery, C. N. and G. Bulmash, "Air Blast Parameters From TNT Spherical Air Burst and Hemispherical Surface Burst," Ballistic Research Labs., TR-02555, April 1984.
- (4) Magee, R. J. "The 'SECUREPLAN' BOMB UTILITY -- A PC-Based Analytic Tool for Bomb Defense," 28th Annual Meeting -- Institute of Nuclear Manage-

ment, July 14, 1987, Newport Beach, California.

- (5) The positive phase duration associated with this blast wave also varies considerably -- from about 0.3 msec at 1 foot to 8.8 msec at 100 feet.
- (6) A structural "component" is typically a surface -- such as a wall section -- or a finite element represented by a rectangle in plan view -- such as a column.
- (7) Mainstone, R. J., "The Breakage of Glass Windows by Gas Explosions," Building Research Current Paper CP 26/71, Building Research Establishment, September 1971.
- (8) Doering, W., and G. Burkhardt, "Contributions to the Theory of Detonation," TR F-TS-1227-1A, Wright-Patterson AFB, Ohio, 1949.
- (9) Brode, H. L., "Quick Estimates of Peak Overpressure from Two Simultaneous Blast Waves," Defense Nuclear Agency Report No. DNA4503T (December 1977).
- (10) These calculations are adapted from the method outlined by BAKER et al (Reference 2 above) -- pages 238 to 252.
- (11) Hirsh, F. G., "Effects of Overpressure on the Ear -- A Review," Annals of the New York Academy of Sciences, 152, Article 1, October 1968.
- (12) Ross, R., et al, "Criteria for Assessing Hearing Damage Risk From Impulse-Noise Exposure," Human Engineering Laboratory, Aberdeen Proving Ground, Maryland, AD 666206, August 1967.
- (13) White, C. S., "The Scope of Blast and Shock Biology and Problem Areas in Relating Physical and Biological Parameters," Annals of the New York Academy of Sciences, 152, Article 1, October 1968.
- (14) Bowen, I. G., et al, "Estimate of Man's Tolerance to the Direct Effects of Air Blast," Technical Report to Defense Atomic Support Agency, DASA 2113, Lovelace Foundation for Medical Education and Research, AD 693105, October 1968.
- (15) White, C. S., "The Nature of the Problems Involved in Estimating the Immediate Casualties From Nuclear Explosions," CEX-71.1, Civil Effects Study, U.S. Atomic Energy Commission, DR-1816, July 1971.

# Stress Wave Propagation in Thick Slabs Subjected to Blast or Impulsive Loads

J. Ballmann / K.S. Kim / W. Nachtsheim

Technical University Aachen, Templergraben 64, D-5100 Aachen, FRG

ITAM Consultants, Lousbergstr. 16; P.O.Box 1847, D-5100 Aachen, FRG

## Abstract

A realistic analysis of structures subjected to blast or impulsive loads needs a correct representation of the different wave phenomena forming within the system. A numerical bi-characteristics method is presented here proved to be well suitable with respect to the mechanical nature of wave propagation.

The different wave effects are explained in detail by means of a numerical example. Particularly the Rayleigh surface wave with its extreme stress peaks, steep gradients and the concentration of energy has a strong influence on the total transient behaviour. It propagates over wide ranges of the slab front face with approximately unchanged intensity.

Furthermore the development of cracks and the wave reflections are outlined; material spalling or scabbing may occur at the slab rear face.

## 1. Introduction

The first processes after the very beginning of the load may already strongly affect the complete subsequent behaviour of the subjected structures, depending on the intensity and the increasing velocity of the impulsive or impact load. The wave effects determine whether the structural part will be locally damaged by penetration/perforation. Even it may fail, long before measurable deflections are able to form. A prevailing bending behaviour to be described by usual dynamic beam or slab methods can be excited only a long time afterwards.

In the first period however, a realistic analysis of structures subjected in this way needs a correct consideration of the propagation, reflection and superimposition of the different generated stress waves. But as known from theoretical physical treatises (e.g. already by Lord Rayleigh), very steep stress gradients and high concentrations of energy may be produced within the scope of wave effects especially near a free surface. Seismic waves are a good example from nature propagating approximately without energy dispersion. Hence, the computational procedures must accomplish certain requirements e.g. relating the numerical dispersion and dissipation. Most of the usually used computational methods e.g. based on Finite Element or Finite Difference schemes may easily fail to give correct results.

In this paper a numerical bi-characteristics method is presented to solve the wave problem based on a linear theory for homogeneous isotropic structures. The discretisation in space and time follows the physical wave surfaces. So the procedure is in good conformance with the mechanical nature of the wave propagation process. It guarantees the accuracy necessary to compute the special phenomena under consideration.

## 2. Computational method

The equation of motion of a differential slab element resp. the local balance of momentum combined with the time derivative of the constitutive relation result in a system of partial differential equations (PDE's, /1/). Dealing with linear elastic material Hooke's law is written herein using the shear modulus  $G$  and the modified Lamé constant  $\lambda$ .

$$\rho \frac{dy}{dt} - \text{div } \underline{g} = 0 \quad (1)$$

$$\frac{\partial \underline{g}}{\partial t} = \lambda \underline{\underline{E}} \text{ div } \underline{v} + G (\text{grad } \underline{v} + (\text{grad } \underline{v})^T) \quad (2)$$

This is a hyperbolic system; so in general singular surfaces can exist where the normal derivatives of the stresses and of the particle velocity are discontinuous. Therefore the numerical difference scheme has been especially organized to follow the singular surfaces. Thus, undue evolutions in the before-mentioned normal directions are avoided a priori.

All the characteristic surfaces passing through one point envelop a cone in space and time (a so-called Monge-cone), generated by the bi-characteristics (figure 1). Regarding elastic solids two such cones exist, a dilatational and a shear one. The directions of bi-characteristics are as follows in difference form

on the dilatational cone (index  $L$ )

$$\underline{r}(t_0 + \Delta t) - \underline{r}_L(t_0) = \underline{m}_L \Delta t \quad (3)$$

on the shear cone (index  $S$ )

$$\underline{r}(t_0 + \Delta t) - \underline{r}_S(t_0) = \underline{m}_S \Delta t \quad (4)$$

A characteristic surface touches the equivalent cone along such a bi-characteristic. Using linear combinations of (1), (2), the equations (3) and (4) yield

on the dilatational cone

$$\begin{aligned} & \left[ \rho c_L \dot{u}_x + \dot{u}_x \frac{\partial \sigma_x}{\partial x} - q \operatorname{grad}(\lambda \dot{u}_x + c_L \dot{u}_x) \frac{\Delta t}{2} \right]_{P_0} = \\ & \left[ \rho c_L \dot{u}_x + \dot{u}_x \frac{\partial \sigma_x}{\partial x} + q \operatorname{grad}(\lambda \dot{u}_x + c_L \dot{u}_x) \frac{\Delta t}{2} \right]_{P_1} \end{aligned} \quad (5)$$

on the shear cone

$$\begin{aligned} & \left[ \rho c_S \dot{u}_x + \dot{u}_x \frac{\partial \tau}{\partial x} - q \operatorname{grad}(G \dot{u}_x + c_S \dot{u}_x) \frac{\Delta t}{2} \right]_{P_0} = \\ & \left[ \rho c_S \dot{u}_x + \dot{u}_x \frac{\partial \tau}{\partial x} + q \operatorname{grad}(G \dot{u}_x + c_S \dot{u}_x) \frac{\Delta t}{2} \right]_{Q_1} \end{aligned} \quad (6)$$

By this means the relations are gained using only derivatives within the surface element. Normal derivatives possibly discontinuous are completely eliminated; hence, (5) and (6) are called the compatibility equations.

Utilizing the initial value surface by means of the equations (5) and (6) with the index  $i = 1, \dots, 4$ , the stress situation and the velocity of every new point  $P^0$  are calculated. From these results the total state of deformations and motions is finally

determined. Regarding mesh points on the boundary of the computational domain an analogous scheme holds with respect to the relations in figure 1.

In order to prove the computational procedure an overall comparison was performed with measurements experimentally established. These results were originated by the model tests described in reference /2/. Araldite-B-plates have been loaded by an explosion applied to a local surface region. The transient stresses generated within the models were recorded by an optical method, by means of a Cranz-Schardin-camera allowing photo series with very short time intervals of only a few microseconds. Usually the iso-chromatics are directly observed during an experiment and numerically analysed afterwards. These are the lines of equal maximum shear stresses. For convenience these graphs can be immediately contrasted to the iso-contour plots determined by computational simulations. Reference /3/ shows a rather good agreement between experiments and analyses, with respect to the quality of the different wave effects explained furtheron as well as in a quantitative manner.

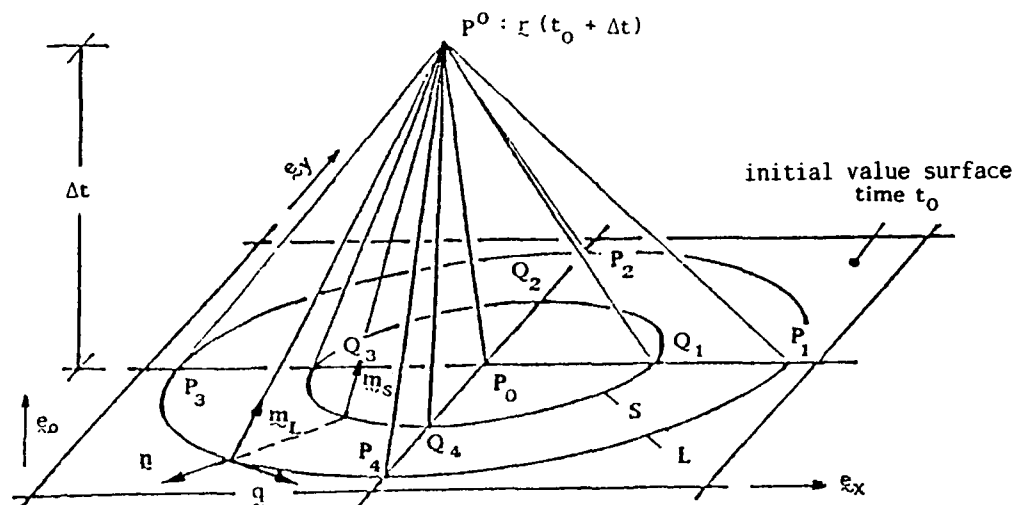


Fig.1 Numerical difference scheme relating to mesh points in the interior

### 3. Numerical results

In the following the numerical results are explained in detail by means of an example. A similar Araldite-B-model as mentioned before was analysed. Figure 2 shows the geometry of the thick unidirectional slab with a 6:1 ratio between length and thickness and the explosive line load at the symmetry axis. The load history in figure 3 and its local concentration have been taken over from the experiment. So all parameter agree with the model test without the modified thickness-span-ratio.

It should be pointed out here, however, that of course the numerical procedure can be used for other elastic material, geometrical conditions as well as arbitrary load distributions in time and space.

The solution of the prevailing PDE-system yields the complete stresses and motions of the structure under consideration strongly varying with time. The longitudinal and shear stresses in an orthogonal base system  $x, y$  are computed as well as the quantities and directions of the equivalent principle stresses. Because of the small spatial mesh pattern in the example given here the time interval  $\Delta t$  amounts to only 1.35  $\mu s$ . So an extensive data material is obtained.

In the following certain graphs from these total results are exemplarily presented, mainly relating to a simulation time  $t = 215 \mu s$ . The different wave types passing through the computational domain I can be identified. After the beginning of loading they propagate each with its own velocity. At the chosen time step they are already

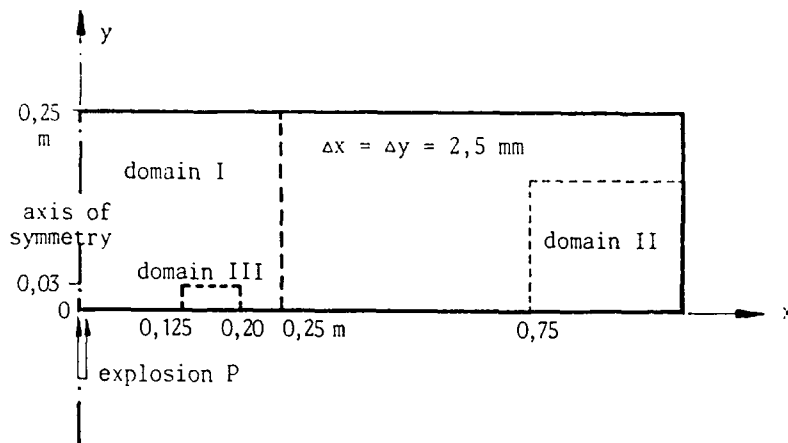


Fig. 2 Section of slab

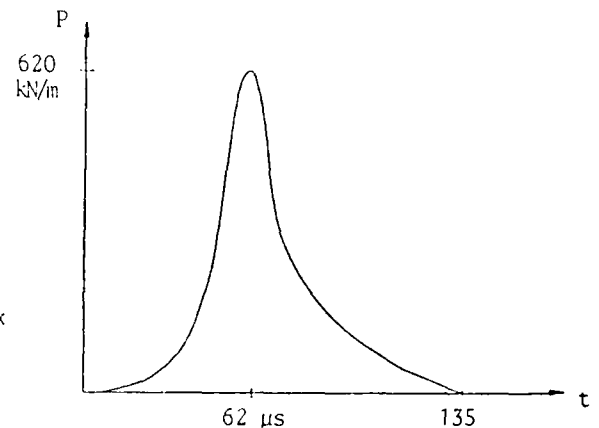


Fig. 3 Explosion force time history

so far separated from the iso-chromatics below the explosion load so that they can be well distinguished.

At first figure 4 shows the field of maximum shear stresses (so-called "principle" shear stresses). The iso-contour plot in figure 4a would be directly comparable with the appropriate iso-chromatic graph of a corresponding optical model test. Furthermore in figure 4b the shear stress amplitudes are pictured in a 3D view for a better illustration of wave effects.

The compression wave propagates fastest into the slab (longitudinal P-wave,  $c_L = \sqrt{E/\rho}$ ). The shear wave follows with a velocity about 40 % smaller (transversal S-wave,  $c_S = \sqrt{G/\rho}$ ). Furthermore the transverse von-Schmidt- or head-wave appears connecting the longitudinal wave from the free surface tangential to the shear wave.

Moreover figure 4 shows that the compression wave has already reached the slab rear face and is reflected. The oblique incident stress components are split up into a tension and a shear wave superimposing the still propagating slower stresses. At the axis of symmetry the compression is reflected by pure tension.

On the free front face, - the surface condition of zero stresses is satisfied, - the shear wave changes into a surface wave, the so-called Rayleigh wave (R-wave). This phenomenon indicates a strong concentration of stress peaks also propagating, with a typical face easily to identify in all figures. Its propagation velocity is even a little smaller than that of the shear wave; the ratio  $c_R/c_S$  amounts to 0.88 - 0.96 according to the Lamé constant ( $\nu/4$ ).

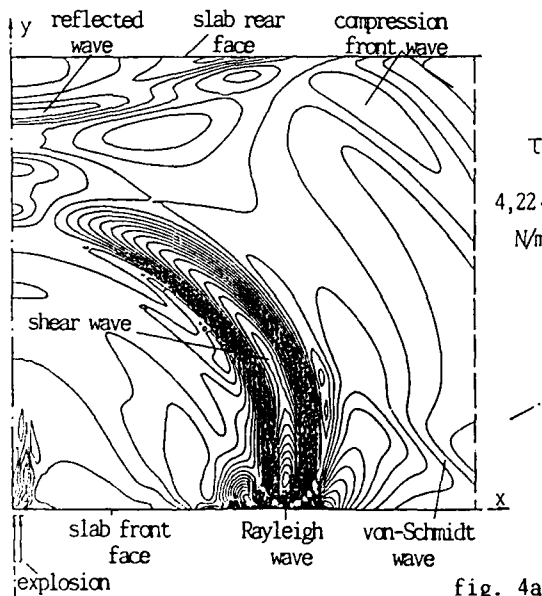


fig. 4a

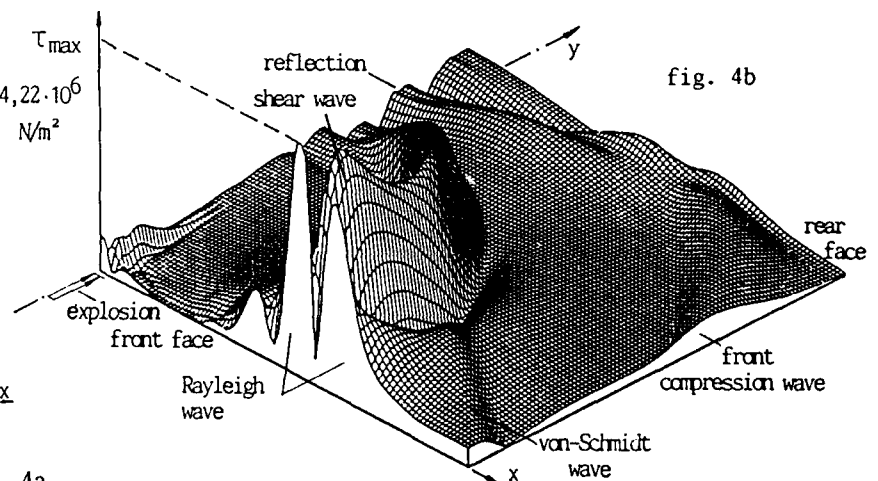


fig. 4b

Fig. 4 Field of maximum shear stresses (domain I,  $t = 215 \mu s$ )



The stress peaks of the Rayleigh wave concentrate only on a thin surface layer; note the steep decrease of shear stresses normal to the surface and again an increase when changing into the shear wave.

While the compressive front wave rapidly diminishes due to propagation and dispersion, the stress peaks of the Rayleigh wave in contrast reduce only very slowly. They pass with approximately unchanged intensity over wide ranges of the slab front face, with appropriate consequences on the total subsequent structural behaviour.

At the transversal slab surfaces, - e.g. when reaching the supported end, - the propagating Rayleigh wave is split up into a reflected as well as a diffracted R-part. Figure 5 shows the shear stress amplitudes in the region of the slab edge (domain II in figure 2) after reflection/diffraction.

With the reflected wave fronts first information relating the type of supports arrive at the slab center resp. the loaded area. Until this time no influence of the supports could be felt on the stress and deformation behaviour. Hence, the supports will predominantly affect the global vibrations taking place later.

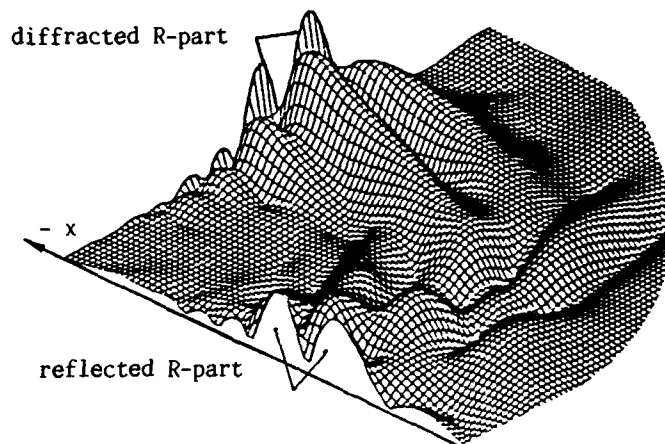


Fig.5 Maximum shear stresses (domain II)

In contrary, maximum, shape and duration of the impulsive load play a dominant role on the wave phenomena already from the very beginning of stress propagation, primarily with a great influence on the Rayleigh wave and its face.

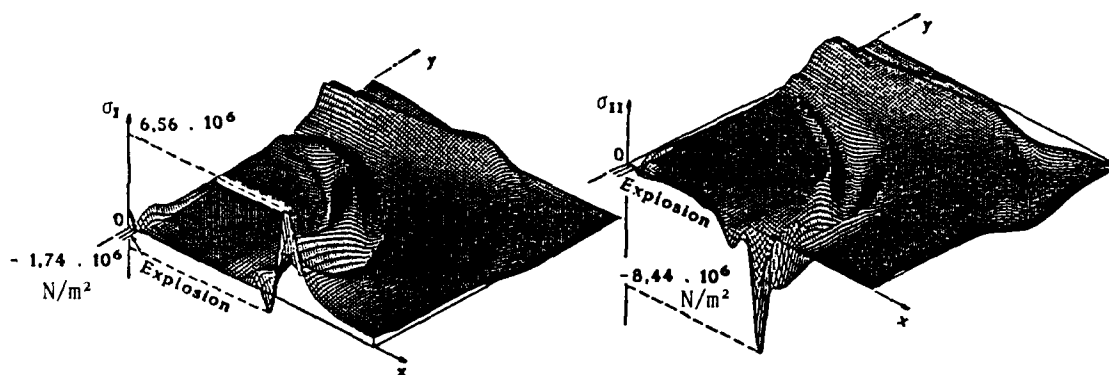


Fig.6 Principle stresses  $\sigma_I$  and  $\sigma_{II}$  (domain I,  $t = 215 \mu s$ )

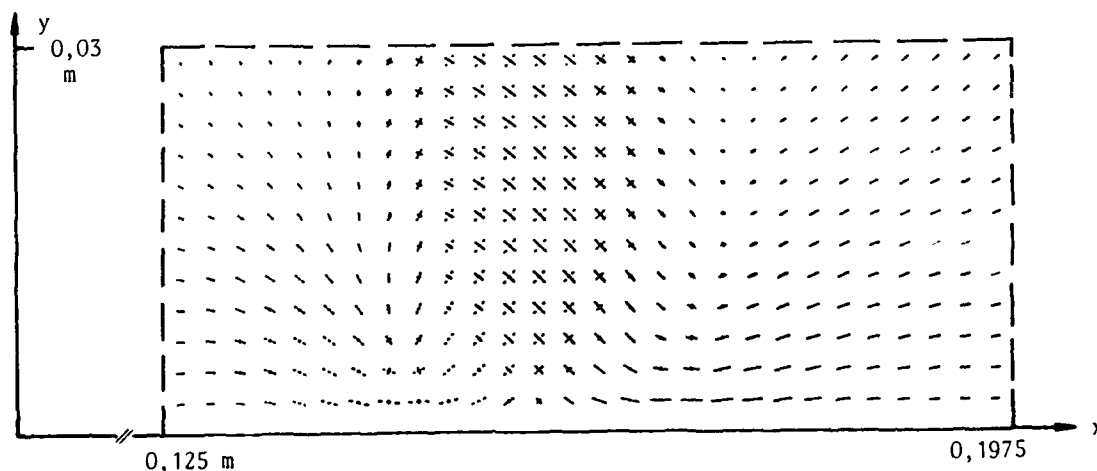


Fig.7 Principle stress directions (domain III)

In addition to the shear stresses discussed up to now for demonstration of wave effects, the analysis of the slab stress situation is mainly based on the principle stresses  $\sigma_I$  and  $\sigma_{II}$  and their directions. Figures 6a and b present the quantities of principle stresses for the same simulation time and in the same view as the maximum shear stresses in figure 4. The positive sign in figure 6 indicates tension. The wave phenomena explained before clearly follow from figure 6, too. In the region of the Rayleigh wave the stress peaks with their steep gradients can be observed; obviously a tension wave moves in front of a compression wave along the surface as parts of the R-wave, initiated by the pressure pulse.

A similar impression is obtained from the directions of principle stresses in figure 7, with respect to the heading tensile and following compressive stresses at the surface. In this detail of the computational domain (domain III, figure 2) the type of stresses is marked (full line for tension, dotted for compression), and the quantities of the amplitudes are outlined by the line lengths. Towards the slab interior principle tension and compression are approximately of the same amount in pairs and inclined with a  $45^\circ$  angle.

With respect to the crack development to be expected, the following conclusions can be drawn from figures 5 and 6 for the example given here. Within the loaded area a structural disturbance must be assumed depending on the explosion intensity. Beyond, the development of cracks may begin at the subjected surface in the front R-tension wave where the tensile strength or the associated admissible strains are exceeded. These cracks are normal to the surface. When the shear wave immediately passes afterwards the cracks may propagate to the interior in the direction rectangular to the oblique principle tensile stresses. Then they may form a cone opening to the rear face, as familiar from appropriate experiments.

In addition to the before-mentioned stresses the particle velocities in the x,y base directions are presented in figures 8a and b over the domain I. As expected the maxima coincide with the R-wave stress peaks.

Resulting from the stresses and the velocities, the distribution of the energy density  $e = e_{el} + e_{kin}$  follows in figure 9. As already pointed out the strong concentration of energy within the Rayleigh-wave is evident; the maximum values of the S- and the P-wave are exceeded many times. The portion

Fig.8 Particle velocities  $v_x$  and  $v_y$  (domain I,  $t = 215 \mu s$ )

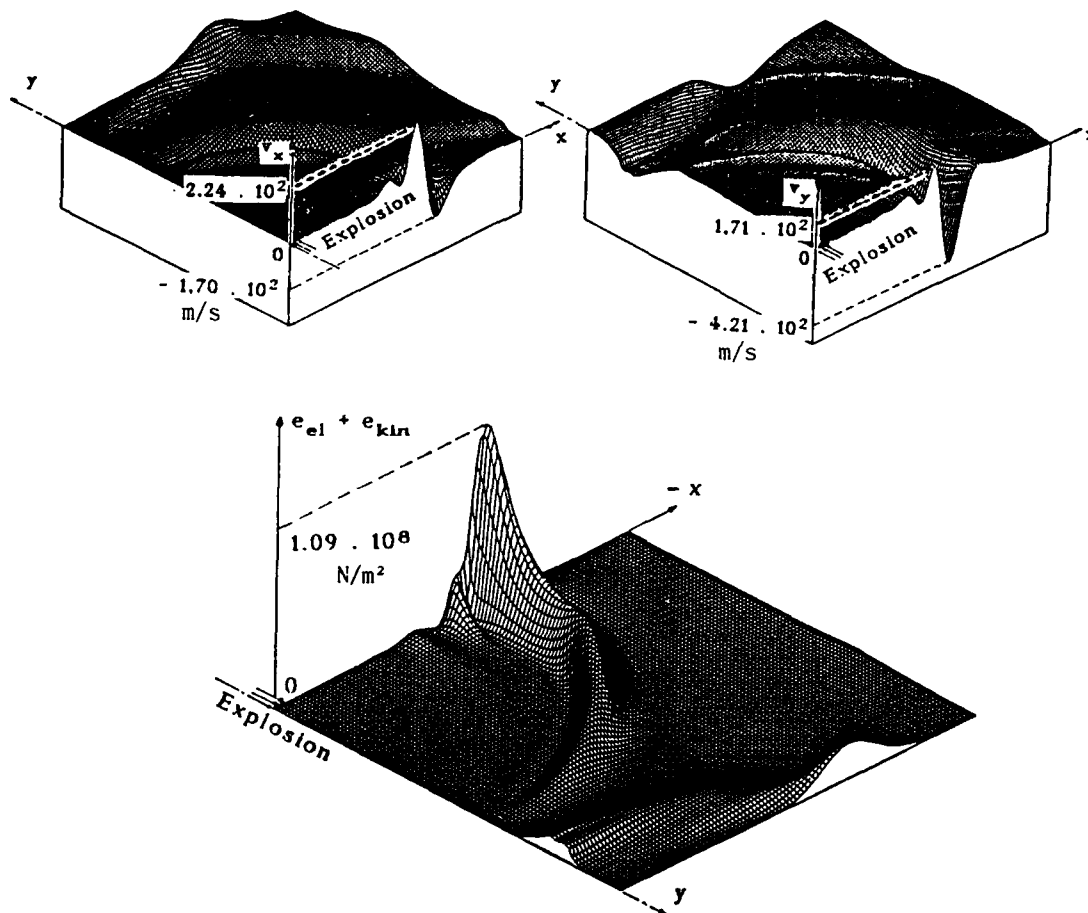


Fig.9 Energy density  $e$  (domain I,  $t = 215 \mu s$ )

included within the R-wave can amount up to 2/3 of the total induced energy according to the pulse shape and the material properties (/5/).

#### 4. Conclusions, further progress

The numerically determined wave phenomena described before in comparison with the experimental measurements proved the computational procedure to be well suited; the calculated results are in good agreement with real effects.

In order to analyse the capacity resp. the state of strain of a subjected structure, the following aspects show to be predominant.

Along the loaded front face the Rayleigh wave is propagating with a high energy intensity, also known from theoretical mechanics. It consists of a combined tension/compression-wave with high amplitudes and steep gradients. Regarding the linear load distribution in the example given here, the R-wave passes over wide structural ranges with approximately unchanged intensity, until the wave is reflected and diffracted at lateral surfaces. With respect to a point load the R-wave must be assumed to decrease with a ratio of about  $1/\sqrt{r}$ , with the distance  $r$  from the load center.

In contrary the surface energy dispersion of all other waves takes place much quicker with a higher power of  $r$  ( $1/r^2$ ).

Because of the extreme tensile stresses as part of the Rayleigh-wave, the crack development will probably begin at the front face where the tensile strength is exceeded. Due to the following shear wave the cracks may propagate to the slab interior in the direction of the principle compressive stresses (region of prevailing shear bands resp. punching cracks known from impact experiments).

Furthermore the strong tension/compression-change due to the passing Rayleigh wave induces a shock-like load into all the instruments attached on the surface, even far beyond the area actually subjected by the impulse.

At the slab rear face, the reflection of the compressive wave by tension may cause the formation of cracks, too, and even may result in material spalling or scabbing.

Considering material with only limited or without linear elasticity (e.g. brittle material as con-

crete), other constitutive relations have to be taken into account within the numerical code using appropriate stress or distortion limits. The only condition for the applicability of the method is that the system of PDE's remains hyperbolic. After the formation of a crack tension in the normal direction is eliminated. This approximately corresponds with the introduction of additional free or contact surfaces into the continuum model.

Relating to the crack propagation with finite velocity, the direction of crack tip propagation could be determined depending on the actual strain situation at the tip (dynamic crack problem). This step would include a combination of the stress theory used herein with an analytical treatment of fracture mechanics.

Thus, the numerical procedure developed on the basis of bi-characteristics method operates under very general conditions. So composite material structures can also be analysed where particular additional wave effects arise especially at the interfaces between the layers.

#### 5. References

- /1/ J. Ballmann/ H.J. Raatschen/ M. Staat: High Stress Intensities in Focussing Zones of Waves.  
in P. Ladevese, Local Effects in the Analysis of Structures; Elsevier, Amsterdam 1985
- /2/ H.P. Rossmanith: Ausbreitung elastischer Wellen in Festkörpern.  
Wiss. Film, 33, Wien 1985; Begleitveröffentlichung zum Film, PWF
- /3/ J. Ballmann/ K.S. Kim: Numerische Simulation von Oberflächenwellen in linearelastischen Festkörpern.  
in Mitteilungen des FKI, RWTH Aachen, Heft 20, 1989
- /4/ Y.C. Fung: Foundations of Solid Mechanics.  
Prentice Hall, 1965
- /5/ K.F. Graff: Wave Motion in Elastic Solids.  
Clarendon Press, Oxford, 1975

# BURIED PROTECTIVE STRUCTURES SUBJECTED TO SURFACE IMPACT LOADING - AN EXPERIMENTAL STUDY

Dr. Michael C.R. Davies

School of Engineering, University of Wales College of Cardiff, U.K.

## ABSTRACT

Experimental and analytical studies of surface impact loading of buried flexible structures are described. In the experimental study instrumented model cylinders were buried at varying depths and subjected to an impact load at the surface. A series of static loading tests were also performed. From the results of each test the dynamic magnification factor and the stresses in the cylinder and the soil adjacent to it were obtained. A method for predicting the dynamic magnification factor is presented. Predicted values were in agreement with those measured.

## 1. INTRODUCTION

In common with all buried flexible structures, buried protective structures have to support the dead loading of the soil providing cover and any live loading at the surface. Live loading can be a static load, moving loads or dynamic loading. Surface dynamic loading may be in the form of a local impulse e.g. as a result of munitions. Loading from munitions may be in the form of an impulse overpressure being applied over a large area of the ground surface, as in the case with large conventional or nuclear munitions, or the kinetic and blast wave components of a localised impulse i.e. a terrorist bomb. There is a necessity to predict response - and ultimately the collapse loads - of buried structures subjected to dynamic loading in order to protect buried structures and vital "lifeline" services from accidental or deliberate damage and, ultimately, to protect life.

Because of the military requirement for field shelters to withstand blast loading, investigations into the dynamic loading of buried structures have tended to concentrate on the effects of dynamic overpressures. Comparisons of the static and dynamic overpressures necessary to cause failure of buried cylindrical shells have been reported by a number of workers in the UK and USA e.g. (1,2,3). An analytical approach using a dynamic version of the finite element method has also been developed (4). The results of this analysis indicated that for buried cylindrical shells of varying stiffness, with depths of cover greater than 0.5 of the radius, a value of 1.2 was obtained for the dynamic magnification factor - the ratio of the maximum dynamic response to the static response of the system. This value compares well with the values of dynamic magnification factor

obtained experimentally (2,3). It was concluded (4) that a dynamic magnification factor of 1.2 could be generally applied in design as a means of avoiding the computational effort involved in a full finite element analysis for each application. However, although there was variation in the stiffness and depth of burial of the structures, the comparisons of the experimental and finite element results were for a single loading boundary condition only i.e. an overburden pressure.

An experimental study was conducted to obtain a greater understanding of the response of buried flexible structures to localized impulse surface loading resulting from conventional munitions. In the study the response to impact loading of structures embedded in soil was investigated. Special attention was paid to the capacity of soil in damping and absorbing impact energy in order to assess the ability of soil to prevent impact loads being transmitted to buried structures.

## 2. EXPERIMENTAL STUDY

### 2.1 Apparatus and experimental procedure

The structure used in the laboratory tests was a brass cylinder of diameter  $d=100\text{mm}$  and wall thickness  $t=0.127\text{mm}$ ; resulting in a very flexible structure. The models were placed in a 1.5m cubic tank, Fig. 1,

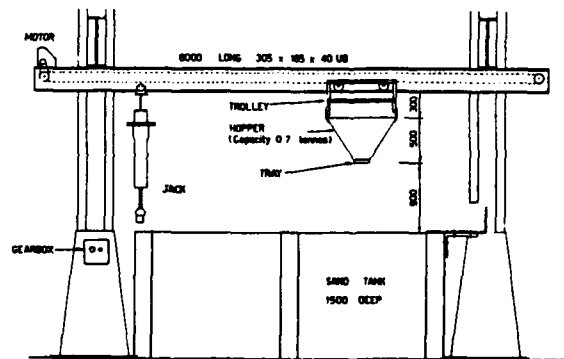


FIG. 1 General arrangement of testing apparatus and buried at varying depths of cover. The cylinders were fabricated from five lengths - joined together with adhesive tape - to span the tank. Segmental construction prevented the instrumented central section from experiencing any end effects (as a result of confinement in the tank); thus ensuring plane

strain conditions for the instrumented section. Circumferential strains in the cylinder wall were measured by 9 pairs of strain gauges (one on the inside and the other outside) positioned symmetrically around the middle segment. Stresses in the soil around the cylinder were measured using miniature pressure cells located in the soil.

A dry sand foundation with a repeatable uniform density of  $16.8 \pm 0.1 \text{ kN/m}^3$  was achieved using a hopper. The 700kg capacity hopper was mounted on rails above the tank, Fig. 1, and driven at a constant rate by an electric motor using a chain drive. A baffle tray fixed below the base of the hopper ensured a uniform rain of sand, which fell through at least 1.0m into the tank.

Two series of buried cylinder tests were performed. The geometry of the models was similar in both cases, as shown diagrammatically in Fig. 2.

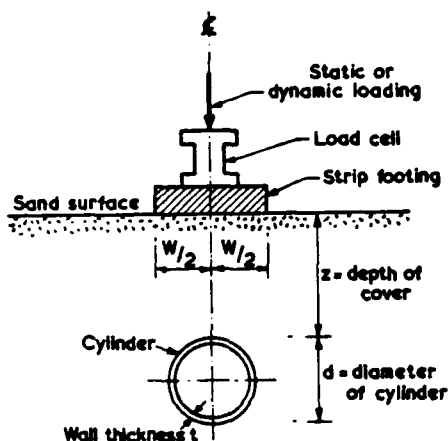


FIG. 2 Geometry of model

Tests were conducted on cylinders buried at different depths of cover,  $z$ . In the first series, the ground surface above the buried cylinder was loaded with an increasing static pressure until the cylinder failed. Surface loading was applied using a hydraulic jack acting on a footing of width,  $W=100\text{mm}$ ; the force acting on the footing being measured using a load cell and the stress in the soil by pressure cells located in the soil immediately below the footing.

The second series of tests repeated the model configurations of the static tests. Dynamic loading of the soil/structure system was an impulsive force provided by dropping a weight (a beam to maintain plane strain conditions) onto the footing. Cylinders buried at different depths were subjected to the same surface impact allowing an assessment of the effects of stress wave attenuation on the structural response.

## 2.2 Results of Loading Tests

### 2.2.1 Dynamic Magnification Factor

The results of the two series of tests were used to quantify the dynamic response of the soil/structure system in terms of a dynamic magnification factor,  $D$ , which for an elastic system this can be shown to be :

$$D = P_S/P_D$$

where  $P_S$  and  $P_D$  are the static and dynamic loads to produce the same structural response respectively.

Values of peak stress recorded at the soil/footing interface in the dynamic loading tests are plotted v. depth of cover in Fig. 3, together with static stresses at the equivalent cylinder responses. The

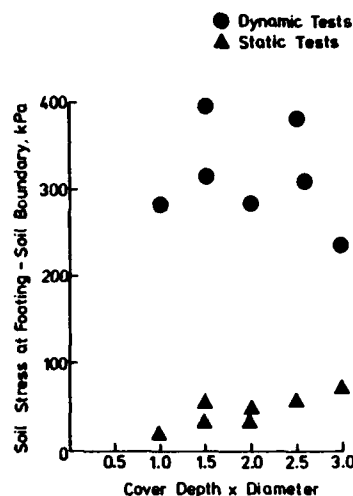


FIG. 3 Dynamic and static soil/footing interface stresses at equivalent cylinder responses

results indicate that to produce the same structural response the peak dynamic stresses were much larger than static values. The dynamic magnification factor for the soil/structure system was  $D=0.15$ . If this value is compared with the dynamic magnification factor for the case of an overburden pressure, i.e.  $D=1.2$ , (1,3,4) it is clearly evident that a large variation in the value of dynamic magnification factor results from a change in loading boundary conditions.

### 2.2.2 Attenuation of Stress Wave

A "free field" test was conducted to investigate the effect of the structure on the stress propagation through the soil. The soil was instrumented with pressure cells located below the centreline of the footing at varying depth. The peak stress recorded in each pressure cell is plotted v. depth in Fig. 4. When elastic body waves are propagating along a cylindrical wave front (as is the case for the plane strain surface loading) attenuation due to geometric damping is proportional to  $x^{-0.5}$ , where  $x$  is the distance from the source of the impact. A curve of this form is plotted together with the results in Fig. 4. The agreement is very good although at greater depths the measured attenuation was slightly greater than that predicted - probably due to the effect of viscous damping.

The results indicate that the stress immediately above the crown of the cylinder was very similar to the free field value, Fig. 4. Pressure cells located adjacent to the springing of the cylinder indicated that at depths greater than  $1.5d$  the lateral stresses were of similar value to the crown stresses. Thus for depths greater than  $1.5d$ , radial stresses acting on the cylinder may be reasonably presented by the

value of free field vertical stress at the crown.

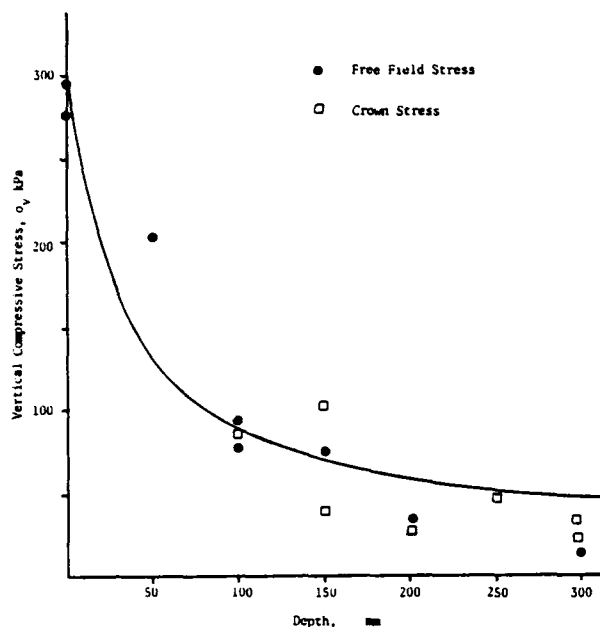


FIG. 4 Attenuation of vertical stress

### 2.2.3 Structural Response

The peak normal (hoop) strains in the cylinder, plotted against half circumference, are shown in Fig. 5. As the cover depth was increased so the distribution of normal strain around the circumference became more uniform, reflecting the more

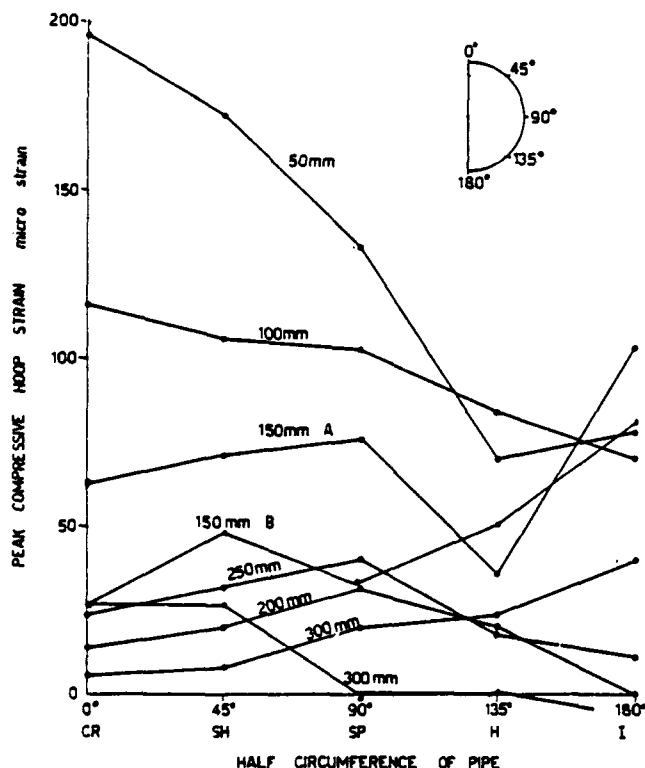


FIG. 5 Hoop strain profiles

uniform stress field (see 2.2.2) with depth. The effect of increased protection with depth of burial may be more clearly observed by comparison of the cylinder crown strains, Fig. 6. With increasing depth of burial the value of peak strain initially

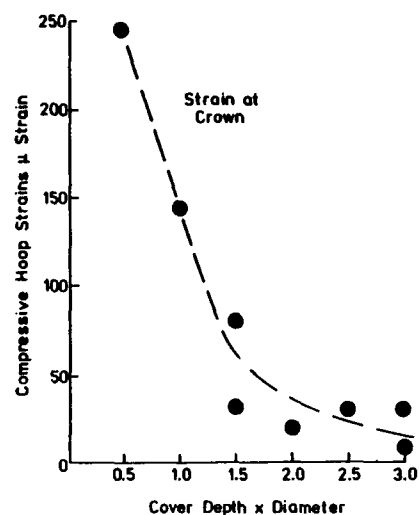


FIG. 6 Decay of hoop strain with depth

decreased very rapidly. At depths greater than 1.5 diameters increasing depth of burial only resulted in a small reduction in measured strain. Thus for the range of cover depths in the experimental programme 1.5d cover appears to be optimum.

## 3. ANALYTICAL STUDY

### 3.1 Method of Analysis

The experimental evidence indicates that if the response of a buried structure to static loading is known it is possible to predict the dynamic response by applying a dynamic magnification factor. The static response of a buried structure may be found either through measurement or predicted using an analytical technique (e.g. (5)). If the dynamic magnification factor for the system can be obtained then the dynamic response may be predicted.

3.1.1 Prediction of dynamic magnification factor, D. Dynamic loading in the experimental study was an impulsive force (in the form of a half-sine-wave) of duration,  $t_1=1.22\text{ms}$ . When considering the response of a system to a dynamic impulse, the maximum response will be reached in a very short time. During this time there will be very little energy absorbed in the system by damping forces. Consequently damping forces will not be considered in this analysis.

A solution has been presented (6) for the dynamic magnification factor, D, of an undamped single degree of freedom subjected to impulsive loading. For the type of impulse observed in the experiments the dynamic magnification factor is given by :

$$D = \frac{v_{\max}}{P_D/k} = \frac{2\beta}{1-\beta^2} \cos \frac{\pi}{2\beta} \quad (1)$$

where  $v_{\max}$  is the maximum dynamic response,  $P_D$  is the peak pressure and  $\beta$  the ratio of the applied load frequency to the natural free-vibration

frequency viz:

$$\beta = \frac{|\omega|}{\omega} \quad (2)$$

In order to calculate the dynamic magnification factor,  $D$ , it is necessary, therefore, to obtain the natural free-vibration frequency of the system under impact loading.

### 3.1.2 Calculation of natural free-vibration frequency, $\omega$

The natural frequency,  $\omega$ , of a free-vibrating system may be obtained using Rayleigh's method. The method assumes that the system deforms at the fundamental frequency - which corresponds to the frequency in the first mode of vibration. The results of a rigorous dynamic finite element analysis (4) indicated that the first mode of vibration was by far the most dominant, supporting this assumption. It is necessary to assume the shape that the system takes up in the fundamental frequency. For an elastic system this may be considered to be the deflected static shape under the same loading boundary conditions as the dynamically loaded system. By assuming the deflected shape the multi-degree of freedom system is reduced to a single-degree of freedom. This also results in the solution for dynamic magnification factor,  $D$ . Equation 1, to be used.

In a free-vibrating system the total energy in the system does not vary i.e. the sum of potential energy,  $V$ , and the kinetic energy,  $T$ , is a constant, hence,

$$\frac{d}{dt} (T + V) = 0 \quad (3)$$

and, therefore, the maximum kinetic energy equals the maximum potential energy. In a free-vibrating system the kinetic energy is a function of the natural frequency, hence, if the mode shape is known this equality may be used to calculate the natural free-vibrating frequency.

If an elastic system is freely vibrating with a frequency,  $\omega$ , the maximum variation of potential energy in the system is given by,

$$V = \frac{1}{2} \int \delta \sigma_i \cdot \delta \epsilon_i \, d \text{ vol} \quad (4)$$

where  $\sigma_i$  is the vector of stresses in the system and  $\epsilon_i$  the vector of maximum strains. The maximum value of kinetic energy of the system is given by,

$$T = \frac{1}{2} \int m \cdot \delta v_i^2 \cdot \omega^2 \, d \text{ vol} \quad (5)$$

in which  $m$  is the mass/unit volume and  $v_i$  the maximum value of the assumed displacement function. By equating Equ. 4 and Equ. 5 the free-vibration frequency may be found from,

$$\omega^2 = \frac{\int \delta \sigma_i \cdot \delta \epsilon_i \, d \text{ vol}}{\int m \cdot \delta v_i^2 \, d \text{ vol}} \quad (6)$$

### 3.2 Analysis of Experimental Results

A program was written to calculate the natural free-vibration frequency of the soil foundation in the model tests. The foundation was divided into elements to form a mesh and for the appropriate loading boundary conditions, the normal and shear stresses

and strains - hence the displacements - for each element in the mesh were calculated using an elastic stress distribution for the free field condition. The value of  $\omega$  was obtained by summing the contribution of each element to the potential energy and kinetic energy for the whole foundation.

The forced frequency due to the impact was 2575 rad/s and the calculated circular natural frequency of the soil 297 rad/s. This resulted in a dynamic magnification factor,  $D=0.23$ . The calculated dynamic magnification factor predicted the trends in the experiments, i.e.  $P_D \gg P_S$ , and was of similar magnitude to the experimentally obtained value of 0.15.

A further assessment of the accuracy of this method for calculating the dynamic collapse pressure of buried cylinders was conducted by predicting experimental results reported in the literature (1). The dynamic loading in these tests was an overpressure provided by an explosion, the blast surface pressure v. time curve being of the typical Friedlander form with a maximum duration,  $t_1=20$  ms. This approximated to a triangular loading impulse, for which there is a solution for the dynamic magnification factor, of a similar form as that in Equ. 2 for sinusoidal loading (6). A dynamic magnification factor of  $D = 1.31$  was obtained from this analysis. This result is consistent with the experimentally obtained value of 1.2 obtained in the experiments (1) and by complex numerical calculations (4).

Predictions of the dynamic collapse pressure of buried cylinders in both the cases presented above are most encouraging. In the experiments described herein the peak value of the dynamic collapse pressure is much greater than the static collapse, conversely, in the overpressure loading tests (1) the peak value of the dynamic collapse pressure is only slightly less than the static value. These trends are modelled well in the analyses. In the impact loading tests the sinusoidal loading was applied over a duration much shorter than the natural period of the soil mass. The impulsive overpressure, caused by the shock pressure wave resulting from an explosion, was a triangular wave form, the duration of which, 20ms, was only slightly less than the natural period of the soil mass (which was calculated to be 28ms). The different loading boundary conditions, i.e. the nature and duration of the impulse, resulted in the varying response.

### 4. CONCLUSIONS

Experimental and analytical investigations have been conducted into the response of buried structures to dynamic surface pressures. The following conclusions can be made:

1. The experimental observations indicated that a dynamic magnification factor,  $D$ , could be used to predict the dynamic collapse pressure from the static value.
2. Geometric damping dominated the attenuation of the stresses in the foundation above the buried structure. Stresses immediately above the crown were similar in magnitude to the free field values.
3. The experiments indicated that 1.5 diameters was the optimum depth of cover.

4. Assuming that the foundation layer vibrates as a single degree of freedom system and the stress distribution is given by the free field response, Rayleigh's method may be used to calculate the free-vibration natural frequency of the foundation. Hence the dynamic magnification factor may be obtained.

5. Dynamic collapse loads predicted from the static values closely followed the trends observed in the experiments, giving reasonably accurate quantitative results.

#### ACKNOWLEDGEMENT

This work has been carried out with the support of the Procurement Executive, Ministry of Defence.

#### REFERENCES

- (1) Bulson, P.S. Stability of buried tubes under static and dynamic overpressure. Part I: Circular tubes in compacted sand, Military Engineering Experimental Establishment, Research Report RES 47.5/7, 1966.
- (2) Marino, R.L. and Riley, W.F. Response of buried structures to static and dynamic overpressures, Proc. Symp. on soil-structure interaction, University of Arizona, Tucson, 1964.
- (3) Albritton, G.E., Kirkland, J.L., Kennedy, T.E. and Dorris, A.F. The elastic response of buried cylinders, U.S. Army Waterways Experiment Station, Technical Report 1-750, 1966.
- (4) Dunns, C.S. and Butterfield, R. Flexible buried cylinders - Part II: Dynamic response, Int. Journal Rock Mech. Min. Sci. 1971, Vol. 8, 601-612.
- (5) Gumbel, J.E., O'Reilly, M.P., Lake, L.M. and Carder, D.R. The development of a new design method for buried pipes, Europipe Conference, Basle, 1982, 87-98.
- (6) Clough, R.W. and Penzien, J. Dynamics of structures, McGraw-Hill, 1975.



# Numerical Simulations of Reinforced Structure Response Subjected to High Explosive Detonation.

J.M. TERRIER      J.F.X. BOISSEAU      SNPE Centre de Recherche du Bouchet  
B.P.02 91710 Vert-le-Petit  
France

January 1989

## Abstract

Within the context of explosive hazard structures, SNPE<sup>1</sup> was led to take an active interest in the behavior of concrete with or without reinforcements under dynamic loadings. The concrete model introduced in the code Dyna2d allows to analyse structures behavior under high dynamic loadings, and to estimate correctly the initial velocities of concrete fragments when a safety wall breaks up.

Most of structures submitted to explosions are verified using pseudostatics methods based on experimental results ( TM5-1300 ; Biggs ; ... ). Since few years new rheological models are able to take into account the non-linearities in material behavior. For the concrete with or without reinforcements few models are able to take correctly into account these non-linearities, specially under high dynamic solicitations.

With the context of explosive hazard structures, SNPE was led to take an active interest into behavior of concrete under dynamic loadings. Sackett's laws introduced in the codes Dyna2d [1] and Dyna3d [2] from the Lawrence Livermore Laboratory have been tested and compared with the pseudostatic-methods. This concrete model includes volume hysteresis (compaction) and will be constructed primarily from Hugoniot data (Gregon). The shear behavior is controlled by a pres-

sure dependent yield stress which has cohesion that is broken by fracture or spall.

The goal of this study is the application of this law to check structures behavior under explosions and to compute fragments velocities at breaking time.

After a short presentation of the concrete model, we will present comparisons computational results with pseudostatic methods achieved on simple structures. If maxima deformations are in good agreements, we will point out that the pseudostatic methods are not able to give realistic residual deformations and in the same way the stresses. On the other hand the model is in good agreement with experimentations.

On the second part of this paper we will present a comparison computed fragments velocities with experimental results.

## 1 Constitutive Model

The concrete model introduced by Sackett into the code Dyna2d allows high dynamic pressure loads. The hydrodynamic formulation connected with an equation of state takes so into account material compaction.

The law part driving the behavior of the concrete is issued from the soil plasticity model developed by L.M. Taylor at the Sandia National Laboratory [3]. The volumetric and deviatoric responses are completely independent.

<sup>1</sup>Société Nationale des Poudres et Explosifs

The mean pressure is updated with a compaction equation of state :

$$P = C(\epsilon_v) + \gamma T(\epsilon_v) E$$

$$\begin{cases} \epsilon_v & \text{volumetric mean strain} \\ C, \gamma, T & \text{parameters} \\ E & \text{internal energy} \end{cases}$$

The mean volumetric strain is computed at each time's step :

$$\begin{aligned} \epsilon_v^{n+1} &= \epsilon_v^n + \Delta t \epsilon_v \\ \epsilon_v &= \frac{1}{3} \text{tr}(\underline{d}) \end{aligned}$$

Tensile failure is assumed to occur if the mean pressure is less than a specified tensile pressure :

$$\begin{aligned} p &\leq p_t^f \\ \epsilon_t^f &= \frac{P_t^f}{K_n} \end{aligned}$$

If the failure criteria is active, the pressure is limited to the value  $P_t^f$  until the mean volumetric strain respect the condition:

$$\epsilon_v \leq \epsilon_t^f$$

On the other case, tests are:

$$\begin{aligned} \epsilon_v \leq \epsilon_{max} &\Rightarrow P^{n+1} = P^n - K(\epsilon_v) \Delta \epsilon_v \\ \epsilon_v \geq \epsilon_{max} &\Rightarrow \epsilon_{max} = \epsilon_v^{n+1} \end{aligned}$$

Unloading is possible from  $P^{n+1}$  to  $P_t^f$ .

For the deviatoric part, the yield surface is assumed for the material which is a surface of revolution about the hydrostat in principal stress space. The radius of the surface about the hydrostat is taken to be a quadratic function of the mean pressure. This surface equation is :

$$\begin{aligned} J_2 &= a_0 + a_1 P + a_2 P^2 \\ \begin{cases} J_2 & \text{second invariant of the stress tenseur.} \\ P & \text{pressure} \end{cases} \end{aligned}$$

Von Mises effective stress is given by :

$$\bar{\sigma}_v^2 = 3J_2$$

The relation between the Von Mises effective stress and the pressure is given by :

$$\sigma_v = \sqrt{3a_0 + 3a_1 P + 3a_2 P^2}$$

$$* a_1 = a_2 = 0 :$$

$$\begin{aligned} \bar{\sigma}_v &= \sqrt{3a_0} \\ a_0 &\geq 0 \end{aligned}$$

The yield surface is a cylinder.

$$* a_2 = 0 :$$

$$\begin{aligned} \bar{\sigma}_v &= \sqrt{3a_0 + 3a_1 P} \\ \Rightarrow \begin{cases} \bar{\sigma}_v^2 - 3a_1(P + \frac{a_0}{a_1}) = 0 \\ P_t^f = -\frac{a_0}{a_1} \end{cases} \end{aligned}$$

The yield surface is a conic.

$$* a_0 \neq 0, a_1 \neq 0, a_2 \neq 0 :$$

A valid set of constants results in a parabola.  $P_t^f$  is the negative root of the following equation :

$$a_0 + a_1 P + a_2 P^2 = 0$$

The deviatoric part of the response is computed as Von Mises effective stress  $\bar{\sigma}$ . The yield condition is checked to determine whether  $\bar{\sigma} \leq \sigma_{yd}$ . If this relation is true, the trial stress is the correct deviatoric stress at the end of the time step :  $S_{n+1} = S^{tr}$ . If the yield stress is exceeded a simple radial return is performed to calculate the deviatoric stress at the end of the time step :  $S_{n+1} = \frac{\sigma_{yd}}{\bar{\sigma}} S^{tr}$ .

Tensile failure is assume to occur if the maximum principal stress (tension is positive) based on the trial stresses exceed a specified tensile strength :  $\sigma_{tr}^{max} \geq \sigma_t^f$ . If failure occur the concrete is assume to be fractured. The material is only able to resist to compressive stress field and shear is limited to an angle of friction.

It is possible to take into account the influence of the concrete damage on the stress tensor. In this case the user has to introduce the variation of the effective stress as a function of plastic deformation including damage effects:

$$\begin{cases} \sigma &= f(D) \\ D &= \int \frac{b_v}{(1 + \frac{b_v}{\sigma_t^f})^{b_1}} d\epsilon^p \end{cases}$$

The reinforcements are modelised with an isotropic steel percentage ( $f_s$ ). The behavior is isotropic elasto-plastic. Reinforcement contribution is taken by :

$$\begin{cases} K &= (1 - f_s)K^c + f_s K^s \\ G &= (1 - f_s)G^c + f_s G^s \\ \sigma_v &= (1 - f_s)\sigma_v^c + f_s \sigma_v^s \end{cases}$$

The concrete model included in the code Dyna3d is quite the same [4].

## 2 Numerical Examples of Structures Behavior

A lot of simple structure elements have been studied under dynamic loadings. Comparisons have been made with pseudo-statics methods (TM5-1300; Biggs ...) and experimental data [4]. We want to present here only the results obtained with a slab under blast effects.

### 2.1 Slab Geometry

The rectangular slab has the following dimensions:

$$\begin{cases} e = 30. \text{ cm thickness} \\ L = 600. \text{ cm length} \\ l = 400. \text{ cm width} \end{cases}$$

Embedded on each side, the slab is reinforced on its two faces in the two direction with  $n^{\circ} 4$  rebar at 20. cm centers.

### 2.2 Applied Loadings

Using all the symmetries we have modelised only one quarter of the slab. The dynamic loadings are issued from charges explosions. These charges are supposed centered on the slab at different levels. The modelling is carried through elementary pressure loadings defined for each elementary area by (24 elementary loaded areas) :

$$\begin{cases} t < t_a \text{ or } t_a + t_o < t & P = 0. \\ t_a \leq t \leq t_a + t_o & P = P_r \left(1 - \frac{t-t_a}{t_o}\right) \end{cases}$$

Three charges have been studied. They give the following pressure loads :

1. loading  $n^{\circ} 1$  :  $P_r = 2.20 \text{ MPa}$   
 $t_a = 1.703 \text{ ms}$   $t_o = 4.732 \text{ ms}$
2. loading  $n^{\circ} 2$  :  $P_r = 3.80 \text{ MPa}$   
 $t_a = 1.485 \text{ ms}$   $t_o = 1.320 \text{ ms}$
3. loading  $n^{\circ} 3$  :  $P_r = 1.53 \text{ MPa}$   
 $t_a = 2.425 \text{ ms}$   $t_o = 10.46 \text{ ms}$

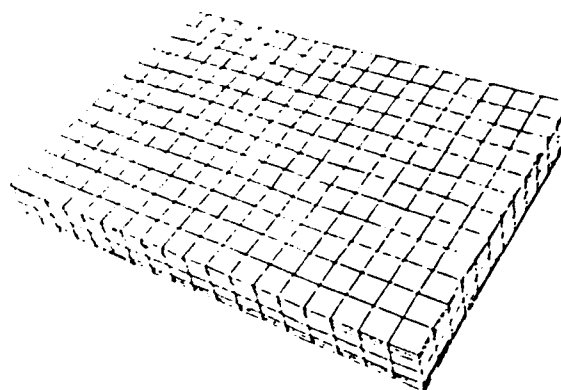


Figure 1: Cell layout for simulation of slab response under blast effect

### 2.3 Modelisation and Materials Characteristics

The modelling was made using four nodes brick elements :

→ 6 in the thickness.

→  $12 \times 18$  on the surface.

The cell layout for the computer simulation is shown in figure 1.

The reinforcements characteristics choosen for this simulation are :

$$\begin{cases} E = 2.1 \cdot 10^5 \text{ MPa} & \text{Young modulus} \\ \nu = 0.3 & \text{Poisson ratio} \\ \sigma_y^c = 0.44 \text{ MPa} & \text{Compression yield stress} \end{cases}$$

The concrete characteristics are :

$$\begin{cases} K = 0.147 \text{ MPa} & \text{Unloading bulk modulus} \\ \gamma = 0. \\ E_o = 0. \\ V_o = 0. \\ P = f(\epsilon_v) & \text{Gregson works} \end{cases}$$

The pressure versus volumetric strain curve for equation-of-state is shown in figure 2.

### 2.4 Results

Dyna results are given table  $n^{\circ} 1$ . They are compared with those obtained with pseudostatics methods and the finite element code EPHYD-3D [5][6].

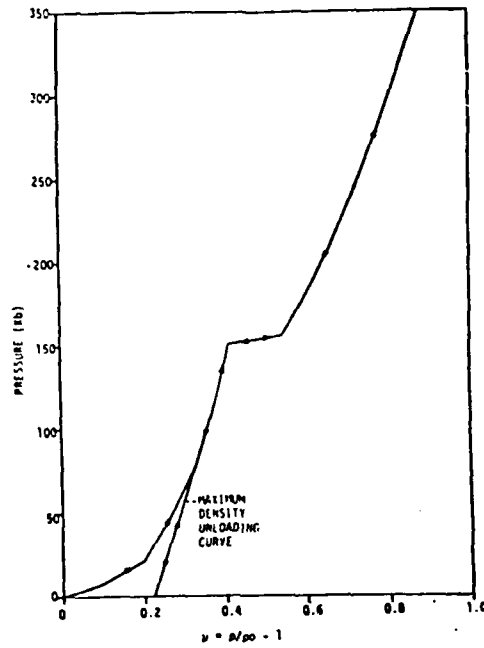


Figure 2: Hugoniot pressure

|             | Slab                       | DYNA3D | EPHYD3D | BIGGS | TM5-1300 |
|-------------|----------------------------|--------|---------|-------|----------|
| Loading n°1 | Maximum displacement (cm)  | 6.9    | 3.6     | 5.7   | 8.6      |
|             | Corresponding time (ms)    | 19.2   | 10.     | 18.   | -        |
|             | Residual displacement (cm) | 6.5    | 0.      | 3.6   | -        |
|             | $\theta_{max}$ (deg.)      | 2.     | -       | 1.6   | 2.5      |
|             | $\theta_{res}$ (deg.)      | 1.9    | -       | 1.    | -        |
| Loading n°2 | Maximum displacement (cm)  | 1.9    | -       | 1.7   | 1.7      |
|             | Corresponding time (ms)    | 12.5   | -       | 10.1  | -        |
|             | Residual displacement (cm) | 1.4    | -       | 0.3   | -        |
|             | $\theta_{max}$ (deg.)      | .55    | -       | .50   | .50      |
|             | $\theta_{res}$ (deg.)      | .40    | -       | .10   | -        |
| Loading n°3 | Maximum displacement (cm)  | 10.9   | -       | 12.5  | 24.7     |
|             | Corresponding time (ms)    | 24.5   | -       | 26.3  | -        |
|             | Residual displacement (cm) | 10.2   | -       | 11.2  | -        |
|             | $\theta_{max}$ (deg.)      | 3.1    | -       | 3.6   | 7.0      |
|             | $\theta_{res}$ (deg.)      | 2.9    | -       | 3.2   | -        |

$\theta_{max}$  = maximum rotation angle

$\theta_{res}$  = residual rotation angle

Table n° 1 : Simulations results.

### 3 Computation of Initial Fragment Velocity due to Wall Failure under an Explosion.

In 1981 the S.W.R.I. (SouthWest Research Institute) have published results on a program to determine the fragmentation characteristics of reinforced concrete and masonry dividing walls subjected to close-in blast effects [8]. Fragment data such as fragment velocities, shapes, sizes, and density downrange were obtained for  $\frac{1}{6}$ th-scale model reinforced concrete walls.

We have decided to compute the behavior of such structures under blast effects to search for the possibility to approach correctly the initial velocity of concrete fragments with numerical simulations.

#### 3.1 Geometry, Boundary Conditions and Materials Characteristics.

The dimensions of the scaled model wall are :

$$\begin{cases} L = 0.46 \text{ m} & \text{length} \\ l = 0.46 \text{ m} & \text{width} \\ t = 0.051 \text{ m} & \text{thickness} \end{cases}$$

The wall was embedded on one side. 14 gage galvanized steel wire was used to simulate the reinforcing bars : 0.21cm wire at 5.1 cm centers.

Material characteristics choosen for this simulation are :

Concrete :

$$\begin{cases} \nu = 0.19 & \text{Poisson ratio} \\ \sigma_t^f = 0.8 \text{ MPa} & \text{Spall strength} \\ a_0 = 155.2 \cdot 10^4 (\text{MPa})^2 \\ a_1 = 1.875 \cdot 10^5 \text{ MPa} \\ a_2 = -221.9 \\ \varphi = 35.^\circ & \text{friction angle} \\ \rho = 2470. \text{ kg/m}^3 & \text{density} \end{cases}$$

The parameters which define concrete compaction equation of state are the same as shown in figure 2.

Reinforcements :

$$\begin{cases} E = 2.1 \cdot 10^5 \text{ MPa} & \text{Young modulus} \\ \sigma_y = 400. \text{ MPa} & \text{Yield stress} \\ \nu = 0.3 & \text{Poisson ratio} \\ E_t = 362.5 \text{ MPa} & \text{Hardening modulus} \\ f_s = 3. \% & \text{Percent reinforcement} \end{cases}$$

#### 3.2 Loadings.

Four configurations have been computed. They are summarized in the following table. The charge type is C4 (91% RDX). Blast characteristics are obtained using the TM5-1300 [7]. It was possible to compute the pressure loads but all the interpretations of experimental results have been made with this manual.

|               | 1     | 2     | 3     | 4      | 5     |
|---------------|-------|-------|-------|--------|-------|
| W (g)         | 226.8 | 226.8 | 453.6 | 1360.8 | 907.0 |
| R (m)         | .152  | .076  | .183  | .320   | .183  |
| h (m)         | .229  | .229  | .152  | .152   | .152  |
| $i_r$ (KPa-s) | 2.46  | 9.86  | 3.38  | 3.45   | 5.10  |

$$\begin{cases} W & \text{charge weight} \\ R & \text{standoff distance} \\ h & \text{charge height} \\ i_r & \text{reflected impulse} \end{cases}$$

#### 3.3 Results

Velocities fields are shown at time 450.  $\mu$ s, for the fourth computations, in figures 5 to 8. At this time the wall is assumed to be completely broken. Fragments emerging from the back side of the wall may be hazardous. Therefore we have retained their velocities. Computed largest velocities of rebar cover and concrete fragments which are assumed to behave like a rigid body (figure 4) are given figure 3. The experimental measurements are reported on the same figure as a function of the reflected impulse.

Nevertheless, comparisons with experimental data show reasonable agreement. Taking into account the results obtained with rebar cover fragments, the largest velocity increases roughly linearly with the reflected impulse applied on the wall. The set of data were curve fit and the resulting linear equation is :

$$V = -4.04 + 8.08 i_r \quad \begin{cases} V & \text{m/s} \\ i_r & \text{MPa.ms} \end{cases}$$

The impulse given by zero velocity corresponds to the necessary impulse to failure concrete.

## 4 conclusions

- This concrete model can represent correctly reinforced concrete structure behavior under dynamic loadings. The deflections are in good agreements between pseudostatics methods and the computations. On the other hand the pseudostatics methods do not predict realistic residual deflections because their don't take precisely into account concrete nonlinearities.
- In munition manufacturing facilities, reinforced concrete dividing walls are used as shields for staff protection and as physical barriers between explosive production steps. Should an explosion occur, the dividing wall may break up under the overpressure loading. Fragments emerging from the back side of the wall may impact an adjacent explosive source with sufficient energy to cause a secondary initiation. In the majority of design applications, the spall fragment velocity is a determining value for the safety zone evaluation. The good simulation of the behavior of such walls allows to evaluate correctly the initial fragment velocities due to concrete failure under blast effects.

### Aknowledgement

This research was supported by S.N.P.E and specially under the authority of the Safety Technical Group (GTS).

## References

- [1] John O. HALLQUIST  
"User's manual for DYNA2D . An explicit twodimensional hydrodynamic finite element code with interactive rezoning ". L.L.N.L. UCID 18756 rev 3
- [2] John O. HALLQUIST - D.J. BENSON  
"DYNA3D user's manual. An explicit three dimensional hydrodynamic finite element code ". L.L.N.L. UCID 19592 rev 3
- [3] D.V. SWENSON - L.M.TAYLOR  
"A finite element model for the analysis of tailored pulse stimulation of boreholes."  
International Journal for Numerical and Analytical Methods in Geomechanics. vol 7 p469-484, 1983.
- [4] J.M. TERRIER  
"Calculs non-linéaires de structures en béton armé ou non-armé soumises à des explosions." Journal de Physique, Colloque C3 DYMAT, Septembre 1988.
- [5] A. CURNIER  
"A crackable reinforced concrete model " Engineering Systems International Report 1980.
- [6] Z.P. BAZANT  
"Finite elements analysis of reinforced concrete" American Society of Civil Engineers. 1982
- [7] M. DEDE - F. SOCK - S. LIPVIN-SCHRAMM - N. DOBBS  
"TM5-1300.Structures to resist the effects of accidental explosions"  
Special Publication ARLCD-SP-84001 Ammann & Whitney Two World Trade Center New York NY 10048.
- [8] L.M. VAHGASY, J.C. HOKANSON, H.W. HINDNER  
"Explosive fragmentation of dividing walls." Jul. 1981, SWRI-02-5793.

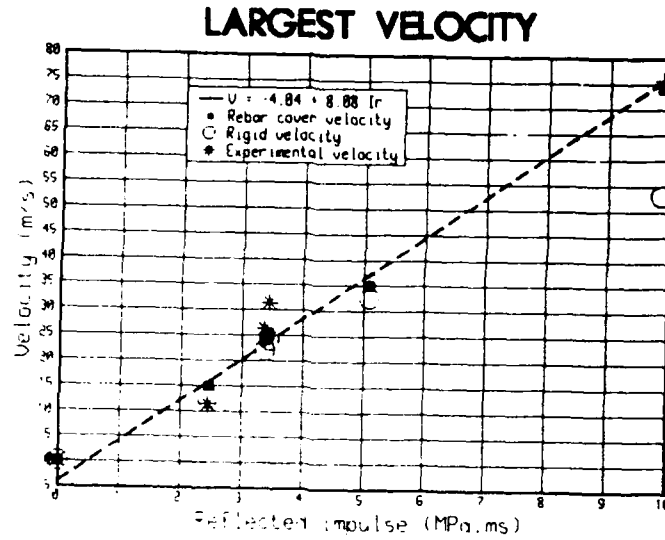


Figure 3: Velocity versus reflected impulse

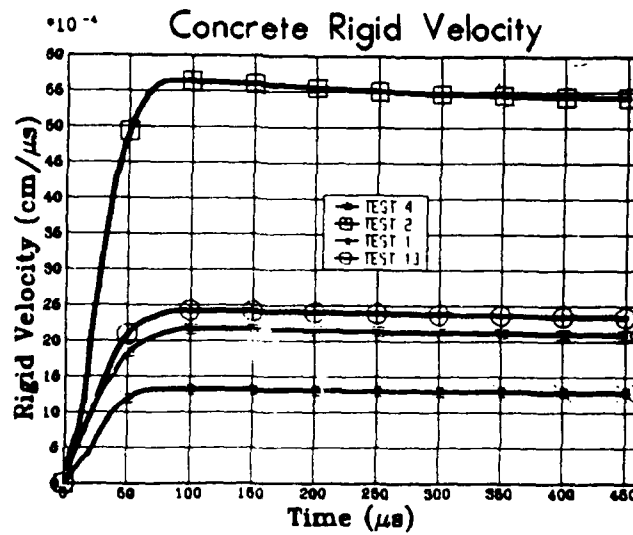


Figure 4: Concrete rigid velocity versus time for tests 1 to 4.

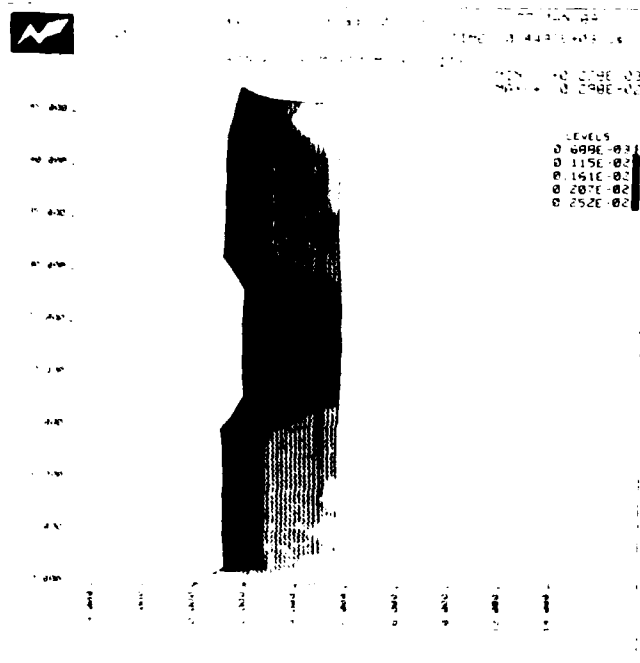


Figure 5: Fringes of maximum velocity. Test 1.

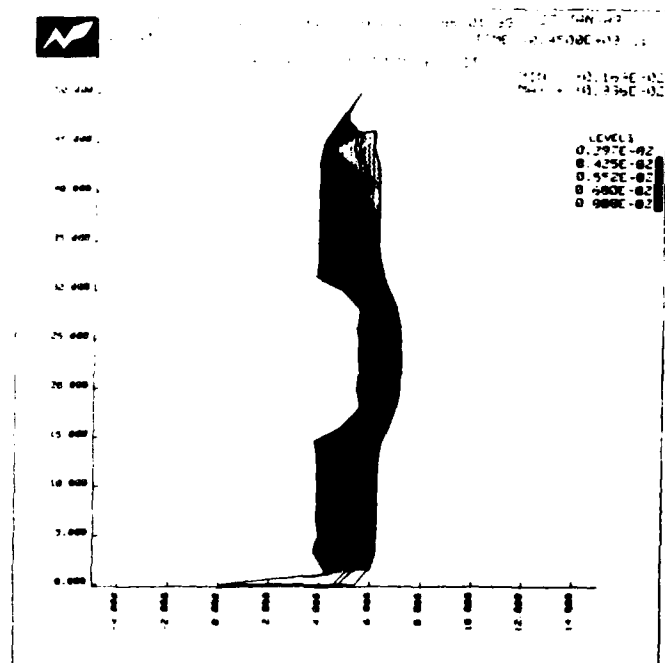


Figure 6: Fringes of maximum velocity. Test 2.

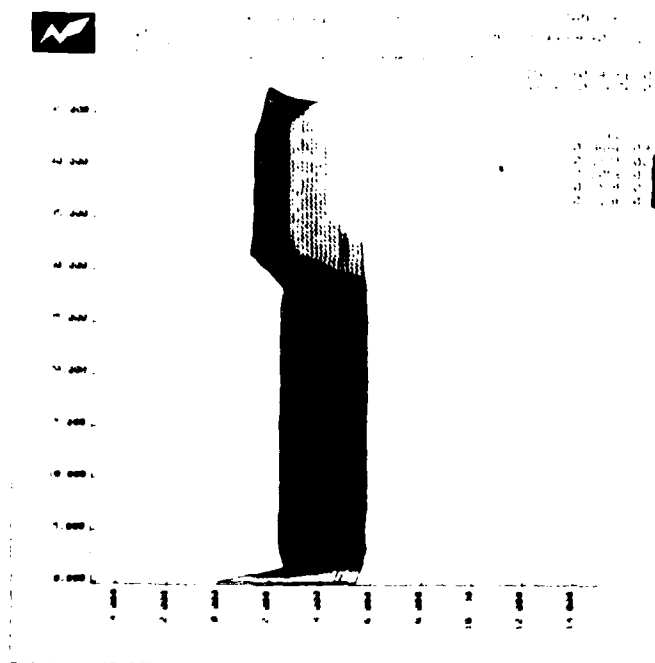


Figure 7: Fringes of maximum velocity. Test 3.

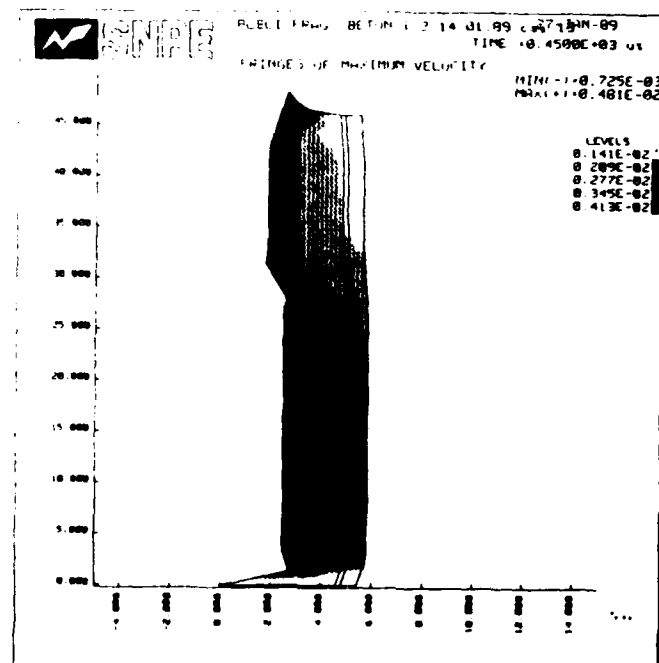


Figure 8: Fringes of maximum velocity. Test 4.



# Large Plastic Deformation of Steel Plates at Impulsive Blast Load

Gerhard H. Guerke

Fraunhofer-Institut fuer Kurzzeitdynamik  
Ernst-Mach-Institut  
Freiburg, West Germany

## Abstract

Large plastic deformation of homogeneous square and rectangular steel plates at high impulsive blast loading has been investigated. The plates were clamped along all edges to a rigid support. The typical pyramidal shape of the test objects proves that the movement is completely different from static loading effects. High peaks of shear force cause tearing off the plates along the support at impulsive overloading. The targets can withstand high impulsive loading only if they are designed in such a manner that tearing off is prevented and large deflection is possible.

Small-scale experiments at plates of  $1 \text{ m}^2$ ,  $1/4 \text{ m}^2$  and  $1/16 \text{ m}^2$  were conducted to find the deformation of homogeneous steel plates as a function of blast impulse. The distribution of blast impulse at the plate's surface was carefully measured. The test results from differently sized plates are in agreement with Hopkinson-Cranz scaling. The observed pyramidal shape of the test objects and the maximum deflection at the plate's center are in agreement with Finite Element structural dynamic calculations. Acceleration, velocity and displacement at any point of the plate as a function of time can be calculated by the code.

## Introduction

Square and rectangular steel plates clamped along all edges to a rigid support are loaded by a very short, uniformly distributed blast impulse. Experiments show clearly that the dynamic motion under impulsive load is completely different from displacement at static loading. A simple explanation may be that any point of the plate moves at a velocity that was imparted by the impulse, until it is stopped by stress that results from the clamping. In contrast to the result of static test, the plates tear off along the support in case of overloading.

In many tests it has proved difficult to carry out direct measurements of the initial deflection of plates caused by a high-explosive airblast environment. In the case of large plastic deformation of steel plates, the final test result can be compared to finite element structural dynamic calculations. If the final results are

in agreement, the transient acceleration, velocity and displacement at any point of the plate as a function of time can be calculated by the code.

Prototype tests at containers built of steel plates as well as model tests have shown a tendency that a whole wall panel will be torn off and thrown away at a remarkable velocity under impulsive overloading. No substantial deformation has been observed before tearing off. High peaks of shear force appear at the support immediately after loading. These peaks are a qualitative explanation of the catastrophic failure behaviour of the plates. It is difficult to quantify the peaks by means of finite element methods: a large number of elements at a small area is needed, together with a small time step. Besides, it is necessary to know the material behaviour at extremely high deformation rates.

## Impulsive Load

Impulsive loading is characterized by the fact that an impulse is imparted to the plate from the reflected airblast in such a short time that no deflection occurs and the material-strength cannot be activated. The impulse load can be replaced by an initial velocity imparted to the mass of the plate by equating the total blast impulse to the change in momentum of the plate. From the initial velocity, the initial kinetic energy is obtained. Equating the initial kinetic energy to the strain energy absorbed by the plate during plastic deformation results in equations that give a suitable theoretical explanation to the experimental results. Dimensionless parameters have been found that allow the application of the model results to prototype dimensions. Equations can be derived to give the impulse asymptote of the P-i diagram for plates.

## Test Arrangement

The test arrangement is shown in Figs. 1 and 2. It looks simple to have just a spherical charge detonated at some distance from a square steel plate that is clamped to a rigid frame. But there are many details that must be taken into consideration in order to obtain reliable results.

The experiments were conducted to find the deformation of homogeneous steel plates as a function of blast impulse. Two parameters of the test object are important: Plate area  $F$  and plate thickness  $d$ . The

quadratic shape has been chosen in order to describe the plate shape and area by just one parameter, the lateral length  $l$ . Only if the two plate parameters  $l$  and  $d$  can be put into one scaled parameter, according to Hopkinson-Cranz similarity, a clear description of the test results can be found.

Some other aspects of the test arrangement are that the impulse must be distributed sufficiently uniform over the plate area, that the frame must be sufficiently rigid and that the edges must be clamped sufficiently strong to the frame. None of these requirements can be perfectly fulfilled. It depends mainly on the experimenter's skill and expertise to find well-balanced conditions that lead to reliable test results.

### Experimental Results

A very obvious experimental result is shown in Figs. 3 and 4. The shape of the impulsive loaded plate can be approximated by a pyramid whilst the static loaded plate results in a spherical segment. It is important to obtain a good approximation by a simple shape, as one needs a method to calculate the amount of strain for the theoretical model that equates the strain energy to the initial kinetic energy. The scaled maximum deflection as a function of the specific loading impulse is shown in Fig. 5. The line in the diagram belongs to the theory.

The validity of Cranz-Hopkinson scaling has been checked by means of 3 geometrically similar test arrangements, as shown in Fig. 6. The  $1 \text{ m}^2$ -plate was 2 mm thick and the 1 kg HE-charge detonated at HOB 0.6 meter above the plate, as shown in Fig. 1. The  $1/4 \text{ m}^2$ -plate was 1 mm thick and the 0.125 kg HE-charge detonated at HOB 0.3 meter above the plate's center. The  $1/16 \text{ m}^2$  plate was 0.5 mm thick and the 0.0156 kg HE-charge detonated at HOB 0.15 meter. All the plates showed similar shape after the tests. The maximum deflection at the plate's center was 100 mm for  $1 \text{ m}^2$ , 50 mm for  $1/4 \text{ m}^2$  and 25 mm for  $1/16 \text{ m}^2$ . The volume of the deformation was 31.5 liters for  $1 \text{ m}^2$ , 4 liters for  $1/4 \text{ m}^2$  and 0.5 liter for  $1/16 \text{ m}^2$ . As a result, the validity of Cranz-Hopkinson scaling was stated.

Another experimental result was that all the cracks start at the center of one side, as shown in Fig. 7. Any state of crack formation can be reproducibly generated, as shown in Fig. 8. Tearing off always happens along the clamped edges. If the plate is hardly overloaded by impulse there is no time for large deformation. A test object with a steep rim and a flat bottom is shown in Fig. 9 that escaped at high velocity before all the kinetic energy imparted by the blast impulse was transformed to stress energy. It is impossible to measure the load function at the testplate itself. Acceleration is very high and pressure gages will be torn off the thin plates or even destroyed. In case of impulsive load, there is a possibility of putting a thick steel plate as a platform into the support and measure the same pressure-time history that appears at the test plate. The test arrangement is shown in Fig. 10. Test results are given in Fig. 11. Only if the impulse is known, the experimental results can be compared to theoretical models and numerical calculations.

### Numerical Results

The displacement along the plate's cross-section from the centerpoint (left) to the middle of one clamped side (right) at 12 instants of motion is shown in Fig. 12. The 2 mm-thick plate of  $1 \text{ m}^2$  square dimension is exposed from top to a uniformly distributed specific blast impulse of  $570 \text{ kPa} \cdot \text{ms}$  at a positive duration of 400 microseconds. It is clear from this diagram that any point of the plate moves down at a constant velocity of 40 m/s until a signal from the clamped edge arrives at time step 1.125 ms at the center. This signal runs at a constant velocity of about 500 m/s from the clamped edge to the plate center. Now the velocity at the centerpoint changes from step to step with a maximum of 80 m/s between time steps 1.875 and 2.125 where a type of "snap-effect" happens. The maximum deflection of 80 mm at the centerpoint is reached at that time. The cross-section forms a straight line from the clamped side to the centerpoint, indicating the pyramidal shape of the deformed plate.

The motion of the plate's center can be studied in more detail from Figs. 13 to 15. It is accelerated during the positive phase of reflected pressure impulse, e.g. for 0.2 millisecond at  $1080 \text{ kPa} \cdot \text{ms}$  the peak acceleration is about 60 000 g (Fig. 13). Then for about 1 millisecond there is zero acceleration until a signal from the clamped edges arrives at the centerpoint. Highest acceleration happens to this point when it is abruptly stopped at the end of plastic deformation. At the time of 1.95 milliseconds about 1000 00 g were calculated. It is easily understood now that direct measurement by accelerometers at that point is extremely difficult.

For the load impulse of  $1080 \text{ kPa} \cdot \text{ms}$  a constant velocity of 70 m/s is reached at the end of the positive duration of 0.2 millisecond (Fig. 14). At 1.2 milliseconds the signal from the clamped edges arrives. It causes a velocity reduction to 45 m/s. At 1.6 milliseconds the velocity changes again and reaches a maximum value of 125 m/s at 1.95 milliseconds. This effect may be understood as an analogy to the motion of the tip of a whip-lash that causes the crack of a whip.

The displacement has been calculated up to 10 milliseconds for specific blast impulses of  $100 \text{ kPa} \cdot \text{ms}$  and  $250 \text{ kPa} \cdot \text{ms}$ . The impulse load of  $100 \text{ kPa} \cdot \text{ms}$  results in a displacement of 25 millimeters at 3 milliseconds that by far exceeds the elastic range. But the elastic energy stored in the plate is big enough to cause a positive deflection of about 10 millimeters at 7.5 milliseconds. There are tests with a plastic deformation in the positive direction of blast loading. That may be understood as the "Instability Phenomenon" in plates subjected to impulsive loading, as discussed in Ref. 4. At the highest load of  $1080 \text{ kPa} \cdot \text{ms}$ , a deflection at the center of about 150 millimeters is reached at 2 milliseconds. Relative small elastic oscillations at 2 millimeters amplitude are calculated. The relative strain belongs to 4.4 per cent for this example. A plate that is clamped to a rigid frame with sharp edges will tear off along the edges at that load. But the loading capacity has been improved up to a relative strain of 40 per cent by means of measures that prevent tearing off. Many

details of the dynamic response of steel plates to impulsive loading can be studied if experimental results and numerical calculations for identical systems are available.

## References

1. Bücking, P. and Gürke, G., et al.  
Experimentelle Untersuchungen zum Versagen schifftechnischer Bauteile unter Blastbelastung, Fraunhofer-Institut für Kurzzeitdynamik, Ernst-Mach-Institut, Bericht No. E 7/87, June 1987.
2. Karhaus, W. and Leussink, J. W.  
"Dynamic Loading: More than just a Dynamic Load Factor", Symposium Proceedings "The Interaction of Non-Nuclear Munitions with Structures", Colorado, May 1983.
3. Mercx, W. P. M. and Harmanny, A.  
"The Normal Mode Technique: A Useful Tool to Investigate the Behaviour of Structures to Local Impulsive Loading", Symposium Proceedings "Die Interaktion konventioneller Munition mit Schutzbauten", Mannheim, March 1987.
4. Iankelevsky, D. Z.  
"Instability Phenomenon in Plates Subjected to Impulsive Loading", Symposium Proceedings "Die Interaktion konventioneller Munition mit Schutzbauten", Mannheim, March 1987.
5. Belliveau, L. J.  
"A Method for Measuring Initial Motions from the Acceleration-Time Records of Shelters Exposed on a High-Explosive Event", Tenth International Symposium on Military Application of Blast Simulation (MABS 10), September 1987.

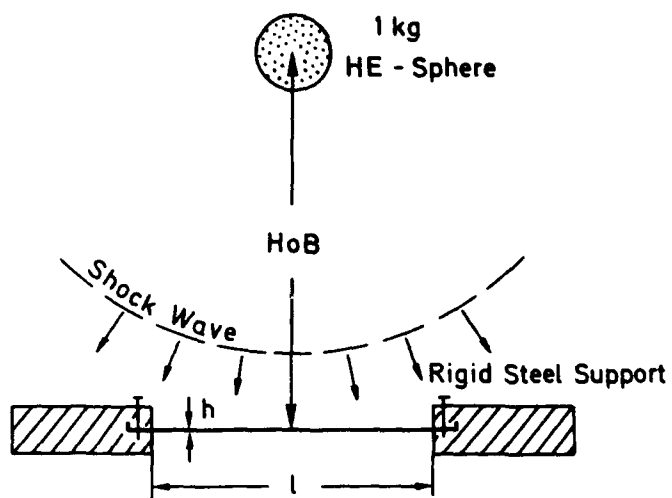


Fig. 1 Test Arrangement:  
Clamped Quadratic Steel Plate  
Parameters:  
Plate Side Length  $l$   
Plate Thickness  $h$   
Charge Height  $HoB$



Fig. 2 The test arrangement - a flat square steelplate 1m · 1m clamped and bolted to a rigid support. The 1kg charge made of plastic explosive is wrapped into thin fabric and detonated at some height above the plate center.

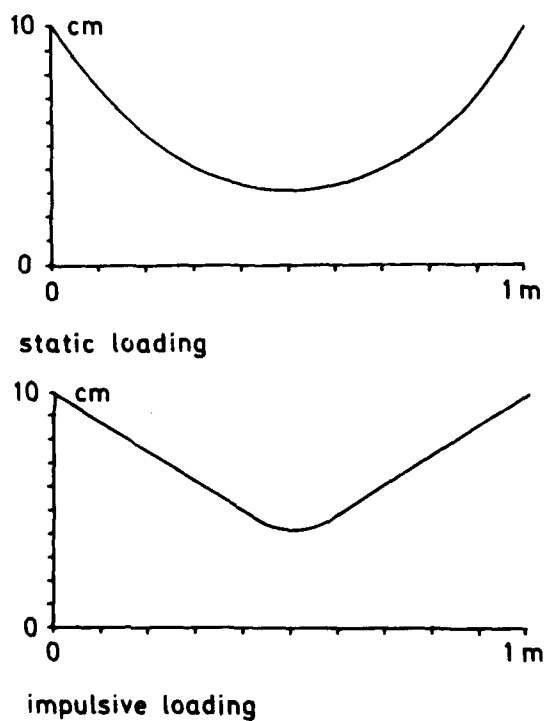


Fig. 3 Typical Shape of Homogeneous Steel Plates at Static and Impulsive Loading

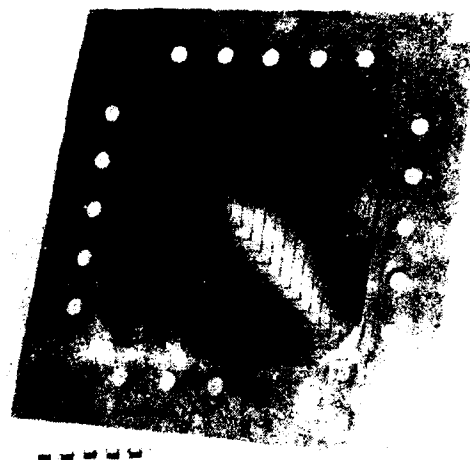


Fig. 4 A clamped square steelplate deforms to a pyramid at high impulsive loading. The straight line pattern at the flat plate remains straight at the pyramid after deformation.

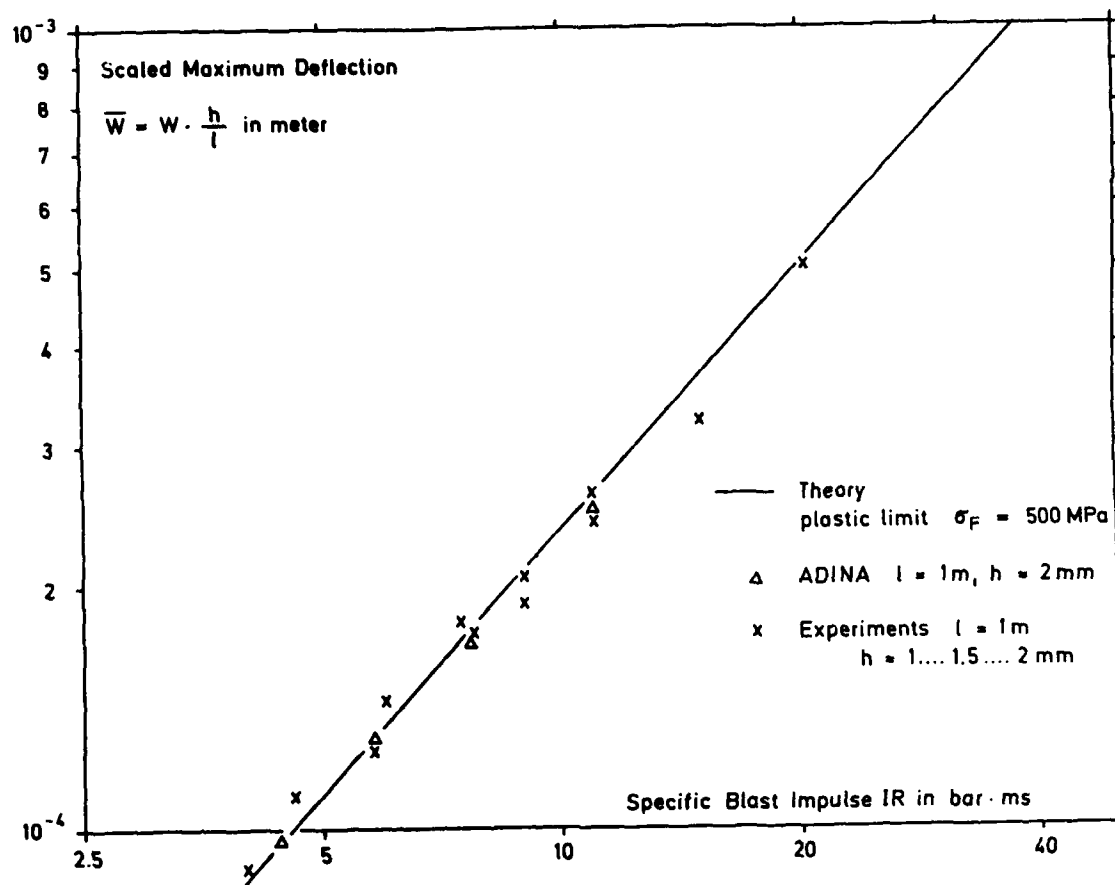


Fig. 5 Scaled Maximum Deflection at Centerpoint vs. Specific Blast Impulse

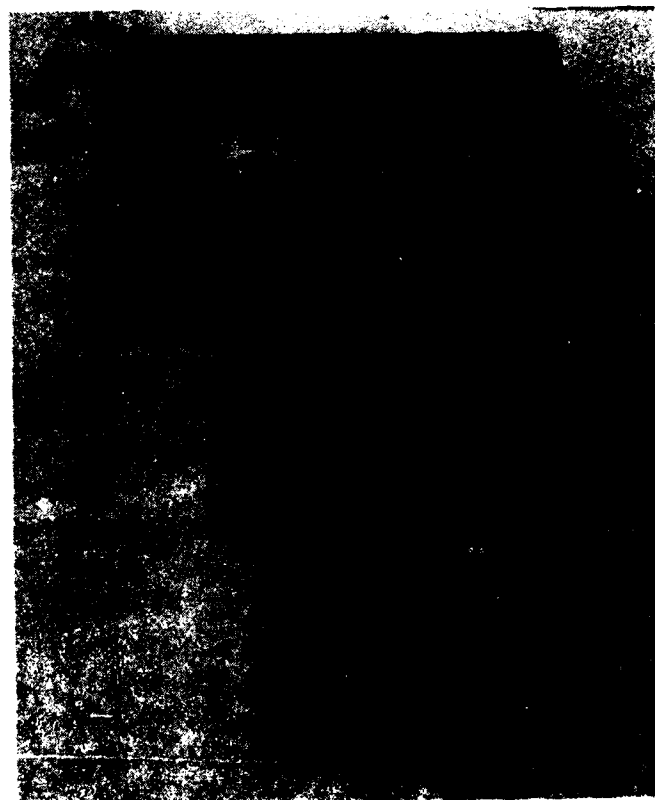


Fig. 6 The validity of Cranz-Hopkinson Scaling has been tested by means of 3 geometrically similar test arrangements  
 $1 = 1 \text{ m}^2$   $0.5 = 0.5 \text{ m}^2$   $0.25 = 0.25 \text{ m}^2$

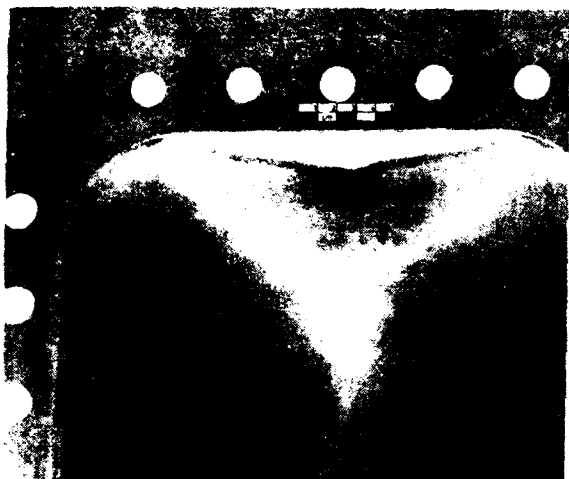


Fig. 7 The crack formation at an impulsive loaded steel plate starts in the middle of one clamped side.

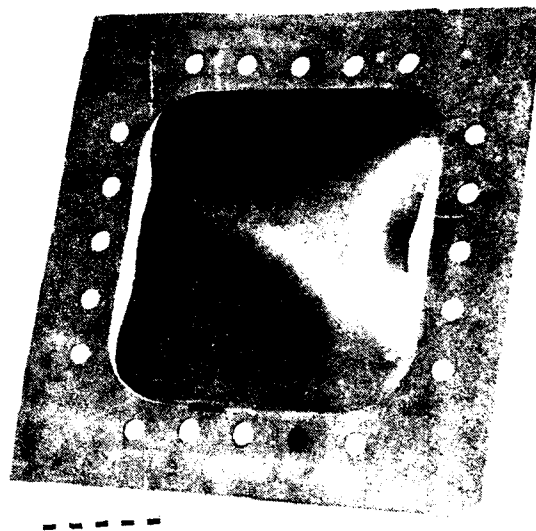
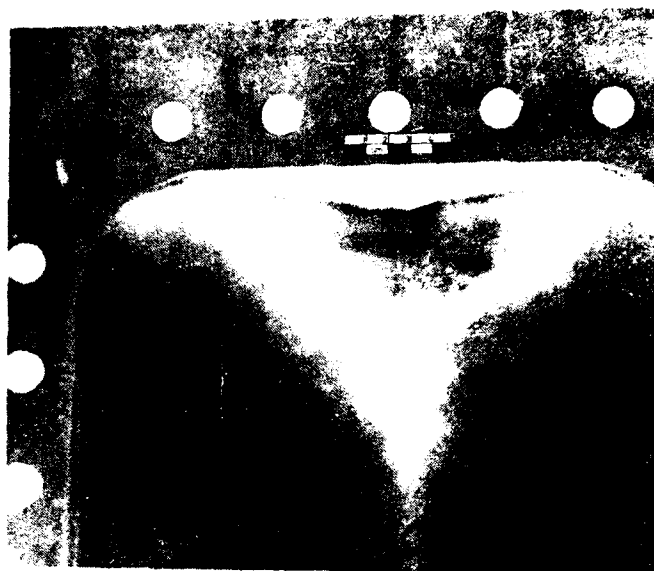


Fig. 8 Any shape of crack - formation can be reproducibly generated at the impulsive loaded steel plates. Tearing off always happens along the clamped edges.



Fig. 9 A plate with a steep rim and a flat bottom that was torn off along the clamped sides before the plastic stresswaves reached the center



Fig. 10

A thick steel plate is put into the support in order to measure the pressure - time history at 11 points at the test object. The load function is calculated from these measurements.

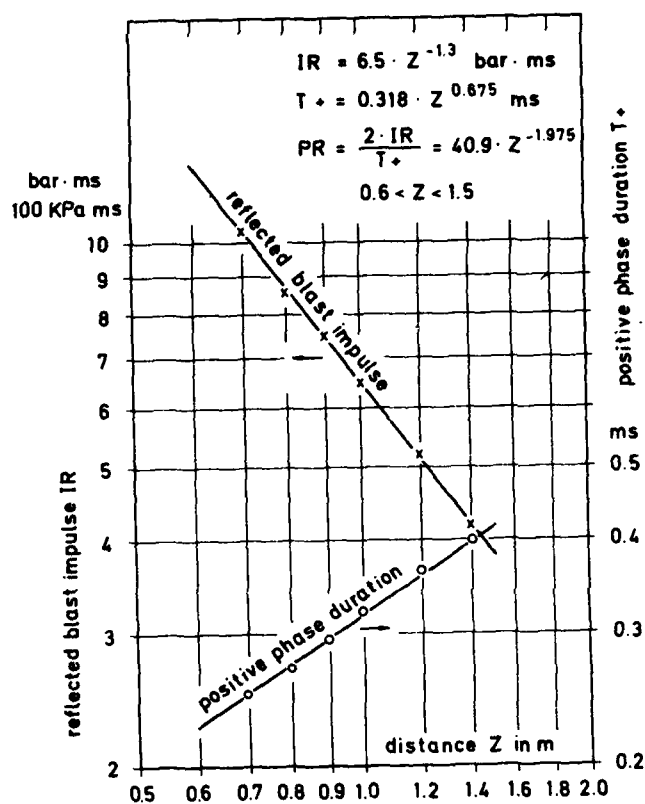
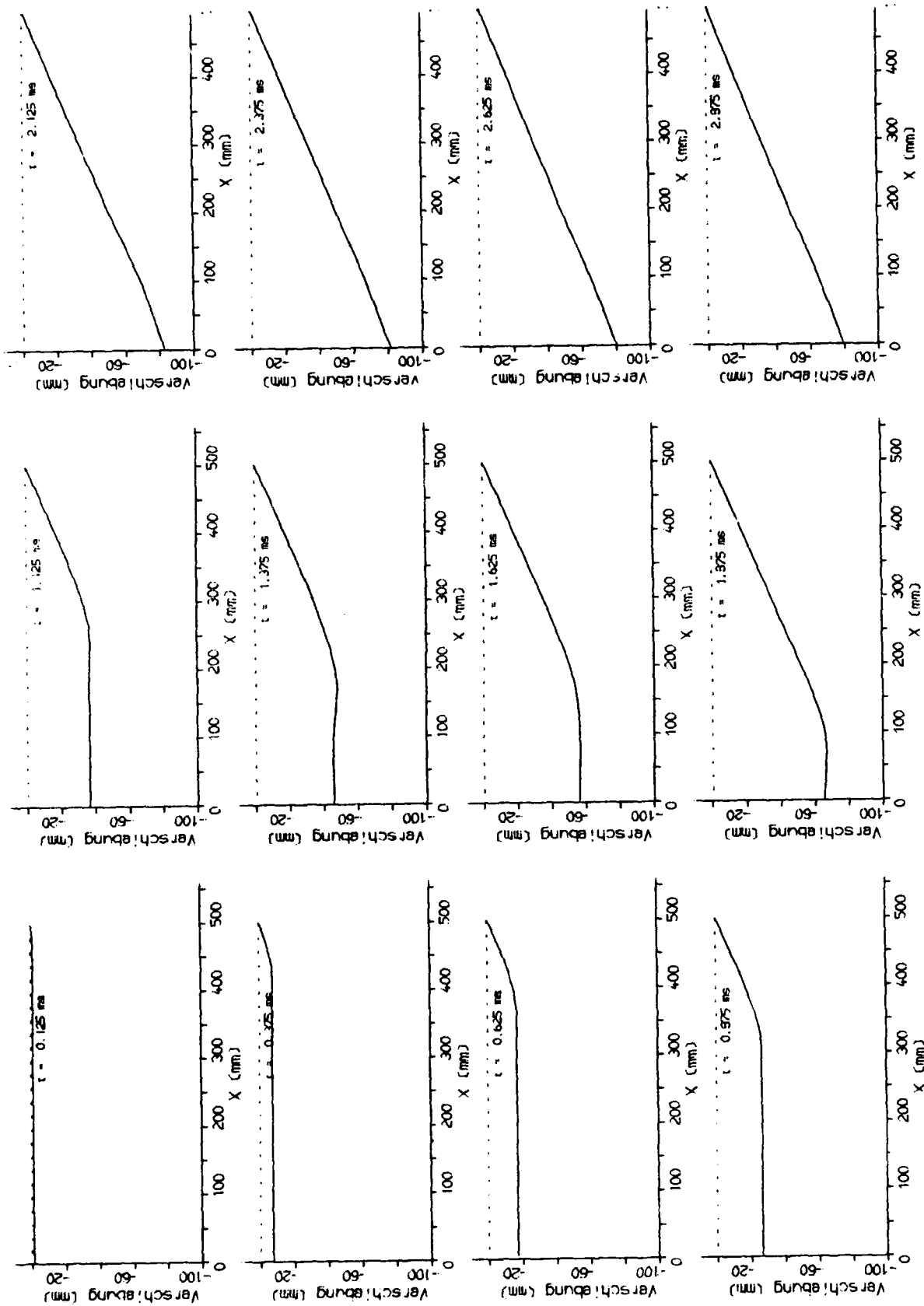


Fig. 11

Reflected Blastimpulse and Positive Phase Duration at the Plate's Surface



The displacement of the plate's cross-section from the centerpoint to one clamped side at different instants of motion.

Fig. 12



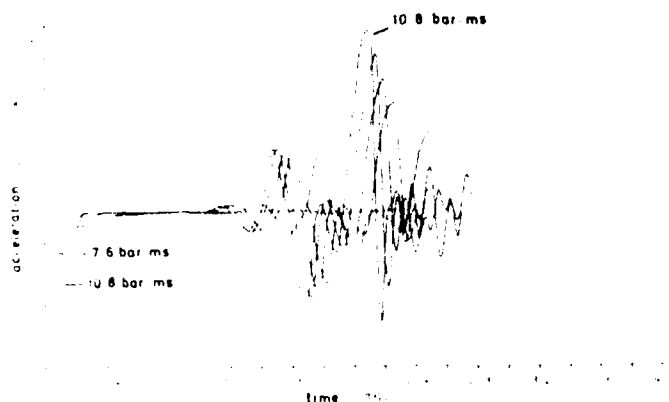


Fig. 13 Acceleration of plate center as a function of time after shockfront arrival for different specific blast impulses ( $l = 1\text{m}$ ,  $h = 2\text{mm}$ )

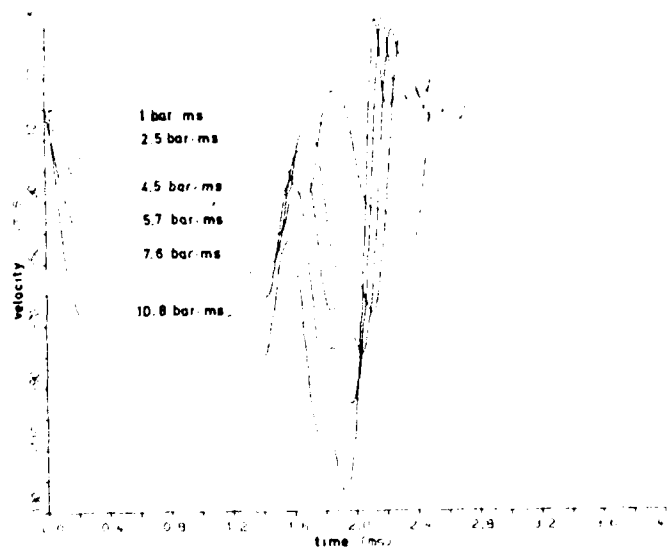


Fig. 14 Velocity of plate center as a function of time after shockfront arrival for different specific blast impulses ( $l = 1\text{m}$ ,  $h = 2\text{mm}$ )

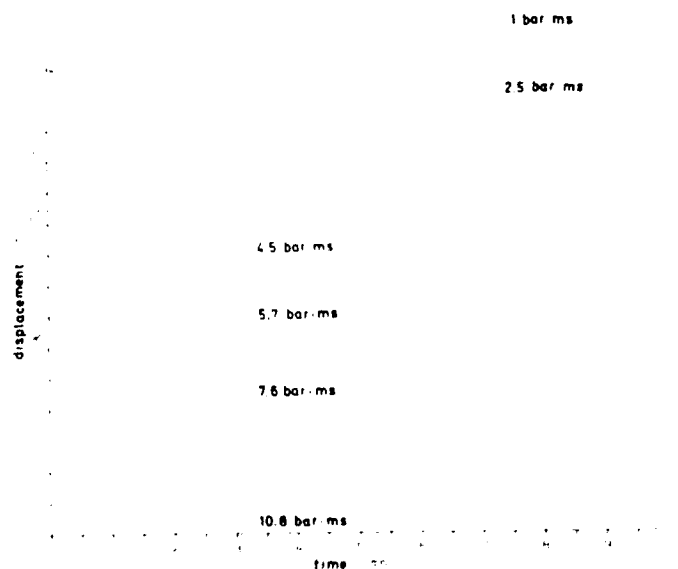


Fig. 15 Displacement of plate center as a function of time after shockfront arrival for different specific blast impulses ( $l = 1\text{m}$ ,  $h = 2\text{mm}$ )

# THE IMPORTANCE OF DYNAMIC REACTIONS IN THE DESIGN OF EXPLOSIVELY LOADED FLEXURAL MEMBERS

THOMAS P. CARROLL

CENTER FOR BLAST RESISTANT DESIGN  
SILVER SPRING, MARYLAND

## ABSTRACT

The purpose of this paper is to alert designers to the importance of dynamic reactions in the design of blast resistant flexural members, and to several instances of paradoxical behavior. Dynamic reactions generally govern the shear design and produce the loading on supporting members. Methods for calculating the dynamic reactions of explosively loaded flexural members are reviewed and dynamic reaction coefficients are compiled for several cases. Two conditions of practical interest are examined. An impulsively loaded flexural member can fail in shear before it has had a chance to respond in flexure. Conditions under which premature shear failure can occur are defined. A detonation, which is very close to a member in relation to its span, can produce pseudo-concentrated loading resulting in (initial) dynamic reactions in a direction which opposes intuition. This apparent anomalous behavior should be taken into account in the design of members and their supports.

## INTRODUCTION

In the design of explosively loaded flexural members, dynamic reactions are needed to determine the required shear strength and to adequately design supports and supporting members. The dynamic reactions of an idealized equivalent single degree-of-freedom system are not the same as the dynamic reactions of the real system. The inertia forces of the member, as well as the distribution of the applied loading, affect the dynamic reactions of the real system and must be taken into consideration. A reasonably reliable method for approximating the dynamic reactions of flexural members which was presented more than 30 years ago (See Reference 1), is discussed below.

The flexural member shown in Figure 1 is subjected to explosive loading  $p(x,t)$ . In response to the loading inertia forces  $I(x,t)$  are produced, which at all times have a spanwise distribution related to the accelerations and deflected shape of the member. The true deflected shape of explosively loaded flexural members has been studied by several researchers (for example, References 2,3, and 4). It is generally recognized that the dynamic deflected shape is not the same as the static deflected shape. However, an approximate

and simple approach to obtaining dynamic reactions is to assume that the spanwise distribution of inertia forces, in dynamically loaded flexural members, is the same as the curve of the static deflection of the member subjected to the same distribution of loading as the explosive load. The dynamic reactions  $V(t)$  can be evaluated by considering the "dynamic equilibrium" of the system and taking into account the relationship

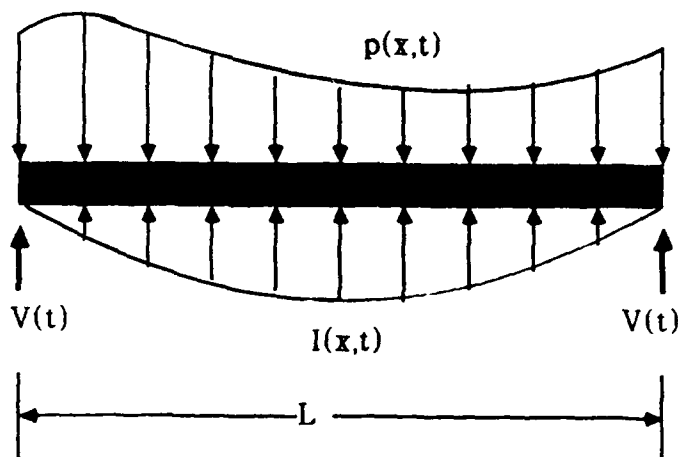


Figure 1 Applied Loading and Inertia Forces in Dynamically Loaded Flexural Member

between loading and resistance  $r(t)$ . The dynamic reactions can be expressed in the form:

$$V(t) = C_r r(t)L + C_p p(t)L \quad (1)$$

in which  $C_r$  and  $C_p$  are "dynamic reaction coefficients" and  $L$  is the span. These coefficients depend upon the distribution of the applied loading, support conditions, member sectional properties, and the strain range (i.e. elastic, elastic-plastic, plastic, etc.). Only elastic response will be discussed here, although the methodology is applicable to all strain ranges. Dynamic reactions for a wide variety of structures and loadings are given in Reference 1, including: beams and one-way slabs; two-way slabs; flat slabs; tee-beams; deep beams; and trusses. Some of these dynamic reactions are also contained in References 5 and 6. Dynamic

reactions for a few selected cases of elastic response of beams are given in Table 1.

Table 1 Dynamic Reactions and Minimum DLF for Support Shears

| MEMBER | DYNAMIC REACTIONS (ELASTIC RANGE) | MIN. DLF FOR SUPPORT SHEARS |
|--------|-----------------------------------|-----------------------------|
|        | $0.39r(t)L + 0.11p(t)L$           | 0.22                        |
|        | $0.36r(t)L + 0.14p(t)L$           | 0.28                        |
|        | $0.78R(t) - 0.28P(t)$             | 0.56                        |
|        | $0.71R(t) - 0.21P(t)$             | 0.42                        |

#### DISCUSSION

Equation (1) shows that the dynamic reactions depend upon the resistance of the member as well as the applied loading, both of which are functions of time. Consider a simply supported beam of uniform cross-section subjected to a uniformly distributed time dependent loading  $p(t)$ . From Table 1, the expression for the dynamic reactions (for elastic response of the beam) at each end is:

$$V(t) = 0.39r(t)L + 0.11p(t)L \quad (2)$$

Note that in the static case  $r = p$  and the reactions are  $0.5p$ , which means that half of the applied loading goes to each support as expected. Also note in Table 1 that the sum of the dynamic coefficients always totals 0.5.

#### Impulsive Loading

Consider the case of impulsive loading (i.e. suddenly applied loading in which the duration is very short compared to the natural period ( $T$ ) of the member). For example, a suddenly applied triangular loading with a duration of  $1/20$  of the natural period of the beam. The maximum "dynamic load factor" (DLF) of the equivalent single degree-of-freedom (elastic) system is about 0.15, and the member could be designed with a flexural

capacity of 0.15 times the peak value of  $p(t)$ . However, equation (2) shows that at the instant the load ( $p$ ) first hits the member, and before any significant resistance ( $r$ ) develops, the reactions at both ends of the beam add to 0.22 times the peak value of  $p(t)$ . This is equivalent to a DLF of 0.22 for the dynamic reactions. The ends of the member must be designed with a shear resistance of at least 0.22 times the peak value of the applied loading. If not, the member-- although adequately designed for flexure--can fail in shear, before it has a chance to respond in flexure. "Equivalent" minimum DLFs for support shears, to prevent premature shear failure, are tabulated in Table 1 for several cases.

#### Concentrated Loading

Another case of interest to designers of protective structures is a very close-in detonation in which the blast loads are distributed over such a short portion of the span that the loading may approach a pseudo-concentrated loading. The expression for the dynamic reactions for elastic response of a simply supported beam of uniform cross section subjected to a concentrated load  $P(t)$  at midspan is given in Table 1 as:

$$V(t) = 0.78R(t) - 0.28P(t) \quad (3)$$

in which  $R(t)$  is the resistance of the member. Note that these two coefficients add to  $1/2$  and that the coefficient for the loading term is negative. The implication of the negative dynamic reaction coefficient is that at the instant the loading is applied (and before any significant deflections take place), the dynamic reactions (and hence the loading on supports and supporting members) are in the opposite direction to what would be expected intuitively based on static considerations. Designers should take this reversal into account in the shear and rebound design of the member as well as in the design of supports and supporting members. Note also that the design for shear would be based on an "equivalent" minimum DLF of  $2 \times 0.28 = 0.56$ . Designers should consider this apparent anomaly in the shear design of the member, in the design of supporting members, and in providing "rebound" resistance. Also note that since the equivalent minimum DLF for support shear is 0.56, premature shear failure is theoretically possible for loads with durations as long as about  $1/5$  of the members' natural period.

#### COMMENTARY

Approaches for estimating dynamic reactions, and support shears presented here do not agree with recommendations given in Reference 7, the manual which replaces TM 5-1300. Special Publication ARLCD-SP-84001 "Structures to Resist the Effects of Accidental Explosions, Volume III, Principles of Dynamic Analysis," Section 3-15 states that "...for short duration blast loads, the support shears can be reasonably estimated by neglecting the applied load. Therefore, the ultimate support shear can be assumed to be

developed when the resistance reaches the ultimate value..." The fallacy of this approach is that for very short duration loads (i.e. impulsive loads), the required ultimate resistance may be only a fraction of the applied load, and as shown herein, the loading term may govern the maximum value of support shears and dynamic reactions.

#### CONCLUSIONS

Dynamic reactions play an important role in the design of explosively loaded flexural members. Actual support shears can be larger than those obtained using traditional Dynamic Load Factor considerations, and instances of premature shear failure are possible. Dynamic reactions and support shears for pseudo-concentrated loading may initially be in a deceiving direction. Dynamic reactions given in References 1, 5, and 6 are a first approximation, but are based on assumptions of (static) deflected shape which may not be valid under explosive loading conditions. Recommendations given in the Special Publication which replaces TM5-1300 could produce unsafe designs for short duration blast loads.

#### REFERENCES

1. "Design of Structures to Resist the Effects of Atomic Weapons," U.S. Army Corps of Engineers Manual EM 1110-345-416, March 1957.
2. Karthaus, W. and J.W. Leussink, "Dynamic Loading: More Than Just A Dynamic Load Factor," Symposium Proceedings, The Interaction of Non-Nuclear Munitions with Structures, U.S. Air Force Academy, Colorado, May 10-13, 1983.
3. Leussink, J.W., Respons van een dynamisch balaste ligger. Analyse op basis van eigentillingsvormen. M.Sc. Thesis, University of Technology, Delft, June 1983.
4. Millavec, William A. and Jeremy Isenberg, "The Response of Reinforced Concrete Structures Under Impulsive Loading," Symposium Proceedings, The Interaction of Non-Nuclear Munitions with Structures, U.S. Air Force Academy, Colorado, May 10-13, 1983.
5. Fundamentals of Protective Design for Conventional Weapons, Department of the Army, Technical Manual TM 5-855-1, 3 November 1986.
6. Biggs, John M., Introduction to Structural Dynamics, McGraw-Hill Book Company, 1964.
7. Structures to Resist the Effects of Accidental Explosions Volume III - Principles of Dynamic Analysis, U.S. Army Armament Research and Development Center, Special Publication ARLCD-SP-84001, Dover, New Jersey, June 1984.

## " A NEW BLAST METHOD FOR CONCRETE BRIDGES "

Prof. Dr.-Ing. D. Kraus

Universität der Bundeswehr München  
Lehrstuhl für Massivbau

### Abstract:

The new blast method is based on the generation of a certain number of hinges in the end-span of a concrete-bridge, that the structure fails as a kinematic system. To produce the necessary hinges, the concrete of the compressive zone is blown out by an explosion. The aim of the present research project is the determination of the necessary amount of explosives for typical concrete bridge-members as deck-plates, webs and bottom-plates.

### 1. Indroduction

The principal idea of the proposed method is the demolition of the end span of a continuous beam by blasting out the concrete.

This can be achieved by creating two hinges in the end span of the girder, which has usually moveable supports.

Due to the resulting kinematics, the beam will bend in and drop off its supports.

In order to obtain the necessary hinges, the concrete of the structure in the compressive zone is subjected to an explosion. This leads to a significant reduction of the concrete's compressive strength. The result is, that the concrete in the compressive zone cannot resist the stresses caused by the dead load of the system.

This method is carried out by the University of the German Federal Armed Forces in Munich and is sponsored by the Ministry of Defence.

### 2. Kinematics of the end span

By means of an explosion a triangular zone of the beam is blown out, which provides the hinges. The size of these triangles depend on the necessary rotation capacity of the so formed hinges and has to be big enough that the beam can drop off the abutment. Fig. 1 shows the arrangement of the hinges. This arrangement is made by taking into account the following criterions.

Hinge (1) in the mid span area is situated at a distance of  $0.3 l$  of the end support. In this section the bridge plate is exposed to relatively high longitudinal compressive stresses, which will increase the demolition caused by the explosion.

Hinge (2) near the inner column is situated at a distance of  $0.1 l$  of the first intermediate support, because usually the bottom plates in this area of a box-girder-bridge are very thick. In addition cross girders, which are usually situated over the bearings, will affect the free reflection area, which is necessary for the blast effect.

The size of the triangular zones can be estimated by the length parameters  $x_1$  and  $x_2$  according to equation (1) and (2).

$$x_1 \approx 2 \cdot d \cdot \sqrt{\frac{a + b}{0,6 \cdot l - a + b}} \quad (1)$$

$$x_2 \approx \frac{x_1}{3} + 1,10 \cdot \frac{c}{l} \cdot d \quad (2)$$

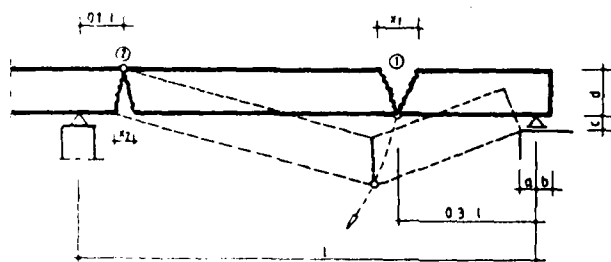


Fig 1: Arrangement and dimensioning of the necessary hinges

It is very difficult to completely blast out the concrete. Also the steel reinforcement will reduce the rotation capacity. This means, the length-variables  $x_1$  and  $x_2$  should be multiplied by a safety factor between 1.5 and 2.0.

### 3. Explosive-Technique

Besides the generation of sufficient kinematics, it is necessary to determine the amount and the arrangement of the required charges.

The intended demolition of the concrete in the compressive zone is based on the principle, that the tensile stresses, induced by the direct and reflected detonation waves, exceed the relatively low tensile strength of the concrete. As a consequence

the concrete is blown out of the steel reinforcement.

The present dimensioning of the charges is based on empirical equations according to /1/. The intention of the current research work is to develop a possibility to define the charge by analytic methods.

Acc. to /1/ the necessary amount of a "demolition charge" can be determined by equation (3):

$$M_{L1} = W^3 \cdot a \cdot c \quad (3)$$

$M_{L1}$  : demolition charge in kg TNT/explosive charge

$W$  : effective radius in m

$a$  : tamping factor  $c=4,5$  for a free untamped charge

$c$  : resistance factor depending on  $W$

| $W$ | $\leq 1,5 \text{ m}$ | $\leq 2,0 \text{ m}$ | $\leq 3,5 \text{ m}$ | $> 3,5 \text{ m}$ |
|-----|----------------------|----------------------|----------------------|-------------------|
| $c$ | 6                    | 5                    | 4                    | 3                 |

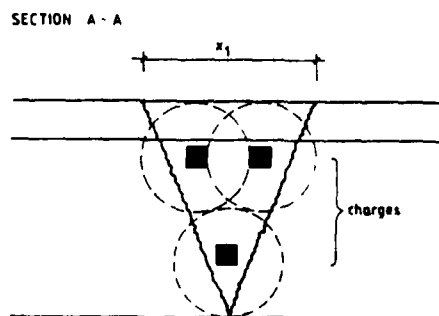
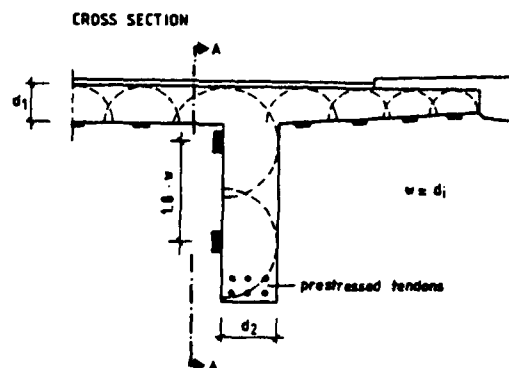


Fig 2: Arrangement of the charges for a T-beam cross section

#### 4. Theoretical Investigations

The effective technical part of the explosive energie depends on the combination of the explosive properties and the mechanical properties of the concrete structure.

The effect of an explosion, beginning in the center of the charge, can be classified in 3 zones:

- (1) The crushing zone within the range of the charge
- (2) The following smashing and cracking zone
- (3) The seismic or vibration zone, where no compression destruction takes place, but where the resistance properties of the material are severely disturbed by irreversible processes

An investigation of the stress conditions of a continuum subjected to an explosion beyond the crushing zone may be analysed by the theory of wave propagation [2], [3], [4].

The 3 equations of motion for an elastic medium, shown in cartesian coordinates, are as follows:

$$\rho \frac{\partial^2 u}{\partial t^2} = \frac{\partial \sigma_x}{\partial x} + \frac{\partial \tau_{xy}}{\partial y} + \frac{\partial \tau_{xz}}{\partial z} \quad (4)$$

$$\rho \frac{\partial^2 v}{\partial t^2} = \frac{\partial \tau_{yx}}{\partial x} + \frac{\partial \sigma_y}{\partial y} + \frac{\partial \tau_{yz}}{\partial z} \quad (5)$$

$$\rho \frac{\partial^2 w}{\partial t^2} = \frac{\partial \tau_{zx}}{\partial x} + \frac{\partial \tau_{zy}}{\partial y} + \frac{\partial \sigma_z}{\partial z} \quad (6)$$

The left part of the equations (4), (5) and (6) describes the inertia forces by d'Alembert and the right part the elastic restoring forces.

The waves of the explosion, propagate in a spherical way, beginning in the center of the charge. They are reflected at the free surface and they will be superposed with the following waves.

The particles of the material oscillate in the same direction as the wave propagation (compression wave) or perpendicular to its propagation (shear-wave).

The compression wave is producing radial compressive stresses and the according tangential tensile stresses (see fig. 3).

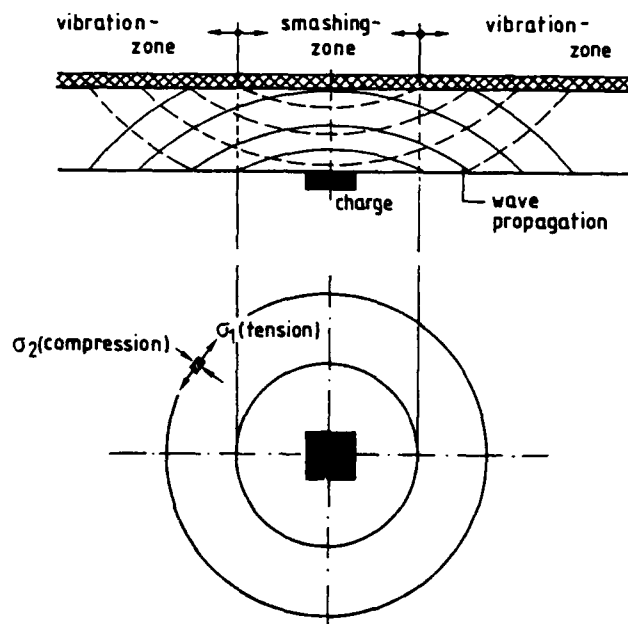


Fig 3: Wave propagation caused by a blast-impact

In order to obtain practical computations, a numerical solution of the wave equations is performed, considering the nonlinear and heterogenous properties of reinforced concrete. It has to be taken into consideration that concrete increases its strength, when it is subjected to a high rate of load application [5]. By means of this solution, it is possible to compute the quantity of charge that is necessary to reduce the compressive strength of concrete.

## 5. Field-Tests

Apart from the theoretical investigations, typical plates of concrete bridge constructions are investigated by explosive field-tests. The stresses existing on the real construction in the compressive zone are produced by extraneous prestressed tendons (see Fig 4).

The following investigations are carried out:

- (1) The reduction of the compressive strength of concrete as a function of the quantity and the distance of the charge.
- (2) Variation of the reinforcing steel.
- (3) Comparison of the theoretical investigations with the measured wave propagation in the vibration zone.

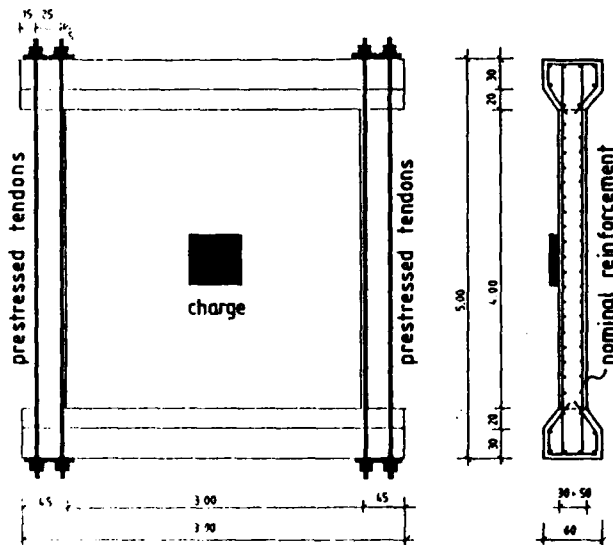


Fig 4: Samples for the field-test

## References

- /1/ "Anwendung für Führung und Einsatz Sprengen" Anw FE 286/200 VS-NfD
- /2/ H. Kolsky "Stress Waves in Solids" Dover Publications Inc. New York, 1963
- /3/ J. Henrych "The Dynamics of Explosion and its Use" Elsevier Scientific Publishing Company New York, 1979
- /4/ W. Johnson "Impact Strength of Materials" Edward Arnold (Publishers) Limited, Landau, 1972
- /5/ M. Curbach "Festigkeitssteigerung von Beton bei hohen Belastungsgeschwindigkeiten" Schriftenreihe des Instituts für Massivbau und Baustofftechnologie der Universität Karlsruhe 1987



# FINITE ELEMENT ANALYSIS OF CIVIL DEFENSE SHELTER SUBJECTED TO BLAST LOAD

Jonas Palm

FortF - Royal Swedish Fortifications Administration  
Eskilstuna, Sweden

## ABSTRACT

The behavior of a civil defense shelter subjected to blast load has been analyzed by using the finite element method (FEM). The response of the above-ground concrete structure was calculated by the SOLVIA code, which assumes nonlinear constitutive laws. Results from the calculations are compared with test-results. It's shown that a large part of the structure has to be analyzed and that it should be allowed to respond not only in flexural and shear modes, but in a compressive/rigid body mode as well. Moreover, separate load-time functions - including separate times of arrival - have to be defined for each node in order to get the load adequately defined. If the analysis is restricted to the front wall, boundary conditions are set to clamped supports and the load is assumed to be uniformly distributed, the results are influenced by artificial stiffness-increases. The concrete modelling by a hypoelastic model and a plasticity cap model, respectively, are discussed.

## INTRODUCTION

Full-scale testing of concrete structures subjected to blast loads are rather expensive and time consuming if several parameters are going to be studied. It is, however, necessary in order to study the overall structural response and to identify material properties of importance. A number of blast-response tests have been conducted on structural members like beams and slabs. By numerical analysis it's possible to reduce the number of tests and to apply findings from calculations of structural members to analyses of full-scale structures. One objective of numerical analyses is to calibrate material models, constitutive equations etc and hereby close the gap between calculated and experimental results. Recently performed blast-response tests at White Sands Missile Range, New Mexico, USA, on an aboveground civil defense shelter /3,4/, now presents results for a full-scale structure for which such calibrations could be executed.

Finite element analysis of a civil defense shelter subjected to long duration blast load has previously been performed at FortF /3/. The objective of this paper is to describe analyses of a civil defense shelter subjected to blast load from high explosives. The use of conventional weapons beside

the blast load normally result in impact by fragmentation. To simplify the analysis only the blast load is studied here. Because of the space limitations only the main aspects can be treated here.

## TEST SETUP

The tests have been extensively reported in /4/, and only a brief description is made here. The structure was designed according to the existing design codes for civil defense shelters in Sweden and Norway. The structure was tested in the 1985 MINOR SCALE Event to verify these design codes. The structure received only minor cracks at the event.

Figure 1 shows plan and elevation views of the structure. Principal wall steel reinforcement ratio at midspan varied between 0.12 and 0.19 percent in the Swedish section. The floor had a comparatively low reinforcement ratio, 0.08 percent. Moreover, the floor face against the soil was unreinforced. All reinforcing steel was Swedish Specification Ks 40 S, having a yield strength of 450 MPa. Tests on concrete specimens showed a compressive strength of 32 MPa for concrete from the casting of the walls and 35 MPa for the floor. At time for the blast load testing Schmidt Hammer-tests showed a concrete compressive strength of 40 MPa.

The charges, placed vertically on the ground, consisted of 29 kg TNT cylinders and 96 kg Mk 82 bombs containing Tritonal explosive. Far-out shots as well as close-in shots were conducted. The far-out shots (scaled distance of  $2.0 \text{ m/kg}^{1/3}$ ) were conducted before the close-in shots (scaled distance of  $0.5 \text{ m/kg}^{1/3}$ ). Fifteen tests were conducted. All but 4 of the tests were instrumented with pressure gages, deflection gages and accelerometers, giving results suitable for comparisons with finite element analyses. However, the exterior pressure gages of the structure were placed at midheight of its walls. In order to get more detailed blast load measurements to put in the finite element calculations some additional blast load tests have been performed at FortF, giving pressure-time histories at 15 gage locations. Some pressure-time data from the gages at the front wall are shown in Figure 2.

## ANALYSIS

The SOLVIA code is based on the ADINA code /10/, which has been frequently used to analyze concrete

structures subjected to dynamic loading /9,16,17, 18,21/. Several important improvements have been implemented in the SOLVIA code; some will be discussed later. The SOLVIA system also includes pre- and postprocessing /6,7/.

In the analysis two different kinds of direct integration methods have been tested. The implicit Newmark integration method and the explicit central difference method, respectively. The former is a so called unconditionally stable method, and the latter is a conditionally stable method.

The explicit analysis is conditionally stable since the time step is limited by the Courant stability restriction. Despite the need of a small time step, the method can be computationally efficient since no stiffness and mass matrices of the complete element assemblage need to be calculated. The velocity of the stress waves vary in a nonlinear analysis. Hence, the time step required can only be roughly estimated; some guidelines can be found in /15,21/. In this kind of analysis the mass matrix has to be lumped.

In the implicit analysis a consistent mass matrix was used in most of the calculations and by Rayleigh damping mass-and/or stiffness proportional damping was included in the analysis. Within each time step equilibrium iterations were performed with the BFGS-method (Broyden-Fletcher-Goldfarb-Shanno). In this kind of analysis the time step can be longer than that required by the Courant stability restriction. It can be adequately estimated if the maximum frequency of the load is known - which can be determined by Fourier-transformation of the load-time function. Moreover, the time step must be small enough to define the arrival time of the load at each node.

#### Concrete model

Two different kinds of constitutive laws have been studied for concrete. The SOLVIA concrete model /6/, and the Drucker-Prager cap model of SOLVIA /6/ respectively. Beside the official version of the former a pre-release version has been tested as well /8/.

The SOLVIA concrete model is a hypoelastic model based on a uniaxial stress-strain relation that is generalized to take biaxial and triaxial stress conditions into account /10/. The model employs three basic features to describe the material behavior, namely (1) a nonlinear stress-strain relation including strain-softening to allow for the weakening of the material under increasing compressive stresses, (2) a failure envelope that defines cracking in tension and crushing in compression, and (3) a strategy to model the post-cracking and crushing of the material. In the solution, the material can be subjected to cyclic loading conditions, i.e., the numerical solution allows for unloading and reloading including deactivation of tensile failures /10/. In the pre-release version several important improvements have been implemented. Examples of such are the tension stiffening effect and a gradual stress release in the strain softening

region /8/. The use of tensile and compressive failure criteria prevents that unrealistically large stress and strain conditions are predicted as can be the case when using some plasticity models.

To overcome such deficiencies of the Drucker-Prager plasticity model a second yield function has been introduced in the SOLVIA code which, in the case of concrete, hardens with increasing hydrostatic compression /6/. This yield function is the cap; so called because it closes the cone in the principal stress space.

In the analysis the concrete strength properties were increased initially according to /14/ to take the strain rate effects into account.

#### Steel model

Tensile tests on unmachined steel bars show a significant influence of strain rate on the mechanical properties. The yield strength, ultimate strength, uniform strain, and ultimate strain increase with increasing strain rate /18/.

Four different kinds of constitutive laws have been studied for the reinforcing steel. (1) Ideal plastic, (2) Plastic linearly strain-hardening, (3) Multi-linear plastic and (4) Strain rate dependent version of (3). Models (1) to (3) are not influenced by strain rate, whereas such influence is taken into account in (4) by a strain rate dependent constitutive equation /6/. In a literature survey, /5/, the maximum strain rate of the tensile reinforcement of concrete structures subjected to blast loads from high explosives was found to be about  $5 \text{ s}^{-1}$ . For this maximum strain rate an average increase in yield strength of 7 % is reasonable, /5, 18/. No limit is set for the inelastic strain in models (1) and (2), whereas a strain-value greatly exceeding the static ultimate strain is set in models (3) and (4) (partially to avoid numerical problems).

#### Soil model

A simplified approach to soil modelling is adopted here. In the z-direction (horizontally according to Figure 2) the soil is modelled by linear springs and dampers. In the x-direction (vertically) two different kinds of soil models were tested. Linear springs and dampers and contact elements which only are transferring compressive forces, respectively. In the latter case a realistic modelling of a (local) deflection upwards of the floor is possible, for instance inside the shelter. When using these contact elements as a soil model the weight of the structure must be taken into account to get the initial compression of the contact elements. The soil properties are set according to /2/.

The FE-model is shown in Figure 2. The concrete part of the structure was modelled by isoparametric 3-dimensional elements. Two different kinds of elements were tested; 8-node and 20-node elements respectively. The reinforcing steel was modelled by truss elements; 2-node elements. In the analysis perfect bond is assumed between concrete and rein-

forcing steel. In reality this doesn't exist. However, since not local strains or discrete cracks are studied a rather coarse mesh is adequate in this respect /15/. The mesh dependence of the results is studied by a 2668 degrees of freedom system, and a 12138 degrees of freedom system, respectively.

To validate the code a one-way slab subjected to blast load from high explosives was analyzed, and results were compared with test-results, /12/. The slab is a plate-strip of a wall of a typical civil defense shelter and its properties are similar to those of the walls of the shelter studied here. Slabs in the test-series have been analyzed in /13/ using an orthotropic elasticity model for concrete, and in /19/ using a plasticity model for concrete. The major findings from the present analyses of the slab were that it was necessary to not only take the "elastic part" of tensile energy absorption capacity of the concrete into account - to yield a stable solution - but the total. This means including that originating from tension stiffening. Concerning modelling of the reinforcing steel it was found that it was necessary with a detailed description of the stress-strain curve. The multilinear plastic model was found to be superior to the other models tested.

In the analysis of aboveground civil defense shelters it's common practice to restrict it to the front wall and to neglect the rest of the structure. In order to get "realistic" boundary conditions often springs and dampers are added. A similar approach was adopted here beside some early analyses which studied the front wall as a slab; simply supported, and with clamped supports, respectively. Hence, the front wall was studied as a slab and the rest of the structure was only taken into account in the sense that its stiffness, damping and inertia were represented by springs, dampers and masses mounted at the edges of the slab. However, the resulting masses at reasonable agreement of calculated and experimental peak displacements were too large to match actual physical properties. Some results of interest, on the other hand, were found in those analyses. By using an uniformly distributed load unrealistically large hydrostatic compressive stresses of the concrete resulted in artificial stiffness-increases. These resulted in higher frequencies in comparison with test-results. When the results of the previously mentioned additional blast load tests were used as input, by defining separate load-time functions for each node - including separate times of arrival - substantially lower stresses were found. As a result the frequencies got lower, but were still about twice as high as those of the test-results.

Detailed studies of the experimental response were made to get a clearer picture of the structural motion. This concerned displacement-time histories, including numeric two-time integrations of acceleration-time data. Although, the latter displacements not always being of top quality, some general trends were found for the test-series. The z-direction displacements, horizontal towards the end wall, became increasingly larger for the AHF1, AHF2

and AHF3 gage locations (located at the floor, see Figure 1). The location closest to the front wall being the most displaced. A similar behavior was found for the roof gage locations. Furthermore, displacements obtained by integrations of acceleration-time data for the center point of the front wall, showed larger values than deflections for the same point obtained by a mechanical deflection gage. (The deflection gage was mounted on the floor close to the front wall in location A, see Figure 1.) This reflects the fact the deflection gage is measuring in a local coordinate system, whereas the accelerometer is measuring in a global one. It was evident that not only the front wall of the structure displaced, but rather the entire structure - or at least a major part of it. This showed that it should be desirable to analyze the whole structure, since one does not generally a priori know the time for maximum response.

Results for the far-out shot (no. 8), using the hypoelastic concrete model of the SOLVIA pre-release version, are shown in Figures 2 and 3. It's obvious from the deformation plots, that not only the front wall is responding to the blast load, but rather the entire structure. Beside the upward deflections of the roof, the floor is partially deflecting upwards as well; reflecting the fact that the floor face against the soil is unreinforced. Response in a compressive/rigid body mode can to some extent be seen as well, but becomes clearer by studying displacement-time histories. Consequently, it had to be taken into account in interpreting the results, that the motion of the structure had a substantial influence on the measured deflections of the front wall, as previously discussed. That's the reason why the difference between the calculated displacement-time histories  $DW_c$  and  $DA_c$  should be compared with the experimental deflection-time history  $DW_e$ . The former being calculated in a global coordinate system, the latter being measured in a local one. The calculated acceleration-time history (for location AHW) shows a somewhat more oscillating shape in comparison with test-results, but seems reasonable. Moreover, the peak acceleration agrees fairly well with that of the test-results; it's about 15 % larger.

After the far-out shot, the calculated results of which just have been mentioned, a close-in shot (no. 10) was conducted at the same front wall. Some simplified analyses were performed for this close in shot (scaled distance of  $0.5 \text{ m/kg}^{1/3}$ ). The tests had shown a shear failure along the lower edge of the front wall. Truss elements were mounted perpendicular to this front wall edge and the edge was modelled to be free to displace from the rest of the structure in the z-direction. The properties of the trusses were defined by having the same "force" at yielding as that of the reinforcing steel in the x-direction. Reasonable agreement with test-results was achieved, but the approach seem to be regarded as a general way of analyzing a very complicated problem. Further refined analyses are planned.

Additional analyses were performed to check the

stability of the code/FE-model at large bending deformations/large plastic reinforcing steel deformations. The blast load data for a Mk 82 bomb test with the same standoff as that of the previously analyzed far-out shot were used as input. The test were conducted with wall Ss as front wall, which had almost identical material properties to wall Se, the same span in the short direction (x-direction), but about twice the span in the long direction. The test-results showed a maximum deflection of 19.0 mm. The calculated results, using wall Se as front wall (being able to use the previously studied model), is shown in Figure 3. The deflections have increased as well as the time for peak deflection, compared to the far-out shot results. This seems reasonable. Because of the dissimilarities only rough comparisons to the Mk 82 bomb tests could be made. The calculated deflections are smaller, which again seems reasonable, taking the shorter span of the studied front wall into account.

### DISCUSSION

It could be argued that the solution is strongly dependent on the properties of the soil model, and that the FE-model in this form bears resemblance to a mass-spring-damper system. However, it turns out by studying the influence of the soil properties, that even if these are set to upper bound values (of the scatter), or to extremely small values, the results only show minor changes compared to those in Figure 3. For extremely large values of the soil properties, the results show some similarities to those of the previously mentioned early analyses, which were restricted to the front wall. Hence, the results were hampered by artificial stiffness-increases. Increases in frequencies and reductions of deflections were partially a result of the increased hydrostatic compressive stresses of the concrete, and partially a result of loss of structural flexibility/compressibility. It was evident that especially the flexibility of the floor had to be taken into account to get realistically low frequencies. The modelling of the soil with contact elements, only transferring compressive forces, proved to be useful to obtain these results.

Still the calculated results show somewhat higher frequencies than the test-results. To some extent this could be explained by a rather coarse mesh, but similar results have been found in other FE-analyses /15,20,22/. It's, however not reasonable to use a too fine mesh for the concrete models studied, since these describe the macroscopic concrete behavior. In such cases a locally arising stress peak, which is larger than the tensile strength, can result in a crack that propagates and causes failure of the entire structure /15/. Moreover, experimental values of the tensile strength are evaluated for the total cross-sectional area, and the stresses can be substantially larger locally, e.g. in the aggregate. The stresses vary over a cross section. Provided that their mean value is smaller than the tensile strength, failure doesn't occur in a real test. Normally the minimum element length shouldn't be set smaller than 2-3 times the maximum

aggregate diameter, /15/.

Another possible reason to the comparatively high frequencies is the energy dissipation to the soil not being modelled to realistically high values by the dampers in the soil model. This is something that not yet have been explicitly studied.

Comparisons of results for 8-node elements and 20-node elements showed that the 8-node element gave a better definition of the blast load, especially for its time of arrival at each node (for a given number of degrees of freedom). Furthermore, the 8-node element is more suited to explicit analysis. For large bending deformations, on the other hand, the use of one 20-node element in the cross direction of the structural members can result in a somewhat more stable solution. In general terms, however, the differences were small.

The refined hypoelastic model shows better agreement with test-results than the Drucker-Prager cap model, which results in comparatively smaller deflections and higher frequencies. However, the choice of input to the models is complicated by the fact that (to the author's knowledge) few results exist for the triaxial stress behavior of concrete under high strain rates /1/, particularly for unloading/reloading. This is especially true for the cap model since the entire cap concept is governed by input of triaxial stress properties - the initial position of the cap, as well as its hydrostatic compression dependence. However, the use of static triaxial stress properties can still be appropriate, as shown in /15/.

Numerical instability can arise in an explicit analysis if the Courant stability restriction is violated. As a result, for instance an artificial crack can develop in the concrete. Then the crack will be present throughout the analysis. A similar crack can occur in an implicit analysis - if the time step has been chosen too optimistically - but the equilibrium iterations will "close" the crack and assure a stable and accurate solution (provided that the convergence tolerances are tight enough). It's necessary to model the tension stiffening effect to yield a stable solution. In implicit analysis it could either be represented by the constant,  $\eta_N$ , in the stiffness matrix for cracked concrete, or - more physically relevant - by  $\alpha$  of the tension stiffening effect itself. In explicit analysis, however, the tension stiffening effect only can be modelled by the latter, since no stiffness matrix is entering the equation of motion. In order to develop a feel for a FE-model in an initial analysis, the constant,  $\eta_N$ , is a suitable way of simulating the tension stiffening effect. To present knowledge little is known about the strain rate dependence of the concrete triaxial ultimate tensile strains (uniaxial tests indicate increases with increasing strain rate, /14/). Instead of using  $\alpha$  set to uniaxial values, in such an analysis, the use of a the constant,  $\eta_N$  - set to values according to /16/ - results in a considerably more stable solution. This, furthermore, implies the comparatively "safe" approach of implicit analysis, but explicit analysis can be extremely computatio-

nal efficient - and by obeying its restrictions - the results can be satisfactory.

#### CONCLUSIONS

The numerical results obtained indicate that the present FE-model is capable to satisfactorily predict the response of the shelter subjected to blast load. The concrete has to be adequately modelled to yield a stable solution. A realistic modelling of the reinforcing steel, on the other hand, is of utmost importance to obtain agreement with test-results.

Generally speaking many uncertainties are inherent in the analysis of full-scale structures. Still the present analyses have provided insight in a complex problem. It's obvious that a large part of the structure has to be analyzed, and that it should be allowed to respond not only in flexural and shear modes, but in a compressive/rigid body mode as well. Moreover, separate load-time functions - including separate times of arrival - have to be defined for each node in order to get the load adequately defined. If the analysis is restricted to the front wall, boundary conditions are set to clamped supports, and the load is assumed to be uniformly distributed, the results are influenced by artificial effects. These include inertia-reductions and stiffness-increases, respectively. Beside the obvious reason for the former, the latter partially is a result of loss of structural flexibility/compressibility, and partially by unrealistically large hydrostatic compressive stresses of the concrete.

#### ACKNOWLEDGEMENTS

The assistance provided by Mr. Gunnar Larsson, and Mr. Jan-Anders Sundberg, SOLVIA Engineering AB, Östra Ringvägen 4, Västerås, S-72214, Sweden, is gratefully acknowledged.

#### REFERENCES

- /1/ BAKHTAR, K. et al, Concrete material properties, TerraTek Research, DNA Concr. Meeting, 1985
- /2/ PHILLIPS, B.R. et al, Geotechnical investigation for Direct Course and related events, Rep. SL-86-18, Waterways Exp. Station, Vicksburg, 1986
- /3/ VRETLAD, B., Joint Swedish-Norwegian Civil Defense Shelter, Fort F/F, C1:86, Eskilstuna, 1986
- /4/ WRIGHT, R.S. et al, Blast Response Tests of a Swedish-Norwegian Structure, C8:87, 1987, *ibid*
- /5/ PALM, J., On Concrete Structures Subjected Dynamic Loading, in Swedish, to be publ., 1989, *ibid*
- /6/ SOLVIA-PRE 87, SE 87-1, SOLVIA Engineering AB, Västerås, 1987
- /7/ SOLVIA-POST 87, SE 87-2, *ibid*
- /8/ BATHE, K.-J. & SUNDBERG, J.-A., A Concrete Material Model, Computer Modelling of Reinforced Concrete Structures, Pineridge Press, 1986
- /9/ BUTLER, T.A. & BENNET, J.G., Nonlinear Response of a Post-Tensioned Concrete Structure to Static and Dynamic Internal Pressure Loads, *Comp. & Struct.*, Vol. 13, Pergamon, 1981, pp 647-659
- /10/ ADINA, AE 84-4, ADINA Engineering, 1984
- /11/ BATHE, K.-J., Finite Element Procedures in Engineering Analysis, Mass. Inst. of Tech., 1982
- /12/ JOHANSSON, I., Försök med enkelspända betongplattor utsatta för luftstöt vågsbelastning, FOA Rapport C 20256-D4(A3), Stockholm, 1978
- /13/ NILSSON, L. & JOHANSSON, I., Analys med Finit Element Metod av Luftstöt vågsbelastade, Enkelspända Betongplattor, C 20204-DA(A3), 1977, *ibid*
- /14/ CURBACH, M. Festigkeitssteigerung von Beton bei hohen Belastungsgeschwindigkeiten, Diss., Massivbau Baustofftec., Heft 1, Univ. Karlsruhe, 1987
- /15/ SCHLÜTER, F.-H., Dicke Stahlbetonplatten unter stossartiger Belastung, Diss., Heft 2, *ibid*
- /16/ HOCH, A., Trag- und Formänderungsverhalten von Stahlbetonbalken bis zum Bruch bei grosser Belastungsgeschwindigkeit, Diss., 1983, *ibid*
- /17/ DESNOYERS, J.F. et al, Impact Behaviour of Concrete Beams with Corroding Reinforcing Steel, 9th Conf. SMIRT, Vol. H, Balkema, 1987, pp 277-284
- /18/ HERTER, J. et al, Nonlinear Finite Element Analysis of Reinforced Concrete Beams, Concrete Structures under Impact and Impulsive Loading, BAM, Berlin, 1982, pp 455-471
- /19/ MIKKOLA, M.J. & SINISALO, H.S., Nonlinear Dynamic Analysis of Reinforced Concrete Structures, pp 535-547, *ibid*
- /20/ STANGENBERG, F., Shock Induced Response of Structural Systems, Struct. Analysis and Design of Nuclear Power Plants, Porto Alegre, 1984, pp 87-98
- /21/ STEBERL, R., Berechnung Stossartig Beanspruchten Stahlbetonplatten mit Endochronen Werkstoffgesetzen, Univ. Berlin, Werner-Verlag, 1986
- /22/ DARGEL, J., Zur Rechnerischen Analyse von Stahlbetontragwerken unter Stossartiger Beanspruchung, Diss., TH Darmstadt, 1984

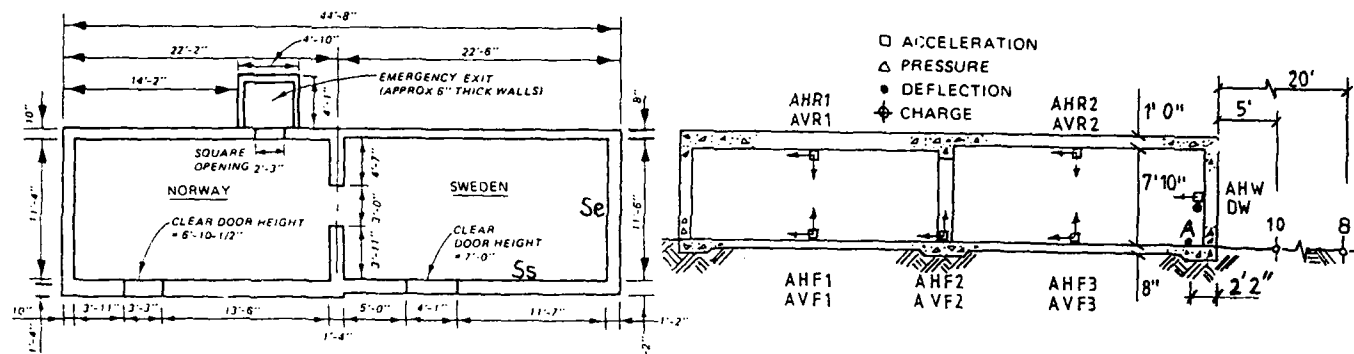


Figure 1. Plan view, elevation view, and gage layout. Point A indicate position of the deflection gage mounting

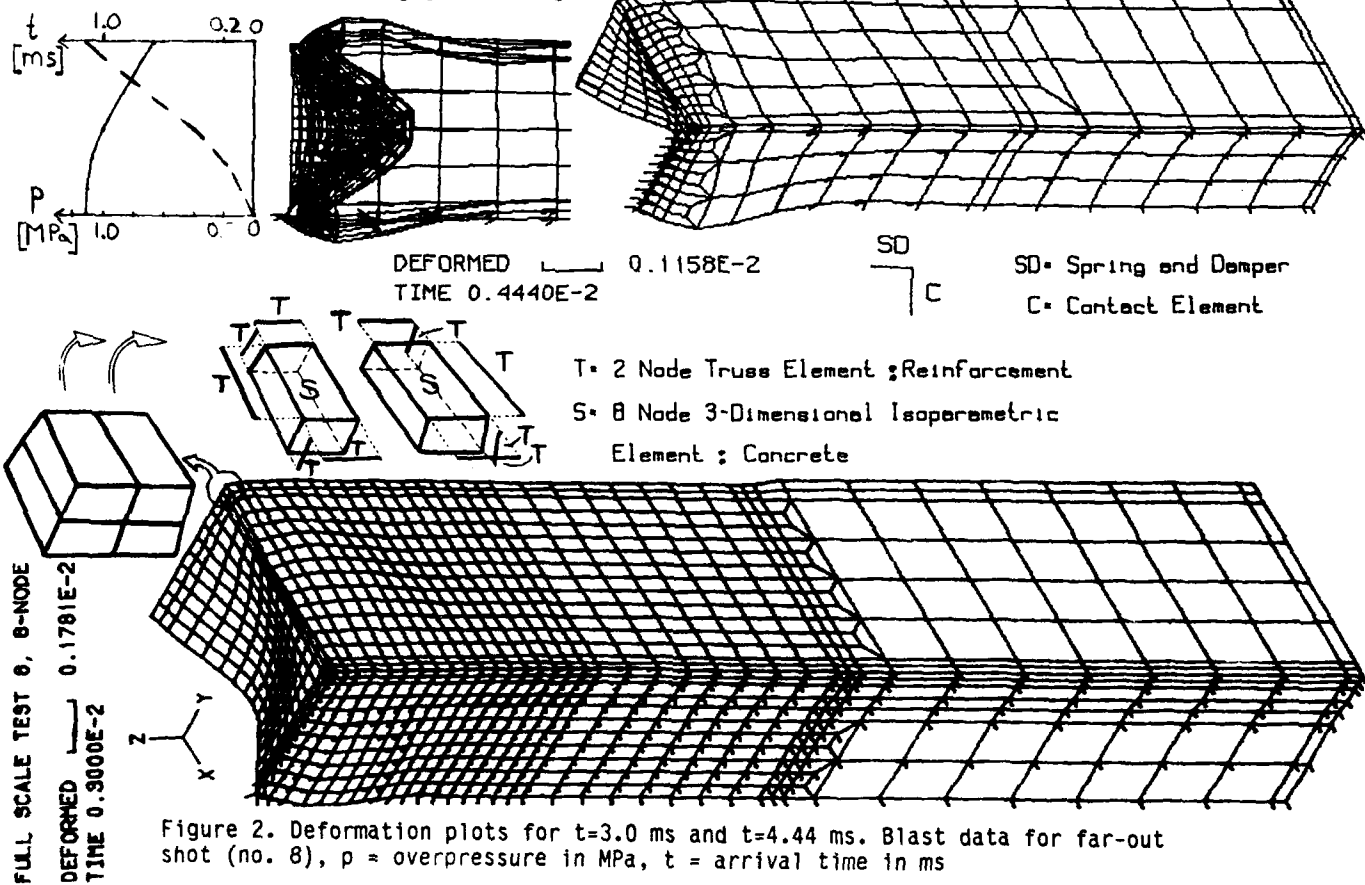


Figure 2. Deformation plots for  $t=3.0$  ms and  $t=4.44$  ms. Blast data for far-out shot (no. 8),  $p$  = overpressure in MPa,  $t$  = arrival time in ms

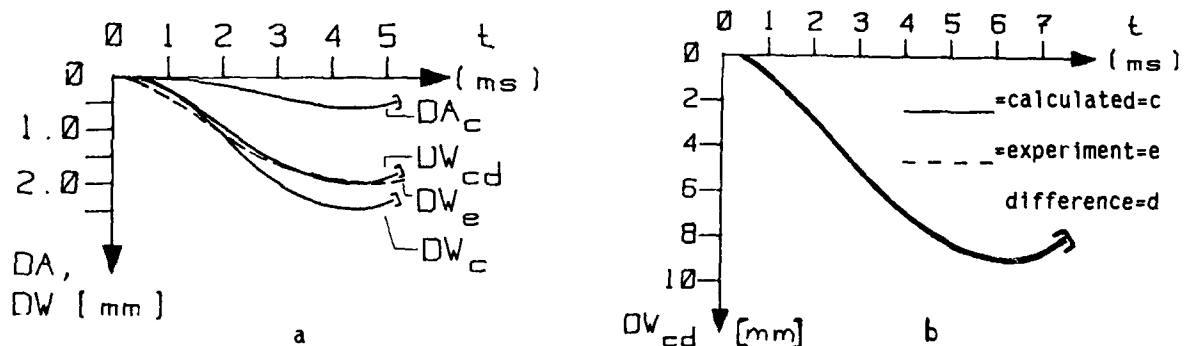


Figure 3. Displacement-time histories for far-out shot (no. 8) fig a, and Mk 82 bomb test, fig b, respectively. Calculations are performed in a global coordinate system and deflection measurements in a local one. This explains why the "difference history"  $DW_{cd}$  should be compared with the experimental  $DW_e$ . Note that no experimental displacement-time history exists for point A, located according to Figure 1. This should be taken into account in comparing the time for maximum displacement

The Normal Mode Technique: applications for  
the analysis of transient loaded structures.

W.P.M. Mercx

Prins Maurits Laboratory TNO  
P.O. Box 45, 2280 AA Rijswijk, The Netherlands

1 ABSTRACT

The application of the Normal Mode Technique in the linear analysis of structural response yields analytical solutions, which are compared with a simplified analysis method. A brief overview of the technique is given, with references of publications about this subject that were presented during former symposia.

Solutions for the response of cases beyond the application range of the simplified method are shown. The benefit of the application of the technique in non-linear and finite element calculations is demonstrated. Subjects in linear analysis which require research effort are discussed.

2 INTRODUCTION

The application of the normal mode technique (NMT) in the analysis of the response of transient loaded structures is not very common, although the method has been known for some time. The reasons for this limited use will be discussed in the following text.

In Norris et al. 1959, the technique is used for the verification of a simplified analysis method which calculates the deflection, bending moments and support reactions with a single degree of freedom (SDOF) system under the assumption of the static deflection shape. It was concluded that the simplified analysis was accurate enough in the calculation of the maximal values of the quantities for those cases where the quotient of the load duration and the lowest natural period exceeds the factor 0.4. Lower values for this factor were not to be expected in practical problems.

As the NMT can only be applied in linear systems, the use in blast resistant design, in which the non-linear structural and material behaviour are of main importance, is not very obvious.

This restriction to a linear (elastic) system becomes less important if one realizes that the first stage of the response of a structure will be elastic and that the outcome of this early time response determines the next, possible non-linear stages. As it is known that on the one hand highly peaked stress waves can occur due to an impulsive loading (Leussink and Karthaus, 1983) and that on the other hand material properties are rate dependent (Weerheijm and Karthaus, 1985), the outcome of the elastic early time response cannot easily be predicted.

There are however also cases for which the quotient of load duration and first natural period is smaller than 0.4, for instance structures loaded with an explosion at small distance. Here the simplified analysis cannot be applied.

Finite element codes (FEC) could be applied in order to study the elastic response but in cases where wave propagation becomes important, these codes are less suitable. Also, the correct choice of the element size and time step, to describe the high frequency response accurately, is a problem.

Here is where the NMT comes into the picture. By using the technique to resolve the equations of motion, analytical expressions can be found for the response of beams and plates with different support conditions, loading configurations and loading histories. These expressions are almost free of numerical approximations and, because of the relatively small computer effort, they can be used for extensive parameter studies.

This paper briefly describes how the analytical expressions were found and describes how they contribute to a better insight in the dynamic response. Applications are shown and restrictions are discussed.

3 SUMMARY OF THE METHOD

The NMT consists of the splitting up of the place function of the applied load into a number of contributions which correspond with the normal modes of the structure. Because of the orthogonality of the modes, each component is independent of the other, and each loading component will only activate the corresponding normal mode. The total response can be found by adding up all individual response components.

A first attempt to analyse the phenomenon of shear and bending moment waves, travelling through structures under impulsive loading, was made with an analytical solution of the Timoshenko equations of motion (Leussink and Karthaus, 1983). This was done for a simply supported beam subjected to a uniformly distributed load with a triangular shaped pulse with zero rise time and variable duration.

The method was generalized for plates as well as for different support conditions (Merckx and Harmanny, 1987). It appeared to be also possible to generalize the place and time function of the load and to introduce damping. In order to do this, the rotatory inertia was disregarded. The result of this exclusion was that, instead of two groups of natural frequencies as appear with the Timoshenko theory, now only one group appears which almost coincides with the first Timoshenko group. The disregarding of the rotatory inertia has almost the same effect on the total response as the discounting of the second Timoshenko group which is often done. The advantage of disregarding the rotatory inertia is the consistency of the model which is not present if the second group is disregarded.

In the next chapter a comparison is made with the simplified analysis method as is often described in technical literature.

#### 4 SHEAR FORCES

In simplified blast resistant design the structure is schematized to a SDOF system (for instance Norris et al., 1959). Under the assumption of a deflection shape (usually the static or lowest normal mode shape), load- and mass factors are derived in order to adjust the displacement of the system with the maximal deflection of the real structure. Under the assumption that the distribution of the mass inertia has the same shape as the deflection, the support reactions can be calculated from the equilibrium of forces. As the maximal shear force in the structure is often equal to the support reaction and as wave propagation is recognized, it is proposed to use the maximal support reaction as the design shear force for the whole structure.

By using the abovementioned method, the support reaction is a function of time and consists of contributions of the applied load and the resistance of the structure. The resistance at a certain point of time is conceivable as the static load that would cause the same deflection as exists with the dynamic system at that point of time.

In this paper the results of the NMT will be compared with the SDOF system for a simply supported beam for the sake of simplicity and recognizability, although other support conditions are possible as well. For a uniformly distributed load the support reactions are:

$$V(t) = 0.39R(t) + 0.11P(t)$$

in which  $P(t)$  equals the distributed load  $q(t)$  times the span  $L$  of the beam and  $R(t)$  is the resistance.

The dynamic support reactions will be calculated for a triangular time function of the load with zero rise time and load duration  $tp$ . Figure 1 gives the dynamic load factor (DLF) for the support reaction as a function of  $tp/T$  with the natural period  $T$  of the SDOF system. While in the static case  $V = 0.5P$  it follows that:

$$DLF(t) = 0.78R(t) + 0.22P(t).$$

A problem arises in the case of  $tp/T$  being smaller than about 0.1. There the maximal support reaction occurs at  $t = 0$  where there is no deflection at all yet, so the derivation is not valid. The second maximal that occurs, and for which the deflection differs from zero (dotted line in Figure 1), is only due to the resistance. The real support reaction will presumably have a value in between the two.

In Figure 1 the maximal support reaction according to the theory mentioned in chapter 2 is depicted also. In the theory, the material is represented only by its Poisson ratio  $\nu$ . The other parameter that has to be chosen is the height over length ratio  $h/L$ . The calculations were made by adding up the contributions of 400 normal modes for  $\nu = 0.2$  and  $h/L = 0.1$ . The number of normal modes is far too high for large values of  $tp/T$  but becomes more realistic for the very small values of  $tp/T$ .

With regard to the straight line in Figure 1 of the simplified analysis the NMT predicts higher values for the support reaction for practical values of  $tp/T$ . The differences in DLF increases to percent for a  $tp/T$  of about 0.08.

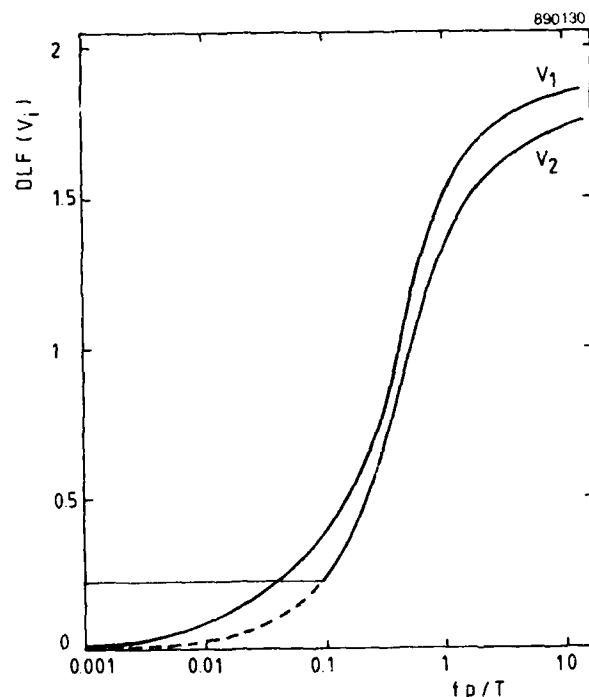


Figure 1: DLF for the support reactions according to different models.

V1 : analytical solution of Timoshenko

V2 : SDOF system.

model without rotatory inertia.



It is clear that the assumed deflection shape is not valid for small values of  $tp/T$  where higher natural frequencies become important. In other load configurations the assumption of a deflection shape can be a problem as well. For instance if the load is distributed over a limited part of the span, the usual choice of the static deflection shape is debatable.

Figure 2 shows the DLF for the support reaction of a simply supported beam that is loaded by a load uniformly distributed over a part  $x$  of the span (symmetrical in regard to the center of the span). The DLF for ratio's  $x/L$  of 1.0, 0.5, 0.3 and 0.1 as a function of  $tp/T$  is shown. With the NMT unsymmetric parts could be also loaded, even by nonuniform loads and even combined with concentrated loads. However, with the symmetrically loaded part, a comparison can be made for small values of  $x/L$  with the DLF for a concentrated load according to the SDOF system. The dotted line in Figure 2 represents this SDOF solution. Also here the SDOF system underestimates the support reaction.

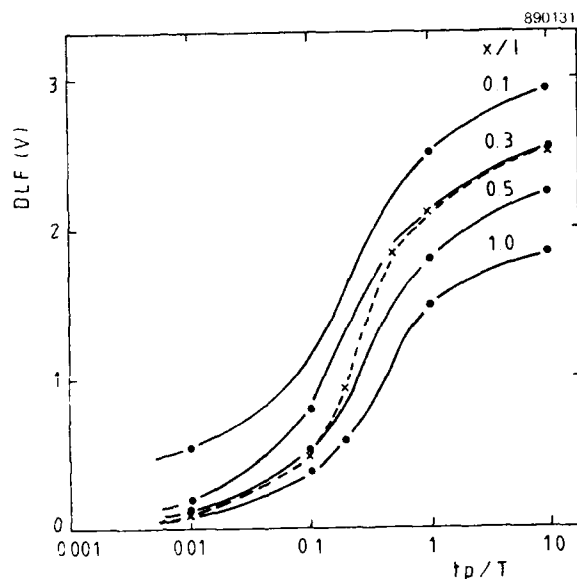


Figure 2: DLF for the support reaction of a partially loaded simply supported beam.  
 -----: Timoshenko without rotatory inertia.  
 .....: SDOF for a concentrated load.

The assumption, that the support reaction will be the maximal shear force to count with for the whole structure, can also be verified with the NMT. In Figure 3 the shear force is calculated for a simply supported beam loaded over  $x/l = 0.1$  symmetrically with regard to the center of the span and for  $tp/T = 0.1$ . The shear force is depicted for two sections: at the support and at the edge of the load, where the shear force is expected to be the highest. As can be seen in Figure 3 the maximal shear force at the support is higher than the maximal shear force at the edge of the load during a time period equal to the first natural period.

As a matter of facts, a parameter study, in which the shear force was also calculated for other sections and for other values of  $x/L$ , showed the correctness of the assumption that the maximal support reaction according to the NMT will always be the largest shear force to count with.

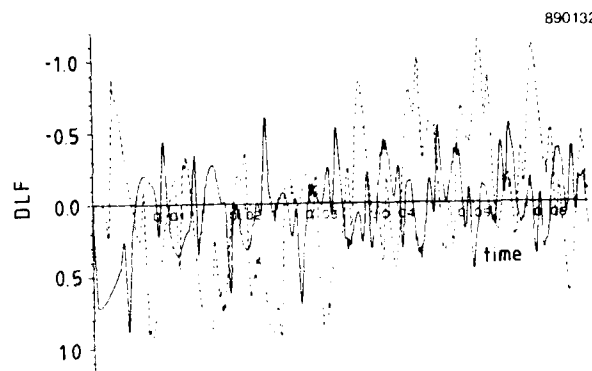


Figure 3: Shear force divided by  $0.5q(t)x/L$  (DLF) during the first natural period.  
 -----: at the edge of the load.  
 .....: at the support.

## 5 APPLICATION FOR NONLINEAR ANALYSIS

In general, a structure will be designed to fail due to the bending moment instead of the shear force in order to obtain a ductile behaviour before failure occurs. Usually the design is such that the elastic bending moment capacity is sufficient to absorb a certain part of the load while the remaining part is absorbed by the ductility due to plastic rotation of the yield hinges. The shear force capacity must be larger than the maximal shear force due to the load.

For the SDOF system, it can be derived that in most cases the shear force reaches its maximum at the point of time the bending moment reaches its elastic limit.

The consequence of this approach using the SDOF system are demonstrated in Figure 4 for a uniformly distributed load with  $tp/T = 0.2$ . If the design level for the bending moment is chosen as, for instance, 55 percent of the bending moment  $M$  that would occur if the load would be taken totally elastic, the shear force  $V$  to count with will be 60 percent of the maximal value that would occur in the pure elastic case. The extra 5 percent is caused by the contribution of the load; the load is still acting at the time of the maximal shear force. The SDOF requires a ductility of about 2 in this case.

The NMT predicts a higher value of the maximal shear force because of the higher frequencies have a larger influence on the shear force than on the bending moment. According to Figure 4 the shear force is reduced to 75 percent for a choice of 55 percent for the elastic limit. Together with the underestimation that was already made for the maximal elastic support reaction, the SDOF system calculates a maximal shear force which is only 65 percent of the maximal shear force calculated with the NMT. It is clear that in this case the SDOF cannot be applied.

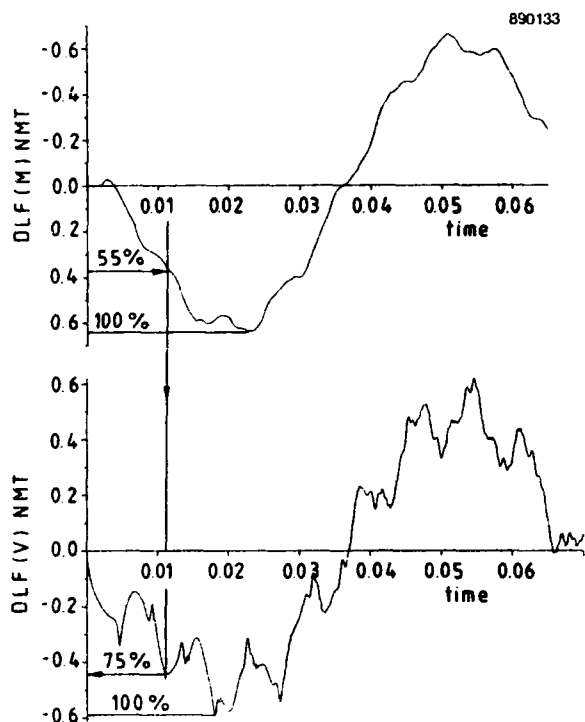
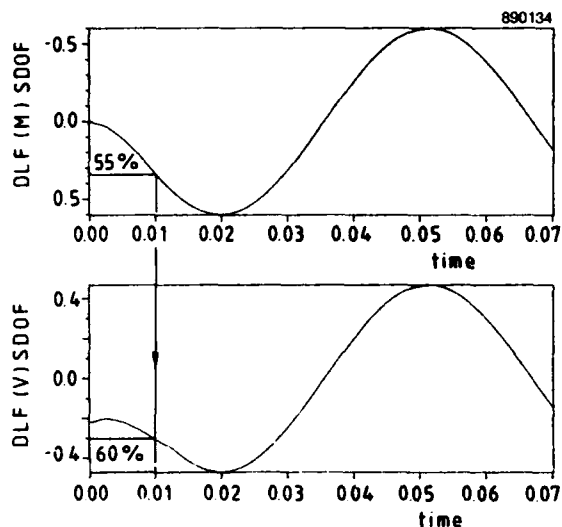


Figure 4: Example of the maximal shear force in elasto-plastic design according to SDOF and NMT for  $tp/T = 0.2$ .  
V: shear force at support.  
M: bending moment at mid-span.

Another phenomenon that is noticed by using NMT is that temporary maximal bending moments can occur outside the mid-section due to the influence of higher numbered normal modes. In the very early stage of the response the section with this maximum travels from the support to the mid-section where it, in most cases, stays until the ultimate elastic moment is reached. Figure 5 shows the general path of the section with a temporary maximum for the whole range of  $tp/T$ . For values  $tp/T > 0.5$  the maximum shifts to another section temporarily after reaching the mid-section.

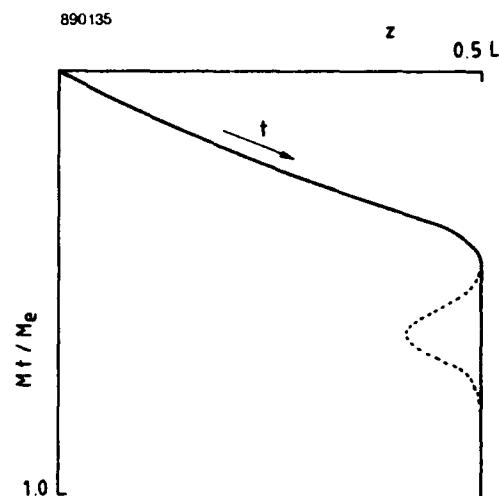


Figure 5: Impression of the time path of section with temporarily maximal bending moment for a simply supported beam loaded uniformly distributed for all  $tp/T$ .  
z: distance to support  
Mt: temporary maximal bending moment  
Me: maximal elastic bending moment  
.....:  $tp/T > 0.5$

For elasto-plastic design the SDOF system assumes a plastic hinge in the centre of the beam and the acquired amount of ductility can be calculated. However, the assumption does not hold if the chosen bending moment resistance is such that it will be reached outside the mid-section.

A finite element code will be applied in cases where a rigorous elasto-plastic analysis is required. The NMT offers the possibility for the FEC to model the problem in order to describe accurately the elastic response required to enter the non-linear stage of the response. The NMT yields the number of normal modes that is required and the element size and the time step of the FEC can be adjusted to that number. Figure 6 shows the shear force near the support for an impulsive load with  $tp/T = 0.0085$  calculated with the NMT and with the FEC calculation. There were 32 quadratic isoparametric plain stress elements needed along the length for the FEC and a division of the height into two elements of the same type with a time step of  $1/20$  of the period of the 15th normal mode. According to the NMT only 15 normal modes were required for an accurate description of the shear force at the support (Weerheijm et al., 1988). The required size of the time step depends on the stage of the response under consideration. The size becomes larger if the response during respectively wave propagation, load duration or thereafter, has to be studied.

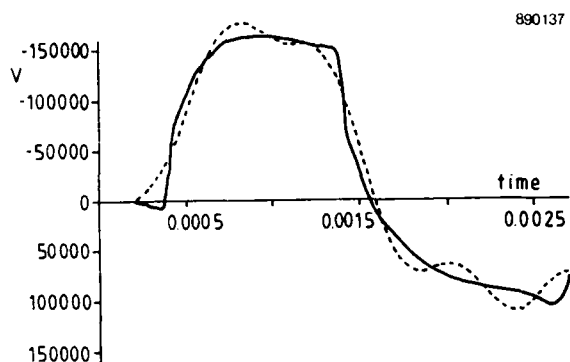


Figure 6: Shear force near the support calculated with NMT and FEC.

The element size and the time step have to be smaller as follows from the required number of normal modes. Due to the discretization, inaccurately described higher modes disturb the FEC solution. Although the influence of the separate higher modes is small, the sum of the contributions causes considerable deviation. The results of a study to eliminate this numerical distortion of normal modes by means of numerical damping will be presented in (van Wees, 1989).

## 6 FURTHER RESEARCH

Although the NMT offers a method to enlarge the knowledge about the linear response of transient loaded structures, there are still subjects which it cannot handle.

The maximal shear forces predicted with the NMT occur in the section of the support or in the section where there is a sudden change in the place function of the load. The schematization of the structure to a line (beam) or a plane (plate) to which section quantities are attached, is in fact not valid in those specific sections. Due to the three-dimensional stress situation, the introduction of the forces into the structure will lead to lower shear force peaks.

The stiffness of the supports which is assumed infinite in the NMT, will also reduce the maximal internal forces (however, the peaks in the wave propagation from a concentrated load towards the support is not influenced).

Another point of uncertainty is the time period during which a shear or bending moment peak must be present, in order to cause damage to the structure. In study, discussed in this paper, it was assumed that elastic failure occurred or that plastic response started, at the moment the internal forces equal the elastic resistance. It is easy to imagine that a very short claim of the maximal resistance will cause only minor damage, without influencing the overall response.

In this respect also, the strain rate dependent material strengths are important: it is possible that the high shear forces that can arise cause no damage to the structure because of the high frequency response to which high strain rates match with.

In fact, damage will occur due to the stresses being equal to the strength; in the NMT the section quantities are derived for a static stress distribution. References can be found which predict a frequency dependent stress distribution in impulsive loaded structures.

The application of FEC to study the above mentioned subjects is possible because of the reliability, obtained with the NMT, in the FEC linear calculations.

## 7 CONCLUSIONS

The NMT offers the possibility to find analytical solutions for the response of transient loaded structures with which extensive parameter studies can be performed in a short time period.

A comparison of the NMT with the simplified SDOF analysis method showed the inaccuracy of the latter which can amount to 35 percent for the maximal elastic shear force and the restrictions of its application both in relative time period ( $t_p/T$ ) and load configuration.

The benefit of the NMT in non-linear analysis for FEC was demonstrated. The NMT showed the restrictions in non-linear SDOF analysis depending on the chosen elastic limit.

There remain subjects in the linear response which the NMT cannot handle. Other methods, for instance the FEC, are required there. A comparison of NMT with FEC increased the confidence in accurate FEC linear analysis without an overreduction of the element size and time step and created a firm base for fundamental non-linear FEC analysis of transient loaded structures.

- Karthaus W. and Leussink J.W.  
Dynamic loading: more than just a dynamic load factor.  
Proceedings of the symposium of the interaction of non-nuclear munitions with structures. Colorado, 1983.
- Mercx W.P.M. and Harmanny A.  
The Normal Mode Technique: a useful tool to investigate the behaviour of structures subjected to local impulsive loading.  
Proceedings of the symposium of the interaction of conventional munitions with protective structures. Mannheim, 1987.
- Norris C.H. et al.  
Structural design for dynamic loads.  
Mcgraw-Hill book company, 1959
- Weerheijm J. and Karthaus W.  
The tensile strength of concrete under dynamic loading.  
Proceedings of the second symposium of the interaction of non-nuclear munitions with structures. Panama Beach City, Florida, 1985.
- Weerheijm J., P.J.H. van Zantvoort, G. Opschoor.  
The applicability of the FE-technique to dynamic failure analysis of concrete structures.  
Proceedings of the 23rd DoD Explosives Safety Seminar. Atlanta, Georgia, 1988.
- Wees R.M.M. van and Weerheijm J.  
Calculation of explosively loaded concrete beams with the finite element method.  
Proceedings of the symposium of structures under shock and impact (to be published).  
Cambridge, Massachusetts, 1989.

## ENGINEERING - QUANTITY/DISTANCE ANALYSIS OF AMMUNITION AND EXPLOSIVES OPERATIONS

David Kussover<sup>1</sup>, Norval Dobbs<sup>1</sup>, and Joseph Caltagirone<sup>2</sup>

Ammann & Whitney, Consulting Engineers, New York, NY<sup>1</sup>  
U.S. Army Armament Research, Development and Engineering  
Center, Picatinny Arsenal, NJ<sup>2</sup>

### ABSTRACT

A mathematical model and test results have been used to determine hazardous debris distance for 56 structures at Picatinny Arsenal. The hazardous debris distance is assumed to be the inhabited building distance (IBD) for secondary fragments (Ref. 1). The model not only considers the distance the debris travels in air, but also includes an additional factor which accounts for rolling, debris interaction, debris breakup and other uncertainties. The model is especially useful for Picatinny Arsenal-type structures where the donor offers nominal resistance to the blast and the charge weights are generally less than 3,000 pounds.

### BACKGROUND

The Department of Defense Explosive Safety Board (DDESB) has established guidelines for the minimum safe separation between buildings containing explosives and buildings of adjoining facilities (Inhabited Building Distances). These distances are established for both blast overpressures and fragments formed from the break-up of donor buildings (structures containing potential explosions). For fragment projections from an accidental explosion, the present guidelines do not permit the storage of explosives if the separation between the donor and inhabited building is less than 670 feet. The explosive weight is limited to 100 pounds if the separation is at least 670 feet. At a separation of at least 1,250 feet, the allowable explosive limit becomes 30,000 pounds. The explosive weight may be increased and/or the separation distance decreased if it can be proven analytically that fragments from a donor structure impact a section outside an acceptor structure with a density not to exceed one fragment per 600 square feet and an impact force not to exceed 58 foot-pounds.

Ammann & Whitney was engaged by the U.S. Army Armament Research, Development and Engineering Center (ARDEC) to establish analytical procedures to determine actual distances in which secondary fragments will be projected and to analyze 56 buildings at Picatinny Arsenal for conformance to these distances.

### ANALYTICAL MODEL

The analytical model for predicting the maximum debris distance consists of the development of three model components. The first component involves the determination of the initial fragment velocity. The second

component consists of the determination of the in-flight range of the fragment, while the third component accounts for the post in-flight range of the debris. However, as will be explained later, the maximum debris distance differs from the hazardous debris distance which must be correlated to the IBD criteria.

Once the internal structure blast loading and quasi-static loading (hereafter referred to as gas loads) are established either by computer programs or by charts in Reference 2, the debris velocity can be calculated. With the velocity and debris launch angle as input, the flight range (travel through the air) is derived either by use of a computer program or by equations of motion. Finally, a factor is then applied to the debris flight range which accounts for debris rolling, break-up and other uncertainties to arrive at the hazardous debris distance. At this distance, the fragment is at rest, and, therefore, must be less than the IBD to meet the DDESB criteria for fragment impact.

The model considers two types of structure debris that are ejected during an explosion. The first type consists of debris ejected immediately opposite the charge in a direction normal to the wall surface, due to the localized high intensity of the shock load. This debris is considered low-angle and its initial velocity is a function of the high intensity region of the shock loading only. The second type consists of debris ejected at higher angles and its initial velocity is related to the average shock loading as well as the gas load.

### DEBRIS INITIAL VELOCITY

For buildings of the type at Picatinny Arsenal where the resistance of the structure is small in comparison to the intensity of the blast loading, the following equation is used to determine the initial debris velocity:

$$V_i = i_t / m \quad (\text{eq. 1})$$

where

$V_i$  = maximum velocity of debris

$i_t$  = total unit impulse

$m$  = effective unit mass

For debris located directly opposite the charge and which is ejected in a direction normal to the wall (low-angle debris),  $i_t = i_{r \max}$  and

$$V_i = i_{r \max} / m \quad (\text{eq. 2})$$

where  $i_{rmax}$  = the maximum normal unit reflected shock impulse.

For debris located at some distance from the charge, the effects of the average shock impulse and the gas impulse govern the velocity (high-angle debris). For this case,

$$i_t = i_{ravg} + i_g \text{ and} \\ V_i = (i_{ravg} + i_g)/m \quad (\text{eq. 3})$$

where  $i_{ravg}$  = the average normal, unit reflected shock impulse.

$i_g$  = the gas unit impulse.

The unit mass of the debris, which is a function of the wall or roof material density and thickness, is used in Equations 1, 2 and 3. The debris shape, as it affects the trajectory, will be discussed later.

### SHOCK IMPULSE

The values of impulse are calculated by the computer program "SHOCK". This program is a modification of the program "IMPRES" developed by Ammann & Whitney for ARDEC and adapted by the Naval Civil Engineering Laboratory (NCEL). The program SHOCK computes the values of scaled impulse for up to 1,100 grid point locations.

Figure 1 depicts a typical shock impulse surface shape caused by the detonation of a charge. From the plotted shape it is obvious that the concentration of impulse is almost constant outside a region bounded by the locus of all the points making an angle of approximately 45 degrees from the center of the charge; and within the region its value rises sharply. The debris ejected from this high impulse region are considered low-angle debris with the numerical value of its velocity described in Equation 2. The debris ejected outside the region of high intensity are considered high-angle debris. In this region, the shock load is governed by the average impulse and the numerical value of its velocity is described in Equation 3.

In lieu of using the program SHOCK to generate average impulse loadings on a blast surface, the impulse charts contained in Reference 2 may be used.

### GAS IMPULSE

When an explosion occurs within a confined area, gaseous products accumulate and temperatures rise forming gas pressures whose magnitude is less than the shock pressures but whose duration is significantly longer. The magnitude of the gas impulse depends on the charge weight, room volume, area of vent openings and unit weight of vent opening covers.

The computer program FRANG developed by NCEL was used to determine the magnitude of the gas impulse. This program is based on tests performed and documented in Reference 3 as well as subsequent tests performed by NCEL.

Theoretically, all surfaces of the structure begin to vent once impacted by the reflected shock impulse since none of these structures has been designed for containment. However, in modeling the structure for venting, only

lightweight elements, such as windows, doors, roofs, and frangible panels, provide the relief due to their small mass compared to the larger unit mass of the concrete or block walls. In cases of the Picatinny structures where the venting was provided by the roof, a unit weight of 10 psf has been chosen for the model to account for the dead weight of the roofing (corrugated asbestos, plywood or corrugated metal) and a significant snow load. This is a conservative estimate since the higher the unit load of the roof vent, the higher the gas impulse.

### DEBRIS IN-FLIGHT RANGE

The debris in-flight range, that is, the distance that the debris travels in the air, is governed by the following parameters:

1. Initial velocity
2. Initial launch angle
3. Debris density and shape (i.e., drag coefficient) and
4. Relative location (in elevation) of donor structure and landing point of debris.

The launch angle will differ for the low-angle and high-angle debris and is presented below.

### LAUNCH ANGLE ESTIMATION

High-angle debris is influenced by the average, normal reflected shock impulse and the gas impulse, and the low-angle debris is influenced primarily by the peak normal reflected shock impulse. Figure 2 depicts the ejection of low-angle and high-angle debris and the time-dependence for each case.

From various test results it has been established that the majority of fragments ejecting from the low-angle debris region emerge normal to the wall surface even though some fragments are propelled at small angles from the horizontal.

The fragments ejecting from the region of lower intensity shock load can take off at angles other than zero degrees. These fragments attain the maximum range when the initial launch angle is close to 45 degrees over level terrain.

The depiction of launch angle for the model for the high and low-angle debris is illustrated in Figure 3.

### EFFECTS OF DRAG

A study has been performed which evaluated the effects of drag versus fragment velocity. As a result of this study:

1. The effect of drag which is expressed in terms of the drag coefficient,  $C_D$ , is negligible at velocities up to 100 ft/sec. regardless of the initial angle of flight,
2. For an initial angle of flight of zero degrees, the effect of drag, at velocities up to 300 ft/sec. is not significant. Therefore the effect of drag can be neglected for the fragments projected at low angles of flight, especially at velocities below 300 ft/sec., and
3. The maximum range was obtained for an initial angle of approximately 45 degrees independent of the initial velocity and/or coefficient of drag.

4. The effect of drag may be significant at velocities over 100 ft/sec. and initial launch angles of about  $45^\circ$ . As an example, at a velocity of 200 ft/sec and a launch angle of  $45^\circ$ , the range of missiles was decreased 20 percent when  $C_D$  varied from 0.5 to 2.0 (Figure 4).

It may be noted that the ranges used in the above study constitute the in-flight distance of the missile (i.e., when the missile first hits the ground). It has been assumed that the ground is level and the initial height of the missile from the ground surface was taken as 10 feet.

For Picatinny Arsenal structures, the low-angle debris velocity was usually less than 300 ft/sec while the velocity of high-angle debris was usually less than 150 ft/sec. Based on the aforementioned study a drag factor of 1.0 was assumed. This drag factor corresponds to a cubical type of missile. This implies that, for an 8-inch thick wall, the hazardous debris analyzed will be that for an 8-inch cube.

### DEBRIS FLIGHT

Once the debris initial velocity, launch angle, size and drag factor are established, the next step in the development of the model is to simulate the flight of the missile. To do this, the computer program "TRAJECT", as developed by the Ralph M. Parsons Co., for the U.S. Army Engineer Division, Huntsville (Ref. 4) is utilized. Briefly, the program operates by analyzing the flight of the missile in two phases, namely, the ascent phase and the descent phase. For each phase the differential equations of a free body under dynamic equilibrium have been formulated and analytically integrated to yield a closed-form solution for the time of ascent, the time of descent, the maximum height attained by the missile, the final impact velocity and the in-flight range of the missile.

This program can evaluate five possible cases of missile flight as depicted in Figure 5.

In those cases where the initial velocities of the high- and low-angle fragments are less than 100 ft/sec and 300 ft/sec, respectively, and the ground surface is horizontal, the use of the computer program can be substituted by using simplified equations of motion and neglecting drag effects.

Up to this point, the model has estimated the maximum in-flight range for high-angle and low-angle debris. In addition, the model must account for fragment roll, break-up, fragment interaction and other uncertainties. The following section discusses the application of multiplication factors which account for this post in-flight range phenomena. This phenomena is expressed in terms of a multiplication factor,  $f$ , which is defined as the ratio of maximum debris range to the in-flight range.

### CORRELATION FACTOR FOR LOW-ANGLE DEBRIS

The correlation or multiplication factor for low-angle debris has been derived by utilizing data from tests performed on scale-model dividing walls (Ref. 5). These tests consisted of one-sixth scale model reinforced concrete dividing walls tested in the open. The wall dimensions were 18" by 18" and the thickness varied from 2 to 3 inches for different test set ups. Deformed wire was used to simulate the steel reinforcement. The charge

weight varied from 1/2 lb to 3 lbs. The charges were located at mid-height in the walls. The standoff distance varied from 5 to 7-1/4 inches. Test results included the determination of the maximum velocities and the range of debris for two types of walls (i.e., one-side and three sides supported). Most debris was ejected normal to the wall in each test.

A correlation between total debris distances obtained from the tests and the computed in-flight ranges has been made. The in-flight ranges have been calculated using the program TRAJECT with the initial velocities obtained from the test results and assuming a launch angle of zero degrees. This correlation formed the basis of determining the value of the multiplication factor,  $f$ , for low-angle debris.

The values of the multiplication factors,  $f$ , obtained from the individual tests have been plotted against corresponding values of maximum observed velocities (Fig. 6). A value of the multiplication factor,  $f$ , equal to 5.1 has been obtained from this plot and represents a confidence level of 85 percent which has been deemed acceptable in light of the conservatism used in developing the analytical model.

### CORRELATION FACTOR FOR HIGH-ANGLE DEBRIS

The correlation or multiplication factor,  $f$ , for the high-angle debris has been established in a manner similar to that for low-angle debris. This was accomplished utilizing data obtained from tests performed on scale model aircraft shelters (Ref. 6). These tests consisted of one-tenth scale models of reinforced concrete arch shelters subjected to interior explosions.

A comparison of the test results is given in Table 1. The values of the maximum observed range and debris velocity have been obtained from the test results while the maximum in-flight ranges were calculated in a manner similar to that described for the low-angle debris. Again the ratio of the observed range to the calculated range was used to establish the multiplication factor,  $f$ , for the high-angle debris. An upper value of the multiplication factor,  $f$ , obtained from the tests was equal to 1.7. However, a multiplication factor equal to 2.0 is recommended for use in the model. This value corresponds to a confidence level of 85 percent which is consistent with that of the low-angle debris multiplication factor.

### HAZARDOUS DEBRIS DISTANCE

As previously mentioned, the maximum debris distance differs from the hazardous debris distance, the latter always being less than the former. While this report does not statistically analyze the debris density, a number of other reports discuss this phenomena in detail. Table 2 lists these reports and it can be seen that the ratio of maximum range to hazardous range is almost never greater than 0.9. Therefore, it is recommended that a correction factor of 0.9 be used to define the hazardous distance compared to the maximum distance. For an acceptable solution, the hazardous debris distance must always be equal to or less than the IBD for the charge considered.

In summary, the hazardous debris distance,  $R$ , becomes:

$$R = 0.9 \times f \times r \quad (\text{eq. 4})$$

where  $f$  = multiplication factor which  
= 5.1 for low-angle debris and  
= 2.0 for high-angle debris  
 $r$  = in-flight range

### EFFECTS OF TERRAIN AND BARRICADES

Terrain and barricades can affect the path of travel of debris. Where no barricades are present and when the acceptor structure is on the same or a lower elevation as the donor, debris from low-angle and high-angle trajectories can reach the acceptor building unimpeded, as illustrated in Figure 7. Debris will travel a greater distance when the acceptor structure is at a lower elevation than the donor. When barricades are present, or when the acceptor is at a higher elevation than the donor, low-angle debris cannot reach the acceptor structure as illustrated in Figure 8. In this case, only the high-angle debris is analyzed.

### ILLUSTRATION OF MODEL RESULTS

Most of the separation distances for Picatinny structures were governed by the high-angle debris. For that reason, a set of curves has been generated for a typical structure where the hazardous debris distance,  $R$ , for high-angle debris has been plotted against varying charge weights. The structure has plan dimensions of 30'x30' and a height of ten feet.

Venting was assumed to be through the roof and the unit roof load was taken as 10 psf to account for the dead load and a significant snow load.

The resulting set of curves is plotted in Figure 9 for four unit weights of wall, varying from W/A of 25 psf (corresponding to lightweight brick) to 200 psf (corresponding to 16 inches of concrete). The charge was placed at the center of building in plan, one-foot off the ground. The acceptor structures were assumed to be at the same elevation as the donor.

Upon reviewing this chart, a number of observations can be made:

1. Lighter weight wall material is generally ejected further. The only exception is in the very high ranges (greater than 2,500 feet) where the more massive debris can travel further.
2. For a charge weight of 100 pounds, the hazardous debris range is less than 670' when the unit weight of the wall is 100 psf or greater, (this corresponds to an 8" concrete wall).
3. The 1,250' distance is exceeded in all cases of unit wall weight when the charge weight is approximately 3,000 pounds (extrapolated). This verifies the usefulness of the model in the range of charge weights up to 3,000 pounds.

### MODEL CONSERVATISMS

Since this analysis is a state-of-the art application to the debris hazard problem, many aspects of the model represent a conservative approach namely:

1. The peak reflected shock load was used to determine the debris velocity for low-angle particles.

2. The average reflected shock impulse, which includes the peak region, and the maximum gas impulse were used to determine the debris velocity for high-angle particles.
3. A worst-case launch angle, approximately 45 degrees, was used to determine debris range for high-angle particles.
4. Worst-case charge locations were taken for analysis.
5. A substantial roof load that accounts for snow was assumed. This high roof load results in a longer confinement of the explosion thereby increasing the gas impulse load on the debris.
6. No hazardous debris density analysis was performed. In general the maximum distance debris can travel, as a result of an explosion, was taken as a measure of hazardous debris distance.
7. No attempt was made to account for the effects that trees and shrubs may have on impeding debris travel on the ground.
8. By assuming that the vent panel remains rigid, the model does not consider the additional venting of the gas pressures due to fragmentation of the vent panel, which undoubtedly occurs.

### REFERENCES

1. Safety Manual, AMC-R 385-100, Department of the Army, Headquarters U.S. Army Materiel Command, Alexandria, Virginia, August 1985.
2. Ayvazyan, H., et al., Structures to Resist the Effects of Accidental Explosions, Volume II, Blast, Fragment, and Shock Loads, Special Publication ARLCD-SP-84001, Prepared by Ammann & Whitney Consulting Engineers, New York, NY, in association with Southwest Research Institute, San Antonio, TX, for US Army Armament Engineering Directorate, Picatinny Arsenal, Dover, New Jersey, December 1986.
3. Keenan, W.A. and Tancreto, J.E., Blast Environment from Fully and Partially Vented Explosions in Cubicles, Technical Report 51-027, Civil Engineering Laboratory, Naval Construction Battalion Center, Port Hueneme, CA., February 1974.
4. Donor Building Fragmentation and Missile Hazard Study, RDX/HMX Production Facility, prepared by The Ralph M. Parsons Co., in association with Hercules, Inc., A.T. Kearney, Inc. for US Army Engineer Division Huntsville, Huntsville, Alabama, Contract No. DACA 87-75-C-0041, AUGUST 1976.
5. Vargas, L.M., Hokanson, J.C., Explosive Fragmentation of Dividing Walls, prepared by Southwest Research Institute for US Army Armament Research and Development Command, Picatinny Arsenal, Dover NJ, July 1981.
6. Ward, J., et. al., Modeling of Debris and Air Blast Effects from Explosions Inside Scaled Hardened Aircraft Shells, Research and Technology Department, Naval Surface Weapons Center, Dahlgren, VA, Silver Springs, MD, May 1985.



TABLE 1

Comparison of Aircraft Shelter Scaled Model Debris Data  
with Trajectory Computer Program

| Test No | Max. Observed Range (Feet) | Max. Observed Velocity (Feet/Sec.) | Max. Calculated (2) In-Flight Range (Feet) | Ratio of Observed Range to Calculated Range, 1 |
|---------|----------------------------|------------------------------------|--|--|
| 1       | 689                        | 138                                | 402  | 1.71   |
| 2       | 689                        | 177                                | 557  | 1.24   |
| 3       | 518                        | 118                                | 320  | 1.62   |
| 4       | 620                        | 262                                | 854  | 0.73   |
| 5       | 712                        | 262                                | 854  | 0.84   |

(1) From Side of Aircraft Shelter

(2) From the Trajectory Program Max Observed Velocity as Input

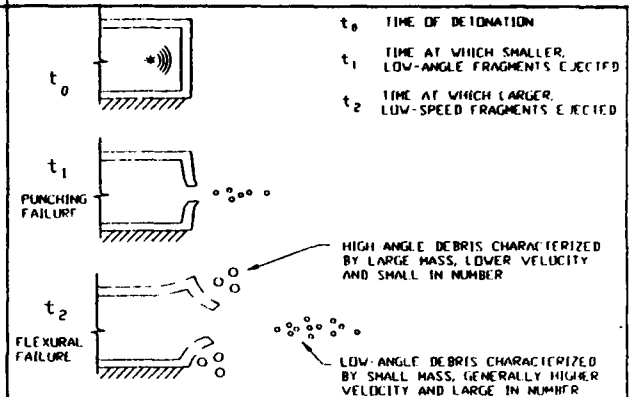
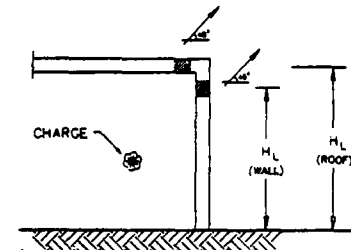


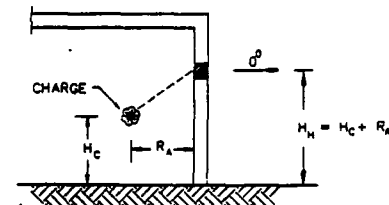
Figure 2 Low-angle and high-angle debris ejection

TABLE 2  
Comparison of Hazardous Debris Distance  
with Maximum Debris Range

| Event or Report  | Element or Direction | Hazardous Debris Distance (Ft) | Maximum Debris Distance (Ft) | Ratio of Hazardous Range to Maximum Range |
|--|----------------------|--------------------------------|------------------------------|---|
| Distant Runner Event 5 (Aircraft Shelter)                                | Front Wall           | 1034                           | 1356                         | 0.761                                     |
|  | Side Wall            | 1293                           | 1480                         | 0.874                                     |
|  | Rear Wall            | 807                            | 1486                         | 0.543                                     |
| Huang Analysis & Prediction of Debris Hazards in Buildings IM M-63-83-10 | N-S Direction        | 801                            | 1537                         | 0.521                                     |
|  | E-W Direction        | 1265                           | 1537                         | 0.823                                     |
| Distant Runner Event 4 (Aircraft Shelter)                                | Front Wall           | 645                            | 682                          | 0.950                                     |
|  | Side Wall            | 659                            | 1309                         | 0.500                                     |
|  | Rear Wall            | 564                            | 1253                         | 0.450                                     |



(a) HIGH-ANGLE DEBRIS



(b) LOW-ANGLE DEBRIS

Figure 3 Location of wall or roof debris and initial launch angle

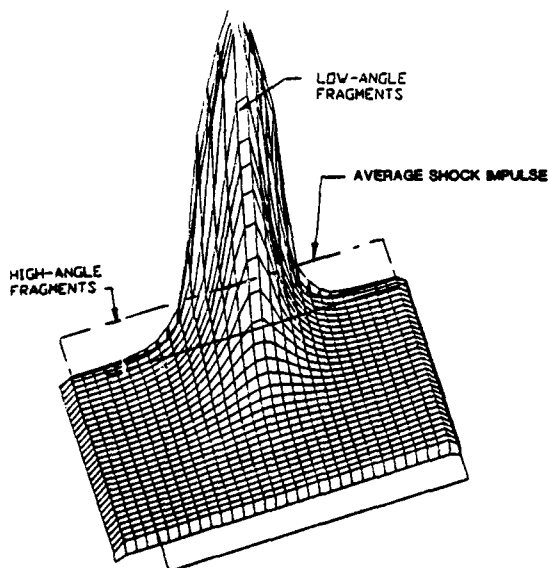
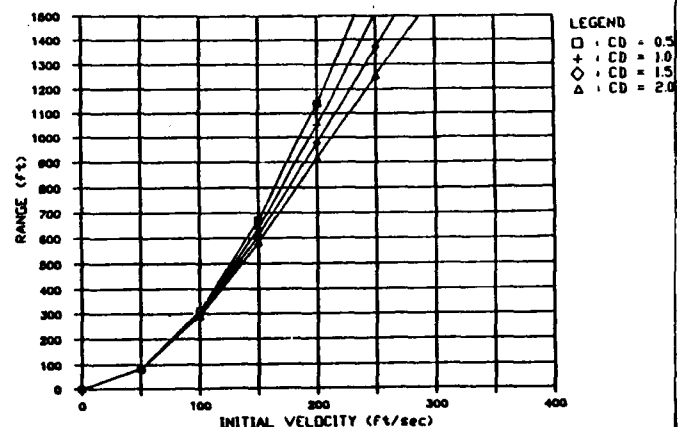
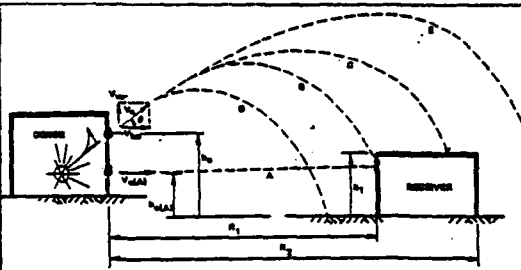


Figure 1 Typical impulse surface from output of the computer program SHOCK

Figure 4 Effect of drag for launch angle of  $45^\circ$



#### CASES:

- (A) WALL IMPACT DURING THE ASCENT PHASE OF TRAJECTORY.
- (B) WALL IMPACT DURING DESCENT.
- (C) ROOF IMPACT DURING DESCENT.
- (D) FRAGMENT FALLING SHORT.
- (E) FRAGMENT FLYING OVER.

Figure 5 Flight paths for the program TRAJECT

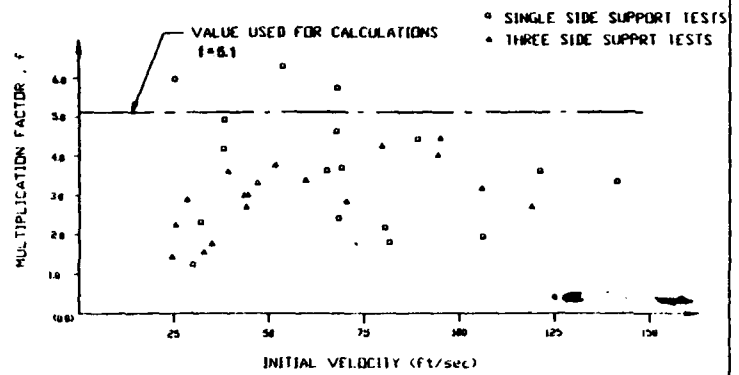


Figure 6 Multiplication factor,  $f$ , versus debris velocity.

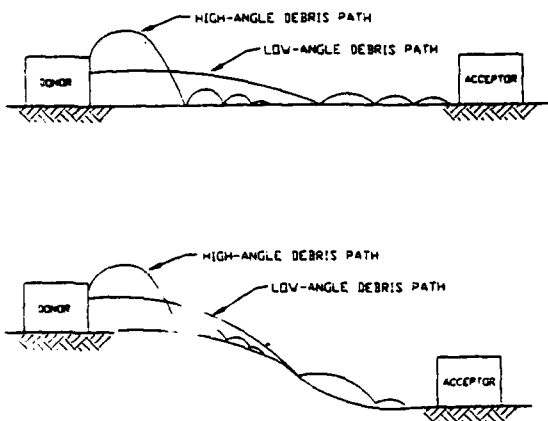


Figure 7 Debris trajectories without barricades

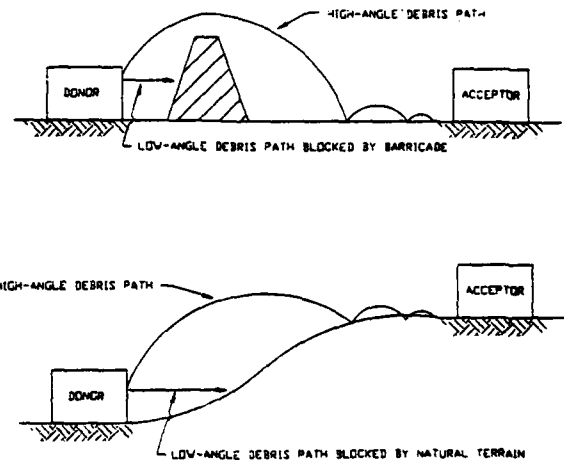


Figure 8 Debris trajectories with barricades or terrain impediments

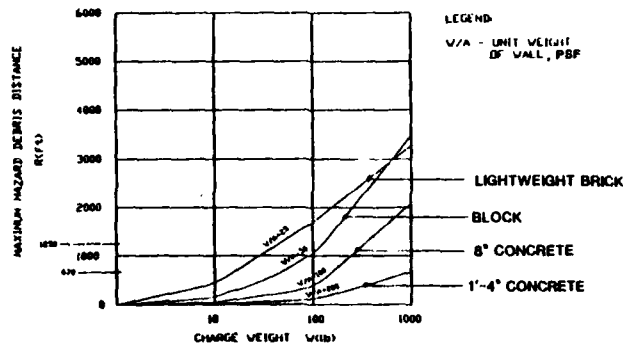


Figure 9 Hazardous debris distance for Case III structure - 30'x30'

## FRAGMENT AND DEBRIS HAZARD EVALUATION--A NEED FOR NEW Q-D CRITERIA FOR DOE FACILITIES

Patricia Moseley Bowles, Senior Research Analyst

Southwest Research Institute, 6220 Culebra Road  
P.O. Drawer 28510, San Antonio, Texas 78284

### ABSTRACT

The threat of costly expansion of plant real estate or hardening of existing structures in order to comply with the fragment/debris hazard criteria in DOD 6055.9 has prompted the DOE safety community to question the applicability of the broad ranged DOD fragment separation criteria for siting DOE structures. In most cases, the DOE structures contain relatively small quantities of high explosives and may require less separation distance to provide intended safety levels. A safety assurance plan was developed to establish new siting criteria for DOE facilities. The plan includes assembly of existing data, a collection of information on DOE operations, structures, and explosives to develop structure/explosives groups of similar hazard, the use of predictive computer models and hazard analysis to define the worse case situations and identify areas of low confidence in hazards prediction, and the use of testing to develop an adequate database to improve hazard predictions to levels of high confidence. This paper summarizes progress made to date in resolving each step of the safety assurance plan.

### 1.0 INTRODUCTION

The Department of Energy (DOE) Explosives Safety Manual, DOE/EV/06194-3, requires that the DOE and its contractors use fragment/debris hazard criteria in addition to the blast criteria outlined in the Department of Defense (DOD) "Ammunition and Explosive Safety Standards", DOD 6055.9, for determining safe separation distances for explosives facilities. This has caused great concern at existing DOE facilities. Some of the now required separation distances exceed current boundaries, and exceed distances between structures at these facilities, because the original siting was based on blast hazard protection alone. The threat of costly expansion of plant real estate or hardening of some structures has prompted the DOE safety community to question the applicability of the broad ranged DOD fragment separation criteria for siting DOE structures which house, in many cases, small quantities of high explosives (HE).

The need to provide safe clearance for hazardous debris which can evolve from accidental explosions or detonations of energetic materials

is not disputed, but more specific data to develop criteria to supplement the quantity-distance tables for combinations of structure and explosives types found at DOE facilities would be cost effective in making existing facilities comply with criteria, without compromising the intended safety. These new criteria need to be established by a careful examination of the structures and explosives present at DOE facilities, a study of existing data on fragmentation of these explosive configurations and structural breakup caused by accidents, and possible subscale or full scale testing of combinations of structure and explosives types.

### 2.0 PLAN OF ACTION

A safety assurance plan has been developed for the Department of Energy to use to establish new siting criteria for DOE facilities which handle high explosive material. The plan has encouraged technical exchange between the DOE and the DOD in order to maximize the quality of the work and application of results. Both a DOE Explosives Safety Steering Committee and a Technical Advisory Group composed of representatives from the DOD explosives safety community have served as mentors for the study since its inception.

The plan which has been developed includes sufficient analytical and experimental investigations to address and satisfy the concerns of the DOE. The plan includes assembly of existing data and technologies for defining fragment/debris hazards; collection of information on DOE operations, structures, and explosive configurations; development of structure/explosives groups of similar hazard and associated accident scenarios; the use of predictive computer models and hazard analysis to define the worst case situations; identification of areas of low confidence in hazards prediction; and the use of testing to develop an adequate database to improve hazard predictions to levels of high confidence.

The plan flow is identified in Figure 1. The following paragraphs describe a brief history of the project, a summary of work completed on Steps 1 through 9 of the plan, and the approach to be taken to resolve the remaining steps of the plan.

The original plan was presented in Reference 1 in August 1987. At that time Step 1, "Establishment of Current Database and Fragment Hazard Technologies," had been completed. Shortly thereafter, the Explosives Safety Steering Committee developed the form for the technical data sheets to be used during Step 2. These forms were then sent to all major DOE facilities with a request for the necessary information on structures and operations at each facility. Collection of the information awaited funding of a contract to begin Steps 2 through 8 of the plan. In July 1988, Southwest Research Institute (SwRI) and Bernard Johnson, Inc. were funded by Mason & Hanger - Silas Mason Co., Inc. to resolve Steps 2 through 8. Resolution of Step 9 was added to the contract in December 1988.

### 3.0 SUMMARY OF RESULTS

#### Step 1: Establishment of Current Database and Fragment Hazard Technologies

The first task was to collect and review existing data and debris hazard prediction methodologies in the form of related reports and published papers to prevent repetition of efforts. To establish the current database, computer aided literature searches were conducted to locate pertinent documents. The resulting abstracts were reviewed, and relevant reports were obtained so they could be examined for possible addition to the debris hazard database. In addition to the computer aided searches, fact gathering efforts by DOE safety personnel and Southwest Research Institute (SwRI) personnel were compiled and included in a summary of the existing fragment/debris hazard prediction database. Results of the literature search are discussed in Reference 1.

#### Step 2: Collection of Information on Structures and Explosive Configurations for DOE Facilities

Each of the major DOE facilities was examined to determine the various types of structures (construction materials, characteristics such as frangible walls, vented roofs, or reinforced concrete walls and roofs, operations conducted, etc.) and the types of explosives processed. A general form with an attached letter requesting information on the structures and explosives was sent to each facility with an explanation of the nature of information needed and the reason for requesting it.

In addition to the information retrieved from the forms, several site visits were made to obtain structural drawings and examine some of the structures.

#### Step 3: Identification of Structures of Similar Construction

Once information on all the DOE facilities had been collected, structures of similar construction were grouped together. In reviewing all the data and doing preliminary sorts in the

database, it was decided that structural response could not always be predicted by noting the database entries from the technical data sheets since different people filled out forms in different ways. Thus, a big effort was expended looking at drawings and making engineering judgments on structural response as well as sorting in the database.

#### Step 4: Identification of Explosives of Like Assembly

Information collected on explosive configurations processed or handled at each DOE facility were grouped by configuration (casing, characteristics, shape) and HE quantity similarities. The explosive amounts played a major role in establishing the groups since they greatly effect structural response.

#### Step 5: Establishment of Structure/Explosive Groups of Similar Hazard

The structure categories and explosives groups identified following the facility data collection were combined into groups of similar hazard. Out of over 300 database entries, 26 groups were established. Quantity-distance criteria need to be based on these structure/explosives groups, not just on HE quantity, to reflect true safe separation distances from debris hazards since the structure contributes much of the debris following an accidental explosion or detonation. Since the two entities are combined, a series of tables or charts may be necessary to properly display the safety criteria in a manual.

#### Step 6: Definition of Explosion Accident Scenarios and MCE

The facility data collection was also used to define explosion accident scenarios for each structure/explosives group. For some groups, more than one scenario was analyzed to cover the range of explosive quantities in a single group. Other groups contained so few structures or such uncommon structures or explosive amounts that they were not analyzed at all. Still other groups represented structures for which quantity-distance relationships have already been established and, thus, did not require analysis.

#### Step 7: Use of Predictive Computer Model to Analyze Structure/Explosives Groups for MCE

A debris/fragmentation hazard refinement analysis was performed for the accident scenarios for each structure/explosives group using a predictive model. The model is a combination of computer codes and applications of data analysis results. The breakup of a structure and, thus, debris characteristics are based on the quantity and configuration of the explosives involved in the MCE and the construction of the building. The final product of the predictive model should be data which can be used to establish Q-D relationships for each group.

Existing computer models in the areas of blast loading and debris distribution prediction were located and examined for applicability in analyzing the structure/explosives groups. In addition, several test reports were studied to determine structural response and debris formation characteristics and to develop a means of incorporating the prediction of these characteristics into the model.

The initial step of the model is a structural analysis of the wall or roof component response to a blast load at the explosive weight limit associated with a particular group or section of a group. The NCEL computer code SHOCK (Reference 2) is used to predict the impulsive load on a component and determine the degree of failure expected. The wall and roof components absorb energy up until "failure". At failure, all the unabsorbed applied impulse is converted into initial velocity of fragments. Failure criteria and fragment size criteria were determined using analysis of test data from Reference 3. Fragment trajectory criteria are also based on data from this reference and other observations of tests. For cases where quasistatic loading is important, the effect of this loading on fragment size and velocity is included. The NCEL computer program FRANG (Reference 4) is used to determine gas loads when necessary. Characteristic fragment size, initial trajectory, and initial velocity are used in the second step of the model to determine debris flight for each component group or section of a group.

The hazardous debris arcs for each structure analyzed were determined using the MUDEMIMP computer code (Reference 5). This code uses a probabilistic approach to cover variations and uncertainties of launch/flight characteristics of each individual debris missile from an explosion. It starts by using the Monte-Carlo random sampling technique to select a set of launch/flight parameters for a single debris piece. It will then calculate the trajectory, impact range, and terminal kinetic energy of that piece. The Monte-Carlo process and trajectory calculations are then repeated for all the debris missiles from an explosion. The code outputs a histogram of the accumulated number of critical (kinetic energy greater than 58 ft-lbs) debris missiles as a function of impact range. Hazardous arcs were established using these histograms.

The model was used to predict a separate hazardous debris arc for each structure analyzed for each group. For a building, the debris distribution used to determine an arc in a certain direction is that of the wall facing that direction plus a "worst case" portion of the roof debris. The hazardous debris arcs indicate safe clearance distances for each group and, thus, could be used to designate appropriate quantity-distance criteria.

#### **Step 8: Identification of Level of Confidence of the Data, Technology, and Results for the Analysis of the Various Structure/Explosives Groups**

Approval of new quantity-distance criteria based solely on the analyses of the structure/munition groups requires identification of the level of confidence in the input data, the prediction methodologies, and the resultant safe separation distances. Prediction of building breakup and debris throw has a low level of confidence unless specific testing of structural components or models has been performed. Accuracy of the prediction methodologies for blast loading, time of failure, structural breakup, debris/fragment velocities, maximum clearance distances, etc. greatly depends on any proof-testing or data comparisons which have been done in the past. The confidence level associated with the resultant hazardous debris arcs and quantity-distance relationships is based on the perceived accuracy of the analysis methods and the quality of the debris data used as input. If confidence in the results is low, specific testing for a structure/explosives group is necessary.

#### **Step 9: Establishment of Small Scale Test Requirements and Test Plans**

The level of confidence in any new quantity-distance criteria needs to be high in order to use them to supplement the DOE Explosives Safety Manual. If the hazard refinement analysis for any of the structure/explosives groups does not result in a high degree of confidence in given criteria, small scale testing will be required.

The small scale test requirements have been incorporated into a detailed test plan. The test plan indicates which structure/explosives groups need test data, the nature of the tests to be performed, materials necessary for testing, the number of tests required, the sequence of the tests, a proposed schedule for the tests, instrumentation to be used, and measurements to be made. The test plan has been presented to DOE for approval.

#### **Step 10: Performance of Small Scale Tests**

The approved test plan developed under Step 9 will be followed in the performance of required small scale tests. The test plan may be modified as lessons are learned during the performance of tests. The model and surrounding area will be instrumented to obtain debris/fragment distribution data and secondary information such as ground shock measurements, shock and blast loads down corridors (if applicable), and near and far field pressures outside structures. Results of the tests will establish an improved database in debris/fragment hazard evaluation and will help define the blast pressure field near the donor structure.

#### **Step 11: Repetition of Predictive Analysis for Structure/Explosives Groups**

The predictive analysis will be repeated for those structure/explosives groups for which data collection from small scale testing was accomplished. The results will again be in the form of hazardous debris area or quantity-distance relationships which will be presented for review by the DOE and DDESB. Any blast data collected can be used to establish overpressure contour maps.

#### **Step 12: Establishment of Large Scale Test Requirements and Plans**

If the confidence level of the quantity-distance relationships and quantity bench marks established after small scale testing is still not high enough, large scale testing will be necessary. This testing will probably be done in half or full scale. Careful and detailed instrumentation will be required since the larger scale models will be expensive and as much data as possible need to be collected. This testing will be performed only on a limited number of worst case situations for the structure/explosives groups due to the prohibitive cost. As with the small scale testing, a detailed test plan will be submitted for DOE review prior to testing.

#### **Step 13: Performance of Large Scale Tests**

The large scale tests, if necessary, should confirm results of the small scale tests or, in some way, increase the level of confidence in the debris hazard prediction methodologies and quantity-distance relationships. The results should be well documented as they will greatly improve the database available in this area.

#### **Step 14: Repetition and Refinement of Predictive Analysis for Structure/Explosives Groups**

The results of the large scale tests will be used to refine the predictive model, and thus, the hazard analysis results for those structure/explosives groups affected by the new data. The refined missile maps and quantity-distance relationships will establish the criteria to be included in tables to supplement the DOE Explosives Safety Manual.

#### **REFERENCES**

1. Bowles, P.M., Whitney, M.G., and Baker, W.E., "Fragment and Debris Hazard Evaluation Problem Definition and Safety Assurance Plan," SwRI Project 06-1819, prepared for Mason & Hanger--Silas Mason Co., Inc., August 1987.
2. "SHOCK Users Manual," Version 1.0, Naval Civil Engineering Laboratory, Port Hueneme, CA, January 1988.
3. Vargas, L.M., Hokanson, J.C. and Rindner, R.M., "Explosive Fragmentation of Dividing Walls," ARRADCOM Contractor Report ARLCD-CR-81018, July 1981.
4. Connett, J., "FRANG Users Manual," Naval Civil Engineering Laboratory, Special Paper 6046SP, October 1988.
5. Huang, L.C.P., "Theory and Computer Program for the Multiple Debris Missile Impact Simulation (MUDEMIMP)," Naval Civil Engineering Laboratory, Program No. Y-0995-01-003-331, June 1984.

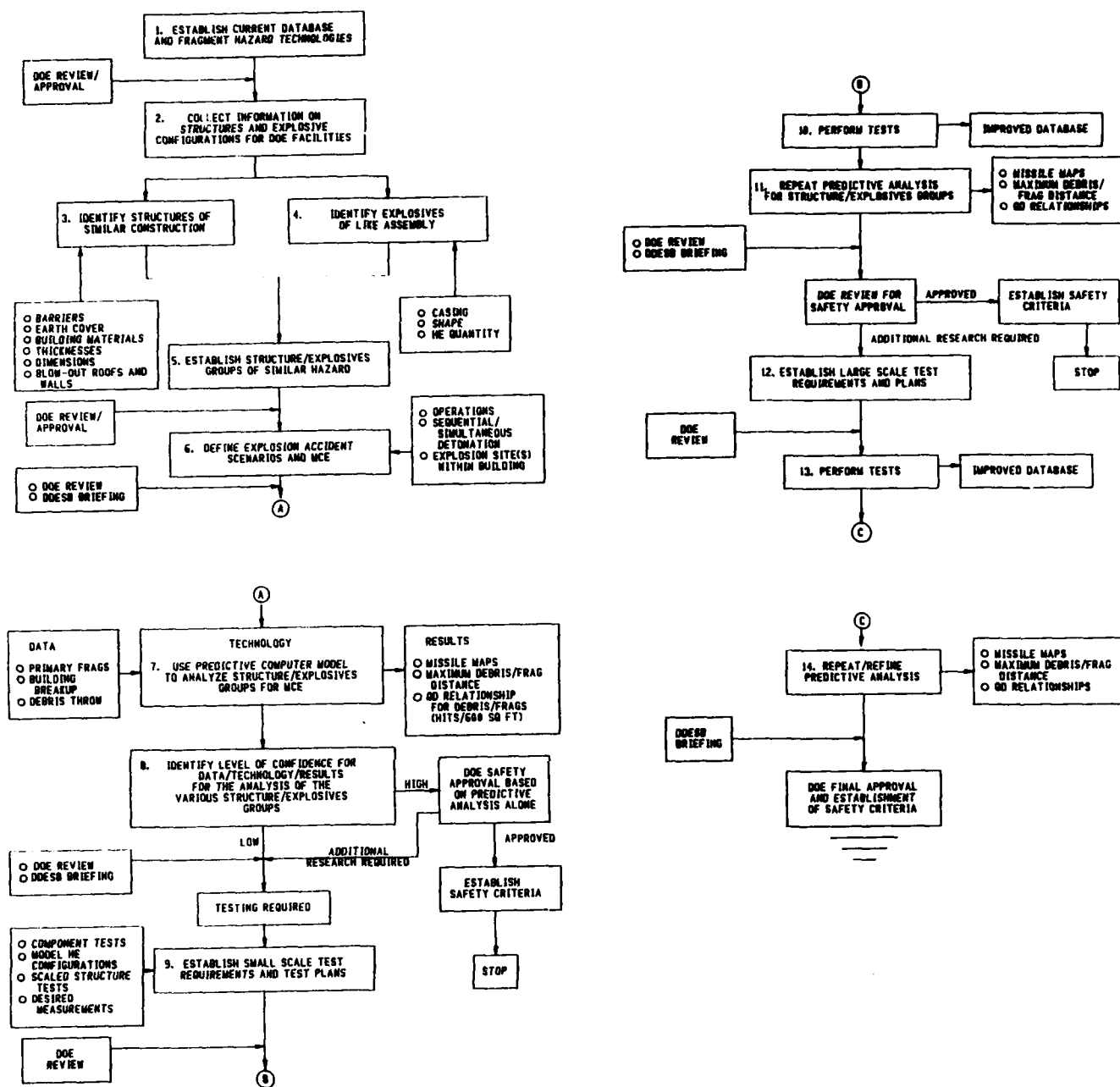


Figure 1. Safety Assurance Plan

## INTERACTION OF DEFORMATION AND SHOCK RESPONSE FOR BURIED STRUCTURES SUBJECT TO EXPLOSIONS

Eve Hinman, Structural Engineer

Weidlinger Associates, 333 Seventh Avenue,  
New York, NY, 10001

**Abstract:** An approximate method is presented for determining the rigid body response of buried structures subject to explosions; the effects of exterior wall deformation and interface shear friction are included. The structure is modeled by a three-degree-of-freedom system. The two exterior walls perpendicular to the blast direction are modeled by lumped masses and elasto-plastic resistance functions. These are attached to either side of a third rigid mass, representing the remainder of the structure. A decoupling procedure is used to model structure-medium interaction effects.

### Introduction

This is a progress report on our current research on the response of buried structures to groundshock. In March 1987, we presented a paper at this symposium on the deformation response of an exterior wall subjected to the effects of a below ground explosion. The wall was modeled using an elasto-plastic, single-degree-of-freedom (SDOF) system with structure-medium-interaction (SMI) effects included by using the decoupling approach of Ref. (8). This solution method was shown to compare well with finite-element computations. Similar work by Drake [3] was also presented at that time. Further work was presented in August 1987 at a NATO Workshop conference at Tyndall Air Force Base. A preliminary, closed-form solution was given for rigid body response where the structure was modeled by a rigid mass and the same decoupling approach is used to model interface stress. A numerical example is solved in Ref. (7) using this solution method.

In this paper the rigid body response model is improved by including the deformation of the exterior walls perpendicular to the blast, and also the effect of interface friction. Deformation of the exterior walls is modeled using the SDOF method of Refs. (5) and (7).

A more detailed solution to this problem is obtained by using the "soil island" method [6]. In this method the soil, the structure, and the interface are modeled using finite elements (FEM) and velocities are applied at the boundaries. These models have many degrees of freedom and require constitutive equations for all the materials used. The calculations are time consuming and are performed on main-frame computers.

Unfortunately, the free-field stress is not well defined for these problems and there are only limited test data. Ref. (2) provides a semi-empirical expression for the free-field stress based on test data from the early 1970's. Reservations have been expressed regarding the uncertainty of some of the parameters in this free-field definition, particularly use of seismic velocity to characterize the soil.

Considering the degree of uncertainty in the definition of the free-field source function, elaborate FEM computation are not justified at this time. The method presented here is sufficient for our purposes. It is not intended as a design tool in its present form but as a research tool, to highlight the areas which need further investigation.

An example problem is solved using numerical methods, and the effect of varying the stiffness of the walls is investigated. The effect of interface friction on the response is explored. Results of parametric variations are compared with the solution for rigid exterior walls and the solution method of Ref. (2). Peak response comparisons, time histories, and response spectra are presented.

### Problem Formulation

A buried, box-shaped structure is subjected to an explosion located at a range,  $R_0$ , from the nearest surface. Three generic configurations are shown in Fig. (1).



The explosion produces a radially expanding shock wave that propagates through the soil. As the stress wave envelops the structure, it moves as a rigid body. This motion is used to define the internal shock environment. It is affected by the threat, the deformation response of the structural components, rigid body rotation, interface shear friction, structure mass, and the soil characteristics.

The primary exciting force is the pressure acting on the surface nearest to the explosion. It is assumed that the walls and slabs are able to survive this loading. The peak pressure varies along this surface [see Fig. (2)]. Only a portion of the wall or slab directly across from the explosion responds through plastic deformation. The remainder responds elastically.

When the structure velocity exceeds the velocity of the surrounding soil particles, a gap forms and the structure becomes unloaded. Relative velocity also causes interface friction to occur on the sides parallel to the blast direction.

The rigid body response is used to predict the response of the contents in the building by using the structure velocity as the exciting function on a linear elastic oscillator of variable frequency. This is the in-structure shock. Fragility curves of equipment are used to determine the frequency ranges in which shock isolation is needed.

#### Lumped Mass Model

The lumped mass model shown in Fig. (3) is used. It models the deformation response of the exterior walls perpendicular to the blast [7] and the interface friction. The two walls are referred to as the "near wall" and the "far wall" to indicate their locations with respect to the charge, and it is assumed that the center of gravity (c.g.) of the explosive source is located direct-

ly across from the mid-point of the near wall.

The lateral motion of the exterior walls, as a function of time,  $t$ , consists of two parts:

- the deformation with respect to the box structure,  $y(t)$ , and
- the rigid body displacement of the c.g. of the structure,  $w(t)$ .

The total displacements of the near (n) and far walls (f) are therefore

$$u_n(t) = y_n(t) + w_n(t) \quad (1)$$

$$u_f(t) = y_f(t) + w_f(t) \quad (2)$$

The displacement  $y_n(t)$  in Eq. (1) is the displacement of the near wall along the effective width  $ab$  in Fig. (2). The remaining width of the near wall is assumed to remain rigid.

The interface pressures [4,7] acting on these walls, are

$$\sigma_n(t) = 2P_{n\alpha}(t) - \mu \dot{c}u_n \quad (3)$$

$$\sigma_f(t) = -\mu \dot{c}u_f \quad (4)$$

where  $(\dot{\phantom{x}})$  indicates differentiation with respect to time,  $\mu c$  is the average acoustic impedance of the soil and,  $P_{n\alpha}$ , is the average free-field stress acting on the effective near wall area  $abL$  shown in Fig. (2). Ref. (2) provides formulas and tables for evaluating  $P_{n\alpha}$  and  $\mu c$ .

For walls of mass,  $m$ , elasto-plastic flexural resistance,  $r$ , subjected to the interface pressures of Eqs. (3) and (4), the equations of motion of the near and far walls [4] are respectively,

$$K_{LM}m\ddot{y}_n + \mu c\dot{y}_n + r(y_n) = 2P_{n\alpha}(t) - m\ddot{w} - \mu c\dot{w} \quad (5)$$

$$K_{LM}m\ddot{y}_f + \mu c\dot{y}_f + r(y_f) = -m\ddot{w} - \mu c\dot{w} \quad (6)$$

where  $K_{LM}$  is the ratio of the mass factor,  $K_M$ , to the load factor,  $K_L$ , [1] and all

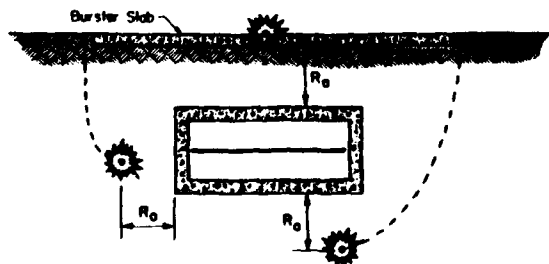


Figure 1. Buried Protective Structure

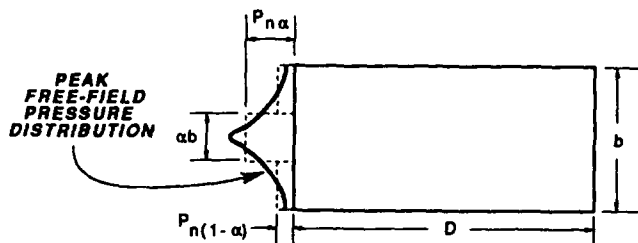


Figure 2. Effective Width of Near Wall

terms are expressed in units of force per unit area.

Eqs. (5) and (6) must satisfy the initial conditions

$$u_N(0) = u_F(0) = w(0) = 0 \quad (7)$$

$$\dot{u}_N(0) = \dot{u}_F(0) = \dot{w}(0) = 0 \quad (8)$$

and the load cut-off conditions:

$$\text{when } 2P_{Na} < \mu c \dot{u}_N \text{ we set } 2P_{Na} = \mu c \dot{u}_N = 0 \quad (9)$$

$$\text{and when } \mu c \dot{u}_F < 0 \text{ we set } \mu c \dot{u}_F = 0 \quad (10)$$

The loading acting on the exterior walls is transmitted to the box structure by: the elasto-plastic reactions,  $R_N$  and  $R_F$ , acting over the effective width,  $ab$ ; the average pressure,  $P_{N,1-\alpha}$  acting along the remainder of the width,  $(1-\alpha)b$  [see Fig. (2)], and the interface friction,  $F$ . The equation of motion for the box structure is:

$$M\ddot{w} + F = \alpha(R_N + R_F) + (1-\alpha)P_{N,1-\alpha} \quad (11)$$

where

$$R_N = 2P_{Na}(t) - m\ddot{w} - \mu c\dot{w} - K_{Ln}[m\ddot{y}_N + \mu c\dot{y}_N] \quad (12)$$

$$R_F = -m\ddot{w} - \mu c\dot{w} - K_{Lf}[m\ddot{y}_F + \mu c\dot{y}_F] \quad (13)$$

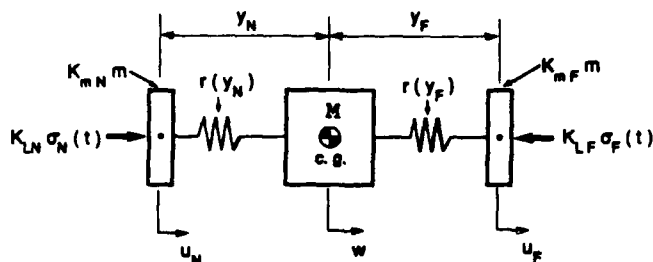


Figure 3. Lumped Mass Model

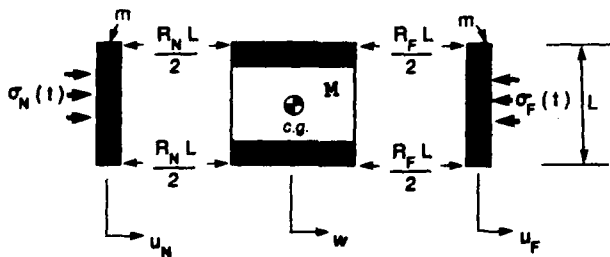


Figure 4. Exterior Wall Reactions

and the total mass of the structure is

$$M_t = M + 2m \quad (14)$$

The interface friction expressed as an equivalent pressure is taken to be

$$F = \phi g M_t D/L \quad (15)$$

where  $\phi$  is the friction coefficient,  $g$  is the acceleration of gravity,  $D$  is the structure length, and  $L$  is the structure height [see Fig. (2)].

Eqs (5), (6), and (11) are expressed in matrix form by substituting Eqs. (12) and (13) into Eq. (11) and rearranging terms. Symbolically this is expressed:

$$[M](\ddot{X}) + [C](\dot{X}) + \{R\} = \{P\} \quad (16)$$

where the initial conditions are

$$\{X\} = \{\dot{X}\} = 0 \text{ at } t=0 \quad (17)$$

and the load cut-off conditions of Eq. (9) and (10) are satisfied.

These matrices are defined as

$$[M] = m \begin{bmatrix} K_{MN} & 0 & K_{Ln} \\ 0 & K_{Mf} & K_{Lf} \\ \alpha K_{Ln} & \alpha K_{Lf} & (2\alpha + M/m) \end{bmatrix} \quad \{X\} = \begin{bmatrix} y_N \\ y_F \\ w \end{bmatrix}$$

$$[C] = \mu c \begin{bmatrix} K_{Ln} & 0 & K_{Ln} \\ 0 & K_{Lf} & K_{Lf} \\ \alpha K_{Ln} & \alpha K_{Lf} & 2\alpha \end{bmatrix} \quad \{R\} = \begin{bmatrix} K_{Ln} r(y_N) \\ K_{Lf} r(y_F) \\ F \end{bmatrix}$$

$$\{P\} = \begin{bmatrix} 2K_{Ln}P_{Na} \\ 0 \\ (1-\alpha)P_{N,1-\alpha} + \alpha 2P_{Na} \end{bmatrix}$$

This model reproduces the following response sequence [Fig. (5)]:

- 1) The first surface to encounter the shock wave is the near wall [Fig.5(a)]. This wall responds by deforming inward [Fig. 5(b)]. Depending on the threat, the soil properties, and structure geometry, a gap may form between the soil and the structure causing the structure to become unloaded.
- 2) The loading is transmitted to the box through the near wall reactions,  $R_N$ , and  $P_{N,1-\alpha}$  [Fig. 5(c)] causing the box to move.
- 3) The box motion causes the far surface to be loaded with pressure  $\sigma_F(t)$ , resulting in far wall deformation. Load cut-off may occur at this face.

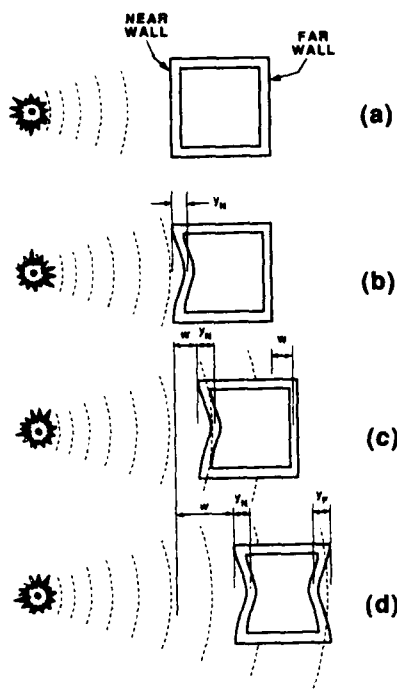


Figure 5. Response Sequence

- 4) The box velocity is reduced by the reactions,  $R_f$ , of the far wall and the interface friction,  $F$ .

Limitations of the model are:

- 1, Asymmetrical effects are neglected.
- 2) Stress wave propagation through the structure is neglected. The box motion is defined solely by the translation of the c.g. of the structure.
- 3) Interface friction acts only on the foundation surface. Soil shear strength is neglected. The effect of relative velocity between the soil and structure is not considered.
- 4) Deformation effects on the sides of the structure parallel to the direction of the blast are neglected.
- 5) Non-linear soil properties, cratering, and reflections from the surface and soil layers are neglected.
- 6) Elastic deformation effects associated with the near wall outside the effective width  $ab$  are neglected.

#### Numerical Example

The rigid body response of a buried structure subjected to a side-on burst is considered for the special case when  $\alpha=1$  and  $F=0$ . Input parameters are shown in Fig. (6).

Eqs (9), (10), (16), and (17) are solved using numerical methods. The peak displacement, velocity, and acceleration

are determined to be

$$w_{\max} = 1.4 \text{ in} \quad \dot{w}_{\max} = .01 \text{ in/msec}$$

$$\ddot{w}_{\max} = 3.4 \text{ g's}$$

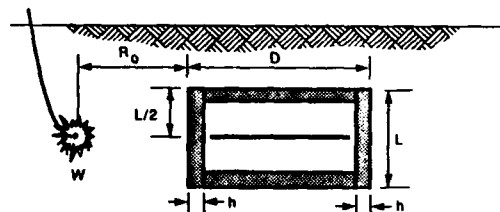
Detailed discussion of this problem is given in Ref. (4).

#### Effect of Wall Stiffness and Resistance

The effect of stiffness and ultimate resistance of the walls is considered by varying the wall thicknesses from  $h=20"$  to  $h=90"$  while keeping the total mass,  $M_t$ , constant. The peak displacement, velocity, acceleration, and deceleration of the box structure are plotted against the wall thickness,  $h$ , in Fig. (7). Response values in Fig. (7) are normalized with respect to the following rigid (i.e., non-deforming) wall solution:

$$w_{\max} = 4.1 \text{ in} \quad \dot{w}_{\max} = .029 \text{ in/msec}$$

$$\ddot{w}_{\max} = .0026 \text{ in}^2/\text{ms} \quad \ddot{w}_{\min} = -.00031 \text{ in}^2/\text{ms}$$



#### FREE FIELD:

$w = 1014 \text{ lbs TNT}$   
 $R_0 = 10 \text{ ft (3m)}$   
 $I = 1.0$   
 $pc = 22 \text{ psi/ft}$   
 $n = 2.75$

#### EXTERIOR WALLS:

$L = 65.6 \text{ ft}$   
 $n = 38 \text{ in}$   
 $\rho_s = 0.0045 \text{ ea. face, ea. way}$   
 $f_c = 4 \text{ ksi (25% enhancement)}$   
 $f_y = 60 \text{ ksi (20% enhancement)}$   
 $m = 14 \text{ lbs}^2/\text{ft}^3$   
 $D = 210 \text{ ft}$

#### BOX STRUCTURE:

$M_t = 370 \text{ lbs}^2/\text{ft}^3 (1807 \text{ kg/m}^3)$

Figure 6. Numerical Example

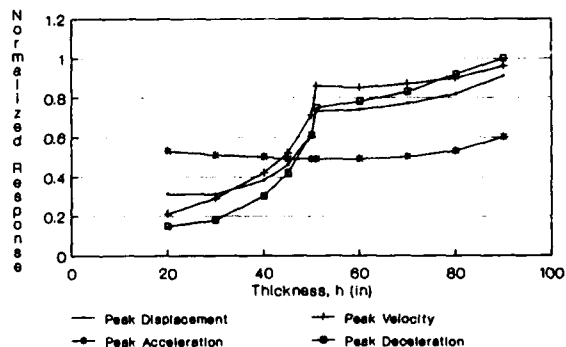


Figure 7. Peak Response (normalized w/r to rigid wall solution)

Fig. (7) shows that there are two distinct response regimes. For more flexible slabs ( $h < 51"$  or  $h/L < 1/15.4$ ) the peak displacement, velocity, and deceleration are markedly affected by wall deformation -- with peak values that are 20-80% of the rigid wall solution. For stiffer slabs ( $h > 51"$  or  $h/L > 1/15.4$ ) these quantities are less affected by wall deformation -- with values that are 80-100% of the rigid wall response.

This sensitivity to wall stiffness is due to the load cut-off condition of Eq. (9). This is illustrated in Fig. (8), where the load cut-off time,  $t_1^*$ , is plotted as a function of wall thickness,  $h$ . This figure shows that flexible slabs experience early time load cut-off and stiffer slabs experience load cut-off only at later times. At the critical stiffness ( $h=51"$  or  $h/L = 1/15.4$ ), there is a sharp discontinuous transition between these two regimes.

Fig. (8) also shows that for flexible slabs, the loading returns after a time,  $t_2^*$ . As the stiffness approaches the critical value ( $h=51"$ ) the reloading time,  $t_2^*$ , approaches the cut-off time,  $t_1^*$ .

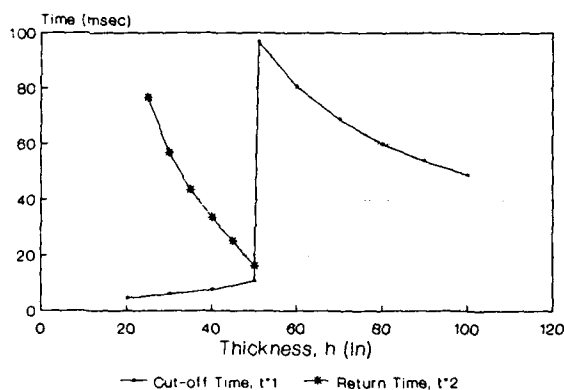


Figure 8. Times of Load Cut-off and Reload

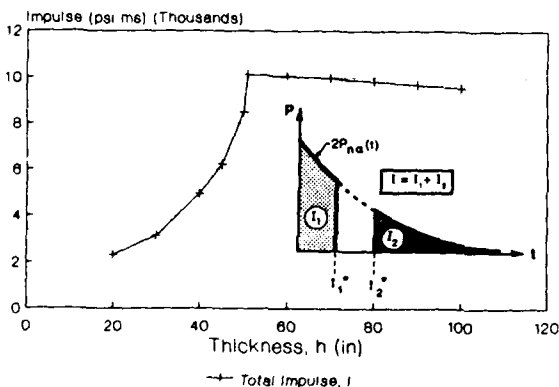


Figure 9. Total Impulse on Near Wall

This load cut-off behavior affects the impulse acting on the system, as shown in Fig. (9). The transition at the critical stiffness is not as abrupt as in Fig. (8) due to the impulse contribution of reload. Note that the response curves of Fig. (7) are similar to the pressure impulse of Fig. (9). The peak acceleration shown in Fig. (7) is insensitive to stiffness because it occurs before load cut-off (at  $t \approx 0$ ).

Load cut-off occurs at early times for flexible slabs because these walls experience large plastic deformations which cause a gap to form between the soil and structure, and consequently cause the unloading of the stem. Stiffer slabs, experiencing smaller deformations maintain contact with the soil at these times. Load cut-off occurs at later times for stiffer slabs due to the increased rigid body motion of the box structure.

The velocity time histories for the box structure are used as input to predict the response of a linearly elastic oscillator. Damping is taken to be 5% of critical in this study. Results are plotted in the form of response spectra in Fig. (10), for a structure having flexible walls,  $h=36"$ , stiff walls,  $h=72"$ , and the rigid wall case. Results are compared with the semi-empirical solution method given by the WES manual [2] (which is independent of wall thickness).

Fig. (10) shows that the in-structure values show trends that are similar to the peak response values of Fig. (7). The WES manual solution shows greater in-structure displacements and accelerations and a smaller pseudo-velocity for this particular numerical example.

#### Effect of Interface Shear Friction

In this study, the interface friction defined by Eq. (15) is not intended to precisely reproduce the physical behavior but to given insight into system sensitivities.

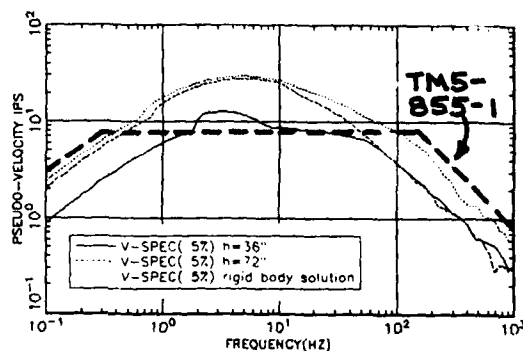


Figure 10. In-Structure Shock Response

For a friction coefficient [Eq. (15)] of  $\phi = .3$ , the interface friction is represented by the equivalent pressure of  $F = 79$  psi for this example. This is a constant force acts when  $\dot{w} > 0$ .

Peak response values for the box motion are presented in Fig. (11). Values are normalized to the no-friction, rigid wall solution given previously.

This figure shows that the presence of interface friction does not eliminate the abrupt transition found in Fig. (7), however, magnitudes are affected. There are increases in the peak deceleration of the box and decreases in the peak displacements and velocities.

In Fig. (12) in-structure response spectra, including the effect of interface friction, are given for  $h=36"$  and  $h=72"$ , and the rigid wall case. These are compared with the WES solution given previously. Interface friction has the effect of reducing the in-structure values particularly for the flexible wall case,  $h=36"$ .

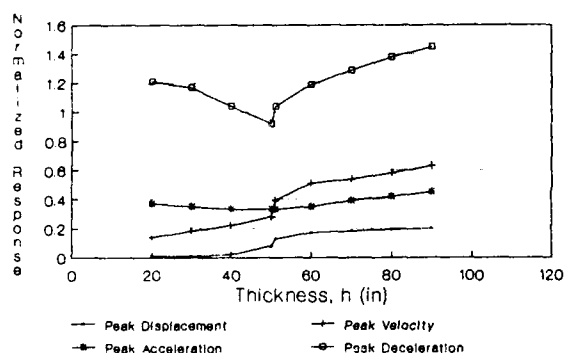


Figure 11. Peak Response (including effect of interface shear)

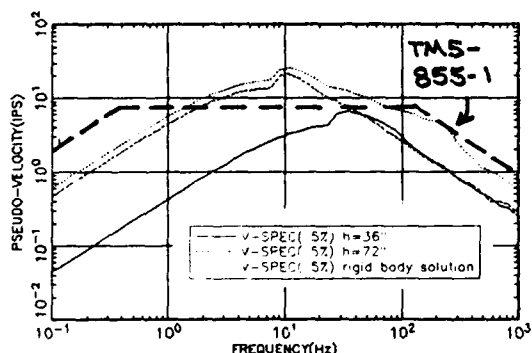


Figure 12. In-Structure Response (including effect of interface shear)

## Conclusion

The results of this study indicate a sensitivity to the depth-to-span ratio of the exterior walls/slabs. Deformation mitigates rigid body response by absorbing energy through plastic deformation. Also, load cut-off effects reduce the rigid body response of structures having flexible walls. In-structure shock is similarly affected by wall stiffness. Validation by detailed finite element analysis and explosive testing is urgently needed.

## References

1. Biggs, John, M., Introduction to Structural Dynamics, McGraw-Hill Book Company, New York,, 1964.
2. Fundamentals of Protective Design for Conventional Weapons, TM5-855-1, Headquarters, Dept. of the Army, Wash. DC, Nov. 1986.
3. Drake, J.L., R.A. Frank and M.A. Rochefort, "A Simplified Method for the Prediction of the Ground Shock Loads on Buried Structures," Proc. International Symposium on the Interaction of Conventional Munitions with Protective Structures, Mannheim, West Germany, March 09-13, 1987.
4. Hinman, E., "Shock Response of Buried Structures Subject to Explosions," Proc. ASCE Speciality Conference on Structures for Enhanced Safety and Physical Security, March 8-10, 1989, Arlington, VA.
5. Hinman, E., and Weidlinger, P., "Single Degree of Freedom Solution of Structure-Medium Interactions," Proc. International Symposium on the Interaction of Conventional Weapons With Structures, Mannheim, West Germany, March 9-13, 1987.
6. Nelson, I, "Numerical Solution of Problems Involving Explosive Loading," Proc. Dynamic Methods in Soil and Rock Mechanics, Karlsruhe, 5-16 Sept., 1977, Vol. 2, A.A. Balkema Rotterdam, Holland, pp. 239-297.
7. Weidlinger, P., and Hinman, E., "Analysis of Underground Protective Structures," Journal of Structural Engineering, ASCE, Vol. 114, No. 7, July 1988, pp. 1658-1673.
8. Wong, F.S., and Weidlinger, P., "Design of Underground Protective Structures," Journal of Structural Engineering, ASCE, Vol. 109, No. 8, August, pp. 1972-1979.

## TEST PROGRAM FOR DETERMINATION OF REFLECTED PRESSURES IN ACCEPTOR BAYS

Darrell D. Barker  
Steven L. Young, PE

Mason & Hanger - Silas Mason Co., Inc.

**ABSTRACT:** Criteria for protection of personnel in DOE facilities requires that, for Class II operations, all personnel in occupied areas other than the bay of occurrence not be exposed to overpressures greater than 15 psi. Several of the operating bays used at DOE facilities are WW II-era structures consisting of two or three wall cubicles with a "soft" roof. Of particular concern are bays which have a clay tile wall adjacent to the open front. A test program was initiated to determine the pressures reflected by this wall into an adjacent bay. A 1/8th scale steel model of two adjacent bays was built, instrumented and tested to determine these pressures. Charge and gauge locations were varied to determine relationships between pressure and scaled distance from a reflecting surface. Test program, model fabrication, and results are discussed.

### INTRODUCTION

A test program was initiated to determine overpressures reflected into adjacent occupied areas by an accidental detonation in an explosives operations bay. An overstrong steel model was built to model donor and acceptor bays to verify compliance with protection criteria.

### BACKGROUND

Department of Energy (DOE) criteria requires that, for Class II operations, all personnel in occupied areas, other than the bay of occurrence, be protected from overpressures greater than 15 psi. Several explosives operating facilities are in use today which are in excess of 40 years old. These facilities were designed to conform to criteria which was not as stringent as that required today. Facilities which cause particular concern are those with adjacent operating bays with open front walls and a connecting corridor. The corridor is composed of a concrete floor slab, clay tile exterior wall and a "soft"

roof. The bays are two and three wall cubicles with 12" reinforced concrete walls. Roofs are either reinforced concrete or asbestos cement panels. A typical bay is 19 ft. wide, 17.5 ft. high, and 23.5 ft. deep. "Thru" bays are 48 ft. deep two wall cubicles (open front and rear).

Explosives limits in the bays are 12 lbs. of high explosives (HE), normally PBX and HMX compounds. The design charge weight for determining overpressures is taken as the bay limit converted to TNT with an equivalency factor of 1.10. The postulated accident is a handling error which can occur at any location within the bay which is more than three feet from any wall.

### TEST PROGRAM

#### Description of Model

The 1/8th scale model was designed to remain elastic under the design loading to allow a large number of tests to be conducted. The model was constructed of A36 steel with welded and bolted (A307) connections. A plan view of the model is shown in Figure 1. The 1/2" floor plate was connected to 1/4"x 6" continuous plates on 6" centers to allow access to gauge mounting holes. The 1/2" front wall was bolted to the floor and the 1/4" roof plate to allow removal. This provided a method for determining "wrap-around" pressures without the effects of a reflecting front wall. The roof was also bolted to the 1-1/2" side walls to allow testing of the model as a three wall cubicle without a roof. The back wall of the donor bay was bolted to allow modeling as a "thru" bay.

Gauge mounting holes were provided at four locations in the floor along the front of the donor bay and at the front, 1/4 point, and center of the acceptor bay to measure side-on pressures. Six inch angles were bolted to the floor of the acceptor bay with pressure gauges installed at 3" above

the floor to measure reflected pressures at each gauge line. Gauges were installed in the front wall at eight locations to measure reflected pressures 3" above the floor. The model was placed in an 11 ft. diameter test fire chamber to allow testing in all weather conditions.

#### Instrumentation

Pressure gauges were PCB Model 102A02, high resolution transducers with built-in amplifier. The gauges were installed flush with the mounting surface and covered with an opaque material to protect against flashes from the detonation. All gauges performed well during testing and appeared to sustain no appreciable damage during the first 10 tests. The gauges are rated for 0-100 psi but will remain functional up to 1000 psi. The highest pressures measured during testing were less than 150 psi. The gauges were coupled to a Neff Model 122 DC amplifier with a PCB Model 483A power unit and Beldon RG58-AU cabling. Signals from the amplifier were fed into a Sangamo 80, 14 channel magnetic tape recorder operating at 120 ips. The analog signal for each channel was digitized

at 200 samples per millisecond using a Biomation Model 8100 Digital Waveform Recorder. The digitized voltages were recorded on magnetic disk and converted to pressure values using calibration voltage data and an HP 9845 computer. Pressure data was plotted using a thermal plotter. A typical pressure plot is shown in Figure 2.

#### Test Plan

The high explosive used for each test was a single pressed, cylindrical charge of LX-10 weighing 10.64 grams with a diameter of 0.75" (L/D=1.05). This explosive has a TNT equivalency of 1.1. An RP-2 detonator was used to detonate the HE. The orientation of the charge was varied to determine directional effects of the cylindrical charge and detonator. End effects from the cylinder were negligible in the confined model and detonator effects were limited to an increase in reflected pressures from the back wall. It was determined that a forward orientation would be used because the accident scenario was a handling error not involving a detonator.

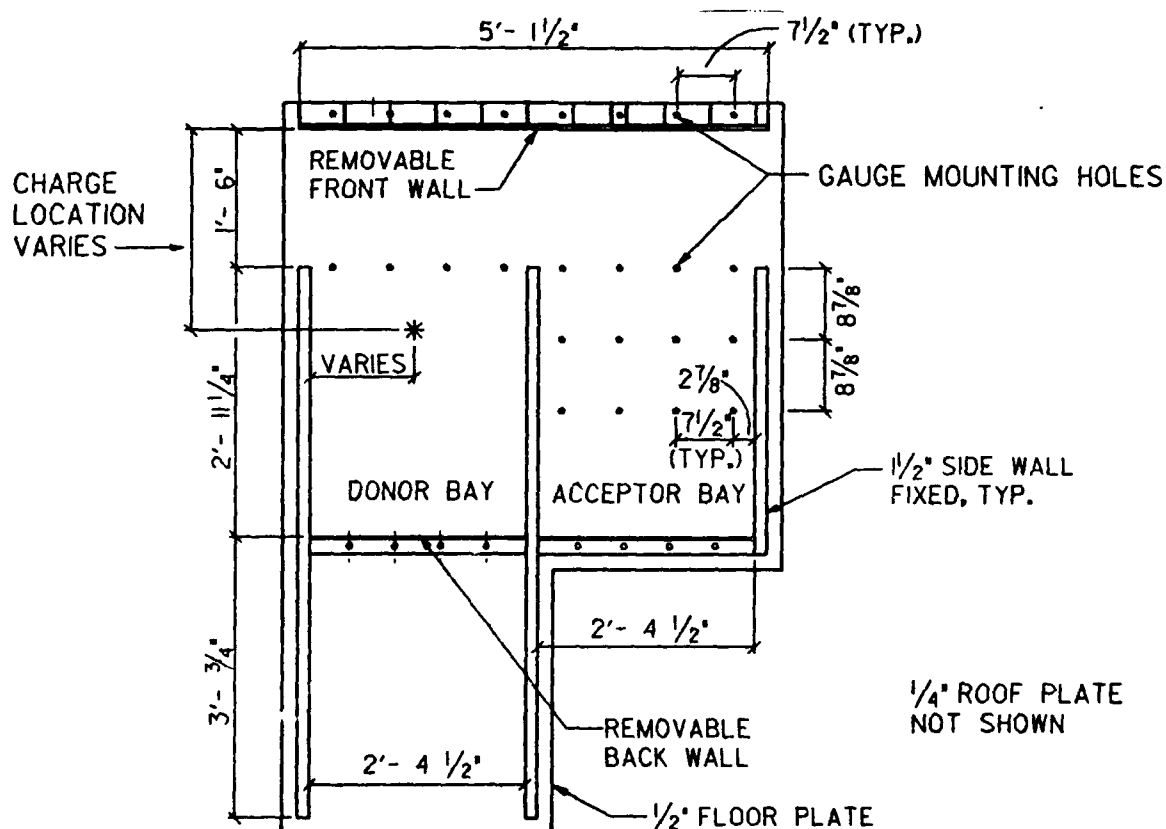


FIGURE 1.  $\frac{1}{8}$  SCALE MODEL, PLAN VIEW

Several model configurations were used to determine the effects of distance, reflective surfaces, and angle of incidence. Initially the charge was placed in the center of the donor bay and reflected pressures were measured at the reflecting wall and the face of the acceptor bay. Measured pressures were compared to predicted pressures to verify that results were within the range for which the gauges had been calibrated. The pressures were approximately 50% higher at the reflecting wall than anticipated and gauge calibration voltage steps were adjusted accordingly. The higher pressures were the result of adjacent reflective surfaces, especially the back wall. Blast pressures for the charge positioned at the front of the donor bay were predicted by doubling the charge weight and using Figure 2-15 of ARLCD-SP-84001, Vol. II. These values were then used to recalibrate the gauges. Measured pressures for the charge in the front position were less than predicted by this procedure and allowed data to be recorded within the calibration limits of the transducers. Results of these two tests allowed a calibration pressure to be established for each gauge location.

Three gauge lines were used in the acceptor bay to establish side-on and reflected pressures at various obliquities and distances from the reflecting wall. These lines covered the front half of the bay and were used to describe pressure contours for the bay. The front wall and roof were removed for three of the test shots to allow separation of "wrap around" pressures from the reflected pressures caused by the front wall.

## RESULTS

### Pressure Measurements

Peak pressures were read directly from the plotted traces. A Fast Fourier Transform filter was applied to the data from the first two tests but did not significantly change the output. Because the filter required a long period of time to run and did not significantly affect the results, it was not used for subsequent tests. A summary of the measured pressures for a charge in the center of the donor bay is given in Table 1.

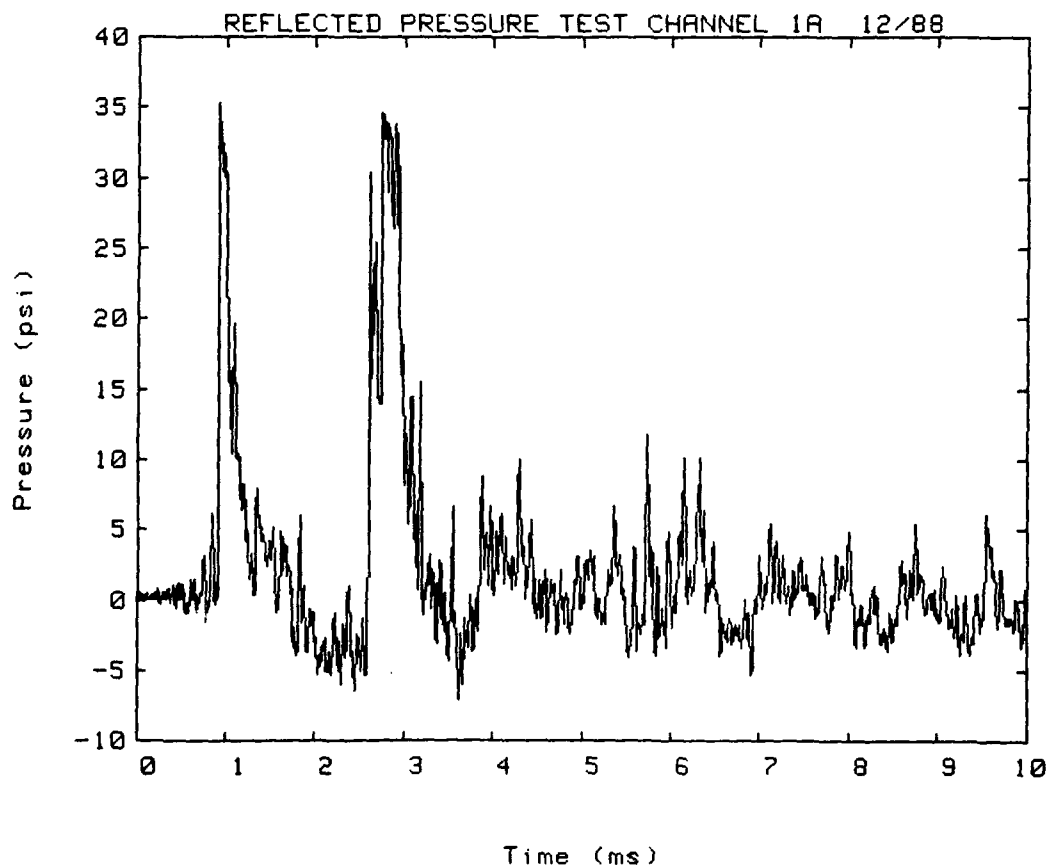


Figure 2 Typical Pressure Plot



Four locations were provided along each gauge line to allow comparisons of measured values in close proximity to each other. This provided a means for evaluating results and determining the validity of the pressure measurements. Measurements which differed greatly from those of nearby gauges were analyzed to determine if the difference resulted from reflections or gauge malfunctions. These locations will be monitored in subsequent testing of the same configuration.

#### Reflected pressures

Reflected pressures were measured at the reflecting front wall and at each gauge line in the acceptor bay. A 6"x3"x1/4" angle was used to provide a reflecting surface and was bolted to the floor so that the front face was flush with the gauge line. The pressure gauges were installed in the angle 3" above the floor. Influence of floor reflections was measured at these gauges by comparing reflected and side-on pressure values.

Pressures at the reflecting front wall ranged from 12 to 35 psi with the charge in the center of the donor bay and 50 to 145 psi with the charge in the front of the bay. At the face of the acceptor bay, pressures were 12 to 22 psi for a center charge and 17 to 25 psi for a front charge. Pressures averaged 17 psi at the second row and 12 psi at the third row for a center charge.

When the front wall and roof were removed, reflected pressures remained approximately the same at the front of the acceptor bay for a front charge position. This configuration with a center charge will be included in future testing.

#### Side-on pressures

Side-on pressures were measured only at gauge lines in the acceptor bay. These pressures were measured to establish a relationship between side-on and reflected

pressures in the model. These pressures were also useful in determining the actual pressures personnel would be exposed to during a detonation.

Pressures along the first gauge line ranged from 8 to 16 psi for a charge in the center position of the donor bay and 12 to 15 psi at the second gauge line. When the charge was moved to the front of the donor bay, the side-on pressures at the first gauge line averaged 13 psi. Removal of the front wall and roof reduced pressures only slightly at the first gauge line with the charge in either position.

#### Analysis

##### Objectives

The principal objective of this test program was to determine whether or not personnel protection requirements were being met. The criteria requires that maximal effective pressures in adjacent occupied areas be less than 15 psi. Reflected pressures at the first gauge line with the charge in the front position are approximately 5 psi higher than allowed by this criteria; however, this configuration is not a realistic design basis. The operations in the explosives facilities are performed on work benches at several locations in a bay. Only a portion of the total HE weight in the bay is located at any given work location. The center of these charges as a group is likely to be between the center of the bay and the back wall. This makes the center bay charge location a suitable configuration for evaluating the true overpressure hazard.

The test results indicate that for the charge in the center of the donor bay the reflected pressures are slightly higher than 15 psi at the face of the bay; however, several important considerations should be noted. As would be expected, pressures in the middle of the gauge line are less than at the ends because they are affected less by reflections from the

Average Measured Pressures (psi)

| Pressure Type | Gauge Location  |          |          |          |
|---------------|-----------------|----------|----------|----------|
|               | Reflecting Wall | 1st Line | 2nd Line | 3rd Line |
| Reflected     | 33.8            | 16.2     | 17.4     | 12.0     |
| Side-on       | N/A             | 13.0     | 13.2     | N/A      |

Table 1. Summary Of Pressures For Center Charge

side walls. Pressures at locations at a greater distance from the floor will likely be less due to less reflection from the floor. The side-on pressures were less than 15 psi for all locations along the first gauge line. Therefore most of the area at the face of the bay will experience pressures less than 15 psi. An interesting result of tests is lack of decay in reflected pressure between gauge lines.

A secondary objective of the test program was to develop a method of predicting overpressures in similar facilities. Several attempts were made to predict pressures in the acceptor bay using various multipliers on the charge weight, total scaled distance to the point of interest, and Figure 2-15 of ARLCD-SP-84001, Vol. II. A multiplier of 4.0 was required to predict pressures equal to those measured with the charge in the center position and 1.5 for the charge in the front position. Another alternative for predicting pressures is to produce graphs relating pressure to: scaled distance to the reflecting surface, angle of obliquity, and scaled distance from the

reflecting surface to the point of interest. Additional testing with variations in charge weight and location will be required to establish meaningful values for either method.

#### Reflected pressures

Reflected pressures at the reflecting wall were approximately three times higher for the charge in the front position than in the center as would be expected. Pressures at the first gauge line, however, were only slightly less for the center position. This was attributed to a reduction in side wall reflection due to the open ends of the corridor area near the charge and less back wall influence due to greater travel distance.

When the front wall and roof were removed, pressures were not reduced at the first gauge line for a front position charge because the direct-path wave equaled or exceeded the reflected wave and was not affected by removal of the wall. Pressures at the third gauge line were reduced by one-half when the front wall was removed.

#### Side-on pressures

Analysis of the results for side-on pressures was difficult because of inconsistent values for adjacent gauges. Measured pressures did not appear to be dependent on charge location, gauge location, or presence of the front wall. Further testing will be required to establish relationships between these variables.

#### Application

The results of the test program will be used to verify compliance with protection requirements for a particular facility; however, a large number of facilities in use today have similar geometries, construction, and explosives limits. Variations in charge weight, charge location, and gauge positioning used in this test will allow prediction of pressures in many of these facilities in which the protection provided is not accurately known. Many times explosives limits are set artificially low because these values are not available; however, there will also be instances in which limits will have to be lowered based on the results of this test program. Results of the tests could also be used to reduce personnel exposure by allowing evaluation of restrictions on HE location in a donor bay and physical barriers for personnel in critical locations of an acceptor bay.

#### SUMMARY

##### Test Plan

The test program provided a means for evaluating personnel exposure to hazardous overpressures for a particular configuration of explosives operations bays. Existing methods for accurately determining pressures reflected into adjacent bays have not been available. This has resulted in the use of simplifying, normally conservative, assumptions to predict these pressures. The test plan varied charge location, gauge position, and reflective surface configuration to accurately measure reflected and side-on pressures.

##### Results

The measured pressures for the most realistic charge location indicated that protection requirements were met for most locations in the bay. Pressures which were above the limits were due to localized reflections from the floor and walls. Upon completion of the tests, HE limits, accident scenario, and restriction on personnel occupancy will be examined to determine what measures must be taken to bring the facility into strict compliance.

##### Application

The abundance of similar facilities necessitated the variation of charge location and gauge positioning to allow application of the results to other operating bays. The methods for determining pressures, which will be developed upon completion of testing, will be used to set HE limits and evaluate personnel protection in these facilities.

### Future Testing

Currently 10 test shots have been completed. The configurations tested were used to establish boundaries for pressure measurements and to determine critical locations. Only one shot was made for any given configuration; however, future tests will use some of the same configurations to establish a level of confidence for the results. Additional tests will use variations in charge weight and location to determine the resulting pressures at the reflecting wall and at acceptor bay gauge lines.

The back wall of the donor bay will be removed for some of the test shots to model a "thru" bay and evaluate the effects of reflections from the wall. The roof will be removed to measure leakage pressures in the acceptor bay for a charge placed in the rear of a "thru" bay. Pressures will also be measured on the roof of the acceptor bay with the donor roof removed. This will allow evaluation of protection provided by the "soft" roof. Pressures outside the model will be measured to determine personnel exposure outside the building. All testing is scheduled to be completed during the third quarter of FY 1989.

# A MODIFIED TIMOSHENKO BEAM APPROACH FOR THE ANALYSIS OF REINFORCED CONCRETE STRUCTURES UNDER IMPULSIVE LOADS

A. Assadi-Lamouki, AM. ASCE

T. Krauthammer, M. ASCE

AEC Engineers, Minneapolis

U. of Minnesota, Minneapolis

Preventing catastrophic failures of reinforced concrete structures under blast loads is a fundamental requirement for safe protective structures. This study was aimed at understanding the nature of structural failures, and at developing an analytical approach for evaluating the observed responses of structures tested under such conditions.

## Background

The interest in the dynamic shear failure of reinforced concrete slabs is relatively recent, and the subject attracted the attention of a number of researchers after the problem was observed experimentally at the Waterways Experiment Station (WES). Three series of tests were conducted at WES. The first group consisted of six box-type structures with single bay two-way roof slabs and one multi-bay two-way roof slabs tested between July 1977 and July 1980 (Kiger *et al* 1980-84). The second group consisted of five reinforced concrete box-type structures with one-way roof slabs tested in 1981. As a continuation to the first series, another group of six box-type structures were tested in 1982 (Kiger and Slawson 1981-82, and Slawson 1984).

These structures were tested in a shallow-buried configuration using a HEST (High Explosive Simulation Technique) loading that simulated the peak pressure, duration, and the rate of decay of the anticipated overpressure. The three structural test configurations were 1/4 scale test elements, and the major parameters varied were the span-to-thickness ratio, steel reinforcement ratio, concrete strength, and charge density. Here, only the last eleven cases (Kiger and Slawson 1981-82, and Slawson 1984) will be investigated. The values of average peak

pressure, rise time, and duration used for this analysis were the average values of interface pressure gauge readings. These loads represent the combined effect of the actual blast overpressure and soil-structure interface pressure-time histories. To determine the mode of failure of the test structure, post-failure photographs, high speed photography data, and the interface pressure readings have been used here.

In these tests it has been observed that roof slabs of reinforced concrete shallow-buried structures subjected to severe dynamic loads may fail in a distinct shear mode, in which the plane of failure is nearly vertical and parallel to the shear resisting stirrups. The direct shear failure happens when the deformations due to shear, at early loading stages, grows at a rate much faster than those due to flexure, and failure occurs when the capacity of the member in direct shear is attained. In other cases, diagonal shear, as opposed to direct shear, was an important factor effecting the response of the structure. Consequently, any reliable analytical model, for predicting the response of reinforced concrete structures subjected to severe dynamic loads, should be able to consider the shear deformations, as well as the complete shear stress-shear strain relationship for diagonal shear and shear stress-shear slip relationship for direct shear, in conjunction with the flexural behavior. In this paper, the non-linear, inelastic responses of reinforced concrete structural elements are examined, and the differential equations of motion that include these non-linearities are solved numerically by an explicit finite difference technique, as presented by Assadi-Lamouki and Krauthammer (1988).

## Analytical Approach

Since all the roof slabs of the tested box-type systems were either one-way or acted as one-way systems (length to width ratio of 4), a beam theory capable of

predicting their responses could be utilized for the analysis. Further, due to the importance of shear in conjunction with flexural response, a model capable of assessing both these mechanism is needed. The Timoshenko beam theory had been shown to be suitable for this purpose (Ross 1983, Goodman 1951), and therefore is adopted in this study. For the reinforced concrete structures under consideration, failure is most probably to occur in the nonlinear domain of behavior, hence, this theory is modified to account for nonlinear, inelastic material behavior. The roof slabs were modeled as beams with nonlinear, inelastic supports in order to investigate the shear slip and bending rotation influences. It should be noted that the end restraints are provided by adjoining structural elements, and the effect of such an interaction could be modeled by linear elastic or nonlinear inelastic springs, as shown in Figure 1.

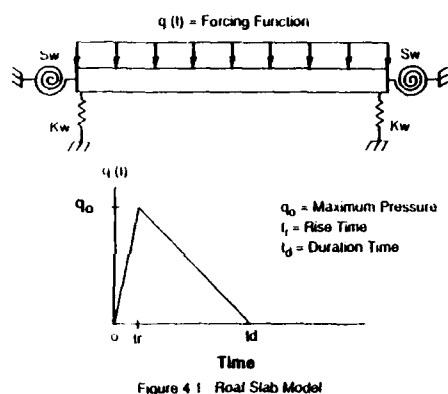


Figure 1. Roof Slab Model

The general equations of motion of the Timoshenko beam can be written as:

$$\frac{\partial M}{\partial x} - Q = -\rho I \frac{\partial^2 \beta}{\partial t^2} \quad (1a)$$

$$\frac{\partial Q}{\partial x} + q = \rho A \frac{\partial^2 w}{\partial t^2} \quad (1b)$$

where,

- $M, Q$  = bending moment and shear force, respectively
- $I, A$  = cross sectional moment of inertia and area, respectively
- $\rho$  = material density
- $\beta$  = rotation of the cross section due to bending
- $w$  = transverse displacement of midplane of the beam

$q$  = distributed dynamic load transverse to beam length

For simplicity, Timoshenko (1921) and Mindlin (1951) assumed that the shear stress is constant over the cross sectional area, but, then introduced a factor  $K$  to correct for the error stemming from this assumption. Therefore,

$$Q = KA\tau_{xz} \quad (2)$$

where:

- $K$  = shear deformation coefficient, and
- $\tau_{xz}$  = shear stress

For high frequency vibration, Mindlin (1951) suggested

$$K = \pi^2 / 12 \quad (3)$$

The same coefficient was also used by Ross (1983). In general, bending moment and shear force can be rewritten as follow:

$$Q = (KA) f_1(\gamma_{xz}) \quad (4a)$$

$$M = f_2(\mu) \quad (4b)$$

where:

- $f_1$  = function defining the shear force shear strain relationship
- $f_2$  = function defining the moment-curvature relationship
- $\gamma_{xz}$  = shear strain of the cross section
- $\mu = (\partial w / \partial x) - \beta$
- $\mu$  = curvature of the cross section subsequent to bending =  $-\partial \beta / \partial x$

At the boundary,

$$Q_b = K_w(W_b) \quad (5a)$$

$$M_b = S_w(\beta_b) \quad (5b)$$

where,

- $Q_b, M_b$  = shear and moment at the boundary, respectively
- $W_b, \beta_b$  = vertical slip and rotation at the boundary, respectively
- $S_w$  = function defining the rotational constraint at the boundary
- $K_w$  = direct shear force - shear slip relationship

One may assume that the ends of the beams are infinitely restrained against rotation. Experimental observation indicated that the walls of the reinforced concrete box-type structures have shown little damage at failure, and it has been noticed further that the rotation at the bases of the walls were nearly zero. The vertical shear slip phenomenon, however, cannot be ignored since the direct shear failure is a result of the relative movement of the slab with respect to the supporting walls.

## Material Behavior

The material models for steel and reinforced concrete used in this study were presented previously in the literature. The steel model is the one proposed by Park and Paulay (1975), and the concrete model is similar to the one proposed by Krauthammer et al. (1987) by modification of a model that had been developed by Hognestad (1951). The moment-curvature relation of the reinforced concrete element was then determined by incorporating these material models in the requirement for strain compatibility and force equilibrium. The popular Gaussian Quadrature integration technique has been utilized for computing the resultant forces and moments corresponding to the nonlinear distribution of stresses. The calculated moment-curvature relationship was then used to define the function  $f_2$  (in Eq. 4B).

The present empirical model for direct shear is based on studies by Hawkins (1974, 1981) and is referred to as the Hawkins shear stress-shear slip model as described by Murtha and Holland (1982). The model has been developed based on the experimental data and material behavior within the static domain and the resulting curve is a non linear relationship between the shear stress and the relative vertical slip across a section. Here, in order to preserve consistency with the models proposed for moment and diagonal shear, the complete shear stress-shear slip curve is not utilized. Since failure for both moment and diagonal shear is defined when the member reaches its ultimate moment capacity, or diagonal shear capacity, respectively, the direct shear failure is also assessed when the member reaches its ultimate direct shear capacity. Ross (1983) proposed the same failure criterion, and a similar failure criterion has also been utilized by Karagazian and Case (1973). Thus a bilinear shear force-shear slip model is proposed, as shown in Figure 2. The two regions in the model are as follows:

Region 1:  $0 \leq \Delta \leq \Delta_1$ , elastic relation

$$V_d = A_c \tau_e (\Delta / \Delta_1) \quad (6a)$$

Region 2:  $\Delta_1 < \Delta < \Delta_2$ , inelastic region

$$V_d = A_c \left[ \tau_e + \left( \frac{\tau_u - \tau_e}{\Delta_2 - \Delta_1} \right) (\Delta - \Delta_1) \right] \quad (6b)$$

where:

$$\tau_e = 165 + 0.157 f'_c \quad (6c)$$

$$\tau_u = 2/f'_c + 0.8 \rho_{vt} f_y \leq 0.35 f'_c \quad (6d)$$

$f'_c$  = ultimate compressive strength of concrete, psi

$f_y$  = yield strength of reinforcement crossing the slip plane, psi  
 $\rho_{vt}$  = ratio of area of reinforcement crossing the shear plane to the cross section area  
 $A_c$  = cross sectional area, in<sup>2</sup>  
 $\Delta_1$  = 0.004 in  
 $\Delta_2$  = 0.012 in

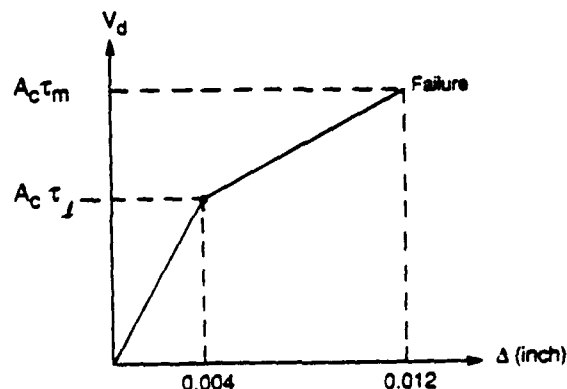


Figure 2. Direct Shear Force - Shear Slip Relationship

For simplicity, a bi-linear relationship between average shear force (shear stress) and average shear strain has been proposed, as shown in Figure 3. This relationship is based on the Compression Field Theory as proposed by Mitchell and Collins (1974), Collins (1978), and Vecchio and Collins (1986). The theory, which is analogous to the Tension Field Theory adopted by Wagner (1929), is capable of predicting the response of the reinforced concrete members in shear within the linear as well as nonlinear inelastic domain where the stirrups enter well into the yield region.

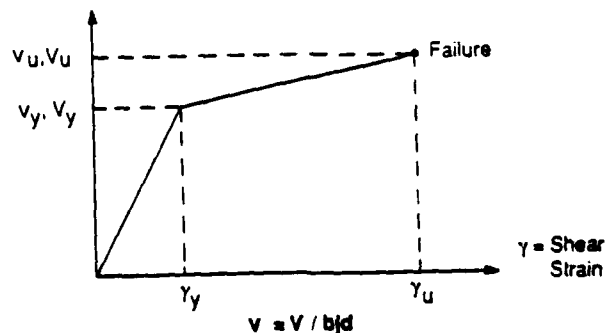


Figure 3. Bi-Linear Shear Force (Shear Stress) - Shear Strain Relationship

## Dynamic Rate Loading Effects

The inclusion of rate effect is handled by an increase of the stress properties of concrete and steel (it is assumed that the rate effect has identical effect on both concrete and steel). The enhancement factor is determined as a function of the load rate (assumed to be equal to stress rate) simply from the previous experimental studies (Watsein and Borese 1952), as discussed by Ross (1983). The new values of material stress properties are then incorporated into the  $M-\mu$ ,  $V-\gamma$ , and  $V_d-\Delta$  curves discussed earlier. The dynamic resistance functions are constructed to incorporate the effect of load reversal on the material resistance functions. The dynamic resistance model utilized here was first proposed by Krauthammer et al. (1984) for modeling a dynamic shear-stress shear-slip resistance. Shahriar (1988) has successfully applied the model for a dynamic force-displacement resistance function for nonlinear analysis of reinforced concrete beams and the results appeared to be attractive.

## Application and Results

Incorporating the nonlinear dynamic resistance function into the equations of motion of the Timoshenko beam (Eq. 1) results in nonlinear differential equations form solutions for this case are not feasible.

Eleven cases were investigated, and the procedure was applied for obtaining the dynamic deflection profile, dynamic shear distribution, and dynamic moment distribution, as well as the time and mode of failure. The results (mode and time of failure) for all eleven cases are summarized in Table 1. These results demonstrate clearly the accuracy of the present analytical approach. For all the present eleven cases the results agreed well with the experimental findings. The results are further illustrated by Figures 4 through 7 for the structure DS1-1.

## Conclusions

These results confirm that shear dominates the structural behavior at early stages of the impulsive loadings (for certain geometrical, material, and load parameters) especially in the presence of very high peak pressures. The modified Timoshenko beam theory is shown to be an accurate approach for predicting of the behavior of reinforced concrete structures under severe dynamic environments.

Table 1  
Summary of Time and Mode of Failure  
for Eleven Beams

| Beam  | Time of Failure(msec) | Mode of Failure** |            |
|-------|-----------------------|-------------------|------------|
|       |                       | Theory            | Experiment |
| DS1-1 | 0.186                 | DTS               | DTS        |
| DS1-2 | 0.166                 | DTS               | DTS        |
| DS1-3 | 0.233                 | DTS               | DTS        |
| DS1-4 | 0.223                 | DTS               | DTS        |
| DS1-5 | 0.188                 | DTS               | DTS        |
| DS2-1 | 0.212                 | DTS               | DTS        |
| DS2-2 | 0.548*                | FL                | FL         |
| DS2-3 | 0.595*                | FL                | FL         |
| DS2-4 | 0.178                 | DTS               | DTS        |
| DS2-5 | 0.614*                | FL                | FL         |
| DS2-6 | 0.609*                | FL                | FL         |

\* Formation of Hinges at the Supports

\*\* DTS - Direct Shear Mode

FL - Flexural Mode

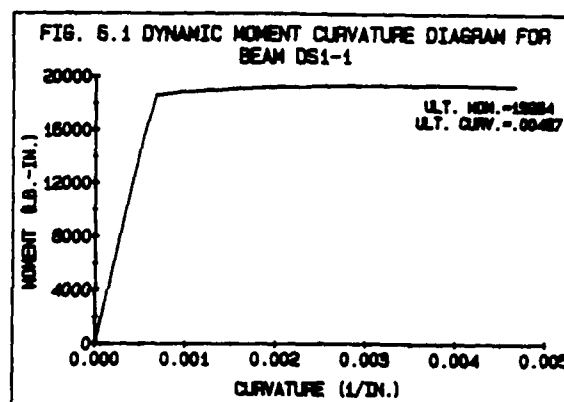


Figure 4. Dynamic Moment-Curvature Diagram for DS1-1

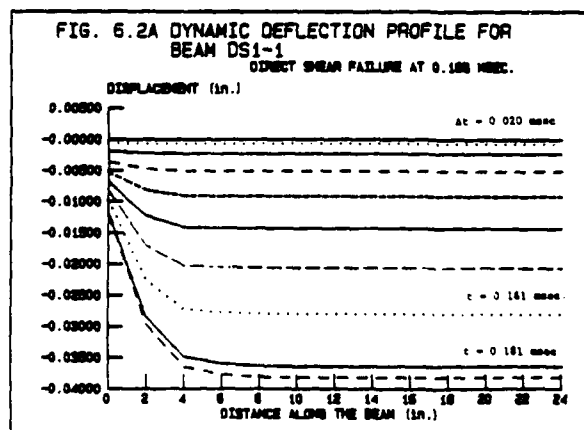


Figure 5. Dynamic Deflection Profile for DS1-1

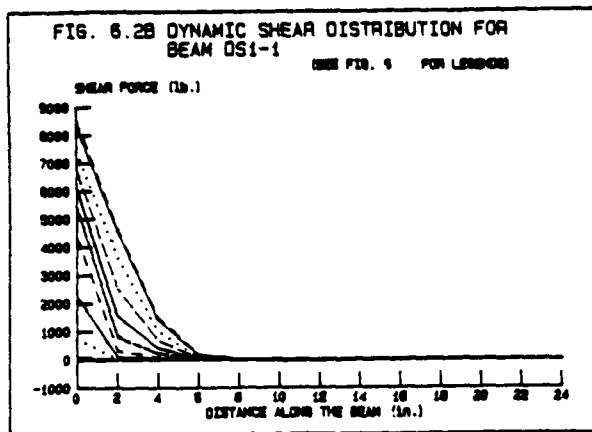


Figure 6. Dynamic Shear Distribution for DS1-1

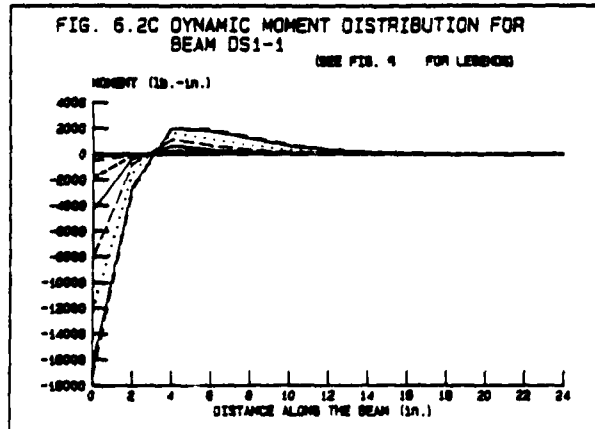


Figure 7. Dynamic Moment Distribution for DS1-1

## References

- Assadi-Lamouki, A. and Krauthammer, T. (1988), "Development of Improved Timoshenko Beam and Mindlin Plate Theories for the Analysis of Reinforced Concrete Structures Subjected to Impulsive Loads," Structural Engineering Report No. ST-88-02, Civil and Mineral Engineering Department, University of Minnesota.
- Collins, M.P. (April 1978), "Toward a Rational Theory for RC Members in Shear," ASCE Journal of Structural Division, ST4, pp. 649-666.
- Goodman L.E. (1951) with Sutherland J.G., "Vibrations of Prismatic bars Including Rotatory Inertia and Shear Deformations," Department of Civil Engineering, University of Illinois Project NR-064-183.
- Hawkins, N.M. (28 August 1981), "Dynamic Shear Resistance of Reinforced Concrete," Letter Report to U.S. Navy.
- Hawkins, N.M. (December 1974), "The Strength of Stud Shear Connections," Civil Engineering Transactions, Institute of Engineers, Australia, pp. 39-45.
- Hognestad, D. (November 1951), "A Study of Combined Bending and Axial Load in Reinforced Concrete Members," University of Illinois Engineering Experimental Station, Bulletin Series No. 399, 128 pp.
- Karagozian and Case, Structural Engineers. (1973), "Construction Joint Test Program," Final Report, Air Force System Command, Space and Missile System Organization Contract F0701-72-C-0358, Los Angeles, California.
- Kiger S.A. and Slawson, T.R. (September 1981 and July 1982), "Data Report for Dynamic Shear Tests," Two Reports, FY81 and FY82, U.S. Army Corps of Engineers, Waterways Experiment Station.
- Kiger, S.A., Getchell, J.V., Slawson, T.R., and Hyde, D.W. (September 1980-September 1984), "Vulnerability of Shallow-Buried Flat-Roof Structures," Technical Report SL-80-7, U.S. Army Waterways Experiment Station, Parts 1-6.
- Krauthammer, T. (March 1984), "Shallow-Buried RC Box-Type Structures," Journal of Structural Engineering, ASCE, Vol. 110, No. 3, pp. 637-651.
- Krauthammer, T., Shahriar, S., and Shanaa, H.M. (November-December 1987), "Analysis of Reinforced Concrete Beams Subjected to Severe Concentrated Loads," ACI Structural Journal, Vol. 84, No. 6, pp. 473-480.



Mindlin, R.D. (March 1951), "Influence of Rotatory Inertia and Shear on Flexural Motion of Isotropic Elastic Plates," ASME Journal of Applied Mechanics, Vol. 18, pp. 31-38.

Mitchell, D. and Collins, M.P. (August 1974), "Diagonal Compression Field Theory-A Rational Model for Structural Concrete in Pure Torsion," ACI Journal, Vol. 71, pp. 306-403.

Murtha, R.N., and Holland, T.J. (December 1982), "Analysis of WES FY82 Dynamic Shear Test Structures," Technical Memorandum 51-83-02 Defense Nuclear Agency.

Park, R., and Paulay, T. (1975), Reinforced Concrete Structures, Wiley.

Ross, T.J. (September 1983), "Direct Shear Failure in Reinforced Concrete Beams Under Impulsive Loading," Air Force Weapon Laboratory, Kirkland Air Force Base, Report No. AFWL-TR-83-84.

Shahriar, S. (1987), "Response of Reinforced Concrete Structures Subjected to Severe Localized Static or Dynamic Loads," Ph.D. Thesis, University of Minnesota.

Slawson, T.R. (April 1984), "Dynamic Shear Failure of Shallow-Buried Flat-Roofed Reinforced Concrete Structures Subjected to Blast Loading", Final report No. SL-84-7, U.S. Army Waterways Experiment Station.

Timoshenko, S.P. (1921), "On the Correction for Shear of the Differential Equation for Transverse Vibrations of Prismatic Bars," Philosophical Magazine, Series 6, Vol. 41, pp. 744-746.

Vecchio, F.J. and Collins, M.P. (March-April 1986), "The Modified Compression-Field Theory for Reinforced Concrete Elements Subjected to Shear," ACI Journal, No. 2, Proceedings V. 83, pp.219-231.

Wagner, H. (1929), "Ebene Blechwandtrager mit sehr dunnem Stegblech," Zeitschrift fur Flugtechnik und Motorluftschiffahrt, V. 20, No. 8 to 12, Berlin.

Watstein, D. and Boresi, A.P. (March 1952), "The Effect of Loading Rate on the Compressive Strength and Elastic Properties of Plain Concrete," National Bureau of Standards Report 1523, 1001-22-4703, and ACI Journal, Vol. 24 (1953), 729 pp.

A COMBINED SYMBOLIC-NUMERIC PROCESS FOR STRUCTURAL ASSESSMENT  
WITHIN A LARGE SCALE DECISION SUPPORT SYSTEM  
FOR POST ATTACK ENVIRONMENTS

Theodor Krauthammer  
Walter Schimdt  
Raman Muralidharan

Department of Civil and Mineral Engineering  
University of Minnesota  
Minneapolis, Minnesota 55455, U.S.A.

**ABSTRACT**

A combined symbolic-numeric approach to addressing the ill- and well-defined components of structural damage assessment is presented in the format of an expert system which, similar to the method a human engineer would follow, directs the flow of an analysis with high level symbolic reasoning and calls low level numeric programs to verify uncertain conclusion or supply missing data. It is proposed that similar symbolic-numeric tools be created and combined to address the various domains of decision making at each level of a four-level hierarchical large scale system focused on supporting decision making in post attack environments.

**INTRODUCTION**

Structural damage assessment following an enemy attack, such as a preemptive first strike or sabotage operation, could be one of the most difficult tasks an engineer faces. He is required to inspect the structure, determine its condition and reserve capacity, and explain the sequence of behavioral events that caused the observed condition. The high stress environment and the great time constraints on the engineer often cause him to make mediocre or poor decisions. This could be potentially disastrous, possibly causing the loss of vital operational facilities and possibly also human lives. Hence it is imperative that the engineer be provided with comprehensive decision support tools in order to ensure high quality decisions.

In this paper, a proposed architecture for a large scale, inter-disciplinary, decision support system (DSS) for assisting military personnel in post attack recovery operations is presented, and a combined symbolic-numeric process, for structural assessment in such an environment is discussed in detail. The latter forms a small but essential part of the former. It assesses damage inflicted upon structures by conventional and/or nuclear weapons, determines the sequence of structural responses, and provides recommendations as regards the future serviceability of the structure.

**THE ENVIRONMENT**

A scenario after an enemy attack could be characterized by shock, confusion and even panic. It is not an environment conducive to thoughtful

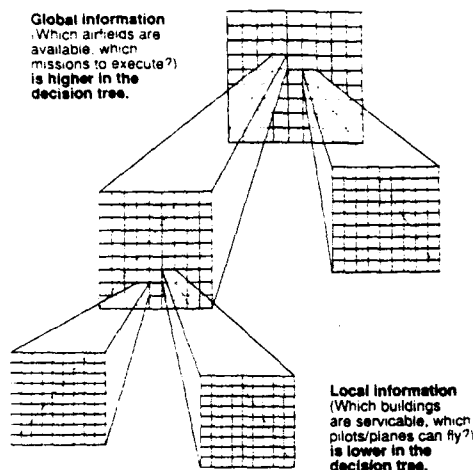
and rational decision making. But it is one in which many vitally important decisions have to be made.

In order to understand the environment better the following example is provided. When the enemy bombs airfields as part of a preemptive strike, several questions have to be answered. At the local level, (ie. the airfield), the staff themselves have to determine how many of the important facilities such as runways, hangers, hospitals, maintenance facilities and planes are still operational. They have to assess the number of dead or wounded personnel, such as pilots, groundcrew, and others performing vital tasks. Airfield defense facilities such as missile launchers and anti-aircraft gun emplacements have to be checked with respect to serviceability. Several of these tasks require the services of a civil engineer who is understandably hardpressed for time.

At the global level, (ie. the military headquarters), several tactical and strategic decisions have to be made. These include deciding which airfields can be considered operational, which have to be evacuated, how many aircraft are combat-worthy and what damage-control procedures need to be initiated. All such global decisions require as information inputs, decisions made at the local level. Global decisions themselves are split into several categories or levels, decisions at each level requiring as information multiple choices made at lower levels. For example in order to decide what missions can be mounted one would have to know which air bases are operational, how many and which planes are available, what number of pilots are still fit enough to fly etc.. So what exists is what we term a "Zoom in checker board effect" (see figure 1); each decision level being a checker board with individual decisions in individual squares. If we zoom in on any one of these squares/decisions, it dissolves into another checker board of lower level decisions, each of which needs to be resolved before the higher level decision can be addressed. In other words the decision tree is complex and has a high degree of branching. The important attributes of a system to support such a multi-level decision making process are:

- 1) Fast and efficient information exchange between components and levels.
- 2) Truth maintenance, to maintain the accuracy

- of transferred information and to ensure a logically consistent inference process.
- 3) Balancing the integration of the entire process with the independence of its various parts.
  - 4) High speed processes: Decisions have to be made fast.
  - 5) High quality results: The decisions need to be as "correct" as possible.



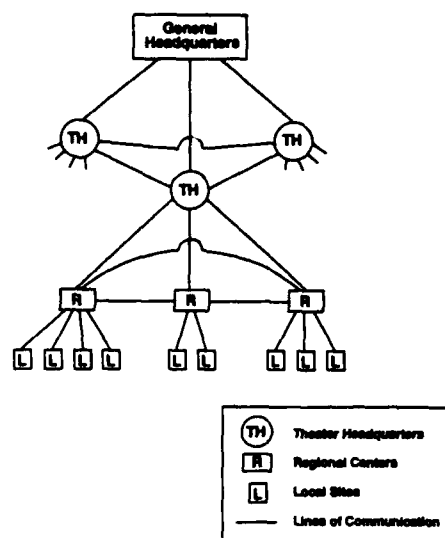
Zoom in Checker Board  
Multi-Access Data Base.

Figure 1

#### THE LARGE SCALE NETWORK SYSTEM

The large scale inter-disciplinary system proposed herein has been designed with respect to the above mentioned attributes of a decision making system in a post attack environment. The proposed architecture is a network of hierarchically ordered command, control, communication and intelligence (C<sup>3</sup>I) centers. Each C<sup>3</sup>I center is located at a distinct physical site and consists of a data base and data base management system, decision support tools for processing data in the data base, and communication links for receiving data from and sending data to other nodes in the network.

Four hierarchical levels are proposed: General, Theater, Regional and Local. Decisions are made at each level based on decisions made at lower levels and guidelines created at higher levels. The general (or global) node controls all of the theater nodes, each theater controls many regional nodes, and each region controls many local nodes. In addition to these hierarchical lines of communication, all theaters can communicate with each other, and all regions within a theater can communicate with each other (see figure 2). In order to allow robust communication, connections are not constrained to just those previously described; lines of communication may exist between any two components of the network. For example the general headquarters may communicate directly with local stations or regional centers. Components can communicate using hard wire lines, microwaves, radiowaves or via a backup satellite system.



Logical Network of Command, Control,  
Communication, and Intelligence Centers.

Figure 2

Although the large-scale system generally filters and summarizes data from lower levels into more manageable and useful information for higher levels, the higher levels are able to access all of the data and duplicate all of the processes that are available at lower levels; in effect the lower levels are subsets of the higher levels. Higher levels are also superior to lower levels in that more knowledgeable personnel exist at high level installations to address the problems that arise but may not be resolvable by personnel at lower levels; a higher level of expertise exists at general or theater headquarters than exists at a local site.

The large-scale system (see figure 3) consists of the following basic components:

- 1) Automatic sensors for collection of data at local sites. In case of damage to these sensors a backup mode which provides for manually input data, which is often ambiguous, is also created. This mode can also be used in conjunction with sensors, to provide values to parameters that are inherently judgmental.
- 2) Local, regional, theater, and general command, control, communication and information centers, where each higher level addresses a larger domain. Each C<sup>3</sup>I center is used to analyse the impact of recommendations made at lower levels and help support strategic decision making at that level. Each C<sup>3</sup>I is made up of the following components.
  - a) A data bank and a data bank management system, which can be accessed easily by connected centers.
  - b) A number of decision support tools to facilitate decision making at the current level. Separate tools for each type of decision should be provided at each center. For example structural

assessment, aircraft surveying, and medical support analysis tools should exist at each local level center.

- c) Communication links which use multiple means such as cables, microwave transmission and satellites to tie centers together. The network should be able to support a high level of interaction between various levels.
- 3) A global data bank and data processing center which is potentially accessible by all components in the network. This component is different from a C<sup>3</sup>I center, in that it is not used to originate decisions; it is used only to store information and perform expensive data processing.
- 4) Drones (remote control planes) and/or intelligence satellites which carry cameras may be used to acquire additional visual data. Drones provide information to regional centers, whereas satellites transmit information to the global data bank.

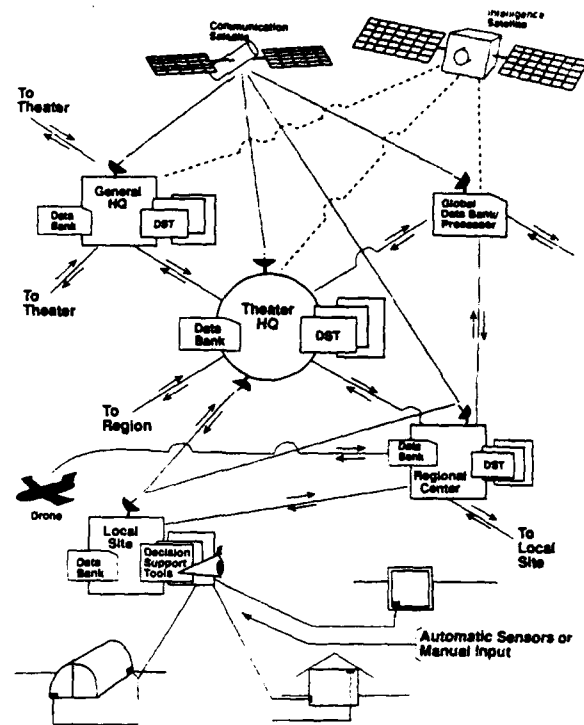
Such an architecture would allow the speed, quality and reliability required in the decision making process, also a number of backups are provided. The cost of building such a network however, would be very formidable. It is with respect to such a network that a small structural damage assessment tool to be used at the local level has been developed, as discussed later.

#### COMBINED SYMBOLIC - NUMERIC EVALUATION FOR DECISION SUPPORT TOOLS

As stated earlier a number of decision support tools are to be provided at each level to facilitate decision making in various areas. Aircraft management, medical support analysis, supplies inventory control, and structural assessment are typical examples of areas of concern at the local level. It is proposed that decision support tools which combine symbolic and numeric processes be developed for each of these domains and then combined into an aggregate C<sup>3</sup>I center for each local station; similar symbolic/numeric combinations would be created for centers to address concerns at each level.

The need to combine symbolic and numeric approaches is not new, almost all solutions of physical problems contain some form of such a combination. The simplest example of such a combination of approaches is a diagnostic session at the physician's office. In most cases, the physician will ask the patient questions, then if a diagnosis is not obvious, the physician will require the patient to undergo some tests. The type of tests to be performed will depend on initial clues obtained from the answers provided by the patient. The results from the tests will be coupled with the patient's answers for obtaining (or confirming) a diagnosis and the corresponding treatment. This issue can be defined in more general terms as follows.

There are two types of problems, those that are well-structured and others that are ill-structured. Similarly, there are two types of solution procedures, those that are based on strong mathematical methods and others that are founded on weak, rule of thumb, procedures. Numerical methods belong to the strong approach group, while symbolic



Example of Physical Global System

Figure 3

methods are weak approaches. For well defined problems for which mathematical approaches can be employed there is no need to employ symbolic methods; similarly, symbolic approaches should be employed for ill-structured problems and not be used for well defined problems. The problems addressed by the decision support tools we have mentioned, have both well-structured and ill-structured components, the proposed solution is to combine strong (numeric) processes to address the well-structured parts with weak (symbolic) processes to address the ill-structured parts.

#### ASSESSING STRUCTURAL DAMAGE WITH SYMBOLIC AND NUMERIC PROCEDURES

In the following, a structural damage assessment tool which combines symbolic and numeric processes to assess damage inflicted upon a structure by conventional or nuclear weapons is presented to fulfill the requirement that a structural analysis decision support tool exist at the local level.

General rules which can be expressed easily in words but not expressed easily using numbers, represents the ill-structured, symbolic part of structural damage assessment. For example, given a cross-section area of a beam, a general rule says: if a crack exists on the beam starting at the bottom and inclines upward to the left and another crack (to the right of the first crack) begins at the bottom of the beam and inclines upward to the right then it is possible that the beam experienced a punching shear behavior in this area, where a load was applied from below.

Mathematical, sometimes computationally complex, algorithms represent the well-structured,

numeric, part of structural damage assessment. For example, the deflection of a slab can be calculated by invoking an algorithm which takes as inputs a numeric description of a slab and the measurement of a load applied to it.

Since the problem of structural assessment is relatively unstructured when considered as a whole, overall general control of the assessment process should be handled by symbolic reasoning; however, the well structured subparts of the problem should be addressed by numeric processes. Symbolic methods provide an understandable and modifiable control structure; numeric procedures which supplement this symbolic control, provide precision and accuracy.

#### AN EXPERT SYSTEM FORMAT

We have chosen to combine symbolic and numeric processes in the form of an expert system and numeric procedures which it calls. In general terms, an expert system is an interactive computer code that can represent the intelligence and knowledge of one or more experts by employing heuristic knowledge embedded in a symbolic representation. The expert system imitates a civil engineer's "high level thinking". When the expert system reached indeterminate conclusions, it can call numeric procedures to verify or deny uncertain results or provide missing data that can not be obtained easily by observation.

An expert system format was chosen considering the environment in which the decision support tool must work. After an attack, quick, high quality decisions regarding the safety of surviving buildings must be made so that personnel may be placed in safe shelter before another attack which is likely to follow. Since expertise is needed to provide high quality recommendations and it is likely that human structural engineering experts are not at or near the site, an artificial expert is appropriate. Since time is limited, computationally demanding codes such as finite element analyses may not be adequate, instead it is appropriate that symbolic reasoning be used to control calls to less extensive, more specific numeric codes. However, the expert system may contact advanced computational tools if they are determined to be helpful.

An expert system consists of two major components: 1) a knowledge base containing facts and rules about the specific domain to which the system pertains, and 2) an inference engine, which is the control structure for manipulating the knowledge base. The main contribution of artificial intelligence is the inference engine's heuristic search process, required for progression through a collection of rules as discussed by Buchanan and Shortliffe (1984), Hayes-Roth et. al. (1983), and Rich (1983). The process can start with an initial set of rules and facts and progress toward a goal fact by considering antecedent conditions of rules that allow sensible deductions to be made (forward chaining). The search can also be executed in a backward manner starting at a goal fact and regressing to a set of initial facts; logical pre-conditions that are necessary for set post-conditions are determined for all intermediate rules until the pre-conditions of the rules necessary to initiate the chain are met. The purpose of an expert system is to provide a search

procedure by making use of plausible inferences based on knowledge supplied by the user, these possible inferences are stored as rules in the knowledge base.

Since the control structure (the inference engine's search procedure) of a rule-based system is separable from the domain knowledge, it is possible to implement general purpose inference engines which are typically called expert system shells. Adeli (1988) presented an extensive discussion on this topic. By using an expert system shell a developer makes his task easier, he does not have to design the control of his program, all he has to do is declare the knowledge of an expert and the inference engine does the rest. Theoretically, it is easier to construct and modify rule-based knowledge bases than it is to create and modify a procedural program used to accomplish the same task. Conceptually a rule-based system permits one to accomplish tasks by stating what is required to be done rather than stating explicitly how to do it.

#### AN EXPERT SYSTEM FOR ASSESSING STRUCTURAL DAMAGE

Any structural damage inflicted on a building is caused by a loading environment applied to it. In our context, that environment can be either a nuclear detonation, as defined in the literature (ASCE, 1985) or a conventional detonation generated by chemical explosives. These environments differ mainly in the pressure time histories they generate and the types of damage they cause.

When an explosive device is detonated in the air an airblast is applied to the soil free surface, and a corresponding shock wave is induced in the soil directly beneath it. That ground shock will propagate in the soil until it meets with the structure, and as a result of the soil-structure interaction a loading environment on the structure will be produced. The structural response is controlled by structural mechanisms which respond to the induced loads. Such mechanisms may be represented by direct shear which could cause failure at specific locations at a very early time, by flexure where a slab may exhibit membrane effects initially in compression and later in tension, by a compression mode in the event that the structure is loaded in the vertical direction, or by combinations of these structural mechanisms.

The purpose of the system we have constructed is to act as a consultant, assisting a civil engineer to interpret observed damage and make recommendations to military personnel. The system reports the cause of damage and more importantly it reports the extent of damage in terms of it's effect on the structure's ability to withstand future loading applications.

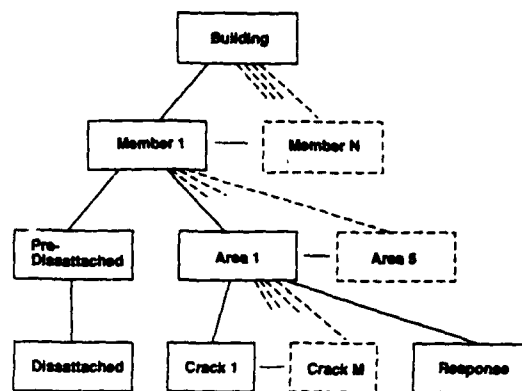
The Expert System shell which we have used for development is Texas Instruments' Personal Consultant Plus (PC+) (1987). A knowledge base consists of three basic structures: frames, parameters, and rules. Each frame represents a concept, each parameter represents a fact, and each rule is a method of creating new facts from old. Frames are organized in a tree-like structure, subframes (child frames) of a (parent) frame represent a logical, more detailed division of the concept the parent frame represents. Parameters and rules are placed in groups within frames that they are related to. Each frame is associated with

one group of parameters and one or more groups of rules. Descendent frames can refer to (inherit) values of parameters in ancestor frames, and ancestor frames can call upon rules of descendent frames. Each frame, parameter, and rule has a set of properties associated with it. Properties provide information that further describe specific frames, parameters, and rules.

Two particularly important properties of frames are 1) initial data and 2) goals, both of which are lists of parameters. When a frame is created the first thing PC+ does is attempt to find values for the parameters in the initial data list. After PC+ finds values for these parameters and performs operations called for by the found values, it searches for values of the parameters listed in the goal property. In attempting to fulfill a goal, PC+ may set additional parameter values and create new frames.

The value of a parameter may be found in one of three ways 1) calculated by a 'predetermined function, 2) entered by the user when asked for, and 3) set by the consequent part of a rule which fires. As an example if our goal is to determine if C is true and we have a rule that says: 'if A and B then C', PC+ will try using a function to calculate C, if this is not possible, PC+ will ask the user for the value of C, if this is not possible, PC+ will check to see if A and B are true, this implies repeating the process (backward chaining) to find the values of A and B. Although PC+ searches for parameter values primarily via backward chaining through appropriate rules and by asking for user input whenever possible, forward chaining can also be specified.

The frame structure we have designed is shown in figure 4. The building frame represents the composite structure which is being considered. The building is expected to be either a box, frame, or arch type structure. The main goal of the building frame is to consider each component or member of the structure, therefore one frame for each member of the building is created under the building frame. A member is expected to be either a beam, slab, or column. The initial data to be determined for each member frame is where the member is damaged. The goals of the member frame are to test and report on each of these structural mechanisms: direct-shear, punching shear, flexure, diagonal tension, and shear compression. If a member is disattached on any of it's originally attached sides, a pre-disattachment frame is created under the member frame to test how this member should be analyzed. A member which is completely disattached from a side, is likely to have extensive damage throughout due to the disattachment; therefore it is analyzed as a whole using the goals and rules of a disattachment frame created under the pre-disattachment frame. Other members are analyzed using area frames created under the member frame. Up to five area frames, (left-connection, left, middle, right, right-connection), are created per corresponding member. The goals of an area frame are to explain all appropriate damage in an area. The possible types of damage are: deflection, discontinuities, spalling concrete, crushed concrete, pulled out bars, broken bars and concrete teeth. The types of damage that actually exist in an area are solicited from the user as initial data. Crack frames are created under an area frame



Frame Structure for Local Expert System  
For Structural Damage Assessment.

Figure 4

to gather information about each family of cracks that exist in an area. A response frame created under an area frame provides rules to explain observable damage by relating it to structural mechanisms. For example flexure response rule039 says: if spalling concrete and deflection damage occur on the same side of a middle area of a member, then a flexural mechanism was present and spalling concrete and deflection damage are explainable; in PC+ terms this is:

```

IF :: (A-POS = MIDDLE AND D-TYP = SPALLING-
      CONCRETE AND D-TYP = DEFLECTION AND
      SC-DF = SAME-SIDE)
THEN :: (FLEXURE CF (MAX (CF SPALLING-
      CONCRETE) (CF DEFLECTION))) AND E-
      SPALLING-CONCRETE AND E-DEFLECTION)
  
```

Notice that the system maintains certainty factors (CF) which indicate how strongly a user should believe that a parameter has a certain value. An example of a rule which reports the effects of damage is response shear rule051:

```

IF :: (A-CON AND D-TYP = DISCONTINUITIES AND
      ESTIMATE-DFL-MORE-THAN-0.024)
THEN :: (DIRECT-SHEAR CF (CF DISCONTINUITIES)
      AND MEM-FUTR-RES-SHEAR = "is
      nonexistent because it has exceeded
      the peak capacity" AND E-
      DISCONTINUITIES)
  
```

If discontinuities exist in a connection area of a member and the estimated deflection is more than 0.024 inches, then a direct shear mechanism was present, the member's future resistance to shear is nonexistent because it has exceeded it's peak capacity, and discontinuity damage is explainable. MEM-FUTR-RES-SHEAR is a parameter which will be used by rules in the member frame to report damage effects on the structure's ability to withstand future loading applications.

For the previous rule to fire, the user must guess at the size of a deflection. A more robust method involves calling a numerical program to estimate a deflection. For example, presume that the type of weapon used, the distance from the

detonation center to the structure, and the burial conditions are known by the user who enters this data into the expert system. To determine the amount of deflection that theoretically should have been caused by such a blast, the expert system can call a numeric program which may access a data bank to retrieve weapons effects data and a numerical description of the building. By putting all of this data together the numeric program can calculate appropriate pressure-time histories and determine theoretical results. Notice that observations made on-site are combined with information that has been set up in advance in data banks for use in crisis situations.

There are two basic ways in which symbolic and numeric processes can be coupled. One approach is to integrate the two different types of programs into a single unit. This requires extremely careful programming in order to allow the two parts to interact satisfactorily. When changes are introduced in one part of the program, corresponding changes are required in the other part. The second approach is to create different modules for the numeric and symbolic parts that are actually independent programs, but which can be linked through another program acting as a "controller" of the combined symbolic-numeric process. The issue of coupling these two distinct programming capabilities has been discussed by Degroff (1987) and Wong et al. (1988). We have chosen to emphasize the second approach. Our expert system acts both as the symbolic part and as the controller. The expert system calls programs to perform numerical evaluations for specific problems. The input for each problem is sent via batch files and/or command lines. When the numeric process is finished it places its output in a batch file and notifies the expert system. We hope that the symbolic and numeric processing can be accomplished in parallel on separate machines or in a multi-tasking environment.

#### SUMMARY

We have presented an expert system based decision support tool within the context of a large scale decision support system. The expert system presented here addresses the domain of assessing structural damage. This system uses symbolic reasoning to both effectively interact with an engineer and to control the flow of an analysis; numeric programs are called to verify uncertain data and to provide missing data. It is proposed that similar expert systems be created to address other domains of decision making that exist at the local level of the large scale decision support system. Once the local level systems are created, similar regional, theater, and general level expert systems support tools should be created and linked together with a robust communications network.

We have stressed that a combined symbolic-numeric process is required to efficiently deal with the problems that occur in post attack environments because the problems themselves need to be solved through a mixture of high level thinking and low level processing. Symbolics provide computers with the ability to model the basic human thinking needed to outline solutions to complex problems occurring in post attack environments, while numerics provide the accuracy and precision needed to make confident judgements.

#### POSSIBLE IMPROVEMENTS

This system, like any other computer system can be separated into its input, process, and output components. The three steps are: 1) data is put into the system, 2) this data is processed creating useful information, and 3) information is transmitted to the end user as an aid in decision making. There are three criteria by which we can improve the usefulness of any system: 1) output more information, 2) output information quicker, and 3) improve the quality of information being output; make it more relevant, more useful.

The collection of data can be made faster and more fruitful by automation. For example, vision sensors may be placed on buildings to automatically determine deflections, and accelerometers may be used to keep a history of velocities and accelerations which may respectively cause cracking and damage equipment.

Processing may be sped up by simply improving the interfacing among parts of the network, or by implementing parallel processing at each site.

Improved methods of transmitting information to the user offers the greatest potential for improving the quality of information. In particular, allowing the user to interactively question an expert system, creates several new alternatives; the expert system can: explain how it reached its conclusions, and set certain values; output more information that has already been created but not yet reported because it was not considered relevant by the system; and initiate new processing to answer new questions.

#### REFERENCES

- Adeli, H., *Expert Systems in Construction and Structural Engineering*, Chapman and Hall, 1988
- ASCE, *Design of Structures to Resist Nuclear Weapon Effects*, American Society of Civil Engineers, Manual 42, 1985.
- Buchanan, B.G., and Shortliffe, E.H., *Rule-Based Expert Systems*, Addison-Wesley, 1984.
- Degroff, L., "Conventional Languages and Expert Systems", *AI Expert*, April 1987.
- Hayes-Roth, F., Waterman, D.A., and Lenat, D.B., *Building Expert Systems*, Addison-Wesley, 1983.
- Rich, E., *Artificial Intelligence*, McGraw-Hill, 1983.
- Texas Instruments, Inc., "Personal Consultant Plus (PC+)", Versions 3.01, and 3.02, 1987.
- Wong, F.S., Dong, W.M., and Blanks, M., "An Integrated PC-Based Computer System for Protective Structures Application", Final Report TR-88-91, Air Force Weapons Laboratory, 1988.

# STOCHASTIC METHODS FOR PROTECTIVE STRUCTURES DESIGN

Timothy J. Ross  
Department of Civil Engineering  
University of New Mexico  
Albuquerque, NM 87131

Shyh-Yuan Kung  
Intelligent Systems Integration, Inc.  
Los Altos, CA 94040

## Abstract

*This paper describes a research effort conducted for the Air Force Engineering Services Center (AFESC) [1]. The objective of the research was to demonstrate the feasibility of developing a more balanced and effective tool for designing protective structures to conventional weapons effects which: (1) can take into account the natural random variability of quantitative design parameters; (2) can assess uncertainty in nonrandom issues such as modeling and boundary condition assumptions; and (3) can accommodate flexibility in modeling structure behavioral changes (different physics of response) caused by evolutions in the weapons environment.*

## The Design Problem

Protective structures designed to withstand the effects of conventional (nonnuclear) munitions are built primarily according to deterministic design procedures. These procedures assume precise knowledge about the parameters that play a significant role in the structure's final design. Real-world variabilities in site characteristics, structural attributes like strength and stiffness, and weapon delivery characteristics are generally not accounted for in current design schemes. In fact, current design procedures are overly conservative in that, to ensure high confidence in sustaining the facilities' mission, they presume a "worst-case scenario" in selecting values for design parameters. For example, some typical "worst-case" presumptions would involve underestimating structural strength, overestimating the loading imparted to the structure, ignoring complex details like three-dimensional and nonlinear effects, overestimating joint stiffness, and ignoring issues that typically are not quantitative in nature. Examples of the latter would include construction quality control, weather conditions during construction, ad-hoc construction changes and short-cuts, and the validity of the design procedure to emulate real-world situations.

The problem is compounded by the fact that the loading is caused by a weapon environment whose effects on a structure are highly variable, and where significant changes in some parameters can require a complete change in the design model. For example, peak interface pressure at a soil-structure interface is inversely proportional to the distance from the explosive source. But at some point when the explosive source gets very close to a structural element, the response behavior can change

from a forced-vibration problem to a wave-propagation, breaching, or penetration problem. A simple Monte-Carlo simulation of the range versus pressure function would completely miss this change in behavior unless the correct phenomena are captured within the design framework.

Furthermore, current design procedures are based on a deterministic set of parameters describing loadings based on standard and documented weapons configurations. If the problem of interest requires knowledge about potential future weapons configurations, or if the configuration is not documented, then the designer's only recourse is to interpolate between, or, worse, extrapolate beyond existing situations.

Based on the problem described here it is evident that a balanced (in the sense of accommodating various sources of data, knowledge, and design methods) and effective design tool is needed. This new tool would address random and nonrandom variability and would be flexible in use and adaptable to changes in user requirements.

## Extent of Uncertainty in Design

Consider a typical problem of designing a facility to survive a conventional weapons threat which might be vaguely specified, to be built in a NATO-based country, and to be sized according to an unknown budget. The designer must consider several real-world "nonalgorithmic" issues. Some of these issues might include: local material availability, constructability (things are built according to different practices in Germany and Turkey, for example), local restrictions on architectural, esthetic, planning, zoning and environmental concerns, and built-in flexibility to future threats. It is easy to ignore these non-algorithmic issues, but the development of a new design algorithm should be adaptive to changing requirements if it is to achieve acceptability.

Another issue is that there are at least five types of designs which meet a specified threat. These design types are: (1) hardened (usually for nuclear threats), (2) protective (usually for a direct impact from a conventional threat), (3) semi-hardened (usually designed to some stand-off distance from a conventional threat), (4) splintering (expected fragment damage), and (5) collateral (damage based on proximity to a higher-priority target). It is not uncommon for an agency (USAFE, NATO, etc.) to want a structure to be designed to survive a combination of the threats mentioned above.



After deciding which design type is to be considered for a particular structure (or a modification to an existing structure, for that matter), one must consider the variability (uncertainty) in the parameters of the threat, the loading mechanism, the structural response, and the survivability of the structure contents. It is also necessary to estimate the uncertainty in the design algorithm itself (e.g., an empirical relation, a finite element model, boundary conditions, etc.), which currently is rarely considered.

In the determination of the threat there are numerous options and, within each threat option, several parameters should be considered in terms of their own uncertainty. There are several kinds of projectile weapons such as small arms, direct fire weapons, armor piercing (AP) solid shot and capped projectiles, HE shells, mortar shells (such as the large Soviet 240 mm used against R/C structures), and grenades. Several kinds of bombs exist: general purpose (GP), AP and semi-AP, fuel-air explosives, light-case, fire and incendiary, special-purpose (chemical), and dispenser/cluster types. Rockets and missiles exist as tactical and battlefield (U. S. LANCE, Soviet SCUD and FROG) types. Special purpose weapons such as fuel-air munitions, shaped-charges, cratering charges, and heat-gas types are prevalent. And if these categories aren't enough to contend with, the new and evolving weapon threats are more accurate and "smarter". Smart weapons include such features as target hardness sensors which alter the fuzing option according to target rigidity, and damage mechanism sensing where a two-stage weapon will first penetrate with a shape-charge, then detonate at depth with an HE warhead. The newer threats make it increasingly important to consider the synergistic effects of airblast, fragmentation, breaching, spall, etc. as the expected miss distance decreases for these threats.

Another factor to be considered is the uncertainty in the propagation of these weapon effects through the medium surrounding the structure. For above-ground structures this would include a characterization of the airblast, the fragmentation and thermal (and/or chemical) patterns, penetration mechanisms, and the near-surface ground shock propagation. For buried structures this would include a characterization of coupling issues, ground shock, cratering, ejecta, and sub-surface munitions fragmentation characteristics. For example, for airblast the uncertainty in explosive type, in cube-root scaling, in blast-wave phenomena, and in the nature of pressure increases internal to the structure all should be considered.

After propagation effects are considered the resulting loads on the structure must be computed. This is a critical point in a typical design, because the structural loads are a function, not only of the propagation path of the disturbance (airblast, shock, penetration) but also, of the physics of the phenomenon. The physics of a pressure-force relation are different from those of a fragment-penetration relation and the specification in the load environment should accommodate changing physics due to the uncertainty in some parameters; for example, in the miss-distance.

The structural response and associated internal component response is generally decoupled from the specification of the external loads in most design algorithms. This is a mistake since it ignores the interaction effect. The assumption of a flexural response of a slab due to an air-blast pressure might be appropriate for a deterministic design, but in the stochastic case the variability in the miss-distance could produce a situation where a direct-shear failure near the slab support is the governing failure mechanism [2]. In this phase of the design, special attention needs to be focused on the fact that most design criteria in Europe and the Pacific basin do not account for

dynamic phenomena directly, but rather use design "factors" to account for such things as dynamic material properties, higher-mode response, and the relation between the frequency content of the disturbance and the frequency and non-linearity of the response. The response of internal objects is also based on assumptions of rigid-body response without consideration due to the uncertainty in local behavior, joint behavior, and the influence of damage locations on rigid-body behavior.

### Specific Design Case Study

The research described here considered the design of a reinforced concrete (R/C) one-way wall section from a typical, partially buried Air Force facility, as provided by AFESC. The loading on the wall was modeled as a free-air burst of a 1000-pound General Purpose (GP) bomb. The dynamic load was assumed to act uniformly across the wall height and it was modeled in the time-domain as an initially peaked triangular loading. The study considered the effects on the design of: (i) four stochastic methods, (ii) four numerical engineering models, and (iii) three different response physics.

#### Stochastic Methods

The research reported in this paper considered the following four stochastic methods, and they are readily adapted to design-type problems, where parametric uncertainty plays a key role.

- \* Monte Carlo simulation
- \* Partial Derivative
- \* Point Estimates by Probability Moments (PEPM)
- \* Response Surfaces

The last three methods are all considered as first order, second moment methods (FOSM) [3]. The Direct Monte Carlo method involves a large number of theoretical realizations of the design model and the results are generally analyzed in terms of the mean and variance of parameters of interest within the model.

The partial derivative method (also known as the Taylor's series expansion method) involves the expansion of the design equation in a power series about the mean value of a parameter of interest. This method is valid only for analytically described processes (such as an equation) and for small excursions of the variables away from their mean values. The first and second moments of this parameter are then computed directly from the polynomial describing the expansion.

The PEPM method is based on the assumption that the first three moments of all independent variables are known prior to the determination of the first two moments (mean and variance) of the dependent variable. This method approximates the true density function of a random variable as Dirac-delta functions located one standard deviation (points) from the mean for all the variables. These delta functions therefore approximate the actual random realizations of the process at these points.

The response surface method is similar to the PEPM method in that it approximates the true response at only a few discrete points in the solution space, but the response surface method can sample a random variable at more than two discrete points. Both the PEPM and response surface methods can be used to estimate the correlation among random variables and, unlike the partial derivative method, are both well suited to problems which do not require analytic solutions but rather require numerical treatments.

## Numerical Engineering Models

Uncertainty in design also arises from the user's choice of a numerical model. Numerical models differ according to their level of sophistication and different assumption requirements. The following four models were addressed in the research.

- \* Simple static design algorithm
- \* Dynamic Single-degree-of-freedom (SDOF) model
- \* Dynamic Four-degree-of-freedom (4-DOF) model
- \* Dynamic continuum model

### Response Physics

Sometimes the physics of the design algorithm changes for the same structure when one or more of the parameters in the model change to certain magnitudes. For example, if the standoff distance between a weapon and a structure approaches zero, the structural response physics will change from a forced-vibration response to a penetration response to a breaching failure. For this research effort three model physics were explored.

- \* forced vibration failure from airblast
- \* penetration failure (perforation or fragment spall)
- \* breaching failure (from a near-direct hit)

### Stochastic Simulations

The design case study explored numerous design outcomes by addressing all the various stochastic methods, numerical engineering models, and response physics in several simulation studies. Table 1 shows the random variables used in the simulation studies. These studies were divided into three groups: *Series 1 Simulations* studied the effects on design of the four stochastic methods; *Series 2 Simulations* studied the effects on design of the four numerical engineering models; and *Series 3 simulations* studied the effects on design of the three various response physics. Only summaries of these studies are presented here for brevity; details are available in [4].

#### Series 1 Simulations

In Series 1 simulations the four stochastic methods were compared in the computation of the variability of the shear strength of the R/C wall section (modeled as a beam) with stirrups regularly spaced along the length. The resulting probability density functions (PDFs) of shear strength were compared. The beam system was represented by the ACI Committee 426 Design equation:

$$V_{ACI} = B * D * [2 * (F'_c)^{1/2} + r * F_y]$$

where  $V_{ACI}$  = the shear strength of the cross-section ( $V_{ACI}$  was divided by the nominal cross-sectional area to get the shear strength per unit area),  $B$  = width of beam,  $D$  = effective depth of beam, i.e., depth to tensile flexural reinforcement,  $F'_c$  = concrete strength in psi,  $F_y$  = yield strength of stirrup rebars in psi,  $r = A_v/(B * S)$  where  $A_v$  is the total cross-sectional area of the stirrups (2 x bar area), and  $S$  is the longitudinal spacing of the stirrups. The shear strength is random because the parameters  $B$ ,  $D$ ,  $F'_c$  and  $F_y$  are random (the reinforcement ratio,  $r$ , was assumed deterministic).

#### Series 2 Simulations

Using a recently successful direct shear-strength criteria [5], the physics of forced vibration from airblast, and one stochastic method (Monte Carlo simulation), probability of failure results

for the four numerical engineering models for the R/C design were conducted for the Series 2 simulations.

TABLE 1-RANDOM VARIABLES FOR SIMULATIONS

| General Gaussian Random Variables          |               |  |
|--|---------------|--|
| Parameter; units                           | Mean          | Standard Deviation   |
| Slab Thickness (inches)                    | 25.5          | 1.0  |
| Unit Thickness (inches)                    | 5.0           | 0.5  |
| Concrete Strength (psi)                    | 4028          | 600  |
| Steel Strength (psi)                       | 48800         | 5220   |
| Charge Weight (lbs)                        | 555           | 55.5   |
| Static Random Variables                    |               |  |
| Parameter                                  | Type          | Values   |
| Stirrup steel ratio                        | Deterministic | 0.0026   |
| Long. steel ratio                          | Deterministic | 0.0066   |
| Beam Length                                | Normal        | $\mu = 156$ in.; $\sigma = 12$ in.                           |
| Miss-distance (range)                      | Beta          | $4 \text{ ft} < R < 40 \text{ ft}$ ; $\alpha = 2, \beta = 2$ |
| Dynamic Random Variables                   |               |  |
| Parameter                                  | Type          | Values   |
| Damping                                    | Deterministic | 2%   |
| Long. steel ratio                          | Deterministic | 0.0066   |
| Mass Density                               | Deterministic | 0.0002247 #-sec <sup>2</sup> /in <sup>4</sup>                |
| Miss-distance (range)                      | Beta          | $4 \text{ ft} < R < 40 \text{ ft}$ ; $\alpha = 2, \beta = 2$ |
| Wall height                                | Normal        | $\mu = 15.25$ ft; $\sigma = 1.52$ ft                         |
| Penetration and Breaching Random Variables |               |  |
| Parameter                                  | Type          | Values   |
| Casing Thickness                           | Deterministic | 0.5 in.  |
| Bomb Weight                                | Deterministic | 1000-#   |
| Casing inside dia.                         | Deterministic | 17.8 in.   |
| Long. steel ratio                          | Deterministic | 0.0066   |
| Miss-distance (range)                      | Beta          | $0 < R < 40 \text{ ft}$ ; $\alpha = 2.2, \beta = 1.8$        |
| Fragment wt ( $W_f$ )                      | Beta          | $0.2 \text{ oz} < W_f < W_{fmax}$ ; $\alpha = 1, \beta = 3$  |

In these simulations the Monte Carlo method is used to sample from the probability density functions of all the random variables of the static model and the three dynamic models. Failure in each Monte Carlo loop is defined to occur when the maximum shear-stress (in the time-domain) induced in the beam from the loading exceeds the shear-strength. The simulation simply counts the proportion of cycles in which a failure is indicated. For dynamic models the maximum shear-stress can occur at any time during or after the triangular load is applied to the beam. The beam is assumed to be fixed at the supports and to exhibit linear properties through the simulation process.

For direct shear the following formulation [5] is used for direct-shear resistance,  $V_u$ :

$$V_u = [8 * (F'_c)^{1/2} + 0.8 \rho_s f_y] < 0.35 F'_c \text{ (psi)}$$

These strength relations are functions of the concrete compressive strength,  $F'_c$ , the percentage of longitudinal steel,  $\rho_s$ , and the yield strength of the steel,  $f_y$ , in the slab. In the dynamic simulations the strength properties of the concrete and steel are enhanced by 30% to crudely account for strain rate effects. All these parameters can be random. Table 1 shows the variability of each of the random variables in the static and

dynamic models. In the case of Gaussian (Normal) random variables the mean and standard deviation are expressed and in the case of Beta-distributed random variables the end-points (min, max) are specified along with the two parameters of the Beta:  $\alpha$  and  $\beta$ . In the Beta distribution, when  $\alpha=\beta$  the distribution is symmetric; when  $\alpha=\beta=1$  the distribution becomes the uniform distribution; and when  $\alpha<\beta$  the distribution is skewed to the right.

Figure 1 displays the probability of failure ( $P_f$ ) curves for the ACI and direct-shear ( $V_u$ ) criteria. As can be seen, a significant decrease in miss-distance (range) for the same  $P_f$  can be realized by using the less-conservative direct shear criteria. This translates to a significant cost savings for the same survivability if the designer elects to use a less-conservative shear-failure criterion.

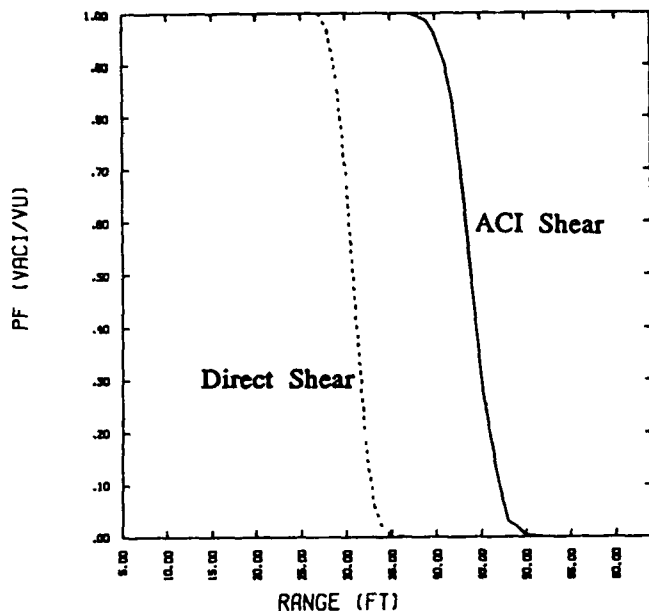


Figure 1. Comparison of Shear Failure Criteria for Static Simulation

In the dynamic simulations, Figure 2 compares the probability of failure ( $P_f$ ) curves for the four models: (1) static response, (2) SDOF response, (3) 4-DOF response and (4) continuum model with many degrees of freedom. From a design point-of-view the static calculation is the least conservative (for a given range, the static simulation provides the lowest  $P_f$ ) for this particular problem, but the interesting feature is that there is not much significant difference between the simulations among the dynamic models.

### Series 3 Simulations

In *Series 3* simulations probability of direct-shear failure is compared for three different kinds of model response physics. In these calculations the Monte Carlo simulation is used to sample from the probability density functions of all the random variables of the three physics models. These models all attempt to address the question of whether different physical responses can govern the probability of failure if a framework is developed to exercise them. The three physics (response modes) models are: (1) failure from forced-vibration from airblast in direct shear (this model has been addressed in the *Series 2* simulations); (2)

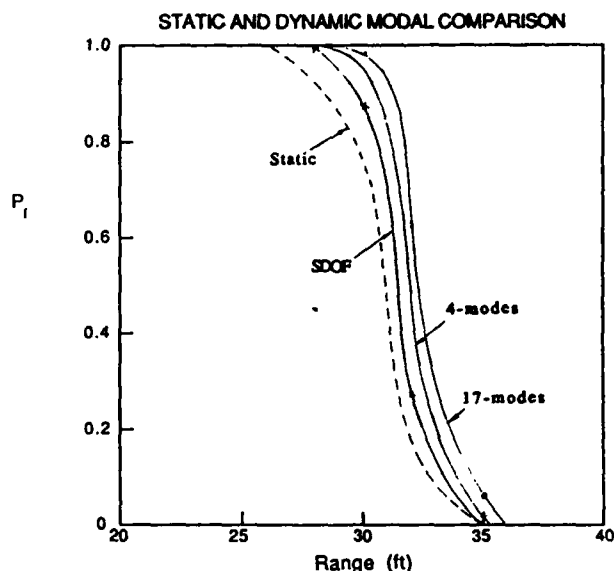


Figure 2. Comparison of Probability of Failure Curves for (1) Static Response, (2) Dynamic SDOF Response, (3) Dynamic 4-DOF Response, and (4) Dynamic Continuum Model

failure from penetration of bomb casing fragments; and (3) failure from breaching (punch-through) of the R/C wall due to a near-direct hit. Two of the response physics, forced vibration and breaching, compare pressure-induced shear stress in the structure to the direct shear failure criteria. The physics of penetration depth from perforation or spalling to the thickness of the wall. In the stochastic analysis the range of detonation of the 1000-pound GP bomb from the wall slab is a random variable. If a single realization of this variable makes it very close to the wall, penetration or fragmentation may govern. If a realization of the random variable for range makes it far from the wall slab, a forced-vibration shear failure may govern. Details on the empirical and theoretical developments of the penetration modes (perforation and spalling) are provided in design manuals [6]. Information on the theoretical development of the breaching mode of failure is derived in the Appendix. Details on the implementation of these modes of failure for this work are available in the literature [4].

Figure 3 reveals some very interesting phenomena relating to the need for design models to account for uncertainties in weapons and structural parameters. From a design point of view the physics of breaching would impose the least conservative constraint on structural requirements while the physics of forced-vibration from airblast would impose the highest constraints (i.e., for this example design the wall would fail due to airblast before it would fail due to breaching). Failure due to penetration also seems to be abnormally high at larger ranges (ranges above 35 feet; scaled ranges above about  $\lambda = 4$ ). This is because the probability of a given fragment even hitting the wall was not addressed in the simulation. This uncertainty is a function not only of miss-distance, but also the azimuthal location between the bomb and the structural element. Perhaps the biggest conclusion from Figure 3 is the fact that synergistic effects between the various modes of physics are clearly revealed but have not been accounted for explicitly in the physics models! For example, at a range of about 30 feet fragmentation and airblast would produce combined effects on a wall and at a range of about 15 feet fragmentation, airblast, and breaching would all come into play. Not only should uncertainties be

accounted for in this case, but research into the true physics of synergistic effects is warranted.

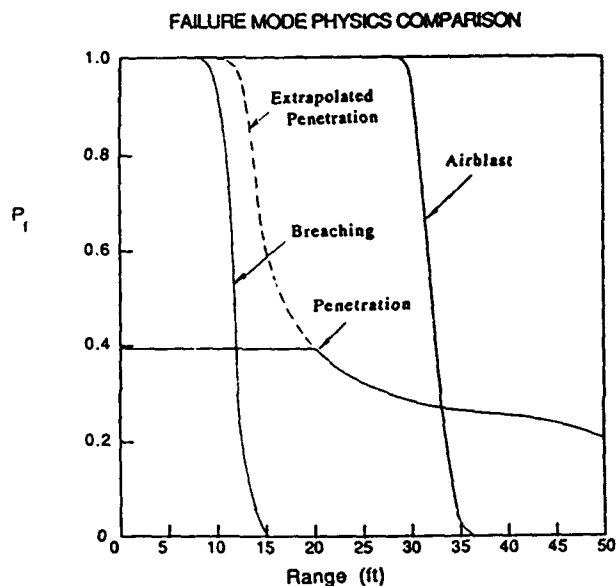


Figure 3. Comparison of  $P_f$  curves for (1) Airblast, (2) Penetration and (3) Breaching failure modes

### Summary

Stochastic simulations for a simple design example show that uncertainty in major variables such as the miss-distance or the strength criterion tends to obscure the minor differences between engineering models of varying degrees of sophistication. Other results show that, from a design point of view, the physics of breaching would impose the least conservative constraint on structural requirements while the physics of forced-vibration from airblast would impose the highest constraints. Perhaps the biggest conclusion is the fact that synergistic effects between the various modes of physics are clearly revealed but have not been accounted for explicitly in the physics models. Research into the true physics of synergistic effects is worthy of closer scrutiny in future design approaches.

This paper has discussed the considerable breadth and depth of variability in parameters and models involved in protective structure design. The technical overview can take on an added perspective when the importance of how protective structure design, and a consideration of the design uncertainties, is related to the overall air base operability issue. There are many general philosophical, but realistic, issues associated with protective structure design on an air base which could be resolved through the use of more advanced design procedures. Addressing these issues, at the air base level, would help support the operational Air Force needs in the area of survivability and operability. Such stochastic methods will reduce design and construction costs by optimizing structural performance under the influence of uncertain loadings and the uncertain degradation of material properties with time.

### ACKNOWLEDGEMENTS

This research was sponsored by the Air Force Engineering Services Center under their Small Business Innovation Research (SBIR) program, Contract F08635-87-C-0371. This support is gratefully acknowledged.

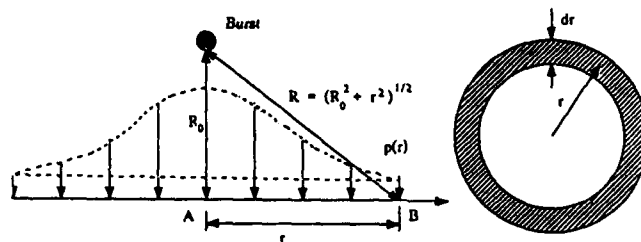
### REFERENCES

1. Ross, T.J., Kung, S.Y., and Wong, F.S., "Stochastic Methods in Protective Structures Design: An Integrated Approach", Small Business Innovation Research Report to the Air Force Engineering and Services Center, July 1988.
2. Ross, T. J., Matsumoto, E. E. and Wong, M. K., "High Frequency Structural Effects from Local Impulsive Loads," submitted for publication.
3. Wong, F. (1985) "First-Order, Second Moment Methods," *Journal of Computers and Structures*, Vol. 20, 4, pp. 779-791.
4. Ross, T.J., "The Use of Stochastic Methods in the Design of Protective Structures", to be submitted for publication.
5. Ross, T.J. and Krawinkler, H., "Impulsive Direct Shear Failure in Reinforced Concrete Slabs," *ASCE Journal of Structure Engineering*, Vol 111, No. 8, August 1985, pp 1661-1677.
6. Crawford, et. al., "Protection from Nonnuclear Weapons", Air Force Weapons Laboratory Report, AFWL-TR-70-127, Feb., 1971.

### APPENDIX

#### Breaching Analysis

When a conventional munition detonates close to a structural element ( within a scaled range of about 1.5) it imparts a spherical shock front to the element. Hence, the maximum pressure from the detonation on the element face is proportional to the cube of the distance between the burst and the element face. In the schematic shown below,



the pressure at point B is given by

$$p(r) = \left( \frac{R_0}{R} \right)^3 P_r \text{ and } R = (R_0^2 + r^2)^{1/2}$$

where  $P_r$  is the peak reflected pressure at point A. The value of  $P_r$  is a function of  $R$  and the charge weight,  $W$ , as shown in Figure B.1. For a small annulus of area on the face of the element with a radius of  $r$  and a width of  $dr$  (see schematic) then the total force on this annulus from the blast pressure is given by

$$\Delta F(r_0) = \left( \frac{R_0}{R} \right)^3 P_r \cdot 2\pi r dr$$

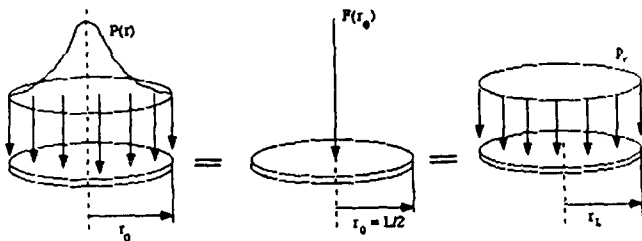
and the total force on an area of the element face of radius  $r_0$  is then,

$$F(r_0) = \int \Delta F(r,t) = 2\pi p_r R_0^3 \int_0^{r_0} \frac{r}{R^3} dr = 2\pi p_r R_0^3 \frac{r dr}{(R_0^2 + r^2)^{3/2}}$$

which, through the substitution  $Y = R_0^2 + r^2$  and  $dY = 2r dr$ , yields

$$F(r_0) = 2\pi R_0^2 P_r \left[ 1 - \frac{R_0}{(R_0^2 + r_0^2)^{0.5}} \right]$$

So  $F(r_0)$  is the total force on a circular area of radius  $r_0$  as shown in the figure below.



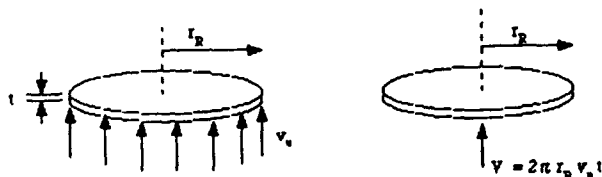
Normally, the parameter  $r_0$  is taken to be one-half the slab length ( $L/2$ ). Now, if the total force  $F(r_0)$  on the slab is presumed to be produced by the uniform pressure,  $p_r$ , the relationship is determined,

$$r_L = \left[ \frac{\phi F(\frac{L}{2})}{\pi p_r} \right]^{1/2}$$

where  $r_L$  is the radius of an equivalent circular area with the same force,  $F(r_0)$ , acting on it and  $\phi = 0.57$  is a factor accounting for the fact that the peak reflection factor only occurs at normal incidence (where  $R = R_0$ ) and most of the pressure occurs for  $R > R_0$ . Now if the maximum shear stress capacity of the structural element is set equal to the direct shear stress,  $v_u$ , given by

$$v_u = 8(f'_c)^{1/2} + 0.8 \rho_s f_y \leq 0.35 f'_c$$

where  $f'_c$  is in psi,  $\rho_s$  is the longitudinal steel percentage, and  $f_y$  is the tensile strength of the steel, and assume this stress acts on the perimeter of a circular "punched" area of the element, as shown below,



then the total resisting shear force acts over an area with a radius given by,

$$r_R = \frac{\phi F(\frac{L}{2})}{2\pi v_u t}$$

where  $t$  is the element thickness and  $r_R$  is the radius. Finally, failure occurs for the condition  $r_R > r_L$ .

# FUZZY PROBABILITY ANALYSIS OF BASEMENT TYPE SHELTERS

X.L.Liu C.N.Liu

Tsinghua University, Beijing, 100084, China

## ABSTRACT

In the present paper, a new method for predicting the survival probability of basement type shelters is introduced. Some variables, such as the variability in peak overpressure and the positive phase duration of the blast load, are treated as fuzzy variables. On the other side, however, the resistance parameters, such as the material and geometric parameters of the reinforced concrete slab, are considered as random variables. Two numerical algorithms are proposed. Some calculation results are given together with some necessary recommendations.

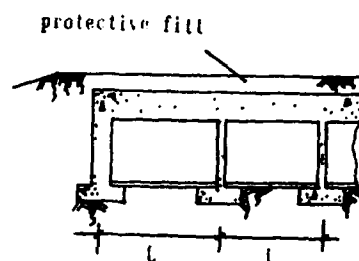


Fig.1 Shelter Structure

The blast load form is taken as

$$F(t) = F_0(1 - t_0) \exp(-t/t_0) \quad (1)$$

## 1. INTRODUCTION

It is well known that the loading condition and the designed condition of basement type shelters are entirely different from most conventional structures. Besides, it is very difficult to perform loading tests for this kind of structures. In the present paper, the fuzzy set is introduced to describe the uncertainties in design and the fuzzy statistics is used for the survival probability analysis. Some results and recommendations are presented, which should be very useful for designers.

## 2. STRUCTURE, LOADING CONDITION, AND RESISTANCE FUNCTION

The shelter considered in the present paper is shown in Fig.1, which is similar to that of Ref. [1].

Since the roof slab is the weakest structure components, whose collapse results in casualties, and the walls and the foundation of shelters are not expected to fail prior to the slab failures, only the collapse of roof slab is considered in the analysis. The roof is modeled as a single degree-of-freedom system and the midpoint deflection is taken as a judgment parameter. Thus, the survival probability of the roof slab subjected to the blast effects can be estimated.

in which,  $F_0$  is the peak overpressure, and  $t_0$  is the positive phase duration of the overpressure.

The distribution of the blast load is assumed to be uniform over the slab surface. The depth of soil cover and the slope of the mounding are assumed to be sufficiently shallow to preclude the attenuation of blast load with depth and the dynamic side effect, respectively. In other words, there is no need to modify Eq.(1).

Resistance function for two-way reinforced concrete slabs is shown in Fig.2.

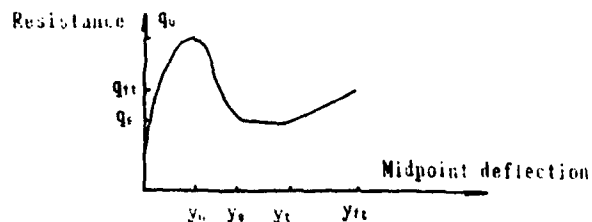


Fig.2 Resistance Function

It is divided into three parts: (i) the compressive membrane resistance stage; (ii) the secondary resistance stage; and (iii) the tensile membrane resistance stage.

For a square, clamped, and uniformly reinforced slab, assuming the edge restraints are so great that no displacements occur at the edges. The resistance parameters in Fig. 2 are given as follows [2]

$$y_u = h \sqrt{h^2 - L^2 [\epsilon_u(1 + \epsilon_s) + \epsilon_s]} / 2 \quad (2)$$

where,  $h$  is the slab thickness,  $\epsilon_u$  is the ultimate compressive strain of concrete, and  $\epsilon_s$  is the total axial strain.

$$q_u = 24 \cdot L^2 (2\bar{M}_u - y_u \cdot 6 [N_u(0) + 2N_u(L/2)]) \quad (3)$$

$$\bar{M}_u = [M_u(0) + M_u(L/2)] / 2 \quad (4)$$

$$M_u(x) = 0.5 \beta_1 f'_c C(h - \beta_1 C) + f'_y A'_s (h - 2d') + f_y A_s (d - h/2) \quad (5)$$

$$C = 1/2(h - x - Ly_u - \epsilon_s L^2 / 4y_u) \quad (6)$$

$$N_u(x) = \beta_1 f'_c C - f_y A_s + f'_y A'_s \quad (7)$$

where  $M_u(x)$  is the ultimate moment resistance about midthickness of sections along the diagonal by the average thrust acting across the span.  $\beta_1$  is the equivalent stress block factor,  $f_y$  is the yield strength of tensile steel,  $f'_y$  is the yield strength of compressive steel,  $f'_c$  is the compressive cylinder strength of concrete,  $A_s$  is the tensile steel area per unit width,  $A'_s$  is the compressive steel area per unit width,  $d$  is the effective depth of tensile steel, and  $d'$  is the effective depth of compressive steel.

$$q_u = 48 \cdot L^2 M_u^0 \quad (8)$$

where  $M_u^0$  is the ultimate moment capacity per unit width at the center of an edge with zero thrust.

Neglecting the effectiveness of compressive steel, then

$$M_u^0 = A_s f_y (d - 0.59 A_s f_y / f'_c) \quad (9)$$

$$y_u = \min(y_u, 3y_u) \quad (10)$$

Assuming in the tensile membrane stage, the slab has the following properties: (i) the concrete has cracked throughout its depth, and therefore is ineffective in resisting internal stresses; (ii) all reinforcing steel has yielded; (iii) the strain hardening of steel does not occur. Therefore,

$$y_t = q_u L^2 / (k'_t A_{ts} f_y) \quad (11)$$

$$k'_t = 1.5k_t = 1.5\pi^2 / \{4 \sum_{n=1,3,5} (1/n^2)\} \quad (12)$$

$$(-1)^{(n-1)/2} [1 - \text{sh}(n\pi/2)] \}$$

where  $A_{ts}$  is the total reinforcing steel area per unit width.

$$q_{tt} = k'_t A_{ts} f_y y_{tt} \quad (13)$$

$$y_{tt} = 0.15L \quad (14)$$

From test data, the resistance function at every stage can be approximately expressed by

$$q(y) = \begin{cases} q_u [1 - (1 - y/y_u)^{1.8}]^{1/1.8} & 0 \leq y \leq y_u \\ q_u / 2 \{1 + q_u/q_u + (1 - q_u/q_u) \cos [\pi(y - y_u)/(y_u - y_u)]\} & y_u \leq y \leq y_s \\ q_s & y_s \leq y \leq y_t \\ k'_t (A_{ts} f_y / L^2) y & y_t \leq y \leq y_{tt} \end{cases} \quad (15)$$

The dynamic differential equation is

$$K_{LM} M_t \ddot{y} + q(y) = F(t) \quad (16)$$

where  $K_{LM}$  is the load-mass factor,  $M_t$  is the total mass of the slab per unit area,  $q(y)$  is the resistance function, and  $F(t)$  is the load-time history per unit area.

Since both the load and the resistance are complex functions, it is necessary to use a numerical procedure to obtain the peak midpoint deflection of the slab.

$$y_p = f(q_u, y_u, q_s, y_s, y_t, q_{tt}, F, t_d, M_t) \quad (17)$$

### 3. ANALYSIS OF UNCERTAINTIES

Since the parameters deciding  $y_p$  in Eq. (17) are influenced by many uncertain factors, they are all uncertainties. Among them,  $q_u, q_s, y_u, y_t, q_{tt}$ , and  $y_{tt}$  are resistance parameters, they can be described as random variables.  $F, t_d, M_t$ , and  $y_u$  are treated as fuzzy variables, and their membership function are taken as follows (Fig. 3).

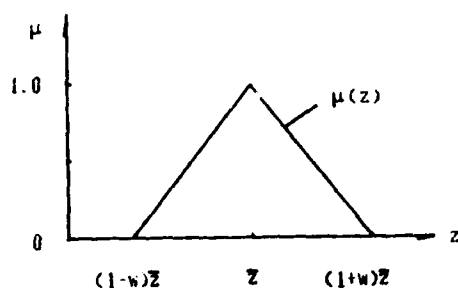


Fig.3 Membership Function of Fuzzy Variable

The value of  $z$  and  $w$  can be determined from survey data. If  $y$  is a function of  $n$  independent fuzzy variables as

$$y = f(x_1, x_2, \dots, x_n) \quad (18)$$

where  $x_1, x_2, \dots, x_n$  are independent fuzzy variables, their membership function are  $\mu_1(x_1), \dots, \mu_n(x_n)$ , respectively. Therefore,  $y$  is a fuzzy variable also, whose membership function can be determined [4] as

$$\mu(y) = \sup_{y=f(x_1, x_2, \dots, x_n)} \{ \min [\mu_i(x_i)] \} \quad (19)$$

A numerical procedure based on the fuzzy simulation is employed to obtain  $\mu(y)$ . If  $y$  is a function of  $n$  independent random variables, the means and variances of  $x_1, x_2, \dots, x_n$  are  $\bar{x}_1, \bar{x}_2, \dots, \bar{x}_n$ ,  $v(x_1), v(x_2), \dots, v(x_n)$ , respectively. The covariance of  $x_i$  and  $x_j$  is  $C(x_i, x_j)$ . Using linear terms of Taylor's series to approximate  $y = f(x_1, \dots, x_n)$ , the means and variance of  $y$  can be obtained as

$$\bar{y} = f(\bar{x}_1, \bar{x}_2, \dots, \bar{x}_n) \quad (20)$$

$$v(y) = \sum_{i=1}^n (y_i - \bar{y})^2 v(x_i) + 2 \sum_{i=1}^{n-1} \sum_{j=2}^n \left[ \frac{\partial y}{\partial x_i} \frac{\partial y}{\partial x_j} C(x_i, x_j) \right] \quad (21)$$

where all terms in the expression are evaluated at  $x_i = \bar{x}_i (i = 1, 2, \dots, n)$ .

#### 4. THE SURVIVAL PROBABILITY OF SLABS

From the dynamic analysis of slabs, the relationship between  $F_1$  and  $y_p$  is found as Fig.4.

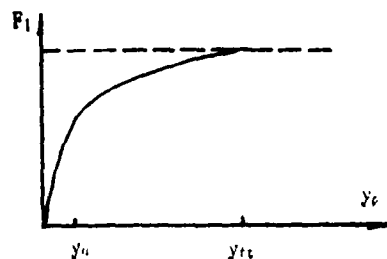


Fig.4 Relationship between  $F_1$  and  $y_p$

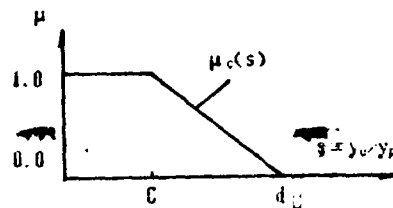


Fig.5 Membership Function of the Slab's Collapse,  $\mu_c(s)$

The collapse of slabs is a fuzzy occurrence, whose membership function  $\mu_c(s)$  is chosen as Fig.5.

Considering the properties of  $F_1 - y_p$  relationship and other factors, the  $c$  and  $d$  are chosen as

$$\begin{cases} c = y_0 - y_{tc} \\ d = 1.0 \end{cases} \quad (22)$$

Since  $y_p = f(q_0, y_0, q_1, y_1, q_2, y_2, \dots, q_n, y_n, F_1, t_0, M_0, \dots)$  is a function of fuzzy and random variables, the membership of  $y_p$ ,  $\mu_{y_p}(y_p)$  at a  $y_p$  can be obtained from the method introduced previously.

To avoid some numerical difficulties arising from sharp turn point of  $y_p$  at  $y_{tc}$ ,  $s = y_0 - y_p$  is used to represent the response of the slab instead of  $y_p$ . The membership function of  $s = y_0 - y_p$ ,  $\mu_s(y, s)$  can be obtained from  $\mu(y_0)$  and  $\mu_{y_p}(y, y_p)$ , as in Fig.6.

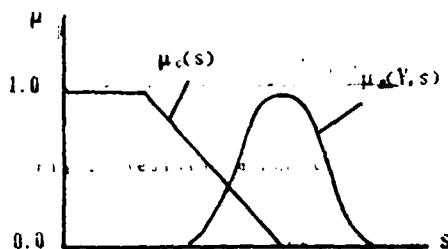


Fig.6 Membership Function of the Slab's Response  $\mu_s(Y, s)$  and the Collapse Criterion of the Slab



The relative position of  $\mu_r(Y, s)$  with respect to  $\mu_c(s)$  represents the satisfactory degree of the slab's response to the collapse criterion of the slab ( Fig.6 ). Thus, the membership function of the slab's collapse is defined as [3]

$$\beta(Y) = \frac{\int_{-\infty}^{\infty} \min \{ \mu_c(s), \mu_r(Y, s) \} ds}{\int_{-\infty}^{\infty} \mu_r(Y, s) ds} \quad (23)$$

Thus the probability of the slab's collapse can be found as [3]

$$p = \int \beta(Y) f_n(Y) dY \quad (24)$$

where  $f_n(Y)$  is the joint probability density function of  $Y$ .

Finally the survival probability of the slab is

$$p_s = 1 - p \quad (25)$$

If the response of the slab is independent of any random variable, the probability of the slab's collapse is

$$p = \int \beta f_n(Y) dY = \beta \quad (26)$$

Two numerical algorithms are proposed to obtain  $p_s$  in this paper. Method 1 is to simulate the random variables and obtain  $p_s$  using Eq.(24) and Eq.(25). Method 2 is based on the assumption that all uncertainties can be considered as fuzzy variables and then  $p_s$  is obtained using Eq.(26) and Eq.(25).

## 5. CALCULATION RESULTS

The design parameters and resistance parameters are shown in Table 1.

Survival probability of the slab is obtained using method introduced previously, results are shown in Fig.7 and Fig.8.

On the basis of results obtained, the following conclusions are made.

(1) Since the compressive membrane action has not considered in the design, the survival probability of the shelter is bigger than that expected in the design. Thus, in this case, the design is conservative.

(2) The distribution of the peak overpressure and the positive phase duration of the overpressure are very important in determining the survival probability of the slab, and the wider the distribution is, the more smooth the curve of survival probability is. It means that the determination of the blast effects is very important factor for the design.

(3) In the design of shelters, the reinforcing ratio is relatively low. This leads to the resistance in the tensile membrane stage is comparatively lower with respect to the resistance in the compressive membrane stage. There exists a sharp-turn point in  $y$ , and the shelter collapse in a brittle failure type, which is not good for structure safety. Therefore, reinforcing ratio should be modified in the design of shelters to improve the ductility of the slabs.

(4) The results of survival probability obtained in this paper is very useful in the design of basement type shelters.

## ACKNOWLEDGEMENT

Helpful suggestions from Prof. Z.Y.Chen are gratefully acknowledged.

Table 1 Data and Resistance Function Parameters  
( 20 psi Design )

| Parameter                 | Mean Value | Coefficient of Variation | Parameter     | Mean Value | Coefficient of Variation |
|---------------------------|------------|--------------------------|---------------|------------|--------------------------|
| $L(ft)$                   | 16.00      | 0.000                    | $q_u(ksi)$    | 118.76     | 0.190                    |
| $h(in)$                   | 15.00      | 0.000                    | $y_u(in)$     | 2.48       | 0.042                    |
| $d(in)$                   | 12.75      | 0.041                    | $q_s(ksi)$    | 36.38      | 0.105                    |
| $A_s$ and $A'_s(in^2/ft)$ | 0.32       | 0.024                    | $y_s(in)$     | 7.89       | 0.042                    |
| $f_{cy}(ksi/in^2)$        | 84.02      | 0.092                    | $y_t(in)$     | 14.69      | 0.063                    |
| $f'_{dc}(ksi/in^2)$       | 4.75       | 0.176                    | $q_{rt}(ksi)$ | 71.38      | 0.095                    |
| $k'_t$                    | 20.37      | 0.000                    | $y_{rt}(in)$  | 28.80      | 0.100                    |
| $\phi$                    | 1.00       | 0.047                    | $m_t(ksi)$    | 1.97       | 0.023                    |

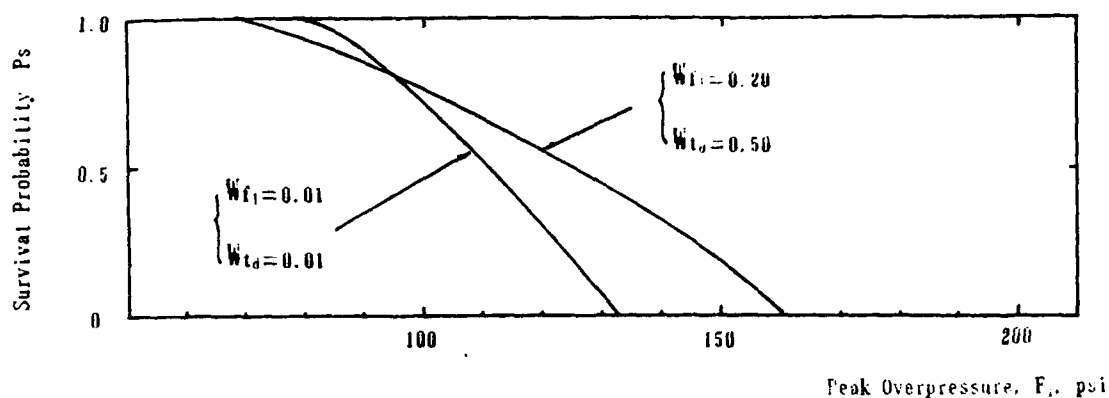


Fig. 7 Survival Probability of the Slab,  
20 psi Design

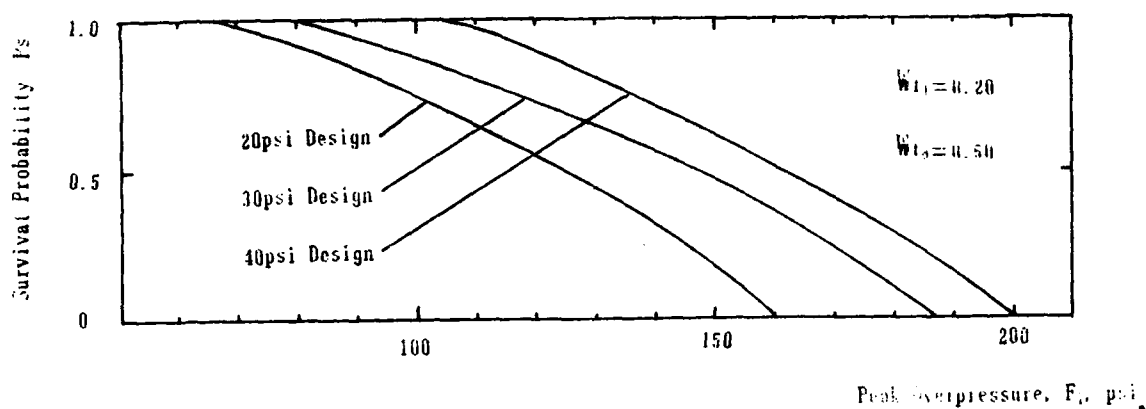


Fig. 8 Survival Probabilities for Different Loads

#### REFERENCES

[1] Longinow, A., "Probability of People Survival in Nuclear Weapon Blast Environment", for Federal Emergency Management Agency, FEMA Contract DCPA01-79-C-0240 Work Unit 1621, IIT Research Institute, Chicago, ILL., May, 1980.

[2] Wiehle, C.K., "Dynamic Analysis of a Building Element", April 1974.

[3] Zadeh, L.A., "Fuzzy Sets", Information and Control, No. 3, 1965.

[4] Zadeh, L.A., "Probability of Measures of Fuzzy Events", Journal of Mathematical Analysis and Applications, Vol. 23, 1968, pp. 421-427.

## **TWO-POUND HIGH EXPLOSIVE TEST FIRE CHAMBER DESIGN, CONSTRUCTION AND TESTING**

**Steven L. Young, PE  
Darrell D. Barker**

**Mason & Hanger - Silas Mason Co., Inc.**

**ABSTRACT:** A test fire chamber was designed and fabricated to routinely contain the effects of a 2 lb detonation of high explosives (HE). The chamber was designed such that the charge could be located 3 feet from any surface, allowing maximum use of the working platform. The test fire chamber is a horizontal, cylindrically shaped vessel. The chamber has a flat bulkhead front containing the door opening, and a torispherical aft housing two camera ports. Final chamber certification included a 125 percent HE overtest of the chamber capacity and a hydrostatic test. Additionally, the chamber was instrumented to determine strains at specific locations during the 125 percent overtest. Principal and maximum shear stresses were calculated and compared with allowable values.

### **INTRODUCTION**

The Trident II Test Fire Facility, located at the Pantex Plant in Amarillo, Texas was designed in 1986 and construction began in 1987. Construction was completed in 1988. The facility houses two test fire chambers used for qualifications testing of small explosives components. The chambers were designed to resist the effects of a planned detonation with limited venting to the atmosphere. Two chambers were designed; one chamber was designed to contain the effects of a one pound detonation and the other was designed for two pounds of explosives. The chamber welds were radiographically tested and chambers were stress relieved. In addition to a hydrostatic test, the chambers were subjected to a 125 percent proof test prior to acceptance. Both chambers have essentially the same configuration and were designed similarly. The two pound chamber, because of the greater loading and larger size, presented the greater design challenge and will be the focus of the discussion.

### **DESCRIPTION OF CONTAINMENT CHAMBER**

The chamber is a horizontal cylinder with a flat bulkhead containing the door and a torispherical aft incorporating the camera ports. The front bulkhead is made from a series of stiffeners and beam framing elements for the door opening. The length of the vessel is approximately 27'-0" and the outside diameter is approximately 12'-6". The door opening for the chamber is 4'-10" by 7'-0" with an outward door swing. There are two camera ports in the chamber mounted on swivel mechanisms allowing full coverage of the working platform. The working platform is continuously welded to the cylinder walls with the void beneath the platform filled with concrete. The working platform size is 10'-0" by 25'-0". The main chamber components are made from SA 516, grade 70 steel with the exception of the door pins and inserts which are made from 4140 tool steel. The main shell and floor thickness of the chamber are one inch. The door pins are air actuated with spring retract. The chamber has exhaust capabilities that can be manually activated after an explosive test. Optic ports are in the aft end and chamber center. The ports have steel plate shielding capabilities but were designed to be left in the locked open position during the test. The shields can be used to protect the ports from fragments generated from the explosive detonator. Apart from the inherent penetration resistant of the chamber walls, no other fragment provisions were made.

### **DESIGN METHODOLOGY**

The chamber was designed to routinely contain the effects of a 2 lb detonation of high explosives (HE) located approximately 3 feet from any interior surface. An additional design requirement, was a one time 2.5 lb HE proof test which was part of the chamber certification process. No fragment

calculations were necessary, since explosive testing conducted within the chamber will be bare HE. Port covers were designed to protect the optic port from small detonator fragments, however the plate thickness was dictated by the blast loading and not by fragment parameters.

The multipliers on the explosive weight to provide a factor of safety and a TNT equivalence were 1.2 and 1.3 respectively. The 1.3 TNT equivalence is used to permit maximum flexibility of explosive testing within the chamber. The 2.5 lb HE proof test was not increased and used as the design charge since the proof charge was placed in the center of the chamber and was a one time event. Rather, the 2 lb HE weight was increased by the multipliers and used as the design basis charge.

The primary challenge during design of the chamber was to determine the blast loading on the cylindrical shell and torispherical surface caused by an off-center detonation. Reference (1) provides a clear, step by step procedure to account for off-center detonations within an explosive containment vessel:

1. Partition the ring element into several subareas connected by nodes.
2. Use curves for Normally Reflected Blast Wave Properties for Bare, Spherical TNT in Air at Sea Level to determine reflected pressure ( $P_r$ ) and reflected impulse ( $i_r$ ) for the standoff distance ( $R$ ) from the charge location to each node.
3. Calculate time of duration ( $t$ ) for each node by  $t = 2 i_r / P_r$
4. Increase  $P_r$  and  $i_r$  by 1.75 to account for secondary shocks within the chamber.
5. Calculate quasi-static pressure ( $P_{qs}$ ) and blow down time ( $t_{qs}$ ) using available volume and vent area. Follow procedure in Reference (2) to determine  $t_{qs}$ .

In addition to the off-center load calculation, the design of the cylindrical shell also included a center charge loading, using the radius of the chamber as the standoff distance, the curves in step 2 to determine  $P_r$  and  $i_r$ , and calculating  $t$  as outlined in step 3. The pressure and impulse were again increased by 1.75 to account for secondary shocks.

A procedure provided in Reference 2 was used to calculate the blast loads on the bulkhead and door.

After determination of the loading on the vessel, response calculations were accomplished using a structural analysis program for dynamic response of linear

systems, Reference (3), and a locally developed, nonlinear, single degree of freedom system program.

As the chamber approached final design, the hydrostatic pressure magnitude and origin was questioned. 200 psig, though a contractual requirement, was not related to the dynamic loading of the vessel. Further investigation revealed that the number was based on past, not necessarily related, chamber designs. As a result, additional calculations were performed to relate 200 psig hydrostatic pressure to actual dynamic response of the chamber components. Since the hydrostatic test was part of the verification process, it was determined that a hydrostatic pressure producing deformation at least equal to the dynamic deformation resulting from the actual chamber working load, would be a more appropriate test of the completed chamber. The magnitude and time of maximum response, natural period and dynamic load factor were calculated for each vessel component. A center charge location was used for the cylindrical shell calculations. An equivalent static pressure was calculated from the dynamic load factor obtained from Reference (4). The limiting static pressure was obtained and, per ASME Pressure Vessel Code, increased by 1.5. The equivalent static pressure recommended was 340 psig. Unfortunately, the contract documents did not require a hydrostatic loading to that level. The equivalent static pressure without the ASME increase was 225 psi. Since the design charge was increased by a 20 percent safety and a 30 percent TNT equivalence factor, it was determined that 225 psig would adequately test the chamber.

## TEST PROGRAM

### Introduction

A vessel designed to contain the effects of an explosion must be designed well within the elastic limit of the material. An elastic design eliminates the need for a detailed and expensive inspection after each test shot.

Generally, the design and response of a symmetric shell does not present a design problem. However, because of user requirements, such as off-center detonations, or construction requirements, components are added that affect the symmetry and thereby alter the stress distribution and response of the vessel.

The purpose of the test program was to obtain stress values at specific locations on the chamber to ensure chamber response was within the elastic region of the

material. Additional objectives were to monitor areas of high localized stress concentration, verify design safety factors, and gather data for future chamber designs.

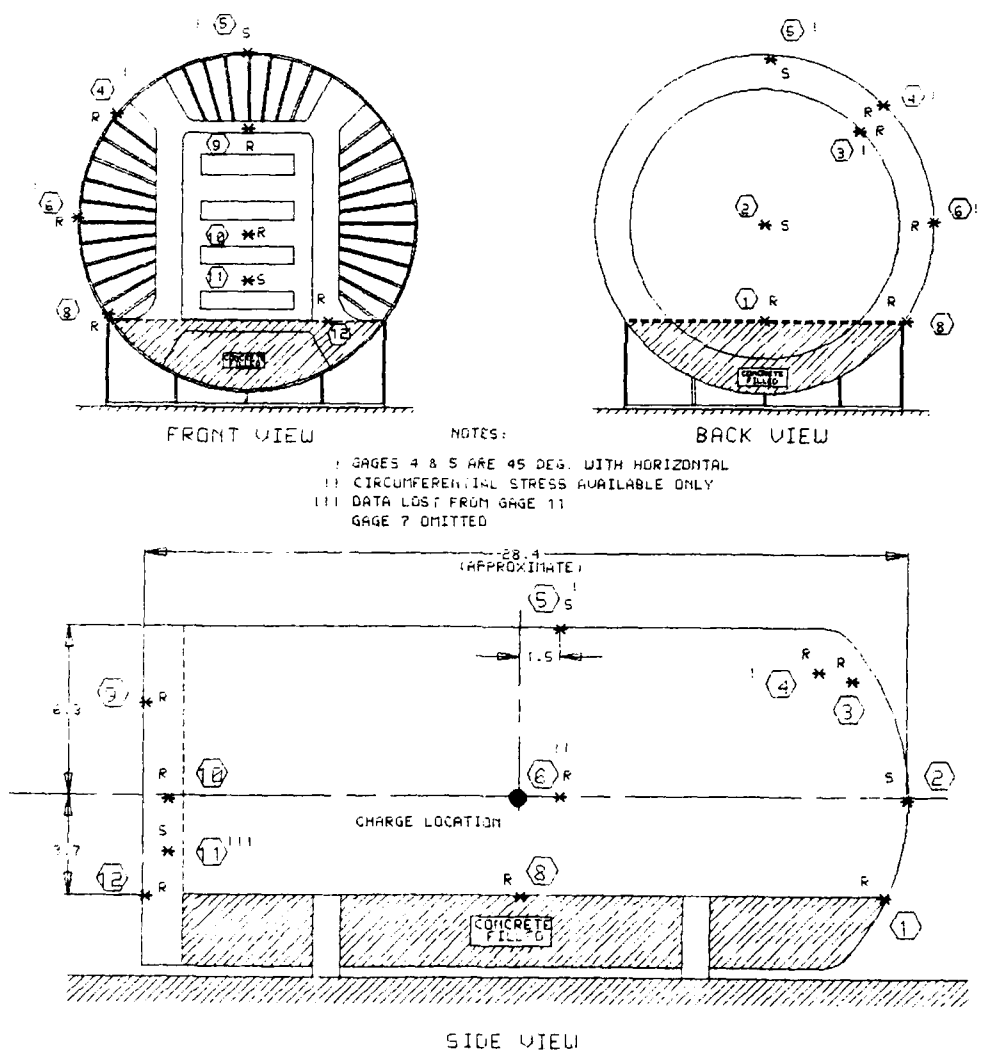
### Proof Charge/Location

The proof charge was cylindrical, with a length to diameter ratio of 1. The longitudinal axis of the charge was parallel to the long axis of the chamber. In addition, the charge was placed in the center of the chamber, 44" from the floor. The charge location was selected to best test all chamber components rather than concentrating on one specific component. In future validation testing of explosive containment chambers, a more appropriate explosive test procedure may be to conduct

several tests with the design charge weight, or at 125 percent of the design charge weight, at several locations to test all components, including an off-center condition.

### Instrumentation

The chamber was instrumented with single and rosette strain gages as shown in Figure 1. The output of the gages were recorded on two, Sangamo 80-14 channel magnetic tape recorders. The magnetic tapes were played through a Biomation Model 8100 Digital Waveform Recorder to digitize the analog signals. The digitized data was recorded on magnetic disk with an HP 9835 computer and converted to strain values on an HP 9845.



The signals were digitized at two sampling rates, 2 and 100 samples per millisecond, to allow analysis of responses during shock and long term gas loads. Plots of these values were provided over 20 and 1000 millisecond time intervals. The data was filtered by a Fast Fourier Transform.

## TEST RESULTS

### Methodology

Principal and maximum shear stresses were calculated from peak strain values and gage orientation, as appropriate, using basic mechanics principles. A locally written computer program was developed to facilitate analysis of several cases.

### Single Gages

Stresses at the single gage locations were obtained using the peak strain values and calculating the corresponding stresses. Actual principal stress values ranged from maximum positive and maximum negative

values of 4,634 psi and -3,435 psi at the door center, to minimum positive and negative values of 2,040 psi and -1,410 psi at the torispherical center.

The data on gage 11 was lost during the shot. The gage was to monitor actual stress in the bottom center door beam. Gage 7 was redundant and was intentionally omitted prior to the shot.

### Rosettes

The peak strain values and times of occurrence were taken from a single leg of each rosette. The strains occurring at that time were then read from the remaining legs of the rosette, and corresponding principal and maximum shear stresses calculated. The process was repeated for the peaks of the remaining two legs of the rosette and the worst case principal and maximum shear stresses obtained for that gage location.

The maximum principal positive stress

| GAGE NUMBER     | GAGE TYPE | PRINCIPAL STRESSES<br>(Max,Min-psi) |       | MAXIMUM SHEAR<br>(psi) |
|-----------------|-----------|-------------------------------------|-------|------------------------|
| 1               | Rosette   | 1972                                | -1941 | 970                    |
| 2               | Single    | 2040                                | -1410 | -                      |
| 3               | Rosette   | 2817                                | -6208 | 507                    |
| 4               | Rosette   | 4940                                | -4005 | 1694                   |
| 5               | Single    | 3900                                | -3000 | -                      |
| 6 <sup>!</sup>  | Rosette   | 4050                                | -3300 | -                      |
| 7               | omitted   | ****                                | ****  | ****                   |
| 8               | Rosette   | 2038                                | -2744 | 848                    |
| 9               | Rosette   | 2811                                | -3103 | 948                    |
| 10              | Rosette   | 4084                                | -3435 | 1358                   |
| 11              | Single    | "                                   | "     | "                      |
| 12 <sup>!</sup> | Rosette   | 900                                 | -600  | -                      |

! Partial data available

!! Data lost

TABLE 1. MAXIMUM PRINCIPAL SHEAR AND STRESSES

(4,940 psi) occurred at gage 4. This gage was located at the junction of the torispherical head and cylinder at a 45 degrees angle with the longitudinal axis of the chamber (refer to Fig 1). The maximum principal negative stress was 6,208 psi, located in the torispherical head at the junction of the radius change. Again, the gage was located 45 degrees with the chamber longitudinal axis.

Some channel information for gages 6 and 12 were lost during the shot, providing only partial information at those locations. Gage 6 was located on the cylindrical shell at the same height as the charge. Gage 6 data was available to determine circumferential stress at that location. However, data from gage 12, located at the base of the door support,

came from the vertical leg of the rosette and provided little information.

The principle stresses and shears for both gage types are presented in Table 1.

#### Conclusion of Test Program

The allowable primary bending stress for SA 516, grade 70 steel per ASME is 25,600 psi. In all cases the values were well within the elastic region of the material.

As time permits, additional calculations will be performed to compare actual stresses obtained from the test program to predicted values incorporating test conditions.

#### REFERENCES

- (1) Whitney, M.G., G.J. Friesenhahn, W.E. Baker, L.M. Vargas. "A Manual to Predict Blast and Fragment Loadings from Accidental Explosions of Chemical Munitions Inside an Explosive Containment Structure", Final Report to USA Toxic Materials Agency and USA Corps of Engineers, Huntsville Division, Prepared by Southwest Research Institute, April 1983.
- (2) DOE/TIC-11268, "A Manual for the Prediction of Blast and Fragment Loading of Structures", Prepared for U.S. Department of Energy, Albuquerque Operations, Amarillo Area Office, Facilities and Maintenance Branch, Prepared by Southwest Research Institute, November 1980, Revised April 1982.
- (3) Bathe, K., E.L. Wilson, F.E. Peterson, "SAP IV - A Structural Analysis Program for Static and Dynamic Response of Linear Systems", June 1973, Revised April 1974.
- (4) Biggs, J.M., "Introduction To Structural Dynamics", McGraw-Hill

# THE DESIGN OF UNDERGROUND MASS TRANSIT STRUCTURES TO RESIST CONVENTIONAL WEAPON EFFECTS

C. A. MILLS

WS ATKINS & PARTNERS, UK

## ABSTRACT

The paper outlines the concepts that can be adopted for underground mass transit structures that are to be designed to serve a dual role as civil defence shelters during wartime.

## INTRODUCTION

During the Second World War, the stations of London Transport's mass transit system were used as air raid shelters during the night time bombing raids on London<sup>(1)</sup>. On the whole the structures used were deep, bored tunnel stations which provided protection by virtue of their depth below ground. More recently, shallow mass transit structures constructed by cut and cover techniques have been designed to withstand a direct hit by conventional weapons.

The operational requirements of a mass transit system conflict with those of a civil defence system and hence there has to be a compromise between civil defence and mass transit requirements. The time between a warning of an attack and the actual attack is unlikely to allow sufficient time to convert from mass transit to civil defence operations and unless mass transit operations are to be suspended during hostilities, structures need to be designed to meet both requirements simultaneously.

Desirable features of a mass transit station include:

- \* minimal distance and level between the street and platforms.
- \* clear sight lines enabling visual orientation of passengers.
- \* spacious entrance structures and passages to allow the easy ingress and egress of passengers.

The ideal characteristics of structures to meet the above requirements would include minimum number of columns, large voids in the concourse slab to create sight lines between ticketing and platform areas, and large openings in the station box between the concourse areas and the street. These characteristics are the opposite of the ideal requirements for structures to provide protection against blast and fragments that result from the detonation of conventional weapons where the requirement is to provide a sealed environment and heavy civil engineering structures.

## DESIGN PARAMETERS

In order to design a weapon resistant structure it is necessary to define the threat, the weapon characteristics and the acceptable level of damage. It is not possible to provide complete protection, even against conventional weapons, and hence there has to be an appropriate balance between the risk of the protection being compromised and the cost of providing higher levels of protection. In practice, the level of protection provided is likely to be influenced by cost considerations which require some design work and hence the selection of design parameters becomes an iterative process.

With regard to risk, a characteristic of mass transit stations is their relatively large size allowing large numbers of people to be accommodated. When selecting the weapons against which protection is to be provided it is necessary to consider the consequences of concentrating large numbers of people in relatively open structures which, if penetrated by a weapon larger than that selected for design, could have catastrophic results. A typical mass transit station can accommodate approximately 2000 people plus two train loads of passengers giving a total of about 5000 people.



It is possible to design mass transit structures to resist nuclear, biological and chemical weapons but this leads to severe restrictions on mass transit operations and hence it is reasonable to limit protection to the effects of conventional weapons. With respect to conventional weapons, air raids are the most likely form of attack and conventional bombs dropped from high altitude pose the most serious threat to the underground structures. As a form of attack, high altitude bomb runs are highly vulnerable to modern air defence systems and hence the likelihood of such an attack being carried out needs to be included in the overall assessment of risk.

The depth to which bombs are likely to penetrate the ground is an important design parameter. Information collected by bomb disposal authorities in the United Kingdom during the Second World War and collated by Christopherson<sup>(2)</sup> shows that penetration depths follow Normal probability distributions dependant upon soil type. One such probability plot is given in Figure 1 and such plots can be used to assess the risk of different penetration depths being exceeded.

#### CUT AND COVER STRUCTURES

A typical general arrangement of an island platform cut and cover station is given in Figure 4. As can be seen, the station box can be divided into public areas, ancillary operational areas and plant areas. Attached to the station box are entrances leading to street level, and emergency exits and ventilation ducts leading to shafts shown located behind existing building lines. The major openings in the structure are due to the ventilation system, the entrances and the running tunnels.

In order to carry out a structural design, it is first of all necessary to divide the floor area of the station into suitable levels of protection. Assuming that the purpose of providing weapon resistant civil defence structures is to shelter people rather than provide a weapon resistant transit system, three grades of required protection can be identified:

- GRADE A: Suitable for the protection of personnel sheltering in the station. Covers public and ancillary operational areas manned by mass transit staff.
- GRADE B: Suitable for the protection of equipment required for the operation of the shelter including the maintenance of the shelter environment.
- GRADE C: Required for areas adjacent to Grade A and Grade B where penetrating weapons could compromise the protected zones. It includes, for example, the running tunnels where an exploding weapon could cause casualties on the platforms of adjacent stations.

There are two basic structural options for creating the protected environment. They are:

- (a) by shielding the structure with an additional sacrificial layer;
- (b) by strengthening the structure to resist the direct effects of weapons.

Frequently a satisfactory sheltering system will be best achieved by a combination of both methods. Alternative structural forms for hardened cut and cover station cross-sections are given in Figure 5. Information for establishing preliminary structural sizes has been previously summarised by the author<sup>(3)</sup>.

The structural sizes are governed by two requirements. First, a thickness requirement that is independent of span dimensions to prevent perforation and spalling due to weapon effects, and second, a strength requirement that depends upon the applied loads and span dimensions. The loads applied by conventional weapons are typically of large magnitude and short duration and hence can be absorbed by post elastic response. The degree of post elastic response is measured by the ductility which is defined as the ratio of the maximum displacement to the yield displacement. A ductility of one or less implies an elastic response and a ductility greater than one, a plastic response. Increasing values of ductility imply increased levels of damage.

The cost implications of the level of ductility adopted for design are illustrated in Figure 2. This figure shows the variation in the cost of a reinforced concrete structural element as a function of the ductility required to absorb a given blast loading. The element varies from a thick, heavy member with an elastic response, to a thin, lighter member responding plastically. As can be observed, adopting a design ductility of three approximately halves the cost of the element. This curve illustrates the importance of maximising acceptable damage levels when establishing the cost and design parameters for hardening a mass transit station.

The relationship between the required wall thickness and burster slab overhang, necessary to keep weapons away from the walls of the structure, is another important design parameter to consider. A structural analysis of the wall thickness required for different proximities to a bomb exploding below ground produces a curve like the one shown in Figure 3. As can be seen, the thickness required reduces rapidly as the proximity decreases, especially if the origin is taken as the inside face of the wall which correlates with the land take.

The desire to maintain mass transit operations during hostilities and the lack of time to make substantial changes to the operation of the system after a specific warning of an attack imposes major constraints on the design of the main openings in the station box.

It is desirable to maintain relatively easy ingress and egress of passengers during alerts while at the same time providing protection against blast. A possible solution is to provide access via two blast doors, one of which is always shut, but this imposes severe constraints on passenger flows. An alternative illustrated on the general arrangement (Figure 4) is to close off the main entrance with a single blast door while providing an alternative means of entrance via passages containing a suitable number of blast attenuating features.

The massive ventilation requirements of a mass transit system preclude the use of mechanical blast protection devices on the air intake and exhaust shafts resulting in the need to design the structure for the environmental control system (ECS) as a blast attenuation chamber. A possible arrangement for the ECS is illustrated on the general arrangement (Figure 4). This arrangement incorporates a series of blast walls perforated by ventilation openings that function as a series of baffles to reduce the blast pressure to acceptable levels. An exploding weapon would destroy the equipment but the ECS can be duplicated at each end of the station. In the event of one ECS being destroyed, the second can be designed to maintain the shelter environment at a reduced but safe level.

From the mass transit operations point of view, the provision of blast doors between the station ends and running tunnels presents a possible safety hazard during normal operations due to the accident risk of trains running into closed doors. Blast pressures show little attenuation with distance in tunnels and with large numbers of people sheltering on the adjacent platforms, there is a need to ensure weapons do not detonate in the running tunnels.

The design of cut and cover running tunnels to resist weapon effects is the same as for a cut and cover station, although the level of protection required is much less.

#### BORED TUNNEL STRUCTURES

To establish the levels of damage that segmentally lined bored running tunnels and stations can sustain, bomb damage reports on the London Underground during the Second World War have been extracted from archives and analysed to produce proximity factors for varying levels of damage.

Linear dimensions such as the proximity of an explosion to a structure can be expressed in terms of a scaling factor and the cube root of an equivalent weight of TNT causing the explosion. This allows the direct comparison of explosions involving different amounts of explosive but in otherwise similar situations. The proximity factor,  $Z$ , of an explosion to a structure can thus be defined as:

$$Z = r/w^{1/3}$$

where  $r$  = distance in metres from the point of detonation to the structure.

and  $w$  = the equivalent charge weight measured in kilograms of TNT.

The information on bomb damage included the necessary repairs, the depth of the tunnel, and the crater size with its plan distance from the tunnel. From the crater dimensions, the likely bomb size and depth of detonation were calculated from which proximity factors relative to the tunnel were determined. On the basis of this analysis it was estimated that although tunnels would be heavily damaged, they would prevent blast pressures entering the tunnel at proximity factors greater than 0.6. Minimal damage that would provide adequate protection to people sheltering in a station constructed by bored tunnelling methods occurs at proximity factors greater than 3.0. These proximity factors are for cast iron segmentally lined tunnels in London clay.

#### CONCLUSIONS

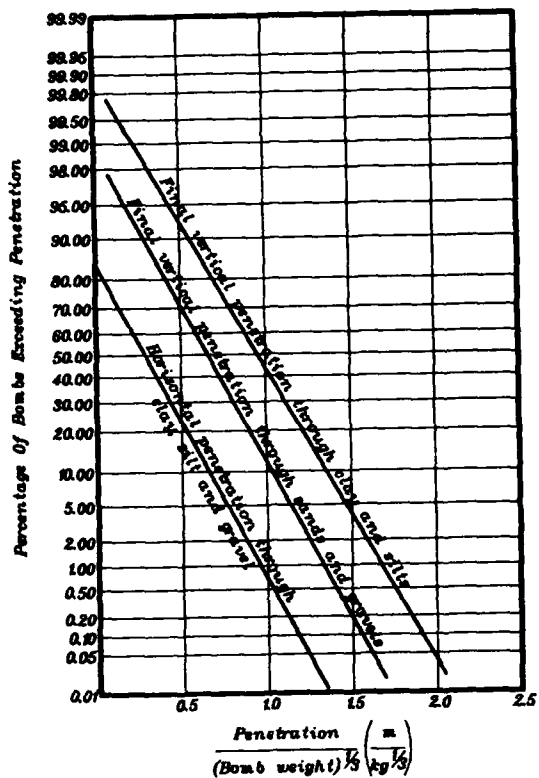
The foregoing outlines the structural considerations required when incorporating civil defence facilities within a mass transit system. The civil defence and mass transit requirements are to a certain extent in conflict and there is a clear need to establish their relative priorities early on in the design process. The level of protection to be provided is likely to be influenced by cost and as has been indicated, this is not only determined by the threat definition but also by the levels of damage that can be accepted. The threat and damage levels will also determine the range of construction methods that can be employed for cut and cover construction which will have a further effect on the cost of incorporating civil defence facilities. A good level of protection can be provided for an additional structural cost in the order of twenty percent.

#### ACKNOWLEDGEMENT

The author wishes to acknowledge the valued contribution from Mr M A Soubry of Freeman Fox and Partners to the concepts outlined in the paper.

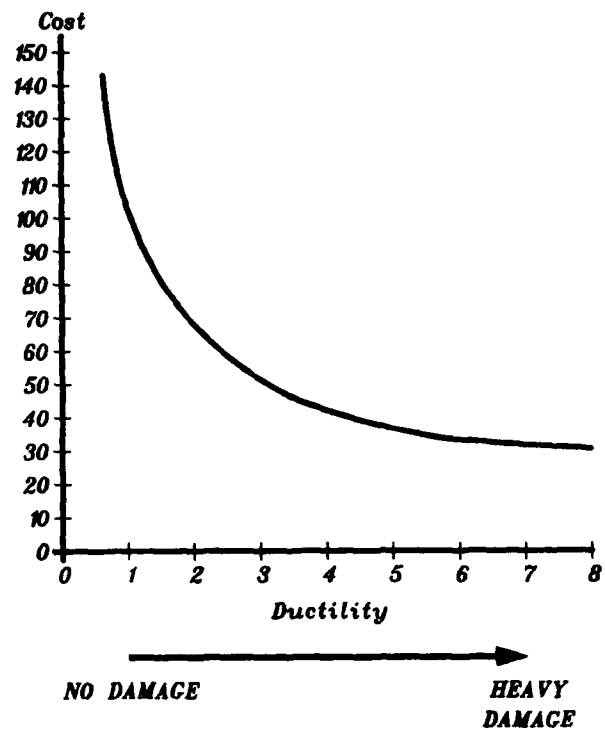
#### REFERENCES

- (1) Graves C, (1947). London Transport Carried On. London Passenger Transport Board, London.
- (2) Christopherson D G, (1945). Structural Defence. British Ministry of Home Security, London.
- (3) Mills C A, (1987). The Design of Concrete Structures to Resist Explosions and Weapons Effects. The First International Conference on Concrete for Hazard Protection, Edinburgh, 27-30 September 1987.



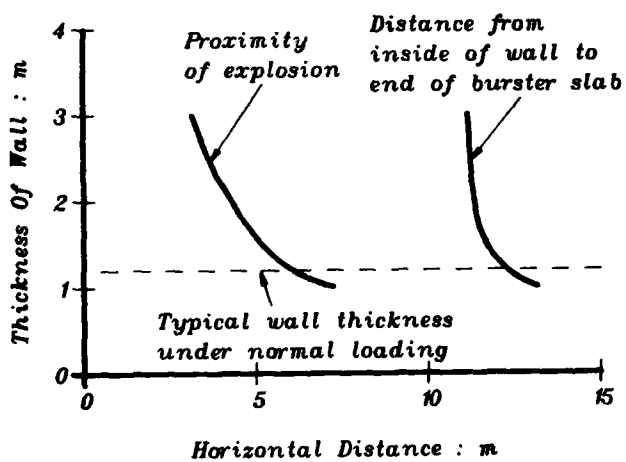
Probability Plot Of The Ground Penetration Of A Bomb

Figure 1



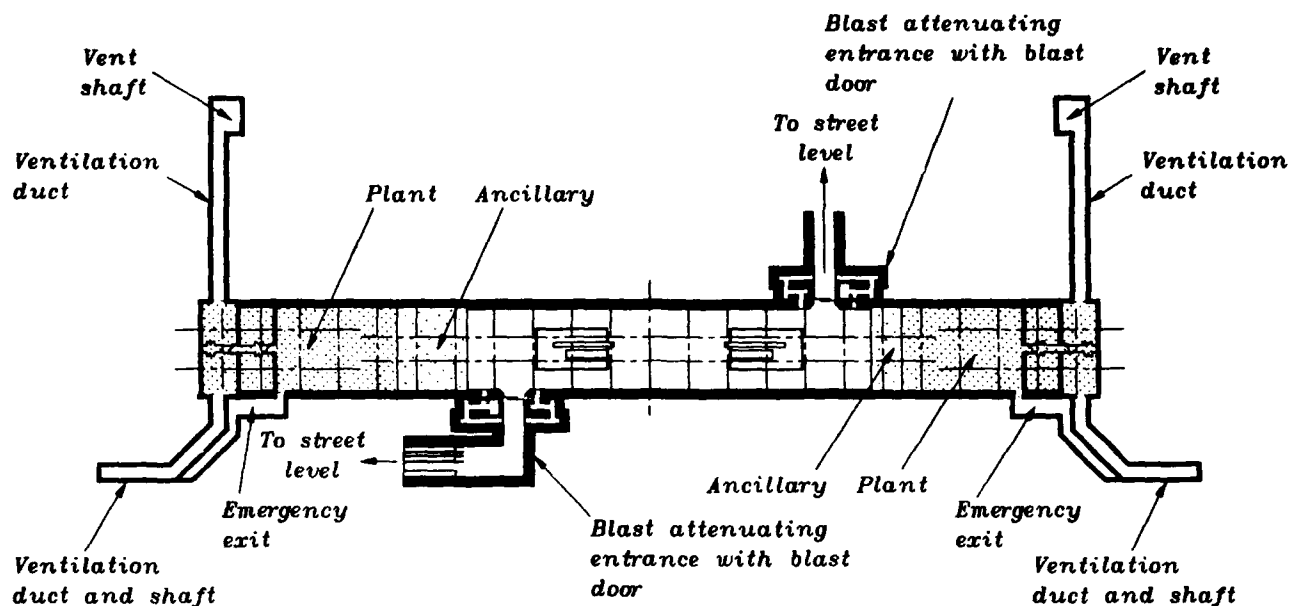
A Cost Versus Design Ductility Curve For A Reinforced Concrete Element Subjected To A Specified Blast Load

Figure 2



Burster Slab Overhang Versus Wall Thickness

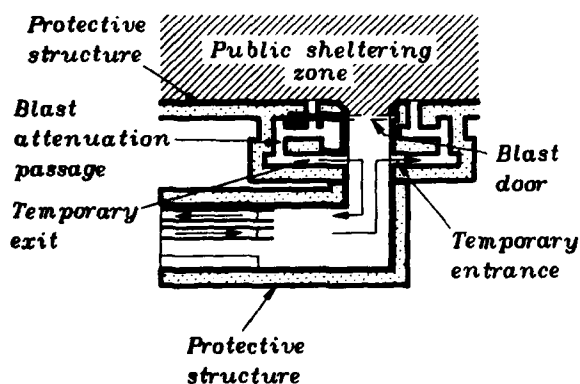
Figure 3



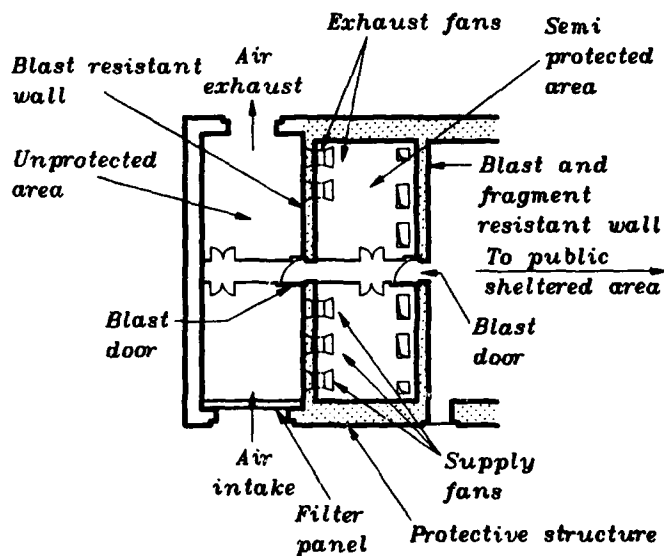
*Plan At Concourse Level*



*Plan At Platform Level*



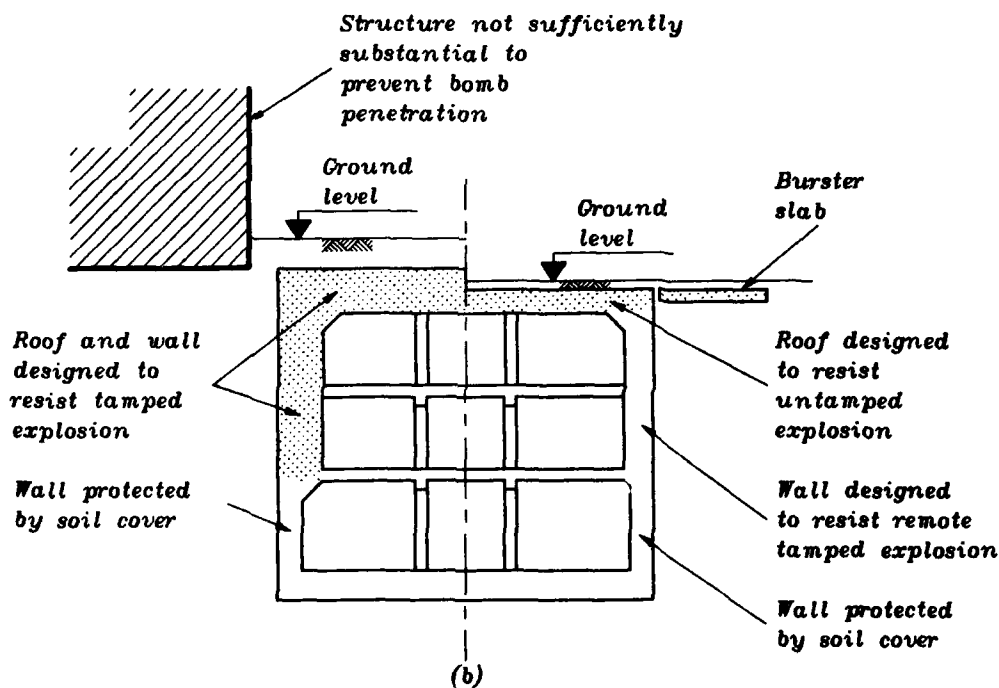
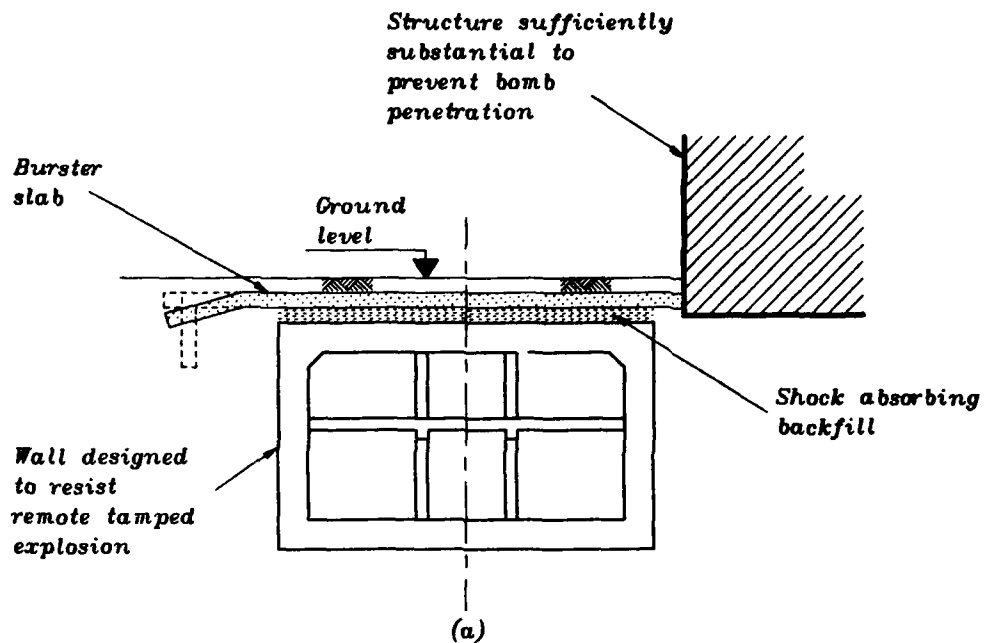
*Blast Attenuating Entrance Structure*



*Blast Attenuating Ventilation Structure*

## *A Typical General Arrangement For An Island Platform Station*

*Figure 4*



Structural members and/or burster slab designed to resist effects of direct exposure to explosion and/or impact shown thus



Some Alternative Arrangements For  
A Cut And Cover Station Box

Figure 5

# DESIGN, DEVELOPMENT AND TESTING OF A HARDENED UNDERGROUND TRANSPORTABLE COMPOSITE HYPERBOLIC PARABOLOID (HUTCH) SHELTER

T. F. Moriarty and P. von Buelow

The University of Tennessee  
Knoxville, Tennessee

## ABSTRACT

Two blast shelter modules, each providing approximately 500 sq ft (46 sq m), were prefabricated, transported, erected, bermed and tested. Each module was designed using modular structural panels based on hyperbolic paraboloids. The hyperbolic paraboloid shape is an efficient structural form for carrying impulsive type loadings due to its inherent ability to provide tensile as well as compressive load paths. This dual structural nature also lends itself well to composite designs. The precast panels were built up as composites, utilizing layers of polyester, reinforced concrete, fiberglass and asphalt. Three different levels of steel fiber reinforcement were examined. Each module contained three sets of panels with 0%, 1.25% and 5.5% fiber reinforcement, respectively. In addition, one module was designed with a pinned panel to panel connection, and the other module employed a bolted connection. The two methods of connection were assessed with regards to fabrication, field erection, inspection, and blast load resistance. A total of six blast tests were conducted using Mk 83 1000 lb bombs. The bombs were buried in the berm at distances producing either moderate or severe blast loads. Two tests were conducted on the pinned module and four on the bolted module, with one being a double shot on the same panel. Fabrication, erection, testing, cost estimates and applications are discussed.

## DESIGN CONCEPT

The USAF has a need for a strong, versatile, economical structural shelter system that can protect equipment and personnel from near miss detonations of conventional weapons. In response to this need the Hardened Underground Transportable Composite Hyperbolic Paraboloid (HUTCH) shelter has been developed and tested (References 1 and 2). The major criteria considered in this design are:

- **HIGH STRENGTH** - controlled, factory fabrication
- **HIGH MODULARITY** - only two panel types per module - modules can be connected in a variety of configurations.
- **TRANSPORTABILITY** - lightweight, nesting panels
- **EASE OF FIELD ERECTION** - prefabricated to minimize field construction - strength not dependent on field conditions
- **LOW COST** - common construction materials

The HUTCH shelter, because it is based on geometries using hyperbolic paraboloids, is more effective at meeting these criteria than either a conventional flat walled box or a barrel vault shelter.

A single HUTCH shelter, shown in Figures 1, provides 500 usable square feet (46 sq m). It is octagonal in plan and completely assembled with just two panel types. To erect one module, eight apex (upper) panels and from four to seven base (lower) panels are required. The number of base panels used depends on the number of access points desired (from one to four.) Individual modules are designed to fit together to form larger building configurations as show in Figure 2.

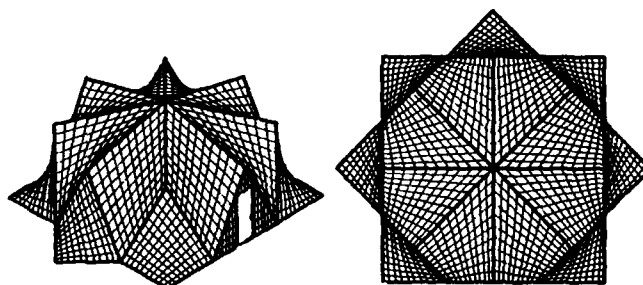


Figure 1. Isometric and plan views of a HUTCH module

Three panel material composites and two panel connection methods were tested. The three composite material systems were essentially: 1) high strength concrete with steel rebar reinforcement, 2) high strength concrete with steel rebar reinforcement plus 1.25% steel fiber reinforcement, and 3) a portland cement/fly ash slurry filled with 5.5% steel fiber and steel rebar reinforcement. The three material composite systems were evaluated on their ease of fabrication and quality control, strength under high impulse blast loadings, and cost. The two panel connection methods used were pinned connections and bolted connections. Both methods were evaluated on the same criteria as the material composites, plus a comparison was made on their ease of erection.

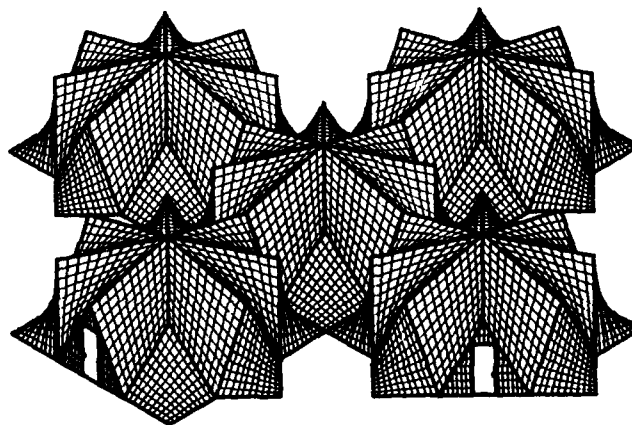


Figure 2. A "cross" configuration using five HUTCH modules

## Strength

The HUTCH shelter panels are hyperbolic paraboloids which have double opposing curvature. This means that any point on the surface is simultaneously part of a concave curve and part of a convex curve. Both tension and compression load paths are provided at every point on the panel. Having both tensile and compressive load paths makes possible the use of composite material systems that would be structurally ineffective in any flat wall, arch or dome geometry. For example, the double opposing curvature of the HUTCH panels makes possible the structural application of high strength, lightweight fabrics.

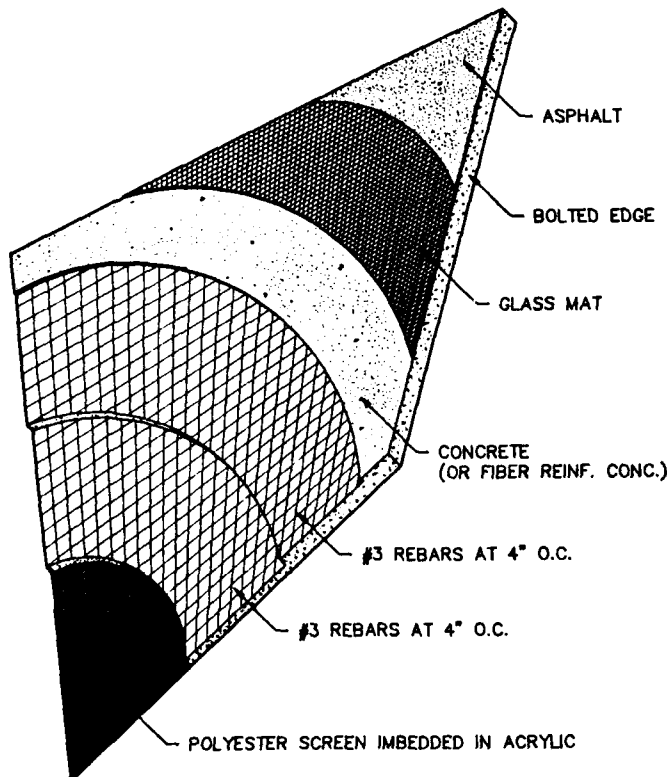


Figure 3. Cut-away view of a HUTCH panel material composite

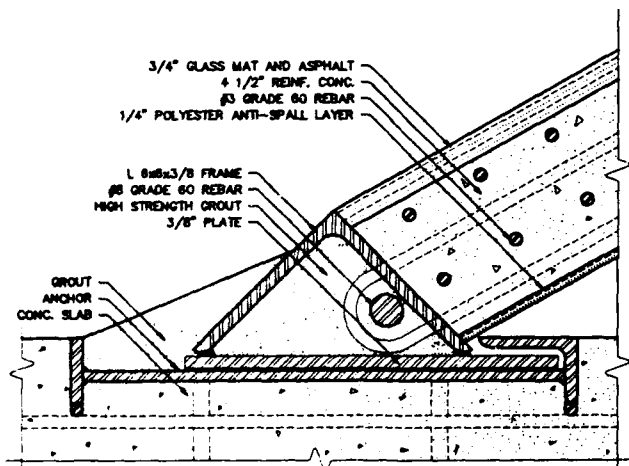


Figure 4. HUTCH slab to panel connection detail

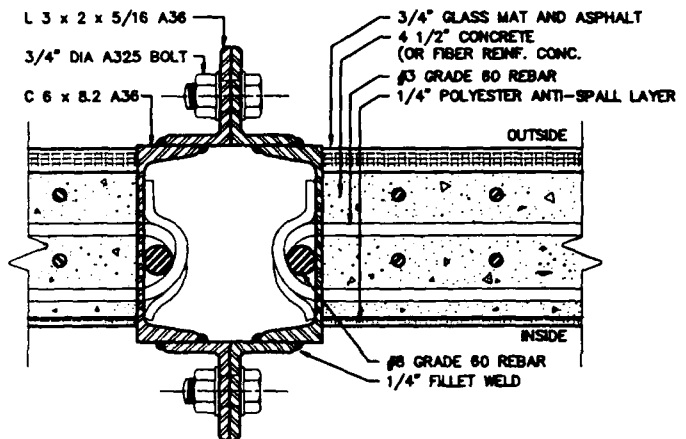


Figure 5. HUTCH bolted panel to panel connection detail

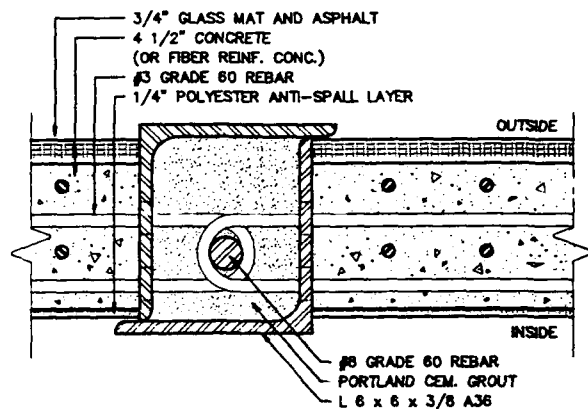


Figure 6. HUTCH pinned panel to panel connection detail

## Modularity

Each HUTCH module is made up of just two types of panels: apex panels and base panels. To erect one module requires eight apex panels and from four to seven base panels depending on the number of access points. The fact that there are only two major building parts simplifies fabrication in that only two types of forms are needed to cast the panels. The fact that any base or apex panel is interchangeable with any other base or apex panel, simplifies the logistics of procurement, storage and deployment.

Because of the regular geometry of each HUTCH module, and the patterned way in which they connect to one another, a large variety of building configurations can be achieved. Each module contains 500 sq ft (46 sq m) and can be hermetically sealed from the adjacent modules. In case of damage to one module, that module can be sealed off to maintain a chemical/biological safe condition in the rest of the surrounding modules. Building configurations can be developed to fit a variety of site conditions and functional requirements.

## Transportability

The HUTCH shelter has been designed as a system which will be prefabricated at a remote facility, and shipped to the erection site. The maximum dimensions are small enough to allow transport by either truck or rail. In addition the geometry of the individual panels allows for nested packing. This reduces the number of loads required to transport the panels. Everything required to erect the two modules tested at Tyndall AFB was shipped from Knoxville, Tennessee on the two rail cars. Figure 7 shows the way in which the panels nest, reducing shipping cubage. The base and apex panels weighing 2 and 3 tons (1.8 and 2.7 metric tons) respectively, have built in lifting points, and are easily moved and loaded with a crane.

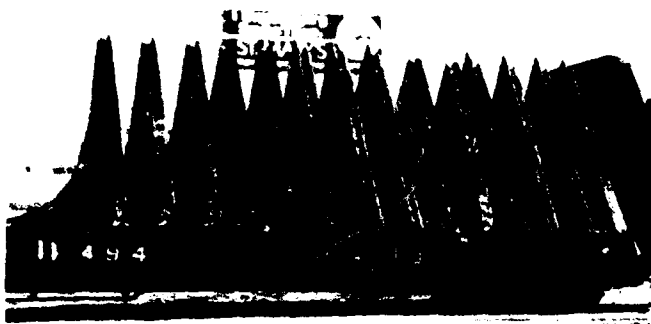


Figure 7. HUTCH panels loaded on rail car

## FABRICATION PROCESS

The panels were built on open face forms. The steel frame, which is laid on top of the form, becomes the edge of the form, and an integral part of the completed panel. The different layers of each panel are laid up individually on the wooden forms starting with the inner layer and working out. The entire process takes on the average about 80 man hours per panel to complete once the materials are prepared.

### Polyester Antispall Membrane

The first layer applied to the form is the polyester fabric which forms the interior surface of the shelter. Because of the tensile curve present in the panel, polyester fabric provides the same spall protection as heavier, more expensive steel plate. For this test prototype four layers of uncoated fabric were laid on the form and impregnated with acrylic. For production panels the same polyester fabric will be used, but with a commercially available, heat sealed, vinyl coating that offers a much more maintainable, fire resistant finish in the final product.

### Steel Reinforcement

The major reinforcement is in four layers forming a double grid of grade 60 #3, deformed steel rebars. The rebars are placed through holes pre-punched in the steel frame. The pre-punched holes in the frame set the position and spacing for the rebars. The layers are separated and held in place during casting by 5/8" (1.6 cm) spacer rebars (see Figure 8).

### Concrete

The concrete was batched at the fabrication site, placed with a small front end loader, and leveled in the form with shovels and hoes. A 1/4 hp (1000 watt) electric vibrator with a 1 1/2" (3.8 cm) diameter head was used to compact the concrete as shown in Figure 9.



Figure 8. Base panel on form with steel reinforcement in place

Three batch designs were used containing different levels of steel fiber reinforcement. The three levels were 0.0%, 1.25% and 5.5% with average 28 day compressive strengths of 8,526 psi (58.78 MPa), 7,498 psi (51.70 MPa) and 8,955 psi (61.74 MPa), respectively. The addition of the steel fiber was intended to increase the plastic range of the concrete.

The casting process is virtually the same for plain concrete and the 1.25% steel fiber reinforced concrete. The 5.5% steel fiber reinforced concrete is more labor intensive to cast because the densely matted fiber must be rodded into place one handful at a time to achieve penetration through the four rebar layers.

### Fiberglass and Asphalt Layer

The fiberglass and asphalt layer is applied after the panels are removed from the forms and placed outdoors. 24 oz/sq yd (0.81 kg/sq m) woven roving fiberglass is applied in 50 in. (1.27 m) widths and mopped with hot roofing asphalt. A total of four layers are built up. This layer provides a sealed outer skin strong enough to prevent soil from entering the protected space in the event of a local failure in the concrete.



Figure 9. Placing and compacting concrete in base panel form

## ERECTION PROCESS

With the slab set, the first step is to place all of the base panels for a module into their anchor mountings on the slab. Next, every other apex panel is put in place and attached to the adjacent base panels. Two methods of connection were used. One module was designed with pinned connections, and the other with bolted connections. A center support aids in the placing of the apex panels. Finally, the remaining apex panels are secured in place and a center cap is bolted on. In the pinned module the cavity between the panels formed by the connected edges is filled with a portland cement grout, bonding the pin to the rebar loops of both panels. The grout is not used in the bolted module. The bolted module uses 3/4" ASTM A-325 structural bolts in the panel to panel connection. This was found to make the erection much easier than the pinned method. All of the bolts were in plain sight and easy reach which made inspection much easier and more reliable.

After the erection of both modules was complete, a soil berm was placed.



## COMPUTER ANALYSIS

The responses of the HUTCH shelters to blast loads were predicted with the computer program DYNA3D (Reference 3) which is an explicit, three dimensional, finite element code for calculating the dynamic response of bodies that are comprised of solids with nonlinear, elastic/inelastic, stress/strain relations, that can undergo large deformation, and that are subjected to high time rates of loading.

The computer models for determining the blast loading response of the modules, used the quadrant of the base panel nearest the weapon. The edges of the quadrant which coincided with the panel edge were modelled as fixed; the edges of the quadrant which bisected the base panel were modelled as attached to roller planes which allowed motion perpendicular to the panel surface. A panel was modelled in five layers corresponding to the material thicknesses and properties used in the actual panels. The total thickness of a panel was 5.5 in. (13.97 cm).

The Drake/Little model (Reference 4) was used to generate the blast loadings in the computer analyses.

There was general agreement between the blast resistance predicted by the computer analyses and those observed in the tests.

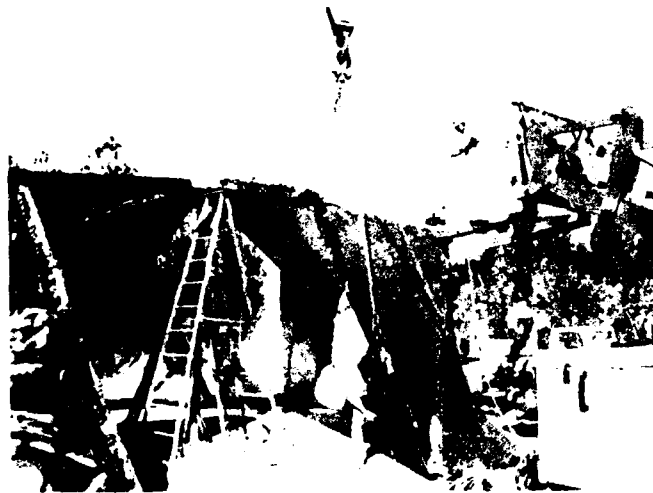


Figure 10. Erection of the pinned HUTCH module



Figure 11. Both modules in place before berming



Figure 12. Tightening the bolts of the bolted HUTCH module

The permanent displacements for tests one, three and six (moderate blast loads) differ from the computer predictions (permanent displacement equals zero) because of the rigid body motion of base hypars relative to their anchor plates. The computer models modelled these anchor connections as rigid.

The permanent displacements for tests two, four and five (severe blast loads) differ from the computer predictions (permanent displacement equals: 3.8 in. (9.7cm), test two; 3.9 in. (9.9cm), test four; and 4.0 in. (10.2cm), test five) because of the rigid body motion of base hypars relative to their anchor plates just mentioned as well as the twisting inward and local buckling of the base panel to apex panel edge connections. The computer models modelled all of these connections as rigid. In test two, the actual inward displacement was further increased by the failure of a flawed panel to panel edge connection.



Figure 13. Test 4 of bolted 1.25% fiber module - exterior berm before the shot

## TEST PROGRAM

### Instrumentation

For each of the six blast tests the following data was recorded:

- o Free Field Pressure
- o Soil-Structure Interface Pressure
- o Panel Acceleration
- o Slab Acceleration
- o Final Deformation
- o Acoustic Pressure

The data was recorded on three, 14 channel recorders.

Free field pressures were recorded at distances of 12, 16 and 20 ft (3.7, 4.9 and 6.1 m) from the center of the charge. They were buried unmounted in the soil at the same depth as the center of gravity of the charge.

The soil/structure interface pressure gages were used at regular locations on the base and apex panels. The gages were mounted in steel receptacles which had been cast into the panels during fabrication. The active diaphragm was placed flush with the outside surface of the panel with all wiring routed out the back of the mount to the inside of the module.

Three directional accelerometers were mounted at the top and middle of each frame member and single directional accelerometers were mounted at the center of each panel tested. The slab accelerations were also recorded by three directional gages.

Selected geometric measurements were made of the modules before and after each test by hand with a tape measure. These measurements include the eight interior diameters of the module, and the midpoint of the base panel being tested. These measurements were made in order to have a spot check on the displacement data generated by integrating the accelerometer data.

Acoustic pressure data was recorded with gages mounted in a 1 in. (2.5 cm) diameter acrylic disk which in turn was attached by rubber bands to a 14 in. (35.6 cm) steel inertia ring. The inertia rings were hung at a height of 5.5 ft (1.68 m) above the slab by elastic cord tied to the midpoints of the upper edges of the apex frames.



Figure 14. Test 4 of bolted 1.25% fiber module - interior before the shot



Figure 15. Test 4 of bolted 1.25% fiber module - crater

### TEST RESULTS

The six blast tests were performed using two different stand off distances. On the pinned module one moderate shot and one severe shot were made on the panels with plain concrete and 5.5% fiber concrete, respectively. The four tests made on the bolted module were two moderate shots repeated on the same plain concrete panel, and two severe shots, one each on panels with 1.25% and 5.5% fiber concrete.

The moderate shot on the plain concrete panel of the pinned module caused some ridged body shifting of the panel, but no plastic deformation. The severe shot on the 5.5% fiber concrete panel of the pinned module resulted in the failure of the pinned connection, allowing the panel to tilt inward 14°.

In the two successive tests made on the plain concrete panel of the bolted module, some shifting of the panel in the foundation anchor took place (about 2 in. (5 cm)), but again there was no plastic deformation in the panel.



Figure 16. Test 4 of bolted 1.25% fiber module - interior after the shot

The two remaining shots on the bolted module tested the 1.25% fiber concrete panel and the 5.5% fiber concrete at close range. In both cases, no breaching or spalling was observed. More movement was present in the foundation anchor connection, and some of the foundation slab surrounding the anchor plates broke up. Plastic deformation of the shells did occur and the steel edge members were bowed inward on the tested panels. The concrete layer showed cracks but remained intact. Figures 15 and 16 show views of the interior of the bolted module before and after a severe blast test on the 1.25% fiber concrete panel.

### COST ESTIMATE

Since this effort included the actual construction of two full scale modules, each with three different material composites, it was possible to collect sufficient data from actual purchases and work done to assemble accurate cost comparisons. The cost estimate shown in Table 1 is for the 1.25% fiber concrete with bolted connections. Data on labor expenditures was also collected. The figures presented indicate that the HUTCH system is more cost effective at providing blast protection by a factor of 3 over conventional, flat wall systems. The modular, prefabricated, HUTCH shelters are more labor efficient, and provide better quality control than field built systems.

### CONCLUSIONS

#### Method of Joining Panels

During fabrication, additional effort was needed to place and orient the rebar loops used for the pinned connection above that needed for the bolted connection. During erection, the proper placement of the pins through adjoining panel rebar loops proved to be more difficult than anticipated, verification of proper placement of the pins was difficult and grouting the pinned connection cavities containing the pins and rebar loops was an erection step that was unnecessary for the bolted connection. Further, the bolted connection had the significant erection advantage of being able to align and pull together adjacent panels using the connection bolts. The bolted connections experienced only minor crippling due to blast loading. On the other hand, a pinned connection, that was flawed because a pin could not be properly inserted through all the required rebar loops, failed during a severe blast test. The bolted connection is superior to the pinned connection from the standpoint of fabrication, erection and blast response.

#### Panel Composite System

The three composite systems tested (with 0%, 1.25% and 5.5% steel fiber reinforcement) exhibited excellent blast resistance. The 0% steel fiber composite was subjected to moderate blast loads, while the 1.25% and 5.5% steel fiber composites were subjected to severe blast loads. The 1.25% and 5.5% steel fiber composites showed comparable blast resistance; however, for the bolted connection panels made with these composites, the 5.5% steel fiber composite was 22.7%, 5.4% and 10.1% more expensive than the 1.25% steel fiber composite in material, unskilled labor, and skilled labor, respectively. The 0% steel fiber composite was not blast tested to as high a load as the 1.25% steel fiber composite so that there is no direct test data to show how close the 0% steel fiber composite blast resistance is to the 1.25% steel fiber composite blast resistance. However, the material cost of the 0% steel fiber composite (for the bolted connection panels) was only 6.1% less than that for the 1.25% steel fiber composite while the unskilled and skilled labor costs for both composites were the same. Of the three composites tested, the 1.25% steel fiber composite was the most cost effective.

### Slab/Anchor System

The HUTCH modules were erected on a cast in place slab/anchor system for a series of blast tests that was primarily concerned with the blast response of the composite panels and the panel to panel joining systems. For future deployments of HUTCH modules, to further reduce field work and erection time and to maximize the panel to anchor connection strength and rigidity, it is recommended that a prefabricated slab/anchor system be designed.

| BOLTED SYSTEM - 1.25% FIBER CONCRETE |                |            |               |            |
|--------------------------------------|----------------|------------|---------------|------------|
| MATERIAL COSTS                       |                |            |               |            |
| ELEMENT                              | MATERIAL       | QUANTITY   | UNIT COST     | TOTAL COST |
| EDGE                                 | steel channel  | 1,3620 #   | \$0.55/#      | \$7,491.00 |
|                                      | base plate     | 1,400 #    | \$0.40/#      | \$560.00   |
| CONNECTION                           | 3/4 in. bolts  | 528 pcs.   | \$65.55/100   | \$293.30   |
| CAP PLATE                            | steel          | 340 #      | \$0.50/#      | \$200.00   |
|                                      | 3/4 in. bolts  | 48 pcs.    | \$65.55/100   | \$26.66    |
| CONCRETE                             | cement         | 9.3 tons   | \$86.11/ton   | \$791.52   |
|                                      | sand           | 12.4 tons  | \$15.00/ton   | \$186.00   |
|                                      | 3/8 in. agg.   | 10.9 tons  | \$10.00/ton   | \$109.00   |
|                                      | admix.         | 25.75 gal. | \$2.49/gal.   | \$64.13    |
| REINFORCEMENT                        | #3 reinf.      | 8,963 #    | \$0.23/#      | \$2,068.09 |
|                                      | steel fiber    | 2,772 #    | \$0.50/#      | \$1,386.00 |
| TENSILE MEMB.                        | 24 oz. glass   | 1,320 #    | \$0.86/#      | \$1,174.80 |
|                                      | asphalt        | 3,400 #    | \$0.10/#      | \$340.00   |
| SPALL COAT                           | polyester      | 806 sq.yd. | \$2.50/sq.yd. | \$1,512.50 |
|                                      | acrylic        | 475 #      | \$0.50/#      | \$237.50   |
| ANCHOR                               | steel          | 3,114 #    | \$0.40/#      | \$1,245.60 |
|                                      | shear connect. | 217 pcs.   | \$1.20/each   | \$260.40   |
| FOUNDATION                           | concrete       | 49 cu.yd.  | \$60./cu.yd.  | \$2,940.00 |
|                                      | #3 reinf.      | 7,280 #    | \$0.23/#      | \$1,674.40 |

TOTAL FOR MODULE \$22,557.00  
COST PER SQUARE FOOT \$51.27

Table 1. Material cost estimate for the bolted HUTCH module with 1.25% steel fiber concrete

### REFERENCES

- Moriarty, T.F., von Buelow, P., Development and Testing of an Underground Protective Shelter Constructed of Hyperbolic Paraboloid Shell Elements, ESL-TR-86-37, Engineering and Services Laboratory, Air Force Engineering and Services Center, Tyndall Air Force Base, Florida 32403, September 1986.
- Moriarty, T.F., von Buelow, P., final report for Development of Prefabricated Hyperbolic Paraboloid Shell Structural System, for Engineering and Services Laboratory, Air Force Engineering and Services Center, Tyndall Air Force Base, Florida 32403, 1989. (to be submitted)
- Hallquist, John O., DYNA3D User's Manual (Nonlinear Dynamic Analysis of Solids in Three Dimensions), UCID-19592, Lawrence Livermore Laboratory, Nov 1982.
- Drake, James L., Little, Charles D., Jr., "Ground Shock from Penetrating Conventional Weapons," Symposium on the Interaction of Non-Nuclear Munitions with Structures, USAF Academy, Colorado Springs, CO, May 9-13, 1983.

# PRACTICAL EXPERIENCE IN THE DESIGN AND CONSTRUCTION OF RAPID ERECTABLE PRE-ENGINEERED HARDENED STRUCTURES

Micaela and Reuben Eytan

Eytan Building Design Ltd.  
Tel Aviv, Israel

## ABSTRACT

The paper includes the description of the authors practical experience in the design and construction of rapid erectable hardened (REH) structures in the last 21 years. The discussed pre-engineered REH structures are hardened against different types of conventional weapons and explosive devices. The requirements for which the REH structures are designed include their rapid erection on sites with difficult conditions (such as forward areas with enemy attacks during construction) as well as standardization and use of pre-engineered structural elements. The special problems encountered in the design and in the field assembly of the REH pre-engineered structures are presented and discussed and different real structures are described.

## INTRODUCTION

Rapid erectable hardened (REH) structures were developed due to two basic requirements: rapid erectability and hardening against enemy attacks.

In real attack situations it was found that construction of normal hardened structures is often made impossible by enemy fire; the level of injuries to the construction personnel was also very high.

In order to provide the best protection in the least time, REH structures were designed and built, sometimes under continuous enemy shelling and bombardment.

Two types of REH structures are described:

- light steel REH structures constructed without heavy mechanical equipment.
- heavy reinforced concrete REH structures requiring lifting equipment.

With the increase in terrorist attacks, the need for structures withstanding the effects of light weapons and different explosive devices including car bombs lead to the development of aboveground single and multi-storey REH structures.

Several types of aboveground REH structures are described with special emphasis on the conflicts between the functional and aesthetic requirements and the desire to provide the best survivability with the most cost-effective hardening solutions and the least construction time.

## REH STRUCTURES AGAINST DIRECT HITS OF ARTILLERY SHELLS AND AIR BOMBS

REH structures designed to withstand direct hits of artillery shells and air bombs were urgently required in forward areas subjected to daily enemy fire.

Special tridimensional reinforced concrete units were developed for rapid erection and with sufficient strength to support protective layers covering the REH structure assembled from the basic units.

Thousands of REH reinforced concrete units were manufactured, transported to the sites and assembled rapidly.

The site emplacement of a REH reinforced concrete unit is shown in figure 1.

To provide the hardening strength for withstanding direct hits of conventional weapons, the REH structures were covered with protective layers:

- a top burster layer, made of strong materials, designed to stop the weapon's penetration and induce it's explosion (burst).
- an absorption layer, made of soil, designed to absorb the explosion energy and reduce the shock pressures on the REH structures to allowable levels.

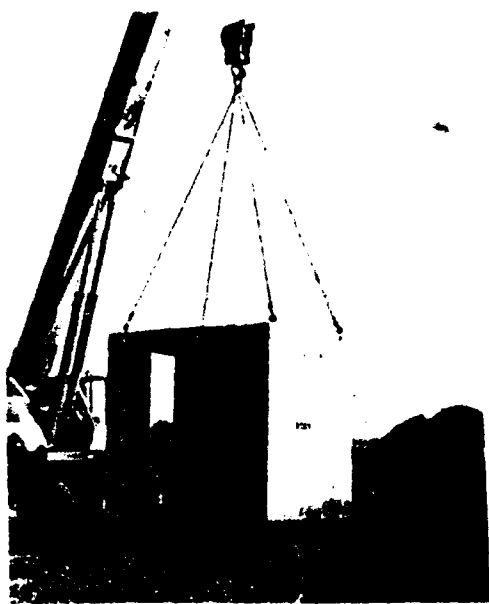


Figure 1. Emplacement of a REH reinforced concrete unit.

A real REH structure covered with a top rock burster layer over a soil absorption layer is shown in figure 2.

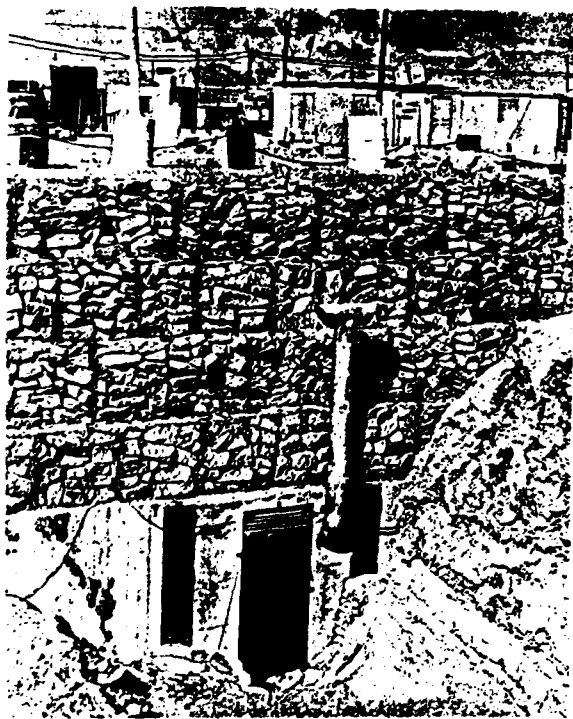


Figure 2. REH structure covered with protective layers.

The above described REH structures were subjected to numerous attacks by enemy shelling and bombardment and performed as expected, providing full protection to the people and equipment; only repairs of the

burster layers were required which were relatively easy and quickly performed.

The pre-engineered and standard typical REH reinforced concrete units (no more than 6 types were developed) were used extensively in the construction of many REH structures with different configurations and uses.

The REH structures were built as single-storey but also as two-storey and provided a great design flexibility.

In critical situations of enemy fire, partial protection was provided to the construction crew during erection and the number of injured personnel decreased considerably.

Appropriate waterproofing details for the joints between the REH basic units were developed and performed satisfactory.

No foundations were required and the REH structures were emplaced directly on a leveled soil base.

A great advantage of the REH structures was the possibility of upgrading the level of protection when required. This was practically done several times in a period of ten years and proved to be extremely easy to construct and most cost-effective.

Another major advantage of the REH reinforced concrete units was the possibility of their dismantling, transporting to a new location and reassembly in any required configuration.

REH reinforced concrete units dismantled and transported to a new site are shown in figure 3.



Figure 3. Reinforced concrete REH units.

## LIGHT STEEL REH STRUCTURES

For forward installations different light steel REH structures were developed responding to the requirement of assembly without heavy mechanical equipment.

Thousands of light REH structures using steel elements were assembled by personnel only in all types of conditions varying from scorching heat in the desert to below-freezing and snow on high mountains. The pre-engineered and standard light steel elements were improved as more practical experience was gathered and now different types of REH structures for varied uses can be rapidly assembled.

A light steel REH structure during erection on site is shown in figure 4.

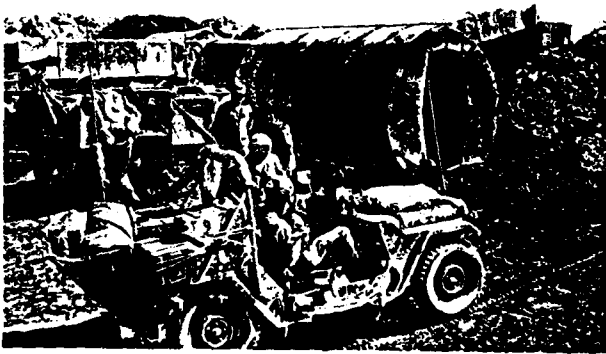


Figure 4. Light REH structure during erection.

The internal configuration of a light steel REH structure with its occupants is shown in figure 5.



Figure 5. Inside a light REH structure

The light steel REH structures were also designed to support protective layers and provided adequate protection against direct hits of artillery shells and air bombs.

## RAPID ERECTABLE PROTECTIVE LAYERS

Following the development of REH structures, the requirement for rapid erectable protective layers, especially the top burster layer, was addressed and different appropriate construction methods were developed.

For the widely used rock burster layers, the addition of steel mesh gabions, in which the rocks were placed prior to their emplacement above the REH structure, provided rapid erection capability. An example of rock filled gabions is shown in figure 2.

Burster layers using steel elements were also extensively built with very rapid erection times. A typical steel burster layer is shown in figure 6.



Figure 6. Steel burster layer over REH structure.

Pre-engineered concrete elements for burster layers were also developed and extensively used (see figure 7).

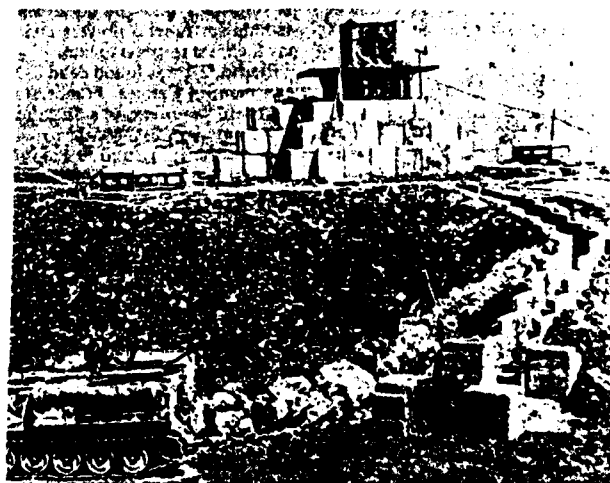


Figure 7. Concrete protective layer around a REH structure.

## SINGLE STOREY ABOVEGROUND REH STRUCTURES

For the lower protection criteria of light weapons and nearby explosions aboveground REH structures were developed.

A conceptual layout of a single storey aboveground REH structure is shown in figure 8.

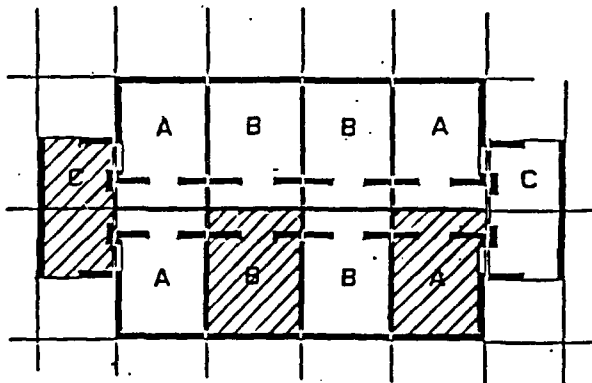


Figure 8. Conceptual layout and section of a single-storey aboveground REH structure.

A basic unit for single storey aboveground REH structures including reinforced concrete walls, floor and roof with internal antispalling steel plates is shown in figure 9.

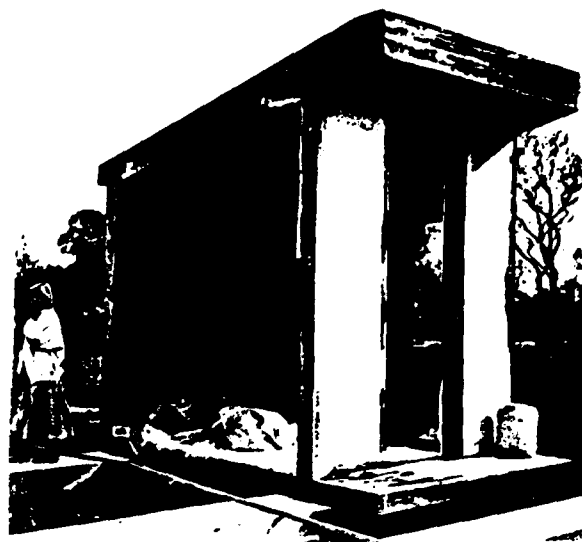


Figure 9. Basic unit for single-storey REH structure

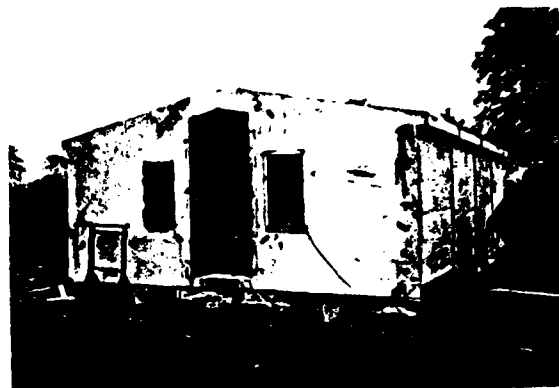


Figure 10. Single-storey REH structure during assembly.

A single storey REH structure during assembly in the manufacturing plant is shown in figure 10.

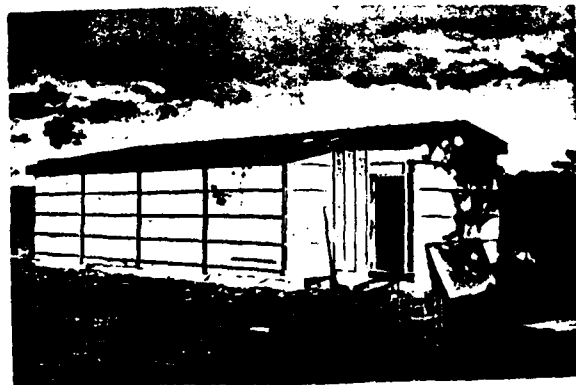


Figure 11. Assembled REH structure

The fully assembled REH structure including steel connectors between the basic units is shown in figure 11.

The REH basic units during their transport to the site are shown in figure 12.

## MULTI-STOREY ABOVEGROUND REH STRUCTURES

The need of providing hardening against terrorist attacks for multi-storey aboveground structures increased lately and REH multi-storey structures composed of tridimensional basic units were developed.

A conceptual description of a REH multi-storey structure is presented in figure 14.



Figure 12. Transporting the REH units from the assembly plant to the site.

The finished reassembled REH structure on site is shown in figure 13.

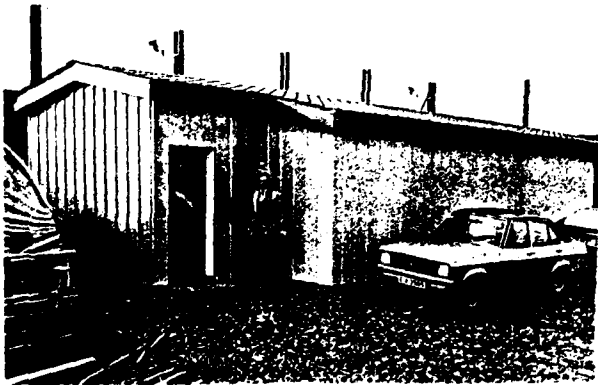


Figure 13. Finished REH structure on site.

The use of tridimensional pre-engineered reinforced concrete units for single-storey REH structures proved to be extremely expedient and most cost-effective.

Single storey REH structures were erected "over night" in sensitive forward areas and provided adequate protection practically in no-time.

Many REH structures were easily dismantled, transported to new sites and reassembled.

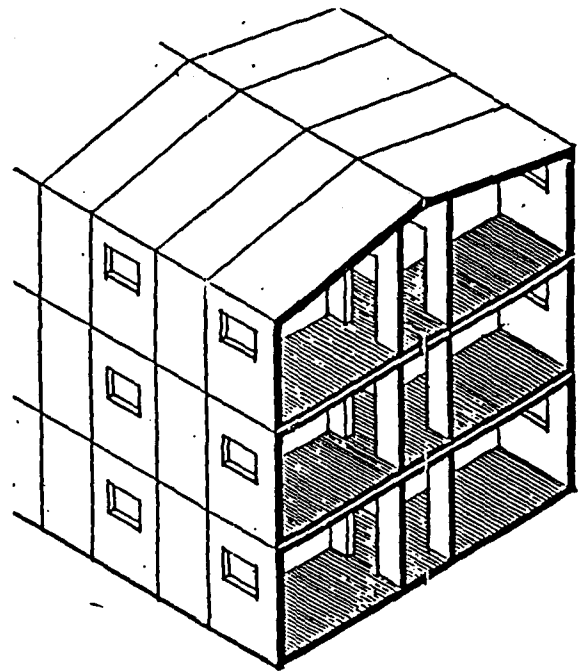


Figure 14. Conceptual view of multi-storey REH structure.

The assembly of multi-storey REH reinforced concrete basic units is shown in figure 15.



Figure 15. Multi-storey REH structure during assembly.

The site erection of a multi-storey REH structure is described in figure 16.



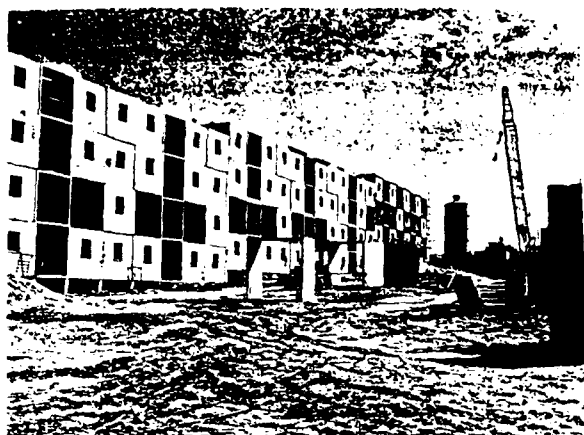


Figure 16. Multi-storey REH structure being erected on site.

A finished multi-storey REH structure is shown in figure 17.



Figure 17. Finished multi-storey REH structure

#### DESIGN FLEXIBILITY WITH REH UNITS

The use of pre-engineered REH units allows the flexibility of designing many types of structures for varied uses.

Underground fully hardened structures covered with protective layers as well as aboveground semihardened "normal looking" structures were designed and built in many configurations including multi-storey buildings.

Military as well as civilian installations were designed using REH structures.

An example of an observation post/guard house REH structure is shown in figure 18.



Figure 18. REH observation structure

#### SUMMARY

Pre-engineered rapid erectable hardened (REH) structures were developed and built during the last 21 years for many uses and protective requirements.

The major advantages of REH structures were found to be the design flexibility, the rapid erection, the possibility of easy repairs and units replacements and the relocation and re-use capabilities.

The constraints imposed by the use of REH units were mainly encountered during their transport and erection.

However, the use of REH structures enabled the construction of functional and aesthetic facilities which also resist the defined weapons and explosive devices effects.

In many practical applications the REH structures proved to be the most cost-effective solution compared to normally hardened structures.

# TESTS PERFORMED ON THE ASP CONSTRUCTION SYSTEM

Yaakov Yerushalmi

The ASP Group, Washington, D.C.

*ASP is a new type of construction system developed for use in protective structures. The system was invented by the author and is manufactured under license in the United States. To date, the ASP system has been tested in about 20 different weapon tests in four different countries. These tests show significant price and performance advantages of the ASP system as compared with reinforced concrete alternatives in a wide range of accident and malevolent threat scenarios. This paper describes the system, its applications, and recent tests.*

## TESTS PERFORMED ON THE ASP CONSTRUCTION SYSTEM

### 1. INTRODUCTION

ASP is a new type of construction system developed for use in protective structures. The system was invented by the author and is manufactured under license in the United States and other countries. To date, the ASP system has been tested in about 20 different weapon and accidental explosion tests. The ASP is a new type of construction system that can be used for protective walls as well as multistory buildings. The ASP system offers advantages over reinforced concrete, especially in high-threat environments. ASP construction techniques typically provide for cost savings over reinforced concrete construction.

The wall element is a composite structure of exterior steel panels and diagonal interior steel lacing panels with a concrete fill. The ASP wall is erected on conventional concrete foundations. Roof slabs are constructed using a bottom ASP exterior panel in a manner similar to floor decking. Reinforcement bars are used to tie the walls to the foundations or to any roof or intermediate slabs. ASP beams and columns are used when required. Almost any exterior or interior finish can be applied on ASP walls and buildings. Standard ASP walls

are 8-, 10-, and 12-inches thick. If a single ASP does not provide the required protection, a layered or "sandwich" design is utilized. A representative ASP sandwich wall consists of two separate 8-inch thick ASP walls, separated by 16 inches. The 16-inch void is filled with crushed stones or sand. The ASP construction system is illustrated in Figure 1.

### 2. ADVANTAGES OF THE ASP SYSTEM

The main advantages of the ASP system are the following:

- o ASP provides significant potential cost savings compared with reinforced concrete for all levels of protection.
- o ASP sections are approximately half as thick as reinforced concrete alternatives providing the same level of protection. The weight saving is significant for movable walls and shelters.
- o ASP structures have a higher safety factor compared with reinforced concrete offering the same level of protection.
- o ASP construction provides reinforcement, formwork, anti-spalling protection, and RF shielding in one integral system.
- o ASP construction offers speed and ease of construction using unskilled labor. There is typically no need for scaffolding or extensive support during construction.

### 3. APPLICATIONS

The ASP system is in use for the following applications:

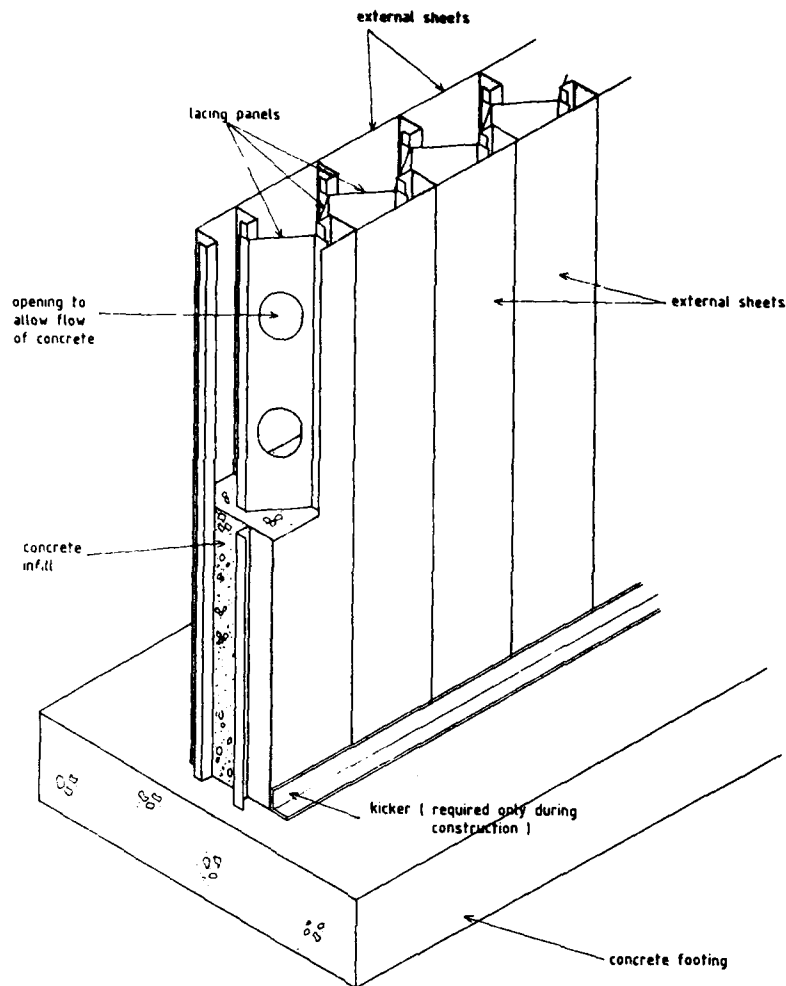


Fig. 1

Isometric View of the Basic Component of the  
ASP Walling System

- o Structures and walls to prevent and contain the effects of accidental explosion of ammunition magazines, and dividing wall structures for the explosive and chemical industry.
- o Military structures to withstand near miss and localized effects of air bombs, as well as ground and buried installations, such as ground stations, and fixed and movable shelters.
- o Protective structures and walls that are effective against such terrorist and demolition attacks as car bombs, direct hits of hollow charges, heavy-placed charges, and forced entry. Typical projects are computer centers, embassy and foreign mission buildings, perimeter protection for power stations, oil

and gas chemical tanks, and transmission stations.

- o Structures with requirements for RF or EMP shielding.

#### 4. TESTS

The ASP system has been tested in four different countries. Tests include the following:

- o Near miss and localized effects of general-purpose air bombs such as 500-lb MK-82, 1,000-lb MK-83, and 2,000-lb MK-84 (four different tests)
- o Penetration of armor piercing projectiles (two tests)

- o Penetration of hollow charge rockets (three tests)
- o Placed charges (four different tests)
- o High reflected pressure with relatively long duration to simulate ammunition magazine explosions (one test)
- o Movable panels designed to prevent chain detonation of ammunition trucks (one test)

A brief description of four of the tests is given below.

#### **4.1 Near Miss of Air Bombs**

Israeli Defense Force (IDF) tests assessed ASP system resistance against fragments generated by near miss of air bombs (Nebi Musa 1981). An above ground ASP structure with 10-inch thick ASP walls was subjected to static detonation of 500-lb and 500-kg general-purpose air bombs. Similar tests were conducted by other countries using 1,000 and 2,000 lb general-purpose bombs.

At a distance of about 30 feet, the ASP sections resisted blast and fragmentation of air bombs well. Comparing the measured penetration into ASP sections against calculated penetration in massive concrete suggests that the penetration in ASP sections is about one-third to one-half of the penetration of reinforced concrete structures.

High resistance to penetration is achieved for the following reasons: anchored anti-spalling "back plate" with continuous deep rib connections to the diagonal panels; confinement of concrete between the external and diagonal panels, providing high resistance compared with standard reinforced concrete; front spall plate (decreasing "front cratering" and crack propagation); resistance to penetration via composite sections of concrete and steel plates as compared with penetration through homogeneous reinforced concrete; elimination of "edge effects" in ASP sections; and protection against repeated hits by localizing damage.

#### **4.2 Penetration of Shaped Charge Warheads**

The Naval Surface Weapons Center (DeJarnette 1986) conducted tests for the Defense Nuclear Agency to assess the resistance of the ASP sandwich construction against repeated direct hits of RPG-7 rockets. Five rockets were detonated with optimal static stand off distance on a circumscribed

target area (1.65 SF). The sample tested was a sandwich section consisting of 20 cm ASP wall, a 40 cm gap filled with granite stones, and a rear 20 cm ASP wall.

The 80-cm thick ASP sandwich section resisted penetration from repeated RPG hits in a localized area. Average penetration was about 40 cm (16 inches). The impact crater of the rockets in the ASP section was confined, providing protection from repeated hits. A comparison of penetration in ASP sandwich sections with penetration in massive concrete suggests that the penetration in the ASP sandwich is about 50 percent of the penetration of the same rocket in massive concrete.

#### **4.3 Dynamic Response of ASP Magazine Gable Wall**

French Defense Forces (Groupe Nucleaire Protection 1987) conducted tests to assess the dynamic response of ASP walls when used as gable walls for ammunition magazines. The test applied high-reflected pressures with relatively long duration on ASP gable walls, simulating accidental ammunition magazine explosion.

An ASP wall panel 11.5 feet long (10 feet between the center of the supports) and 10 feet wide was constructed on a heavy steel frame. The steel frame was bolted to an existing heavy concrete structure. The ASP wall was bolted to the top and the bottom of a steel frame, precluding movement of the ASP wall. Blast loads were generated by detonation of 1,750 lbs of TNT at various distances. Four detonations were used starting with a peak reflected pressure of 7 psi, and reaching peak reflected pressures of about 200 psi with positive duration of about 15 msec. Free field and reflected blast parameters were measured, as were strains, accelerations, and displacements.

Sensor data have not yet been analyzed in detail. However, the main conclusion from the test is that standard calculations for reinforced concrete sections are conservative compared with ASP results. Strains and displacements of ASP are much smaller than calculated values (particularly in the plastic range), and ASP resists loads through internal plastic deformation.

#### **4.4 Movable Panels To Prevent Chain Detonation**

The Ballistics Research Laboratory (BRL) (Collis 1988) tested movable ASP panels for prevention of chain detonations. Large quantities of ammunition

for US military units are stored on flat-bed trailers in compounds near inhabited buildings. Most of the ammunition consists of mass-detonating munitions. If one trailer load detonates, currently no fully satisfactory method exists to prevent detonation of munitions in other trailers. Initial BRL tests suggest that the ASP system may have significant advantages over other methods.

The ASP test was part of a series of tests in the "quickload" program. (Previous tests in 1987 by the French Corps of Engineers indicate that an ASP wall subjected to localized effects of artillery rounds will not be penetrated by the primary fragments--although the wall itself may be destroyed.) The purpose of the BRL test was to determine whether ASP movable panels can prevent chain detonation of ammunition trucks. Movable ASP panels 12 inches thick and 8 feet high were placed between two trucks loaded with ammunition. The distance between the center line of the trucks was 20 feet. The donor trailer contained 160 M107 projectiles (155 mm) and 160 M3A1 propellant charge cans. The acceptor trailer contained 96 projectiles and 96 M3A1 propellant charges.

Accidental detonation was simulated by simultaneous detonation of four rounds on the Donor truck. A crater 58 inches deep and about 24 feet in diameter was created by the explosion. Although the ASP wall was destroyed, the test was successful because the ASP wall prevented the chain detonation. This result is significant for operational requirements demanding moveable barriers. Additional tests are being conducted.

## 5. SUMMARY

Several additional tests and applications of the ASP system are planned or in process both in the United States and other countries. These tests and

applications include the use of ASP construction for relocatable shelters in which the weight advantage of ASP over reinforced concrete is significant. Other ASP applications include use of the ASP system in environments where RF, EMI, or EMP shielding is required. Many of these applications are sensitive, but it is clear that the ASP system offers significant advantages in environments requiring shielding and hardening. Unclassified reports are available for certain tests and applications, describing tests more fully and discussing the price-performance advantages of the ASP system over reinforced concrete alternatives (Yerushalmi 1988a and 1988b).

## REFERENCES

- "Protective Structures Tests." Nebi Musa, IDF, Corps of Engineers. April 1981.
- "Testing of the ASP Sandwich Barrier with Shaped-Charge (RPG-7) Warheads." H. M. DeJarnette, Naval Surface Weapons Center. February 1986.
- "Comportement Au Souffle Et Aux Eclats De Murs Forts." Groupe Nucleaire Protection. November 1987.
- "ASP Walling System Concrete Barrier Test Results: Ammunition Quickload Test Series." D. Collis, New Mexico Institute of Mining and Technology, TERA Group, Socorro. June 1988.
- "ASP System for Protective Structures." (TR89-02) Y. Yerushalmi, ASP Group. October 1988.
- "ASP Protective Construction System: Price and Performance Comparison with Reinforced Concrete." (TR89-01) Y. Yerushalmi, ASP Group. October 1988.

## Earthquake Damage Repair Technology Applied to Blast Damaged Structures

Phillip T. Nash

Southwest Research Institute  
San Antonio, Texas

James O. Jirsa

Amador Teran

University of Texas  
Austin, Texas

### ABSTRACT

Damaged airbase facilities critical to restoring aircraft operations must be repaired quickly after an attack to provide the needed support. Repair technologies have been developed in earthquake damage research which have potential application to bomb damage repair. This paper describes repair techniques developed for earthquake damage and their potential application to bomb damage repair. Although the damage mechanisms from earthquake loads are quite different from damage mechanisms of blast loads, the damage resulting to structural elements can be quite similar. Typical damages and failure mechanisms are categorized and compared for earthquake and conventional weapon loadings. Typical structures are selected based upon design guidelines. Damages expected to the typical structures from conventional weapon attack are described. Functional damages are defined and methods for accomplishing facility repairs are then recommended depending upon the facility function and degree of damage. Materials, equipment, and procedures developed for repairing earthquake damage are described along with their potential use in repairing bomb damages.

### BACKGROUND

To reduce or nullify the effects of an enemy attack on an installation, the Air Force uses protective construction measures to protect critical assets. These passive measures include dispersion and duplication of structures and activities, strengthening (hardening) of structures, camouflage or "tonedown" painting, and physical protection against chemical, biological and radiological agents. Protective construction includes buildings or facilities that minimize effects of enemy weapons on the operation of weapon systems, and permit weapon systems to return to operation quickly after damage from attack.

The purpose of the research reported in this paper was to support improvement of Air Force capabilities to recover aircraft operations quickly after an enemy attack through expedient repair of damaged facilities. The goals of the research were: 1) Identify and define typical damage to critical structures or structural elements; 2) Identify failure mechanisms for each

type of damage caused by impact and blast loads; and 3) Provide preliminary recommendations of repair procedures for impact and blast load damage using the considerable data which has been accumulated in structural engineering studies for repair of buildings damaged in earthquakes. The general approach was to identify and define technical issues pertinent to the expedient repair of bomb-damaged facilities. Specific steps included: 1) Identify predominant structure types and structural elements; 2) Identify and define typical damage; 3) Define failure mechanisms resulting from damage types expected; 4) Compare failure mechanisms resulting from bomb damage with the failure mechanisms expected from earthquake type loadings; 5) Identify materials, equipment, and procedures developed for repair of earthquake damage which apply to repair of bomb-damaged facilities; and 6) Provide recommendations for expedient repair of bomb-damaged facilities.

### PREDOMINANT STRUCTURAL TYPES

A summary of facilities identified on an Air Force list is given in Table 1. The construction types given in Reference 1 were used to categorize frame, wall and roof systems. The descriptions given on the list were very general and therefore the construction categories selected were quite arbitrary. The predominant structural system found from the list of facilities was a reinforced concrete frame with masonry walls. There was insufficient information to determine the predominant type of roof construction; however, the roof systems listed were of common construction and not designed to offer protection against blast loads. It is interesting that of the seventy structures considered, only three were constructed of reinforced concrete walls--a structural element common in most protective structures.

The structures identified were not designed as protective structures. At the outset of the project, it was anticipated that considerable attention would need to be given to protective structures. However, the majority of repair techniques developed in earthquake research will have excellent potential for repairing airbase structures such as those listed.

TABLE 1. CONSTRUCTION CATEGORIES

| Air Base | Frame     |           |     |     |     | Wall |     |     |     | Roof |     |    |     |
|----------|-----------|-----------|-----|-----|-----|------|-----|-----|-----|------|-----|----|-----|
|          | LB<br>R/C | LB<br>MAS | STL | CON | OTH | R/C  | MAS | MTL | CRT | CON  | MTL | WD | OTH |
| 1        | -         | -         | -   | 10  | -   | 7    | 2   | -   | -   | -    | 3   | 4  | -   |
| 2        | -         | -         | -   | 10  | -   | -    | -   | -   | 7   | -    | -   | -  | -   |
| 3        | 1         | 5         | 4   | -   | -   | 1    | 5   | 1   | 3   | -    | 1   | -  | -   |
| 4        | 1         | 4         | -   | 1   | 4   | 1    | 4   | -   | -   | -    | -   | -  | -   |
| 5        | -         | 6         | 2   | 2   | -   | -    | 6   | 2   | -   | -    | -   | -  | -   |
| 6        | -         | -         | 4   | 6   | -   | -    | 6   | 4   | -   | -    | -   | -  | -   |
| 7        | 1         | 1         | 6   | 2   | -   | 1    | 3   | 4   | -   | -    | 2   | 2  | -   |
| TOTAL    | 3         | 16        | 16  | 31  | 4   | 10   | 26  | 11  | 10  | -    | 6   | 6  | -   |

LB - Load Bearing  
R/C - Reinforced Concrete  
MAS - Masonry  
STL - Steel  
CON - Concrete, reinforcement unknown

OTH - Other  
MTL - Metal  
CRT - Curtain  
WD - Wood

Criteria and standards found in Reference 1 are to be applied, "to the extent practicable at Air Force installation in foreign countries." Concrete design for Air Force structures [2] is based on methods developed by the American Concrete Institute Committee 318 "Building Code Requirements" [3]. Air Force requirements call for framing to be rigid or to include load-bearing and/or shear walls. Therefore, design details for the structural types and elements should follow conventional concrete frame designs. The reinforced concrete frame is expected to be a rigid frame made of concrete columns and girders having a rectangular cross section.

Typical architectural detail drawings for composite masonry walls were taken from Reference 4. A typical masonry wall would be a composite wall with a clay or shale brick exterior face and a concrete masonry unit interior face. Because the structural loads are supported by the reinforced concrete frame, the masonry wall is taken as an in-fill wall and is not expected to be reinforced for vertical or flexural loads. However, reinforcement is expected to be present for joining the two wythes and providing crack control. The typical or predominant structural system is considered to include a composite masonry wall similar to that shown in Figure 1.

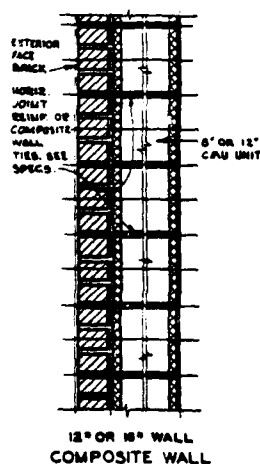


Figure 1. Modular Masonry Coursing, Composite and Cavity Walls (Ref 4b)

## EXPECTED BOMB DAMAGE

Typical damage which may be encountered can be described in two broad categories: 1) local damage; and 2) global damage. Local damage will occur to elements within the structural system and will probably be the result of projectile impact or close proximity detonations of high explosive charges too small to destroy the entire structure. Global damage can occur from high explosive charges large enough to create extensive damage and loading from the blast. The extent of damage will decrease with distance of the charge from the structure. Global damage can also occur when loss of elements from local damage causes progressive collapse of the structure or part of the structure due to inadequate support. One aim of the program was to identify and define typical damage which can be expected for predominant structural types.

A search of the open literature yielded few references on conventional weapon damage to structures similar to the selected critical structure. Incident summary reports from World War II were found which described actual bomb damage to reinforced concrete frame and masonry wall structures. Some information was found on blast and other dynamic lateral loads on masonry walls. There are probably two main reasons for the paucity of applicable information: 1) weapon effects data is not usually found in the open literature; and 2) most of the current research is performed in relation to protective, or hardened structures. It is important to note again that many facilities may not be designed as protective structures.

The damage to a multi-story, reinforced concrete frame apartment building struck by a 500-kg bomb is shown in Figure 2 [5]. Although the bomb detonated inside the structure, damage to the walls and columns illustrate the kinds of damage which can be expected from bombs detonating near a reinforced concrete frame structure with masonry walls. The 500-kg general purpose bomb was determined to contain approximately 550 lbs. of explosive and detonated less than ten feet inside the exterior wall of the building between the seventh and eighth floors. Several reinforced concrete columns completely disintegrated. Other columns were broken up, bowed, or badly damaged. Walls were blown out for several floors and bays in each direction. The authors commented that some of the excessive column damage was probably due to bonding of partitions to columns. Peak overpressures on the structural elements from 550 lbs. of explosives ten feet away can be expected in the order of thousands of psi. Masonry walls cannot survive such extreme loads and thus complete destruction of the walls is typical. The two columns in the right foreground of Figure 2 are obviously no longer carrying load and would require major repairs to restore their original strength. The column shown in the left foreground of Figure 2 is badly deformed, but could regain some of its original load carrying capabilities with expedient repair techniques. Other columns

in the background of Figure 2 appear to be undamaged.

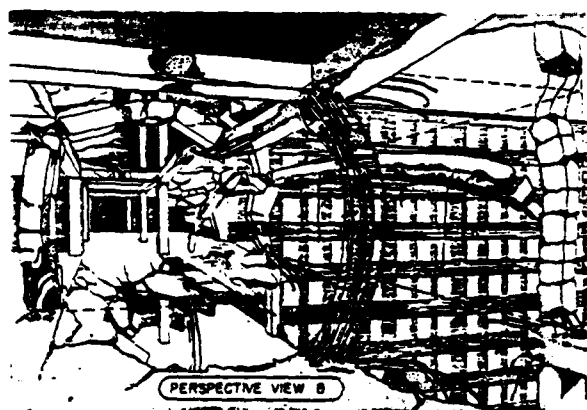


Figure 2. Bomb Damage to a Reinforced Concrete Frame

The blast resistance of a variety of masonry wall panels was studied experimentally and is reported in Reference 6. Although the blast loads were designed to simulate nuclear weapon loadings at large distances, the response modes of the masonry wall panels were of the same type as can be expected from conventional weapon overpressures for large distances or large incidence angles. A variety of wall configurations and mounting techniques were tested. Typical response mode is illustrated in Figure 3. Actual response and failure loads are affected by the rigidity of the supports and the presence of openings such as windows or doors.

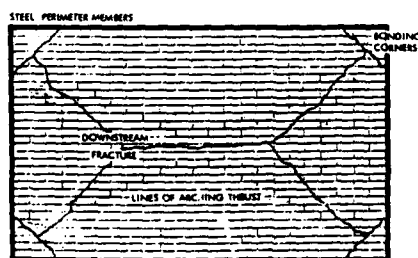


Figure 3. Effect of Steel Perimeter Frame on Crack Pattern

#### COMPARISON OF CONVENTIONAL WEAPON AND EARTHQUAKE DAMAGE

Failure mechanisms under earthquake loads are quite different from those due to blast loads. However, the visible damage to structural elements can be similar. Earthquake damage is due to low frequency ground motions. The ground motions can be from any direction with respect to the structure and structural elements fail when their inertial loadings exceed material strengths. For structural columns, inertial

masses of the structure can be considered to be lumped at the ends of the columns which means the primary mode of response will be relative movement of the individual floors resulting in a general sideways deformation of the structure. Damage to concrete frames often is seen as diagonal shear cracks along the height of the columns. Excessive differential displacements between the top and bottom of the columns can lead to eccentric axial loadings that produce frame stability problems. The cyclic nature of earthquake loadings can cause several cycles of structural response leading to rapid deterioration of the damaged elements.

Masonry walls have little tolerance to lateral cyclic loads of large deformation and may collapse in early cycles of loading. In-plane loadings of masonry walls result in diagonal shear cracks across the face of the wall. Roofs are designed for out-of-place loadings and are not as subject to earthquake damage as vertical walls which are usually designed primarily for axial loading or act as non-structural elements. Damage to the roof generally will depend upon the amount of damage to supporting members under large lateral deformations.

Blast damage occurs due to the excessive overpressure from the explosion or the forces from the fragments impacting the structure. Areas of the structure subjected to the distributed overpressure or fragment loadings will transmit the loads to supporting elements of the structure. Once the loaded element fails, the dynamic forces cannot be transmitted fully to supporting elements. Damage will be restricted to the failed element. If the element continues to transmit forces to other parts of the structure, the degree of damage will depend on the strengths of other structural elements and the direction and distance from the blast. Columns or beams may be damaged along their entire length or may suffer localized damage from high intensity loads over a small area. Fragments or missiles impacting the reinforced concrete frame members can cause spalling of the concrete and loss of material.

Damage to masonry walls during blast loading is primarily from overpressures normal to the wall, but lateral distortions of the frame in the plane of the walls can cause diagonal shear cracking similar to earthquake damage. Masonry walls damaged from lateral blast loads can remain in place with crack patterns determined by the nature of the loads and boundary conditions.

Structural damage from conventional weapon loading can be categorized according to structural element type, extent of damage, and degree of damage to determine the possible functional failures of the structural system and to identify proper repair measures. Possible functional failures for various combinations of structural elements (for the selected critical structure) and degree of damage are shown in Table 2. Degrees of damage have been given for Local and Global considerations. The following definitions are suggested:



**TABLE 2. PROPOSED DAMAGE CATEGORIES**

| Structural Element                   | Local <sup>a</sup> |              |       | Global <sup>b</sup> |              |       |
|--------------------------------------|--------------------|--------------|-------|---------------------|--------------|-------|
|                                      | Minor              | Intermediate | Major | Minor               | Intermediate | Major |
| <b>Frame (Reinforced Concrete)</b>   |                    |              |       |                     |              |       |
| Columns                              | 0                  | 2            | 3     | 0                   | 3            | 3     |
| Beams, Slabs, Braces                 | 1                  | 2            | 3     | 1                   | 2            | 3     |
| Joints                               | 0                  | 1            | 2     | 0                   | 2            | 3     |
| Walls                                | 0                  | 1            | 2     | 0                   | 1            | 2     |
| <b>Wall (Nonloadbearing Masonry)</b> |                    |              |       |                     |              |       |
| One-Way Support                      | 1                  | 2            | 3     | 1                   | 2            | 3     |
| Two-Way Support                      | 0                  | 2            | 3     | 0                   | 2            | 3     |
| Roof (Concrete and)                  | 0                  | 1            | 2     | 0                   | 2            | 3     |

<sup>a</sup> 0 No loss of structural function  
 1 Reduced level of safety for occupants (falling debris), no loss of structural function  
 2 Loss of strength but temporary possible with temporary repairs or shoring  
 3 Loss of stability of structure or portion thereof, structure not usable without major repair

- **Local Damage** - loss of a structural element or part of an element which probably results from concentrated loading on the element and missile impact or close proximity explosions. Examples of local damage include holes in the masonry wall or loss of concrete over a small portion of a reinforced concrete member.
- **Global Damage** - Structural damage over a large area which may involve several structural members. Loading over a large area of the structure is evident. Progressive collapse due to loss of one or more supporting members may also occur.

Degrees of damage are defined as:

- **Minor** - Slight cracking with no observable permanent deformations of the structural element. Not considered to be a problem for reinforced concrete members, but can lead to undesirable weaknesses in masonry walls.
- **Intermediate** - Significant cracking with observable permanent deformations of the structural element. The load carrying capacity and stiffness of the structural element may be reduced and any subsequent overloading may cause widespread damage or collapse.
- **Major** - Extensive cracking or loss of material with gross permanent local or overall deformations. The strength and stiffness of the element or structure are reduced to dangerously low levels and failure under dead loads is possible due to general instability of the system.

#### REPAIR TECHNIQUES

Three main aspects should be considered in any repair project: quality, cost, and time. These variables are closely inter-related, the faster the operational level of a structure is restored, higher costs and lower quality can be expected. As can be seen, time is a parameter

that strongly influences the selection of any repair process.

Repair is defined as the procedure(s) carried out to restore the load carrying capacity and stability of a structure element. Normally the restoration of the original level of resistance of any element can be achieved; however, the same is not true for the element stiffness. Very fine cracks in the concrete or masonry are impossible to repair completely. If the element is repaired to recover its stiffness, it generally will be strengthened as well. In emergency situations, the repair of non-structural elements such as partitions and ceilings consists of restoring their function as fast as possible by any means.

In the study materials and construction techniques were investigated as they apply to all types of repair procedures. The description of repair procedures is divided into three categories: (1) Basic techniques which involve temporary measures to stabilize the damaged structure, but in many cases may become permanent repair solutions; (2) Intermediate techniques which involve restoration of the damaged elements; and (3) Advanced techniques which require considerable time and effort, and may involve development of added parallel load carrying elements or systems. It is expected that any of the three levels of repair could be used to return a damaged structure to service. The level of damage (Table 2) and the time and personnel available to return the structure to service will dictate the sophistication of the repair technique selected.

In the repair and/or strengthening of any structural element, a monolithic behavior between the old and new material must be accomplished for satisfactory behavior of the elements and the structure. In general, any repair material should meet the following guidelines: 1) Be durable and protect reinforcement; 2) Be dimensionally stable (low shrinkage) to avoid loss of contact between the old and new materials; 3) Achieve adequate bond between materials, including bond between steel and concrete; and 4) Be able to develop resistance at early ages, whenever the need to restore the damaged element capacity as soon as possible exists.

To achieve satisfactory behavior of the repaired element, the compressive strength of the new material should be higher than that of the original material. The use of materials of diverse strength must be carefully studied to avoid bond failure and crushing of the contact surface. It is advisable that the repair material properties match relatively well the existing materials uniform structural properties of the repaired element. The elastic moduli and time or temperature effects on the materials must be compatible to avoid problems under high stresses, sustained loads, or temperature changes [7, 8, 9].

In the case of repair by the addition of new elements, a proper connection must be provided to adequately transfer forces between new and existing elements without further damage to the structure. The new elements must be anchored and/or attached to provide for development of design capacity.

### Materials

Resins are used to repair cracks and to anchor or attach new (steel or concrete) elements to concrete and masonry members. Low viscosity resins are used for small width crack injection while higher viscosity resins can be used to fill larger cracks or voids [10]. In general, the properties, application, preparation, and curing are specified by the manufacture [7, 9, 10].

When new concrete is used to replace damaged parts, to increase the capacity of an element, or to cast new elements, special care must be taken to obtain monolithic behavior. Cast-in-place concrete has been extensively used in repair projects. In many cases, poor behavior has been observed due to volume changes and shrinkage of concrete which destroy contact between the old and new materials and prevent proper transfer of stress across the contact surface [9, 11].

Preparation techniques for the concrete surfaces are important to assure adequate contact between new and existing materials. Prior to the placement of new concrete, damaged and deteriorated concrete must be removed, by mechanical means. The old concrete surface should be roughened, cleaned and, in some cases, prepared with epoxy or mortar to improve bond of the new concrete with the existing surface [7, 9, 11]. Concrete properties can be enhanced by the addition of glass, plastic or steel fibers to the mix.

Shotcrete often is used to repair and strengthen concrete or masonry walls and to jacket (encase) different types of concrete elements. Special equipment, as well as trained personnel (nozzlemen), are required in the shotcrete process. The repair job will only be as good as the technician's workmanship and his knowledge of the material properties.

To provide a monolithic behavior in a repaired structure, complex techniques may be needed when high shear forces must be transferred from one element to the other. Such techniques include shear dowels and concrete interlock. Shear keys are formed by removing concrete in the existing surface or by bonding precast concrete shear keys with epoxy adhesives to the surface of the existing element. The shear force between new and old material is transferred through the shear keys and the dowel action of the anchored bars.

### Temporary Measures

Temporary support is needed when structures and facilities suffer serious damage. Unloading

of critical damage elements is required until the capacity to resist its own weight (gravity load) and other possible loads is restored properly. Temporary support may involve emergency measures that need two main requirements (1) to transfer vertical loads from damaged elements to "provisional" auxiliary elements, and (2) to protect the structures as a whole against lateral instability. In many cases "temporary" protection may serve longer term needs or be incorporated into a more permanent repair scheme.

Vertical load capacity must be restored as quickly as possible by installing auxiliary vertical load bearing elements around damage columns and bearing walls. In some cases it is possible to limit the inclusion of new elements to the damaged story as can be seen from Figure 4. The shear capacity of sections t-t, which includes slab and beams, must be sufficient to carry the floor load plus the shore load [9]. It is difficult to determine the shear capacity (Section t-t) in a damaged structure. Providing vertical support at every level below and above the damage element diminishes significantly the shear forces on Sections t-t at both sides of the element. Shoring all floors (Figure 4) is recommended whenever it can be implemented.

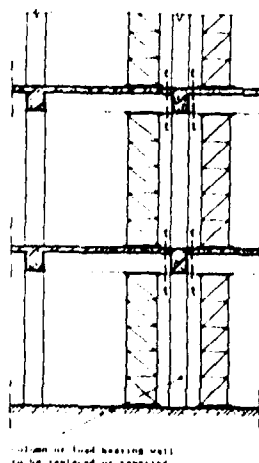


Figure 4. Shoring Configuration for Damaged Vertical Elements

All structures have some capacity to resist lateral loads, even if not specifically designed for this purpose. If the damage appears to be located only on vertical load bearing elements, special concern must be given to the possibility of reduced lateral load resistance of the structure as a whole. To prevent the building from collapse in future shocks, the lateral capacity must be restored or enhanced.

### Intermediate Techniques For Repair

Intermediate solutions do not imply just a temporary transfer of loads to auxiliary elements, but require restoration or upgrade of damaged element strength. Intermediate solutions are considered to be such that implementation is possible within a short time immediately following

any emergency situation. Although in most cases a trained staff is needed to implement and supervise the repair project, the relative simplicity of implementation makes these techniques applicable to emergency situations.

A repair or strengthening scheme is classified as an intermediate solution when its implementation does not alter the structure's original load paths. The strength is usually restored to its original levels, however, in some cases, the stiffness cannot be recovered completely. The basic failure mechanisms and overall behavior under lateral loads are not altered.

In some cases, damaged concrete must be removed and new material substituted. All damaged concrete that can be easily removed should be eliminated; however, in many cases, a simple reliable way to determine when all damaged material has been removed does not exist.

Resin and grout injection are used to repair concrete elements with low levels of damage, no crushed or spalled concrete, no fracture or buckling of steel, and small crack widths. Although the original shear and flexural strengths can be restored with injection, a somewhat lower stiffness results because it is impossible to inject all microcracks.

When crack widths larger than 5.0 mm, concrete crushing, or steel buckling are observed, the damaged elements should be replaced with new material to restore the strength and stiffness of the element.

Steel jacketing, as shown in Figure 5, restores, and in many cases, enhances the performance of any element by the addition of steel elements surrounding the original member. When the element is not badly damaged, the steel skeleton can be applied directly without further preparation. If the capacity is significantly reduced, some restoration of the element must be carried out before the jacketing can take place. Special care must be taken to avoid damage to the concrete at the point where high bearing stresses between the steel elements and concrete can develop.

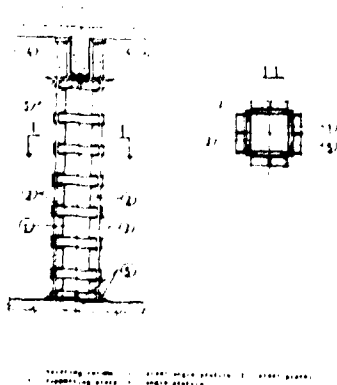


Figure 5. Steel Jacketing for Columns (Ref. 11)

U-shaped metal units with small legs known as stitching dogs can be used to prevent crack growth in slightly damaged concrete (Figure 6). Cracked reinforced concrete flexural elements can be repaired with epoxy and extra reinforcement bar insertion as shown in Figure 7. The shear cracks are externally sealed with gel-type epoxy, inclined holes are drilled through the element to cross the crack at approximately 90°. Steel bars must be inserted in the holes to bridge the crack on each side sufficiently to permit development of the bar tensile capacity. Epoxy is injected at low pressures to fill the cracks and bond the reinforcement to the concrete.

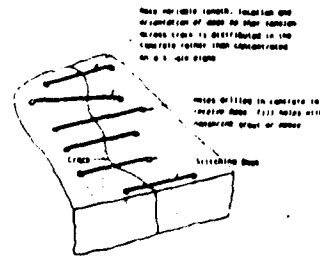


Figure 6. Repair of Crack by Stitching

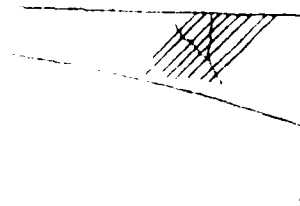


Figure 7. Reinforcing Bar Orientation Used to Effect the Repair

The injection technique is used to restore the capacity of masonry elements with cracks up to 10mm wide, with no loose bricks and no heavily damaged parts. The procedure to repair crack damage in a masonry element is very similar to that discussed for concrete elements with some differences. Finish or surface coatings must be removed from the damaged zone and the cracks cleaned with air or water. In masonry elements with cracks greater than 10mm wide or with loose bricks, damaged bricks should be replaced by new repair materials. In some cases, masonry walls cannot develop their full in-plane shear capacity if an out-of-plane failure occurs prematurely. Steel sections can be used to enhance the wall resistance to force perpendicular to the plane of the wall. The steel elements are tied to the floor diaphragms and confine or "basket" the masonry elements.

## Advanced Techniques For Repair

The techniques described here to restore (or upgrade) the damaged element strength and stiffness require more time and effort. The technical background and preparation of the people that are needed to implement advanced solutions is considerably higher than needed for the solutions described previously. A repair or strengthening scheme is classified as advanced when its implementation alters the overall structural behavior under severe loads. Special care must be focused on avoiding the creation of weak links while repairing the structure. Basic knowledge of the behavior of the structure before and after the implementation of the strengthening scheme is essential to prevent further problems in the structure. Perhaps the most important aspect involved in the repair and strengthening procedures is the achievement of adequate bond between old and new materials. Detailed descriptions of advanced repair techniques are given in Reference 14 but will not be repeated in this paper for the sake of brevity.

## ASSESSMENT OF TECHNIQUES

From the perspective of earthquake damage repair, the techniques which appear to be most advantageous are generally those which are least expensive. In many cases, the primary objective is stabilization of the structure by techniques which do not provide a permanent solution, but rather protect the public and the occupants or contents until more extensive repairs or demolition are possible. In the case of damage due to blast effects, the critical nature of the facilities makes expedient repairs of prime importance. Because operational functions carried out in the structure are likely to be critical, a repair solution which does more than stabilize the structure will be needed. Expedient repair procedures will have to be conducted primarily by personnel on the site using stockpiled materials.

The most promising techniques will depend heavily on the degree of damage and expertise and materials available at the site. Reference 14 contains a summary of the pertinent considerations in selecting a repair procedure for expediently returning the structure to use.

## CLOSURE

The large volume of work reported in the literature and the ongoing repair and strengthening of structures damaged in earthquakes provide a wealth of information for expedient repair of structural facilities.

A thorough review of the literature reveals a number of techniques which can be easily and inexpensively used for expedient repairs. The basic repair measures outlined require only common construction materials, a work force with only limited construction experience, and technician level supervision, provided that simple manuals are developed to guide the repair work.

Intermediate and advanced techniques are also available but may require more time and skill than can be permitted for expedient repair.

## ACKNOWLEDGMENTS

The authors thank the Air Force Engineering and Services Center for sponsoring (through the National Science Foundation) the efforts reported herein.

## REFERENCES

1. Air Force Design Manual - Criteria and Standards for Air Force Construction, AF Manual 88-15(C3), Chapter 1, Policy for Criteria and Design of Air Force Facilities, 20 August 1976.
2. Department of the Army Technical Manual, AF Manual 88-3, Chapter 2, Concrete Structural Design for Buildings, 3 August 1984.
3. ACI Manual of Concrete Practice, Part 3, "Building Code Requirements for Reinforced Concrete," ACI Committee 318, Detroit, Michigan, 1988.
4. Department of the Army Technical Manual, AF Manual 88-3, Chapter 3, Masonry Structural Design for Buildings, 16 January 1985.
5. Summary Technical Report of Division 2, National Defense Research Committee, Volume 1, "Effects of Impact and Explosion," Washington, D.C., 1946.
6. Wilton, C., Kaplan, K. and Gabrielsen, B.L., "The Shock Tunnel: History and Results, Volumes I-V," Defense Civil Preparedness Agency, Final Report No. SSI 7618-1, Work Unit No. 1123H, February 1978.
7. Iglesias, J., Robles, F., et al., Reparacion de Estructuras de Concreto y Mamposteria, First Edition, Universidad Autonoma Metropolitana, Mexico, 1985.
8. Warner, J., "Important Aspects of Cementitious Materials used in Repair," paper presented at the Eighth World Conference on Earthquake Engineering, San Francisco, U.S., 1984.
9. Repair and Strengthening of Reinforced Concrete, Stone and Brick Masonry Buildings, UNDP/UNIDO project RER/79/015, Building Construction Under Seismic Conditions in the Balkan Region, Volume 5, First Edition, United Nations Industrial Development Programme, Vienna 1983.
10. ATC, Appendix A, Chapter 14.

11. Assessment of Concrete Structures and Design Procedures for Upgrading (Redesign), Bulletin D' Information. No. 162, Comité Euro-International Du Béton, CEB General Task Group 12 Assessment of Concrete Structures and Design Procedures for Upgrading, Paris, August 1983.
12. Hutchinson, D.L., Yong, P.M.F. and McKenzie, G.H.F., "Laboratory Testing of a Variety of Strengthening Solutions for Brick Masonry Wall Panels," paper presented at the Eighth World Conference on Earthquake Engineering, San Francisco, U.S., 1984.
13. Lakshmipathy, M. and Santhakumar, A.R., "Repair of Structures Damaged During Earthquakes using Fibrous Concrete," paper presented at the Eighth World Conference on Earthquake Engineering, San Francisco, U.S., 1984.
14. Jirsa, J.O., Teran, A., and Nash, P.T., "Expedient Repair of Structural Facilities", Final Report Submitted to the Air Force Engineering and Services Laboratory, November 1988.

ANALYSIS AND DESIGN RECOMMENDATIONS FOR THE HAYMAN  
IGLOO CONVENTIONAL WEAPONS STORAGE FACILITY

Captain Darell J. Lawver, P.E.

Assistant Professor of Civil Engineering  
United States Air Force Academy, Colorado

ABSTRACT

The purpose of this paper is to analyze the Hayman Igloo conventional weapons storage facility's response to blast loading and present design recommendations for improving the facility's blast loading resistance. This analysis is based on August, 1987, engineering drawings of the structure. The key elements of the structure are the structural steel door, reinforced concrete T-beam roof, and one-way reinforced concrete and steel W-section composite walls. The structure is to be bermed around the walls and has a maximum of two feet of soil on the roof. This paper first models the key elements of the structure and discusses assumptions used for geometric stability and failure limit states. Next, it describes the response of the elements to blast loading. And, finally, general and specific design recommendations and details are presented. This paper is intended to provide engineering guidance for future blast tests and modifications to the Hayman Igloo.

INTRODUCTION

The Hayman Igloo was designed and constructed as a portable conventional weapons storage facility to simulate the blast-structure interaction of permanent weapons storage facilities during conventional weapons quantity distance tests. At a cost of approximately sixty thousand dollars each, the Hayman Igloo represents a tremendous savings over conventional permanent storage igloos often costing well over one million dollars each. Therefore, the logical question is "Can the Hayman Igloo be modified to store conventional weapons at a more reasonable cost than current permanent storage facilities?". Field testing has already begun to determine the answer to this issue. However, the field testing has not been backed up with an in depth analysis of the structure to determine a reasonable expectation of the structure's performance capability.

As part of the United States Air Force Academy's Cadet Summer Research Program (CSRP), Cadet Gary Guy dynamically analyzed the response of key building components of the Hayman Igloo to an unrestrained exterior surface blast of sixty thousand pounds of conventional explosives. Cadet Guy was under the supervision of Captain Ray Bennett, PhD, Section Chief of the Air Force

Weapons Laboratory Civil Engineering Research Structural Response Section (APWL/NTESR), and the author.

The variety of element types and true simple supports make this structure ideal for modeling with single-degree-of-freedom (SDOF) systems (See Figure 1). To account for the dynamic loading effects, the yield stress of the material is increased by twenty percent and plastic moment capacity is utilized. This paper first explains how the structural steel door, reinforced concrete T-beam roof, and one-way reinforced concrete and steel W-section composite walls were modeled as equivalent single-degree-of-freedom (SDOF) systems. During this section, the paper also discusses assumptions used for geometric stability and failure limit states. Next, the paper describes the response of the structure to the given blast loading. This response was found using computer analysis of the SDOF systems and *approximate charts found in Structural Dynamics* by John M. Biggs (Ref 1). Finally, the structural components are evaluated and specific design recommendations and details are presented to strengthen the facility against conventional blast loading. In summary, this paper presents a detailed analysis of the Hayman Igloo, detailed recommendations for future improvements, and provides engineering guidance for future blast tests to determine the capability of the structure.

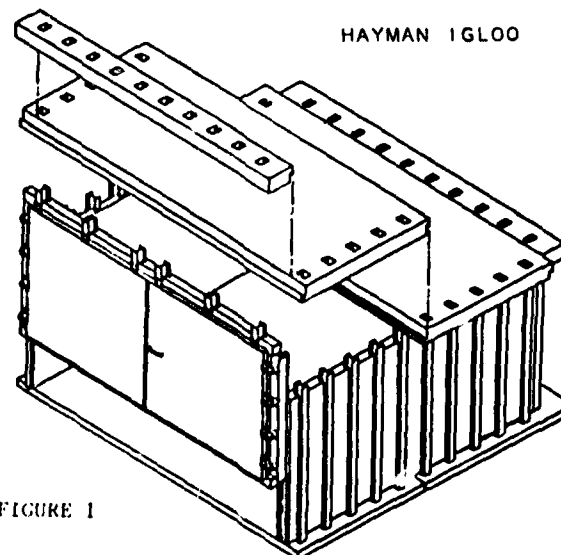
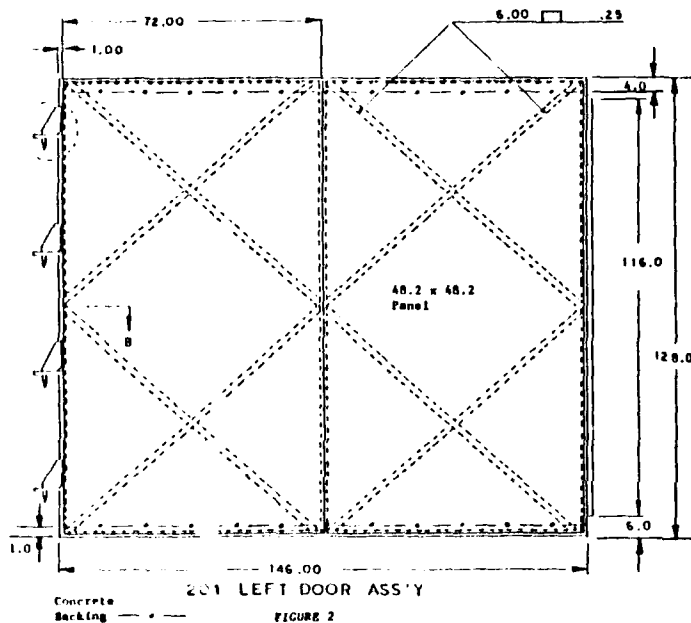


FIGURE 1

## MODELING KEY ELEMENTS

### THE DOOR

The door of the Hayman igloo is composed of inner and outer 3/16 inch, A36 structural steel, plates with A36 C4 x 5.4 American Standard Channels in-between. These channels are placed in a diagonal arrangement with the steel plates welded to their top and bottom flanges (See Figure 2). Due to the large spacing of 48.2 inches between parallel diagonals, the door may not act as a composite plate structure. Therefore, the analysis of the door includes both composite plate action of the door and single plate action of a 48.2 inch x 48.2 inch x 3/16 inch square steel plate.



The first analysis of the door is based upon a composite plate action flexural failure. The plates, spaced four inches apart by the depth of the channel, are assumed to provide all of the composite action stiffness and moment of inertia. Since the moment of inertia of the composite plates is one order of magnitude above the combined moment of inertia of the channels, this assumption seems reasonable. The composite door is modeled as a plate with three sides simply supported and the last side free since it has a pinned hinge on one end and concrete backing at its top and bottom (See Figure 2). Due to the thin outer plates providing the flexural resistance, the plastic moment is only four percent greater than the first yield moment. Therefore, the yield moment is used in both the elastic and yield line failure calculations. Standard plate theory calculations (Ref 2) yield a uniform static loading of 17 psi to reach the first yield moment at the center of the free end of the plate. The maximum deflection at this point and loading is only 1.2 inches. Using yield line theory for ultimate failure (Ref 3), the static uniform loading can increase to 26 psi. Failure is defined when the deflection of the door

is large enough to cause the bottom edge to slip off of the support at its free end. This occurs with a maximum deflection of 11 inches at the center of the free end. From this, the ductility ratio,  $u$ , which is defined as  $y_{\text{maximum}}/y_{\text{elastic}}$ , is 9.1.

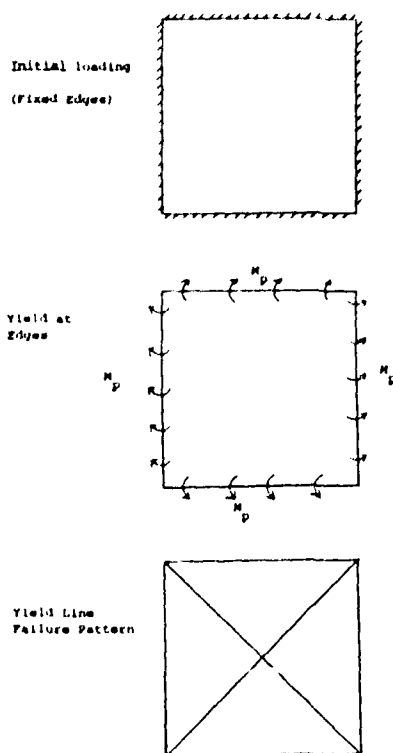
Shear failure is not the primary limit state due to the large area, simple-free end conditions, and uniform loading on the door. Web crippling, local buckling, and lateral torsional buckling of the channels are also not the primary failure mode because of the stocky channel profiles, large distribution of loading, and supported compression flange.

To convert the composite plate door to an equivalent SDOF system, equivalent load, mass, and resistance factors were calculated using integration of the elastic deflected shape and the plastic yield line deflected shape. The mass factors are  $K_m = 0.379$ , for elastic deflections and  $K_m = 0.167$ , for plastic deflections. The load factors, which by definition equal the resistance factors, are  $K_l = 0.525$ , for elastic deflections, and  $K_l = 0.400$ , for plastic deflections. The effective mass and load factors for a ductility ratio of nine are:  $K_m = 0.190$  and  $K_l = 0.414$ .

Other key dynamic parameters are maximum resistance,  $R_M$ , equivalent mass,  $M_E$ , equivalent stiffness,  $K_E$ , and period of the SDOF system,  $T$ . These values are:  $R_M = 486$  Kips,  $M_E = 15.6$  slugs,  $K_E = 110$  Kips/inch, and  $T = 0.022$  sec. Since the composite door has a bilinear resistance function, these parameters will be used directly in the SDOF system to determine the response to blast loading.

The second analysis of the door is based upon a single plate action flexural failure. This analysis is based on the possibility that the two 3/16 inch plates will blow through between the channels before the door fails as a composite plate. The weakest area for single plate failure is the 48.2 inch side diamond panels between the channels on the door (See Figure 2). This area is modeled as a 48.2 inch x 48.2 inch square plate with all four edges fixed. The uniform loading to cause the yield moment of this case is only 2.1 psi with a maximum deflection of 0.820 inches at the center of the plate. Increasing the loading to 4 psi causes plastic moments along most all of the plate edges. This occurs at a center line deflection of 1.66 inches. After the plate edges yield, the plate behaves like a uniformly loaded, simply supported, plate with applied plastic moments at its ends. The plate will then deflect enough to yield at its center and develop yield lines from the center to all four corners (See Figure 3). The loading at center yield is 6.54 psi and the deflection of the center is 5 inches. These values ignore the effects of diaphragm stress. Also, at a center deflection of 4.00 inches, the outer plate will come into contact with the inner plate which introduces new parameters. Since these calculations indicate that the plates will blow through around 6.5 psi, this failure mode controls over composite plate action of the door. To develop a model for the SDOF system, the trilinear resistance function of the plate is converted to an equivalent bilinear resistance function. The single plate is converted from its trilinear response to an equivalent bilinear response using the methods

FIGURE 3  
PLATE FAILURE STAGES



presented in Chapter 5 of Structural Dynamics by John M. Biggs (Ref 1). From these calculations, the bilinear parameters are  $R_M = 15.2$  K,  $K = 4.15$  K/inch, and  $y_E = 3.66$  inches. The "real system" bilinear parameters are converted to SDOF parameters using the mass and load transformation factors. For our range of deflection, the approximate factors come from the elastic-plastic charts of Biggs, page 214, where  $K_1 = 0.46$  and  $K_2 = 0.31$ . From this conversion, the "limiting" deflection for the outer plate can be taken as 4 inches at the center which occurs after the load reaches 6.5 psi. In a static sense, if the outer plate is loaded to failure, the inner plate would fail almost immediately after the outer plate. While this is not necessarily true for dynamic blast loading due to changes in stiffness, mass, and period of the system after the plates come in contact, for simplicity, the inner plate parameters will be neglected. Considering the uncertainty in blast loading, this assumption is reasonable for obtaining an approximate system response. The key dynamic parameters,  $R_M = 15.2$  K,  $M_E = 1.19$  slugs,  $K_E = 1.91$  K/in,  $T = 0.005$  sec, and  $U = 5$  will be used to determine the single plate response to blast loading.

#### THE ROOF

The roof of the Hayman igloo is composed of reinforced concrete T-beams running 26 1/3 feet between supports. The roof is supported at each end by resting on the side walls with extensions of the side wall W-sections coming up through

slots in the roof slab (See Figure 1). From the geometry of this support, the T-beams can deflect almost 25 inches at the midspan before the W-section extensions will "lock up" in the slots and begin end rotations. The deflection of the midspan at first steel yield is only 2.56 inches. Therefore, the concrete T-beams will be designed with simple supports. The ratio of "look up" deflection at midspan, where the section gets additional support, to first steel yield at midspan is 9.77. This will be used to approximate the maximum ductility ratio,  $u$ , as equal to 10. This is a typical value for reinforced concrete construction experiencing moderate to heavy damage, but not collapse. The uniform static loading to produce first yield is 8.65 psi. Since the T-beams do not have any stirrups, they would surely fail in shear well before the flexural limit state is reached. In fact, using the Standard ACI equations (Ref 8) for concrete shear strength, the T-beams would fail under a static loading of only 2.50 psi. This calculation is done without increasing the concrete stress by the "1.2 factor" since this is not prudent for the shear failure mode. Due to this low loading capacity and unusual beam limit state, the roof of the Hayman igloo will fail under very low overpressure and is not suited to a simplified SDOF model. However, the T-beam roof system will still be modeled as a SDOF system since the shear failure mode can easily be corrected with the addition of stirrups and the SDOF model will help to analyse the structure after design modifications are made. With a two foot soil mass cover, the dynamic parameters for this system are  $R_M = 34.5$  K,  $M_E = 158.3$  slugs,  $K_E = 9.88$  K/in, and  $T = 0.229$  sec.

#### THE WALLS

The walls of the Hayman igloo are six inch reinforced concrete slabs with exterior W-sections, W8 x 18's, spaced on 24 inch centers. Directly behind the W-sections, in the slab, are #4 rebars spaced on 12 inch centers horizontally and 24 inch centers vertically. The W-sections are used as "lifting beams" to move the walls into place and extend into slots in the floor and roof slabs to connect the building together (See Figure 1). When exposed to an exterior blast load, the concrete slab provides almost no strength and only acts to tie the W-sections together. The "worst case" static loading on the walls due to the roof slab and two feet of soil is less than eleven percent of the allowable AISC manual value (Ref 4). Also, the side walls perpendicular to the blast loading provide support to the roof and limit sideways. Therefore, the W-sections will be treated as beams and not beam-columns. The W-sections act as simply supported beams until they rotate enough to "look up" their ends in the slots. From geometric analysis, this does not occur until the midspan has deflected 12 inches. First yield occurs at a uniform static loading of 12.6 psi with a midspan deflection of 0.665 inches. The effective plastic moment is 696 K-in and occurs at a uniform static loading of 13.3 psi with a midspan deflection of 0.70 inches. Therefore, the ductility ratio,  $u$ , is approximately 18 if the deflection to "look up" is



used as the limiting failure mode. The W-section's theoretical lateral torsional buckling and local buckling strength is sufficient to reach full plastic moment. However, with a 132 inch unbraced compression flange length, the W-sections may not reach the full 12 inch midspan deflection required to "lock up". Also, the concrete slab between W-sections would fail in shear well before the midspan deflection of 12 inches. While this shear failure might not cause collapse, it would certainly affect the geometric integrity of the wall. Therefore, the maximum ductility ratio will be lowered to 12 to help account for these failure modes. The parameters for the SDOF analysis of the wall are  $R_M = 41.9$  K,  $M_E = 19.75$  slugs,  $K_E = 30.6$  K/in, and  $T = 0.046$  sec. One point worth noting here is that the equivalent periods of the wall and roof vary by a factor of almost five. With most loading cases this validates our assumption that the two act independently and, therefore, will not both experience maximum rotation simultaneously and "lock up" the roof to wall connection prematurely.

#### RESPONSE TO LOADING

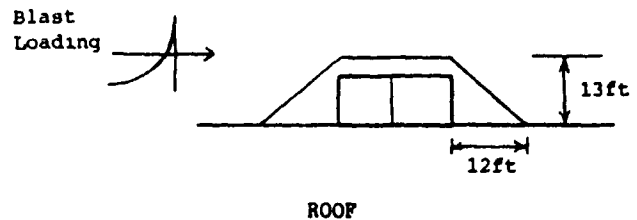
Since the key elements of the Hayman igloo have been modeled as SDOF systems, the response of these systems to any arbitrary loading can now be found. This presents the most uncertainty in the analysis. What is the blast loading on one Hayman igloo when another igloo, some 200 feet away with 100,000 pounds of iron bombs, explodes? Presently, tests are being conducted at Hill AFB, Utah, to find an answer to this type of question. If the distance between igloos is large enough, the primary structural loading will come from the airblast. This could involve overpressure, dynamic pressure, and reflected pressure. Each element of the igloo will be analyzed using an unrestrained 60,000 pound TNT blast load at 200 feet to the side of the igloo. Later, when more data has been gathered, the systems' responses can be analyzed with a more realistic load case and several orientations.

The Hayman igloo is bermed when it is in use (See Figure 4). Therefore, wall and roof calculations include some effects of the soil around the structure. The assumptions used for these effects can also be verified and improved as data from the field tests is made available.

#### DOOR

The door response is based upon the door face oriented perpendicular to the blast load. This eliminates the reflected pressure and leaves overpressure and dynamic pressure as the loading forces. When overpressure and dynamic pressure are combined, the peak load on the door is 18.5 psi. In composite action, this loading creates a maximum ductility ratio of 5 which is well below the failure criteria of 9. However, in single plate action, the loading creates a ductility ratio of over 100 and the panels fail. The ductility ratios for these cases were calculated using approximate methods from Biggs and a numerical analysis computer program.

FIGURE 4  
BERMED HAYMAN IGLOO



The roof response is calculated using two feet of soil mass with the T-beam mass. The soil is not considered to arch. Also, the T-Beams are assumed to have adequate shear and rebound reinforcement. The roof is loaded by the dynamic pressure and overpressure to a peak of 18.5 psi. This loading creates a maximum ductility ratio of 3 which is well below the failure criteria of 10. Therefore, the roof can perform well in flexure if it is adequately designed for shear resistance.

#### WALL

The wall is facing the blast wave for this analysis. Therefore, reflected pressure is added to the dynamic pressure and overpressure as a main loading parameter. The angle of incidence of the berm is used to reduce the reflected pressure, but soil-structure interaction is ignored. The maximum reflected pressure is 112 psi with a stagnation time of .0165 seconds. The combined loading on the wall produces a ductility ratio of over 100 and the wall fails.

#### DESIGN RECOMMENDATIONS AND DETAILS

To make specific design recommendations and details for each element of the Hayman igloo would normally require the development of a specific threat scenario. Elements would then be proportioned to resist this threat. However, it is appropriate to discuss general design recommendations, details for each element, and recommend a preliminary design. This preliminary element design can then be modified for a specific threat.

#### THE DOOR

The weakest element of the Hayman igloo is the door. This is especially important since the door is the only element not protected with a soil covering. One clear way to improve the door strength in both single and composite action is to increase the thickness of the plates. This would increase both the strength and stiffness of the door. Another method for improving the strength and stiffness of the door is to rearrange the placement of the channels. Closer spacing would help prevent single action failure and stiffen the door in composite action. The channels could be placed vertically, horizontally, or in some combination of the two, to make a door element which is relatively easy to analyze and stronger than the existing door. In fact, channels may not

be the best separators for the plates. Other rolled sections, such as a S4 x 7.7 or TS 4 x 2 x 3/16, could provide good separation of the plates with better characteristics for developing and distributing plastic moments. To delay the free end of the door from sliding off the bottom edge, the free end could be stiffened with more separating members and the bottom edge support could be increased from its one inch value. This would help convert our ductility ratio from stability controlled to strength controlled. The door might also be clamped down at the simply supported sides at the top and bottom to help delay the geometric stability failure. For the composite action to be assured, the plates must be adequately connected to the separators. This can be done with full or partial length fillet or slot welds. The preliminary design recommendation for the door is to use structural tubes, TS 4 x 2 x 3/16, as separators with continuously welded 1/4 inch plates on the top and bottom. One tube would be placed horizontally at both the top and bottom of the door. Then, ten tubes would be evenly spaced vertically from the hinge to the free end. This arrangement would increase the composite action stiffness between the simply supported ends by almost 50%, increase the static single plate failure load to almost 30 psi (approximately 6 times stronger), and contain separators which are capable of developing and distributing plastic moments.

#### THE ROOF

The roof of the Hayman igloo is protected from blast loading with up to two feet of soil. However, the weight of the soil and the roof itself decrease the maximum dynamic resistance of the element. The roof has very little shear strength. To correct this shear deficiency, steel stirrups must be closely spaced along the length of the T-beams. These stirrups should be closed and wrap around both the compression and tension steel for maximum ductility. Also, steel mesh could be placed between the T-beams to increase shear resistance. Since the T-beams do not presently have compression, or rebound reinforcement, rebar needs to be placed at the top of the T-beams along with wire fabric at the top of the slab. This double reinforcement in the T-beams could also reduce their total depth. For the ductility ratio to reach 10, which was used in the SDOF model, the T-beam midspan rotation would approach nine degrees. However, even with symmetric flexural and shear reinforcement and lateral restraint, only about eight degrees of rotation could normally be expected. Rotations of up to twelve degrees could be reached if diagonal reinforcement, such as lacing, is placed through the depth of the T-beam. To reach rotations beyond "lock up", the center and ends of the T-beams would have to sustain extensive plastic moments. This would require steel ratios around one half of balanced, reinforcing through the depth of the member and increasing shear reinforcement (Ref 5). The preliminary design recommendation for the roof is to place two number eight rebars at the top of the T-beams, place closed number three stirrups along the T-beam length, and place 6 x 6, 8 gauge, welded wire

fabric 1 1/2 inches from the top and bottom of the six inch slab. The first stirrup would be placed at 5 inches from the support, then fourteen stirrups would be spaced at 10 inches, and finally, 3 stirrups at 4 inches. This arrangement would be mirrored to the other support. This detailing would provide enough ductility to reach the design ductility ratio of ten.

#### THE WALL

As is currently designed, the wall of Hayman igloo gains nothing from the concrete flexural strength and is susceptible to concrete shear failure between the W-sections. Also, the W-sections are not well tied to the concrete slab. The preliminary design recommendation for the wall is to place the W-sections on the inside of the slabs. This allows for composite action and, therefore, gains from the concrete flexural strength and stiffness. The W-section flanges are already buried 2 inches into the slab and are considered naturally bonded with the concrete even without shear connections (Ref 4). However, to insure good composite action and increase the tie between the W-sections and slab, use 1/2 inch diameter x 2 inch long headed stud shear connectors welded to the W-section. Five connectors should be spaced at 22 inch centers beginning 22 inches from the slab edge. The greater depth to the number four rebar and support from the W-section flanges also delays the concrete shear failure beyond the design flexural failure criteria. For a protective structure, the addition of 3/16 inch spall plates between and welded to the W-sections is also recommended. With these design recommendations, the maximum wall resistance is increased almost three-fold.

#### EPILOGUE

Since the research and writing of this paper, several blast tests have been performed on a modified Hayman igloo. This modified Hayman igloo has a much stronger door than the August, 1987, version. These tests have shown that the igloo performs very well for its intended purpose. That purpose is to stop sympathetic explosions from adjacent igloos when one explodes. The igloo is not used as a protective structure, per se. Even with complete collapse, the structure has not had sympathetic explosions occur. Therefore, the Hayman igloo may prove to be a cost effective method of storing conventional weapons. This paper is intended to provide guidance for further testing and improvements to the Hayman igloo.

#### REFERENCES

1. Biggs, John M., Introduction to Structural Dynamics, McGraw-Hill, 1964.
2. Roark, R. J. and Young, W. C., Formulas for Stress and Strain, 5th edition, McGraw-Hill, 1982.
3. Park, R. and Gamble, W. L., Reinforced Concrete Slabs, John Wiley and Sons, 1980.
4. Manual of Steel Construction, Eighth Edition, American Institute of Steel Construction (AISC), 1984.
5. Design of Protective Structures for Conventional Weapons, Draft Document by Applied Research Associates, Inc., for the Air Force Engineering and Services Laboratory, November 1987.
6. Design of Structures to Resist Nuclear Weapons Effects, American Society of Civil Engineers (ASCE), 1985.
7. Schuster, S., et al, The Air Force Manual for Design and Analysis of Hardened Structures, Volumes I and II, By California Research and Technology, Inc. for Air Force Weapons Laboratory, October, 1987.
8. Building Code Requirements for Reinforced Concrete, American Concrete Institute (ACI), 1983.

#### ACKNOWLEDGEMENTS

Funding for this research effort was provided by the Frank J. Seiler Research Laboratory and the Air Force Weapons Laboratory. This paper has been approved for release by HQ USAFA/DFSR, AFISC/SEWV, and AFWL/NTESR. This paper contains no classified information. Special thanks goes to my wife, Diane Elich-Lawver, for her help with typing, editing, and morale.

## DESIGN AND CONSTRUCTION OF THE SEMIHARD TR-1 AIRCRAFT SHELTER

FRANK THEOS

HEADQUARTERS, UNITED STATES AIR FORCES IN EUROPE - DER

**Abstract.** This paper describes some unique features in the development, design and construction of a new semihard shelter for the TR-1 aircraft. The new shelter is designed to withstand the standard NATO threat from conventional weapons. Some unique design problems were: the shelter envelope had to be kept to the minimum. A reduced length was achieved by the elimination of the exhaust port, and hanging the rear door on the outside face of the rear wall. On the front doors, the outrigger was shortened. An armor plate rectangular hollow section was adopted. The larger shelter volume required more ventilation openings placed in less-stressed sections of the arch. The emergency generator fuel tank was placed below the shelter floor, and the plant room is above a ground floor room.

The unique construction problems were: A single pour of 1,150 cubic meters of concrete continuous over 24 hours. The amount of the required reinforcement provided restricted spacing for vibrating the concrete during placement of the downstand beam.

**Background.** Since the mid-1970's the United States Air Force has constructed a substantial number of semihard aircraft shelters in both the European and Pacific theaters. The shelters are designed to house tactical fighters and protect them against an array of specified conventional weapons threats. The threats are those typically identified by NATO. Typical of these structures are the First Generation (TAB VEE, Modified TAB VEE), Second Generation, and Third Generation Hardened Aircraft Shelters (HAS). However, no shelters had been constructed for larger aircraft, such as the TR-1. Such aircraft have essentially no protection from attack while they are parked.

**Objective and Approach.** The requirement was to construct a shelter for the protection of a TR-1 aircraft against conventional weapons threats. This shelter would also be fitted for performing routine maintenance operations, pre-flight activities, taxi-out, and post-flight checks.

The approach taken in establishing a minimum required envelope was to add to the physical dimensions of the aircraft the minimum clearances around and above the aircraft, which

would accommodate the movements of Primary Mission Equipment (PME) around the parked aircraft, and the required clearances for Mechanical and Electrical (M & E) fixtures. The mode of operation and pre-flight activities in wartime conditions also had to be considered.

**Concept of Shelter Use.** The aircraft under its own power taxis toward the shelter and stops its engine with the nose turned away from the opened doors of the shelter. Then a tug with a sulky (tow-bar) tow the aircraft backwards to its final parking position inside the shelter; the tug exits through the rear shelter opening via the tug road. (Figure 1).

Some functional/operational requirements that had to be considered were: a. Refuelling the aircraft while performing pre-flight activities. From an R-9A refueller 2,950 gallons of Jet Petroleum Thermally Stable (JPTS) fuel are pumped into the aircraft's tanks. b. After pre-flight preparation the aircraft must be started in the shelter to supply uninterrupted power to the sensors. c. Positioning the PME at safe distances from the aircraft fuelling points. d. Provide adequate ventilation to prevent concentration of oxygen vapor from Liquid Oxygen transfer, and vapor from fuel spills from tank overfilling. e. grounding the servicing carts.

**Siting and Design Concept Studies.** From the above factors the resulting clear envelope required was: 38.2m - width (W) at a height of 2.4m, a clear height (H) of 7.9m at the crown (shelter center line), and length (L) of 30.5m. A siting exercise, based on a maximum outer footprint of 40m x 33m (WxL), was run simultaneously with a design concept study. The shelter sitings had to comply with NATO, USAFE and U.K. clearance criteria regarding survivability, explosive, and fire requirements. This was necessary in order to establish the limits of additional land required for the construction of the shelters. Land acquisition at the specified base normally constitutes a long-protracted procedure; it was, therefore, a critical path action and a definite restraint in the final design envelope to be developed.

The design threats include conventional bombs, cannon and rocket for which different levels of protection are adopted.

Various shelter concepts were initially analyzed (Reference 1). Four concepts were further analyzed and costed as follows:

| Concept | Protection Level | Out-to-Out Footprint,m | Unit Cost/m |
|---------|------------------|------------------------|-------------|
| <hr/>   |                  |                        |             |
|         |                  | L x W                  |             |
| 1       | Semihard         | 40.8 x 40.5            | £ 17,500    |
| 2       | Splint. Prot.    | 40.8 x 39.3            | £ 13,300    |
| 3       | Splinter Pro.    | 33.0 x 41.0            | £ 15,200    |
| 4       | Spl. Protect.    | 33.0 x 48.0            | £ 13,100    |

The shelter profile was a double-radius arch for Concepts 1 & 2, a rectangular box for Concept 3, and a catenary arch for Concept 4. Originally the front door was of an inverted T shape, the higher central section accommodating the vertical stabilizer of the aircraft. Concepts 1 & 2 considered a door in five independent panels; two lower panels on either side of a central panel. All panels had a pivoting pie-shaped cross section that dropped into a pit. These concepts included an upward sweeping exhaust port. Concepts 3 & 4 involved a full width vertical plate door that translated vertically into a floor slot 10ft deep. The center door was a plate that slid horizontally. The exhaust port was a simple cut-out with drive through capability for the tug. The maximum outer footprint allowed in the siting exercise was 33m x 40m (LxW). From the above table the footprint of Concept 4 was too large for the available sites. Also that of Concepts 1 & 2 was too long, because it included a 7.93m front door pit and 7m long exhaust port. Evaluation of the developed concepts was based on functional suitability, siting (land purchase), survivability, cost, constructibility, system reliability, maintainability, and design and construction time. The separating factors were the functional aspects, siting (shelter size) and cost. The semihard option was preferred by NATO. Further design development proceeded using the arch with vertical rear wall from Concept 1 with the doors and exhaust port of Concepts 3 & 4. A horizontal-sliding bi-parting front door that could be towed open in case of emergency-generator-failure was specified.

#### Probability Study and Stand Off Distances.

A probability study was carried out for various shelter configurations allowing for accuracy of weapon system, target area, and angle of strike. The users-required probability of survival against the specified bomb threat was found to be achievable

Exhaust Port. The aircraft engine angles downward, toward the shelter floor, at a negative angle of 4 degrees 1 minute from the horizontal. This fact caused concern about

possible backflow of engine exhaust inside the shelter.

The original concept study included an upward-curved exhaust port, large enough for a positive exhaust action. However, this arrangement would require a second rear wall opening for tug exiting.

Exhaust port efficiency tests were conducted (Reference 3) which involved the running of a TR-1 aircraft inside a weather shelter which incorporated a 4.6m wide x 7m high rear opening and a blast deflector 10m from its rear door. These tests established: a. The optimum parking position of a TR-1 was with its engine exhaust nozzle within 5.8m, and its nose gear 15.8m from the shelter rear wall; b. For maximum exhaust port efficiency the rear opening need not be higher than 3.4m. The existing 4.6m width, necessary for tug maneuvering, was adequate. From the protection standpoint a 4.6m(W) x 3.4m(H) opening is the smallest to serve both the exhaust and tug drive-through requirements; c. A blast deflector positioned 10m from the rear shelter wall proved very effective in directing the gases upward at 90 degrees and prevented Foreign Object Damage generation on adjacent taxitracks.

The test also proved that an "open" exhaust port with a rear sliding blast door is more effective in aircraft exhaust removal than a complicated exhaust port as incorporated in previous HAS. In addition, by positioning the blast sliding door on the outside face of the rear wall some useful space is gained inside the shelter for pre-flight activities at the rear of a parked aircraft. By eliminating, therefore, the requirement for an exhaust port attachment to the shelter, the result was a shorter shelter.

Shelter Elements - General. The shelter consists of a reinforced concrete (RC) spread footing along three sides and a door foundation at the front; the side footings are tied together by nine transverse tie beams; the footings/grade beams support the RC arch section, which is placed over a double-radius steel shell; a RC floor with grounding points, drains, and centerline markings; front and rear doors with their hydraulic drives and threshold heating in their tracks; a ventilation system with fresh air intake and exhaust ducts; electric power in the form of 50, 60 and 400 Hertz socket outlets supplied via frequency converters; an emergency generator, to be used in case of commercial power failure and fed from an underground diesel storage tank; a power socket is also provided external to the shelter for connecting a mobile diesel generator; a compressed air system for starting the aircraft; both interior and exterior lighting; a fire detection system; Airfield Survivability Measures (ASM) communications system; napalm heat detectors with associated dampers in the ventilation system; conduits and/or stub-ups for a future installation of intrusion detection, fiber optics, and radio antenna systems. There is a storage room in one corner of the shelter, over which the plant room houses all the M & E equipment (emergency generator and control

panel, 3 frequency converters, air compressor and receiver, and hydraulic unit with its Programmed Logical Computer (PLC). The main electrical switchboard and Heating, Ventilation and AirConditioning (HVAC) control panel are located on the shelter floor next to the storage room wall. A tug road is a required accessory.

**Shelter Configuration.** The TR-1 shelter is a double-radius flat arched structure with internal clear dimension of 39.3m span at the springline x 9.238m midspan height x 30.5m length. (Figure 2). Clearance to a parked aircraft is 3.1m at the nose, 3.15m at wing tips and 7.93m at the tail.

**Foundations.** Continuous massive RC footings are provided at arch edges, rear wall, and main door sill. The footings form the floor surface for the 4.6m nearest the springline on either side of the arch. The arch edge strips are tied together with 500mm x 650mm deep RC ground beams at 2.71m c/s to resist the horizontal arch reactions.

**Ground Slab.** The Load Capacity Number (LCN) 60 floor slab is 300mm Pavement Quality Concrete (PQC) reinforced with B785 mesh top and bottom in order to limit floor heave from ground shock. Longitudinal construction joints are tied with a single layer of T20 at 200mm bars. Debonded dowel bars, 1.5m long, are provided between the slab perimeter and the footings. The slab is isolated from the ground tie beams below.

Because of the aircraft characteristics, especially when taxiing out of the shelter fully loaded, the floor gradients to the drains had to be kept quite level.

**Arch Design.** The design adopted arch thicknesses based primarily on fragment and cannon penetration considerations. The arch was thickened at the springline to cater for the higher moments expected at this location. The corrugated liner and the thickness of concrete confined within it were ignored in the analysis (conservative). Various degrees of fixity were considered at the arch springline. The arch was analyzed as a 2-dimensional structure with non-linear response and time varying loads using the ANSYS finite element program. Dead and live loads, air blast and ground shock loads were considered. The air blast and ground shock, plus dead load, cases were found to be critical with maximum bending moments between 30 degrees and 60 degrees from the horizontal; consequently ventilation openings through the concrete arch are located before and after this segment of the arch. Some inelastic response was found to occur in the arch, but no indication of catastrophic collapse.

**Arch.** The arch is of RC (C40 strength) with permanent galvanized corrugated 3mm thick steel liners. R.C. thickness varies from 533mm at

the crown to 1100mm at the springline, plus the corrugation depth of 0 to 356mm. (Figure 3). Reinforcement is T32 at 150mm c/s main, T12 at 250 mm c/s secondary at the crown, equivalent to 5354sq.mm/m (both faces); T40 at 150mm c/s main, T16 at 200mm c/s secondary at the springline (both faces), equivalent to 6793sq.mm/m. The T40 rebars were bent to the arch curvature; their connection to the starter bars from the footing was difficult; (Figure 4) consequently the starter bars were shortened and hydraulically crimped couplers were used to limit congestion; where access made crimping impractical, butt welds were specified. Links were not used in the arch. Limestone aggregates were used in the concrete mix for temperature and shrinkage control. An internal vertical cut-out was designed at the front of the shelter, at the springline of the arch on both sides, where the door drive could be located without impinging on the 38.9m at 2.49m height operational clearance required. This resulted in a corresponding bulge on the exterior face of the arch (Figure 5). The liner is made up from 3mm mild steel doubly-corrugated panels, bolted together at laps to form a continuous shell. Liners are tied into the arch concrete with cast-in bolts; these are not intended to act as shear studs, but some degree of composite action will inevitably occur. In addition to providing permanent formwork, the liners act as spall plates. The liners receive an anti-condensation treatment near the end of the shelter construction operations.

**Main Door.** The main 2-leaf door covers almost the entire front elevation of the shelter, spanning vertically up to 8.2m, between the ground beam and the arch fascia, (Figure 6) instead of the inverted-T shape at the concept stage which would have required unreasonably heavy construction to resist the door rebound reaction.

The hollow door construction of 12mm armor plate, 400x200x10mm mild steel Rectangular Hollow Sections (RHS) at 520mm centers and 12mm inner armor plate all continuously welded (total thickness 424mm), was designed to resist blast and fragments from the specified bomb using simple Single Degree of Freedom methods. Permanent plastic rotation of the door under blast loading would be about 2 degrees. The door construction would resist the largest bomb fragment appropriate for the required level of survivability. Rebound loads are transferred by cantilever plates at top and bottom of the doors onto support structures. Minimum specification for the armor plate steel was MVEE 816 Class II. An equivalent specification (MIL-5-12560 B Class II) was adopted in some instances. Outriggers and counterweights were provided to give the door stability under wind loading. These elements were not taken to contribute in resisting blast loads. However the outrigger construction lends itself to a future door upgrading. Each door leaf, weighing 115 tons, is carried by 4 bogies - two sets of two wheels - under the main door and one set of two wheels

under the outrigger. All wheels run on a rail track.

Downstand Beam. A 1100mm deep downstand beam (Figure 7) was introduced at the central top portion of the front arch elevation in order to allow a reduction in height and saving in weight of the main doors. The heavily reinforced beam cantilevers down from the arch to pick up the considerable reaction from the door head under loading from the separate positive and negative blast wave phases. The effect of this arrangement on the arch structure was assessed, using a three-dimensional finite element analysis which demonstrated that the structure just remained elastic.

Rear Door. The rear door spans across a 3.4m x 4.6m wide clear opening. The door is of hollow construction with 12mm outer armor plate, 300 x 200 x 8mm mild steel RHS at 442mm centers and 12 mm inner armor plate, all continuously welded (total thickness 324mm). The door weight of 3.4 tons is carried by two separate bogies on rail track. The door was designed to the same blast and fragment criteria as the main door but higher permanent rotations were permitted.

Rear Wall. The rear wall is 650mm RC with T20 at 150mm c/s main and T12 at 150mm c/s secondary (both faces), and nominal shear links throughout. It was designed for blast and penetration resistance from the specified threats.

Cowls. Fifteen 850 x 600mm apertures were left through the arch for ventilation ducts. Apertures are covered with armor plate cowls, to prevent bomb fragment penetration, complying with MIL-5-12560 B Class II specification.

Shock. Shock motions were estimated by extrapolation of accelerometer records obtained during full scale tests (the GAS tests) on a Third Generation HAS. Values of predicted motions, including rigid body and flexural values and 100 g, Average Acceleration between 4 and

. An upstairs location for the plant room meant that M & E equipment of lesser shock-resistance could be installed - a cost effective measure.

With the acceleration forces to be resisted known from the design analyses, the M & E equipment was pre-selected from known suppliers of certified shock-tested equipment. This factor enabled the detailed design to be completed, thus allowing adequate space for each piece of equipment, before bids were invited. An added advantage of the pre-selection process is that it compressed the construction time.

Interior walls for storage/plant room. The walls were constructed 6 inches short from the

arch steel liners in order to accommodate the expected deflection from a blast loading. The head-plate of a T shaped steel-plate-saddle was welded to the liners, while the legs straddled the thickness of the RC wall; the six-inch gap between the wall edge and the steel liners, along the sides and ceiling, was packed with fire-rated rockwool.

M & E Services. Each mode of the various systems in every combination, e.g. fuel dumping, protection against napalm attack, smoke removal in the event of fire, has been successfully commissioned. All systems serve the purpose of protecting and minimizing the risk of damage to the resources within the shelter.

All equipment has been designed to withstand shock loadings according to their location within the shelter. Every equipment item has been subjected to a rigorous shock test performed at an independent laboratory. Fans, ductwork, grills, volume control dampers etc. have undergone a simulated test, receiving actual shock treatment on all 3 perpendicular axes. The loadings on all equipment, and its associated supporting structure, were applied at a half-sine wave pulse of pulse width 30 +/- 5 ms. All equipment was certified to be in operating condition, before, during, and after each test. Every test was witnessed in compliance with the project specifications. Provision has also been made within the entire installation for protection against vibration, so that the aircraft can be ran at reduced power inside the shelter without fear of loosening any fixed items.

Door Drive System. A particularly complex and powerful door drive system was incorporated. The main drive power is from a hydraulic power unit situated in the plantroom. This unit is driven by two 30 H.P. electric motors. Each unit contains a PLC system which in effect controls the operation of the doors, and governs the pressure requirements of the hydraulic fluid in accordance with the flow requirement. The PLC is able to detect minor additional functions that may arise as a result of the door track containing a large stone. The system control is such that increased power can be made available automatically to overcome the increase in friction. The drive is applied to the doors through two hydraulic radial piston motors, each driving a pinion that engages the pins in a rack beam fixed on each door leaf. Movement of the doors is made by control of a self-centering joystick and control knobs situated on the control panel. Because reliable door operation is mission essential, the door drive system and the electrical power supply to that system received special design attention. A hydraulic motor was chosen because it requires 37.5 kw to drive all three door leaves, two on the main door and one on the rear door, whereas an electric motor would have required 140 kw only for the two leaves of the main door. The capacity of the emergency diesel generator determined the size of the diesel storage tank

required for 28-day supply to the generator. In case of emergency generator mal-function, the main doors can be opened by a tug pulling one leaf open via a cable fixed to the end of the door with the cable going through an eye on the bumper stand at the end of the door track. The rear door can be pushed open/close by one person.

Additional systems provided in the shelter, whose description is omitted because of limitations to the length of this paper, are: emergency diesel generator, rotary converters, ventilation, compressed air, interior and exterior lighting, fire alarm/detection.

**Construction.** Some unique features are described: a. Concrete placement. The 3mm double-corrugated steel liners, pre-bent to the desired profile, were erected over temporary metal falsework. The supporting falsework consisted of heavier-duty central towers, each with a leg load capacity of 50 tons, and lighter-duty ones at the two ends. The shuttering system incorporated windows spaced at 1.5m c/s horizontally and 2m c/s vertically, through which the concrete was placed and vibrated. The windows were staggered in the vertical direction between successive horizontal rows. The steel shuttering extended up to the change of curvature of the arch; the concrete in the remaining top area was hand trowelled. The entire length of the shelter, except for the 3.5m front portion, was placed in a single pour of 1,150cu.m. For the first shelters the concrete pour was continuous over 24 hours; this time was reduced to 16 hours for the last shelters due to improved techniques used by the contractor. Not having a construction joint on the arch was considered more important than the consequences of bad weather and/or plant breakdown during a scheduled pour. Pumped concrete was placed simultaneously on both sides of the arch.

The 3.5m separate front pour serves a dual purpose: a. The finished front of the shelter, with the downstand beam, is accurately lined up with the front door beam at floor level which incorporates the door track, and b. Provides a neutralizing effect of any creep in the steel liners that may have resulted from the main pour. The construction joint of the arch to the rear wall is horizontal in order to obviate ingress of moisture.

In the concrete mix a plasticizer was used for the concrete placed within the shutters only. Limestone aggregate was used in all arch concrete.

#### Useful facts for each shelter

|  |                                      |
|--|--------------------------------------|
| Floor . . . . .                          | 1,000 cu.m. PQC                      |
| Sub-structure . . . . .                  | 1,070 cu.m. concrete                 |
|  | 30 miles of Reinforcement - 130 tons |
| Super-structure . . . . .                | 3,250 cu.m. concrete                 |
|  | 45 miles of Reinforcement - 320 tons |
|  | 30.5 " in main arch                  |
| Bolts on arch liners . . . .             | 30,000 bolts                         |
| Roof cowls - Weight of largest . . . . . | 4 tons                               |
| Rear wall vents " " " . . . . .          | 3.5 "                                |

|           |   |                |
|-----------|---|----------------|
| Main Door | Weight per leaf . . . . .                 | .115 tons      |
|           | Total surface area . . . . .              | .156 sq.m.     |
|           | Travel dist/Opening time . . . .          | .19.1m/90 sec. |
|           | Weight of fully loaded aircraft . . . . . | 20 tons        |

**Conclusion.** The TR-1 aircraft shelter with an initial construction cost of \$2 million - 1988 prices, Rate of Exchange \$1=£0.59 - and minimum anticipated maintenance costs, protecting a multi-million dollar aircraft is a very good investment in the NATO defence effort.

Features to be considered for improvement in similar type facilities are: a. Front door counterweights on the outrigger could be placed lower to afford additional protection to the bogie-wheels. b. All-metal front door sections, in contrast to RC sections, in large spans are subject to temperature distortion that must be accommodated in the design. c. The heavy blast door for personnel access is subject to abnormal wear and tear. This door can be used less if left open during the day and a light door is added to the inside frame for day use. d. More generous separation of the vents in the rear wall coming from the plantroom would ease concreting operations. (Figure 8).

**Acknowledgement.** Credits are due to the U.S. Air Force Systems Command (AFSC), Eglin AFB, FL for sponsoring the Concept Study, monitored by the U.S. Air Force Engineering and Services Center (AFESC), Tyndall AFB, FL under contract with The University of New Mexico Engineering Research Institute (NMERI), Albuquerque, NM. The U.K. Government Department of the Environment, Property Services Agency (PSA), Explosive Effects and Safety Group at Croydon, acting as consultants for the threat analysis and dynamic design to the PSA DW(USAF), Ruislip, for the detailed design, supervision of construction and project management, in their role as Design and Construction Agents in the U.K. for the U.S. Air Forces in Europe.

#### References

1. Bultmann, E.H. Jr., "Large Aircraft Shelter Concept Study", New Mexico Engineering Research Institute, Task Report NMERI WA2-10 (S.S. 2.04), September 1985, Albuquerque, New Mexico.

3. Environmental Health Laboratory, USAF Regional Medical Center, "Exhaust Port Efficiency Tests, TR-1 Weather Shelter", Technical Report EHL(W)85-31, November 1985, Wiesbaden.



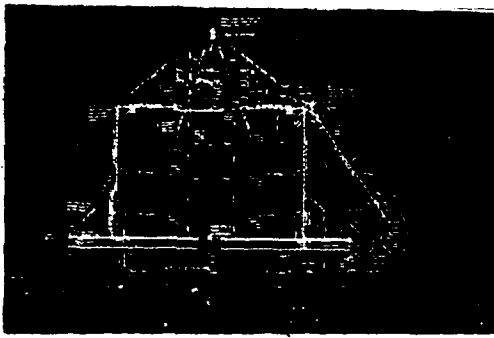


Figure 1. Shelter floor plan & tug road.

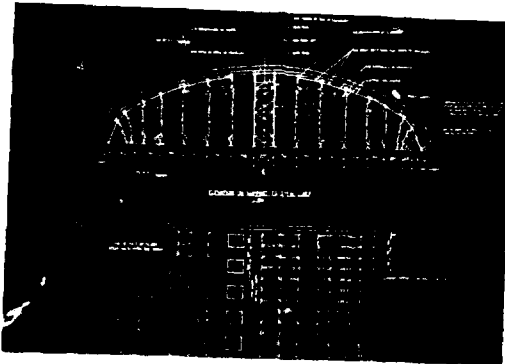


Figure 2. Shelter elevation with designed falsework.

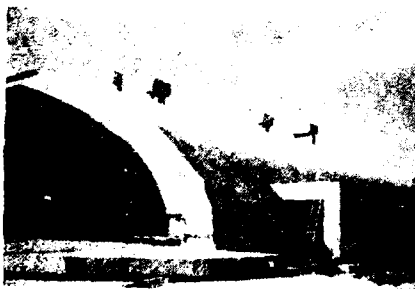


Figure 3. Shelter front & side view.

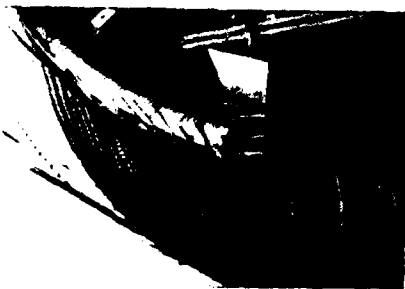


Figure 4. Arch reinforcement & steel liners.



Figure 5. Arch bulge & rear face of door.



Figure 6. Shelter front with doors nearly closed.

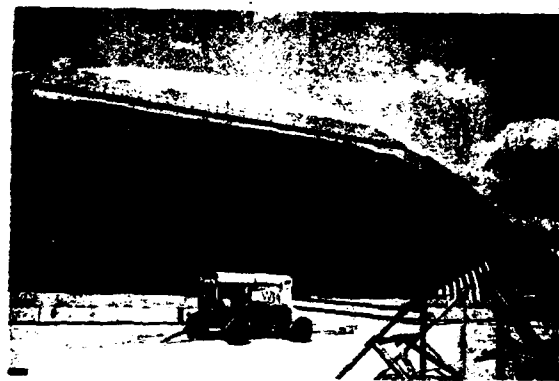


Figure 7. Downstand beam with fascia plate.



Figure 8. Cows on rear wall.

## Non-Propagating One Pound High Explosive Storage Cabinets

Phillip D. Stewart  
Steven L. Young  
A. G. Fapp

Risk Management Department  
Pantex Plant  
Amarillo, Texas

**ABSTRACT:** Operators of explosives processing plants frequently investigate the feasibility of reducing explosives limits in processing bays. Reductions in limits are desired to reduce personnel exposure, satisfy facility constraints, and reduce real estate requirements; however, lower limits hinder process flow and result in increased time to perform operations. An alternative to reducing bay limits is to provide storage cabinets to allow staging of explosives in the bays. These cabinets would prevent propagation of explosives and would reduce the Maximum Credible Event (MCE) to the explosives required for the operation. This paper describes the conditions which initiated the development of the storage cabinets, details of the test program, discussion of the test results, and conclusions of the statistical base development including determination of confidence levels.

### INTRODUCTION

Reduction of explosives limits in existing operating areas of industrial facilities is desirable to increase personnel safety, limit explosive hazards, and meet increasingly stringent protection criteria; however, productivity is usually hampered by these reductions, increasing the time required to perform the desired operations.

### BACKGROUND

In an attempt to maintain current explosives limits for operating areas and decrease the maximum credible event (MCE), a design was developed for a non-propagating storage cabinet. It was proposed that by staging explosives in a cabinet that would not allow propagation from container to container, the MCE would be reduced to the amount of explosives required for the operation being performed while permitting the operating area explosives limit (MCE + amount in storage

cabinet) to remain unchanged. Two tests were conducted in 1974 to establish a design basis for this non-propagating explosives storage cabinet.

Two storage cabinets were constructed for testing. The first cabinet was constructed of a 4'-8" x 4'-2" plywood frame with six cardboard containers arranged in an axisymmetric array around, and 18 inches center-to-center from a center cardboard container. Each container was imbedded with its rim flush with the sand which filled the wooden frame. The assembly was placed on the ground with the opening of each container facing up. The second cabinet was identical to the first except that the cardboard containers were replaced with aluminum cylinders which were rim welded to an aluminum face plate covering the sand fill.

The following is a description of each 1974 test setup:

#### Test #1

Date: May, 1974

Donor Charge: 2.25 lb. pressed LX-04

Six Acceptor Charges:

2.25 lb. pressed LX-04,  
2.25 lb. pressed LX-09,  
2.25 lb. pressed PBX-9404,  
2.0 lb. granules LX-09,  
2.25 lb. pressed LX-09,  
2.0 lb. granules PBX-9404.

#### Test #2

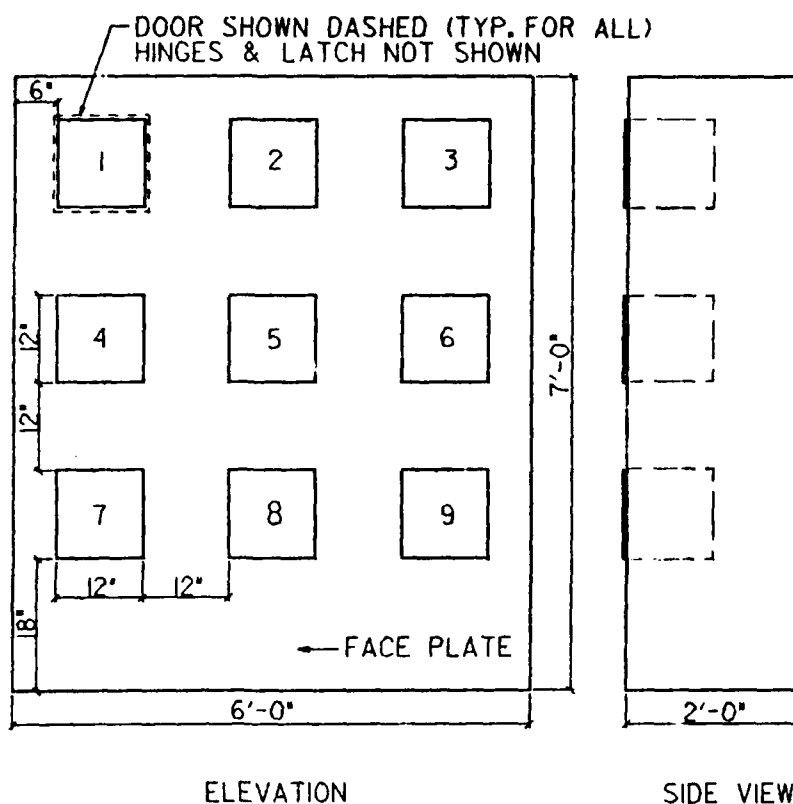
Date: August, 1974

Donor Charge: 2.5 lb. pressed PBX-9404

Six Acceptor Charges:

2.0 lb. LX-04,  
2.375 lb. PBX-9404,  
2.0 lb. LX-04,  
2.0 lb. LX-09,  
2.0 lb. LX-04,  
2.25 lb. PBX-9404.

A formal report was not issued for the two 1974 tests, however review of the information available indicates that no reaction occurred by acceptor charges in either test. A reaction was considered to



#### NOTES:

1. ALL MATERIAL  $\frac{1}{4}$ " ALUMINUM (EXCEPT  $\frac{1}{8}$ " ALUMINUM DOORS).
2. PERIMETER ANGLE BRACING NOT SHOWN.
3. WELDS  $\frac{1}{4}$ " FILLET-CONT.

FIGURE 1. NON-PROPOGATING HE STORAGE CABINET  
(NO SCALE)

be any evidence of burning or detonation from an acceptor charge.

Subsequent to these tests, a design was prepared for non-propagating storage cabinets as shown in Figure 1. This design differed from the second test cabinet in the following ways: the entire cabinet was constructed of aluminum; nine containers were arranged in three rows; separation distances between containers were increased; covers were provided for each container; and, the media surrounding each container was changed from sand to vermiculite. Vermiculite is expanded mica granules commonly used as masonry insulation, and has a density much less than that of sand. Two cabinets were constructed according to this design and are currently in use.

While the design change from sand to vermiculite provided a weight savings of almost 4 tons per cabinet, it was questionable that the vermiculite would provide the protection offered by the sand. This deviation prompted additional testing in 1988 when the cabinets were again reviewed as a means to reduce the MCE in an operating bay.

Two storage cabinets were constructed for testing. Both cabinets were constructed

according to Figure 1 except that plywood was used for the back and sides and the doors were taped in place instead of hinged and latched. The cabinets were filled with vermiculite and placed upright on a steel pad.

The approach to validating the existing cabinet design was to take a full scale model, use similar explosive weights and types as in the 1974 tests, and use the explosive configurations most commonly encountered in an operating bay. The test would be judged on a pass/fail basis; fail being any evidence of a reaction from an acceptor charge. Based on 2.5 pounds of explosives for the tests, should the first test be considered successful, the cabinets would be used to store up to 2 lb. per container. This 25% overload test would allow for a built in safety factor for the cabinet design.

#### 2.5 Lb. TEST

The following is a description of the first 1988 test setup:

##### Test #1

Date: February, 1988

Donor Charge: 2.5 lb. pressed PBX-9404

Eight Acceptor Charges:

2.5 lb. scrap LX-13,

2.5 lb. pressed PBX-9404,  
2.5 lb. granules PBX-9404,  
2.5 lb. pressed LX-10,  
2.5 lb. pressed PBX-9205,  
2.5 lb. granules LX-10 & 14,  
2.5 lb. granules PETN & 9407,  
2.5 lb. granules PBX-9205.

The charges are listed in the order shown in Figure 1 for each container, with the fifth container being the donor charge location.

The test model was completely destroyed. A portion of the aluminum face plate traveled approximately 100 feet with portions of the individual containers traveling over 300 feet. The explosives in the containers directly above and below the donor charge could not be found.

The cabinet pieces were gathered and each piece examined. It was determined that a reaction had occurred with the PETN and PBX-9404 granules located in the bottom container (#8). The walls of this container were pitted and burned. Since this was considered a pass/fail test, it was concluded that the cabinet was not adequate for storage of 2.0 lbs. of explosives.

#### 1.25 Lb. TEST

The second test conducted in 1988 was also designed as pass/fail. The 125% test charge for this test was 1.25 lb. Should this test be considered successful the cabinets would be used to store up to 1 lb. of explosives per container.

The following is a description of the second 1988 test setup:

##### Test #2

Date: February, 1988

Donor Charge: 1.25 lb. press. PBX-9404

Eight Acceptor Charges:

1.25 lb. granules LX-14,  
1.25 lb. scrap LX-13,  
1.25 lb. granules LX-10,  
1.25 lb. pressed PBX-9404,  
1.25 lb. pressed LX-14,  
1.25 lb. granules PBX-9404,  
1.25 lb. pressed PBX-9404,  
1.25 lb. granules PBX-9404.

These charges were also located in accordance with Figure 1. Based upon the first test, the bottom center container was considered to be the most sensitive location for acceptor charges; therefore, a pressed piece of PBX-9404 was placed in this container. Two high speed cameras were used to record this test shot.

The test model was once again destroyed,

however the severe damage to the individual containers was primarily localized to the top and bottom center containers (#2 & #8). In all cases the containers were separated from the aluminum face plate. The four corner containers survived intact with the explosives remaining in the containers. The two side containers (#4 & #6) had the side plates adjacent to the donor charge folded in over the explosives they contained. Containers #2 and #4 traveled approximately 30 feet with pieces of LX-13 from container #2 traveling up to 50 feet. The pressed piece of PBX-9404 located in container #8 were not recovered. Although explosives housed in the acceptor structures were severely shocked, damaged, or destroyed, examination of the cabinet remains showed no evidence of a reaction. The plywood bottom of the cabinet was intact and also showed no sign of a reaction from an acceptor container. Review of the film from the two high speed cameras indicated that no reaction occurred.

Two concepts were involved with evaluation of the 1988 test results:

The first concept assumed that the 25% over test of the cabinets along with the focusing of the blast effects toward the top and bottom containers housing the more sensitive explosives demonstrated the "worst case" scenario. In addition, the blast would hurl the bottom center container into the steel pad which the cabinet was setting on, providing an additional means for propagation. It could be argued that if the cabinets did not allow propagation of acceptor charges in this test configuration, the cabinets would be considered acceptable and would not allow propagation.

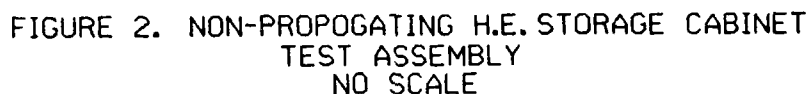
The second concept involved a statistical approach. Due to the unpredictability of explosive detonations from slight variations in test arrangements and the hazards associated with multiple detonations, it could be argued that a statistical base must be established before the cabinets could be considered acceptable for eliminating propagation.

#### DATABASE TEST

It was decided that additional testing was required in order to establish a "level of confidence" considered acceptable for allowing the use of and determining restrictions for the non-propagating storage cabinets. The next series of tests were started in December of 1988 and are currently half complete.

Twelve test models were constructed as

1. ALL MATERIALS - 6061-TS ALUMINUM.
2. ALL JOINTS WELDED EXCEPT AS SHOWN.



As previously discussed, the reasoning behind additional testing was to establish a data base in order to determine a level of confidence for the non-propagating storage cabinet design. The test assembly attempted to model the worst case scenario for each container. It was determined during the first two 1988 tests that the bottom center container (#8) was the most sensitive position. The configuration of this container was used to establish the test assembly design.

surface of the donor container. This is consistent with the separation distance of each container in the non-propagating storage cabinet design.

An octagon concrete frame was provided parallel to each acceptor container and 18 inches from the containers surface to simulate a container of the storage cabinet being hurled into the floor. This frame was also placed horizontally on a steel test fire pad to simulate a storage cabinet being located against a concrete wall of an operating area.

Vermiculite was used to simulate the actual fill material used in the storage cabinets.

The following is a description of the test setup:

Date: Dec. 1988 to Present  
Donor Charge: 1.25 lb. pressed LX-10  
Eight Acceptor Charges: All 1.25 lb.  
pressed LX-10

Each acceptor charge was taped to 3 inches of Styrofoam blocks and wrapped in plastic bags. The Styrofoam blocks were used to raise the charge to the center of the container while the

plastic bags were used to help contain the damaged pieces of explosives and allow recovery for inspection.

### RESULTS

To date, 5 of the 12 tests have been completed. The results of each test have been basically the same. The face plate of each cabinet has been completely or partially split at the centerline weld; however, the face plates have remained on or next to the test assembly. Each container has been torn away from the face plate; however, in most cases the acceptor containers remained within the concrete frame of the test assembly. The sides of the acceptor containers facing the donor charges have been bent in approximately 4 inches, however the containers were all intact. Cover plates for the acceptor containers have traveled up to 100 feet. In all cases to date, the explosives have remained within 5 feet of the test frame. Some charges have remained within the containers. As expected, the donor charge containers have been completely destroyed. Acceptor charges have received minor damage, and in no case has a reaction occurred.

### ANALYSIS

Since the test assemblies were designed for the worst case scenario of the non-propagating storage cabinet, each of the eight acceptor containers of each test assembly is considered to be one test. Ninety-six tests will have been evaluated after the 12th shot has been completed.

As previously discussed, the purpose of the additional testing was to establish a level of confidence considered acceptable for allowing the use of the non-propagating storage cabinets. Figure 3 shows a curve which has been developed to indicate the level of confidence associated with the testing being performed. The x-axis of this curve reflects the percent of the test containers that could show evidence of propagation. The y-axis shows the probability or confidence level that the propagation rate selected or less would be exhibited.

The curve of Figure 3 is based on a statistical approach of random sampling without replacement. The universe size assumed was for over 2000 cabinets with a sample

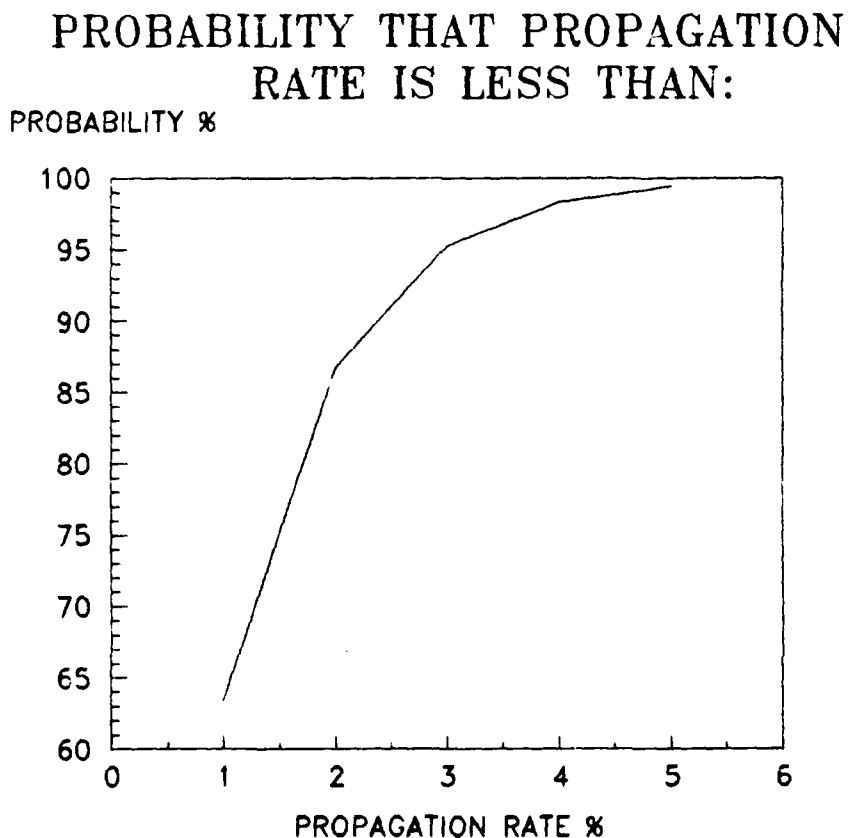


FIGURE 3. CONFIDENCE LEVEL CURVE

size of 100 having no failures (no acceptor charge exhibiting a reaction). For the tests being performed, this curve indicates a confidence level of 99.4% that less than 5% of more than 2000 cabinets would propagate from an accidental detonation within the cabinet.

This level of confidence when considered with the fact the worst case scenario was used for the tests and the tests were performed at 125% of the rated capacity of the storage cabinets, is considered to be adequate for considering the non-propagating storage cabinet design acceptable.

Additional testing could be performed to raise the level of confidence. For example, using the same statistical approach as used for Figure 3, a 99.3% confidence level could be obtained that less than 1% of over 2000 cabinets would propagate, provided that 500 tests were performed without having any propagation.

Funds were not available to perform 500 tests under this project; however the confidence level achieved by the testing performed is considered satisfactory by the authors.

# LARGE SIZE PROTECTIVE DOOR - PART I : STRUCTURAL DETAILS

Dr.-Ing. K-L. FRICKE

Engineering Office KONSTRUKTIV, Hannover, GERMANY

## ABSTRACT:

A new type of protective door was developed for a series of new aircraft shelters of the LUFTWAFFE, the German Airforce. The door was submitted to a rigorous weapon effect testing, which it held out fairly well. More about that in Part II. It therefore seemed senseful to present this door in its technical details to this symposium as a team of experts and to discuss the design at its essential points. This will happen by means of a series of 20 pictures including short comments.

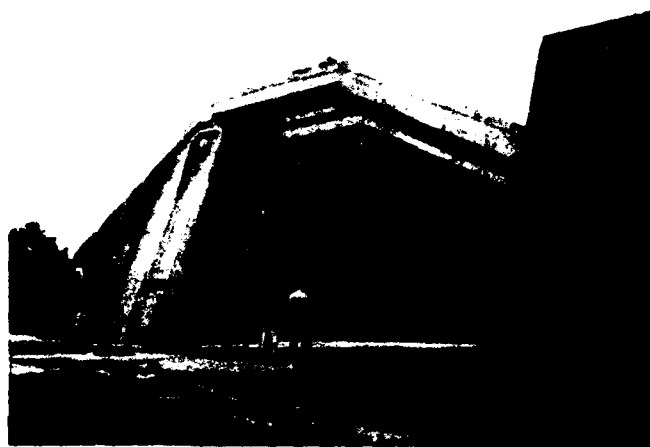


Fig.2 Door, right hand leaf opened

## 1 STRUCTURAL TASK

The task, which the design group was entrusted with, was to close an outline of 22m width and 6.5m height with a protective door.

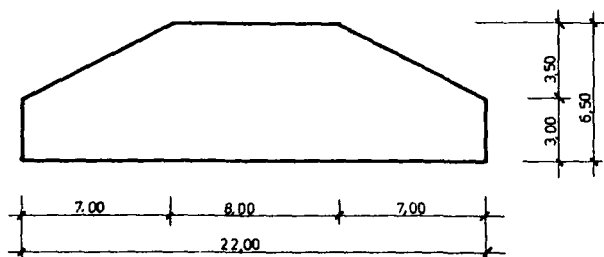


Fig.1 Outline of Required Opening

The protectional requirements for the door were the same as for walls and roof of the shelter. Colonel Russwurm will give some more details on this item. And the door would be exposed to direct weapon effect. Consequently it would be a heavy door.

## 2 DESIGN

### 2.1 Initial History

First of all a couple of alternative concepts were investigated. The falling down type of door was excluded first, because of its intense mechanism, which affords very special mechanical parts far away from any standard machinery. Some time was spent to find out the conditions for a hinged door of that size, the closing mechanism being hydraulic. The door itself and the mechanism was not the main problem. Instead the weight of one door leaf and its leverage lead to additional measures of a considerable extent on the side of the building in order to anchor the hinges and take up the forces. So this type of door was excluded, too. In the end the sliding door proved the most reasonable solution. In this we came to same conclusions as the U.S. design team of 3rd Generation door.



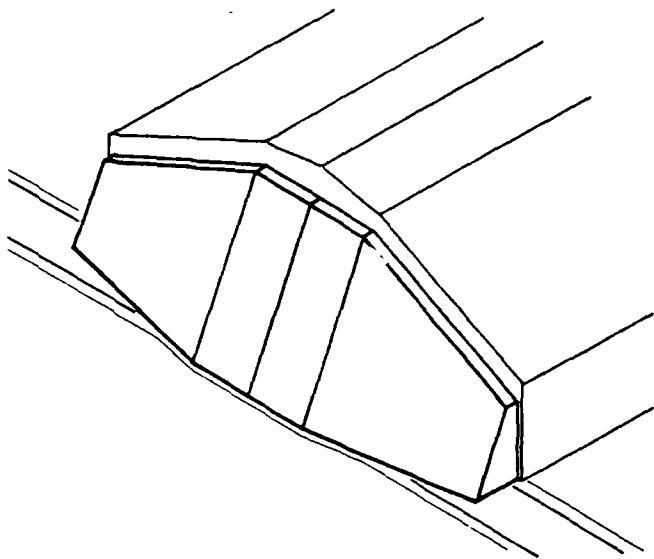


Fig.3 Geometrical Shape of the Door

## 2.2 Guidelines

The main guidelines for design were:

- to give protection for an opening of 22m\*6.5m, covering a couple of aircraft types, which are in use by NATO at present,
- to achieve a short opening time of 1 minute for alert conditions
- to use parts of normal industrial standards for electrical, mechanical equipment of the drive units and for the rails,
- to hide this all totally behind the protectional shield,



Fig.4 Interior of the Door

- to develop a shield in the shape of a steel box, filled up with concrete,
- to develop a continuous peripheral support mechanism, which would be effective against impact and rebound and which should beware the drive units from damage, as far as possible. As a minimum requirement the door should be able to be pulled open by truck after a severe weapon effect.

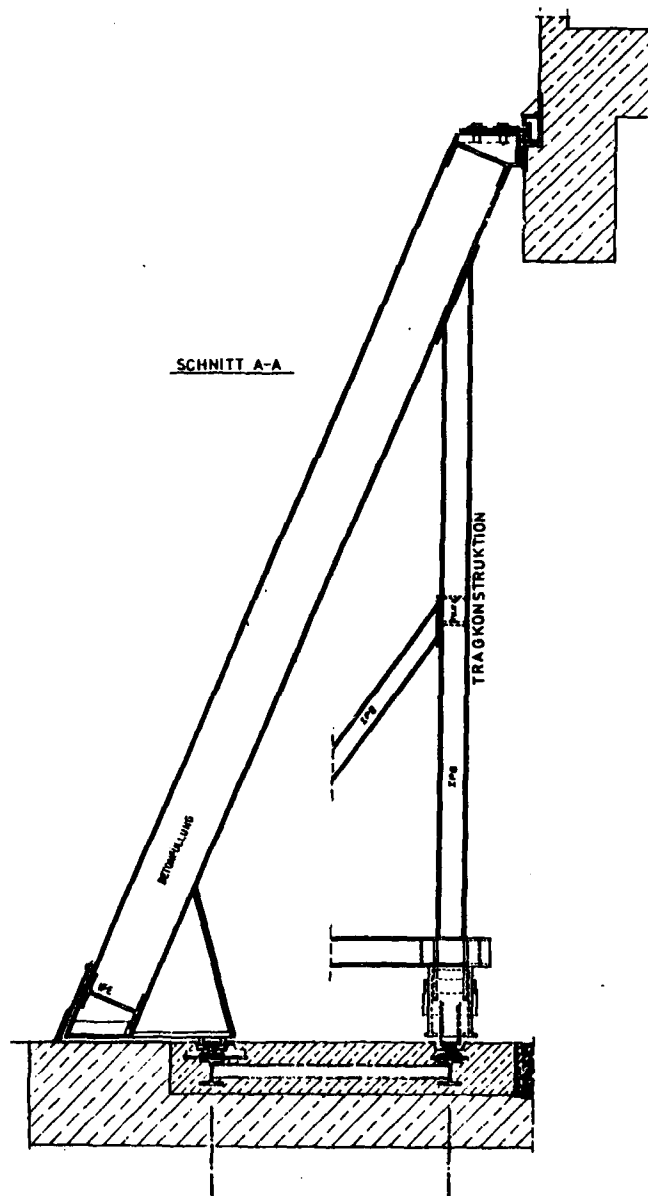


Fig.5 Section

### 3 STRUCTURAL SOLUTION

The structural solution will be discussed in view of 20 additional pictures. Thereby the following details will be addressed:

- 3.1 Shape of the Door
- 3.2 Door Drives
- 3.3 Shield
- 3.4 Bearing Structure
- 3.5 Supports
- 3.6 Fragment Shield
- 3.7 Foundation

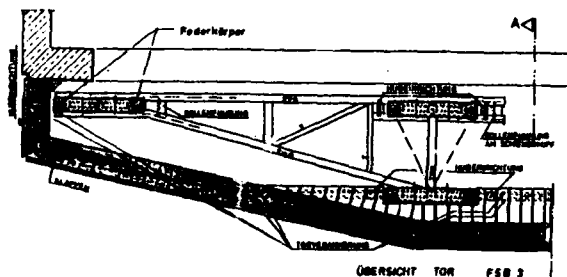
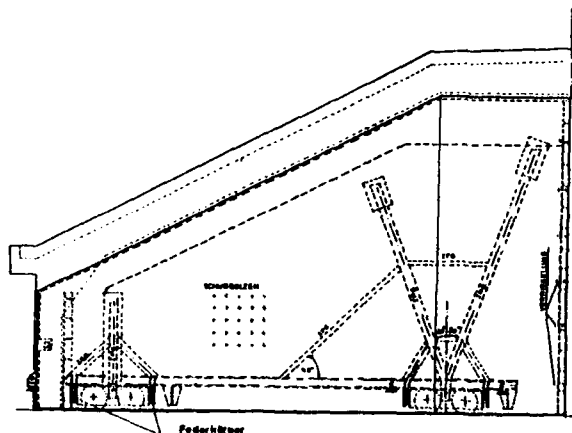


Fig.6 View and Plan



Fig.7 Foundation

### 4 FINAL REMARK

Cornel Russwurm will continue with the discussion of the weapon effects on the door. He will not mind, if this chapter is closed with the remark, that the door stood all the tests without any severe damage. It was a satisfactory experience to the design team, that the door could still be opened with its own drives after the most heavy test series.

## LARGE SIZE PROTECTIVE DOOR - PART II: BEHAVIOR UNDER DYNAMIC LOADING

D. RUSSWURM

### FEDERAL ARMED FORCES OFFICE FOR STUDIES AND EXERCISES SPECIAL INFRASTRUCTURE TASKS DIVISION

#### Abstract

In connection with an extensive protective structures program a large size protective door had to be developed. A mathematical solution only did not seem sufficient. Model tests did not promise good results, either.

Thus, full scale tests were conducted. The tests revealed that the task of developing and designing a protective door with a level of protection to meet a given threat has been fulfilled successfully.

#### 1. Background

Due to the complex nature of the new large size protective door, the in theory hardly predictable behavior of the opening and closing mechanisms, and the large number of protective structures to be equipped with this door, full-scale weapons effects tests were considered absolutely necessary. The Federal Armed Forces Office for Studies and Exercises - Special Infrastructure Tasks Division - therefore initiated tests to determine the protection level of these doors at the Proving Ground at Meppen.

#### 2. Test Program

A total of five explosive tests from different positions and seven live-fire tests have been conducted in the first phase.

A second phase has been established for live shots testing unguided rockets.

The following types of weapons have been used:

- SAPHEI - projectiles, 35mm caliber
- API - projectiles, 35mm caliber
- shells, 155mm caliber
- unguided rockets, small caliber
- GP - bombs
- bare charges

Phase 1 consisted of the following series:

- 3 rounds SAPHEI, impact velocity: 760 m/s
- 3 rounds API, impact velocity: 1350 m/s
- 1 round Shell, impact velocity: 600 m/s
- 5 static detonation tests with GP - bombs/  
bare charges at different stand-off dist.

Phase 2 consisted of the following series:

- 15 rounds of unguided rockets,  
impact velocity: 600 m/s

Pressure, acceleration, and strain have been recorded at several locations of the door during the detonation tests.

#### 3. Test results

##### 3.1. Phase 1

The SAPHEI-projectiles penetrated about 6.5cm while the API-projectile penetrated about 39 cm.

The artillery shell live shot resulted in a palm-sized pockmark in the front steelplate, the typical fragment impact crater pattern of a quick-fuzed projectile.

The door survived all detonation tests. The supporting construction showed no severe

deformations. The door system responded elastically and diverted the dynamic loads as desired.

The fragment crater dispersion was typical for the respective bomb stand-off distance. (Fig. 1) Fragments penetrated 15 to 25 cm dependent on the respective bomb stand-off distance.

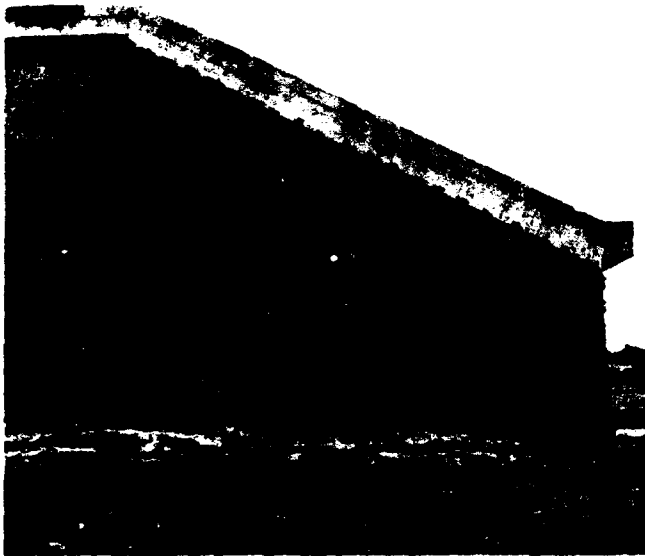


Figure 1 Fragment crater dispersion

The closest stand-off distance of the bomb resulted in a localized severe crushing of the concrete fill of the door. Simultaneously the back steel plate loosened at some points, some welded joints had separated and one of the motor blocks tilted and sagged (Fig. 2).

The door opened by means of its own motor except after the closest stand-off distance of the bomb detonation. In this case, however, the door was opened by means of the winch of an armored vehicle. Door operability was reestablished soon after.

### 3.2. Phase 2

Unguided rocket impact resulted in a palm-sized pockmark in the front steelplate, the typical fragment impact crater pattern of a quick-fuzed projectile (Fig. 3).

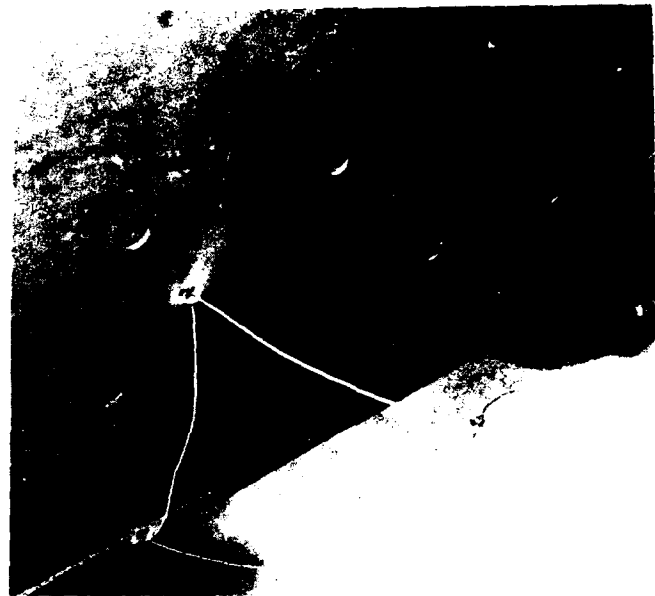


Figure 2 Back steelplate deformation



Figure 3 Palm-sized pockmark

#### 4. Conclusion

The door can be considered to have fully resisted the dynamic loads. In particular, diverting the dynamic loads through the door wing as a shell into the shelter arch and through the tongues into the rail foundation slab turned out to be very effective.

The overall response of the system was more or less elastic.

Structure and design of the door wing have proved reliable. The damage occurred locally in the immediate area of impact.

The near miss bomb detonation and the impact of the API-projectile, however, represent the load limit, which means that weaker design of the door will not be sufficient.

The supporting structure including the wheel assembly worked very well, too. With one exception, opening and closing after impact was possible for all other tests by means of the door's own motor.

# RESPONSE OF A BLAST VALVE TO SHOCK WAVES OF DIFFERENT DURATION

J. Hasler and H. H. Oppliger

Luwa Ltd. Filters + Shelter Equipment

CH-8152 Glattbrugg, Switzerland

## ABSTRACT

In the past there appeared to be some doubts as to whether a blast valve could equally well perform in a long-duration, relatively low-pressure environment associated with nuclear explosions and in the short-duration, high pressure environment of conventional explosions.

A test program with simulation of conventional and nuclear explosions in a shock tube was carried out to establish both, the threshold of failure and the efficiency of such valve as a function of reflected pressure and impulse.

Since the self-activated blast valve ESV-F offers an extremely short closing time due to low mass of moveable parts, practically no influence of the reflected impulse on the penetrating shock wave could be found. The threshold of failure shows a wide range of pressure between first signs of damage and real failure.

## BACKGROUND

During the last two or three decades self activated blast valves to protect mechanical systems and/or people from blast damage were developed. Nuclear threat was for a long time considered the main threat and therefore, the long-duration, relatively low-pressure environment associated with nuclear explosion was the main design criteria (500 to 1000 at 10 to 11 bar respectively 150psi reflected).

Changes in combat models and the increasing precision of weapon delivery systems put the onus back on conventional weapons and the question arose, whether such valves could equally well perform in the short duration (1 to 3ms) high pressure environment of conventional explosions.

## OBJECTIVE

In order to answer such questions, a test program was defined to

- establish the threshold of failure as function of reflected pressure and impulse.
- get to know the efficiency of the valve, that is pressure peaks and impulse behind the valve.

## TEST PROGRAM

Due to limited space and dense population in Switzerland, some restrictions regarding tests with explosives had to be considered. Therefore, three different test methods have been used to create shock waves of various pressures and impulses (Fig.1):

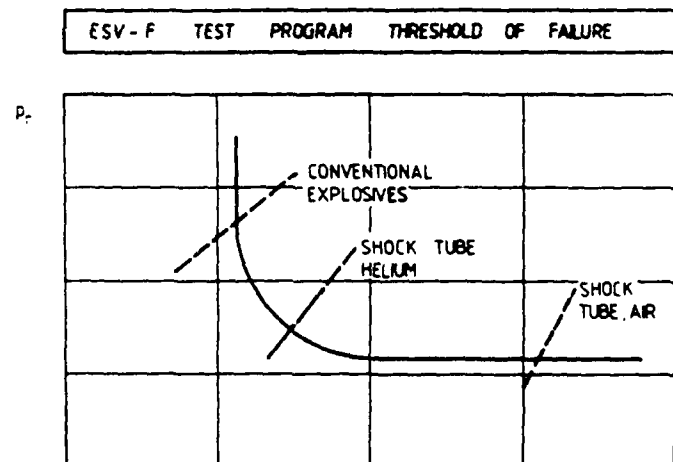


Fig.1

- an air driven shock tube to simulate nuclear explosions,
- a helium driven shock tube to simulate explosions of high conventional yields (5ms positive pressure phase),
- a detonation bunker (Fig.2) where conventional explosives up to 5kp were exploded (2ms positive pressure phase).

# ESV-F TEST PROGRAM CONVENTIONAL EXPLOSIVES

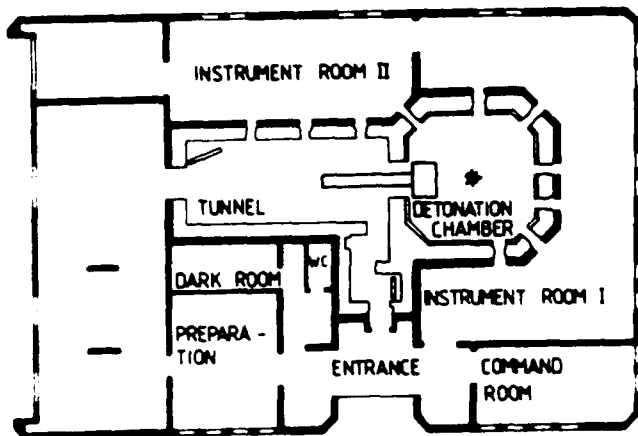


Fig.2

The penetrating shock wave was measured in an identical arrangement for all three test rigs. Reflected pressure and impulse were calibrated against the values of the incident shock wave, using a plate in lieu of the explosion protection valve.

During tests, incident and penetrating shock waves were recorded as well as damages to the valve.

The explosion protection valve ESV-F tested is self-activated by the blast wave. Steel plate springs close within approx. 1(ms) under pressure and reopen again when the pressure pulse has ceased, so air can pass through the valve for normal ventilation without a high pressure drop. The springs react to positive as well as to negative pressures.

The low mass of the springs led us to assume that a fast enough reaction also for short duration pulses was obtainable. The valve can handle 600 m<sup>3</sup>/h (350cfm) of air at 150 Pa (0.6 ins WG), corresponding to the air volume rate of the associated gasfilters used to protect the shelter inhabitants from chemical warfare agents. For larger air volume rates, the valves can be combined to larger units or even to complete valve walls. Although not subject of this paper, it is obvious that the installation of the valve has to be done so as to withstand such air pressure as well as associated ground shock.

## TEST RESULTS

### Threshold of failure

The rigidity of the explosion protection valve ESV-F is shown in Fig.3.

# ESV-F THRESHOLD OF FAILURE

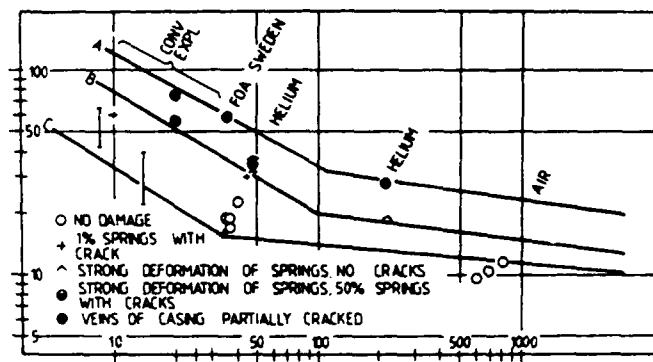


Fig.3

The lines A, B, C represent various grades of failure as a function of reflected pressure and impulse.

In the range between B and C, a small percentage (1%) of the springs may get minor cracks, however, without a negative effect on the valve. In the range between A and B, larger cracks in the springs may occur and the springs show strong deformations, resulting in a higher pressure drop across the valve, thus reducing the air volume rate by about 30% in normal ventilation mode. Blast attenuation, however, remains practically unimpaired.

At line A, cracks in the valve block start developing. However, the valve still can withstand further shock wave without being blown out and without failure regarding protection of the equipment behind. The reflected pressure of approx. 60bar (870 psi) and impulse of 40bar ms (580 psi ms) correspond to a free field explosion of 1000 lb GP-bomb in 4,5 m (15 feet) distance.

It is obvious that the valve must be protected against the effect of fragmentation by means of baffle plates. Better even by builders measures designed so as to reduce peak pressures to a level that the valve gets exposed to loads in the range of line C only and hence, full function without failure can be achieved even under such severe conditions.

The large difference between A and C representing a factor of 3-5 for reflected pressures shows the great insensitivity or "working capacity" of the valve which provides additional safety against unforeseen effects. This has in fact been proved in field tests in Turkey and at Tyndall Air Base where the valves despite of some minor damages from fragments remained fully operational.

# Penetrating shock wave

The test readings of the penetrating shock wave are shown in Fig.4, that is the log of impulse ( $i_r$ ) and pressure peak ( $p_s$ ) as a function of the reflected pressure and impulse. This data has been analyzed using multilinear regression of the logarithm.

$$\text{Log } p_s = A + B \text{ Log } p_r + C \text{ Log } i_r$$

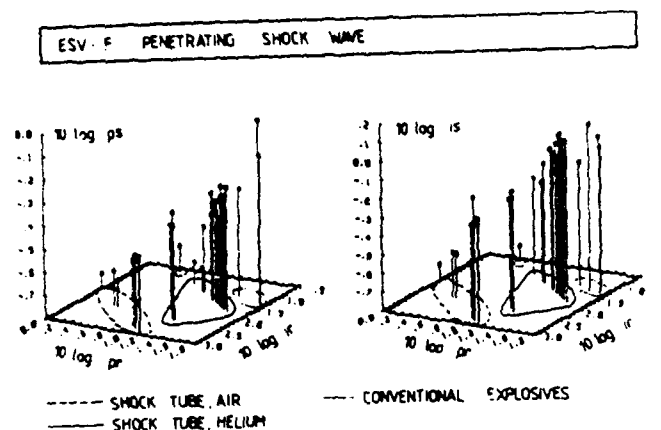


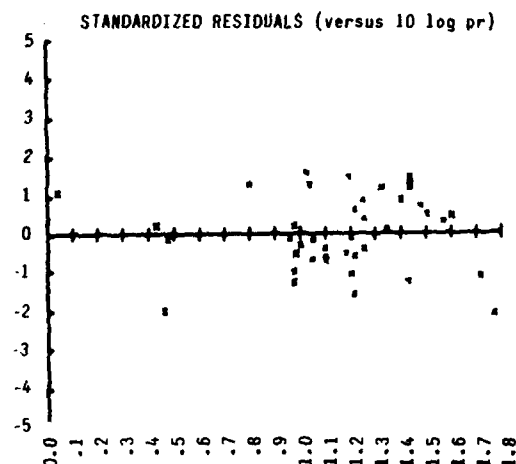
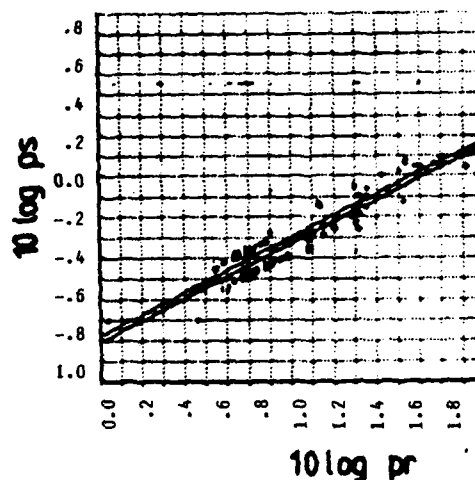
Fig.4

The pressure peaks behind the valve do not significantly depend on the reflected impulse, as shown in fig.5

The constant C has a 90% probability of - 0.049 to 0.013, therefore it was set to zero and the influence of the reflected impulse was neglected.

The best fit is hence given by  $p_s = 0.158 p_r^{0.539}$ .

# ESV - F PENETRATING SHOCK WAVE



$$p_s = 0.158 p_r^{0.539}$$

Fig.5

The impulse behind the valve shows a weaker dependance on the reflected pressure, but also a slight dependance on the reflected impulse see fig.6

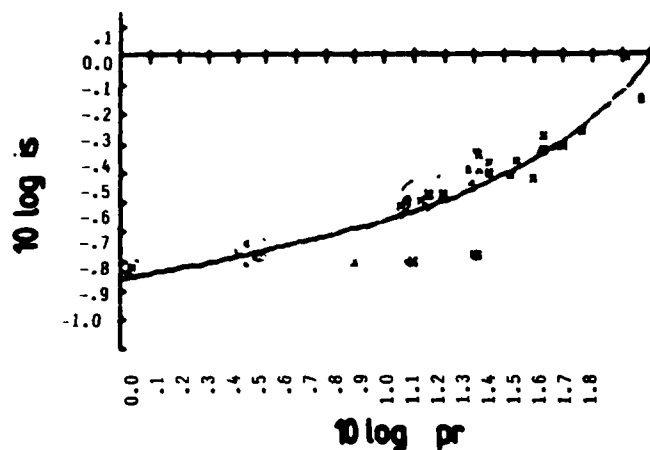
$$i_s = 0.1 p_r^{0.394} \cdot i_r^{0.029}$$

If we postualte a linear decrease of the pressure behind the valve with time, the time of the positive pressure phase can be deduced as

$$t_+ = 1.405 p_r^{-0.145} i_r^{0.029}$$



# ESV-F PENETRATING SHOCK WAVE



$$is = 0.111 pr^{0.394} \times ir^{0.029}$$

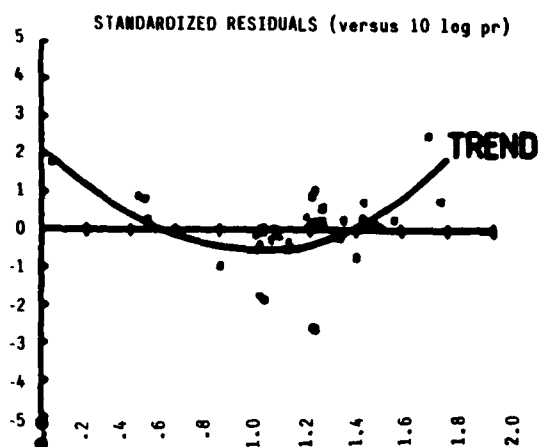


Fig.6

Therefore, the positive pressure phase decreases strongly with increased pressures, but increases slightly with increased impulse. Physically, the following explanation seems to be sensible (Fig.7)

# ESV-F INFLUENCE OF REFLECTED IMPULSE

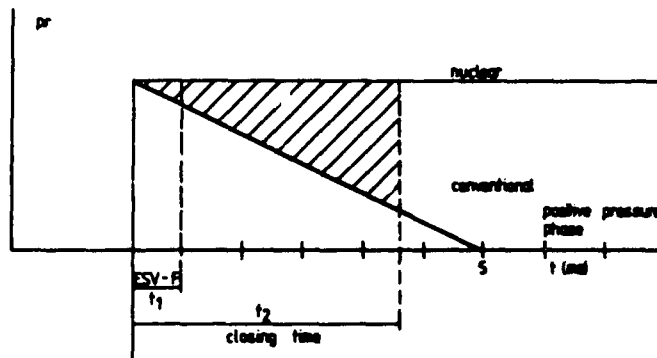


Fig.7

For a given reflected pressure, the penetrating impulse depends on both reflected impulse and closing time of the valve. If the valve has a long closing time, there is a strong influence from the reflected impulse, because of the considerable difference between the nearly rectangular nuclear pulse and the conventional triangle pulse. On the other hand, if the valve has an extremely short closing time like the ESV-F valve tested, practically no influence on the values behind the valve exist, which has been proven by the tests.

To completely specify the efficiency of an explosion protection valve, the documentation according to Fig.8 has been chosen. These two diagrams provide full information on the values behind the valve and the threshold of failure in relation to the reflected shock wave in front of the valve.

# ESV-F PENETRATING SHOCK WAVE

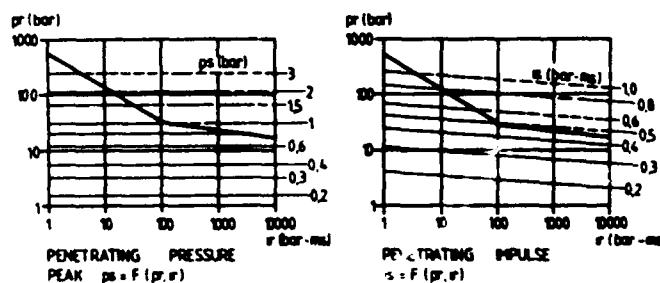


Fig.8

#### SUMMARY

The above test series clearly shows that the blast valve ESV-F originally designed for long-duration and relatively low-pressure environment associated with nuclear explosion equally well works in a conventional blast environment. This provides the designer of shelters with an excellent tool to optimize air in- and outlet configurations.

#### ACKNOWLEDGMENT

We acknowledge the official and professional support of the Test Laboratory in Spiez of the Swiss Defence Technology and Procurement Group (GRD) and

Messrs. Basler & Ptns. Engineers. Zurich who provided the computer based calculations and graphs of the valve characteristics.

## RATE EFFECT ON MIXED-MODE FRACTURE OF CONCRETE

S. P. Shah

Professor of Civil Engineering and Director, NSF Science and Technology Center for Advanced Cement-Based Materials

Northwestern University  
Evanston, IL 60208

### ABSTRACT

Small-scale reinforced concrete specimens were subjected to cyclic loading at rates ranging from 0.0025 Hz to 2.0 Hz. It was observed that the tendency of shear cracking increased with an increased rate of loading. To better analyze the effect of rate of loading on reinforced concrete, an analytical and experimental investigation of mode I (tensile) and mixed mode (combined tensile and shear) fracture of plain concrete subjected to impact loading was conducted. The rate of loading ranged from slow strain rate of  $10^{-6}$  per second to impact strain rate of 0.5 per second. Mixed mode tests were conducted using beams with notches at different locations along the span of the beam. A nonlinear fracture mechanics model was developed to predict the rate sensitivity of mode I and mixed mode fracture of concrete. The predicted results of the proposed model correlated well with the experimental results. Mixed mode experimental and analytical results indicate that impact loading could result in brittle diagonal tension-shear failure of concrete structures as opposed to ductile flexural failure at slow rates of loading.

### INTRODUCTION

Modern computer-aided analysis and use of concrete for special structures such as reactor containment vessels and missile storage silos, have led to a growing interest in the cracking behavior of concrete. Such concrete structures are also likely to be subjected to short duration impulsive and impact loads in addition to static loads.

Previous studies which have been done by several investigators show some influence of monotonically increased dynamic rates [1,2] and some influence of cyclic loading rates [3]. Explosive tests conducted by U. S. Army Waterways Experiment Station on buried reinforced concrete box structures [1] as well as tests conducted by several investigators on reinforced concrete beams loaded at varying rates [2] showed that concrete structures designed to fail in a ductile manner (flexural failure) under slower rates may fail in a brittle manner (shear failure) at higher rates. Reinforced concrete members were tested by Mutsuyoshi and Machida at three different cyclic loading rates, 0.1, 10 and 100 cm/second. It was observed that members subjected to a faster rate of loading failed in a relatively brittle

manner as compared to members subjected to a slower rate of loading. Therefore, it is apparent that the mechanism of failure can be altered by the change of loading rate. However, the previous studies do not reveal the reasoning for the effect of the loading rate on the behavior of reinforced concrete members.

In this study, small-scale reinforced concrete specimens subjected to cyclic loading were tested at rates varying from 0.0025 Hz to 2.0 Hz in order to investigate the effects of several variables including loading rate, shear span to depth ratio ( $a/D$ ) and stirrup spacing.

To predict the rate dependent failure mechanisms in reinforced concrete structures the knowledge of effect of rate of loading on fracture of plain concrete is essential. In general, the fracture of concrete in reinforced concrete elements occurs under combined mode I and mode II loading conditions. This paper discusses the experimental and analytical investigation of the effect of impact loading on mixed mode (modes I and II) fracture of plain concrete.

### SMALL-SCALE REINFORCED CONCRETE SPECIMENS

In order to study the effect of rate of loading, twelve specimens were tested. The test set-up is shown in Fig. 1 whereas the details of reinforcing for a set of specimens are shown in Fig. 2. The test variable included: spacing and stirrups, the shear-span to the depth of the specimen ratio and the rate of cyclic loading (from 0.0025 Hz to 2 Hz). The specimens were subjected to reversed cyclic loading. The maximum amplitude (in terms of deflection-ductility ratio) of cyclic loading ranged from deflection-ductility ratio of 1 to 16. Some of the specimens had reinforcing bars which were grooved to enable the measurement of strain distribution in the bar. The performance of these small-scale specimens at slow rate of loading were satisfactorily compared with the results of large-scale specimens tested by other researchers at comparable slow rate of loading. The details of this comparison as well as other details are given in Ref. 4.

Effect of loading rate on mode of failure is illustrated in Fig. 3. In this figure, crack patterns for 3 sets of specimens are shown. The specimens in each set had the same shear-span to depth ratio and identical stirrup spacing, and were sub-

jected to the same loading history. For each pair of specimens shown, the one to the right was subjected to a faster rate of loading. From such comparisons it was observed that for all fast rate specimens, diagonal shear cracks emerge at an earlier stage of loading than for the corresponding slow rate specimens. The slow rate specimens in general had a larger number of widely distributed cracks as compared to those for the fast rate specimens.

#### MIXED-MODE FRACTURE STUDY

To explore the reasons why the reinforced concrete specimens tested at a faster rate of loading had proclivity at diagonal shear cracking, fracture mechanical type of study was conducted on plain concrete (Ref. 5). A single geometry proposed by Jenq and Shah was tested in this study (Fig. 4). The mode of failure depends on the location of the notch. The location of the notch is defined by  $\gamma$ . The value of  $\gamma = 0$  corresponds to pure mode I configuration (flexural cracking). A value of  $\gamma$  other than zero can result either in a mixed mode failure at the notch tip (diagonal shear cracking) or tension failure at the midspan depending on the values of  $\gamma$  and the depth of the notch ( $a$ ). The main advantage of using this geometry is the ease with which both mode I and mixed mode conditions could be simulated under static and impact loading conditions.

A finite element analysis of the specimen was conducted using quarter-point singular crack tip elements to determine the stress intensity factors at the crack tip [6-9]. The finite element program used in this study was originally developed by Jenq and Shah [10]. To check the validity of this method, the FEM solutions for pure mode I and mode II cases were compared with the 'exact' solutions from the handbook [11]. The FEM solutions correlated well with the results from the handbook.

Using this finite element program, the effect of various locations and depths of the notches on  $K_I$ ,  $K_{II}$ , CMOD and CMSD (crack mouth opening and sliding displacements) were determined. Typical meshes used for the mixed mode case are shown in Fig. 5. Finite element results indicated that the mode I geometry correction factors for the specimens used in this investigation were almost the same as that of specimens with  $L/D=4$  [5,12].

Slow rate ( $<10^{-2}$ /sec) bending tests were conducted using a 20-kip MTS closed loop testing system. The crack opening displacement (COD) was measured using the specially developed clip gage and the midspan deflection was measured using a MTS extensometer described in Ref. 13. For closed-loop testing, either COD or midspan deflection was used as the feedback signal depending on whether the specimen was expected to fail at the notch or at the midspan. Impact tests were conducted using the instrumented modified Charpy impact testing system [5,14]. The guidelines proposed by Gopalaratnam, Shah and John [14] were followed so as to obtain reliable impact load results devoid of inertial effects.

For all tests, applied load, COD, and strain at notch tip or midspan were measured. Midspan deflection was measured for all slow rate tests. A 4-channel digital oscilloscope (Nicolet 4094) with two 2-channel differential amplifier units of high resolution and frequency (up to 500 nanoseconds per point sampling rate) were used to store the data. The data were then transferred directly to an IBM-AT for further analysis of results.

#### STRAIN RATE EFFECTS ON MODE I FRACTURE

Consider a single edge notched beam subjected to three point bending as shown in Fig. 6. The corresponding LEFM equations are [10,15]:

$$K_I = \sigma \sqrt{\pi a F(\alpha)} \quad (1)$$

$$CMOD = \frac{4\sigma a}{E} \cdot V_1(\alpha) \quad (2)$$

$$COD(X) = CMOD \cdot z(\alpha, \beta) \quad (3)$$

in which

$$\sigma = \frac{3PL}{2BD^2} \quad (4)$$

$$F(\alpha) = \frac{1.99 - \alpha(1-\alpha)(2.15 - 3.93\alpha + 2.7\alpha^2)}{\sqrt{\pi(1+2\alpha)(1-\alpha)^{3/2}}} \quad (5)$$

$$V_1(\alpha) = 0.76 - 2.28\alpha + 3.87\alpha^2 - 2.04\alpha^3 + \frac{0.66}{(1-\alpha)^2} \quad (6)$$

$$Z(\alpha, \beta) = [(1-\beta)^2 + (-1.149\alpha + 1.081)(\beta - \beta^2)]^{1/2} \quad (7)$$

Note that  $P, L, B, D, a, x, COD(x)$  and  $CMOD$  are defined in Figure 6,  $\alpha = a/D$ ,  $\beta = x/a$ , and  $E$  = Young's modulus.

A typical load-COD response obtained at 'static' rate of loading is shown in Figure 7. The test was COD controlled. Substantial prepeak nonlinearity can be seen in this figure. Jenq and Shah [15], Bazant [16], and Hillerborg et al. [17] have proposed various models to take into account this prepeak nonlinearity for proper application of fracture mechanics to concrete. The Two Parameter Fracture Model (TPFM) proposed by Jenq and Shah [15] was used for analysis in this investigation.

The Two Parameter Fracture Model utilizes the compliance based estimation of prepeak stable crack growth (also often termed slow crack growth or fracture process zone). A schematic of the load-COD response is shown in Figure 8. By rearranging Eqn. 2 the expression for compliance,  $C$  is obtained as:

$$C = \frac{CMOD}{P} = \frac{6La}{BD^2E} \cdot V_1(\alpha) \quad (8)$$

From Figure 8, the compliance values in the initial stage (linear range) and at the peak load are obtained as  $C_i$  and  $C_u$ , respectively. The Young's modulus,  $E$  of the specimen can be calculated by substituting  $C = C_i$  and  $a = a_0$ , the initial notch depth in Equation 8. Then substituting this value of  $E$  and  $C = C_u$  in Equation 8, the effective crack length at the peak load,  $a = a_p$  can be obtained. Thus the stable precritical crack growth in this case is equal to  $\Delta a_p = a_p - a_0$ . Then using  $a = a_p$  in Equations 1-3, critical stress intensity factor,  $K_{Ic}$ , and critical crack tip opening displacement,  $CTOD_c$  can be determined. To calculate  $CTOD_c$  using Equation 3, one should use  $a = a_p$  and  $x = a_0$ , since  $CTOD = COD$  at the original crack tip. Jenq and Shah [15] showed that  $K_{Ic}$  and  $CTOD_c$  thus determined are essentially size independent fracture parameters. Knowing  $K_{Ic}$  and  $CTOD_c$ , one can determine the peak stress for any structure using equation similar to Equations 1-3 for both notched and unnotched ( $a_0 = 0$ ) specimens.

In this investigation, the strain rate effects on the two fracture parameters,  $K_{Ic}$  and  $CTOD_c$ , and Young's modulus,  $E$  were determined. The experimentally observed effect of strain on  $E$ ,  $K_{Ic}$  and  $CTOD_c$  is shown in Figures 9, 10 and 11, respectively. Young's modulus was found to be relatively rate-independent in the strain rate range of  $10^{-6}$  to 0.5 per second; the increase at  $\dot{\epsilon} = 5/\text{sec}$  is only about 10% of average at the slowest rate (see Figure 9). This trend of relatively rate independent  $E$  was also reported by Gopalaratnam and Shah [13] in flexure, Tinic and Bruhwiler [18] in tension, and Vila and Hamelin [19] in compression. It should be noted that Reinhardt [20] reported that the value of  $E$  increases by about 25% at a strain rate of 1.0 per second based on impact tensile tests. Similarly  $K_{Ic}$  was also observed to be relatively rate independent in the strain rate range of  $10^{-6}$  to 0.5 per second as shown in Figure 10. In contrast,  $CTOD_c$  was observed to decrease with increasing strain rates as shown in Figure 11.

The experimental results obtained in this investigation confirm the assumptions of the rate sensitive fracture mechanics model proposed by John, Shah and Jenq [21]. This model was based on the observation that the prepeak nonlinearity may be attributed to prepeak stable crack growth and that this prepeak crack growth decreases with increase in rate of loading.  $K_{Ic}$  and  $E$  were assumed to be rate independent, and  $CTOD_c$  was assumed to decrease with increasing logarithm of strain rate as given by the following equation.

$$CTOD_{ci} = CTOD_{cs} \cdot \exp[-A(\bar{\epsilon})^B] \quad (9)$$

$$\bar{\epsilon} = \log(\dot{\epsilon}_{imp}/\dot{\epsilon}_{stat}) \quad (10)$$

in which

$\dot{\epsilon}_{stat}$  = static strain rate ( $10^{-7}/\text{sec}$ )

$\dot{\epsilon}_{imp}$  = impact strain rate,  $\dot{\epsilon}_{imp} \geq \dot{\epsilon}_{stat}$

$CTOD_{cs}$  =  $CTOD_c$  at  $\dot{\epsilon}_{stat}$

$CTOD_{ci}$  =  $CTOD_c$  at  $\dot{\epsilon}_{imp}$

$$A = A_1 \sqrt{E_c}$$

and  $A_1$  and  $B$  are empirical constants ( $= 0.048$  and  $3.65$ , respectively). Equation 9 compared well with the data as shown in Figure 11.

#### STRAIN RATE EFFECTS ON MIXED MODE FRACTURE

**Crack Initiation and Propagation:** For crack initiation and propagation analysis, the maximum energy release rate criterion developed by Hussain et al. [22] was used. The first step in the analysis involved calculation of  $K_{II}/K_I$  at the tip of the initial notch. Using this value of  $K_{II}/K_I$  and the maximum energy release rate theory [22], the initiation angle was determined. In the next stage, the crack was propagated at this angle given by the maximum energy release rate theory as shown in Figure 5 (bottom).  $K_I$  and  $K_{II}$  were then evaluated at the current crack tip.  $K_{II}$  was always equal to zero at the tip of the propagating crack. This corresponded to zero initiation angle [22]. The crack was then propagated along the previous crack plane, i.e. continued in a straight line. The crack propagation predicted using LEFM theory is shown as dashed lines in Figure 12. The predicted crack initiation angle and crack propagation path compared reasonably well with the experimental results as shown in this Figure. Arrea and Ingraffea [23], and Jenq and Shah [10] also reported that LEFM is adequate for predicting crack initiation and propagation path in concrete.

#### Final Failure Location:

For the simple mixed-mode beams tested in this investigation, there are two possible locations of failure, i.e., positions 1 and 2 in Figure 13 [10]. When  $\gamma < \gamma_t$ , the failure always occurs at the notch tip, and when  $\gamma > \gamma_t$ , the failure would occur at the midspan. When  $\gamma = \gamma_t$ , the failure could occur at either the notch tip or the midspan.  $\gamma_t$  is termed as the 'transition stage'.

The experimental transition stage is identified in Figure 14, in which the observed failure locations are shown for various locations of the notch and two rates of loading (slow and impact). The transition stage,  $\gamma_t$  corresponds to  $x = 1 \frac{3}{16}$  inches and  $15/16$  inches at slow and impact rates, respectively. At the transition stage, the measured peak load corresponding to failure at the notch tip was the same as that corresponding to failure at the midspan. Many trial tests were done to identify

this transition point. The effect of rate of loading on the transition point can also be seen in Figure 14. Note that for the values of  $\gamma$  between 0.7 and 0.77, the failure occurred at the notch at impact rates whereas for slow rates the failure occurred at midspan.

#### Analysis of Mixed Mode Fracture:

The model proposed for mode I fracture (discussed earlier) was extended for rate sensitive mixed mode fracture of concrete. The approach followed here is an extension to that proposed by Jenq and Shah [10] for slow rate of loading. A mixed mode stress intensity factor ( $K$ ) was defined as the vectorial sum of  $K_I(\theta)$  and  $K_{II}(\theta)$

$$K = [K_I^2(\theta) + K_{II}^2(\theta)]^{1/2} \quad (11)$$

in which  $\theta$  is the crack initiation angle, and  $K_I(\theta)$  and  $K_{II}(\theta)$  are the angular stress intensity factors and  $\theta$  is defined by the maximum energy release rate theory [22]. Consider the deformed shape of the notch with a propagating branch as shown in Figure 15. Crack tip displacement (CTD) is defined as the vector sum of crack tip opening displacement (CTOD) and crack tip sliding displacement (CTSD) as follows (Figure 15):

$$CTD = [CTOD^2 + CTSD^2]^{1/2} \quad (12)$$

Similarly, crack mouth displacement (CMD) is defined as follows:

$$CMD = [CMOD^2 + CMSD^2]^{1/2} \quad (13)$$

The two fracture parameters in this case are  $K_C$  and  $CTD_C$  (critical mixed mode stress intensity factor and critical crack tip displacement), which can be determined from a mode I test. The mode I test ( $\gamma = 0$ ) is a special case of mixed mode failure. Hence

$$K_C = K_{IC} \quad (14)$$

and

$$CTD_C = CTOD_C \quad (15)$$

Using the finite element analysis described earlier, LEFM equations similar to Equation 1-3 were formulated for  $K_I$ ,  $K_{II}$ ,  $CMOD$ ,  $CMSD$ ,  $CTOD$  and  $CTSD$  as functions of location of the notch ( $\gamma$ ) and crack length ( $a$ ). These equations coupled with Equations 11-13 formed the basic equations that were solved in an iterative manner to obtain the peak load and effective crack growth at the peak load simultaneously satisfying the conditions  $K = K_C$  and  $CTD = CTD_C$ . To include the rate effect on mixed mode fracture  $K_C$  and  $E$  was assumed to be rate independent, and  $CTD_C$  was assumed to decrease with increase in rate of loading as given by Equations 9 and 10.

The predicted and measured peak loads values are plotted versus the location of the notch ( $\gamma$ ) in Figure 16. The theory predicted the observed trends satisfactorily. As the notch was moved away from the midspan, the peak load increased gradually and when  $\gamma$  was equal to or greater than  $\gamma_t$ , the beam

failed at the midspan. When the  $\gamma$  was greater than  $\gamma_t$  the beam failed as if the notch did not exist, as indicated by the plateau in the peak load versus  $\gamma$  plot in Figure 15. The peak loads plotted at  $\gamma = 1.0$  correspond to unnotched beam specimens.

The rate effect on the transition point is also predicted by the theory as shown in Figure 16. From the experimental results plotted in Figure 16, it can be seen that when the notch was located between  $\gamma$  equal to 0.70 and 0.77 failure occurred at the notch tip under mixed mode conditions at impact rate in contrast to mode I failure at the midspan at slow rate of loading. This phenomenon coupled with the experimentally observed localization of bond stress at higher strain rates [4] could result in a brittle diagonal tension-shear failure of beams at impact rates as opposed to ductile flexural failure at slow rates of loading.

#### CONCLUSIONS

1. Reinforced concrete specimens subjected to a faster rate of loading showed more propensity for shear cracking.
2. The effect of rate of loading (slow to impact rates) on the mode I fracture parameters was experimentally measured. Based on these observations a rate sensitive fracture mechanics model was proposed.
3. The impact loading effects on mixed mode fracture of concrete was investigated using three-point bend specimens with notches offset from the midspan. The model proposed for mode I fracture was extended to predict the rate sensitive mixed mode failure.
4. This study confirms that LEFM is adequate to predict the crack initiation and crack propagation in concrete, as also shown by other investigators.
5. Experimental and theoretical results from this study imply that structures designed to fail in a ductile manner (flexural failure) at slow rates could fail in a brittle manner (diagonal tension-shear failure) at impact rates of loading.

#### ACKNOWLEDGEMENT

The research reported here was supported, in part, by the U.S. Air Force Office of Scientific Research through a program managed by Dr. Spencer T. Wu.

#### REFERENCES

1. Kiger, S.A., and Getchell, J.V., "Vulnerability of Shallow-Buried Flat Roof Structures," Tech. Report SI-80-7, Report 1, 2, and 3, U.S. Army Engineer Waterways Experiment Station, September 1980.
2. Mutsuyoshi, H. and Machida, A., "Properties and Failure of Reinforced Concrete Members Subjected to Dynamic Loading," Transactions of the Japanese Concrete Institute, Vol. 6, 1984, pp. 521-528.
3. Mutsuyoshi, H. and Machida, A., "Behavior of Reinforced Concrete Members Subjected to Dynamic Loading," Concrete Library of JSCE No. 6, December 1985, pp. 51-68.
4. Chung, L., "Effects of Loading Rate on Response of Reinforced Concrete Model Beam-Column Joints and Anchorage-Bond," Ph.D. Thesis, Department of Civil Engineering, Northwestern University, 1987, 245 pp.

5. John, R., "Mixed Mode Fracture of Concrete Subjected to Impact Loading," Ph.D. Thesis, Northwestern University, Evanston, IL, 1988.
6. Barsaoum, R.S., "On the Use of Isoparametric Finite Elements in Linear Elastic Fracture Mechanics," *International Journal of Numerical Methods in Engineering*, V. 10, pp. 25-37, 1976.
7. Ingraffea, A.R., "Numerical Modeling in Fracture Propagation," in *Rock Fracture Mechanics*, edited by R.P. Rossmanith, published by The International Center for Mechanical Sciences, Udine, Italy, 1983.
8. Ingraffea, A.R. and Manu, C., "Stress Intensity Factor Computation in Three Dimensions with Quarter Point Elements," *International Journal for Numerical Methods in Engineering*, V. 15, pp. 1427-1445, 1980.
9. Saouma, V.E. and Schwemmer, D., "Numerical Evaluation of the Quarter Point Crack Tip Element," *International Journal for Numerical Methods in Engineering*, V. 20, pp. 1629-1641, 1984.
10. Jenq, Y.-S., and Shah, S.P., "Mixed Mode Fracture of Concrete," *International Journal of Fracture Mechanics*, 38, p. 123-142 (1988).
11. Tada, H., Paris, P.C. and Irwin, G.R., *The Stress Analysis of Cracks Handbook*, Del Research Corporation, Hellertown, PA, 1976.
12. John, R. and Shah, S.P., "Effect of High Strength and Rate of Loading on Fracture Parameters of Concrete," in *proceedings of SEM-RILEM International Conference on Fracture of Concrete and Rock* (Eds. S.P. Shah and S.E. Swartz), Houston, TX, USA, June 1987.
13. Gopalaratnam, V.S. and Shah, S.P., "Properties of Steel Fiber Reinforced Concrete Subjected to Impact Loading," *ACI Journal*, Proceedings, V. 83, No. 1, pp. 117-126, 1985.
14. Gopalaratnam, V.S. and Shah, S.P., and John, R., "A Modified Instrumental Charpy Test for Cement Based Composites," *Experimental Mechanics*, SEM, V. 24, No. 2, pp. 102-111, June 1984.
15. Jenq, Y.-S. and Shah, S.P., "A Two Parameter Fracture Model for Concrete," *Journal of Engineering Mechanics*, ASCE, V. 111, No. 10, pp. 1227-1241, October 1985.
16. Bazant, Z.P., "Size Effect in Blunt Fracture: Concrete, Rock, Metal," *Journal of Engineering Mechanics*, ASCE, V. 110, No. 12, pp. 1666-1692, December 1984.
17. Hillerborg, A., Modeer, M. and Petersson, P.E., "Analysis of Crack Formation and Crack Growth in Concrete by Means of Fracture Mechanics and Finite Elements," *Cement and Concrete Research*, V. 8, pp. 773-782, 1976.
18. Inic, C. and Bruhwiler, E., "Effects of Compressive Loads on the Tensile Strength of Concrete at High Strain Rates," *Int. Journal of Cem. Comp. and Lightweight Conc.*, V. 7, No. 2, pp. 103-108, 1985.
19. Vile, M.D., and Hamelin, P., "Comportement au choc des betons et mortiers a matrices hydrauliques," in *Proceedings, 1st International Congress, RILEM-AFREM Combining Materials: Design, Production and Properties*, Vol. II, (Ed. J.C. Meso), Chapman and Hall, London, pp. 725-732, 1987.
20. Reinhardt, H.W., "Strain Rate Effects on the Tensile Strength of Concrete as Predicted by Thermodynamic and Fracture Mechanics Models," in *Cement Based Composites: Strain Rate Effects on Fracture*, Editors: S. Mindess and S.P. Shah, MRS Symposia Proceedings, V. 64, pp. 1-20, 1986.
21. John, R. and Shah, S.P., "A Fracture Mechanics Model to Predict the Rate Sensitivity of Mode I Fracture of Concrete," *Cement and Concrete Research*, Vol. 17, No. 2, pp. 249-262, March 1987.
22. Hussain, M.A., Fu, S.L., and Underwood, J.H., "Strain Energy Release Rate for a Crack under Combined Mode I and Mode II," *Fracture Analysis*, ASTM, STP 560, pp. 2-28, 1974.
23. Arsee, M., and Ingraffea, A.R., "Mixed Mode Crack Propagation in Mortar and Concrete," Department of Structural Engineering Report 81-13, Cornell University, NY, 1981.

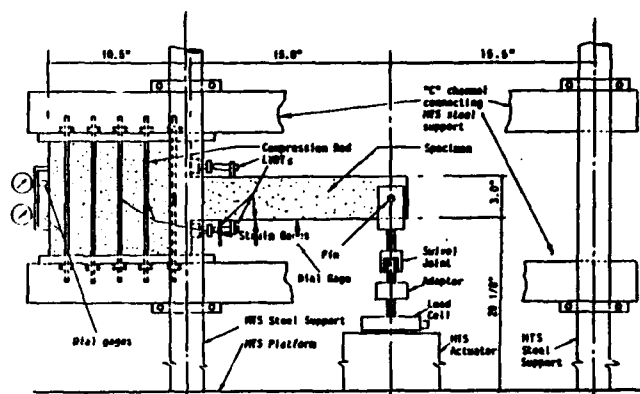


Figure 1. Test Set-up for Reinforced Concrete Specimen (1 in. = 25.4 mm).

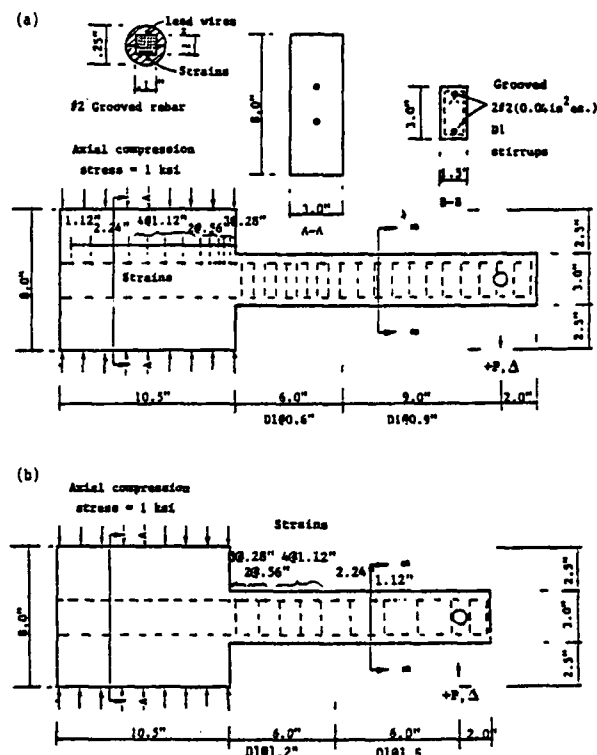


Figure 2. Reinforced Concrete Specimen-Design.

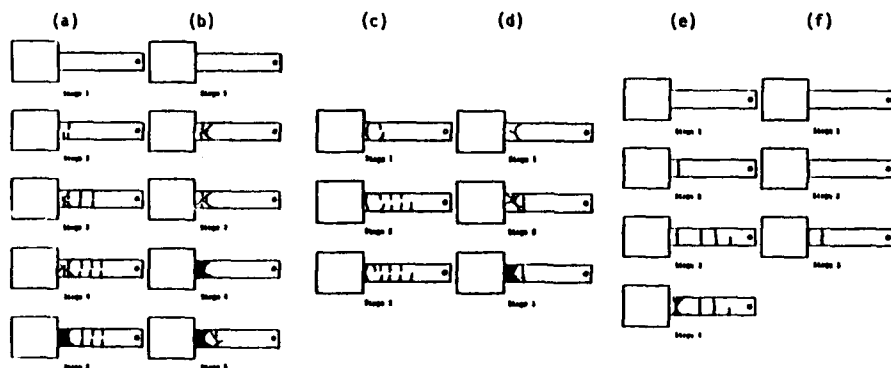


Figure 3.

Failure Modes of Reinforced Concrete Specimens. Note that the specimens (b), (d) and (f) were subjected to faster rate of loading as compared to the specimens (a), (c) and (e).

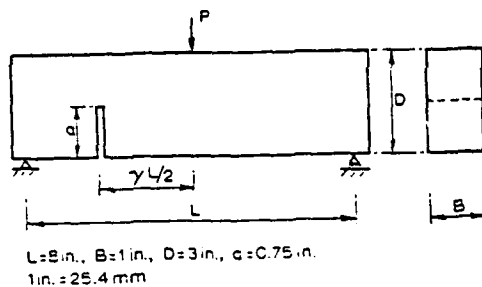


Figure 4. Testing configuration for mixed mode tests.

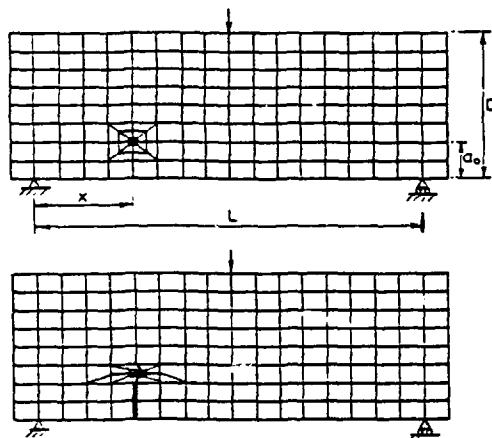


Figure 5. Typical finite element mesh for mixed mode beam subjected to three point bending (top) and for specimen with kinked crack (bottom).

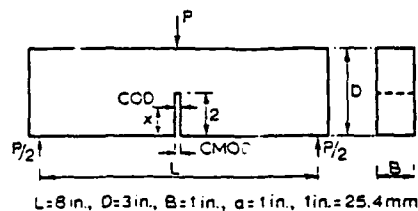


Figure 6. Typical single edge notched beam (SENB) subjected to three point bending.

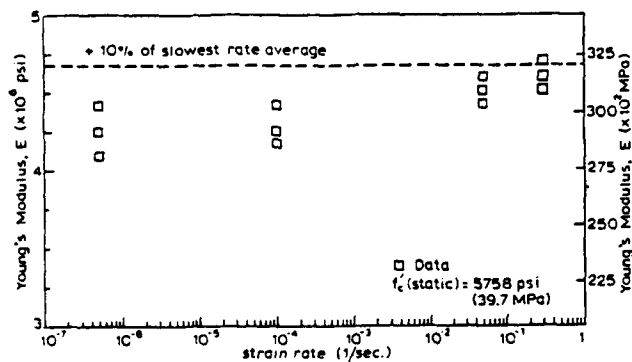


Figure 9. Variation of Young's Modulus with strain rate.

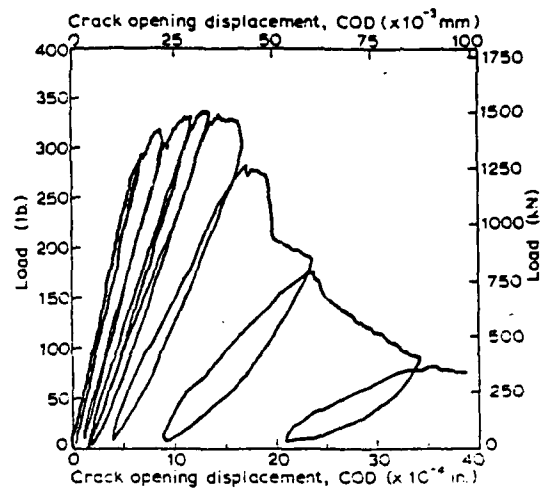


Figure 7. Typical load versus crack opening displacement plot for a single edge notched concrete beam mode I test.

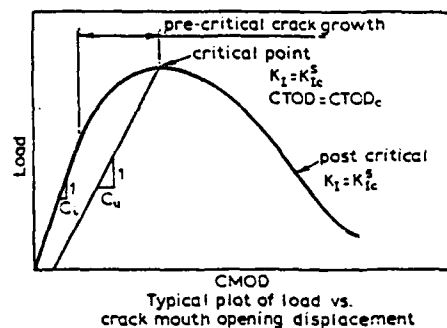
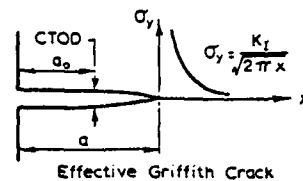


Figure 8. Two parameter fracture model (TPFM) [15].

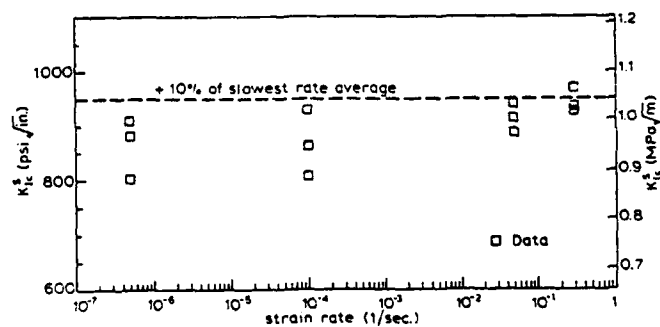


Figure 10. Variation of  $K_{Ic}^S$  with strain rate.



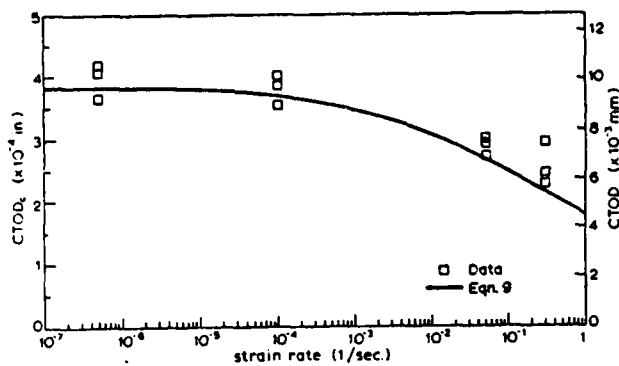


Figure 11. Decrease of  $CTOD_c$  with increasing strain rate.

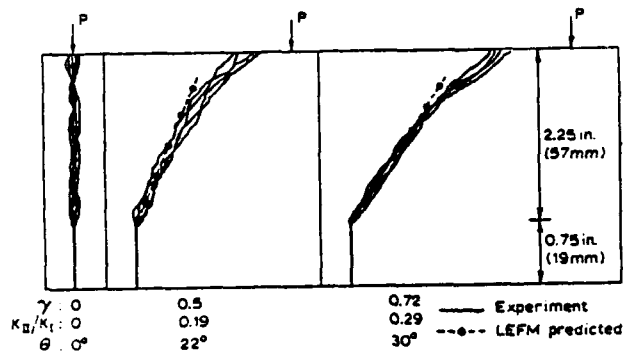


Figure 12. Experimental and predicted crack paths for impact specimens.

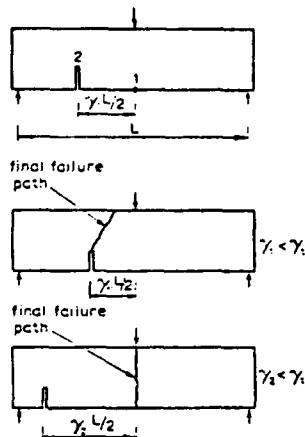
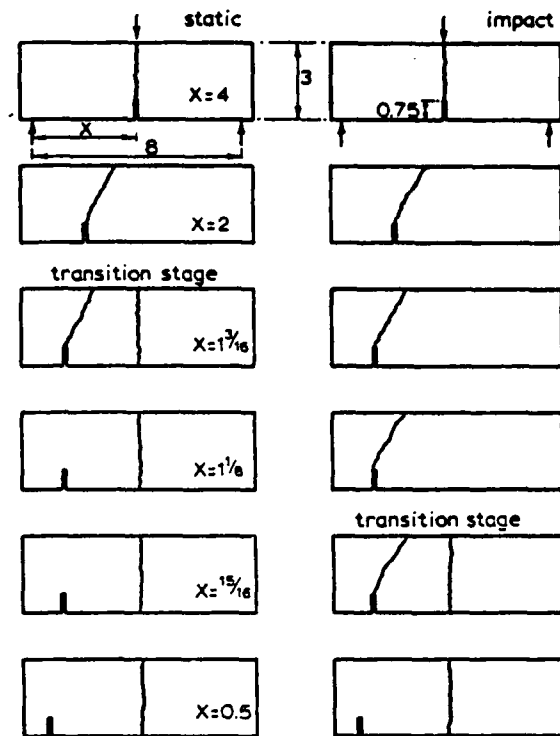
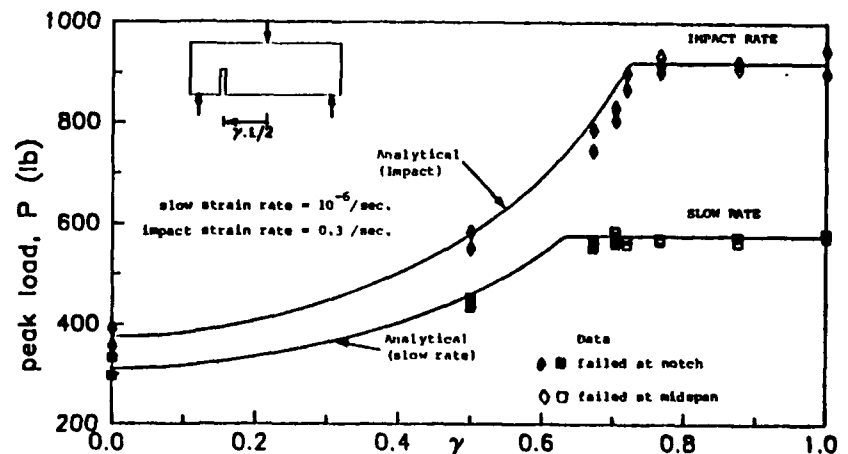


Figure 13. Possible failure locations and effect of location of notch on final failure.

Figure 16. Interaction of location of notch and rate of loading on failure location and peak load.



all dimensions in inches  
1 inch = 25.4mm

Figure 14. Influence of location of notch and rate of loading of final failure location.

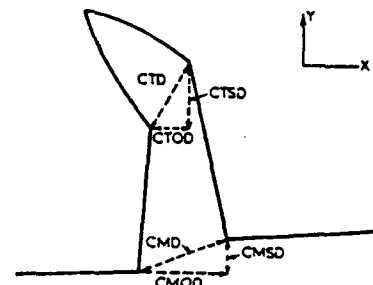


Figure 15. Decomposition of crack tip and crack mouth displacements into their respective opening and sliding displacements.

# STRAIN RATE EFFECT ON STRESS-STRAIN RELATIONSHIPS OF CONCRETE

Hiroshi YAMAGUCHI and Kazuo FUJIMOTO

Fourth Research Center, Technical R&D Institute, Japan Defense Agency  
Fuchinobe 2-9-54, Sagami-hara, Kanagawa 229, Japan

Setsuro Nomura

Department of Architecture, Science University of Tokyo  
Yamazaki 2841, Noda, Chiba 278, Japan

## ABSTRACT

This paper describes triaxial stress-strain relationships of concrete considering the strain rate effect. Triaxial compression tests of cylindrical concrete specimens were conducted by using various axial loading rates under various lateral pressures. As the results of the tests, the stress-strain relationships defined by the tangent shear and bulk moduli were obtained. The tangent shear and bulk moduli are expressed as functions of the octahedral stress and strain, and the rates of increases of the initial elastic moduli and the failure stress due to the octahedral strain rate effect are also taken into account. The calculated results by using the proposed stress-strain relationships reasonably agreed with the test results.

## I. INTRODUCTION

In a concrete structure designed to resist blast and impact loading, concrete is confined by heavy reinforcement in three directions<sup>1)</sup>, which causes rapid triaxial stresses to build up. The behaviors of concrete in this kind of structure may be different from the ones under static loading, because the elastic moduli and the failure stress of concrete depend strongly on the strain rate. The effect has been studied extensively<sup>2,3)</sup>. However, most studies have been limited to uniaxial behaviors. Concerning about the dependence of triaxial behaviors of concrete on the strain rate, no experimental information seems to be reported so far.

The objective of this paper is to propose a simple triaxial stress-strain relationship of concrete considering the strain rate effect for the purpose of rational analyses of concrete structures subjected to blast and impact loading. In the proposed formulation, the tangent elastic moduli are defined as functions of the octahedral stress and strain by correlating with the results of static triaxial compression tests. These moduli are capable of reflecting the hydrostatic nonlinearity and the decrease due to the deviatoric stresses. Then, rapid triaxial compression tests were conducted to investigate the strain rate effect on the initial elastic moduli and the failure stress. The increases of these values due to the octahedral strain rate effect are expressed by empirical equations, and are introduced into the formulation of the tangent elastic moduli.

## II. TEST EQUIPMENT AND PROCEDURES

In order to clarify the characteristics of concrete under rapid triaxial loadings, triaxial compression and hydrostatic loading tests were conducted for cylindrical concrete specimens (10cm in diameter and 20cm in height) under various loading rates. The concrete mixture was based on a water-cement ratio of  $W/C=0.63$ , a mix grading of  $C:S:G = 1:3.25:3.65$  and a maximum aggregate size of 20mm. The specimen was covered with rubber sleeve of 1.5mm thickness and its exposed voids at the cylindrical surface were filled with cement paste in order to prevent intrusion of the rubber sleeve into the concrete voids under high pressures.

The specimen of the triaxial compression test was placed in a triaxial compression cell which is illustrated in Fig.1. Cell pressure was provided by hydraulic oil pump and was transmitted to the specimen. After the cell pressure reached the specified pressure ( $P=0$  (uniaxial), -100, -200, -300, -400, -500, -700 and -900 kgf/cm<sup>2</sup>), the axial load was applied with the main piston corresponding to the specified loading rate. Then, the main piston was loaded by a rapid loading apparatus. To reduce the friction at both ends of the specimen, two thin sheets of teflon discs with lubricating silicon grease inside were placed between the specimen and two end of pedestals((3) and (4) in Fig.1). In each test series, three specimens were used. The loading rates were applied corresponding to four uniaxial strain rate stages: case (S)  $\dot{\epsilon}_1 \approx 10^{-5}$ /sec which is regarded as the value of the static tests, (D1)  $\dot{\epsilon}_1 \approx 10^{-3}$ /sec, (D2)  $\dot{\epsilon}_1 \approx 10^{-2}$ /sec and (D3)  $\dot{\epsilon}_1 \approx 10^{-1}$ /sec. The mean strain rates of each test series are summarized in Table 1. All the triaxial compression tests were conducted by hydrostatic loading first and axial loading successively. During the axial loading, the lateral pressure was attempted to be held constant by controlling the oil pump. However, the lateral pressures of rapid tests (D1~D3) gradually decrease according to the increase of the axial load as well as the loading rate, because the capacity of the oil pump was not enough to control the lateral pressure to be constant under the high loading rates and under the high pressures. The stress paths of the triaxial tests are shown in Fig.2.

The specimen of the hydrostatic loading test was loaded hydrostatically up to about 2000kgf/cm<sup>2</sup> which is

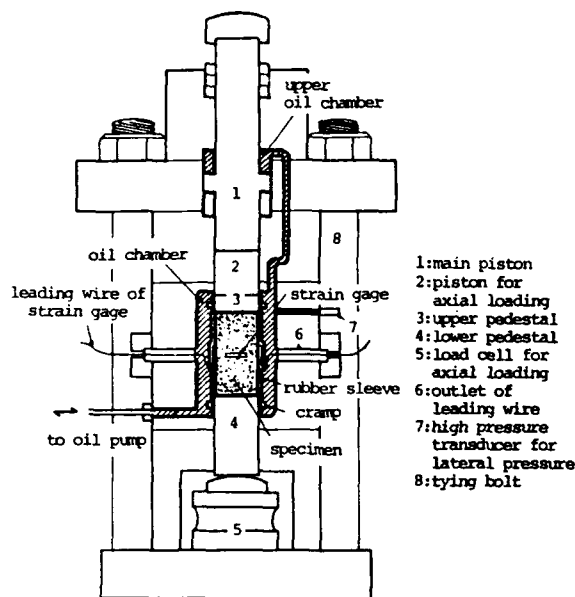


Fig.1 Triaxial compression cell

Table 1 Strain rates of triaxial and hydrostatic loadings

| Rate Notation | Strain Rates   |  |  |                        |
|---------------|--|--|--|------------------------|
|               | Triaxial Loading                                     |  |  | Hydrostatic Loading    |
|               | $\dot{\epsilon}_1$                                   | $\dot{\gamma}_{oct}$                               | $\dot{\epsilon}_{oct}$                               | $\dot{\epsilon}_{oct}$ |
| S             | $-2.61 \times 10^{-5}$<br>( $-3.04 \times 10^{-6}$ ) | $2.44 \times 10^{-5}$<br>( $2.97 \times 10^{-6}$ ) | $-4.06 \times 10^{-6}$<br>( $-1.25 \times 10^{-6}$ ) | $-2.76 \times 10^{-6}$ |
| D1            | $-1.44 \times 10^{-3}$<br>( $-2.31 \times 10^{-4}$ ) | $1.70 \times 10^{-3}$<br>( $3.02 \times 10^{-4}$ ) | $-2.16 \times 10^{-4}$<br>( $-2.46 \times 10^{-5}$ ) | $-1.71 \times 10^{-4}$ |
| D2            | $-2.40 \times 10^{-2}$<br>( $-5.02 \times 10^{-3}$ ) | $2.84 \times 10^{-2}$<br>( $4.89 \times 10^{-3}$ ) | $-2.46 \times 10^{-3}$<br>( $-1.14 \times 10^{-3}$ ) | $-1.68 \times 10^{-3}$ |
| D3            | $-2.54 \times 10^{-1}$<br>( $-7.55 \times 10^{-2}$ ) | $2.52 \times 10^{-1}$<br>( $6.79 \times 10^{-2}$ ) | $-1.68 \times 10^{-2}$<br>( $-8.14 \times 10^{-3}$ ) | $-1.52 \times 10^{-2}$ |

( ) ; Standard deviation

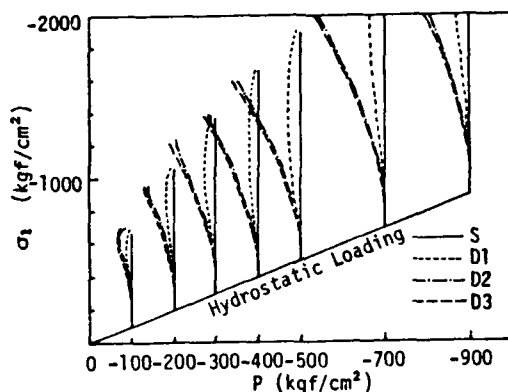


Fig.2 Stress paths in triaxial loading

the maximum capacity of the triaxial compression cell, by pressurizing the oil in the cell. In this case, the piston for axial loading (2) in Fig.1) was removed from the cell and the oil was filled in this part.

### III. TEST RESULTS

#### UNIAXIAL LOADING

The stress-strain curves under uniaxial loadings are shown in Fig.3. The values of Young's modulus,  $E_0$ , and Poisson's ratio,  $\nu$ , for the calculations of initial shear and bulk moduli were obtained from the static stress-strain curves, as  $E_0 = 2.38 \times 10^6 \text{ kgf/cm}^2$  and  $\nu = 0.15$ , respectively. The static uniaxial compressive strength  $F_c$  was  $205 \text{ kgf/cm}^2$ . The compressive strengths increase with the strain rates. At the highest strain rates, (D3), the compressive strengths were on the order of 50 % greater than that of static tests. Fig.4 presents a plot of the compressive strength ratios ( $F_{cd}/F_c$ ) versus the octahedral shear strain rates ( $\dot{\gamma}_{oct}$ ), where  $F_{cd}$  means the dynamic compressive strength. In order to express the strain rate effect on the compressive strengths, the following equations, also shown by the broken line in Fig.4, are derived by least square curve fitting to the test data:

For  $\dot{\gamma}_{oct} \geq 2.44 \times 10^{-5} / \text{sec}$

$$F_{cd}/F_c = f_1 + f_2 \cdot \log(\dot{\gamma}_{oct}) + f_3 \cdot [\log(\dot{\gamma}_{oct})]^2 \quad \dots (1)$$

For  $\dot{\gamma}_{oct} < 2.44 \times 10^{-5} / \text{sec}$

$$F_{cd}/F_c = 1$$

where,  $f_1 = 0.1021 \times 10$ ,  $f_2 = -0.5076 \times 10^{-1}$ ,  $f_3 = 0.2583 \times 10^{-1}$  and  $\dot{\gamma}_{oct}$  is given in the unit of ( $\times 10^{-6} / \text{sec}$ ) and the value  $\dot{\gamma}_{oct} = 2.44 \times 10^{-5} / \text{sec}$  is the mean value of  $\dot{\gamma}_{oct}$  of the static triaxial tests.

#### TRIAXIAL LOADING

Fig.5 shows the stress-strain curves under triaxial loadings on the specified lateral pressures ( $P = -300, -500 \text{ kgf/cm}^2$ ). It can be seen that the tangent elastic moduli increase with the strain rates at the initial points of the rapid axial loading. In the case of high strain rates, the maximum dynamic axial stresses become smaller than static ones, because the lateral pressures decrease by above-mentioned reason.

#### HYDROSTATIC LOADING

Fig.6 shows the hydrostatic loading curves. After an initial decrease, the slope of the hydrostatic loading curve continuously increases. The initial bulk moduli increase with the octahedral normal strain rates ( $\dot{\epsilon}_{oct}$ ).

#### FAILURE ENVELOPE CURVE

Fig.7 presents a plot of the maximum stresses on the octahedral normal stress ( $\sigma_{oct}$ )—octahedral shear stress ( $\tau_{oct}$ ) plane normalized by the static uniaxial compressive strength. The broken line indicates the static failure envelope curve, which can be expressed as follows:

$$\tau_{oct}/F_c = f(\sigma_{oct}/F_c)$$

$$f(\sigma_{oct}/F_c) = \frac{f_1}{\exp(f_2 \cdot \sigma_{oct}/F_c)} + f_3 \quad \dots (2)$$

where,  $f_1 = 7.435$ ,  $f_2 = -0.1113$  and  $f_3 = 7.640$ . The points of maximum stresses under the rapid loadings separate gradually from the static failure envelope curve. Namely, the failure envelope curves move upward with the increase of the strain rates.

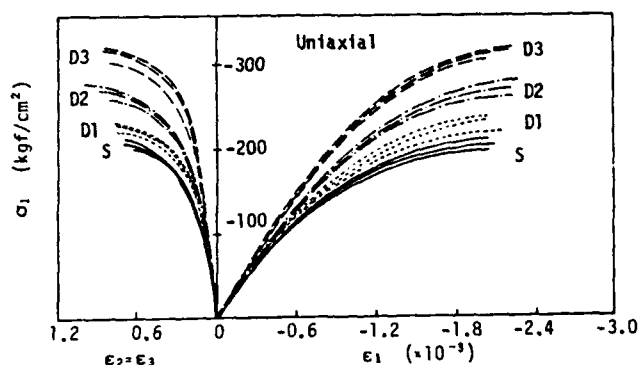


Fig.3 Uniaxial stress-strain curves

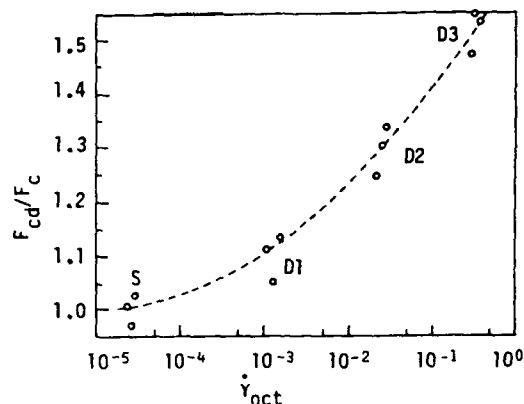


Fig.4 Uniaxial compression strength ratio versus octahedral shear strain rate diagram

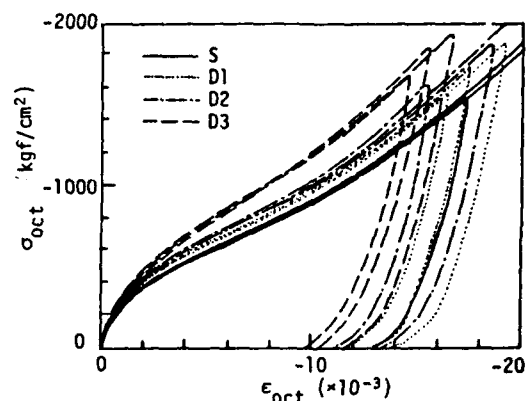


Fig.6 Hydrostatic loading curves

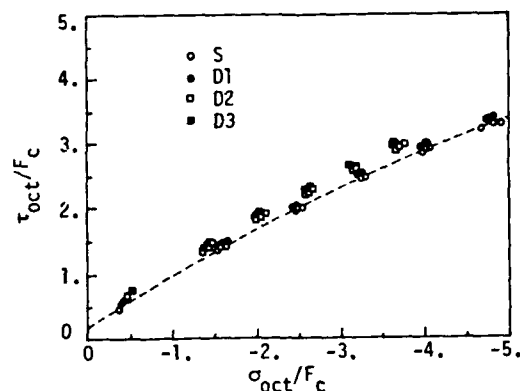


Fig.7 Maximum stresses

#### IV. ELASTIC MODULI

##### TANGENT SHEAR MODULUS

Fig.8 presents a plot of the static tangent shear modulus ratios ( $G^h/G_0$ ) versus the octahedral normal strain, where  $G^h$  is defined at the initial point of rapid axial loading after the specified hydrostatic loading and is regarded as the tangent shear modulus which is decreased solely by the hydrostatic pressure. The initial shear modulus  $G_0$  is obtained by  $G_0 = E_0/2/(1+\nu)$ . In this figure, Each point shows a mean value of three test results. After an initial decrease, the static tangent shear moduli increase with the octahedral normal strains, as shown by the broken line. It is similar to the nonlinearity of hydrostatic loading curve. The tangent shear modulus can be expressed in terms of the octahedral normal strain as follows:

$$G^h/G_0 = \beta_v(\epsilon_{oct}) \quad \dots\dots\dots (3)$$

$$\beta_v(\epsilon_{oct}) = b_1 \cdot \exp(b_2 \cdot \epsilon_{oct}) + b_3 \cdot \exp(b_4 \cdot \epsilon_{oct})$$

where,  $b_1 = 0.5541$ ,  $b_2 = -0.2221 \times 10^2$ ,  $b_3 = 0.4459$  and  $b_4 = 0.8583 \times 10^3$ . Eq.(3) gives the dependence of  $G^h$  on  $\epsilon_{oct}$ , i.e., the variation of the tangent shear modulus due to the hydrostatic pressure only. However, actual tangent shear modulus is also decreased by the deviatoric stress. In order to explain this, the new concept of a graph, where contour lines of the equal rate of decrease of the tangent elastic moduli are shown on  $(\sigma_{oct}/F_0) - (\tau_{oct}/F_0)$  plane, is introduced, and the following assumptions are made:

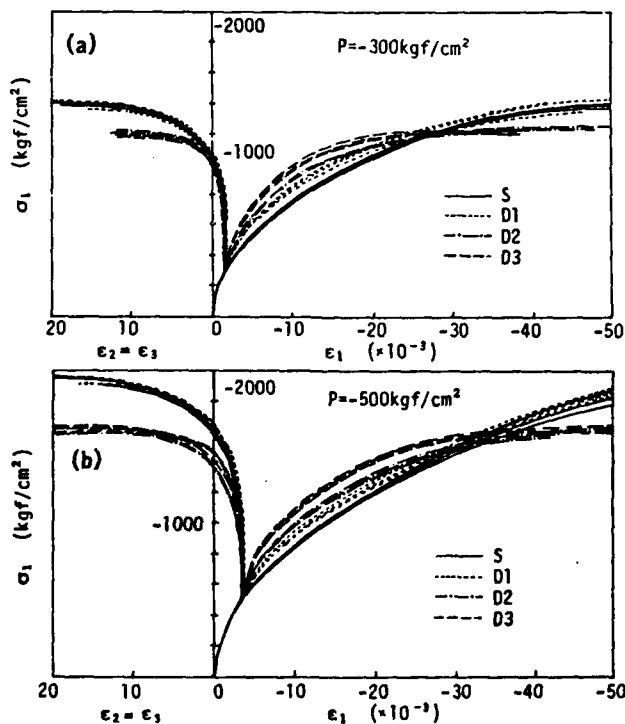


Fig.5 Triaxial stress-strain curves

- (1) The contour line  $\Phi$  is a function of a parameter  $\phi$  ( $0 \leq \phi \leq 1$ ).
- (2) For  $\phi=1$ , the contour line  $\Phi(\phi)$  is equal to the failure envelope curve, and for  $\phi=0$ ,  $\Phi(\phi)=0$ , i.e., the case of hydrostatic loading.
- (3) On each the contour line, the tangent shear modulus ratio ( $G^t/G^{th}$ ) has the same value under various lateral pressures, i.e.,  $G^t$  is uniquely defined by given  $\phi$ .

Under these assumptions, the function form of the contour line shown in Fig.9 can be expressed as follows:

$$\tau_{oct}/F_c = \Phi(\phi, \sigma_{oct}/F_c) \quad \dots\dots\dots(4)$$

$$= \phi \left[ \left( \frac{(1+c)^2}{(\phi+c)} - (1+c) \right) d - \frac{\sigma_{oct}}{F_c} + t \right] \cdot f(\sigma_{oct}/F_c)$$

where,  $t=1/30$  which means the value of  $(\sigma_{oct}/F_c)$  at the tensile failure and the other parameters,  $c$  and  $d$ , are obtained by fitting the test data. The values of these parameters are obtained as  $c=0.02$  and  $d=0.4$ , respectively, and  $f(\sigma_{oct}/F_c)$  is already described in Eq.(2).

Fig.10 indicates the variation of the tangent shear modulus ratios ( $G^t/G^{th}$ ) with the parameter  $\phi$ . It is clear that the decrease of the tangent shear modulus ratio is closely related to  $\phi$  and can be uniquely defined by  $\phi$  under various lateral pressures, where  $\phi$  of the current stress state is given by Eq.(4). The relation between ( $G^t/G^{th}$ ) and  $\phi$ , which is shown in the broken line in this figure, can be expressed as follows:

$$G^t/G^{th} = \beta_D(\phi) \quad \dots\dots\dots(5)$$

$$\beta_D(\phi) = b_5 + b_6 \cdot \phi + b_7 \cdot \phi^2 + b_8 \cdot \phi^3 + b_9 \cdot \phi^4 + b_{10} \cdot \phi^5 + b_{11} \cdot \phi^6 + b_{12} \cdot \phi^7$$

where,  $b_5=1.0$ ,  $b_6=-0.9260 \times 10^3$ ,  $b_7=0.6769 \times 10^2$ ,  $b_8=-0.2730 \times 10^3$ ,  $b_9=0.6110 \times 10^3$ ,  $b_{10}=-0.7601 \times 10^3$ ,  $b_{11}=0.4910 \times 10^3$  and  $b_{12}=-0.1284 \times 10^3$ . Eq.(5) gives the decrease of tangent shear modulus due to the deviatoric stress under the existence of hydrostatic pressure. Therefore, combining Eq.(3) with Eq.(5), the static tangent shear modulus is obtained as:

$$G^t = G_0 \cdot \beta_D(\epsilon_{oct}) \cdot \beta_D(\phi) \quad \dots\dots\dots(6)$$

The strain rate effect on the initial elastic moduli and the failure stress is considered in the formulation of the tangent elastic moduli. The strain rate also influences the shape of stress-strain curve, but this influence is neglected in this study.

Fig.11 shows the ratio of dynamic tangent shear moduli to static ones versus the octahedral normal strain under each loading rate. Note that the dynamic tangent shear modulus  $G^{th}_d$  can be regarded as the initial shear modulus after the specified hydrostatic loading. The initial shear modulus increases with the strain rate and also with the octahedral normal strain. This influence can be approximately expressed as linear functions of  $\epsilon_{oct}$ , which are shown by the broken lines, using the parameters  $g_1$  and  $g_2$  which are defined by the octahedral shear strain rates:

$$G^{th}_d/G^t = g(\epsilon_{oct}, \dot{\gamma}_{oct}) = g_1(\dot{\gamma}_{oct}) - \epsilon_{oct} \cdot g_2(\dot{\gamma}_{oct}) \quad \dots\dots\dots(7)$$

For  $\dot{\gamma}_{oct} \geq 2.44 \times 10^5 / \text{sec}$

$$g_1(\dot{\gamma}_{oct}) = g_{11} + g_{12} \cdot \log(\dot{\gamma}_{oct}) + g_{13} [\log(\dot{\gamma}_{oct})]^2$$

$$g_2(\dot{\gamma}_{oct}) = g_{21} + g_{22} \cdot \log(\dot{\gamma}_{oct}) + g_{23} [\log(\dot{\gamma}_{oct})]^2$$

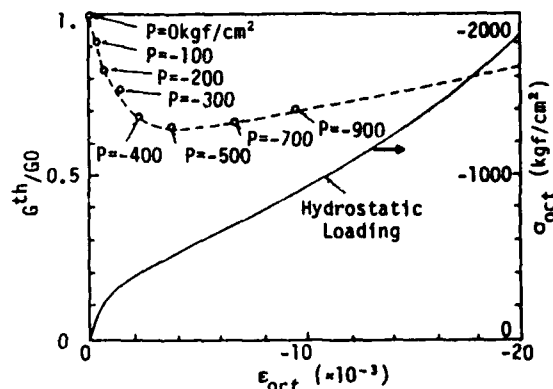


Fig.8 Variation of tangent shear modulus ratio with octahedral normal strain

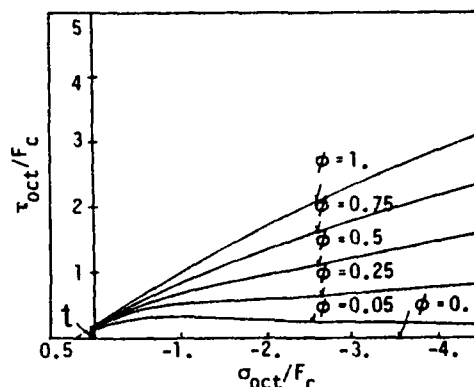


Fig.9 Explanatory diagram of parameter  $\phi$

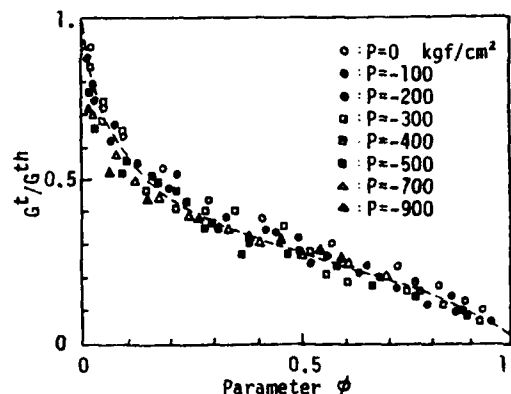


Fig.10 Variation of tangent shear modulus ratio with parameter  $\phi$

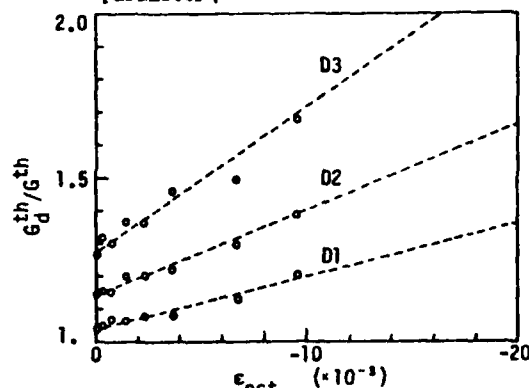


Fig.11 Tangent shear modulus ratio versus octahedral normal strain

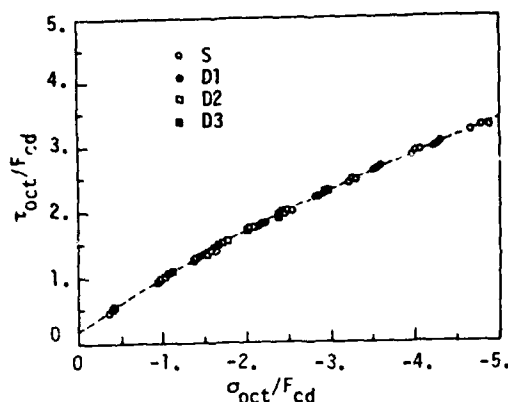


Fig.12 Maximum stresses

For  $\dot{\gamma}_{oct} < 2.44 \times 10^{-5}/\text{sec}$   
 $g_1(\dot{\gamma}_{oct}) = 1, \quad g_2(\dot{\gamma}_{oct}) = 0$

where,  $g_{11}=0.1032 \times 10^{-1}, g_{12}=-0.4673 \times 10^{-1}, g_{13}=0.1684 \times 10^{-1}, g_{21}=-0.2187 \times 10^{-1}, g_{22}=-0.5189, g_{23}=0.1510 \times 10^{-1}$  and  $\dot{\gamma}_{oct}$  is given in the unit of  $(\times 10^{-6}/\text{sec})$ . The value  $\dot{\gamma}_{oct} = 2.44 \times 10^{-5}/\text{sec}$  is the mean value of  $\dot{\gamma}_{oct}$  of the static tests.

Fig.12 presents a plot of the dynamic maximum stress given in a normalized form by the uniaxial compressive strength corresponding to the loading rate. The static failure envelope curve is shown by the broken line in this figure. As shown in Fig.12, the maximum stress points under the rapid loadings lie well on the broken line. It may be regarded that the rates of upward shift of the failure envelope curves with the strain rates are about equal to the rates of increase of the uniaxial compressive strengths. Hence, the failure envelope curve considering the strain rate effect is obtained by substituting  $F_{cd}$  given by Eq.(1) instead of  $F_c$  in Eq(2):

$$f_d(\sigma_{oct}/F_{cd}) = \frac{f_1}{\exp(f_2 \cdot \sigma_{oct}/F_{cd})} + f_3 \quad \dots\dots\dots(8)$$

Corresponding to the dynamic failure envelope curve, the parameter  $\phi$  can be redefined as  $\phi_d$  by combining Eq. (4) and Eq.(8). Therefore, the tangent shear modulus considering the strain rate effect is obtained by substituting  $\phi_d$  instead of  $\phi$  in Eq.(5) and by combining Eq.(3) and Eq.(7):

$$G^t = G_0 \cdot g(\epsilon_{oct}, \dot{\gamma}_{oct}) \cdot \beta_v(\epsilon_{oct}) \cdot \beta_D(\phi_d) \quad \dots\dots\dots(9)$$

#### TANGENT BULK MODULUS

Fig.13 presents a plot of the static tangent bulk modulus ratios ( $K^t/K_0$ ) versus the octahedral normal strain, where  $K^t$  is the tangent bulk modulus under hydrostatic loading and the initial bulk modulus,  $K_0$ , is obtained by  $K_0 = E_0/3/(1-2\nu)$ . This figure shows that the static tangent bulk modulus decrease and then increase with the octahedral normal strain, as shown by the broken line. The tangent bulk modulus can be expressed in terms of the octahedral normal strain as follows:

$$K^t/K_0 = \alpha_v(\epsilon_{oct}) \quad \dots\dots\dots(10)$$

$$\alpha_v(\epsilon_{oct}) = a_1 \cdot \exp(a_2 \cdot \epsilon_{oct}) + a_3 \cdot \exp(a_4 \cdot \epsilon_{oct})$$

where,  $a_1=0.8812, a_2=0.7832 \times 10^3, a_3=0.1188$  and  $a_4=-0.5518 \times 10^2$ . Eq.(10) gives the dependence of  $K^t$  on  $\epsilon_{oct}$ , i.e., the variation of the tangent bulk modulus

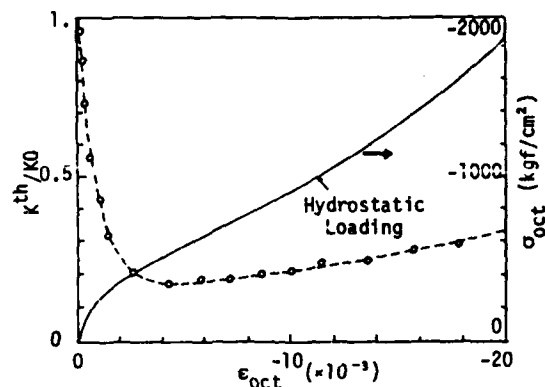


Fig.13 Variation of tangent bulk modulus ratio with octahedral normal strain

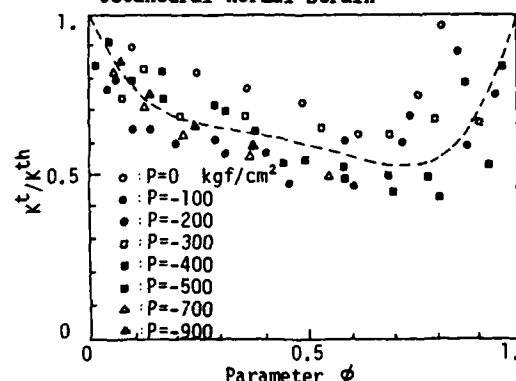


Fig.14 Variation of tangent bulk modulus ratio with parameter  $\phi$

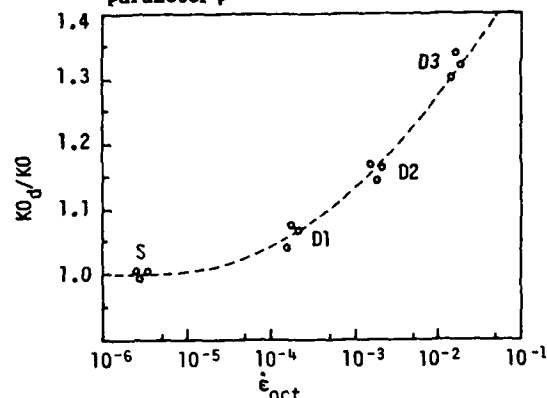


Fig.15 Initial bulk modulus ratio versus octahedral normal strain rate

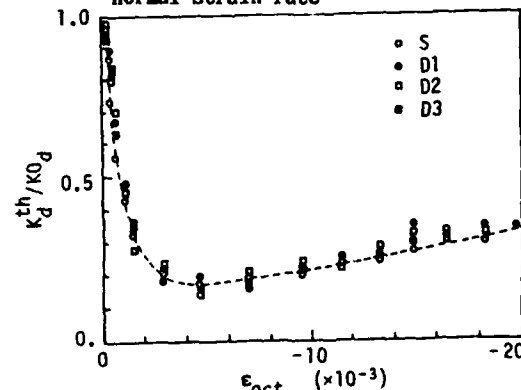


Fig.16 Variation of tangent bulk modulus ratio with octahedral normal strain

due to the hydrostatic pressure only. The decrease of tangent bulk modulus due to the deviatoric stresses is considered in the same manner as the formulation of the tangent shear modulus. Fig.14 indicates the variation of the tangent bulk modulus ratios ( $K^t/K^h$ ) with the parameter  $\phi$ . Although greater dispersions are observed in Fig.14 than the ones in Fig.10, the broken line shown in this figure can approximately express the relation between ( $K^t/K^h$ ) and  $\phi$  as follows:

$$K^t/K^h = \alpha_D(\phi) \quad \dots\dots\dots(11)$$

$$\alpha_D(\phi) = a_5 + a_6 \cdot \phi + a_7 \cdot \phi^2 + a_8 \cdot \phi^3 + a_9 \cdot \phi^4$$

where,  $a_5=1.0$ ,  $a_6=-0.3133 \times 10$ ,  $a_7=0.1071 \times 10^2$ ,  $a_8=-0.1658 \times 10^2$  and  $a_9=0.9012 \times 10$ . Therefore, combining Eq.(10) with Eq.(11), the static tangent bulk modulus is obtained as:

$$K^t = K_0 \cdot \alpha_v(\epsilon_{oct}) \cdot \alpha_D(\phi) \quad \dots\dots\dots(12)$$

Fig.15 presents a plot of the ratios of dynamic initial bulk moduli to static ones versus the octahedral normal strain rate. The following expression shown by the broken line in Fig.15 is obtained in terms of  $\dot{\epsilon}_{oct}$ :

For  $\dot{\epsilon}_{oct} \leq -4.06 \times 10^{-6}/\text{sec}$

$$K_0^d/K_0 = k(\dot{\epsilon}_{oct})$$

$$= k_1 + k_2 \cdot \log(-\dot{\epsilon}_{oct}) + k_3 [\log(-\dot{\epsilon}_{oct})]^2 \quad \dots\dots\dots(13)$$

For  $\dot{\epsilon}_{oct} > -4.06 \times 10^{-6}/\text{sec}$   $K_0^d/K_0 = 1$ .

where,  $k_1=0.1009 \times 10$ ,  $k_2=-0.2875 \times 10^{-1}$ ,  $k_3=0.2362 \times 10^{-1}$  and  $\dot{\epsilon}_{oct}$  is given in the unit of ( $\times 10^{-6}/\text{sec}$ ). The value  $\dot{\epsilon}_{oct} = -4.06 \times 10^{-6}/\text{sec}$  is the mean value of  $\dot{\epsilon}_{oct}$  of the static tests.

Fig.16 presents a plot of the ratios of the dynamic tangent bulk modulus,  $K^h_d$ , to the dynamic initial bulk modulus,  $K_0^d$  under each loading rate versus the octahedral normal strain. The relation between ( $K^h_d/K_0^d$ ) and the octahedral normal strain under the static loading, as shown by the broken line (Eq.(10)), roughly coincides with the ones under the rapid loadings. Therefore, the tangent bulk modulus considering the strain rate effect is obtained by substituting  $\phi_d$  instead of  $\phi$  in Eq.(11) and by combining Eq.(10) and Eq.(13):

$$K^t = K_0 \cdot k(\dot{\epsilon}_{oct}) \cdot \alpha_v(\epsilon_{oct}) \cdot \alpha_D(\phi_d) \quad \dots\dots\dots(14)$$

#### V. COMPARISONS WITH TEST RESULTS

The incremental stress-strain relationship of a axisymmetric model is given as follows:

$$\begin{Bmatrix} d\sigma_1 \\ d\sigma_2 \\ d\sigma_3 \end{Bmatrix} = \begin{bmatrix} D_1 & D_2 & D_2 \\ D_2 & D_1 & D_2 \\ D_2 & D_2 & D_1 \end{bmatrix} \begin{Bmatrix} d\epsilon_1 \\ d\epsilon_2 \\ d\epsilon_3 \end{Bmatrix} \quad \dots\dots\dots(15)$$

where,  $D_1 = K^t + 4G^t/3$ ,  $D_2 = K^t - 2G^t/3$  and the numerical subscripts represent the directions of stresses and strains; 1=axial, 2=3=lateral.

The calculated results of proposed stress-strain relationships using the axial strain increment,  $d\epsilon_1$ , and the lateral pressure increments,  $d\sigma_2 = d\sigma_3$ , of the test data are shown in Fig.17. The strain rates in the calculation were assumed constant, which were given by the mean values of each test series. The calculated results show reasonable agreement with the test results.

#### VI. CONCLUSION

A simple triaxial stress-strain relationship of con-

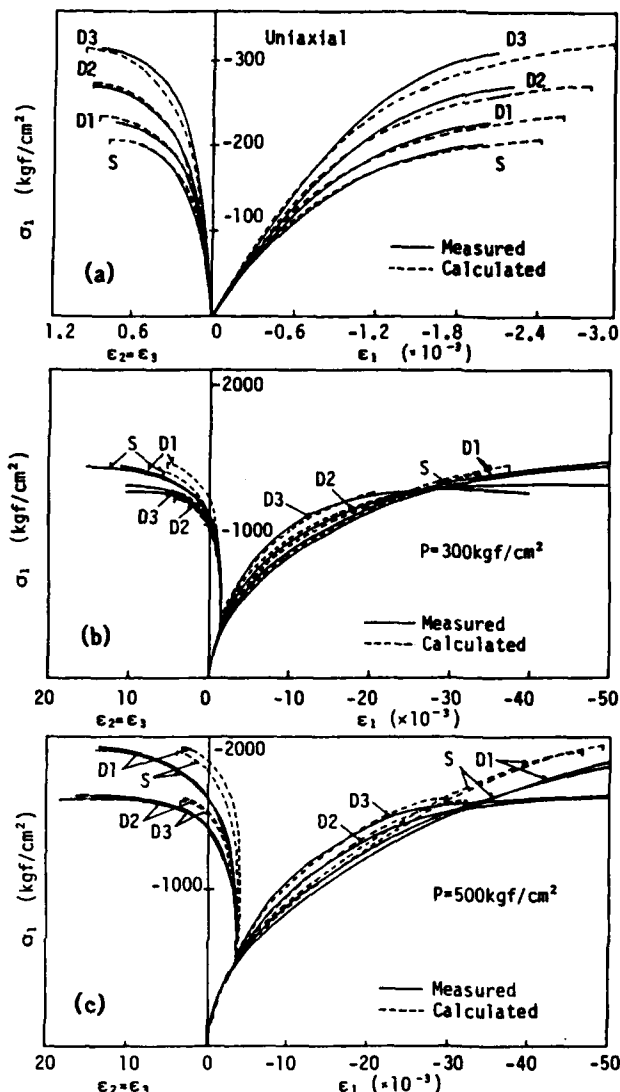


Fig.17 Comparisons with test results

crete was proposed by using the tangent shear and bulk moduli correlated with the rapid triaxial compression test data. Also, the strain rate effect on the initial elastic moduli and the failure stress are considered in the formulation of the tangent elastic moduli. The proposed relationship allows more realistic dynamic analysis of the concrete structure under high loading rate.

#### REFERENCES

- [1] Bažant, Z.P., Bishop, P.C., and Chang, T., "Confined Compression Tests of Cement Paste and Concrete up to 300 ksi," ACI Journal, Vol. 83, No. 48, July-Aug., 1986, pp. 553-580.
- [2] Takeda, J., Tachikawa, H., and Fujimoto, K., "Mechanical Behavior of Concrete under High Rate Loading than in Static Test," Symposium on Mechanical Behavior of Materials, Proceedings of Society of Material Science, Kyoto, Japan, Vol. 2, 1974, pp. 479-488.
- [3] Watstein, D., "Effect of Straining Rate on the Compressive Strength and Elastic Properties of Concrete," ACI Journal, Vol. 49, No. 8, Apr., 1953, pp. 729-744.

## DYNAMIC TESTING OF CONCRETE WITH THE SPLIT HOPKINSON PRESSURE BAR

Lawrence E. Malvern, David A. Jenkins, Tianxi Tang, and Jyh-Cherng Gong

Aerospace Engineering, Mechanics, and Engineering Science Department  
University of Florida, Gainesville, Florida 32611

### ABSTRACT

The objectives of the research reported here were to develop procedures and demonstrate the feasibility of using them to make micrographic examinations of undamaged and damaged Split Hopkinson Pressure Bar (SHPB) compression specimens to determine crack development characteristics in the impacted specimens. Several previously proposed models for concrete failure under impact involve crack initiation, propagation and coalescence assumptions, which had so far not been verified by observations of the crack patterns after varying amounts of damage before general failure. The results of such observations could provide a qualitative understanding of the physical mechanism leading to failure and potentially a quantitative basis for modeling.

### INTRODUCTION

In order to accomplish the objectives two experimental procedures had to be developed. One was the petrographic procedure with which the specimen crack pattern in a longitudinal slice was stabilized by furfural alcohol infiltration and polymerization to fill the cracks with a rigid furan resin before polishing for micrographic examination. To recover specimens with various amounts of deformation before complete failure, a steel collar was placed around each specimen, large enough that it did not provide lateral confinement. Specimens were cut slightly longer than the collar, ends ground to assure flatness and parallelism and to produce a range of excess lengths from 0.0012 to 0.012 times the collar length. Thus after an axial strain of 0.0012 to 0.012 the steel collar began to stop the loading. Similar collar tests were performed quasistatically at comparable levels of axial deformation.

### BACKGROUND

A detailed literature survey related to this investigation was published in 1986 in Reference 1, which also presented results obtained up to that time on high-strength concrete specimens in the SHPB system at the University of Florida under an AFOSR contract. Additional results were reported in the final report, Reference 2. An earlier

paper, Reference 3, described the 3-inch diameter (76.2 mm) bar system and preliminary results on high-strength concrete. Results on mortar in a smaller system were reported in Reference 4.

The SHPB system consists of two long strain-gaged pressure bars with a short specimen sandwiched between them. Analysis of the observed longitudinal elastic stress waves in the two pressure bars furnishes information about both the force and the displacement versus time at each of the two specimen interfaces. From this record the average stress and strain in the specimen are deduced. This facility is the only one of its size in the United States. It has been used for unconfined dynamic testing of five different kinds of high-strength concrete prepared at Waterways Experiment Station, Terra-Tek Inc., and SRI International and also for testing SIFCON (slurry-infiltrated fiber concrete) furnished by the New Mexico Engineering Research Institute for AFWAL, at strain rates from 5 to 200 per second.

As currently configured it provides a loading pulse lasting 300 microseconds, imparted by impact of the 30-inch (762 mm) striker bar against the incident pressure bar. The whole system, including gas gun, pressure bars and a shock absorber at the far end, is almost 30 feet (9.15 m) long.

Figure 1 is a schematic of the pressure bar arrangement, with a Lagrange diagram above it illustrating the elastic wave propagation in the pressure bars. Figure 2 shows an example of the bar strains versus time recorded from the stored signals in a digital oscilloscope. Compressive strain is plotted upward. After the passage of the first incident pulse, there is a dwell time before the arrival of the reflected pulse from the specimen, which is recorded at the same gage station as the incident pulse. Another channel shows the pulse transmitted through the concrete specimen into the transmitter bar. Because the two gage stations are approximately equidistant from the specimen, the transmitted pulse arrives at the transmitter-bar gage station at about the same time as the reflected pulse arrives at the incident-bar station. Also shown are records from two strain gages (axial and hoop) mounted on the specimen.

For purposes of analysis, the pulses are time shifted, so that time zero coincides with the arrival at the first specimen interface, and corrected for wave dispersion in the pressure bars, using a procedure developed under Task Order 85-6 from AFESC/RDC, Tyndall AFB, Florida. The dispersion-correction procedure is similar to that



used by Follansbee and Frantz, Reference 5, and Felice, Reference 6, except that it uses a more efficient Fast Fourier Transform method instead of a Fourier series.

Although the corrected and uncorrected pulses appear similar, the differences in detail, especially for the incident and reflected pulses (which are added algebraically to obtain the pressure bar strain at the first specimen interface) lead to significant differences in the first interface stresses. Figure 3 shows corrected first and second interface stresses in the nominally 3-inch-long (76.2 mm) specimen. The dispersion correction leads to much closer agreement of the two interface stresses, an approximate equilibrium of the two stresses before they have reached half the maximum stress in this case.

The dispersion correction has eliminated the oscillations previously reported in the first-interface stress-time recording in these tests of high-strength concrete with specimens of the same diameter as the pressure bars. As will be seen, the correction procedure was not so successful in tests with a 2-inch diameter specimen.

#### CONCRETE SPECIMENS AND TEST PROCEDURES

Test material was cast in split tube molds with inside diameters of 2 inches (50.8 mm) and lengths of approximately 5 inches (127 mm). After curing, two test specimens 1.75 inches (44.5 mm) long were sawed from the central regions of the resulting cylinders. The ends of the specimens were then ground flat and parallel on a surface grinder to produce a series of finished lengths ranging from 1.709 to 1.727 inches (43.4 to 43.8 mm) for subsequent static and dynamic testing.

A steel collar 1.707 inches (43.36 mm) in length with a bore of 2.050 inches (52.1 mm) and an outside diameter of 3 inches (76.2 mm) was fabricated. The collar, which is shown in Figure 4 (not to scale), stopped each static and dynamic test near the desired level of strain.

The concrete mix used for this group of tests is shown in Table 1. The average density of the specimens was 2.22 g/cm<sup>3</sup>. Unconfined static compressive strength was around 69 MPa (10 KSI).

Table 1. CONCRETE MIXTURE DESIGN

|                                 |          |
|---------------------------------|----------|
| Type II Portland Cement         | 32.7 lb. |
| Brooksville Aggregate No. 89    | 94.2 lb. |
| Sand (Keuka, FL Pit No. 76-137) | 60.4 lb. |
| Water                           | 16.5 lb. |
| Water/Cement Ratio              | 0.50     |
| Slump                           | 2.25 in. |

The Brooksville, Florida, No. 89 is a mixture of coarse and fine manufactured Florida limestone aggregate with a maximum size of 3/8 inch (9.5 mm).

Two series of tests were conducted. The series done in the SHPB will be called dynamic. The six dynamic test specimens were designed for predicted strains of 0.0029, 0.0047, 0.0064, 0.0081, 0.0099 and 0.0116 before the collar began to act. In each of the dynamic tests some further axial deformation of the specimen occurred along with the axial elastic shortening of the collar, so that the measured maximum strains (corresponding to the maximum crack development) were larger than the predicted strains by approximately 0.002.

The second series of tests used a hydraulic press to slowly apply the load and will be referred to as static. Once again, the steel collar was used to arrest the test at a given level of strain. Petrographic examination was made of six specimens with strain levels over a range comparable to that of the six dynamic tests, although the strains in the series are not exactly matched.

#### PETROGRAPHIC EXAMINATION PROCEDURES

After each specimen was tested, it was stabilized by potting it in a polyester mounting resin (IECO Castolite), which helped keep the specimen together throughout subsequent handling. After curing of the polyester, a longitudinal slice approximately 0.060 inch (1.52 mm) thick was cut from the center of each specimen.

In order to further stabilize the structure during mechanical polishing and to provide visual contrast to aid in examination of the crack patterns, a procedure based on the vacuum infiltration and polymerization of furfural alcohol [2-(C<sub>4</sub>H<sub>3</sub>O)CH<sub>2</sub>OH] was used. After infiltration with furfural alcohol, about 20 drops of concentrated hydrochloric acid were carefully added to the approximately 50 cc of alcohol, initiating a polymerization reaction which causes the amber colored furfural alcohol to become a dark brown rigid furan resin within the existing cracks, which reinforced the structure and inhibited further crack development during polishing.

Mounted specimens were ground flat by hand on a succession of silicon carbide grinding papers (180 - 320 - 600 grit), using no lubricant. Finally, each was polished using 6 micron diamond paste on a synthetic fiber polishing wheel, using kerosene as a lubricant.

A macrophotograph was made of each mounted section for later use in marking the paths of cracks. Large cracks could be readily seen in the photographs, but smaller cracks can only be observed by using the metallographic microscope at 5X to 50X. To generate an overall view of the emerging crack patterns, a routine was developed wherein the entire surface of the section was scanned using the microscope and any cracks that were found were marked on a large black and white print of the section macrophotograph using a blue pen. Tracings on plain white paper were made to isolate and enhance the crack patterns.

To deduce the length of cracks per unit area in the cross section and the surface area of cracks per unit volume, the technique of line intercept counting was employed. A grid of sample lines was laid over the traced crack pattern, and the number of intercepts each sample line made with cracks was recorded. The total number of intercepts, divided by the total length of sample line, can be shown to be equal to  $2/\pi$  times the crack length per unit area. The crack length per unit area can further be shown to equal  $\pi/2$  times the total crack surface area per unit volume (counting both surfaces created by the crack), so that the intercept count per unit length gives the crack surface area per unit volume directly; see Underwood, Reference 7.

## RESULTS

The mechanical results of the dynamic tests terminated by the collar will be illustrated by two figures to explain how the measurements were made and then summarized in Table 2. All the collar tests used the same gas-gun firing pressure and striker-bar impact speed as the test without a collar. Ideally the stresses versus time and the stress-strain curves would have the same appearance as the curves for the no-collar specimen until the strain had reached the "predicted strain" value that just reduced the specimen length to the collar length.

The actual results were not so ideal. Even after dispersion correction both Stress 1 and Stress 2 versus time still showed oscillations believed related to the three dimensionality of the wave fronts, induced by the area mismatch between bars and specimen, and possibly to the dynamics of the loose collar, and the two stress plots did not usually reach agreement before the collar took over. Figure 5 shows Stress 1, Stress 2, Strain Rate, and Strain versus time for a specimen with predicted strain of 0.0099 for collar contact (approximately 1 percent strain or 100 on the ordinate scale). Note the three definitions of the ordinate scale. With strain, for example, a reading of 100 is to be multiplied by 1/10,000 to give 0.01 or 1 percent strain.

This strain is reached at time=129 microsec, marked by a square on the strain curve. At this point both the recorded Stress 1 and Stress 2 (also marked by squares) are well above the approximately 100 MPa failure stress of the no-collar test (which occurred at a strain of 0.0064 in the no-collar test). The stress records were not considered reliable for determining collar action. The strain record proved more useful.

The strain record shows a maximum strain plateau of about 0.0128 during the collar action, falling to about 0.0105 at the end of the plot, also marked by a square, after the elastic compression of the collar had been unloaded. The final value of strain after unloading is more easily read on the stress-strain curves of Figure 6 as about 0.0102. This final unloaded value of strain is very close to the predicted strain at collar contact. The indicated stress-strain curves of Figure 6 indicate that both stresses had surpassed the no-collar test strength before this strain was reached. It is clear that by the time the predicted strain of about 0.01 had been reached the collar was already carrying a considerable part of the load.

The strain results summarized in Table 2 show a remarkable consistency. They will be used to correlate with the crack distribution data.

Table 2. PREDICTED STRAIN AT COLLAR CONTACT AND MEASURED RESIDUAL AND MAXIMUM STRAINS.

| SPECIMEN No. | PREDICTED Strain | RESIDUAL Strain | MAXIMUM Strain |
|--------------|------------------|-----------------|----------------|
| F21          | 0.0029           | 0.0023          | 0.0041         |
| F22          | 0.0047           | 0.0046          | 0.0065         |
| F23          | 0.0064           | 0.0068          | 0.0092         |
| F24          | 0.0081           | 0.0082          | 0.0103         |
| F25          | 0.0091           | 0.0102          | 0.0128         |
| F04          | 0.0116           | 0.0106          | 0.0126         |

Figure 7 shows the Stress 2 versus strain curve of a no-collar dynamic test. The six points marked on it are at the maximum strains of Table 2, indicating what points of the unconfined dynamic stress-strain curve were reached before unloading. These points represent approximately the damage conditions for the crack patterns of the dynamic collar tests to be reported. Apparently the first one is at about two-thirds of the failure strain, the second one is just at the failure strain, and the other four are from the strain softening regime. This interpretation takes no account of likely random differences in the mechanical properties of the various test specimens.

## CRACK PATTERNS AND CRACK SURFACE AREA

Figures 8 and 9 show typical crack patterns for one example of each of the two test series. When all 12 patterns are compared, differences between the dynamic series and the static series are apparent. In the dynamic series, the cracks are more uniformly distributed, while the cracks in the static series specimens tend to be concentrated along definite bands between the center and the surface of the specimen.

The results of the crack surface area measurements, as derived from the line intercept counting on each section, are presented in Figure 10. The surface area per unit volume is plotted against the observed maximum strain. Table 3 lists the data on which Figure 10 is based.

For maximum strains up to a threshold strain of about 0.006 (near the failure strains in no-collar tests) there is a moderate amount of cracking. Above a maximum strain of 0.006 (corresponding to the strain-softening regime in the no-collar tests) there is a significantly greater crack development. From the limited data an upward trend of crack density with strain cannot be confirmed in the regime below the threshold or in the regime above the threshold. For the strain-softening regime this may mean that once the major cracks have formed, much of the deformation continues by sliding on the existing cracks. For the lower-strain regime, perhaps a closer examination both of the microcracks not seen by the optical microscope and of more sections from each specimen would be informative.

The very small crack density in the section from the untested specimen confirms that the sectioning, infiltration and polishing operations do not introduce any significant cracking, so that the crack densities seen in the examination slices may be considered to represent the condition in the test-damaged specimens before sectioning.

Table 3. Crack Surface Area per unit volume at various strain levels.

| Specimen No. | Dynamic Test Results |                | Surface/Unit Volume |
|--------------|----------------------|----------------|---------------------|
|              | Predicted Strain     | Maximum Strain |                     |
| F21          | 0.0029               | .0041          | 2.14                |
| F22          | 0.0047               | .0065          | 5.78                |
| F23          | 0.0064               | .0092          | 7.46                |
| F24          | 0.0081               | .0103          | 4.76                |
| F25          | 0.0099               | .0128          | 7.68                |
| F04          | 0.0116               | .0126          | 6.06                |

### Static Test Results

| Specimen No. | Predicted Strain | Estimated Maximum Strain | Surface/Unit Vol. (in <sup>2</sup> /in <sup>3</sup> ) |
|--------------|------------------|--------------------------|---|
| F51          | .0012            | .0014                    | 1.16  |
| F52          | .0029            | .0031                    | 0.28  |
| F53          | .0047            | .0049                    | 0.94  |
| F54          | .0081            | .0083                    | 3.34  |
| F55          | .0099            | .0101                    | 5.92  |
| F56          | .0116            | .0118                    | 3.46  |

### Untested Specimen

|     |     |
|-----|-----|
| F50 | 0.2 |
|-----|-----|

### CONCLUSIONS

1. A substantial increase in crack surface per unit volume occurs at a threshold strain near the strain at peak stress in the no-collar tests.
2. The threshold strains of the dynamic and static tests are about the same.
3. It appears that the crack surface per unit volume is considerably higher in the dynamic tests than in the static tests at the same level of maximum strain. This suggests that in static tests there tends to be on the average more sliding on each crack than in dynamic tests.
4. The distribution of cracks is fairly uniform in the dynamic-test specimens, while there is a tendency for dense bands of cracks to form in the static tests.
5. The aggregate and the aggregate/mortar interface provide a considerable portion of the total crack area in this particular concrete. No great difference between the static and dynamic tests was noted in this respect.
6. The collar method was successful in arresting the tests, so that intact damaged specimens were recovered for examination, and it was possible to deduce the maximum strain level reached in the tests.
7. The sectioning, infiltration, and polishing did not introduce any significant additional macrocracking in the specimens.

### RECOMMENDATIONS

1. The results of this very limited investigation are so promising that a more extensive investigation along these lines seems warranted. The following specific recommendations should be considered in any extended investigation.
2. Specimens near the threshold strain are especially interesting. A closely spaced series to precisely map out the threshold region would be useful, and it should be possible to take a closer look at the process zones around the developing cracks, possibly using Scanning Electron Microscope methods.
3. More sections, on some specimens at least, should be taken to improve the statistics and reduce any orientation bias.
4. Stress measurements in the dynamic tests might be improved by more accurate alignment of the collar and use of strain gages on the elastic collar, which should make it possible to determine the load carried by the collar, so

that the load carried by the concrete could be calculated.

5. The crack identification was a tedious process because of the prominence of other micrographic features. It should be possible to facilitate the procedure by adding a fluorescent dye to the furfural alcohol before infiltration into the cracks and using ultraviolet illumination, so that only the cracks will show up in the micrograph. It might then be possible to automate the crack counting. Fluorescent-dye techniques have been reported previously in examination of very thin slices to observe porosity and microcracking; see References 8 to 10. They should also be useful to observe the macrocracks in thicker slices.

### REFERENCES

1. L. E. Malvern, T. Tang, D. A. Jenkins and J. C. Gong, "Dynamic Compressive Strength of Cementitious Materials," Materials Research Society, Symposium Proceedings, Vol. 64, 119-138, 1986.
2. L. E. Malvern and C. A. Ross, Dynamic Response of Concrete and Concrete Structures, Final Technical Report, Contract AFOSR F49620-83-K007, University of Florida, 30 May 1986.
3. L. E. Malvern, D. A. Jenkins, T. Tang and C. A. Ross, "Dynamic Compressive Testing of Concrete," Proc. Second Symposium on the Interaction of Non-Nuclear Munitions with Structures, Panama City Beach, Florida, April 15-19, 1985, pp. 194-199.
4. T. Tang, L. E. Malvern and D. A. Jenkins, "Dynamic Compressive Testing of Concrete and Mortar," Engineering Mechanics in Civil Engineering, eds. A. P. Boresi and K. P. Chong, ASCE, New York, 1984, pp. 663-666.
5. P. S. Follansbee and C. Frantz, "Wave Propagation in the Split-Hopkinson Pressure Bar," ASME Journal of Engineering Materials and Technology, Vol. 105, pp. 61-66, 1983.
6. C. W. Felice, The Response of Soil to Impulse Loads Using the Split-Hopkinson's Pressure Bar Technique, Ph. D. Dissertation, The University of Utah, 1985.
7. E. E. Underwood, "Surface Area and Length in Volume," pp. 78-125 in Quantitative Microscopy, eds. R. T. DeHoff and F. N. Rhines, McGraw-Hill, New York, 1968.
8. K. L. Gardner, "Impregnation Technique Using Colored Epoxy to Define Porosity in Petrographic Thin Sections," Canadian Journal of Earth Sciences, Vol. 17, pp. 1104-1107, 1980.
9. L. I. Knab, H. N. Walker, J. R. Clifton and E. R. Fuller, Jr., "Fluorescent Thin Sections to Observe the Fracture Zone in Mortar," Cement and Concrete Research, Vol. 14, pp. 339-344, 1984.
10. L. I. Knab, H. Jennings, H. N. Walker, J. R. Clifton and J. W. Grimes, "Techniques to Observe the Fracture Zone in Mortar and Concrete," pp. 241-247 in Fracture Toughness and Fracture Energy of Concrete, ed. F. H. Wittmann, Elsevier Science Publishers, Amsterdam, 1986.

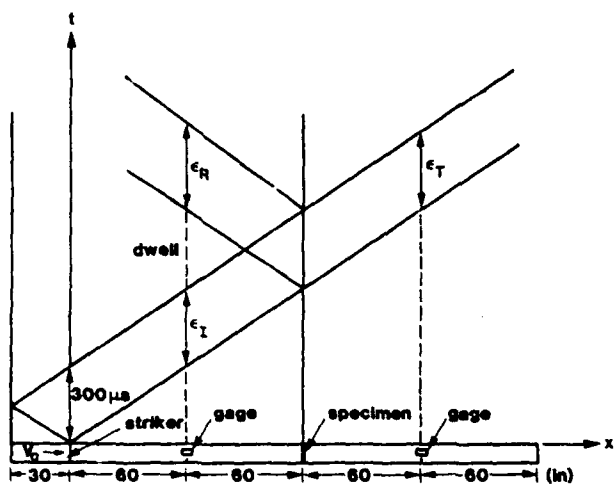


Figure 1. Schematic of SHPB Bars and Lagrange Diagram

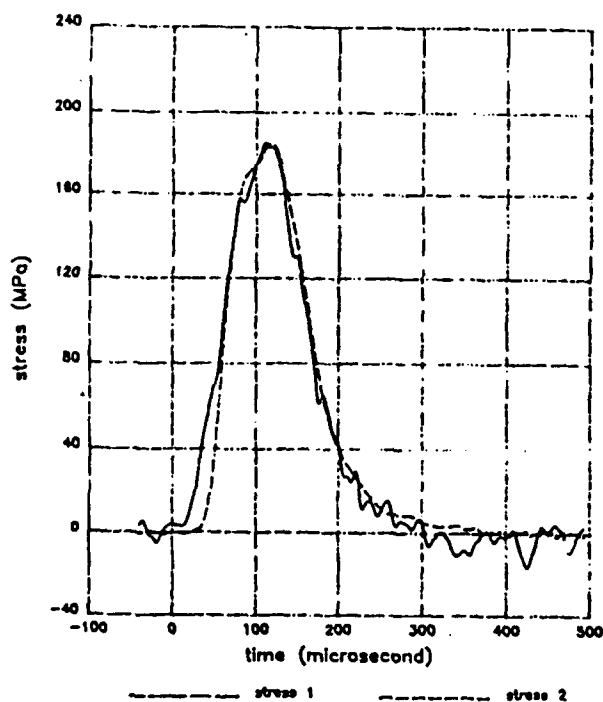


Figure 3. Corrected stresses at two specimen interfaces

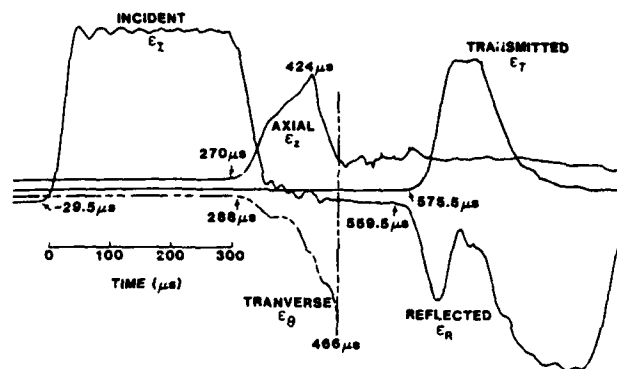


Figure 2. Strain Pulses in Pressure Bars and Axial and Transverse Specimen Surface Strains

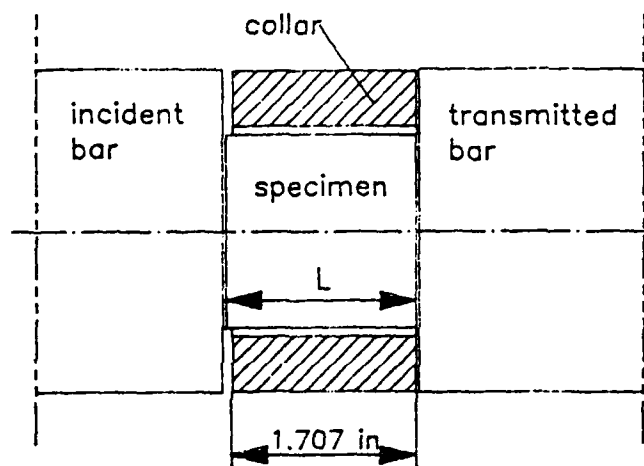


Figure 4. Collar used to interrupt tests

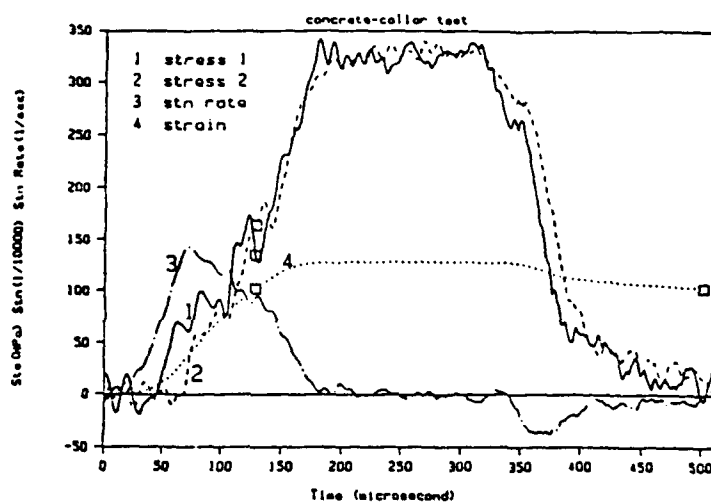


Figure 5. Stresses, strain, and strain rate versus time for collar test of Specimen No. F25

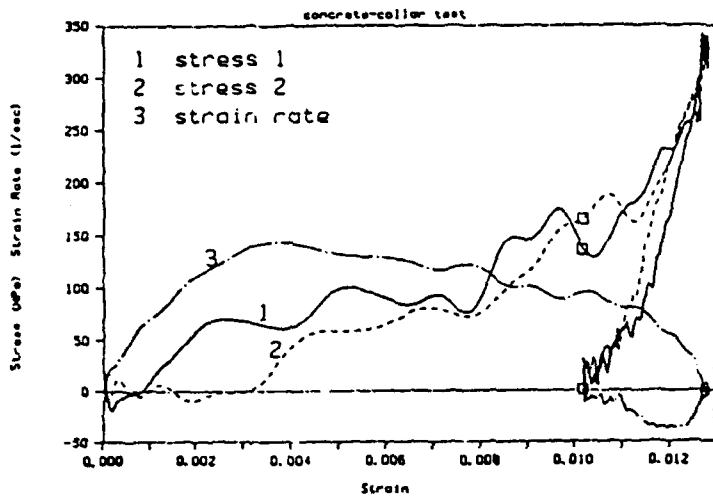


Figure 6. Stresses and strain rate versus strain for collar test of Specimen No. F25



Figure 8. Crack Pattern Tracing of Dynamic Test Specimen with maximum strain of 0.0041

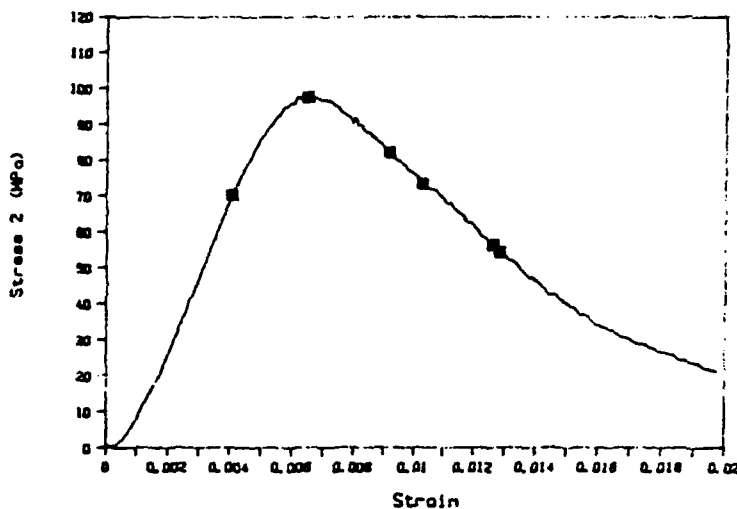


Figure 7. Dynamic stress-strain curve for no-collar test. Points marked correspond to maximum strains in collar-interrupted tests.



Figure 9. Crack Pattern Tracing of Static Test Specimen with maximum strain of 0.0049

#### ACKNOWLEDGMENTS

Research sponsored by the Air Force Office of Scientific Research, Air Force Systems Command, USAF, under Contract No. AFOSR-87-0201. The U. S. Government is authorized to produce and distribute reprints for Governmental purposes not withstanding any copyright notation thereon.

The concrete specimens used in this research were prepared and cured in the laboratory of the Civil Engineering Department at the University of Florida with the assistance of Mr. Daniel S. Richardson.

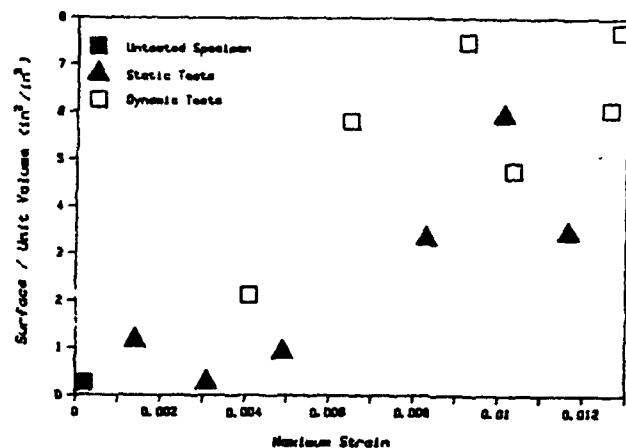


Figure 10. Crack surface area per unit volume versus maximum strain

## HIGH STRAIN RATE EFFECTS ON TENSILE STRENGTH OF CONCRETE

C. Allen Ross  
S. . Kuennen  
W. Strickland

HQ AF Engineering and Services Center  
AFESC/RDCS  
Tyndall AFB FL 32403-6001

### ABSTRACT

Direct tension tests using a Split Hopkinson Pressure Bar (SHPB) were conducted on two different types of tensile test specimens of concrete. In addition, splitting cylinder tests were also conducted using the SHPB. Quasi-static or low strain rate tests were conducted using a standard material test machine. As a comparison, direct compression tests were also conducted on the same material as the tensile specimens. The failure pattern of the splitting cylinder at high strain rates was the same as that of the splitting cylinder tested statically. Preliminary numerical calculations show that the stress distribution in the splitting cylinder tested at high strain rate is very similar to the splitting cylinder tested statically. Based on this, the fracture strength of the splitting cylinder is calculated using the peak SHPB transmitted stress and the statically derived equation for tensile stress. For a given strain rate the splitting cylinder strength ratio (dynamic strength/static strength) is slightly larger than the direct tension strength ratio. However, the results of these 5.10 cm diameter SHPB tests shows that the dynamic tensile strength ratio is approximately three times the compressive strength ratio at high strain rates of 10 to 100/sec.

### INTRODUCTION

Testing at high strain rates usually implies tests conducted at strain rates of approximately 5 to 10 /sec. Several researchers report concrete tensile strength data at strain rates between  $10^{-7}$ /sec to 5.0/sec. The tensile strengths data in the higher strain rate range was collected using a steel projectile impact against a cylindrical concrete bar and is reported in Reference 1. Impact of the projectile on the end of the concrete bar initiates a compressive stress wave which travels the length of the bar and is reflected from the free end as a tensile stress wave. If the tensile stress of the reflected wave exceeds the tensile strength of the bar material then fracture occurs. Data was collected using strain gauges along the bar and an estimate of the tensile stress magnitude at fracture was obtained. Over 50 tests similar to those of Reference 1, are reported for impact on mortar cylindrical bars in Reference 2, however, the dynamic tensile strength was less

than those reported in Reference 1. Several sets of tensile data up to a strain rate of 1.0/sec are presented and discussed in Reference 3. The data contained in Reference 1 and 2 are presented and discussed in Reference 3. The authors of Reference 4 have related the strength ratio (dynamic strength/static strength) as a function of  $\log(10)$  of strain to similar variations in the fracture mechanics parameters of crack tip opening displacement (CTOD) and the stress intensity factor  $K_{IC}$ . A gravity driven (falling weight) SHPB was used in Reference 5 to determine tensile strength of concrete at a strain rate of approximately 1.0/sec. However, the drop height was restricted and the strain rate above approximately 1.0/sec was not attainable.

The major objective in this study was to extend the range of data of concrete tensile strength to obtain rates to at least 10 /sec and above. This was to be accomplished using the HQ AFESC, Engineering and Services Laboratory SHPB (ESL-SHPB). Two different kinds of direct tension specimens and the splitting cylinder specimen were tested in the ESL-SHPB and a low load rate MTS material test machine.

### RESULTS

All specimens tested in this study were purchased from Waterways Experiment Station (WES) and fabricated according to the specifications of Figure 1. The 28 day static compressive strength  $f'_c$  was 43.5 MPa (6300 psi) and a six month static compressive strength was 48.3 MPa (7000 psi). The 28 day static splitting cylinder tensile strength was 3.38 MPa (490 psi). Splitting cylinder strength was not determined for the six month tests. All specimens were cored from a cast block which was cured for 28 days in a humidity chamber. After removal from the chamber all specimens were machined, stored, and tested in air conditioned rooms. All tests on the specimens were completed during the seventh, eighth and ninth month after the 28 day cure cycle.

All direct tension specimens were cemented to the ends of the SHPB and platens of the MTS machine using a nonepoxy cement obtained from the Tridox Products Corp, Philadelphia, PA. The bar surfaces

and specimens surfaces were cleaned in a manner similar to that used for surface cleaning prior to placement of foil resistance strain gauges. This procedure was to clean with a mild acidic solution followed by a neutralizer solution. (These solutions are available from Micromediment Corp.) The worst problem in this cementing process is removal of the broken specimen from the bars and platens. Removal of the broken specimens was accomplished first by chiseling away the large portions and then breaking away the smaller pieces by light tapping of a hammer. A schematic of the specimens mounted in the SHPB and MTS platens are shown in Figure 2. The diameter of the specimens, SHPB, and MTS platens were all 5.1 cm (2.0 in).

The principles of operation of the compressive SHPB are covered in detail in Reference 6 and these same principles apply to the direct tension SHPB. The ESL-SHPB (Figure 3) has both compressive and tensile capability. On the compressive side a solid striker bar is launched by a gas gun and impacts the incident bar. Upon impact a stress wave is set up in the incident bar which impinges on the test specimen sandwiched between the incident and transmitter bars. Electrical resistance strain gauges are mounted on both incident and transmitter bars equidistant from the specimen. These gauges and related equipment record the incident, reflected and transmitted signals. It can be shown that the transmitted strain and the time integral of the reflected strain are respectively proportional to the stress and strain in the specimen. Prior to producing a stress-strain curve these signals are corrected for dispersion and phase shifted back to the front and rear faces of the specimens using a computer code described in Reference 7.

The tensile loading mechanism consists of a hollow cylindrical striker bar sliding on the compressive transmitter bar of the ESL-SHPB. The striker bar impacts a tup threaded into the end of what becomes the tensile incident bar, and sends a tensile stress wave, toward the specimen, cemented between the two bars. In the tensile mode, the strain gauges are used opposite in manner as used in the compressive mode. In each case the strain gauge closest to the active striker bar becomes the incident gauge and the remaining one becomes the transmitter gauge.

The SHPB assumption of uniform stress along the specimen length may be checked by comparing the stresses on the front face (STRESS1, the sum of the incident and reflected stresses) with the stress on the rear face (STRESS2, the transmitted stress). If STRESS1 and STRESS2 are nearly equal, then the assumption is good, but large disagreement is an indicator that the uniform stress assumption is invalid. An alternate method of determining stress uniformity along the specimen length is to measure the wave speed in the specimen and compare the wave-transit time across the specimen with the time of the test. Stress uniformity is usually assumed if the time of test is approximately ten times greater than the specimen wave-transit time.

Figures 4 and 5 show respectively, the uncorrected strain signals for a square notch and saddle notch specimen. Knowing that the transmitted and reflected signals are coincident in time, then the peak of the transmitted signal is observed to occur during the rise time of the reflected pulse (see Figures 4 and 5). For clarity, the inverse of the transmitted pulse is shown as a dotted line in these figures. The question arises as to whether there is sufficient time for multiple reflections within the specimen prior to failure. Figure 6 and 7 show large disagreement between the STRESS1 and STRESS2 of the direct tension specimens. This observation is an indicator that the direct tension specimens used in this study are questionable with respect to uniformity of stress along the specimen length. A dynamic stress analysis of these specimens should answer the question of stress uniformity. An additional problem encountered in the direct tensile specimens was that of multiple fractures along the length of the specimen at strain rates above 20/sec.

It is generally accepted that the peak of the transmitted signal is an indicator of the maximum load or stress in the specimen. Therefore, in the case of the SHPB direct tension specimens, the nonuniformity of stress along the specimen length affects the calculated strain rate, but not the maximum stress. For normal SHPB operation, the strain rate is based upon the reflected strain assuming uniformity of stress in the gauge length of the specimen. An alternative method, which was also employed in the splitting cylinder test, is to measure the loading rate of the transmitted pulse and calculate the strain rate by dividing the loading rate by the elastic modulus. This method was used for both the direct tension specimens and splitting cylinder specimens and the data of Figure 9 reflects this. Assuming stress uniformity the incident strain, reflected strain and a gauge length of 2.54 cm (1.0 in) was used in calculating the strain rate shown in Figures 6 and 7. These strain rates differ from those calculated using the loading rate by a factor of approximately 5.0. Much higher strain rates could be calculated using a smaller gauge length. The pertinent conclusion here is that the test method is sound but modifications in the direct tensile specimen are necessary if stress uniformity along the specimen length is required.

The peak transmitted stress of the splitting cylinder specimen, shown in Figure 8, occurs after the reflected stress reaches an almost constant value. Here again, the inverse of the transmitted pulse is shown as a dotted line. This indicates that there may be sufficient time for the stress distribution to extend across the specimen diameter and become rather stable for a short period of time. Based on a numerical analysis of Reference 8, the dynamic stress distribution behind the initial stress wave front is identical to the stress distribution of a statically loaded splitting cylinder specimen. Using this fact, the dynamic tensile strength  $f_d$  is calculated using the statically derived equation

$$f'_{td} = \frac{2P}{\pi DL} \quad (1)$$

$$P = (\sigma_T)_{\max} A$$

where D is the specimen diameter, L is the specimen length,  $(\sigma_T)_{\max}$  is the peak transmitted stress shown in Figure 8, and A is the SHPB diameter.

For the splitting cylinder test only the tensile strength and load rate may be determined. The tensile strength is determined from Eq. (1) and the loading rate is determined using the strength of Eq. (1) divided by the rise time of the transmitted pulse on Figure 8. The strain rate is then calculated using the static modulus assuming the tensile and compressive moduli are equal. The failure pattern, in which the specimen splits across the loaded diameter, is the same for both the dynamic and static loaded specimens.

Compressive data for the same concrete mix were collected at low and high strain rate using 5.1 cm diameter, 5.1 cm long specimens. Additionally, the same size specimens were tested in the 7.62 cm diameter SHPB at the University of Florida. These test data and all the tensile test data are shown in Figure 9 along with some tensile test data from other researchers of References 3, 4, and 5. The solid line of Figure 9 is based on an equation suggested in Reference 4 and repeated here as

$$\begin{aligned} \frac{f'_{td}}{f'_{ts}} &= \exp(AE^B) \\ E &= \log_{(10)} [\dot{\epsilon}_d / \dot{\epsilon}_s] \\ \dot{\epsilon}_s &= 10^{-7} / \text{sec} \\ A &= 0.0164 \\ B &= 2.086 \\ \dot{\epsilon} &= \text{Strain Rate} \end{aligned} \quad (2)$$

d,s subscripts for dynamic and static

#### CONCLUSIONS

The direct tensile specimens used in this study do not appear to conform to the SHPB assumption of uniform stress along the length of the specimen. Results of the direct tensile SHPB tests are also complicated by multiple fractures at the higher strain rates. It is worth noting that concrete appears to behave as a brittle elastic material under both static and dynamic tensile loads. Using this observation, stress uniformity along the SHPB specimen length may not occur, but the peak transmitted stress is a measure of the tensile strength of the specimen and the load rate

divided by the elastic modulus is a reasonable estimate of the strain rate at fracture.

Tensile fracture patterns of the splitting cylinders were practically identical at all strain rates tested. The dynamic stress distribution of SHPB split cylinder behind the initial passage of the stress wave is very similar to the stress distribution of a statically loaded cylinder. The fracture stress of the splitting cylinders tested in the SHPB are 30 to 50 percent higher than the direct tension specimens for a given strain rate. However, the splitting cylinder specimen may prove to be the better dynamic test specimen for determining tensile strength as a function of strain rate.

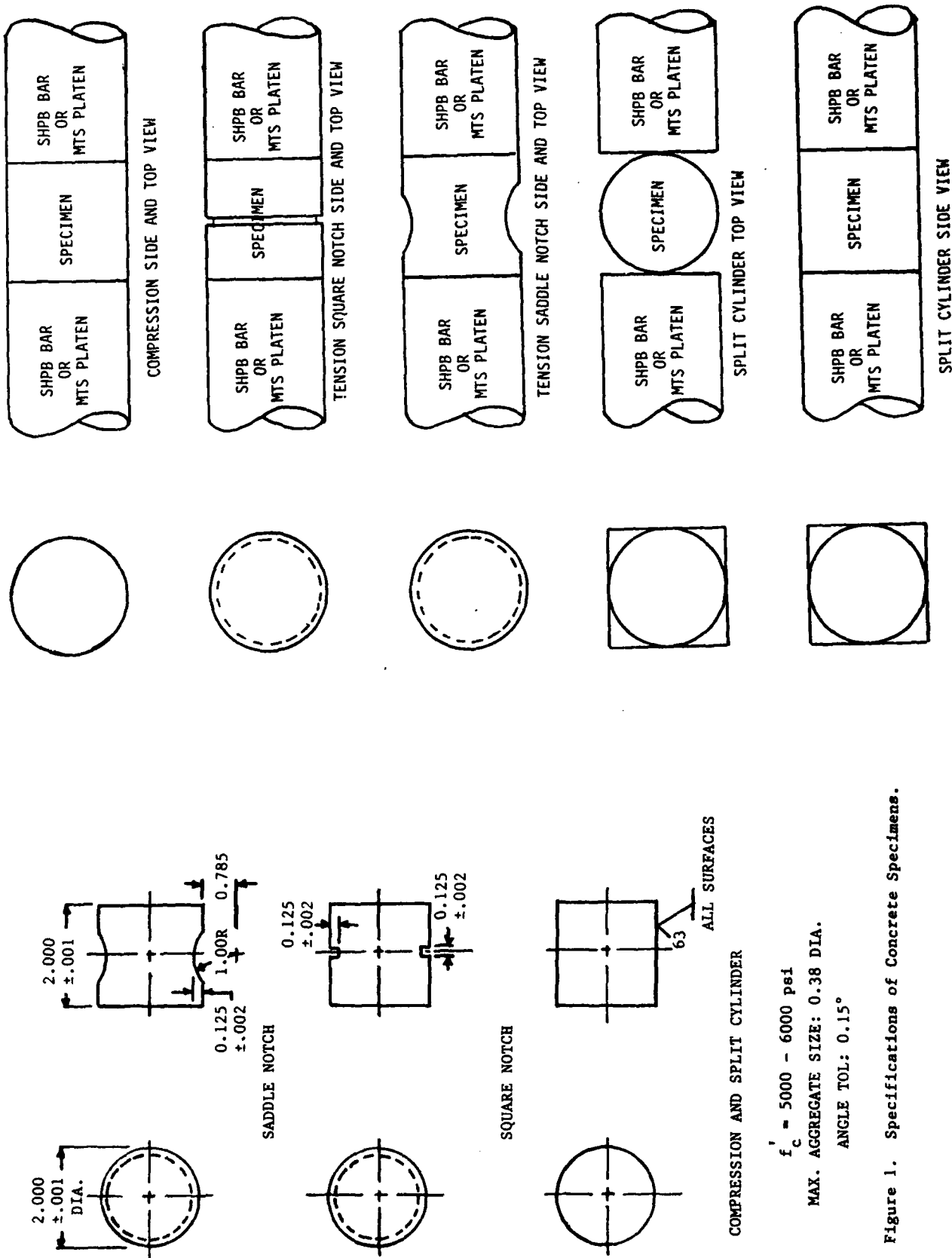
#### ACKNOWLEDGEMENT

Dr. C. A. Ross was supported by the Air Force Office of Scientific Research under a University Resident Research Program. All experimental tests were conducted in the Engineering Services Laboratory, HQ AF Engineering and Services Center, Tyndall AFB, FL.

#### REFERENCES

1. Mellinger, F. M. and Birkimer D. L., "Measurement of Stress and Strain on Cylindrical Test Specimens of Rock and Concrete Under Impact Loading," Tech. Rept No. 4-46 Ohio River Div. Lab. Corps of Eng., Cincinnati, Ohio 45227, Apr 1966.
2. Griner, G. R., Sierakowski, R. L. and Ross, C. A., "Dynamic Properties of Concrete Under Impact Loading," Proceedings 45th Symposium on Shock and Vibration, June 1975.
3. Oh, B. H., "Behavior of Concrete Under Dynamic Tensile Loads," ACI Materials Journal Jan. - Feb. 1987.
4. John, R. and Shah, S., "Effect of High Strength and Rate of Loading on Fracture Parameters of Concrete," Proceedings, RILEM-SEM Int. Conf. on Fracture of Concrete and Rock, Houston, TX, June 1987.
5. Kormeling, H. A., Zielinski, A. J. and Reinhardt, H. W., "Experiments on Concrete Under Single and Repeated Uniaxial Impact Tensile Loading," Rept. 5-80-3, Delft Univ. of Tech., Dept of Civil Eng., Delft Netherlands, Aug. 1981.
6. Nicholas, T., "Material Behavior at High Strain Rates", Chapter 8 of Impact Dynamics, Zukas, J. R., Editor: J. Wiley and Sons, NY, pp 277-332, 1982.
7. Malvern, L. E., Jenkins, D. A., Jerome, E. and Gong, J. C., "Dispersion Correction for Split Hopkinson Bar Data", ESL-TR-88-04, Air Force Engineering and Services Laboratory, Tyndall AFB FL, July 1988.
8. Tedesco, J. W., Ross, C. A., and Brunair, R. M., "Inelastic Analysis of the Dynamic Split Cylinder Test," 4th International Symposium on the Interaction of Non-Nuclear Munitions with Structures, Panama City Beach, FL, April 1989.





$f'_c = 5000 - 6000 \text{ psi}$   
 MAX. AGGREGATE SIZE:  $0.38 \text{ DIA.}$   
 ANGLE TOL:  $0.15^\circ$

Figure 1. Specifications of Concrete Specimens.

Figure 2. Schematic of Specimens in SHPB or MTS.

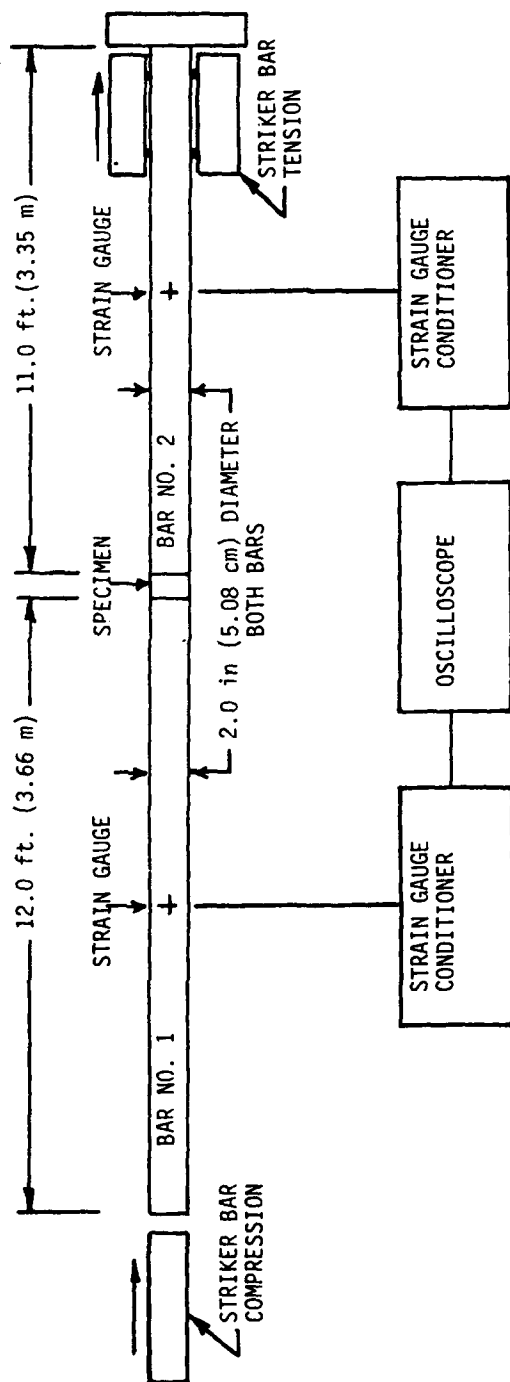


Figure 3. Schematic of the ESL SHPB.

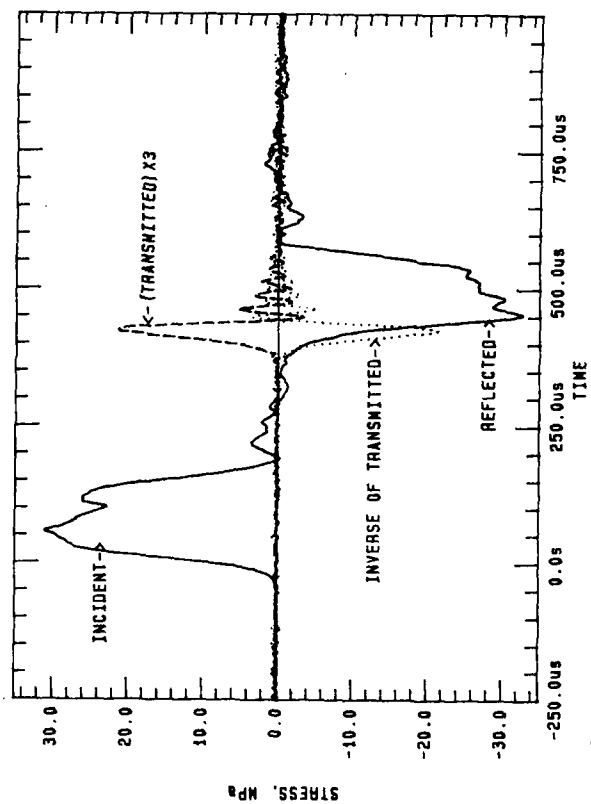


Figure 4. Uncorrected SHPB Stress Signals for a Square Notch Direct Tensile Specimen.

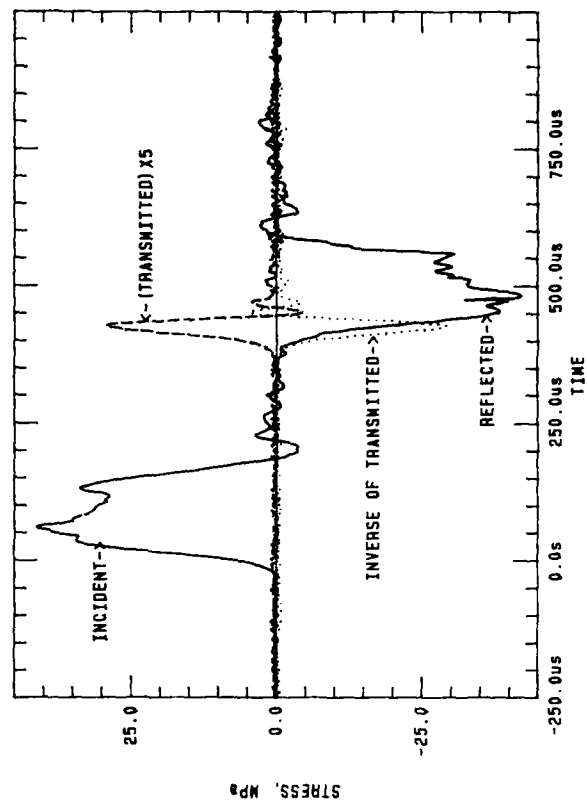


Figure 5. Uncorrected SHPB Stress Signals for a Saddle Notch Direct Tensile Specimen.

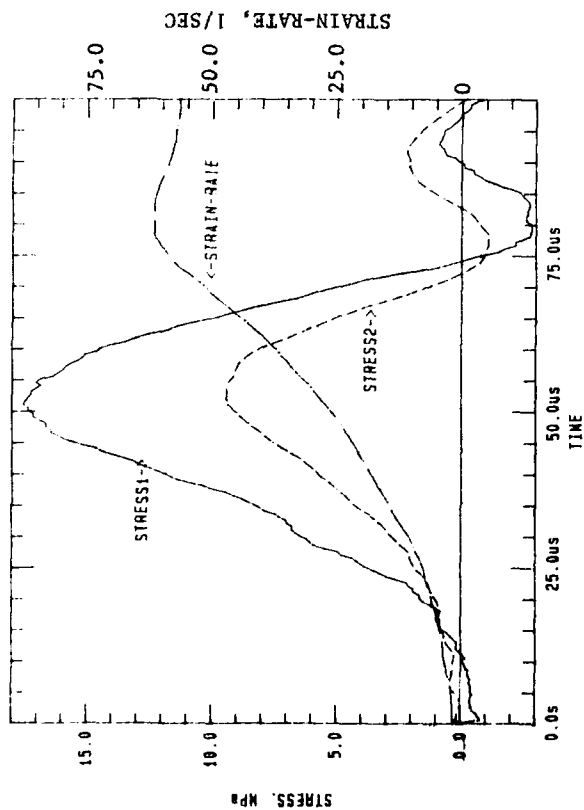


Figure 6. Corrected Front Face (STRESS1) and Rear Face (STRESS2) Stresses of a Square Notch Specimen. Strain-Rate Based on the Reflected Signal.

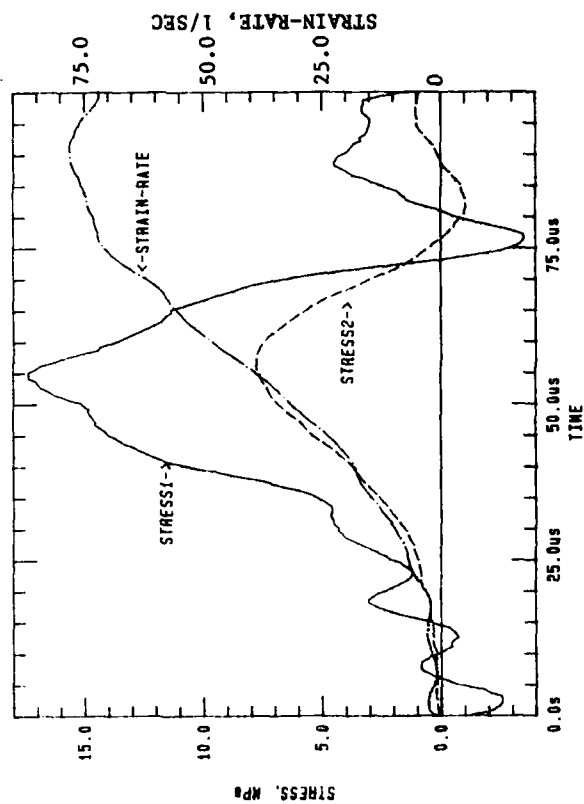


Figure 7. Corrected Front Face (STRESS1) and Rear Face (STRESS2) Stresses of a Saddle Notch Specimen. Strain-Rate Based on the Reflected Signal.

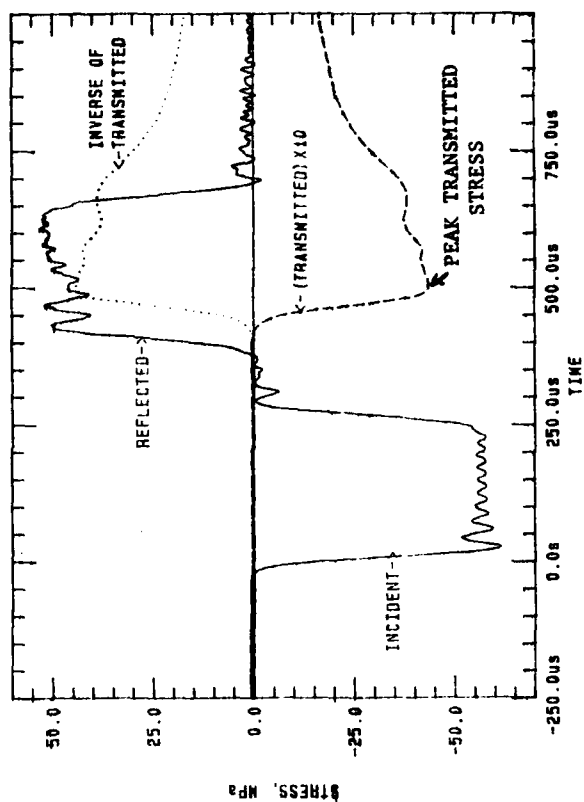


Figure 8. Uncorrected SHPB Stress Signals for a Splitting Cylinder Specimen.

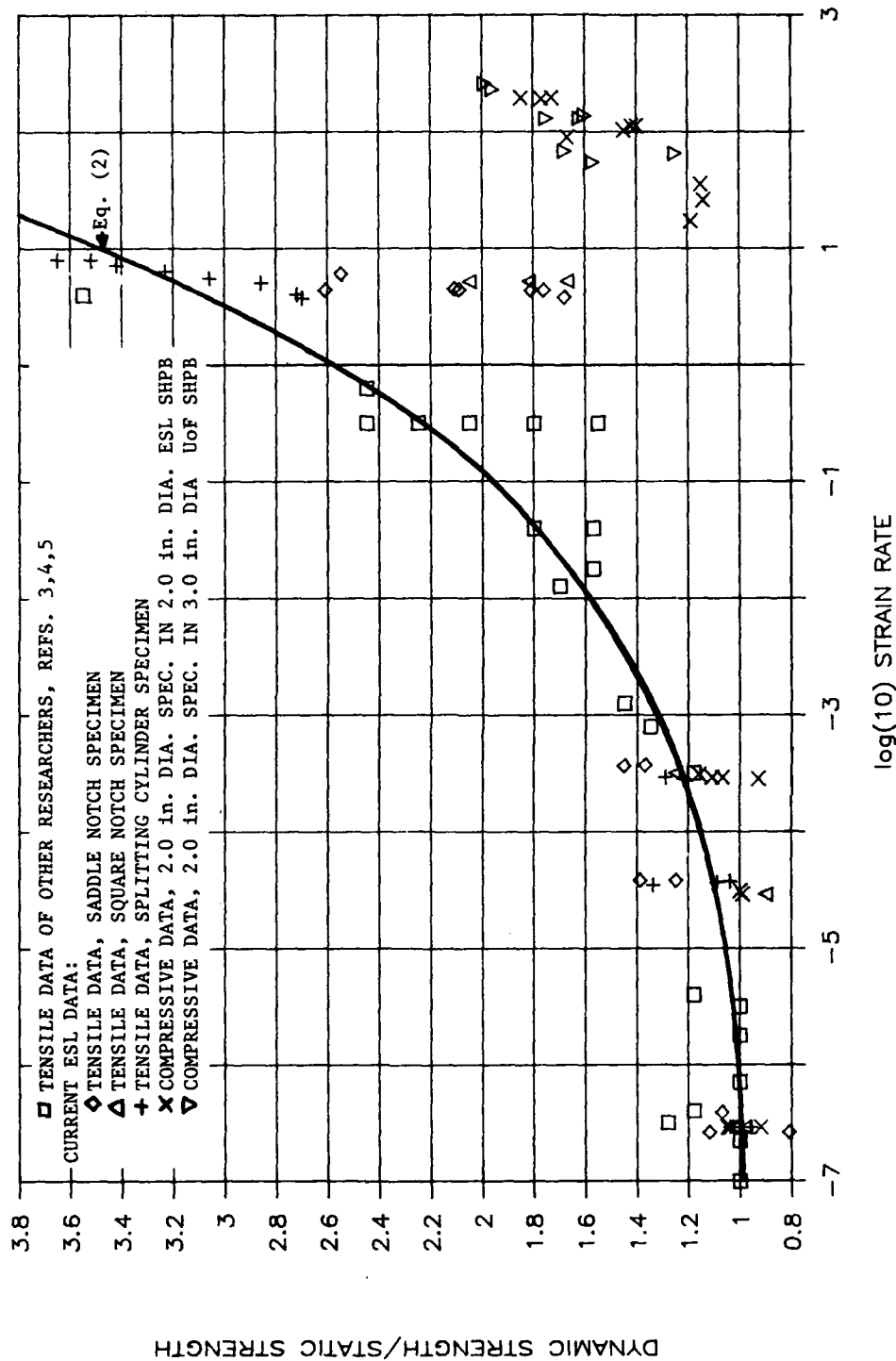


Figure 9. Strength Ratios (Dynamic Strength/Static Strength) vs log(10) of Strain Rate for Concrete.

# INELASTIC ANALYSIS OF THE DYNAMIC SPLIT CYLINDER TEST

Joseph W. Tedesco  
Department of Civil Engineering A.F. Engineering and Services Center  
Auburn University, Alabama 36849

C. Allen Ross  
Department of Civil Engineering  
Tyndall AFB, Florida 32403

Robert M. Brunair  
Department of Civil Engineering  
Auburn University, Alabama 36849

**Abstract** - To investigate the effects of strain rate on the tensile strength of concrete, split cylinder tests of plain concrete specimens were conducted on a Split Hopkinson Pressure Bar (SHPB). To ascertain the stress condition in the material specimens at failure, a comprehensive finite element method (FEM) study was conducted on the SHPB experiments. Both linear and nonlinear analyses were performed. From the results of the numerical analyses, the dynamic states of stress occurring in the split cylinder prior to failure, as well as the mode of failure, are revealed.

## INTRODUCTION

The understanding of material response to high amplitude, short duration, impulse loads generated in a weapons environment is an important problem in protective shelter design and analysis [1]. To model the response in the laboratory requires that the environment must reflect the type of confinement, magnitude of stress change, and the time scale of loading anticipated in the field [2]. The Split Hopkinson Pressure Bar (SHPB) technique [3] can produce the required environment in the laboratory.

In order to investigate the effects of strain-rate on the tensile strength of concrete, split cylinder tests of plain concrete specimens were performed at strain rates between  $10$  and  $10^3$  per second on an SHPB. However, a critical shortcoming with the experiments performed on the SHPB is the inability to ascertain the stress condition in the material specimen. Therefore, in an effort to analyze the dynamic stress distribution in high rate split cylinder tests, a comprehensive finite element method (FEM) study was conducted through implementation of the ADINA [4] computer programs. Both linear and nonlinear analyses were performed.

## SPLIT CYLINDER TESTS ON THE SHPB

The dynamic split cylinder tests were conducted using the 2.0 in. diameter SHPB at the Air Force Engineering and Services Center, Tyndall AFB, Florida. The specimen arrangement for the split cylinder tests is illustrated in Fig. 1. The cylindrical specimens were 2 inches in diameter and 2 inches in length. The static, linear material properties for the specimens were measured as follows: the static compressive strength,  $f'_{cs} = 7000$  psi; the static tensile strength,  $f'_{ts} = 560$  psi; Young's Modulus,

$E = 5.5 \times 10^6$  psi; and mass density,  $\rho = .0006747$  lb-sec<sup>2</sup>/in<sup>4</sup>.

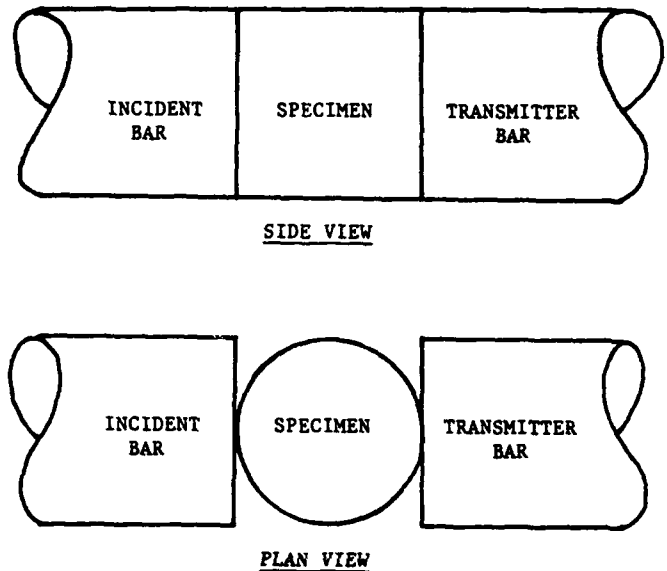


Fig. 1. Split cylinder test arrangement in the SHPB.

SHPB tests were conducted for three different loading conditions. The stress vs. time history for load case 1 is illustrated in Fig. 2. It is assumed that the peak dynamic tensile stress,  $f'_{td}$ , of the split cylinder is proportional to the peak transmitted stress (STRESS 2 of Fig. 2),  $\sigma_T$ , through the closed form solution of Neville [5]:

$$f'_{td} = \frac{2P}{\pi LD} \quad (1)$$

in which

$$P = \pi R^2 \sigma_T \quad (2)$$

where  $L$  is the specimen length,  $D$  is the specimen diameter, and  $R$  is the radius of the SHPB.

Additionally, the loading rate,  $\dot{\sigma}$ , and the strain rate,  $\dot{\epsilon}$ , in the specimen can be estimated from the expressions

$$\dot{\sigma} = \frac{f'_{td}}{\tau} \quad (3)$$

and

$$\dot{\epsilon} = \frac{\dot{\sigma}}{E} \quad (4)$$

where  $\tau$  is the time lag between the start of the

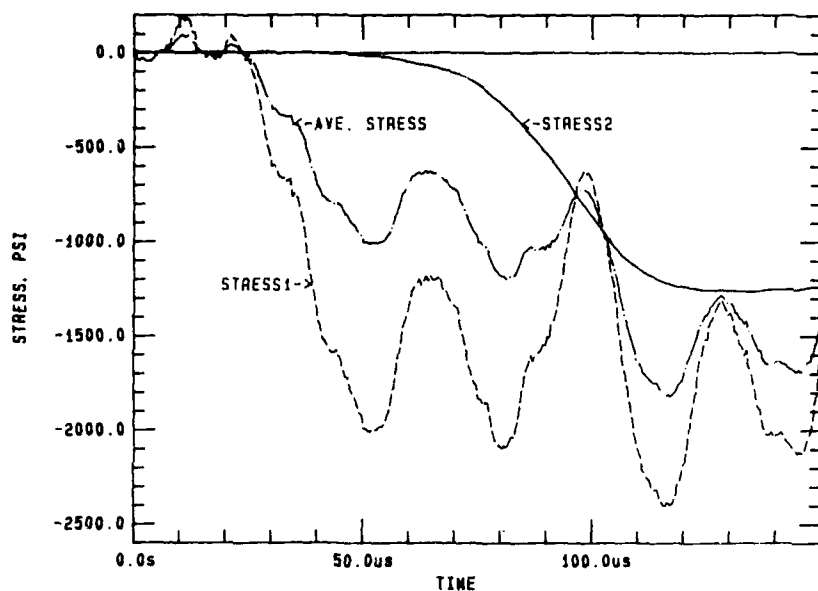


Fig. 2. Split cylinder test data trace for load case 1.

reflected stress wave and the maximum transmitted stress (which is determined from the stress history). A summary of the results obtained from the SHPB tests is presented in Table 1.

Table 1. Summary of SHPB results.

| Load Case No. | Incident Stress $\sigma_i$ (psi) | Transmitted Stress $\sigma_T$ (psi) | Dynamic Tensile Stress $f_{td}$ (psi) | Loading Rate $\dot{\sigma}$ (PSI/sec) | Strain Rate (sec <sup>-1</sup> ) | Experimental Dynamic Increase Factor $\frac{f_{td}}{f_{ts}}$ |
|---------------|----------------------------------|-------------------------------------|---------------------------------------|---------------------------------------|----------------------------------|--|
| 1             | 8740                             | 1270                                | 635                                   | $9.6 \times 10^6$                     | 1.7                              | 1.14   |
| 2             | 10550                            | 3040                                | 1520                                  | $2.1 \times 10^7$                     | 3.8                              | 2.71   |
| 3             | 38320                            | 4080                                | 2040                                  | $4.2 \times 10^7$                     | 7.7                              | 3.64   |

#### LINEAR ANALYSIS

An illustration of the FEM model employed in the study is depicted in Fig. 3. The cylinder is

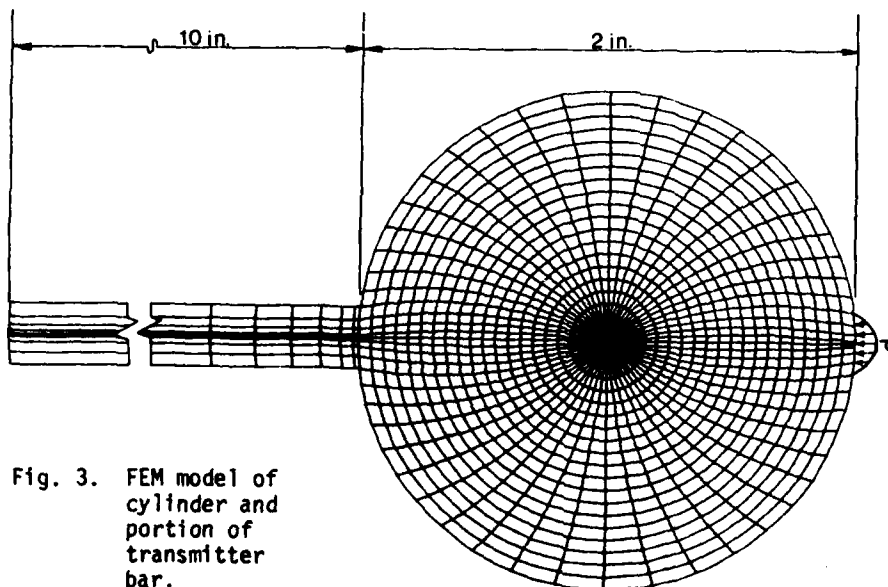


Fig. 3. FEM model of cylinder and portion of transmitter bar.

comprised of 1200 8-node, 2-dimensional finite elements. In order to avoid the development of artificial reflected stresses at the interface between the cylinder and the transmitter bar by the imposition of a rigid boundary, a 10-inch length of the transmitter bar was incorporated into the FEM model. This portion of the model is comprised of 200 8-node, 2-dimensional finite elements. The loading on the split cylinder is applied at the boundary of the cylinder and the incident bar, which is designated as the top of the cylinder.

In order to calibrate the FEM model and verify its accuracy, static analyses of the cylinder portion of the model were conducted for the three load cases summarized in Table 1. The statically applied load was taken as the product of the peak incident stress and the cross sectional area of the incident bar. The numerical results were compared with a closed form analytical solution [5].

The distribution of the horizontal stress,  $\sigma_x$ , along the vertical diameter, obtained from the FEM analysis for load case 1, is presented in Fig. 4. A similar plot for the horizontal stress distribution along the horizontal

diameter is presented in Fig. 5. The numerical results for the horizontal and vertical stresses occurring at the center of the cylinder for all three load cases are presented in Table 2. Excellent correlation with the closed form solutions is noted.

Dynamic analyses were conducted on the SHPB

split cylinder specimens described in the previous section. The loading conditions for the dynamic analyses were determined from the SHPB data curves

of the incident, reflected, and transmitted strain gage traces. These curves were corrected for dispersion and phase change. The stress on the incident face, STRESS 1, the stress on the transmitted face, STRESS 2, and the average of these two stresses, AVE STRESS, are shown in Fig. 2 for load case 1.

Past experience with SHPB experiments [6,7] suggests that the STRESS 2 curve is indicative of the load transmitted to the specimen. In the numerical analyses, the load functions were simulated with a ramp loading. The rise time,  $t_r$ , the stress level,  $P_0$ , and the time of duration,  $t_d$ , for the three load cases are summarized in Table 3.

For problems in which an elastic body is subjected to a short duration impulse loading,

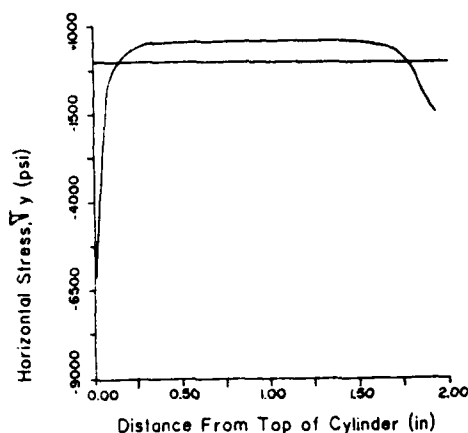


Fig. 4. Horizontal stress distribution along the vertical diameter.

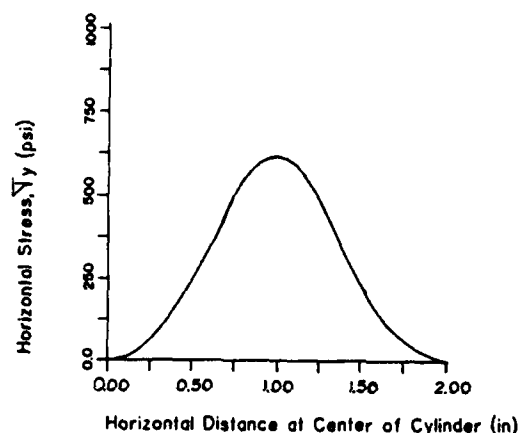


Fig. 5. Horizontal stress distribution along the horizontal diameter.

Table 2. Static stresses at center of cylinder.

| Load Case No. | Vertical Stress, $\sigma_z$ (psi) |         | Horizontal Stress, $\sigma_y$ (psi) |         |
|---------------|-----------------------------------|---------|-------------------------------------|---------|
|               | FEM Analysis                      | Eq. (5) | FEM Analysis                        | Eq. (6) |
| 1             | 1861                              | 1905    | 613                                 | 635     |
| 2             | 4456                              | 4560    | 1468                                | 1520    |
| 3             | 5980                              | 6120    | 1970                                | 2040    |

Table 3. Parameters for ramp load function

| Load Case No. | Rise Time $t_r$ (usec) | Stress Level $P_0$ (psi) | Time of Duration $t_d$ (.sec) |
|---------------|------------------------|--------------------------|-------------------------------|
| 1             | 66                     | 1270                     | 100                           |
| 2             | 72                     | 3040                     | 100                           |
| 3             | 48                     | 4080                     | 100                           |

the propagation of stress/strain waves through the body must be considered in formulating the solution. Modal analyses generally do not yield cost effective, accurate results for wave propagation problems, therefore, a direct numerical integration procedure must be utilized.

In the present study the Newmark method of implicit time integration with a consistent mass formulation is employed. The time step selected

for temporal integration in a wave propagation problem is critical to the accuracy and stability of the solution. Since the Newmark method is unconditionally stable, selection of the time step can be based entirely upon accuracy considerations. In a wave propagation problem, the maximum time step is related to wave speed in the material and element size. The maximum time step is selected so that the stress wave propagates the distance between element integration points within that time increment. The maximum time step is defined by

$$(\Delta t)_{\max} = \frac{L_e/2}{c} \quad (5)$$

where  $L_e$  is the length of an element in the direction of wave propagation, and  $c$  is the velocity of wave propagation, given by

$$c = \sqrt{\frac{E}{\rho}} \quad (6)$$

It has been determined from previous experience [8] that a time step of

$$\Delta t \leq \frac{1}{3}(\Delta t)_{\max} \quad (6)$$

yields accurate results. In the present study, a time step of  $\Delta t = 50$  nanoseconds was used for all dynamic analyses.

Time histories of the horizontal stress,  $\sigma_y$ , for load case 1 at two locations along the vertical diameter are illustrated in Figs. 6 and 7 for

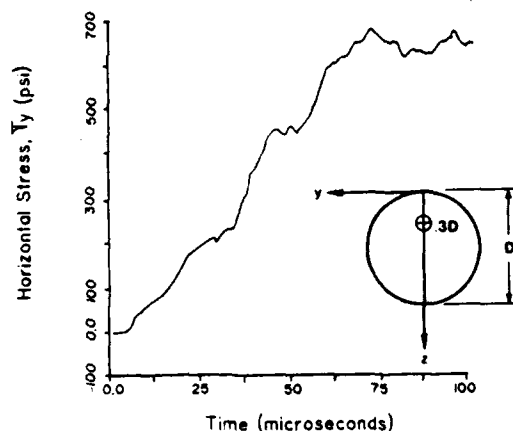


Fig. 6. Time history for horizontal stress at  $z = 0.30$ , load case 1.

$z$  equal to  $0.30D$  and  $0.50D$ , respectively. These time histories indicate that the maximum horizontal stress,  $(\sigma_y)_{\max}$ , occurs at the center of the cylinder ( $z = 0.50D$ ). This observation suggests that, under dynamic loading, the cylinder would begin to crack at its center. The crack would then propagate along the vertical diameter toward the outer boundaries of the cylinder and eventually perpetuate failure.

Profiles for the horizontal stress,  $\sigma_y$ , along the vertical diameter for load case 1 at selected times are illustrated in Figs. 8 and 9. Similar profiles for the horizontal stress along the horizontal diameter are illustrated in Figs. 10 and 11.

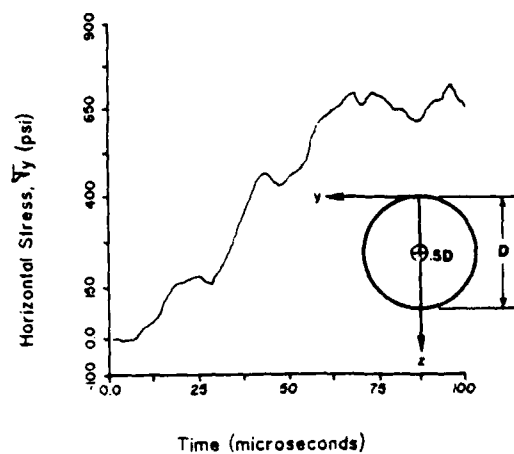


Fig. 7. Time history for horizontal stress at  $z = 0.5D$ , load case 1.

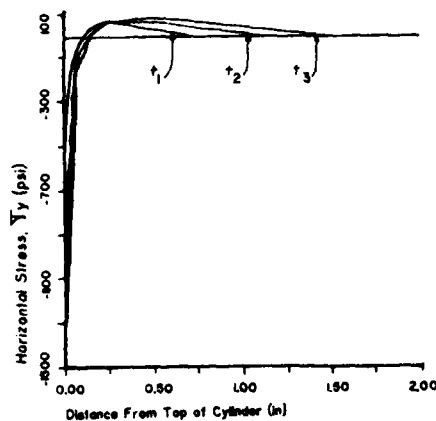


Fig. 8. Profiles for horizontal stress along the vertical diameter, load case 1 ( $t_1$ ,  $t_2$ ,  $t_3$ ).

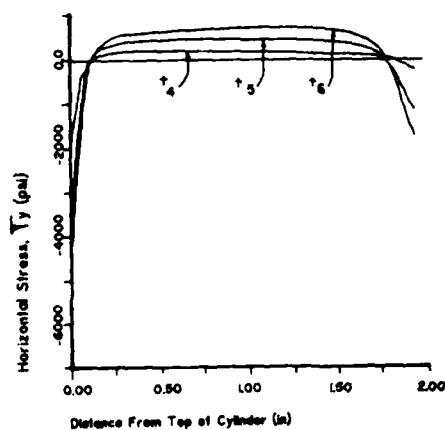


Fig. 9. Profiles for horizontal stress along the vertical diameter, load case 1 ( $t_4$ ,  $t_5$ ,  $t_6$ ).

It is interesting to note the close resemblance the dynamic stress profiles bear to the static stress profiles presented in Figs. 4 and 5.

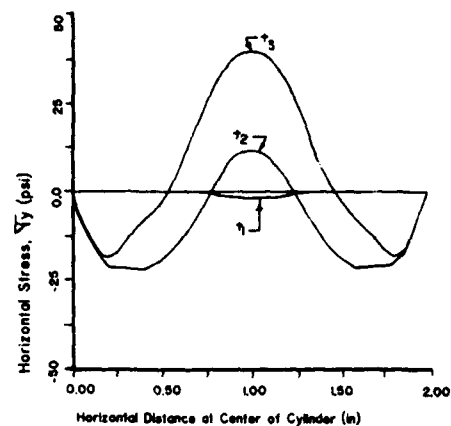


Fig. 10. Profiles for horizontal stress along the horizontal diameter, load case 1 ( $t_1$ ,  $t_2$ ,  $t_3$ ).

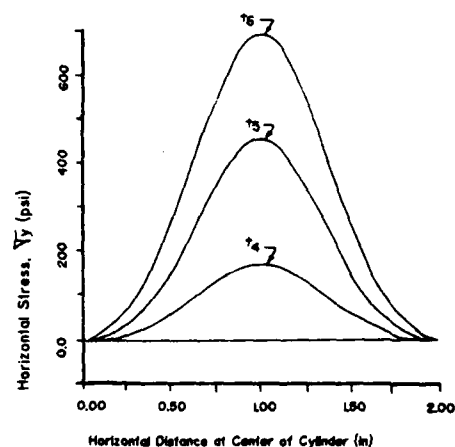


Fig. 11. Profiles for horizontal stress along the horizontal diameter, load case 1 ( $t_4$ ,  $t_5$ ,  $t_6$ ).

The representative times for the stress profiles are presented in Table 4. The numerical results for the maximum dynamic vertical and horizontal stresses occurring at the center of the cylinder for all three load cases are summarized in Table 5. Also presented in Table 5 are the dynamic increase factors (DIF) for each load case.

Table 4. Selected times for stress profiles.

| Designation | Time (usec) | Designation | Time (usec) |
|-------------|-------------|-------------|-------------|
| $t_1$       | 6.28        | $t_4$       | 25.14       |
| $t_2$       | 9.43        | $t_5$       | 50.17       |
| $t_3$       | 12.57       | $t_6$       | 75.86       |

#### NONLINEAR ANALYSIS

In order to ascertain the failure pattern for the dynamic split cylinder tests, a nonlinear material analysis was conducted. The concrete material model employed in the nonlinear analysis is a hypoelastic model based on a uniaxial stress-strain relation that is generalized to take biaxial and triaxial conditions into account [4]. The model employs three basic features to describe the



Table 5. Dynamic Stresses at center of cylinder

| Load Case No. | Vertical $\sigma_z$ (psi) | Horizontal $\sigma_y$ (psi) | Dynamic Impact Factors (DIF) |                        |                        |
|---------------|---------------------------|-----------------------------|------------------------------|------------------------|------------------------|
|               |                           |                             | $(\sigma_z)_{dynamic}$       | $(\sigma_y)_{dynamic}$ | $(\sigma_y)_{dynamic}$ |
|               |                           |                             | $(\sigma_z)_{static}$        | $(\sigma_y)_{static}$  | $f_{ts}$               |
| 1             | 2050                      | 690                         | 1.10                         | 1.09                   | 1.23                   |
| 2             | 4750                      | 1650                        | 1.07                         | 1.09                   | 2.95                   |
| 3             | 7500                      | 2450                        | 1.25                         | 1.20                   | 4.38                   |

material behavior: (i) a nonlinear stress-strain relation including strain softening to allow for weakening of the material under increasing compressive stresses; (ii) a failure envelope that defines cracking in tension and crushing in compression; and (iii) a strategy to model post-cracking and crushing behavior of the material.

In order to establish the uniaxial stress-strain law accounting for multiaxial stress conditions, an appropriate failure envelope must be employed. Since failure of the split cylinder is tension-dominated, a tension failure envelope [4] was used in the concrete model. To identify whether the material has failed, the principal stresses are used to locate the current stress state in the failure envelope. The tensile strength of the material in a principal direction does not change with the introduction of tensile stresses in other principal directions. However, the compressive stresses in the other principal directions alter the tensile strength. The pertinent material parameters for the failure envelope and the uniaxial stress-strain relation are summarized in Table 6.

Table 6. Concrete model parameters.

| Parameter  | Specified Value |
|--|-----------------|
| $E_0$ , initial tangent modulus (psi)  | 5,500,000.0     |
| $\sigma_t$ , uniaxial cut-off tensile strength (psi)   | 560.0           |
| $\sigma_c$ , uniaxial maximum compressive stress (psi)   | 7,000.0         |
| $\sigma_u$ , uniaxial ultimate compressive stress (psi)  | 7,000.0         |
| $\sigma'_c$ , uniaxial compressive failure stress under multiaxial conditions (psi)              | 9,100.0         |
| $\epsilon_c$ , compressive strain at $\sigma_c$  | 0.0022          |
| $\epsilon_u$ , uniaxial ultimate compressive strain  | 0.005           |
| $\sigma_{p1}, \sigma_{p2}, \sigma_{p3}$ , principal stresses in directions 1, 2, 3, respectively | (Fig. 26)       |
| $\sigma'_t$ , uniaxial cut-off tensile stress under multiaxial conditions                        | (Fig. 26)       |

### RESULTS OF NONLINEAR ANALYSIS

The cracking sequence, from the initiation of the first crack until failure, is illustrated in Fig. 12. The first crack occurs at a location approximately 0.25D from the top of the cylinder, at a time  $t = 27.0 \mu\text{sec}$ . (Fig. 12a). At time  $t = 27.07 \mu\text{sec}$ , the crack is observed to propagate in either direction along the vertical diameter (Fig. 12b). At time  $t = 28.65 \mu\text{sec}$ , the crack has propagated along the vertical diameter through the center of the cylinder in one direction, and has nearly reached the top of the cylinder in the other direction (Fig. 12c). Finally, at time  $t = 35 \mu\text{sec}$ , failure occurs (Fig. 12d).

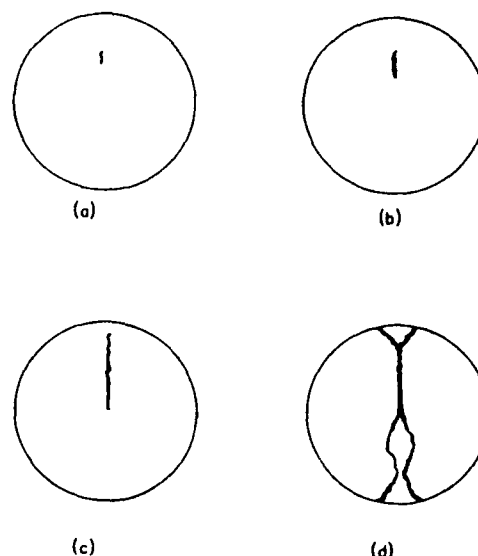


Fig. 12. Cracking sequence for split cylinder, load case 3: (a)  $t = 27.0 \mu\text{sec}$ ; (b)  $t = 27.07 \mu\text{sec}$ ; (c)  $t = 28.65 \mu\text{sec}$ ; (d)  $t = 35.0 \mu\text{sec}$ .

During the failure sequence of the numerical analysis, three different bifurcations of the crack pattern are observed (see Fig. 12d). The first bifurcation occurs just below the center of the cylinder. At approximately the same time, a second bifurcation occurs at the crack front, propagating toward the top of the cylinder at an approximate distance of  $D/7$  from the top. The cracks formed in the top bifurcation eventually propagate to the top surface of the cylinder. However, the two cracks formed by the bifurcation occurring just below the center of the cylinder begin to move back toward each other before bifurcating once again at a distance  $D/7$  from the bottom of the cylinder. The cracks of this final bifurcation eventually propagate to the bottom surface of the cylinder at which time failure occurs.

The pattern of cracking predicted by the numerical analysis is consistent with that observed in the SHPB experiments [9]. Preliminary results of high speed photography (10,000 frames/second) of SHPB tests indicate the development of cracks similar to patterns illustrated in Figs. 12b and 12c, along the vertical diameter prior to the appearance of the bifurcated cracks at the top and bottom of the cylinder. Moreover, the SHPB specimens have exhibited evidence of crack bifurcation occurring just below the center of the cylinder, similar to that illustrated in Fig. 12d. This is substantiated by the observation from high speed photography of a lens-shaped piece of fractured concrete being expelled from the flat surface of the specimen.

### CONCLUSIONS

The results of the linear analyses indicate that the dynamic stress distribution in the cylinder behind the initial stress wave is identical to that exhibited in the static analysis. The crack pattern and the mode of failure predicted by the nonlinear FEM analysis is consistent with that

observed in the SHPB experiments.

In the nonlinear analysis, the failure of the cylinder is predicted at time  $t = 35 \mu\text{sec}$ . (Fig. 12d). This failure is predicated upon a uniaxial tension cut-off stress equal to the static tensile strength of the material. However, experimental strength vs. strain rate data associated with this loading rate indicates that the concrete tensile strength may be three to four times as great as the static tensile strength. Therefore, using the dynamic tensile strength in the material model would delay the time of failure by a factor of two or three.

#### ACKNOWLEDGEMENTS

The experimental work was conducted at the Air Force Engineering and Services Center, Tyndall Air Force Base, Florida. The numerical analysis was sponsored by a research contract from the Air Force Engineering and Services Center, Contract No. F08635-88-C-0195.

#### REFERENCES

1. Fundamentals of Protective Design for Conventional Weapons, Dept. of the Army, Waterways Experiment Station, Corps of Engineers, Vicksburg, MS, July 1984.
2. Felice, C. W. and Gaffney, E. S., "Early Time Response of Soil in a Split-Hopkinson Pressure Bar Experiment," Proceedings of the Third Symposium on the Interaction of Non-Nuclear Munitions with Structures, Mannheim, West Germany, March 9-13, 1987, Vol. II, pp. 508-524.
3. Nicholas, T., "Material Behavior at High Strain Rates," Chapter 8 of Impact Dynamics, Editor: Zukas, J. R., John Wiley and Sons, NY, pp. 280-332, 1982.
4. ADINA, A finite element computer program for automatic dynamic incremental nonlinear analysis, Report ARD 84-1, ADINA R&D, Inc., Watertown, MA, December 1984.
5. Neville, A. M., Properties of Concrete, Pitman Publishing Co., London, UK, pp. 549-552.
6. Malvern, L. E. and Ross, C. A., Dynamic Response of Concrete and Concrete Structures, First Annual Technical Report, AFOSR, Contract F49620-83-K007, 1984.
7. Malvern, L. E. and Ross, C. A., Dynamic Response of Concrete and Concrete Structures, Second Annual Technical Report, AFOSR, Contract F49620-83-K007, February 1985.
8. Tedesco, J. W., Stress Wave Propagation in Layered Media, Final Report, AFOSR, Contract F49620-85-C-0013, August 1988.
9. Ross, C. A., Kuennen, S. T., and Strickland, W. S., "High Strain Rate Effects on Tensile Strength of Concrete," Fourth International Symposium on the Interaction of Non-Nuclear Munitions with Structures, April 17-21, 1989, Panama City, FL.

WEAPONS TESTS  
ON A  
SIFCON DEFENSIVE FIGHTING POSITION

Bruce Schneider  
Senior Research Engineer

New Mexico Engineering Research Institute  
University of New Mexico, P.O. Box 25  
Albuquerque, New Mexico 87131

ABSTRACT

The development of the material SIFCON (Slurry Infiltrated Fiber CONcrete) has resulted in the ability to design and construct hardened structures that are generally more economical than conventional reinforced concrete in resisting the effects of ballistics and bomb fragments. A program to develop, design and test a hardened structural system using SIFCON was recently completed by the New Mexico Engineering Research Institute for the Air Force. This paper presents some of the test results of that program in which SIFCON components were subjected to a variety of threat weapons including the M-60 machine gun, AK-47 rifle, hand grenades and Rocket Propelled Grenades (RPG). The results illustrate the exceptional anti-perforation and strength properties of SIFCON. Also included in the paper is a brief description of the materials and fabrication techniques for SIFCON.

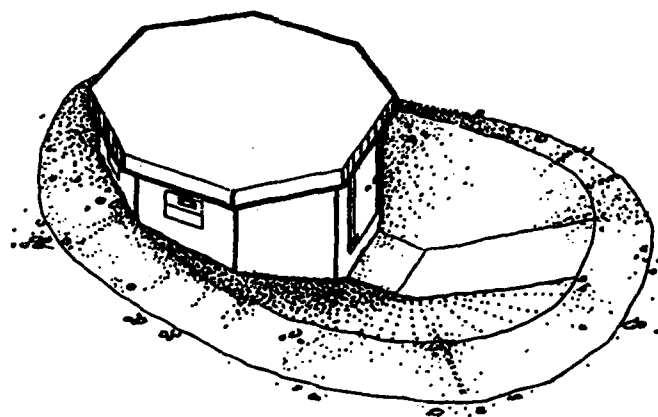


Figure 1. Two-Man Defensive Fighting Position (DFP).

INTRODUCTION

The two-man Defensive Fighting Position (DFP) is part of the U.S. Air Force base defense system in the European and Pacific theaters of operation. In concept the DFP is a small, bunker type structure usually partially buried in the ground or protected with an earth embankment (Figure 1). It is designed to be located at the perimeter of a base or near other assets. It has several small windows, or firing ports, located in its walls, and an entryway usually at the back of the structure. It is designed to be used by two defenders, in conjunction with other nearby DFPs, as a first line defense system against terrorist or commando type attacks.

The New Mexico Engineering Research Institute (NMERI), under contract to the Air Force Weapons Laboratory (AFWL), Kirtland AFB, New Mexico, developed a new design for a two-man DFP that combined the

best features of the existing designs while incorporating additional functional requirements as established by the Air Force. In support of the development program, NMERI fabricated and tested structural components of the design against various weapon threats. Upon completion of the final design, NMERI fabricated and installed a complete DFP structure for further testing and evaluation.

Past experience and recent research conducted at AFWL and NMERI had shown that SIFCON (Slurry Infiltrated Fiber CONcrete) possessed excellent anti-penetration and strength properties making it an obvious candidate material, along with reinforced concrete, for use in the DFP design (Refs. 1 and 2).

This paper is limited to a brief discussion of the material SIFCON, followed by a review of some of the results of the test program in which SIFCON components were subjected to the threat weapons.

## THE MATERIAL--SIFCON

### GENERAL

SIFCON is a relatively new composite material featuring short steel fibers in a Portland cement based matrix. It differs from conventional steel fiber reinforced concrete (SFRC) in which the steel fibers are added directly to a typical concrete mix in the ratio of 0.5 to 1.5 % by volume. SIFCON, on the other hand, starts with a bed of preplaced steel fibers in the range of 5 to 20 % by volume. The fiber bed is then infiltrated with a low viscosity cementitious slurry. The resulting composite material possesses a very high compressive strength as well as toughness and ductility. This is graphically illustrated in Figure 2a. A similar pattern of high strength and ductility is also true for the flexural properties of SIFCON as illustrated in Figure 2b.

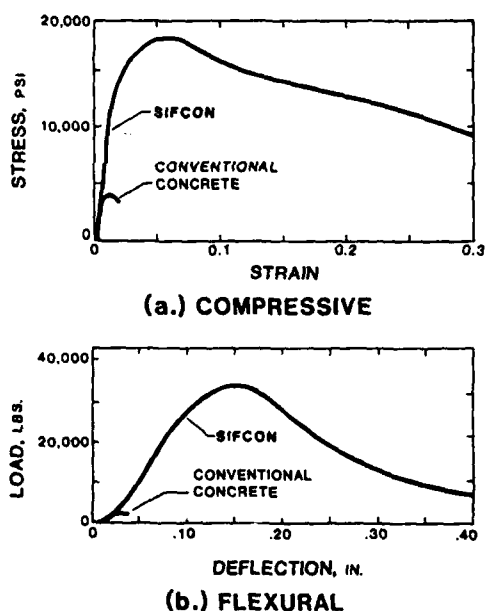


Figure 2.

### MATERIALS

The steel fibers used in SIFCON are the same as those used in conventional steel fiber reinforced concrete. In general, they are manufactured from drawn wire or cut from thin steel sheets. The fibers come in several lengths and diameters and most have some sort of deformation to aid in mechanical bonding.

The slurry ingredients are usually Portland cement, fly ash, and water. A fine sand is often included. In addition, a high-range water reducer (superplasticizer) is used to increase the flowability of the slurry. Other

ingredients, such as microsilica (silica fume), latex modifiers, polymers and other standard concrete admixtures have also been used successfully in SIFCON slurry mixes.

### FABRICATION

SIFCON is manufactured by first sprinkling the fibers by hand or mechanical means into a form or onto a substrate. The form is filled completely to the top with fibers. Depending on the geometric properties of the particular fiber being used and to a lesser degree on the geometry of the form, a unique volume density of fibers will be achieved. Common values of fiber volume densities are in the range of 8 to 15 %.

After the fibers have been placed, the slurry is mixed and then pumped or poured into the fiber bed infiltrating the spaces between the fibers. Mix proportions can vary widely depending on the desired strength or other physical properties of the SIFCON. In addition, form geometry, fiber type, and the particular method of placing the slurry can also determine certain slurry mix parameters. Typical cement/fly ash/sand proportions can vary from 90/10/0 to 30/20/50 by weight. The water/cement plus fly ash ratio can vary from 0.45 to 0.20 and the typical amount of superplasticizer can vary from 0 to 40 ounces per 100 pounds of cement plus fly ash. Because of the wide variation in types of cement, fly ash and sand available across the country, and the large number of brands of superplasticizers, slurry mix proportions usually have to be determined by trial batch methods using the locally available materials.

A recent study of the state-of-the-art in design and construction techniques for SIFCON is reported in Reference 3. In general, it notes that all the necessary materials, formwork and equipment are currently available to fabricate SIFCON as a conventional building material.

### COSTS

SIFCON can be relatively expensive, but it has also been shown to be economical (Ref. 3). The economy is realized when an application using SIFCON is viewed as a total interrelated system. Rather than simply comparing the materials cost of a unit volume of SIFCON versus a unit volume of concrete, one should consider the smaller amount of SIFCON required because of its high strength and toughness compared to conventional concrete.

Next, because highly skilled labor is not required for SIFCON, one should consider that labor costs of placing the fiber and slurry can be considerably lower than the cost of installing reinforcing bars and placing conventional concrete. In fact, it has been shown that the placing of the fibers and slurry can be fully automated in several common applications.

#### OTHER PROPERTIES OF SIFCON

##### Resistance to ballistics

NMERI conducted a comprehensive test program to study the effects of ballistics and fragments on SIFCON (Ref. 1). The study considered different slurry strengths, fiber volume densities and fiber types. The thickness of the specimens ranged from 40 to 60mm (1.5 to 2.4 inches). It was found that at practical velocities, the 0.30 caliber rounds were unable to penetrate the thicker specimens. Instead, 0.50 caliber fragment-simulating projectiles were used for the thicker targets. The ballistic limit (V50) for the 0.30 caliber projectile on most targets ranged from 1050 to 1200 m/s (3500 to 4000 f/s), with a few specimens exceeding 1800 m/s (6000 f/s). The ballistic limit (V50) for the 0.50 caliber projectile averaged about 600 m/s (2000 f/s), with several targets exceeding 750 m/s (2500 f/s).

##### Resistance to fragments

In 1985 a series of SIFCON wall panels, or revetments, were subjected to the fragments and airblast from a 1000 lb. Mark 83 general purpose bomb (Ref. 2). In summary, it was found that the main threats to the revetment were impact damage, penetration and rear surface spall caused by bomb fragments. The SIFCON revetments demonstrated significantly higher resistance to fragment penetration and rear surface spall than conventional reinforced concrete revetments which were 60% thicker than the SIFCON walls. As reported, the SIFCON walls also demonstrated "...a tensile material performance unknown in conventional reinforced concrete....[Furthermore]...SIFCON revetments appear to offer an improved second or third strike capability." (Ref. 2).

##### Resistance to impact

Some limited work on the impact resistance of SIFCON was done by Lankard (Ref. 4). The test procedure, as recommended by the American Concrete Institute (ACI), was to drop a 4.5 kg (10 lb) weight 457mm (18 in) onto a 150mm (6 in) diameter by 65mm (2.5 in) thick specimen and record the number of blows to

crack the material. The plain material cracked at 140 blows and a specimen lightly reinforced with steel fibers cracked at 400 blows. For the SIFCON, the test was carried up to 1500 blows without cracking the specimen and then stopped. The actual number of blows required to crack the SIFCON specimen was never determined.

#### WEAPONS TESTS ON SIFCON

##### THREAT WEAPONS

A listing of the specified threat weapons for testing the DFP is given below. The design of the wall and roof was to be such as to prevent perforation and damaging back spalling resulting from three rifle or pistol rounds, fired from 50m (165 ft), and impacting within a 50mm (2.0 in) diameter area anywhere on the structure. In addition, the design was to prevent perforation and damaging back spalling from a hand grenade detonating on the surface of the structure or a pre-detonated rocket propelled grenade (RPG) impacting on the surface.

##### Threat Weapons

M-60 Machine gun, 7.62 x 51  
(Standard NATO)  
M-16 Rifle, 5.56  
AK-47 Rifle, 7.62 x 39  
HK-21 Machine gun, 9 mm  
Pistol, 9 mm  
M-30 Hand grenade  
RPG-7 Rocket Propelled Grenade

##### SIFCON TEST COMPONENTS

The SIFCON components were approximately 760mm (30 in) wide by 1520mm (60 in) long and were fabricated in four thicknesses: 100mm (4.0 in), 150mm (6.0 in), 200mm (8.0 in) and 250mm (10.0 in). The components were made using the Dramix, ZL 30/50 fiber as manufactured by the Bekeart Steel Wire Corporation. The calculated fiber density was 10.5% by volume.

Quality control specimens tested in uniaxial compression 31 days after being fabricated indicated an average ultimate compressive strength of the SIFCON in the components to be 130 MPa (18,800 psi).

##### TESTING PROCEDURE

For the ballistic type weapons the range was specified as 50m (165 ft.). When instructed by the test director, the marksman fired one round at time at a target painted on the SIFCON component.

The minimum requirements were 3 rounds fired at a 50mm (2.0 in) diameter target. In many cases additional rounds were fired in order to determine the perforation limits or other characteristics of the material. After each round the component was inspected and the results recorded.

The hand grenade was placed in contact with the component. The RPG was pre-detonated by a chain link fence placed in front of the target.

#### TEST RESULTS on SIFCON

100mm (4.0 in) SIFCON,

Weapon: M-60, 3 Rounds, Figure 3.

No chipping, cracking or spalling of the back surface was observed. An approximately 75mm (3.0 in) diameter by 20mm (0.75 in) deep crater was formed on the front surface. The steel fibers were found to be still embedded in the matrix.



Figure 3. Front Surface

100mm (4.0 in) SIFCON,

Weapon: HK-21, 3 Rounds, Figure 4

All the bullets bounced off the front surface. A 40 mm (1.5 in) diameter by 8mm (0.25 in) deep crater was formed on the front surface. No chipping, cracking or spalling was observed on the back surface.



Figure 4. Front Surface

200mm (8.0 in) SIFCON,

Weapon: M-60, 116 Rounds, Figure 5.

Bullets were fired single shot in rapid succession into the same area on the wall until perforation occurred. All bullets struck within a 225mm (9.0 in) diameter area. Many deformed bullets were found in the crater area with steel fibers embedded in the lead. A 38mm (1.5 in) diameter hole was formed at the center of the front crater running through the wall to the back surface. The slurry was knocked out of a 115mm (4.5 in) diameter area on the back surface.



Figure 5. Front Surface

150mm (6.0 in) SIFCON,

Weapon: Hand Grenade, 1 Round, Figure 6.

The crater formed in the top surface was 100mm (4.0 in) in diameter by 12mm (0.50 in) deep (Fig. 6a). No cracks radiating from the crater were observed. A 200mm (8.0 in) diameter, by approximately 3mm (0.125 in) thick, volume of the unreinforced slurry in the top surface had spalled away around the immediate crater area. A volume about 100mm (4.0 in) in diameter by about 3mm (0.125 in) deep of the slurry had also been broken out of the back surface of the panel (Fig. 6b). In this area, it was observed that the hardened slurry had been knocked out from among the fibers. No loose fibers were found on the ground under the panel. All the fibers were still tightly embedded in the surrounding slurry matrix and interlocked with each other. It was determined that the minor loss of slurry would not be detrimental or hazardous to any occupants of the DFP.

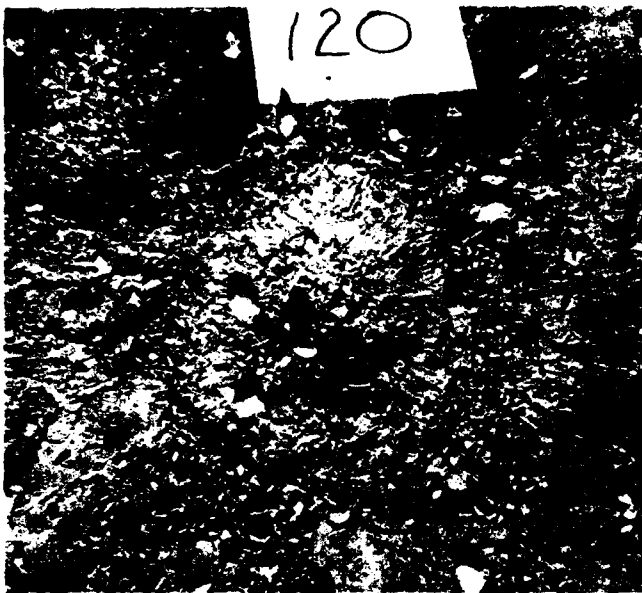


Figure 6a. Front Surface



Figure 7. Front Surface

#### OTHER WEAPONS TESTS

##### Mark 82 General Purpose Bomb

A complete DFP with 150mm (6.0 in) SIFCON walls was subjected to the airblast and fragments of a 500 lb. Mark 82, general purpose bomb detonated within 12m (40 ft) of the structure (Fig 8). In summary, no bomb fragments perforated the walls or produced injury causing spall on the inside wall surface. No tensile cracking or deformation of any kind was observed in any of the SIFCON panels.

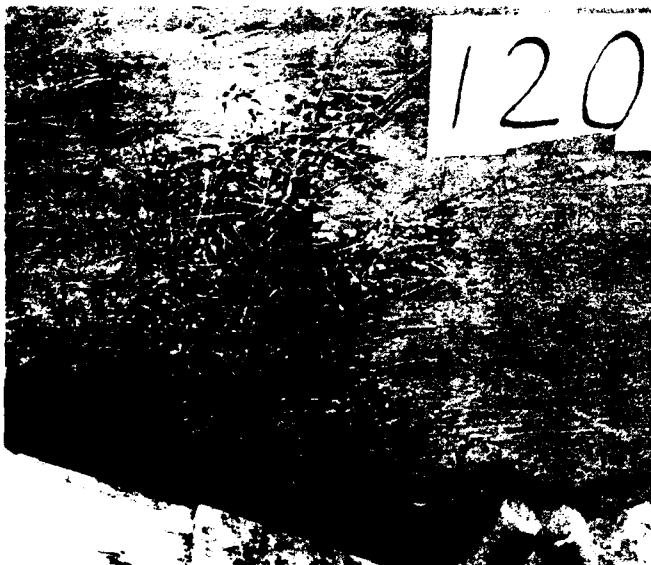


Figure 6b. Back Surface

150mm (6.0 in) SIFCON,

Weapon: RPG-7, 1 Round, Figure 7.

The charge was pre-detonated on a chain link fence placed in front of the component. Several fragments of the weapon struck the front surface of the wall. One large part of the rocket was found embedded 20mm (0.75 in) deep in the front surface. Some minor hairline cracking was observed on the back surface of the wall. No chipping or spalling of the back surface was noted.

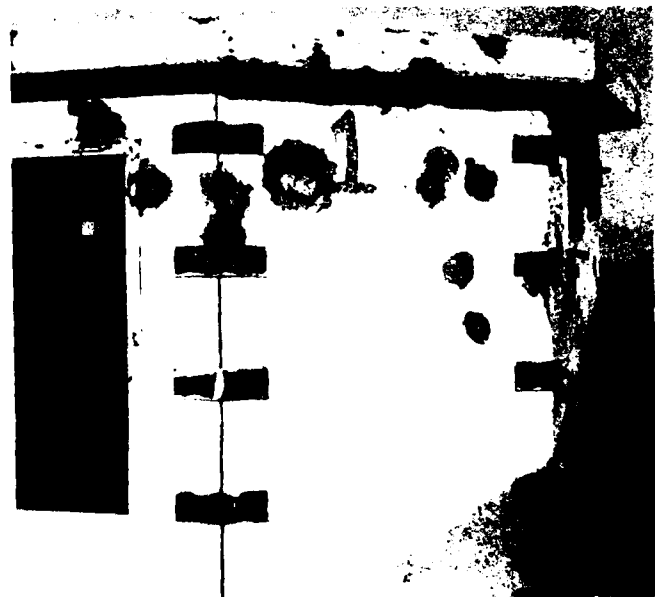


Figure 8. Bomb Test Results

## 0.50 Caliber Munitions

The 200mm (8.0 in) thick SIFCON component was also subjected to 0.50 caliber armor piercing ballistics fired at a range of 50m (164 ft). There was no chipping, cracking or spalling noted on the back surface. A 100mm (4.0 in) diameter by 35mm (1.25 in) deep crater was formed on the front surface. The steel fibers were found to be still embedded in the surrounding matrix. The end of the steel bullet slug was visible approximately 75mm (3.0 in) below the bottom of the crater.

## CONCLUSION

It was found that the 100mm (4.0 in) thick SIFCON panel could resist the specified ballistic type threat of three rounds in a 50mm (2.0 in) diameter area. The ballistic weapon producing the most "damage" was the M-60 machine gun. However, it produced no perforation or spalling for the required three rounds. The effects of the hand grenade, RPG and general purpose bomb were all resisted by the 150 mm (6.0 in) thick SIFCON. It was also shown that the 200mm (8.0 in) thick SIFCON wall could resist 0.50 caliber armor piercing rounds and required more than 100 rounds from a M-60 machine gun impacting at the same location to perforate the material.

The results of these and other tests performed on SIFCON components showed that SIFCON was clearly superior to conventional reinforced concrete in preventing perforation and back spall when subjected to the threat weapons. For an equivalent resistance to the threat weapons, a conventional reinforced concrete wall would have to be 60 to 75% thicker than a SIFCON wall. The test results also indicated that the thinner SIFCON wall could resist 2 to 3 times more ballistic impacts on the same target area than the thicker conventional concrete wall before being perforated.

Using the NMERI SIFCON design, a general contractor has just finished fabricating 25 Defensive Fighting Positions (DFP) at a U.S. military installation in Europe. An additional 200 DFPs are currently scheduled to be installed on other European bases in the near future.

## REFERENCES

1. Carson, James, et al., The Ballistic Performance of SIFCON (Slurry Infiltrated Fiber Concrete), AFWL-TR-86-103, Air Force Weapons Laboratory, Kirtland Air Force Base, New Mexico, July 1986, Unclassified.
2. Carson, James, and Morrison, Dennis, The Response of SIFCON Revetments to a Mark 83 General-Purpose Bomb, AFWL-TR-86-42, Air Force Weapons Laboratory, Kirtland Air Force Base, New Mexico, December 1986, Unclassified.
3. Schneider, Bruce, Design and Construction Techniques for SIFCON, AFWL-TR-88-88, Air Force Weapons Laboratory, Kirtland Air Force Base, New Mexico, April 1988, Unclassified.
4. Lankard, David R., and Newell, Jeffery K., Preparation of Highly Reinforced Concrete Composites, "Fiber Reinforced Concrete-International Symposium", SP-81, American Concrete Institute, Detroit, Michigan, 1984.



# IMPACT RESISTANCE AND MECHANICAL PERFORMANCE OF KEVLAR FIBER REINFORCED CEMENT COMPOSITES

PARVIZ SOROUSHIAN\*, ZIAD BAYASI\*\* & PAUL G. RIEWALD\*\*\*

\*Michigan State University

\*\*Bradley University

\*\*\*E.I. Du Pont De Nemours & Co., Inc.

## ABSTRACT

The mix proportions of mortar and concrete matrices were refined for the incorporation of Kevlar fibers through conventional mixing techniques. The effects of Kevlar fiber reinforcement on the impact resistance, and flexural and compressive performance of mortar and concrete were investigated experimentally. Kevlar fibers were observed to significantly improve the impact resistance, and the flexural strength and energy absorption capacity of mortar and especially concrete. The compressive strength was not much influenced by kevlar fiber reinforcement.

## INTRODUCTION

Cement-based materials provide, for most purposes, economic construction materials with low energy consumption and distinct performance advantages.<sup>1</sup> Cementitious materials, however, suffer from a common shortcoming. They are brittle and have low impact resistance and tensile strength. An effective technique for overcoming this deficiency is through reinforcement by randomly oriented short fibers.<sup>2,3</sup> After about three decades of extensive research and development,<sup>1-5</sup> field applications of fiber reinforced concrete are going through a period of rapid growth.<sup>6</sup> While fibrous concretes with more commonly used steel, polypropylene and glass fibers are now established worldwide as standard construction materials, new fibers such as carbon, wood and Kevlar are also under serious consideration for the reinforcement of cement and concrete, and some have already found growing commercial applications in the

recent years.<sup>1-8</sup> It should be emphasized that each fiber has its own specific advantages and optimum applications in cement and concrete materials.

The research discussed in this paper has been concerned with the application of Kevlar fibers to concrete. Due consideration has been given to the practicality of construction methods and the cost effectiveness of the developed concrete matrices reinforced with Kevlar fibers.

## KEVLAR FIBERS

Kevlar fibers are members of aromatic polyamide fibers.<sup>9</sup> Their tensile strength and modulus of elasticity are relatively high. They are also resistant to corrosion. Kevlar fibers are chemically and mechanically stable at wide temperature ranges.<sup>10,11</sup> Kevlar is commercially available in three different types: (a) Kevlar 49 with a high tensile strength of 400 Ksi (7520 MPa) and a high modulus of 18,000 Ksi (124,000 MPa); (b) Kevlar 29 with the same high tensile strength as Kevlar 49, but a smaller modulus of 9,000 Ksi (62,000 MPa); and (c) Kevlar with properties similar to those of Kevlar 29, but designed for the reinforcement of rubber.

Kevlar 49 was used in this investigation for the reinforcement of concrete. Some key properties of Kevlar 49 are presented in Table 1. Kevlar 49 has a linear tensile stress-strain curve up to failure.<sup>10</sup> In compression, however, the behavior becomes nonlinear at higher stresses. Kevlar 49 has a good thermal stability, retaining a high percentage of its properties when exposed for long periods to temperatures as high as 355 F (180 C). At temperatures as low as -320 F (-196 C) also Kevlar 49 shows essentially no embrittlement or

degradation.<sup>12</sup> Kevlar 49 has an excellent thermal dimensional stability with a slightly negative coefficient of thermal expansion. Some information indicating the excellent chemical resistance of Kevlar 49 (except in a few strong acids) are also summarized in Table 1.

**Table 1. Properties of Kevlar 49.**

Diameter: 11.7 to 18.4 microns  
Specific Gravity: 1.44 to 1.45  
Elastic Modulus: 18,000 Ksi  
Tensile Strength: 400 Ksi  
Elongation: 2 to 2.6%

Coeff. of Thermal Expansion:  $-1.1 \times 10^{-6}/F$   
(in fiber axis direction)

Chemical Resistance  
(% initial strength retained after 100 hrs of exposure)

|                    |     |
|--------------------|-----|
| Acids              |     |
| acetic (99.7%)     | 100 |
| hydrochloric (37%) | 36  |
| hydrofluoric (48%) | 94  |
| nitric (70%)       | 13  |
| sulfuric (96%)     | 0   |

|                        |    |
|------------------------|----|
| Bases                  |    |
| sodium hydroxide (40%) | 97 |

|                 |     |
|-----------------|-----|
| Other Chemicals |     |
| gasoline        | 100 |
| salt water (5%) | 99  |
| boiling water   | 98  |

Equilibrium Moisture Level: 3.5 to 4.5%  
(@72 F and 50% RH)

### **EXPERIMENTAL PROGRAM**

The main thrust of the research reported herein was to develop Kevlar fiber reinforced concretes which can be manufactured through conventional concrete production techniques, and which possess desirable workability characteristics in fresh state and superior hardened material properties. Particular attention had to be given to the proportioning of the mix and deciding the sequence and rate of the addition of mix constituents

during the manufacturing process, in order to ensure the uniform dispersion of fibers.

The materials used in Kevlar fiber reinforced concrete were: natural river gravel, natural sand, type I cement, silica fume (see Table 2), Class F fly ash (Table 3), a naphthalene formaldehyde sulfonate - based superplasticizer, and Kevlar 49 fibers.<sup>13</sup>

**Table 2. Properties of Silica Fume.**

$SiO_2$  (% by weight) = 96.5  
Spec. Gravity = 2.3  
Avg. Particle Size = 0.15 microns

**Table 3. Properties of Fly Ash.**

$SiO_2$  (% by weight) = 47.0  
 $Al_2O_3$  (%) = 22.1  
 $Fe_2O_3$  (%) = 23.4  
CaO (%) = 2.6  
C (%) = 4.3  
Spec. Gravity = 2.245

The mix proportions used in this experimental study on Kevlar fiber reinforced concrete are presented in Table 4. A rotary drum mixer was used in the manufacture of the material, and different mix constituents were added to the mix following the sequence described below:

1. Charge the mixer with a "dispersant mixture" consisting of all the silica fume, 2 to 4 times the weight of silica fume sand, 1.3 to 1.6 times the weight of silica fume water, and about 7% of the silica fume weight superplasticizer;
2. Mix until a uniform mixture is achieved;
3. Gradually add the fibers (avoid fiber balling);
4. Add the remainder of the sand and the gravel;
5. Add the remainder of the mix liquids;
6. Mix for one minute, then stop the mixer and wait for one minute, and complete the mixing process by mixing for one more minute.

All the specimens were kept inside their molds under a plastic sheet for 24 hours, and were then demolded and moist-cured until the test age of 28 days.

Table 4. Mix Proportions of Kevlar Fiber Reinforced Concrete.

|               |       |
|---------------|-------|
| $w/b$         |       |
| 0.42          |       |
| $sf/b$        |       |
| 0.17          |       |
| $fa/b$        |       |
| 0.125         |       |
| $sp/b$        |       |
| 0.0132        | 0.012 |
| $mas$         |       |
| 3/16          | 3/8   |
| $agg/b$       |       |
| 2             | 3     |
| $s/agg$       |       |
| 1             | 0.5   |
| $lf$          |       |
| .5 .25        | .125  |
| $V_f$         |       |
| 0 .3 .2 .1 .1 | .1 .1 |

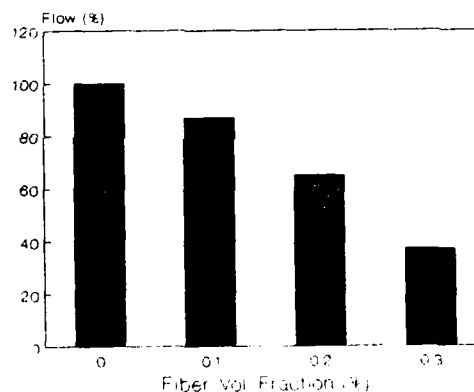
**Note:** w=water; b=binder (cement+silica fume+fly ash); sf=silica fume; fa=fly ash; sp=superplasticizer; mas=max. agg. size (in.); agg=aggregate; s=sand; lf=fiber length (in.);  $V_f$ =fiber volume fraction (%).

The workability of fresh Kevlar fiber reinforced mortar and concrete was assessed through the flow table and inverted slump cone tests, respectively.<sup>14</sup> Hardened Kevlar fiber reinforced mortar and concrete were characterized through the performance of the following tests:

1. Compression strength tests on 6 in. by 12 in. (150 mm by 300 mm) cylindrical specimens (two specimens for each mix);
2. Flexural tests on 4 in. by 4 in. by 14 in. (100 mm by 100 mm by 350 mm) prismatic specimens loaded at one-third points on a span of 12 in. (300 mm), with both load and deflection monitored during the test (three specimens for each mix); and
3. Impact tests on cylindrical specimens 6 in. (150 mm) in diameter and 2.5 in. (64 mm) in height (three specimens for each mix).

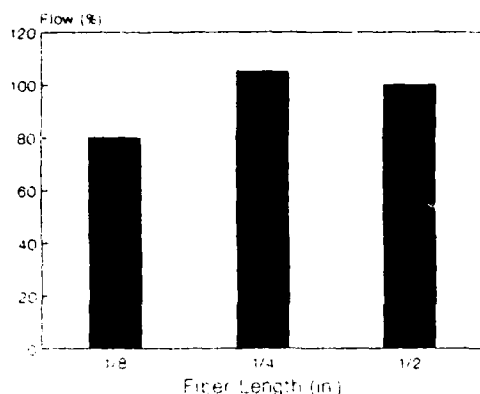
### TEST RESULTS

The flow table test results for mortar (mortar refers to mixtures without coarse aggregate) are shown in Fig. 1. The increase in fiber volume fraction is observed in Fig. 1.a to reduce the flowability of fresh mixtures. As shown in Fig. 1.b, for the limited test data generated in this study, the increase in fiber length from 1/8 in. (3 mm) to 1/2 in. (12 mm) has a relatively small effect on the flowability of mixes with the low fiber volume fraction of 0.1%. As far as the slump test results (performed on concrete mixtures) are concerned, both the fibrous mixes considered in this investigation had relatively high slumps (about 9 in., 230 mm).



(a) Effect of Fiber Volume Fraction

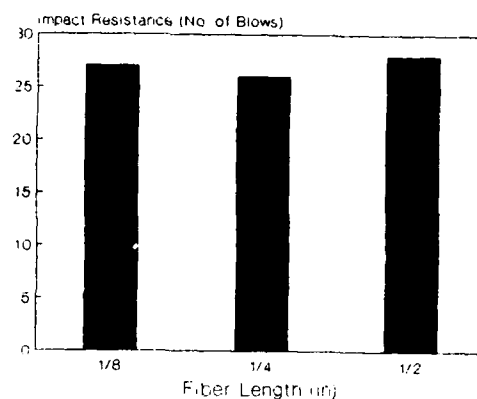
Figure 1. Flow Table Test Results.



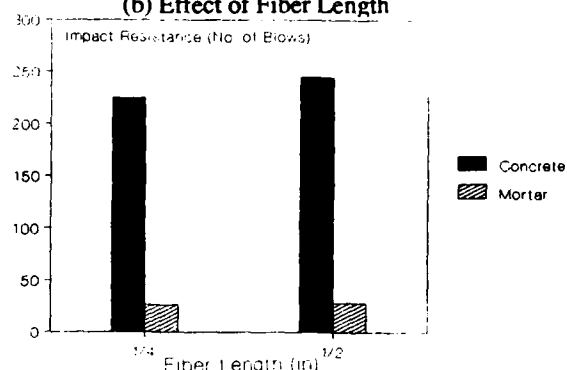
(b) Effect of Fiber Length

Figure 1. Continued

Figs. 2.a through 2.c present the effects of Kevlar fiber reinforcement on the impact resistance of mortar and concrete. Significant improvements (up to 15 times) in the impact resistance of mortar are observed in Fig. 2.a to be achieved as the volume fraction of 1/2 in. (12 mm) Kevlar fibers is increased from 0% to 0.3%. Different fiber lengths ranging from 1/8 in. (3 mm) to 1/2 in. (12 mm) at a fiber volume fraction of 0.1% are observed in Fig. 2.b to produce similar impact strengths in the case of Kevlar fiber reinforced mortar. Fig. 2.c shows that Kevlar fiber reinforced concrete has significantly higher impact strengths when compared with Kevlar fiber reinforced mortar.

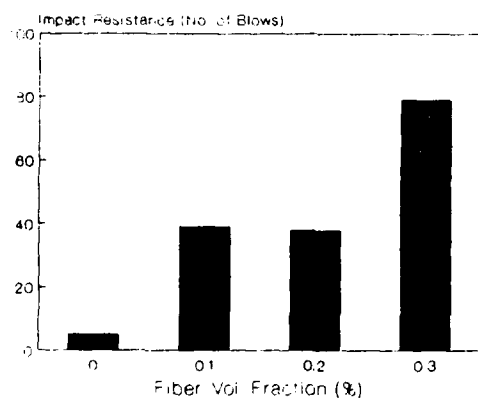


(b) Effect of Fiber Length



(c) Effect of Coarse Aggregates

Figure 2. Impact Resistance Test Results.



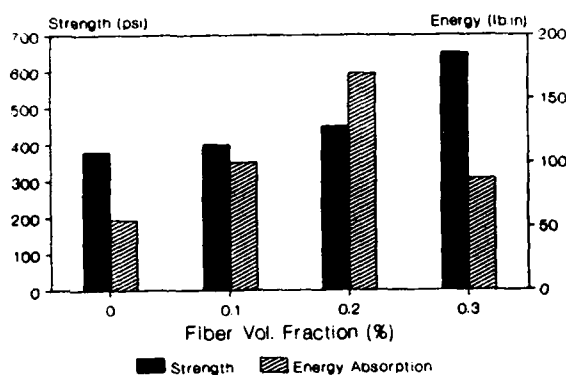
(a) Effect of Fiber Volume Fraction

The effects of fiber volume fraction on the flexural strength and energy absorption capacity of Kevlar fiber reinforced mortar, at a fiber length of 1/2 in. (12 mm) are shown in Fig. 3.a. Flexural energy absorption is defined in this study as the area underneath the flexural load-deflection curve. The increase in fiber volume fraction is observed to consistently increase the flexural strength (up to 80% at a fiber volume fraction of 0.3%). The flexural energy absorption capacity, however, reaches its peak (about three times that of plain mortar) at 0.2% fiber volume fraction, and further increase in fiber content shows adverse effects on this aspect of mortar flexural behavior.

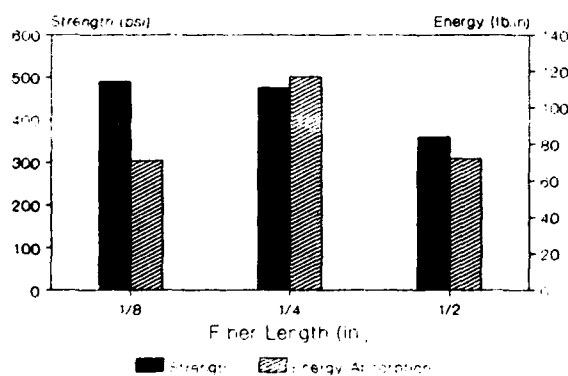
The increase in fiber length above 1/8 in. (3 mm), at a constant fiber volume fraction of 0.1%, is observed in Fig. 3.b to have some negative effects on the flexural strength and energy absorption capacity of Kevlar fiber reinforced mortar.

The effects of incorporating coarse aggregates on the

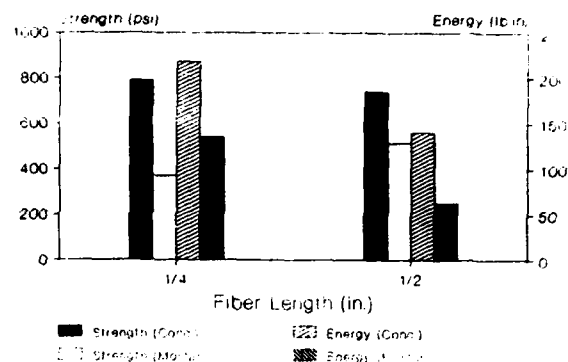
flexural performance of Kevlar fiber reinforced concrete are shown in Fig. 3.c. The flexural strength and energy absorption capacity of Kevlar fiber reinforced concrete (with coarse aggregates at a maximum particle size of 3/8 in., 9 mm) are observed to be 60% to 80% higher than those of Kevlar fiber reinforced mortar (with only fine aggregates at a maximum size of 3/16 in., 5 mm) for both fiber lengths of 1/2 in. (12 mm) and 1/4 in. (6 mm). This observation is consistent with that reported for other fiber types, and it can be attributed to the increase in fiber concentration in the mortar phase of the mix in the presence of coarse aggregates.



(a) Effect of Fiber Volume Fraction



(b) Effect of Fiber Length



(c) Effect of Coarse Aggregates

Figure 3. Flexural Test Results.

The compressive strengths of all the mortar and concrete mixtures of this study were relatively high and ranged from 9 to 12.5 Ksi (62 to 73 MPa). Fiber reinforcement effects on compressive strength were relatively small. This is consistent with the performance of other fiber types in concrete.

## SUMMARY AND CONCLUSIONS

Mortar and concrete matrices were refined to incorporate Kevlar fibers through conventional mixing techniques. The effects of Kevlar fiber reinforcement on the impact resistance, flexural strength and energy absorption capacity, and compressive strength of mortar and concrete were assessed experimentally. From the generated test data it could be concluded that:

1. An increase in fiber volume fraction from 0% to 0.3%, for a fiber length of 1/2 in. (12 mm), leads to an increase of about 80% in flexural strength and about 15 times in impact resistance of mortar. The flexural energy absorption capacity of mortar increases to about three times that of plain mortar at a fiber volume fraction of 0.2%. Compressive strength is not much influenced by Kevlar fiber reinforcement.
2. The increase in fiber length from 1/8 in. (3 mm) to 1/2 in. (12 mm), at a fiber volume fraction of

0.1%, has some negative effects on the flexural performance of mortar, but does not seem to significantly affect the impact resistance.

3. Kevlar fibers at a volume fraction of 0.1% seem to be more effective in enhancing the flexural performance and impact resistance of coarse aggregate concrete when compared with mortar matrices.

### **ACKNOWLEDGMENTS**

The research reported herein was sponsored by the research excellence fund of the State of Michigan, and the Civil Engineering Department of Michigan State University. The Kevlar fibers were provided by E.I. Du Pont De Nemours & Company (Inc.), the superplasticizer by W.R. Grace & Company, the fly ash by the Lansing Board of Water & Light, and the silica fume by Elkem Materials. These contributions are gratefully acknowledged.

A patent (pending) filed by Michigan State University on Kevlar Fiber Reinforced Cement Composites (U.S. Dept. of Commerce Serial No. 174-207) covers the mix proportioning and manufacturing techniques described in this article.

### **REFERENCES**

1. Bayasi, Z., "Development and Mechanical Characteristics of Carbon Fiber Reinforced Cement," A Thesis Submitted to the Faculty of Civil Engineering Department at Michigan State University for the Partial Fulfillment of the Degree of Doctor of Philosophy (Vol. 1), 1989, 199 pp.
2. Mehta, P., "Concrete Structure, Properties and Materials," Prentice-Hall, Inc., 1986, 450 pp.
3. Mindess, S. and Young, J., "Concrete," Prentice-Hall, Inc., 1981, 671 pp.
4. ACI Committee 544, "State of the Art Report on Fiber Reinforced Concrete," Report No. ACI 544.1R-82, American Concrete Institute, Detroit, MI, 1982, 16 pp.
5. Hannant, D., "Fiber Reinforced Cements and Fiber Concretes," John Wiley & Sons, 1978, 219 pp.
6. Soroushian, P. and Bayasi, Z. (editors), "Fiber Reinforced Concrete: Design and Applications," Proceedings, MSU Concrete Technology Seminars-1, Feb. 1987, 217 pp.
7. Ramakrishnan, V., "Materials and Properties of Fiber Reinforced Concrete," Proceedings, International Symposium on Fiber Reinforced Materials, Madras, India, Dec. 1987, pp. 2.3-2.23.
8. Lankard, D., "Opening Paper: Fiber Concrete Applications," Proceedings, RILEM Symposium on Fiber Reinforced Cement and Concrete (London), Vol. 1, 1975, pp. 3-19.
9. Du Pont Company, "Characteristics and Uses of Kevlar 29 Aramid," A Preliminary Information Memo, Du Pont Company No. 375, Sept. 1976, 9 pp.
10. Gale, D. Riewald, P. and Champion, A., "Cement Reinforcement with Man-Made Fibers," Proceedings, International Man-Made Fibers Congress (Australia), Sept. 1986, 11 pp.
11. Burgoyne, C. and Chambers, J., "Prestressing with Parafil Tendons," Concrete (London), Vol. 19, No. 10, Oct. 1985, pp. 12-15.
12. Du Pont Company, "Characteristics and Uses of Kevlar 49 Aramid High Modulus Organic Fibers," Technical Information Brochures, Du Pont Company Bulletin No. K-5, Sept. 1981, 13 pp.
13. Grace Construction Products, "The Daracem Advantage," Product Information Brochure, Grace Construction Products, Cambridge, 1986, 6 pp.
14. ASTM, "1986 Annual Book of ASTM Standards - Section 4: Construction," Vol. .01: Cement, Lime, Gypsum, ASTM, Philadelphia, 1986.

## SATURATED SAND LIQUEFACTION UNDER EXPLOSIVE LOADING

Hassen A. Hassen, Graduate Student  
Wayne A. Charlie, Associate Professor  
Colorado State University, Ft. Collins, Colorado 80523

### Abstract

Explosive-induced shock waves can cause water saturated sand to liquefy. Almost all of the available prediction techniques used for explosive-induced liquefaction problems are based on results of low yield explosive field experiments, the majority of which was conducted by the Russians, Dutch and Germans. All of these tests, however, suffered from problems like incomplete saturation and surface wave disturbances. To overcome such problems and to systematically investigate saturated sand response to explosive loadings, a large scale field testing facility was developed at Colorado State University. This facility is capable of testing large volumes of sand and uses actual explosives to produce ground motions to any level desired. Our paper reviews liquefaction under shock loadings and describes our field testing program that was conducted to study the behavior of saturated sands near the charge point. The material used is described and some results are presented and discussed.

### Introduction

Explosions are characterized by a large and rapid release of energy. When a contained or a surface explosion takes place, a large compressive pulse or a shock wave is generated by either the direct waves or by the air slap, Figure 1. The nature of the vibrations created by blasting activities in dry soils have been studied comprehensively (Henrych, 1979; Crawford, et al., 1974). Techniques to predict ground motions and properties of the transmitting media exist and have been successfully implemented. If the explosion takes place in a saturated cohesionless soil, a larger shock wave will be generated than for an explosion in dry soil. Another important effect of the saturating water is to cause the soil to liquefy. Liquefaction, a phenomenon that is primarily associated with saturated cohesionless soils may be defined as "the act or process of transforming any substance into a liquid. In cohesionless soils, the transformation is from a solid state to a liquefied state as a consequence of increased pore pressure and reduced effective stress" (Committee on Soil Dynamics, 1978). If liquefaction occurs, the soil loses all of its

shear strength and all structures above it or in it are subjected to potentially disastrous effects. In addition to damage from the explosion, structures subjected to liquefaction may sink, float, or tilt. Explosion-induced liquefaction potential effects have been recognized only recently, (International Workshop on Blast-Induced Liquefaction, 1978) and have attracted the interest of researchers in many disciplines: geophysicists, civil and military engineers. Factors affecting shock induced liquefaction of a saturated sand deposit are discussed by Hassen and Charlie (1988).

### Experimental Investigation

Most of the available techniques for prediction and design for problems involving explosive-induced liquefaction are based on results from low yield explosive field tests, the majority of which was conducted in Russia and Netherlands. Laboratory experiments have also been conducted in the United States in the last decade using shock tubes and centrifuge (Charlie, et al., 1988; Schmidt, et al., 1981). Most of these tests, however, suffered from problems like incomplete saturation, boundary conditions effects and surface wave disturbances (Perry, 1972; Van der Kogel, 1981). To overcome such problems and investigate the response of saturated sand to shock loads generated by explosives, a large scale field testing facility was constructed at Colorado State University's Engineering Research Center. As shown in Figure 2, the test facility has a large steel tank that takes up to 80 tons of saturated sand. Explosives are used to produce large ground motions as desired. Many problems of shock wave propagation and dynamic soil-structure interaction have been investigated (Charlie, et al., 1988). However, only results pertinent to testing saturated sand under planar shock loads are reported here. For a full description of the facility, refer to Charlie, et al. (1988). The project was supported by a grant from the Air Force Office of Scientific Research (AFOSR).

## Experimental Set-Up

We conducted a series of six field explosives tests using planar charge geometry on a 50 ton dry weight of placed Poudre Valley sand at a relative density of about 85 percent. The sand has a specific gravity of 2.68, angular grain shape and a D<sub>50</sub> grain size of 0.52 mm. The sample was instrumented so that its pore pressure response during and after the passage of the shock wave is recorded. Porewater pressure transducers, total stress gages and accelerometers were installed at different levels within the sample and connected to a smart high speed digital Transient Data Recorder (TDR). Our data acquisition system is composed of a microcomputer, non-dedicated commercially available software packages, and 20 TDR channels that have 32k bytes of memory per channel (Figure 3). The late or residual response of porewater pressure was measured with a piezometer. To fully saturate this large size of sample, a special procedure was followed. After placing the sand in the tank, it was flushed with CO<sub>2</sub> to displace the air in the soil's voids. Because CO<sub>2</sub> easily dissolves in water, this method insures that water can reach all voids and fill them. Warm deaired water was then introduced to the sand and flushing continued. The degree of saturation was periodically checked by measuring compression wave velocity in the sample using small explosive charges and recording the arrival times at the impeded transducers. After 21 days of continuously flushing the sample, the compression wave velocity reached a steady value of 1,800 m/s. This was considered as an indication of 100 percent saturation.

## Results

Total explosives weight for the six detonations ranged from 0.53 to 2.55 kg, giving charge intensities ranging from 0.15 to 0.73 gm/m<sup>2</sup>. Figure 4 shows a typical transient porewater pressure-time history as measured by the piezoresistive pressure transducer during the passage of the shock wave. It should be noted here that the rise time of the pulse to the peak is in the submillisecond range. This is typical of saturated soils but far smaller than that in dry soils. Piezometer output of the residual pore pressure is in terms of pore pressure ratio-time history is given in Figure 5 (pore pressure ratio, PPR, is the ratio of residual pore pressure to the effective vertical stress at a certain point). This record shows the soil not to have liquefied at the piezometer point but high residual pore pressures were generated and sustained for more than a minute.

The best fit equations for all the tests conducted for the measured peak pressure,  $u_{pk}$ , and the pore pressure ratio, PPR, as a function of scaled distance ( $\frac{R}{w_i}$ ) are

$$u_{pk} = 30,073 \left( \frac{R}{w_i} \right)^{-0.342} \quad \text{Eq. 1}$$

and

$$\text{PPR} = 1.11 \left( \frac{R}{w_i} \right)^{-0.084} \quad \text{Eq. 2}$$

where  $u_{pk}$  is in kPa, PPR ranges from 0 to 1,  $w_i$  is the charge's intensity in gm/m<sup>2</sup> and R is the distance from the charge in m. These two equations allows the prediction of peak pore pressure and pore pressure ratio as a function of the scaled distance or charge's intensity. Equation 2 predicts liquefaction (PPR = 1) at a scaled distance of 3.46. At this scaled distance, Equation 1 predicts a peak transient pore pressure of 19,700 kPa.

## Summary and Conclusions

A brief description of the large scale field testing facility that was developed at Colorado State University under a grant from the AFOSR was presented. The facility allows for testing large samples, and the use of actual explosives. State-of-the-art microcomputer based data acquisition and analysis systems are used. Briefly introduced was the experimental investigation carried out at this test site of the planar shock propagation and liquefaction potential of saturated sands. Some results were presented and discussed. Detailed discussion of all of the results can be found in Charlie, et al., 1988.

## Acknowledgements

This work was partially supported by the U.S. Air Force, Office of Scientific Research (Grant AFOSR-85-0172). We also thank Carol Smoot for typing this paper.

## References

- Charlie, W.A., Doehring, D.O., Veyera, G.E. and Hassen, H.A. (1988), "Blast Induced Liquefaction of Soils: Laboratory and Field Tests," Final Report to the Air Force Office of Scientific Research, Under Grant No. AFOSR-85-0172, Civil Engineering Department, Colorado State University, Fort Collins, Co., July, 184 p.
- Committee on Soil Dynamics (1978), "Definition of Terms Related to Liquefaction," Committee on Soil Dynamics of the Geotechnical Engineering Division, American Society of Civil Engineers, Journal of the Geotechnical Engineering Division, Vol. 104, No. GT9, pp. 1197-1200.
- Crawford, R.E., Higgins, C.J. and Bultmann, E.H. (1974), The Air Force Manual for Design and Analysis of Hardened Structures, Air Force Weapons Laboratory, Air Force Systems Command, Kirtland Air Force Base, NM, 87117.



Hassen, H.A. and Charlie, W.A. (1988), "Blast Induced Liquefaction: Field Explosive Tests," Shock and Vibration Bulletin, No. 59, part 3, pp. 259-267, Oct.

Henrych, J. (1979), The Dynamics of Explosions, Elsevier, 560 p.

International Workshop on Blast-Induced Liquefaction (1978), Dames and Moore/U.S. Air Force, Maidenhead, United Kingdom, Workshop Proceedings, 471 p.

Perry, E.B. (1972), "Movement of Variable-Density Inclusions in Wet Sand Under Blast Loading," U.S. Army Waterways Experimental Station, Vicksburg, Miss., Miscellaneous paper S-72-37, 59 p.

Schmidt, R.M., Fragaszy, R.J. and Holsapple, K.A. (1981), "Centrifuge Modeling of Soil Liquefaction due to Airblast," 7th International Symposium on Military Application of Blast Simulation, Alberta, Canada, July, Vol. 3, pp. 4.2-1 to 4.1-28.

Van der Kogel, H., Van Loon-Engels, C. and Ruygrok, P. (1981), "Wave Propagation in Porous Media, Shock Tube Experiments," Proc. of the 10th International Conference on Soil Mechanics and Foundation Engineering, Vol. 3, pp. 253-256, Stockholm, Sweden.

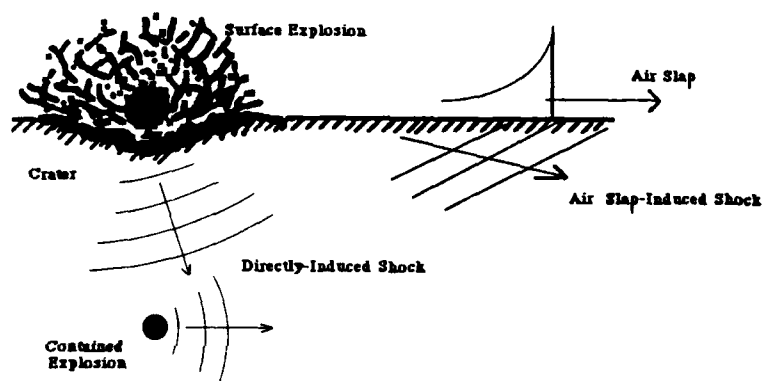


Figure 1. Shock Waves Generated by Explosions

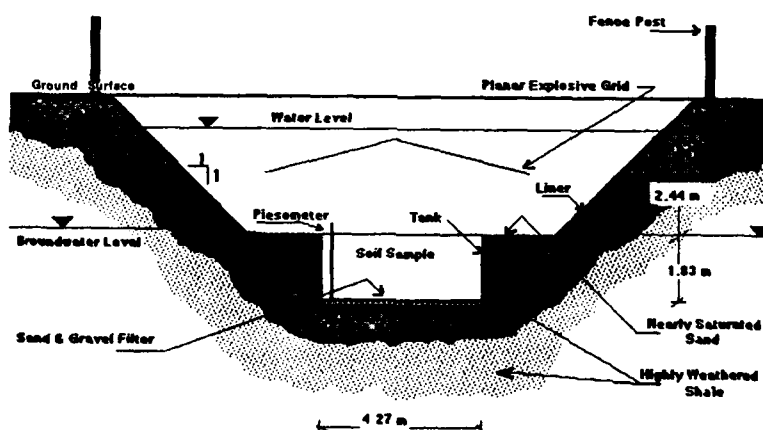


Figure 2. A Sketch Showing X-Section of the Test Pit

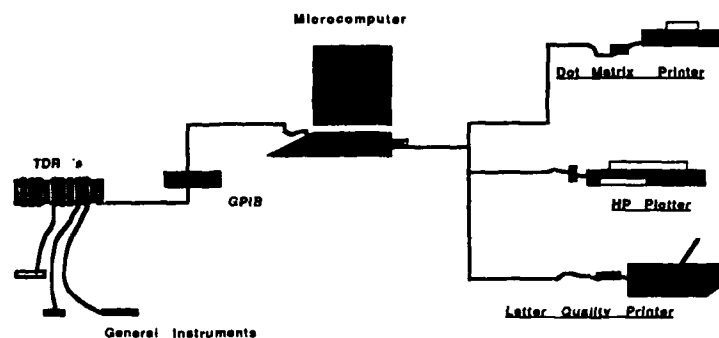


Figure 3. Data Acquisition And Analysis Hardware Arrangement

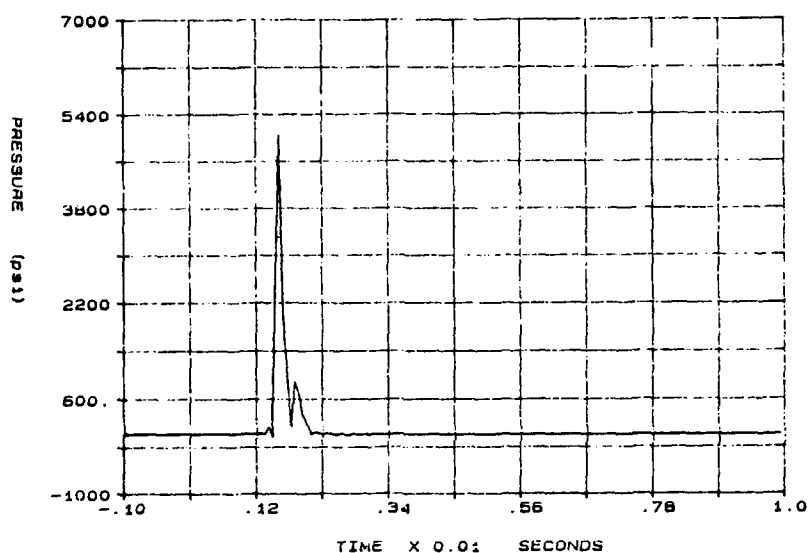


Figure 4. Typical Transient Pressure-time History

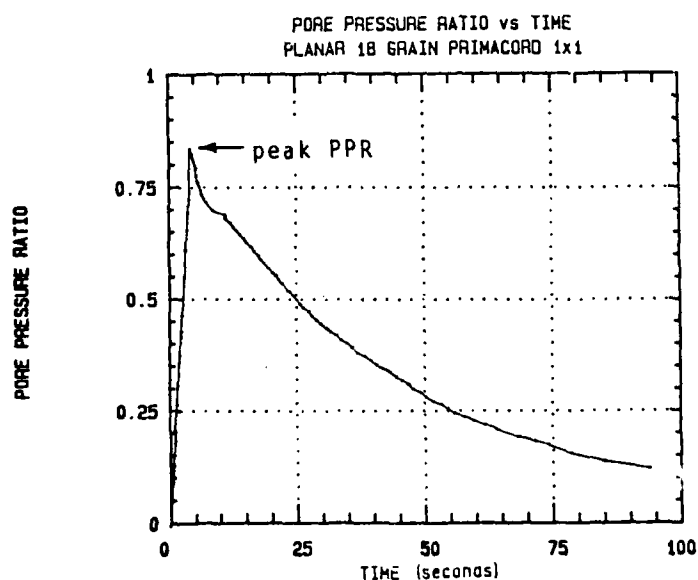


Figure 5. Typical Residual Pressure-Time History

## HIGH AMPLITUDE STRESS WAVE PROPAGATION IN MOIST SAND

Steven J. Pierce, Graduate Student  
Wayne A. Charlie, Associate Professor  
Colorado State University, Fort Collins, Colorado 80523

C. Allen Ross, Visiting Professor  
HQ AFESC (RDCS), Tyndall AFB, Panama City, Florida 32403-6001

### Abstract

We conducted high amplitude, Split Hopkinson Pressure Bar (SHPB) laboratory tests on specimens of 20-30 Ottawa and Eglin sands to evaluate the influence of saturation and capillary pressure on compressional wave velocity and stress transmission. All specimens were compacted to a constant dry density and then subjected to a constant input stress. For specimens compacted at various water contents, both the wave speed and the transmitted stress ratio were found to increase as the saturation was increased from zero to approximately 30 percent and then decreased with increasing saturation. For specimens compacted dry, saturated and then desaturated utilizing the pressure-plate method, both the wave speed and the transmitted stress ratio were found to decrease with increasing saturation.

### Introduction

Stress wave velocity and stress transmission through soils are basic parameters required for the dynamic analysis of soil-structure response of buried structures subjected to blast loadings. However, there are no theoretical, empirical or numerical methods currently available for predicting large amplitude compressive stress wave velocity or stress transmission in partially saturated sand as a function of saturation. Prediction of these values is currently based on the assumption that saturation and changes in saturation have little or no influence. Values are generally determined at in-situ or placed saturation and possible changes in saturation and, hence, changes in these values are ignored.

Research conducted on partially saturated soils by Bishop and Blight (1963), Fredlund and Morgenstern (1976), Hryciw and Dowding (1987), Fredlund (1986) and Wu et al. (1984) have shown that the shear strength, soil compressibility, cone penetration and low-amplitude shear wave velocity is affected by saturation. The only apparent reason for the difference was due to the water content (saturation) and capillary pressure during compaction and testing. Their research suggests that capillarity may also affect high amplitude

stress wave parameters. Our research was conducted to see if soil saturation and hence capillary stress would change compressional stress wave parameters at large strain levels.

Our objective was to determine if differences in wave speed and stress transmission are actually due to capillary pressure. If so, our objective was to determine if it was due to the capillary pressure during soil compaction, the capillary pressure during testing, or both.

### Background

Partially saturated soils are defined for our research as having continuous air and water phases. Because of capillary effects at the air-water interfaces, the porewater pressure,  $u_w$ , is less than the poreair pressure,  $u_a$ . Continuous air and water phases generally occur at water saturation levels less than approximately 85 percent (McWhorter and Sunada, 1977). If the poreair pressure is at atmospheric pressure, ( $u_a = 0$ ), the porewater pressure must be negative ( $u_w < 0$ ). Most soil deposits located a few meters or more above the regional groundwater table are partially saturated and the air pressure is at atmospheric pressure.

Bishop et al. (1963) first suggested that the constitutive relations for partially saturated soils must include total stress,  $\sigma$ , poreair pressure,  $u_a$ , and porewater pressure,  $u_w$ . Bishop defined the effective stress,  $\bar{\sigma}$ , for partially saturated soil as:

$$\bar{\sigma} = (\sigma_n - u_a) + X(u_a - u_w) \quad \text{Eq. 1}$$

where  $X$  is an empirical parameter representing the proportion of soil suction,  $(u_a - u_w)$ , that contributes to effective stress. Fredlund (1986) suggested a theoretical model for the change in volume of a partially saturated soil which does not include an empirical parameter  $X$ . Fredlund has shown that a change in the volumetric strain,  $\epsilon$ , of a partially saturated soil is a function of the total stress,  $\sigma$ , the poreair pressure,  $u_a$ , and the

porewater pressure,  $u_w$ , in the soil. This can be expressed as:

$$\epsilon = C_t [d(\sigma - u_a)] + C_w [d(u_a - u_w)] \quad \text{Eq. 2}$$

where  $C_t$  is the compressibility of the soil structure with respect to a change in  $(\sigma - u_a)$ , and  $C_w$  is the compressibility of the soil structure with respect to a change in  $(u_a - u_w)$ . Because wave speed is a function of soil compressibility, a similar relationship may exist between the wave speed and  $(\sigma - u_a)$  and  $(u_a - u_w)$ .

#### Research Conducted

To meet our objectives, we tested two sands (20-30 Ottawa sand and Eglin sand) at various saturation levels. These sands were compacted both moist and dry and subjected to two confining stresses. The samples compacted moist were compacted at various moisture contents to give various saturation levels. This compaction method was utilized by Ross et al. (1986). The samples compacted dry were saturated after compaction and then desaturated utilizing the pressure plate apparatus. To determine the affect of saturation on the sample compaction process, a compaction-energy apparatus was manufactured. The apparatus is used to measure the amount of energy that is required to compact a sample to a constant dry density at various saturation levels. Energy is applied to a loose sand sample by dropping a Standard Proctor hammer (5.5 lb) from a height of twelve inches. The number of hammer drops required to achieve a constant dry density can then be determined for various saturation levels.

Saturation-desaturation versus capillary pressure curves for the two sands were experimentally determined at Colorado State University. Our dynamic testing was conducted with the Split Hopkinson Pressure Bar Apparatus (SHPB) located at the Engineering and Service Center at Tyndall Air Force Base. Details of the SHPB are given by Ross et al. (1986).

#### Research Results

Experimental results obtained by Ross et al. (1988) for 20-30 Ottawa and Eglin sands compacted moist to a void ratio of 0.51 are given in Figures 1 through 4. These Figures show that both the wave speed and stress transmission increase as saturation increases from 0 to approximately 30 percent and then decrease at increasing saturation levels above 30 percent.

Our experimental results for 20-30 Ottawa and Eglin sands compacted dry to a void ratio of 0.510, then saturated and desaturated by the pressure plate apparatus, are given in Figures 4 through 12. These Figures show that both wave speed and stress transmission increase with increasing confining stress, and decrease with increasing saturation.

The energy required to compact a sample of Eglin sand to a void ratio of 0.51 as a function of saturation is given in Figure 13. This Figure shows that as saturation increases up to 20% the energy required to compact the sample also increases. The energy then decreases as saturation increases above 40%.

The difference in trends obtained by Ross et al. (1988) in Figures 1-4 and those presented in Figures 4-12 may be attributed to the sample compaction process, as all other testing procedures remained constant. The trend obtained from the compaction-energy apparatus in Figure 13 is similar to that presented in Figures 1-4. Since the compressibility of a soil depends very much on the stress level in relation to the stress history, we believe that the differences in wave velocity and stress transmission is directly related to the energy required to compact a moist sample. Based on previous research on partially saturated soil, the additional energy required to compact moist soils is due to the additional effective stress induced by capillary. This increase in effective stress results in higher wave speed and stress transmission ratio values for samples compacted at intermediate saturation levels.

#### Conclusions

The moisture content and hence saturation and capillary pressure during compaction and during testing are important factors to consider in predicting wave velocity and stress transmission in partially saturated compacted sand. Our experimental results show that for sands compacted moist, higher wave speeds and stress transmission can be expected for intermediate saturation levels. For sand compacted dry, wave speed and stress transmission will decrease with an increase in saturation. As the confining stress is increased, values of wave speed and stress transmission can also be expected to increase.

#### Acknowledgements

We wish to thank the Air Force Systems Command, the Air Force Office of Scientific Research and the Air Force Engineering and Service Center for sponsorship of this research. Universal Energy Systems, Inc. provided administrative and directional support. Mr. Stan Strickland provided considerable technical support and encouragement in every phase of the research. Colonel Dale Hokanson's support of the USAF Summer Faculty/Graduate Student Research Program is greatly appreciated.

#### References

- Bishop, A.W., Blight, G.E., "Some Aspects of Effective Stress in Saturated and Partially Saturated Soils," *Geotechnique*, Vol. 13, No. 3, Sept., 1963, pp. 177-179.

Charlie, W.A., and Pierce, S.J., "High Intensity Stress Wave Propagation in Partially Saturated Sand," 1988 USAF-UES Summer Faculty Research Program, Air Force Office of Scientific Research, Contract No. F49620-87-0004, 15 September, 1988.

Fredlund, D.G., "Soil Mechanics Principles that Embrace Unsaturated Soils," Proc. of the Eleventh Int. Conf. on Soil Mechanics and Foundation Eng., SSMFE, San Francisco, 1986, pp. 465-472.

Fredlund, D.G. and Morgenstern, N.R., "Constitutive Relations for Volume Change in Unsaturated Soils," Canadian Geotechnical J., Vol. 13, 1976, pp. 261-276.

Hryciw, R.D. and Dowding, C.H., "Cone Penetration of Partially Saturated Sands," Geotechnical Testing Journal, ASTM, Vol. 10, No. 3, Sept. 1987, pp. 135-141.

McWhorter, D. and Sunada, D.K., Ground-Water Hydrology and Hydraulics, Water Resources Publications, Fort Collins, Colorado, 1977.

Ross, C.A., Nash, P.T. and Friesenhahn, C.J., "Pressure Waves in Soils Using a Split-Hopkinson Pressure Bar," ESL-TR-86-29, AF Engineering and Services Center, Tyndall AFB, Florida, July 1986.

Ross, C.A., Thompson, P.Y. and Charlie, W.A., "Moisture Effects on Wave Propagation in Soils," Abstracts Seventh ASCE/EMD Specialty Conf. Virginia Polytechnic Institute and State University, Blacksburg, Virginia, May 1988.

Wu, S., Gray, D.H., and Richart, F.E., "Capillary Effects on Dynamic Modulus of Sands and Silts," J. of Geotechnical Eng., ASCE, Vol. 110, No. 9, Sept. 1984, pp. 1188-1203.

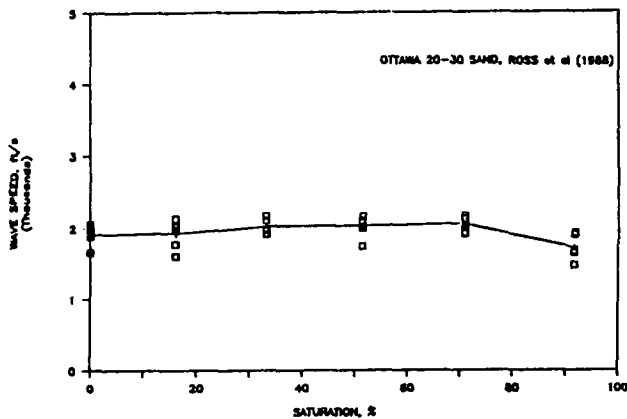


Figure 1. Wave Speed Results for 20-30 Ottawa sand compacted moist and tested with zero confining stress.

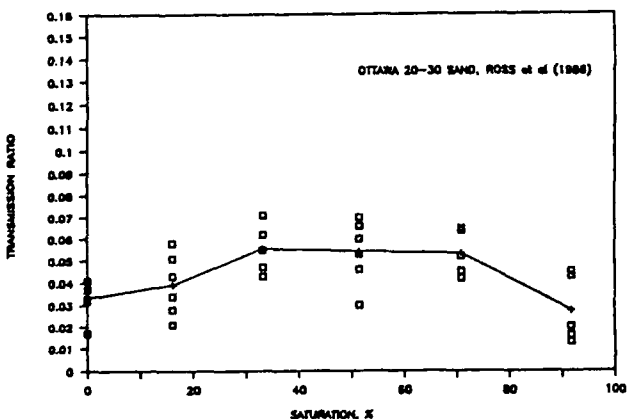


Figure 2. Transmission ratio results for 20-30 Ottawa sand compacted moist and tested with zero confining stress.

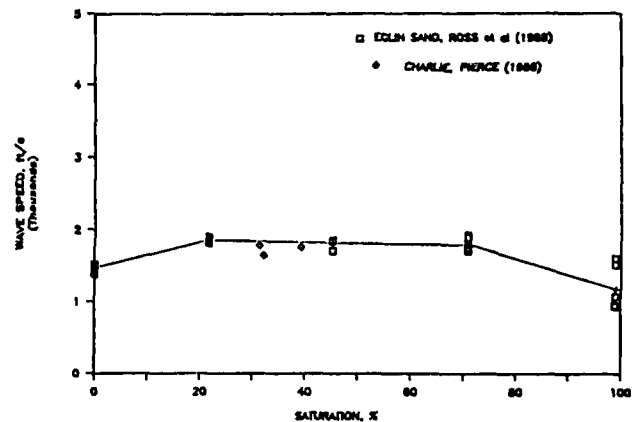


Figure 3. Wave speed results for Eglin sand compacted moist and tested with zero confining stress.

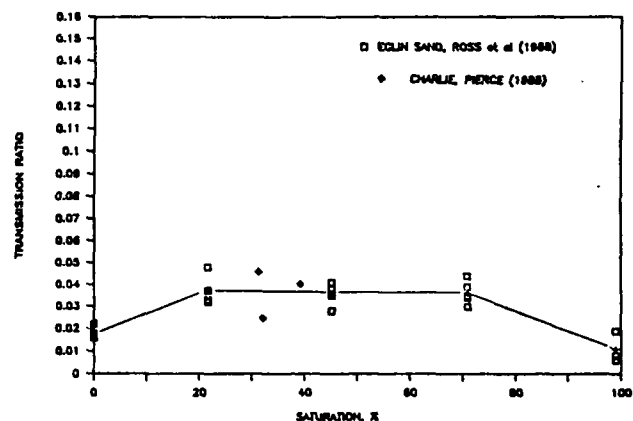


Figure 4. Transmission ratio results for Eglin sand compacted moist and tested with zero confining stress.

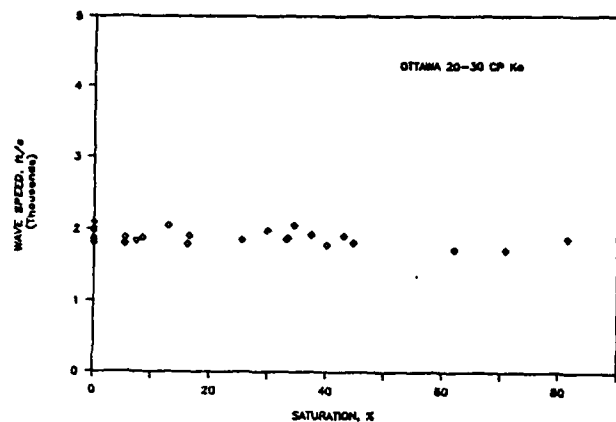


Figure 5. Wave speed results for 20-30 Ottawa sand compacted dry and tested with zero confining stress.

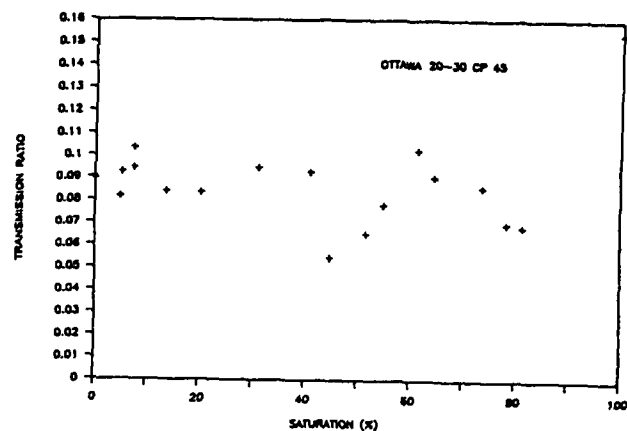


Figure 8. Transmission ratio results for 20-30 Ottawa sand compacted dry and tested with 45 p.s.i. confining stress.

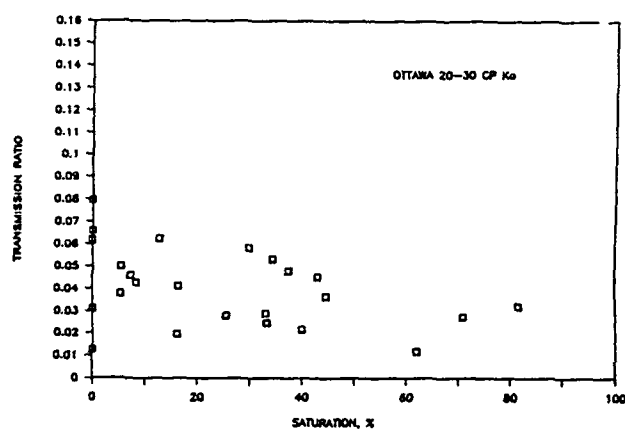


Figure 6. Transmission ratio results for 20-30 Ottawa sand compacted dry and tested with zero confining stress.

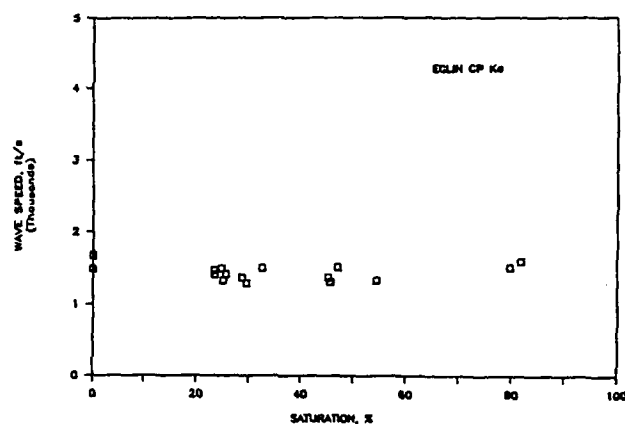


Figure 9. Wave speed results for Eglin sand compacted dry and tested with zero confining stress.

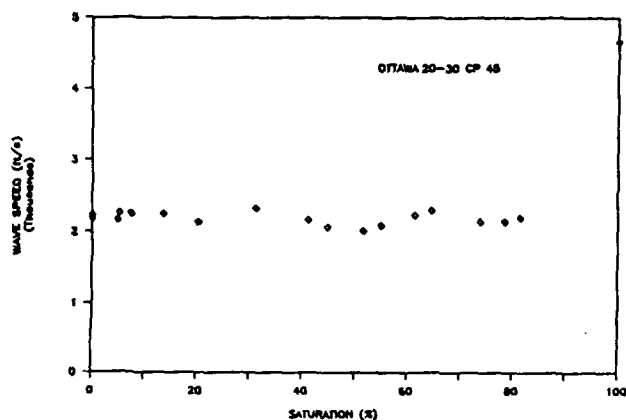


Figure 7. Wave speed results for 20-30 Ottawa sand compacted dry and tested with 45 p.s.i. confining stress.

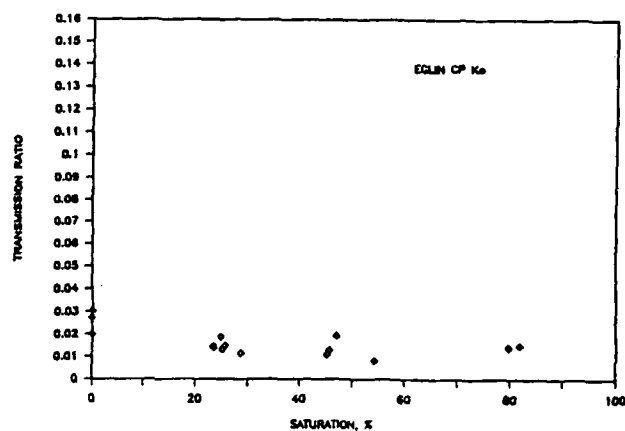


Figure 10. Transmission ratio results for Eglin sand compacted dry and tested with zero confining stress.

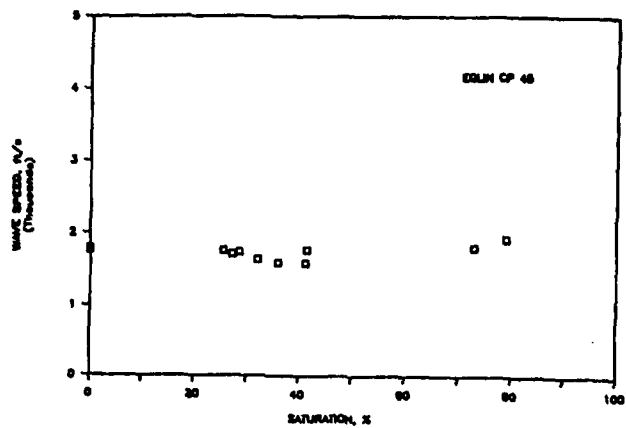


Figure 11. Wave speed results for Eglin sand compacted dry and tested with 45 p.s.i. confining stress.

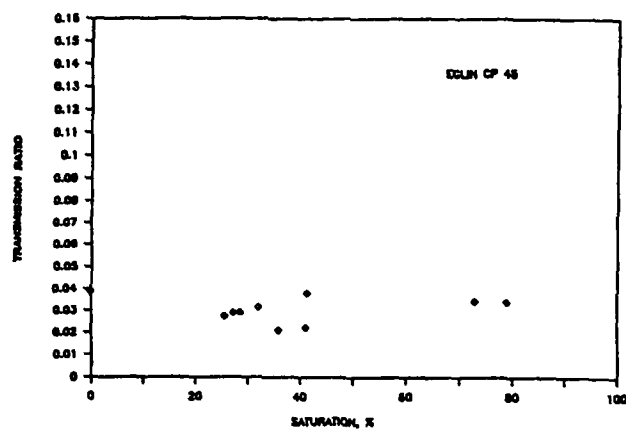


Figure 12. Transmission ratio results for Eglin sand compacted dry and tested with 45 p.s.i. confining stress.

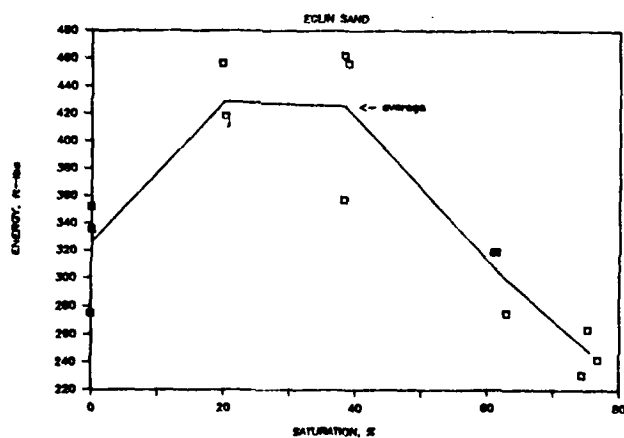


Figure 13. Compaction energy versus saturation level for Eglin sand compacted to constant dry density.

## STRUCTURAL RESPONSE IN IMPACT TENSILE TESTS ON CONCRETE.

J.Weerheijm, H.W.Reinhardt\*

Prins Maurits Laboratory TNO, P.O. Box 45,  
2280 AA, Rijswijk, The Netherlands.

\*Darmstadt University of Technology, Alexanderstrasse 5,  
6100 AA, Darmstadt, West-Germany.

### Abstract

Uniaxial impact tests were performed with a Split-Hopkinson bar apparatus on prismatic concrete specimen with notches. The influence of the structural response of the specimen on the observed ultimate strength, the failure process and the fracture energy appears to be not neglectable. Test results and the structural response are discussed in the paper.

### 1 Introduction.

In a testprogramme on concrete under impact tensile loading and lateral compression, uniaxial impact tests were also performed. The scope of the biaxial programme constrained to a prismatic geometry of the specimen and a local cross section reduction by two saw cuts. This geometry significantly differs from the usual cylindrical geometry in impact tests. The differences offered the opportunity to examine the influence of this geometry on the uniaxial test results by a comparison with former results obtained with the same Split Hopkinson bar apparatus at the Delft University of Technology (DUT).

Due to the application of saw cuts, the deformation inside as well as outside the fracture zone could be measured. Load-deformation curves were determined afterwards to calculate the fracture energy.

In the paper the influence of the geometry, the size of the considered fracture zone and the dynamic loading condition on the measured strength and fracture energy will be discussed.

### 2 Uniaxial experiments.

The objectives of the experimental programme are the determination of the strength, the energy dissipated during the fracture process and to study the process itself.

The experiments were performed with the Split-Hopkinson bar apparatus (SHB) at the DUT. In former years many uniaxial impact tests were successfully carried out (1).

In the current programme the geometry of the specimen is prismatic and notches are applied to fix the failure plane. The strains outside the failure zone, the axial deformation of the whole specimen and the strains in the incident and transmitter bar of the SHB have been registered as a function of time. With these signals the strength can be determined and the failure process can be reconstructed. In former programmes cylindrical specimen were used and only the deformation of the whole specimen was registered besides the strain at the transmitter bar.

In Figure 1 the SHB is depicted and the specimen with the location of the strain gauges is given in Figure 2.

In the programme a high (A) and a low (B) quality concrete was tested to examine the influence of the internal damage on the strength and the fracture process. The loading rate of the incident pulse was not varied in the programme and chosen as high as possible. The applicable loading rate is limited by the notches because the stress concentrations in the adjacent zones will cause brittle failure beyond a certain loading rate, as will be discussed later. Unfortunately the initially applied notches of 5 mm \* 5 mm proved to be insufficient to fix the failure plane in the biaxial tests, so the depth had to be increased to 7 mm.

The dimensions of all specimens are as follows: length 100mm, width 80mm, depth 50mm. The notch depth, the concrete quality and the loading rate in the critical cross section of the tested specimen are listed in Table 1. The mechanical properties of the two concrete qualities are given in Table 2.

Table 1. Different types of specimen.

| type                 | 1    | 2    | 3    | 4    | 5    |
|----------------------|------|------|------|------|------|
| notch depth (mm)     | 5    | 7    | 0    | 5    | 7    |
| concrete quality     | A    | A    | B    | B    | B    |
| loading rate (GPa/s) | 17.7 | 11.5 | 10.0 | 13.8 | 12.6 |



Table 2. Mechanical properties and mix proportions

|                                      | Quality A | Quality B |
|--------------------------------------|-----------|-----------|
| cube compressive strength (MPa)      | 40.       | 27.       |
| splitting strength (MPa)             | 2.3       | 1.7       |
| portland cement (kg/m <sup>3</sup> ) | 375.      | 200.      |
| water-cement ratio (-)               | 0.5       | 0.6       |
| air content (%)                      | 2.1       | 2.5       |

The strain and displacement signals were recorded on tape with a SELABS SE 3000 (14 channels) recorder at a speed of 60ips and a bandwidth of 40kHz. Afterwards all the signals were digitized simultaneously with a 14-channel AD converter (DIFA Benelux TS-9000; 250kHz) and stored at the VAX 11/750 of the Prins Maurits Laboratory. The signals were analysed by means of an extensive software programme for data processing.

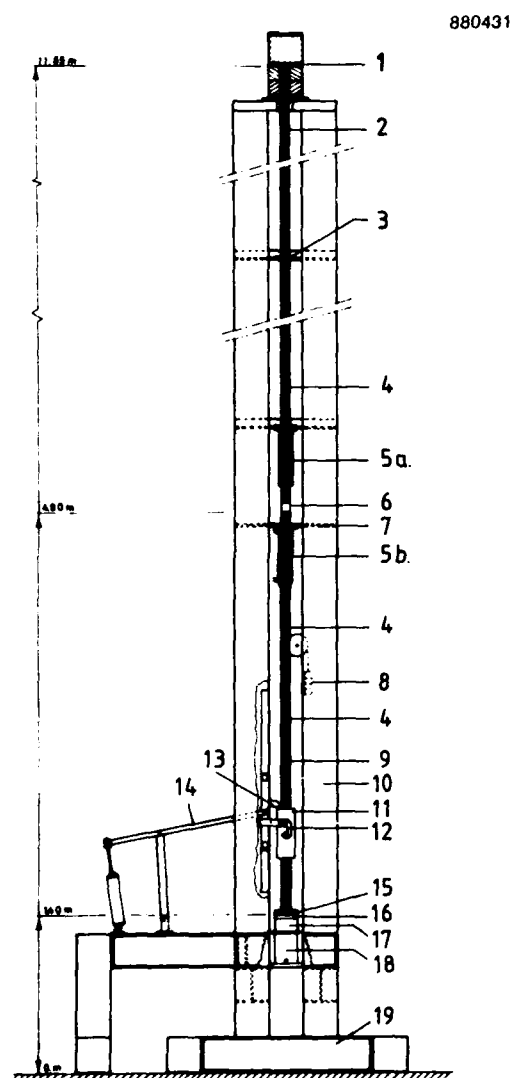


Figure 1. Split Hopkinson bar equipment, schematically.

1, buffer; 2, upper bar; 3, guide; 4, strain gauge; 5a, upper cooling jacket; 5b, lower cooling jacket; 6, concrete test specimen; 7, working platform; 8, counterweight; 9, lower bar; 10, frame; 11, drop weight; 12, coupling; 13, uncoupling; 14, lifting device; 15, damping material; 16, anvil; 17, guide tube; 18, pneumatic jack; 19, frame base.

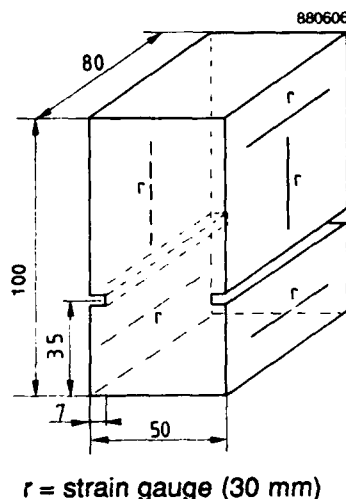


Figure 2. Geometry of specimen and location of strain gauges.

### 3 Test results

In this section the main results will be summarized. These results concern:

the ultimate strength ( $f_d$ );  
the total deformation ( $d_{td}$ ) at ultimate strength;  
the deformation of the fracture zone ( $d_{fd}$ );  
the fracture energy in the whole specimen ( $G_{td}$ );  
the fracture energy in the fracture zone ( $G_{fd}$ );  
the total energy absorbed during the failure process ( $G_f$ ).

Figure 3 shows the shape of the stress-deformation curve inside the failure zone. The data are listed in Table 3.

Table 3. Test results.

| type              | 1    | 2    | 3    | 4    | 5    |
|-------------------|------|------|------|------|------|
| $f_d$ (MPa)       | 4.55 | 4.39 | 2.72 | 2.61 | 2.60 |
| $d_{td}$ (0.01mm) | 1.17 | 1.66 | 2.03 | 1.00 | 1.42 |
| $d_{fd}$ (0.01mm) | 0.61 | 1.08 | -    | 0.42 | 0.94 |
| $G_{td}$ (N/m)    | 26.5 | 30.6 | 30.0 | 15.6 | 23.3 |
| $G_{fd}$ (N/m)    | 15.7 | 22.4 | -    | 10.5 | 17.3 |
| $G_f$ (N/m)       | 98.8 | 93.2 | 110. | 77.7 | 90.0 |

For the high quality concrete the plane of fracture consisted of bond, matrix and aggregate fracture. In case of the low quality concrete the plane was formed by bond and mortar fracture while in several cases multiple fracture occurred. In spite of the uniaxial loading pulse, the specimen did not fail in a symmetrical way. Rotation occurred during the failure process for all types of experiments. These results will be discussed in the following sections.

#### 4 The dynamic tensile strength.

In former programmes an empirical relation for the tensile strength as a function of the loading rate was derived (2). For the mixes A and B this relation is given resp. by:

$$A: \ln(f_d) = 1.48 + 0.042 \ln(\dot{s})$$

$$B: \ln(f_d) = 0.95 + 0.042 \ln(\dot{s})$$

with  $\dot{s}$  as the loading rate (MPa/msec).

These equations predict a strength  $f(A) = 4.92(\text{MPa})$  and  $f(B) = 2.88(\text{MPa})$ . Comparison with the experimental results (Table 3) leads to the conclusion that the strength was affected by the application of notches.

In (3) the influence of notches on the stress distribution, the influence on the failure process and the strength of the specimen are discussed. It is argued that the stress concentrations in the zone next to the notches will not influence the strength when stress-redistribution will occur due to microcracking. With the Dugdale approach the extension of the zone, in which the stresses exceed the material strength, was described. In this zone cracking can occur and consequently redistribution of stresses. The crack speed, however, is limited and so the extension of the zone of stress-redistribution can lag behind when the loading rate exceeds a certain threshold. The consequence is a more brittle failure and an ultimate load which is lower than the product of the cross-sectional area and the true material strength. When for the limiting crack speed the Rayleigh wave velocity is used (about 2000 m/s) then the threshold for loading rate is 50 and 29 GPa/s (A and B quality resp.) for a notch depth of 5mm. This result reflects the increase in rate sensitiveness for decreasing concrete quality. The threshold is proportional with the limiting crack speed.

Assuming that the mentioned approach is correct the data in Tables 1 and 3 lead for a notch depth of 5mm to a limiting crack speed of about 650m/s and 1050m/s for the mixes A and B resp.

From these observations and the data it is concluded that due to the application of notches the response of the specimen does not reflect directly the material response. The velocity of extension for the zone of microcracking is limited. The ultimate speed depends on the concrete quality and can be estimated with the approach described above.

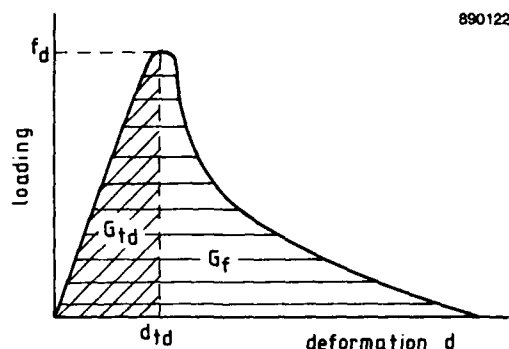


Figure 3. Shape of the load-deformation curve.

#### 5 The deformation capacity.

To determine the deformation capacity of concrete in experiments, the measuring length must be defined. The consequences of a different measuring length emerge from the performed tests.

In type 3, without notches, the results correspond with former tests ( $d_{fd}$  was about 0.015mm (4)); the failure zone is not fixed and multiple cracking can occur, resulting in a large axial deformation of the specimen. In the other tests with notches the deformation of one failure zone was determined. The difference in observed deformation capacity for type 3 and 4 emerges clearly from the results given in Table 3. In type 3 and former tests the structural response obscures the material response. The deformation capacity and the fracture energy  $G_{fd}$  appear to be over-estimated. In the current tests, with one fracture zone, the deformation of this zone appears to be about 60% of the deformation of the whole specimen. From this result it emerges that the deformation capacity observed in former tests, with possible multiple cracking, should at least be reduced to 60%. These results illustrate the carefulness that is necessary in calculations when the deformation capacity or the fracture energy for an element has to be defined in which one or more failure zones can occur (5).

Unfortunately the tests with notches also show a structural response. For each type of tests the failure becomes more brittle for increasing notch depth, as discussed in section 4. The deformation for the tests with 7mm notches is, however, larger and fracture is more ductile than for the other types. This can be explained by a rotation that occurs during the failure process.

In static, deformation controlled, tensile tests it was observed that the boundaries of the softening zone do not remain parallel but rotate when the maximum strength is reached somewhere in the failure zone (6). In a material like concrete with tension softening properties, the deformation will increase for the material in which the strength is

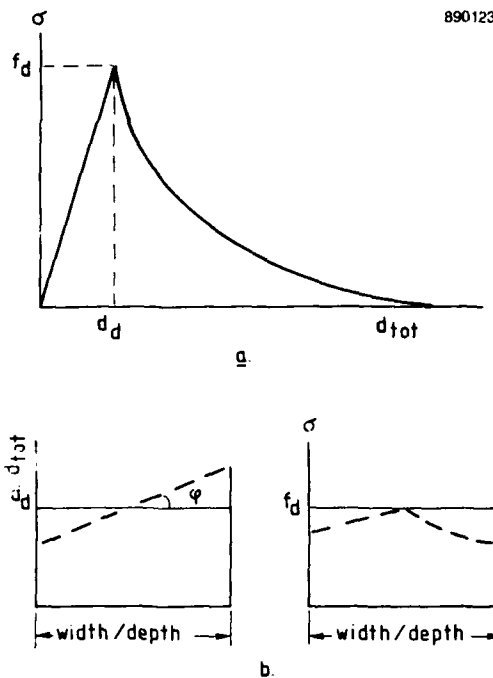


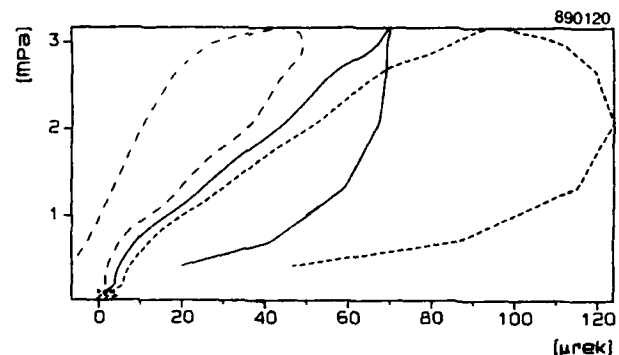
Figure 4. Non-parallel crack opening  
a) stress-deformation diagram  
b) deformation and stress distribution

reached while the stress decreases. Because of the heterogeneity of concrete the ultimate strength will never be reached in the failure plane at once and due to this inhomogeneity rotation will occur. Consider the situation as depicted in Figure 4. When in a spot the ultimate strength is reached the plane will rotate and consequently the material is unloaded (elastically) also at the other side of the specimen. Because of the rotation the average stress decreases and the stored energy in the specimen is lower in case of this non-uniform structural response. The degree of rotation depends on the stiffness of the specimen as discussed in (6).

In the impact tests, which are more or less load-controlled, non-uniform failure was also observed as illustrated in Figure 5. Apparently rotation was not prevented by the stiffness and the inertia of the surrounding material. The specimen could respond with a lower stiffness resulting in a larger deformation at ultimate loading. From measurements non-uniform cracking and rotation was observed for all types of tests. The rotation was the strongest for the "7mm" tests, which is reflected in the larger average deformation  $d(f)$ . Apparently some asymmetric damage was added to the specimens during sawing the notches, causing a more non-uniform structural response.

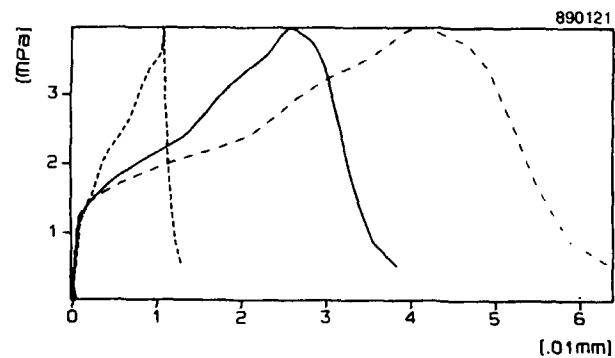
In the dynamic tests the non-uniform response starts before the ultimate load is reached and the failure process becomes more ductile. This explains the larger deformation for the "7mm" tests but also the lower loading rate in the tests with notches (see Table 1) as registered in the transmitter bar of the SHB.

The test results and the given observations show that due to the structural response of the specimen the obtained results cannot be regarded as a pure material response.



(a)

----- strain front side  
- - - strain rear side  
— mean longitudinal strain



(b)

----- deformation front side  
- - - deformation rear side  
— mean deformation (crack width)

Figure 5. Stress-deformation curves outside and inside the fracture zone ("a" and "b" resp.)

## 6 The fracture energy $G_f$ .

In this section the results will be discussed for one failure zone. Concerning the multiple cracking that occurred in former tests, the same comments can be made as for the deformation capacity given in section 5.

The fracture energy is given by the integral for the area under the load-deformation curve for the failure zone. This energy is mainly determined by the descending branch beyond ultimate loading (see Table 3). The descending branch reflects an unstable equilibrium between loading and (material) response or between added energy and dissipated energy in the fracturing process. In deformation controlled tests this can be achieved by a very rigid testing device. In load controlled or dynamic impact tests the energy supply is not coupled to the deformation or the fracture process and the observed curve will differ from the deformation controlled tests. The conclusion is that the load-deformation curve depends on the loading conditions which has also to be considered in dynamic and static calculations.

The obtained curves from the impact tests reflect the separation of both specimen parts including the fracture process and the structural response with inertia effects. Complete separation occurred at a crackwidth of about 0.1mm and corresponds with static results as it should be. The influence of the structural response on the shape of the descending branch cannot be determined with the test results. To study the load-deformation curve the impact experiment will be simulated in a finite-element calculation, as was successfully done for the mentioned static tests (7).

## 7 Concluding remarks.

The determination of material properties appears to be very difficult, and is probably impossible, due to the structural response of the specimen in the loading device. The results of the discussed impact tests emphasize this statement. The conclusions are:

- Application of notches leads to a more brittle failure and a lower ultimate strength of the specimen for loading rates beyond a certain level. The threshold can be estimated as discussed and is about 10GPa/s for the applied geometry.

- The deformation capacity at ultimate loading, as determined in former tests, is too large due to including more than one cracking zone in the measuring length of 100mm. It should probably be reduced to 60% at least when a single failure zone is taken into consideration.

- The load-deformation curve is influenced by rotation of the material adjacent to the failure zone. Due to the rotation the average deformation increases. The rotation occurs during the failure process and depends on the asymmetry of the specimen and the loading. Symmetry and stiffness of the surrounding material will limit the rotation.

- The load-deformation curve is influenced by the loading conditions. The obtained curve in impact tests and the derived fracture energy cannot be regarded as a material property and directly compared with results obtained in static tests.
- Values for the material properties like deformation capacity and fracture energy should be chosen very carefully in (numerical) calculation because of the dependency on the considered element size and the loading conditions.

To study the true material response under impact loading, a combination of experiments and numerical simulation of the experiments will be very fruitful. The structural and material response can be separated in this way.

## References.

- (1) Reinhardt, H.W. et al.  
The Split Hopkinson Bar, a versatile tool for the impact testing of concrete. *Materiaux et Constructions*, Vol.19, No 109, 1986, pp 55-63.
- (2) Zielinski A.J.  
Fracture of concrete and mortar under uniaxial impact loading. Delft University Press, Delft, 1982.
- (3) Weerheijm, J.  
Dynamic properties of concrete 3: Evaluation of biaxial loading device. PML 1989- , to be published in 1989.
- (4) Kormeling, H.A.  
Impact tensile strength of steel fibre concrete. Stevin Report 5-84-8, Delft, 1984.
- (5) Weerheijm, J., Van Zantvoort, P.J.H. and Opschoor, G.  
The Application of the FE-Technique to Dynamic Failure Analysis of Concrete Structures. Proc. 23rd DoD Explosive Safety Seminar, Atlanta, Georgia, 9-11 August 1988.
- (6) Hordijk, D.A., Reinhardt, H.W., Cornelissen, H.A.W.  
Fracture Mechanics Parameters of concrete from uniaxial tensile tests as influenced by specimen length. In: "Fracture of concrete and rock", eds. S.P. Shah, S.E. Swartz, Houston, 1987, pp 138-149.
- (7) Hordijk, D.A., Rots, J.G., Reinhardt, H.W.  
Finite element supported fracture testing of concrete. Proc. IABSE Colloquium, Delft 1987, pp 189-196.

# CRITERIA USED FOR THE PARTIAL SUBSTITUTION OF STEELBARS BY STEEL FIBERS IN PROTECTIVE CONCRETE STRUCTURES

Major NAEYAERT Guido Charles Georges, CE

Design officer, Ministry of Defence.  
Infrastructure Department KGC,  
Kwartier Koningin Elisabeth, B - 1140 Brussels/Belgium.

## ABSTRACT

The dense network of steelbars, stirrups or laced steel in traditional military protective structures is very often a direct cause of poor workmanship on the concrete side.

This consideration, plus the attraction of an equal or better overall performance, has led the Belgian M.O.D. to start designing and constructing shelters by combining traditional steelbar reinforcement with steel fibers.

Whilst maintaining TM 5-1300 as a base for the design, advantage has been taken from the properties of steel fibers to meet the design constraints.

The combination of conventional steelbars and steel fibers has proven to be attractive both from the technical and the economical point of view.

## INTRODUCTION

In the last decennium the durability of (reinforced) concrete constructions has gained increasing attention. The phantastic development of the materials and construction know-how generally has led to a much greater awareness of the durability of a structure and the associated causes of degeneration.

The degeneration of reinforced concrete structures is caused by certain physical (erosion, abrasion, fissuration, frost,...) or chemical (environmental acids, sulphates, chlorides,...) factors or combinations of both.

To stop or retard the degeneration one can create specific thresholds :

- optimize the compaction of the concrete to obtain a low permeability to air and water. This is, by far, the most important durability factor ;
- ensure the internal chemical stability of the reinforced concrete components ;

- provide efficient concrete cover to protect the underlying steel bars ;
- prevent or reduce the formation of cracks to avoid corrosion of the steelbars.

The above recommendations - especially with regard to compaction - are relatively easy to put into practice for concrete with low or medium amounts of reinforcing steel. In the case of heavily reinforced protective structures however, the concrete compaction tends to be a difficult operation. This lack of compaction will touch off a degeneration process throughout the concrete and the reinforcing bars.

## BACKGROUND

In the early eighties, the Belgian M.O.D. has made a countrywide check on the degeneration of aircraft shelters, igloos for ammunition storage and other protective concrete structures. The result was really discouraging : widespread degeneration of concrete and steelbars was found, even on structures of less than ten years old. This widespread damage was mostly due to insufficient concrete compaction. Consequently, the use of conventional reinforced concrete (CRC) was subjected to a critical analysis and alternative methods were sought. The goal was to meet the strength criteria but at the same time find a solution for the high concentrations of steelbars which are systematically at the root of the compaction problems.

When analysing the reasons for the dense steel network in protective concrete structures it appears that these are imposed by the reinforcement design criteria to resist the effect of a nearby explosion. It is known that, for a given wall-thickness, the effectiveness of the steelbar reinforcement is a function of the distance between the inner and outerplane of the reinforcement. This distance should be as big as possible for maximum reinforcing efficiency in bending ; this results in a very high density of bars close to the wall surface both sides. This overconcentration of bars is even worse on places where splicing occurs or in corners where diagonal reinforcement is needed. The problem appeared in its most acute form for shelters which should

resist high nearby explosions where laced reinforcement is added which results in a steel ratio that may be as high as 270 kg per cubic metre (455 lbs per cubic yard) of concrete. These lacing problems have been recently highlighted by Thomas Wuennenberg (1987 - Reference 1), both from the cost and from the placing point of view. Obviously, in these situations, the flow and compaction of the concrete becomes problematic. When the concrete flow is hampered it also happens that the concrete segregates into aggregate-nests which leaves the adjoining bars unprotected.

### OBJECTIVE

In search of alternative reinforcing methods and in view of the above, the following conditions should be met :

- create more space in between the steelbar system, however in a way that the protective function (strength) of the walls is maintained ;
- ensure a well-compacted concrete matrix ;
- optimize the concrete cover. Carbonation and penetration of chlorides through the outer concrete skin should be adequately controlled.

The solution chosen by the M.O.D. was a partial substitution of the traditional steelbars by steel fibers. This alternative reinforcing method has been used in a project comprising five shelters for the Belgian M.O.D.. The purpose of using steel fibers was to :

- try a cost-effective alternative ;
- obtain a solution for the concrete placing and compaction ;
- design at least an equal performance of the reinforced concrete ;
- obtain a significant reduction of the early deterioration of the structure.

### USE OF SFRC

Steel fiber reinforced concrete (SFRC) has a relatively high plastic deformation capability if long deformed fibers from harddrawn steelwire are used. Such fibers have been specifically considered in this presentation. This type of reinforced concrete came up as an interesting alternative for oversaturated compositions of bars and lacing. A design study was done to check if steel fibers, in combination with a reduced portion of standard reinforcing steelbars, can withstand the same loads. The design study was preceded by an in depth evaluation of the characteristics of SFRC under dynamic load.

The most typical aspect of SFRC is that fibers actually change the nature of the concrete itself. Certain important characteristics, especially the ductility, are of a new order of magnitude and fit very well in designs which consider failure modes in plastic deformation. Steel fibers do not only act for load transfer around the first crack but develop their strain throughout the deformation cycle. This characteristic is in fact

generally accepted and backed by testing standards such as ASTM C 1018-85 and the Japanese JSCE standards.

### SFRC + CRC

In reinforced concrete under load, with steel fibers and steelbars combined, a higher number of cracks will occur, with crack-widths that are smaller for the same degree of deformation. Furthermore, in comparison to CRC, the cracks are inhibited until a much higher loading point. The fibers collaborate with the concrete to delay the first crack and interact with the bars to modify the cracking pattern of the structure.

Concrete with only steel fibers as reinforcement (SFRC) is capable of withstanding important loads. The superior crack resistance of SFRC compared to that of CRC is shown by the following formula :

$$1 < \frac{(M_f)_{SFRC}}{(M_f)_{CRC}} < 2 \quad (1)$$

and is a function of the percentage of reinforcement in volume (Reference 4).

Studies have shown (Reference 4) that steel fiber together with steelbar reinforcement attractively combine the advantages of both. This is a.o. resulting from the following formula and (1) :

$$1 < \frac{(M_r)_{CRC}}{(M_r)_{SFRC}} < 2 \quad (2)$$

which is also function of the percentage of reinforcement in volume (Reference 4).

The combination of steel fibers and steelbars is resulting in a remarkable increase of the crack resistance, the ductility, the rigidity and the tensile strength of the material. Furthermore the steel fibers maintain the structural integrity of the concrete element once the ultimate loading is reached. This due to the formation of innumerable little cracks instead of one large crack. This property is being maintained even at rather important deformations. In the compressive zone, the steel fibers will be beneficial because of the ductile behaviour in case of compressive failure (Reference 12). Scabbing is also strongly inhibited by the presence of the fibers throughout the wall section.

### ALTERNATIVE DESIGN METHOD

With these important properties at hand we are able to draw up an alternative for the conventional shelter construction. The design method allows the partial replacement of the normal reinforcements such as steelbars and stirrups by an appropriate quantity of steel fibers. Because of the replacement, more free space is available for the concrete which results into a considera-

bly better flow and compaction of the concrete matrix whilst maintaining the overall degree of reinforcement.

As far as the flexural moments are concerned, seven reliable papers - supported by testing - have been taken into consideration. These studies are giving evidence of the moment of rupture which can be obtained in a beam or a plate. This moment of rupture is the very factor which is used in the normal design procedures for buildings subjected to dynamic loads. The seven studies on review are from Williamson (1973 - Reference 5), Henager and Doherty (1976 - Reference 6), Onet (1978 - Reference 7), Swamy and Al-Ta'an (1981 - Reference 8), Jindal (1982 - Reference 9), Dehousse and Sahloul (1984 - Reference 4), Craig + NJIT (1987 - Reference 10). These different methods produce similar results and are conservative in comparison to certain tests where the ductility increased up to 500 % in comparison to CRC (Reference 10). It is important to note that the effectiveness of fibers in one direction in a concrete matrix can be expressed by a factor between 0 and 1. The factor is a function of the preferential plane of direction of the fibers in the concrete matrix. When SFRC is used in a normal way there is no preferential direction and the factor is 0,5. In the same case however, when SFRC is used in combination with steelbars, the factor goes up to minimum 0,85. This has been evidenced by N.M. Dehousse (Reference 4). On the basis of that remarkable synergy, which results from the combination of fibers and bars, a more balanced design of highly reinforced concrete structures is at our disposal.

The aspect of shear resistance of SFRC has also been studied in extenso. For shear strength the general conclusion is that certain steel fibers can replace stirrups. However, on this subject further tests remain necessary to come to practical values for different fiber dosages and fiber types (Reference 11 and 19).

For protective structures of reinforced concrete the rules of design are given in the well-known TM 5-1300 (Reference 13). These rules are basically not different whether one is considering CRC or combinations of steelbars and steel fibers. In both cases the dynamic analysis is based on the strength characteristics of the (reinforced) structure of which the ultimate moment is certainly the most important. The ultimate moment, in combination with the total deformation and also the elastic deformation, is the key-factor for the dimensioning of protective structures.

According to Craig (Reference 10) the above theories, when applied to SFRC for the determination of the ultimate moment, are equivalent when it comes to the results. Nevertheless, tests have shown that the real ultimate moment is amply larger than the calculated one. This implies that the theoretical value of the ultimate moment is constantly conservative. The difference between the test data and the results obtained by applying the Henager-theory is almost 20 %. Recent

tests in Belgium at the K.U.L. University have shown that, by using suitable fibers and high quality concrete, the difference between the test data and the above mentioned theory can even be a lot higher,

- used fiber : length/diameter ratio of 75, hard-drawn deformed steel with tensile strength min. 1100 N/mm<sup>2</sup> (161,700 psi) ;
- concrete :  $f'_c$  45 N/mm<sup>2</sup> (6,600 psi).

The reason for this is a remarkably higher  $f_t$ -value (fiber tension stress). This conclusion is similar to that given by Hülsewig (Reference 14). An element in CRC can withstand a greater bending moment than an element in CRC + steel fibers considering the same steel quantity in both cases. Purely static it seems at first sight disadvantageous to insert steel fibers in CRC. However, for the dynamic analysis we have to consider that in most cases (Reference 13, Chapter 5, Type II and III Reinforced Concrete Crosssections) the upper ( $A'_s$ ) and lower ( $A_s$ ) reinforcement are the same :

$$A_s = A'_s \quad (3)$$

It is mainly the tensile reinforcement ( $A_s$ ) that intervenes for the determination of the ultimate moment. Even walls with steel fiber concrete require both compressive and tensile reinforcement. However, these reinforcements are considerably smaller than those foreseen in CRC walls. So the addition of steel fibers to CRC can be a more economical solution than pure CRC.

The total and the elastic deformation of the protective structure walls are also important for the dynamic analysis. The deformations of a series of beams with identical dimensions but with different reinforcements, on the one hand CRC and on the other hand CRC combined with steel fibers, have been put on diagram by Craig (Figure 1, 2 and 3 - Reference 10). So by adding steel fibers, the deformation of the beam at failure is almost doubled compared to the conventional solution.

When checking this with the desing rules of TM5-1300 (Reference 18), it immediately appears that an increase of  $X_m/X_E$  results in a greater value  $B/r_u$  if  $T/T_n$  is constant, i.e. for a well defined explosion at a well defined distance from the wall. As the  $B/r_u$  value increases, the wall can sustain a higher explosive load and this on account of the fibers.

A third factor intervening in the wall design is the product  $E \times I$ . It appears from tests and calculations that the influence of this factor is not the decisive one. A realistic estimate of the  $I$ -value, viz. the one given in TM 5-1300 (Reference 13), can be maintained for the combination of CRC and steel fibers. A possible estimate for the  $E$ -value of SFRC is (Reference 4) :

$$E = p \cdot E_a \text{ fibers} + (1 - p) E_b \quad (3)$$

If the amount of steel fibers (harddrawn deformed fibers with  $L/D = 75$ ) is in the order of around one percent in volume, as currently used, there is a small difference between the different values of the elasticity modulus  $E$  and  $E_b$ .

Relying on the forementioned factors a complete dynamic analysis can be done with the manual TM5-1300 for CRC combined with steel fibers.

Considering the properties of SFRC, viz. the increased ductility and the larger total deformation capability of the walls, the positive influence of the fibers is fully revealed if we may assume a larger value for the deformation at the supports in comparison to CRC (Reference 13). This seems justified if you look at the high deformability which SFRC can sustain.

A complete calculation of the optimal design values - wall thickness, total volume of steelbar and fiber reinforcement etc. - for a given explosion at a given distance is a time consuming job. A less complicated approach is to start from a fair assesment of the wall thickness. For CRC the well-known Hader-diagram (Reference 18) is often used. For CRC combined with steel fibers such a diagram is not available yet. However, in analogy with the existing Hader-diagram and using published test data for uncased explosive charges (References 15, 16, 17) we could compute a graphical aid which permits a fair predimensioning of walls with a combined reinforcement of steelbars and steel fibers (Figure 4). For cased explosions it was not possible to do something analogous by lack of sufficient test data.

The diagram (Figure 4) confirms that is possible to reduce the wall thickness considerably for CRC + SFRC in comparison to the traditional CRC solution.

### CONCLUSIONS

The use of steel fibers in combination with CRC in protective structures is an economically justified solution on the condition of using it in a calculated way. The solution consists in increasing the distances between the steelbars or in eliminating some of them. It is possible to drastically reduce the more expensive folded bars and stirrups. Finally we can ensure a maximum of quality control on the concrete placement in between the simplified steelbar-network.

Considering the totally different cracking pattern and the possibility of a bigger plastic deformation without collapsing, it is necessary to admit a larger deformation than currently used in the dynamic analysis.

For structures not needing EMP (Electromagnetic Pulse) protection, it is possible to solve the scabbing-problems with a smaller wall thickness than the one normally used, this without using internal steel plate.

### NOTATIONS

|                |  |
|----------------|--|
| $A_s$          | : area of tension reinforcement                            |
| $A'_s$         | : area of compressive reinforcement                        |
| $B$            | : peak pressure of equivalent triangular loading function  |
| CRC            | : conventional reinforced concrete                         |
| $E$            | : modulus of elasticity of SFRC                            |
| $E_a$ fibers   | : modulus of elasticity of the steel fibers                |
| $E_b$          | : modulus of elasticity of concrete                        |
| $I$            | : moment of inertia  |
| $f_t$          | : tensile stress in the tensile zone of SFRC               |
| $(M_f)_{SFRC}$ | : moment (first crack) for pure SFRC (without rebars)      |
| $(M_f)_{CRC}$  | : moment (first crack) for CRC (without steel fibers)      |
| $(M_r)_{SFRC}$ | : ultimate moment for pure steel fiber reinforced concrete |
| $(M_r)_{CRC}$  | : ultimate moment for conventional reinforced concrete     |
| $r_u$          | : ultimate unit resistance                                 |
| SFRC           | : steel fiber reinforced concrete                          |
| $P$            | : reinforcement ratio                                      |
| $T$            | : duration of equivalent triangular loading                |
| $T_n$          | : effective natural period of vibration                    |
| $x_E$          | : equivalent elastic deflection                            |
| $x_m$          | : maximum deflection                                       |



# REFERENCES

1. Thomas C. Wuennenberg, "Laced Reinforced Concrete Structures", Concrete International, October 1987 also The Military Engineer, May-June 1987
2. ASTM C 1018-85, "Standard Test Method for Flexural Toughness and First Crack Strength of Fiber Reinforced Concrete"
3. Concrete Library of JSCE, "Method of Tests for Steel Fiber Reinforced concrete", June 1984
4. N.M. Dehousse, "Considérations relatives au comportement à la fissuration et à la rupture de béton renforcé de fibres", Journée D'Etudes "Béton armé de fibres d'acier", Groupement Belge du Béton, Liège le 2 avril 1984
5. Williamson G.R., "Compression Characteristics and Structural Beam Design Analysis of Steel Fiber Reinforced Concrete", Technical Report M-62, Construction Engineering Research Laboratory, Champaign, Ill., December 73
6. Henager and Doherty, "Analysis of Reinforced Fibrous Concrete Beams", Journal of Structural Division ASCE, Vol. 102 No St1, Proc. Paper 11847, January 76 - pp. 177 - 188
7. Onet, "The Behaviour of Bar and Steel Fiber Reinforced Concrete Beams in Static Testing", Delft, Stevin Report 5-78-5, June 1978
8. Swamy and Alta'an, "Deformation and Ultimate Strength in Flexure of Reinforced Concrete Beams made with Steel Fiber Concrete", Journal of the American Concrete Institute, Sept.-Oct. 81, N° 5 Proceedings, V. 78
9. Jindal, "Shear and Moment Capacities of Steel Fiber Reinforced Concrete Beams", presented at the 1982 Fall Convention, American Concrete Institute, Detroit, Michigan, September 1982
10. Craig R.J., SP 105-28, "Flexural Behaviour and Design of Reinforced Fiber Concrete Members"  
SP 105 - ACI 1987 - "Fiber Reinforced Concrete - Properties and Applications"
11. L. Van de Loock, "Staalvezelbeton voor konstruktieve toepassingen", literatuurstudie, Katholieke Universiteit Leuven/Belgium, 31-ST-16, 28-04-1988
12. Swamy, "Flexural Behaviour of Fiber Concrete with Conventional Steel Reinforcement", Rilem Symposium on fiber concrete, 1975, p. 187-196
13. TM 5-1300, "Structures of Resist the Effects of Accidental Explosions", US Departments of the Army the Navy and the Air Force, June 1969
14. Hülsewig, Schneider, Stilp, "Behaviour of Fiber Reinforced Concrete Slabs under Impact Loading", The Interaction of Non-nuclear Munitions with Structures, U.S. Air Force Academy, Colorado, 1983
15. H. Pahl, "Ansprengeversuche an einem Schutzbau aus Stahlfaserbeton", Infrastrukturstab des Bundeswehrs, Januar 1979
16. Erp St 52, "Feststellung des Erprobungsergebnisses", T/K 47 EE/81043/45160 vom 14 Juli 78, "Stahlfaserbeton Schutzbau"
17. Williamson G.R., "Response of Fibrous Reinforced Concrete to Explosive Loading", Ohio River Division Laboratories, Corps of Engineers, January 1966
18. Hader, "Effects of Bar and Cased Explosives Charges on Reinforced Concrete Walls", the Interaction of Non-nuclear Munitions with Structures, Colorado, 1983
19. L. Van de Loock, "Influence of Steel Fibers on the Shear Transfer in Cracks", Proceedings of the International Symposium on Fiber Reinforced Concrete, Madras, India, December 1987
20. Craig R.J., Decker J., Dombrowski Jr. L., Laurencelle R. and Federovich J., "Inelastic Behaviour of Reinforced Fibrous Concrete". Journal of Structural Engineering, ASCE, Vol. 113, No. 4, April, 1987, pp. 802-817.

1 Nm = 0.74 lb.ft.  
 1 cm = 0.394 inch  
 1 N/mm<sup>2</sup> = 147 psi

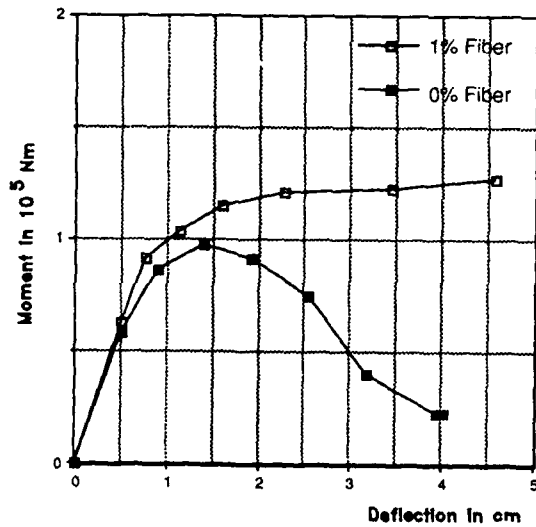


Figure 1 - Comparison of moment deflection curves for steelbar + steel fiber reinforced beam sections with 13,6 N/mm<sup>2</sup> concrete (Reported by CRAIG, Reference 10)

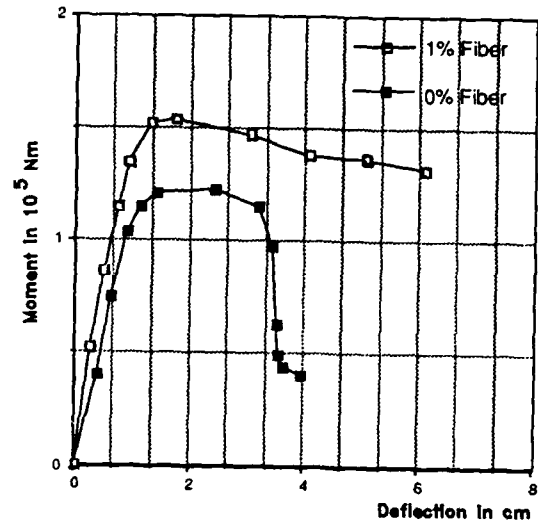


Figure 2 - Comparison of moment deflection curves for steelbar + steel fiber reinforced beam sections with 27,2 N/mm<sup>2</sup> concrete (Reported by CRAIG, Reference 10)

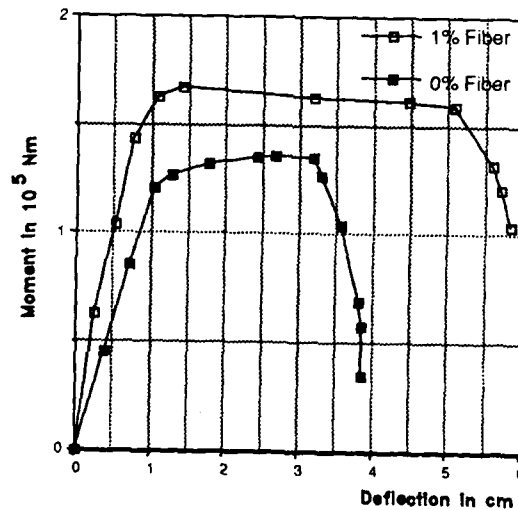


Figure 3 - Comparison of moment deflection curves for steelbar + steel fiber reinforced beam sections with 40,8 N/mm<sup>2</sup> concrete (Reported by CRAIG, Reference 10)

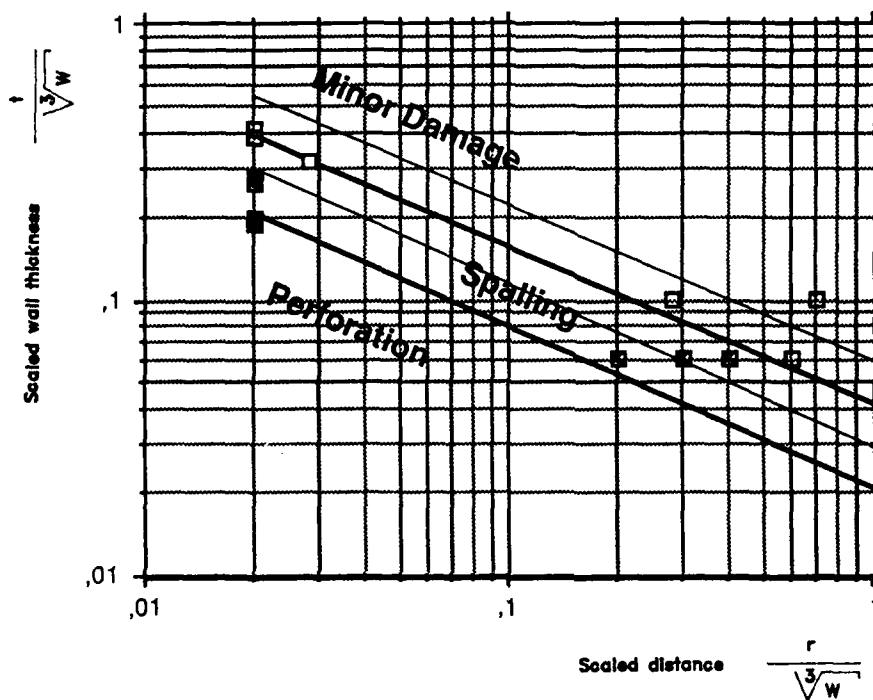


Figure 4 - Damage to reinforced concrete walls caused by detonation of uncased explosive charges

$r$  : distance in meters between wall and center of explosion

$t$  : wall thickness in meters

$W$  : explosive charge weight in kilos

— Conventional Reinforced Concrete (CRC)

— Conventional Reinforced Concrete

+ Steel Fiber Reinforced Concrete (CRC + SFRC)

# STRAIN-DEPENDENT CAP MODEL FOR FITTING MILL YARD TEST BED SOIL BEHAVIOR

GEORGE Y. BALADI

CIVIL ENGINEERING RESEARCH DIVISION  
AFWL/NTE, KIRTLAND AFB, NM 87117-6008

## ABSTRACT

This paper describes the development of a three-dimensional elastic-plastic work-hardening constitutive relationship in which the elastic moduli are functions of stresses and strains. It contains (1) the general description of the new model including proof of its theoretical soundness, (2) selected mathematical forms of its various response functions, tensile behavior, and (3) an example model fit to laboratory shear and uniaxial strain test results of clayey sand backfill-type material. The new model was incorporated into GRALE cratering and ground shock computer code and a calculation is being performed to simulate MILL YARD event.

## INTRODUCTION

Incremental elastic-plastic constitutive models which include both an ultimate failure envelope and a work-hardening yield surface -- or cap -- are commonly used in ground shock calculations to simulate geologic material behavior (Reference 1). The elastic shear modulus in the cap model is usually formulated in terms of the second invariant of the stress deviation tensor and the plastic volumetric strain. Such formulations, however, cannot replicate the highly nonlinear bowl-shaped unloading stress paths that typify clayey sand-type material behavior (Reference 2 and Figure 1).

In 1984, a cap model was developed in which the shear modulus was formulated not only as a function of the second invariant of the stress deviation tensor and plastic volumetric strain, but also as a function of the third invariant of the stress deviation tensor (Reference 3). Although this model is able to duplicate the behavior of clayey sand-type material quite well, it might generate energy under certain stress or strain paths. In order to satisfy all of the rigorous theoretical requirements outlined in Reference 4 and still satisfactorily replicate clayey sand-type material behavior, a new cap model has been formulated in which the shear modulus is expressed as a function of the second invariant of

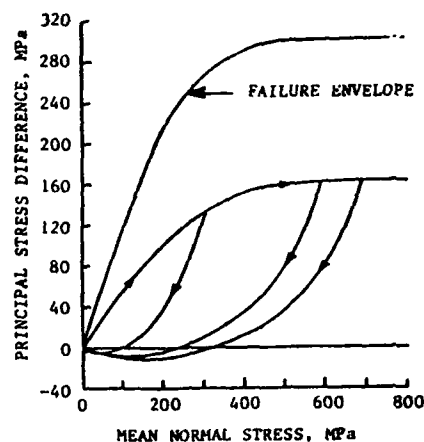


Figure 1. Uniaxial strain stress paths for clayey, sand-type material.

the strain deviation tensor and the second invariant of the stress deviation tensor.

The model has been extended to include high pressure equations of state and used to calculate the MILL YARD event.

## GENERAL DESCRIPTION OF THE NEW MODEL

The basic premise of elastic-plastic constitutive models is the assumption that certain materials are capable of undergoing small plastic (permanent) as well as elastic (recoverable) strains at each loading increment. Mathematically, the total strain increment is assumed to be the sum of the elastic and plastic strain increments, i.e.,

$$d\epsilon_{ij} = d\epsilon_{ij}^E + d\epsilon_{ij}^P \quad (1)$$

The behavior of the material in the plastic range can be described within the framework of the generalized incremental theory of plasticity. The mathematical basis of the theory was established by Drucker (Reference 5), who introduced the concept of material stability given by

$$d\sigma_{ij} d\epsilon_{ij}^P \geq 0 \quad (2)$$

This condition allows considerable flexibility in the choice of the form of the loading function  $f$  for the model, which serves as both a yield surface and the plastic potential. For isotropic materials the yield surface may be expressed, for example, as

$$f(J_1, \sqrt{J_2'}, \kappa) = 0 \quad (3)$$

where  $J_1$  and  $J_2'$  are the first invariant of the stress tensor and the second invariant of the stress deviation tensor, respectively.  $\kappa$  is a hardening parameter and  $\delta_{ij}$  is Kronecker delta. The hardening parameter  $\kappa$  can generally be taken to be a function of the plastic strain tensor. The yield surface of Equation 3 may expand or contract as  $\kappa$  increases or decreases, respectively (Figure 2). The plastic flow rule is:

$$d\epsilon_{ij}^p = \begin{cases} d\lambda \frac{\partial f}{\partial \sigma_{ij}} & \text{if } f = 0 \\ 0 & \text{if } f < 0 \end{cases} \quad (4)$$

where  $d\lambda$  is a positive scalar factor of proportionality, which is non-zero only when plastic deformations occur and is dependent on the particular form of the loading function.

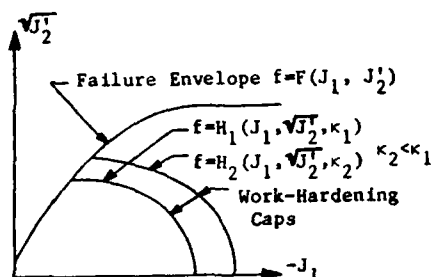


Figure 2. Typical yield surfaces for a cap model.

#### Elastic Strain Increment Tensor

For isotropic elastic materials, the strain increment tensor takes the following form

$$d\epsilon_{ij}^E = \frac{dJ}{9K} \delta_{ij} + \frac{1}{2G} dS_{ij}$$

or

$$d\sigma_{ij} = K d\epsilon_{kk}^E \delta_{ij} + 2G d\epsilon_{ij}^E \quad (5)$$

where  $K$  is the elastic bulk modulus and  $G$  is the elastic shear modulus. These moduli can be functions of the invariants of either the stress or the strain tensor. Accordingly, it is assumed that  $K = K(J_1, J_2', J_3')$  and  $G = G(J_1, J_2', J_3')$  or  $K = K(I_1, I_2', I_3')$  and  $G = G(I_1, I_2', I_3')$ . Equation 5 can be written in terms of the hydrostatic and deviatoric components of the strain and stress increment tensors, i.e.,

$$d\epsilon_{kk}^E = \frac{1}{3K(J_1, J_2', J_3')} dJ_1$$

$$d\epsilon_{ij}^E = \frac{1}{2G(J_1, J_2', J_3')} dS_{ij}$$

or

(6)

$$dJ_1 = 3K(I_1, I_2', I_3') d\epsilon_{kk}^E$$

$$dS_{ij} = 2G(I_1, I_2', I_3') d\epsilon_{ij}^E$$

where  $d\epsilon_{kk}^E$  is the increment of elastic volumetric strain,  $d\epsilon_{ij}^E$  is the elastic strain deviation increment tensor,  $J_3'$  is the third invariant of the stress deviation tensor,  $I_1$  is the first invariant of the strain tensor,  $I_2'$  and  $I_3'$  are the second and third invariants of the strain deviation tensor, respectively. In order not to generate energy or hysteresis within the elastic range, the elastic behavior of the model must be path independent. The material should then possess a positive definite elastic internal energy function  $\bar{W}$  which is independent of stress path. The complementary strain energy function can be written as

$$\begin{aligned} \bar{W} &= \int_0^{\sigma_{ij}} \epsilon_{ij} d\sigma_{ij} \\ &= \int_0^{\epsilon_{ij}} \left( \frac{\epsilon_{kk}}{3} \delta_{ij} + e_{ij} \right) \{ K(I_1, I_2', I_3') d\epsilon_{kk}^E \delta_{ij} + 2G(I_1, I_2', I_3') d\epsilon_{ij}^E \} \quad (7) \end{aligned}$$

Substitution of Equation 1 into Equation 7 leads to

$$\begin{aligned} \bar{W} &= \int_0^{\epsilon_{ij}} \left( \frac{\epsilon_{kk}}{3} \delta_{ij} + e_{ij} \right) \{ K(I_1, I_2', I_3') (d\epsilon_{kk}^E - d\epsilon_{kk}^p) \delta_{ij} \\ &\quad + 2G(I_1, I_2', I_3') (d\epsilon_{ij}^E - d\epsilon_{ij}^p) \} \quad (8) \end{aligned}$$

But  $d\epsilon_{kk}^p$  and  $d\epsilon_{ij}^p$  equal to zero under elastic deformation. Hence Equation 8 becomes

$$\bar{W} = \int_0^{\epsilon_{kk}} \frac{1}{2} K(I_1, I_2', I_3') d\{\epsilon_{kk}^2\} + \int_0^{I_2'} 2G(I_1, I_2', I_3') dI_2' \quad (9)$$

Equation 9 indicates that for  $\bar{W}$  to be independent of the strain path, the integrals in Equation 9 have to depend only on the current values of  $I_1$  and  $I_2'$ . Therefore, the bulk and shear moduli can be expressed as

$$K = K(\epsilon_{kk}) = K(I_1) \text{ and } G = G(I_2') \quad (10)$$

Similarly, it can be shown that (Reference 6)

$$K = K(J_1) \text{ and } G = G(J_2') \quad (11)$$

It can be concluded from Equations 10 and 11 that the bulk modulus should be expressed as a function of either  $I_1$  or  $J_1$  and the shear modulus should be related to either  $I_2$  or  $J_2'$ . Further,  $K$  and  $G$  must always be positive. Since during elastic deformation the hardening parameter  $\kappa$  is constant, the bulk and shear moduli can also be expressed as

$$\begin{aligned} K &= K(J_1, \kappa) = K(I_1, \kappa) \\ \text{or} \quad G &= G(J_2', \kappa) = G(I_2', \kappa) \end{aligned} \quad (12)$$

#### Plastic Strain Increment Tensor

The plastic strain increment tensor is given by Equation 4 where the loading function  $f$  is given by Equation 3. The hardening parameter in Equation 3 could be taken as being equal to the plastic volumetric strain; thus

$$\kappa = \epsilon_{KK}^P \quad (13)$$

The use of Equation 13 will allow the cap to expand as well as to contract (Figure 2).

Like the elastic behavior given by Equation 6, the plastic stress-strain relation can be expressed in terms of the hydrostatic and deviatoric components of strain, i.e.,

$$d\epsilon_{KK}^P = 3 d\lambda \frac{\partial f}{\partial J_1} \text{ and } d\epsilon_{ij}^P = \frac{d\lambda}{2\sqrt{J_2'}} \frac{\partial f}{\partial \sqrt{J_2'}} S_{ij} \quad (14)$$

where, from Reference 6,  $d\lambda$  is

$$d\lambda = \frac{3K \frac{\partial f}{\partial J_1} d\epsilon_{KK} + \sqrt{J_2'} \frac{\partial f}{\partial \sqrt{J_2'}} S_{ij} d\epsilon_{ij}}{9K \left( \frac{\partial f}{\partial J_1} \right)^2 + G \left( \frac{\partial f}{\partial \sqrt{J_2'}} \right)^2 - 3 \frac{\partial f}{\partial J_1} \frac{\partial f}{\partial \epsilon_{KK}^P}} \quad (15)$$

#### Behavior in Tension

The tension cutoff is triggered in this model whenever the following relation is satisfied:

$$\frac{J_1}{3} - T \geq 0 \quad (16)$$

in which  $T$  is the maximum value that the mean hydrostatic tension  $J_1/3$  can attain. The volumetric strain which occurs during tension is computed from the following relation:

$$\epsilon_{KK}^T = \left( \frac{\frac{J_1}{3} - T}{K_1} \right) \quad (17)$$

where  $K_1$  is the bulk modulus of the material at  $J_1/3 = T$  (Figure 3).

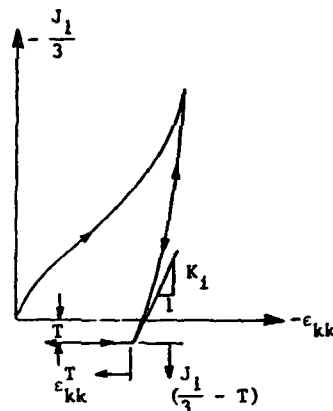


Figure 3. Behavior of the model in tension.

Upon reloading, the material stays in the state of tension until the volumetric strain computed by Equation 17 is completely recovered.

#### Example Model Fit for MILL YARD Clayey Sand-Type Material Behavior

To illustrate the new model's capability for fitting clayey sand-type material behavior, selected mathematical forms of the various response functions were used. In the following model response functions, tension is considered positive.

#### Yield Conditions

The yield conditions consist of an ultimate failure surface of the form

$$f = F(J_1, \sqrt{J_2'}) = \sqrt{J_2'} - \{A - C \exp(B J_1 - B_1 J_1^2)\} = 0 \quad (18)$$

and a work-hardening cap of the form

$$f = H(J_1, \sqrt{J_2'}, \epsilon_{KK}^P) = (J_1 - L)^2 + R J_2' - (X - L)^2 = 0 \quad (19)$$

where  $A$ ,  $B$ ,  $B_1$ , and  $C$  are material parameters (constants),  $L(\epsilon_{KK}^P)$  and  $X(\epsilon_{KK}^P)$  are respectively, the values of  $J_1$  at the center of the cap (Equation 19) and the intersection of the cap with the  $J_1$  axis, and are related as:

$$L - X = R\{A - C \exp(B L - B_1 L^2)\} \quad (20)$$

where  $R$  is the ratio of the major to the minor axis of the cap and is given by:

$$R = \frac{R_0}{1-R_1} \{1 - R_1 \exp(R_2 L)\} + R_3 \left[ \frac{R_4 - 1}{R_4 + 1} + \frac{1 - R_4 \exp(R_5 L)}{1 + R_4 \exp(R_5 L)} \right] \quad (21)$$

where  $R_0, R_1, R_2, R_3, R_4$ , and  $R_5$  are material parameters (constants), and

$$L(\epsilon_{KK}^P) = \begin{cases} L(\epsilon_{KK}^P) & \text{if } L(\epsilon_{KK}^P) \leq 0 \\ 0 & \text{if } L(\epsilon_{KK}^P) > 0 \end{cases} \quad (22)$$

### Hardening Function

The hardening function is chosen to be

$$\epsilon_{KK}^P = W[\exp(D \bar{LL}) - 1 - D \bar{LL} \exp(D_1 \bar{LL})] - D_2 \bar{LL}^2 \exp(D_3 \bar{LL}) - D_4 \left[ \frac{D_5 - 1}{D_5 + 1} + \frac{1 - D_5 \exp(D_6 \bar{LL})}{1 + D_5 \exp(D_6 \bar{LL})} \right] \quad (23)$$

in which  $\bar{LL} = L - \bar{LL}$  and  $W, D, D_1, D_2, D_3, D_4, D_5$ , and  $D_6$  are material constants.  $W$  in Equation 23 defines the maximum plastic volumetric compaction that the material can experience under hydrostatic loading. The numerical value of  $\bar{LL}$  is the solution of the following equation

$$\bar{LL} - R(A - C \exp(B \bar{LL} - B_1 \bar{LL}^2)) = 0 \quad (24)$$

### Bulk Modulus

The bulk modulus is given by

$$K = \frac{K_1}{(1 - K_1)} \{1 - K_1 \exp(K_2 J_{1mp})\} \bar{K} \frac{\hat{K}}{3} \quad (25)$$

where

$$J_{1mp} = \min\{J_1, \max(J_{1m}, K_{10})\} \quad (26a)$$

$$J_{1m} = \min(J_{1m}, J_1) \quad (26b)$$

$$\bar{K} = \frac{K_3 - \frac{1 - K \exp(K_5 (J_{1mp} - J_1))}{1 + K \exp(K_5 (J_{1mp} - J_1))}}{K_3 - \frac{1 - K}{1 + K}} \quad (27)$$

$$\hat{K} = \frac{1 + K \exp(-K \kappa)}{1 + K_7} \quad (28)$$

and

$$\kappa = \frac{\max\{(J_1 - \hat{J}_1), 0\}}{\max\{(\bar{J}_1 - \hat{J}_1), 0\}} \quad (29)$$

where

$$\hat{J}_1 = \min\left\{\frac{1}{K_9} \ln\left(\frac{A - \sqrt{J_2^P}}{C}\right), \frac{1}{K_{13}} \ln\left(\frac{K_{11} - \sqrt{J_2^P}}{K_{12}}\right)\right\} \quad (30)$$

$$\bar{J}_1 = \frac{B}{2B_1} - \sqrt{\left(\frac{B}{2B_1}\right)^2 - \frac{1}{B_1} \ln\left(\frac{A - \sqrt{J_2^P}}{C}\right)} \quad (31)$$

$K_1, K_2, K_3, K_4, K_5, K_7, K_8, K_9, K_{10}, K_{11}, K_{12}$ , and  $K_{13}$  in the above equations are material parameters (constants).

### Shear Modulus

The shear modulus is chosen to be

$$G = \left\{ \frac{G_1}{1 - G_1} \{1 - G_1 \exp(G_2 \epsilon_{KK}^P - G_3 \sqrt{J_2^P})\} + \hat{G} \right\} \bar{G} \frac{\eta}{2} \quad (32)$$

where

$$\sqrt{J_2^P} = \max\{\sqrt{J_2^P}, \sqrt{J_2^P}\} \quad (33)$$

$$\hat{G} = G_7 \left[ 1 - \frac{G_{12} \exp(-G_{11} \sqrt{J_2^P})}{1 + \exp(-2G_{11} \sqrt{J_2^P})} \right] \times \left[ \frac{G_9 - 1}{G_9 + 1} + \frac{1 - G_9 \exp(-G_{10} \sqrt{J_2^P})}{1 + G_9 \exp(-G_{10} \sqrt{J_2^P})} \right] \times \left\{ 1 - \exp\{G_8 (\sqrt{I_2^P} - \sqrt{I_2^P})\} \right\} \quad (34)$$

$$\bar{G} = \frac{G_4 - \frac{1 - G_5 \exp[G_6 (\sqrt{I_2^P} - \sqrt{I_2^P})]}{1 + G_5 \exp[G_6 (\sqrt{I_2^P} - \sqrt{I_2^P})]}}{G_4 - \frac{1 - G_5}{1 + G_5}} \quad (35)$$

$$\eta = \frac{1 + K_7 \exp\{(-K_8 \chi) \exp(-G_{13} \zeta)\}}{1 + K_7} \quad (36)$$

$$\chi = \frac{\max\{(\sqrt{J_2^P} - \sqrt{J_2^P}), 0\}}{\max\{(\sqrt{J_2^P} - \sqrt{J_2^P}), 0\}} \quad (37)$$

$$\zeta = \max\{(\sqrt{I_2^P} - \sqrt{I_2^P}), 0\} \quad (38)$$

$$\sqrt{I'_{2m}} = \max(\sqrt{I'_{2m}}, \sqrt{I'_2}) \quad (39)$$

$$\sqrt{J'_2} = A - C \exp(BJ_1 - B_1 J_1^2) \quad (40)$$

$$\sqrt{J'_2} = \min\{A - C \exp(K_9 J_1), K_{11} - K_{12} \exp(K_{13} J_1)\} \quad (41)$$

$I'_2$  is the second invariant of the strain deviation tensor and  $G_1, G_1, G_2, G_3, G_4, G_5, G_6, G_7, G_8, G_9, G_{10}, G_{11}, G_{12}$ , and  $G_{13}$  are material parameters (constants).

#### Numerical Values of Fitting Parameters

The above model includes a total of 47 fitting parameters (or material constant); the numerical values of these parameters used to fit the material properties specified for MILL YARD clayey sand are given in Table 1.

TABLE 1. Numerical values of fitting parameters for MILL YARD "conventional property" cap model.

| Model Fitting Parameters |                         | Numerical Value    |
|--------------------------|-------------------------|--------------------|
| Name                     | Notation, Unit          |                    |
| Bulk Density             | $\rho, \text{g/cm}^3$   | 1.898              |
|                          | A, MPa                  | 236.7136           |
| Failure                  | B, (MPa) <sup>-1</sup>  | 0.00115            |
| Parameters               | B1, (MPa) <sup>-2</sup> | $6 \times 10^{-7}$ |
|                          | C, MPa                  | 236.6559           |
|                          | R0, --                  | 3.2                |
|                          | R1, --                  | -0.5               |
|                          | R2, (MPa) <sup>-1</sup> | 0.0005             |
|                          | R3, --                  | 10000.0            |
| Hardening                | R4, --                  | $2.0 \times 10^8$  |
| Yield                    |                         |                    |
| Surface                  | R5, (MPa) <sup>-1</sup> | 0.01               |
| Parameters               | W, --                   | 0.173              |
|                          | D, (MPa) <sup>-1</sup>  | 0.015              |
|                          | D1, (MPa) <sup>-1</sup> | 0.2                |
|                          | D2, (MPa) <sup>-2</sup> | $10^{-4}$          |
|                          | D3, (MPa) <sup>-1</sup> | 0.1                |
|                          | D4, --                  | 0.017              |
|                          | D5, --                  | 20.0               |
|                          | D6, (MPa) <sup>-1</sup> | 0.005              |
|                          | K1, MPa                 | 300.0              |
|                          | K1, --                  | 0.994              |

TABLE 1. Continued.

| Model Fitting Parameters |                          | Numerical Value |
|--------------------------|--------------------------|-----------------|
| Name                     | Notation, Unit           |                 |
|                          | K2, (MPa) <sup>-1</sup>  | 0.0005          |
|                          | K3, --                   | 2.0             |
| Bulk Modulus             | K4, --                   | 300.0           |
| Parameters               | K5, (MPa) <sup>-1</sup>  | 0.005           |
|                          | K6, --                   | 1.0             |
|                          | K7, --                   | 0.0             |
|                          | K8, --                   | 0.0             |
|                          | K9, (MPa) <sup>-1</sup>  | 1.0             |
|                          | K10, MPa                 | -1688.46        |
|                          | K11, MPa                 | 243.0           |
|                          | K12, MPa                 | 55.0            |
|                          | K13, (MPa) <sup>-1</sup> | 0.000095        |
|                          | G1, MPa                  | 150.0           |
|                          | G1, --                   | 0.994           |
|                          | G2, --                   | 0.5             |
|                          | G3, (MPa) <sup>-1</sup>  | 0.0025          |
|                          | G4, --                   | 1.2             |
|                          | G5, --                   | 25.0            |
| Shear                    | G6, (MPa) <sup>-1</sup>  | 800.0           |
| Modulus                  |                          |                 |
| Parameters               | G7, MPa                  | 7000.0          |
|                          | G8, (MPa) <sup>-1</sup>  | $10^5$          |
|                          | G9, --                   | 5.0             |
|                          | G10, (MPa) <sup>-1</sup> | 0.02            |
|                          | G11, (MPa) <sup>-1</sup> | 0.04            |
|                          | G12, --                  | 3.6             |
|                          | G13, (MPa) <sup>-1</sup> | 0.0             |
|                          | G14, --                  | 1.0             |

Figures 4 and 5 depict comparisons of the stress-strain and strength behavior predicted by the model with the recommended properties. It is clear from these figures that the proposed model simulates the behavior of clayey sand quite well.

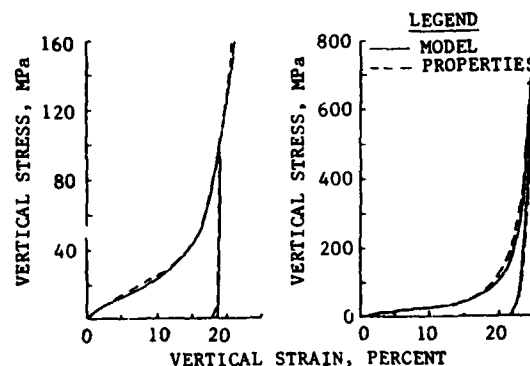


Figure 4. Comparison of model fits with recommended uniaxial strain stress-strain curves.



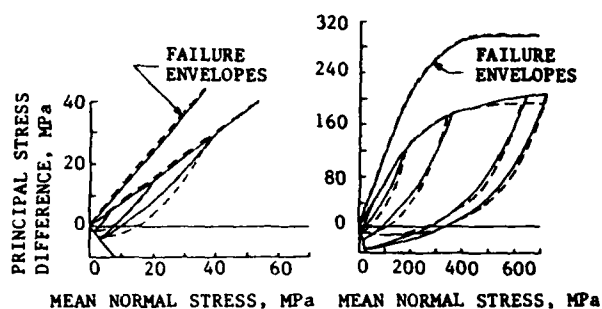


Figure 5. Comparison of model fits with recommended uniaxial strain stress path relations and triaxial failure envelopes.

#### REFERENCES

1. I.S. Sandler, F.L. DiMaggio and G.Y. Baladi; "Generalized Cap Model for Geological Materials"; July 1976; Journal of the Geotechnical Engineering Division, ASCE, Vol. 102, No GT7, Proc. Paper 12243, pp. 638-699.
2. A.E. Jackson, Jr.; "Preliminary Material Property Estimates for ISST Ground Shock Calculations"; January 1984, U.S. Army Engineer Waterways Experiment Station, Vicksburg, MS.
3. G.Y. Baladi; "Constitutive Model Equations and Parameter Values Used for Fitting Preliminary Material Property Estimates for ISST"; April 1984; U.S. Army Engineer Waterways Experiment Station, Vicksburg, MS.
4. I.S. Sandler; "Material Models for Ground Shock Calculations"; 11 July 1984; DNA meeting on Constitutive Models for Ground Calculations at SRI International, Menlo Park, CA.
5. D.C. Drucker, "On Uniqueness in the Theory of Plasticity"; Quarterly of Applied Mathematics, Vol. 14; 1956.
6. W.F. Chen and G.Y. Baladi; Soil Plasticity: Theory and Implementation; Elsevier Science Publishers B.V., 1985.

# STRESS-STRAIN BEHAVIOR OF SANDS - A MICROSTRUCTURAL APPROACH

Ching S. Chang, Associate Professor and Anil Misra, Research Assistant

Department of Civil Engineering,  
University of Massachusetts, Amherst, MA 01003

## ABSTRACT

The initial tangent moduli for granular materials is obtained based on an analytical model considering particle interactions. The Hertz-Mindlin theory of contact of two elastic spheres is used to describe the contact displacement behavior. The analytical model includes the effect of the void ratio, the coordination number, the constituent particle properties, and the structural anisotropy. Results computed from the derived relations are compared with the experimental measurements for initial tangent.

## INTRODUCTION

A rational approach to mathematically model the mechanical behavior of granular soils is by describing of thier overall stress-strain relationship in terms of the force displacement relationship at a contact between two particles. This approach is being increasingly used to study the mechanical behavior of granular packings (2,3,8,16).

In this work the focus is on the study of initial tangent moduli of sands under low amplitude loading conditions. Sand is modelled as made of spherical particles carrying the applied load through the contacts. Considering this simple model of natural sands, the contact forces in a given volume of this material are related to the stress tensor of the volume and the contact displacements are related to the strain tensor. Assuming the contact force-displacement relationship for two elastic spherical particles in contact to be given by the Hertz-Mindlin theory of frictional contacts (11), the stress and the strain for the given volume can be related. Based on this, the initial tangent moduli can be computed for a given loading condition. This stress-strain relationship can account for the packing structure of a granular assembly in terms of the void ratio, the coordination number and the spatial distribution of the vector joining the centroids of two particles. The calculated initial shear modulus are compared with that measured in resonant column and triaxial devices.

## CONTACT FORCE-DISPLACEMENT LAW

Two deformable non-conforming bodies in contact can be conceptually treated as two rigid bodies connected by deformable springs (6). The relative movement of two elastic bodies resulting from the contact forces is accounted by the spring deformations. In this work, the stretch of the springs are termed as contact displacements and the forces in the springs as contact forces.

### Local constitutive law

A general form of the local constitutive law relating the incremental contact force  $\dot{f}_i$  and the incremental contact displacement  $\delta_j$  is given by

$$\dot{f}_i = K_{ij}\delta_j \quad (i, j = x, y, z) \quad (1)$$

where  $K_{ij}$  is the stiffness tensor given by

$$K_{ij} = K_n n_i n_j + K_t (s_i s_j + t_i t_j) \quad (2)$$

where  $K_n$  and  $K_t$  are the normal and the tangential contact stiffnesses respectively. The unit vector  $n$  is normal to the contact surface and  $nst$  forms a local cartesian coordinate system as shown in Fig. 1. Expressed in terms of  $\gamma$  and  $\beta$ ,  $n$ ,  $s$  and  $t$  are given by

$$n = \sin \gamma \cos \beta i + \sin \gamma \sin \beta j + \cos \gamma k \quad (3)$$

$$s = \cos \gamma \cos \beta i + \cos \gamma \sin \beta j - \sin \gamma k \quad (4)$$

$$t = -\sin \beta i + \cos \beta j \quad (5)$$

### Normal contact stiffness $K_n$

Relative movement of two non-conforming deformable elastic bodies in contact resulting from normal force was classically studied by Hertz (9). Considering the contact area to be circular with a parabolic pressure distribution, the deformation at the contact is obtained from elasticity solutions of pressure load on semi-infinite media. Based on this, the relative approach of the two bodies are obtained in terms of the radius  $A$  of the contact area, the normal

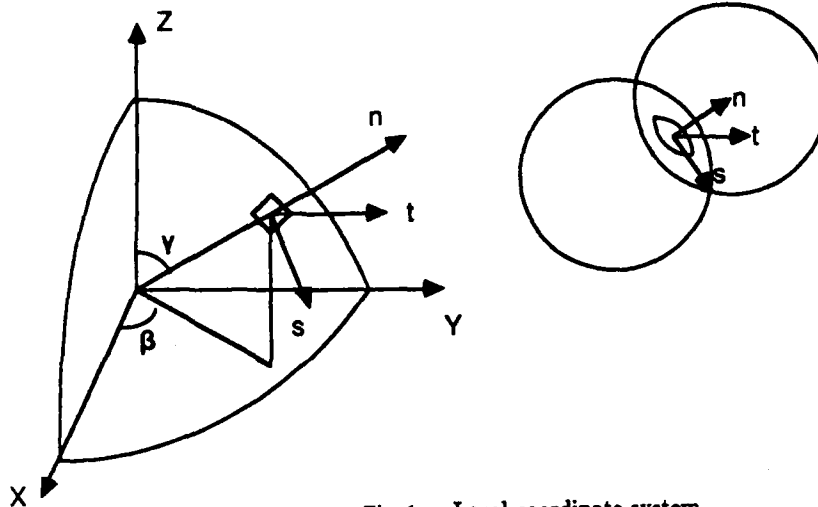


Fig. 1 Local coordinate system.

force  $f_n$  at the contact and the elastic properties of the spheres. This leads to the expression of the normal stiffness at the contact as (9)

$$K_n = \frac{2GA}{1-\nu} \quad (6)$$

where  $A = \left(\frac{3(1-\nu)f_n\rho}{8G}\right)^{1/3}$ ,  $G$  is the shear moduli,  $\nu$  is the Poisson's ratio,  $\rho$  is the radius of the spheres and  $f_n$  is the magnitude of the normal force at the contact. Eq. 6 is valid irrespective of the loading history at the contact.

In natural sands the particles are inelastic and non-linear, have rough contact surfaces and are not perfectly rounded. For these particles, the contact stiffness given by Eq. 6 may not be valid. A general expression for the normal stiffness for the contact of two dissimilar spherical non-linear inelastic rough particles may be written as a power law as

$$K_n = C_1 f_n^\alpha \quad (7)$$

where  $C_1$  is a function of the material and surface properties and the particle size,  $f_n$  is the normal force at the contact and  $\alpha$  is an exponent. In the Hertz theory,  $\alpha = \frac{1}{3}$  and  $C_1 = \left(\frac{3\rho G^2}{(1-\nu)^2}\right)^{1/3}$ .

For two mating bodies having rough surfaces, the contacts occur at the asperity. These asperities tend to undergo plastic deformation, resulting in yielding at the contact at a much lower value of contact pressure than that for the contact of smooth surfaces. The yielding also causes the pressure distribution at the contact to be more uniform rather than being parabolic (9). The pressure distribution in addition to non-linear inelastic material behavior result in exponent  $\alpha$  to be higher and constant  $C_1$  to be lower than that obtained from contact theory for smooth elastic bodies. Experimental data on sands (7) suggests that the exponent  $\alpha$  ranges from 1/3rd to 1/2.

### Tangential contact stiffness $K_t$ .

For a contact of two topographically smooth spheres, the tangential stiffness under oscillating contact force was studied by Mindlin and Deresiewicz (11). The tangential force at the contact causes deformation due the development of slip over a part of the contact surface. When the tangential force exceeds the frictional strength at the contact, sliding takes place. Considering the partial slip, Mindlin and Deresiewicz derived the relationship for the tangential stiffness at the contact under various loading condition. Based on their results, a general expression for the tangential stiffness of two dissimilar non-linear inelastic rough particles can be written as a function of the contact force and the particle properties as follows

$$K_t = C_2 K_n \left(1 - \frac{f_r}{f_n \tan \phi_\mu}\right)^\eta \quad (8)$$

where  $C_2$  and  $\eta$  are material constants,  $\phi_\mu$  is particle to particle friction angle and  $f_r$  is the resultant tangential force at the contact. For the case of topographically smooth spheres the value of  $C_2 = \frac{2(1-\nu)}{3}$  and  $\eta = \frac{1}{3}$ .

### STRESS-STRAIN RELATIONSHIP

Since, in a granular packing, the applied boundary loads are carried through the contacts, it is useful to define an average stress tensor for a given volume  $V$  in terms of the of the contact forces  $f_j$ . The stress tensor is defined as (4)

$$\sigma_{ij} = \frac{1}{2V} \sum_n \sum_m f_j^{nm} l_i^{nm} \quad (9)$$

where the subscripts follow the usual summation convention for the cartesian tensors and the superscripts refer to the  $m$ th contact of the  $n$ th particle. The branch vector  $l_i^{nm}$  is the vector joining the centroid of the  $n$ th particle to the

centroid of another particle which is in contact with the  $n$ th particle at the  $m$ th contact. It is noted that the factor 2 appears in the Eq. 9 as each contact is counted twice in the double summation process. Similar representation of stress tensor in granular media have been reported by Rothenburg and Selvadurai (13) and Kishino (10).

The skew symmetric part of the stress tensor represents the mean torque of the assembly contributed by the contact forces. In absence of any applied torque or couple stresses, the skew symmetric part is zero in order to satisfy Cauchy's law of balance of angular momentum (15).

The granular assembly is conceptually modelled as rigid particles connected to each other by deformable springs at the contacts with the spring constants given by the Hertz-Mindlin theory. Under loading, the particles move as a consequence of the deformation of springs (i.e., contact displacements). Defining an average strain tensor through the equivalence of work done in the assembly we get

$$dW = V \sigma_{ij} \Delta \epsilon_{ij} = \frac{1}{2} \sum_n \sum_m f_i^{nm} \delta_i^{nm} \quad (10)$$

The left hand side of the Eq. 10 represents the work done expressed in terms of the stress  $\sigma_{ij}$  and incremental strain tensor  $\Delta \epsilon_{ij}$ , while the right hand side is the equivalent work done expressed in terms of the contact forces  $f_i$  undergoing the contact displacement  $\delta_i$ . The factor 2 appears in the denominator because of double counting of each contact during the summation process.

Introducing Eq. 9 into Eq. 10 and equating the energy and the work done at each contact, it can be seen that the relationship between the incremental relative displacement  $\delta_i^{nm}$  and the incremental mean strain tensor  $\Delta \epsilon_{ij}$  is given as

$$\delta_i^{nm} = l_j^{nm} \Delta \epsilon_{ij} \quad (11)$$

Eq. 11 is a familiar result for a homogeneous strain field (1,16). It is noted that the effect of relative spinning of particles is neglected.

From Eqs. 1, 9, and 11 and multiplying by the branch vector  $r_j^{nm}$ , the relationship between incremental stress and the incremental strain is obtained as

$$\Delta \sigma_{ij} = C_{ijkl} \Delta \epsilon_{kl} \quad (12)$$

where

$$C_{ijkl} = \frac{1}{2V} \sum_n \sum_m l_j^{nm} K_{ik}^{nm} l_i^{nm} \quad (13)$$

and the incremental stress is defined as

$$\Delta \sigma_{ij} = \frac{1}{2V} \sum_n \sum_m f_i^{nm} l_j^{nm} \quad (14)$$

For a random packing with a large number of contacts, the branch vector distribution can be reasonably treated as continuous. For a packing made of equal sized particles, the branch vector distribution is same as the contact normal distribution. The spatial distribution of the branch

vectors can be defined as  $\xi(n)$  so that Eq. 13 can be rewritten as

$$C_{ijkl} = \frac{N}{2V} \int_{\Omega} l_j^{nm} K_{ik}^{nm} l_i^{nm} \xi(n) d\Omega \quad (15)$$

where  $\int_{\Omega} (\cdot) d\Omega = \int_0^{2\pi} \int_0^{\pi} (\cdot) \sin \gamma d\gamma d\beta$  with  $\gamma$  and  $\beta$  defined in Fig. 1 and  $N$  is the total number of contacts in volume  $V$ .

In Eq. 15, the total number of contacts  $N$  in a given volume  $V$  of a packing of spheres can be obtained from the void ratio, the coordination number and the particle size. For a granular assembly, the void ratio  $e$  is defined as the ratio of the volume of voids to the volume of solids and the coordination number  $\bar{n}$  is defined as the average number of contact points per particle. The ratio,  $\frac{N}{V}$ , can be expressed as follows

$$\frac{N}{V} = \frac{3\bar{n}}{4\pi\rho^3(1+e)} \quad (16)$$

where  $\rho$  is the particle radius. The relationship between the coordination number  $\bar{n}$  and the void ratio  $e$  has been discussed by (12, 17).

## MODULI FOR A PACKING

The initial tangent moduli is the moduli at the initial stress state. The initial moduli are investigated for two types of packings, namely, packings with isotropic material symmetry and anisotropic material symmetry.

### Isotropic packings

For a statistically isotropic packing, the distribution function  $\xi(\gamma, \beta)$  is independent of  $\gamma$  and  $\beta$  given by

$$\xi(\gamma, \beta) = \frac{1}{4\pi} \quad (17)$$

The contact force vector  $f$ , for isotropic packings under initial isotropic stress ( $\sigma_{ij} = P\delta_{ij}$ ), is the same for all contacts, given by

$$f_n = \frac{3VP}{\rho N}; f_s = f_t = 0 \quad (18)$$

Thus the contact stiffnesses (i.e., Eqs. 6 and 8) for all contacts can be expressed in terms of the applied confining pressure  $P$ . Integrating the general expression of the constitutive tensor (Eq. 15) after substituting the contact stiffnesses (Eqs. 6 and 8) and the distribution function (Eq. 17), the stiffness constants for an isotropic assembly of equal spheres can be obtained. The shear modulus  $G_p$  and the Poisson's ratio  $\nu_p$  for the packing are given as

$$G_p = \frac{1}{10} \left( \frac{\bar{n}}{12\pi(1+e)} \right)^{1-\alpha} \rho^{2\alpha-1} C_1 (2 + C_2) P^\alpha \quad (19)$$

$$\nu_p = \frac{1 - C_2}{4 + C_2} \quad (20)$$

It is noted that if  $C_2$  is zero (i.e.,  $K_r = 0$ ) then  $\nu_p = 0.25$ . Bathurst and Rothenburg (2) have also found a value of 0.25 for the Poisson's ratio of packings with only normal contact interactions. The value of constant  $C_2$  is in general less than 1. From Hertz-Mindlin theory the value of  $C_2$  for smooth elastic spheres ranges between 0.67 to 1. If the Hertz-Mindlin theory is used, the Eqs. 19 and 20 reduce to

$$G_p = \frac{1}{5} \left( \frac{\sqrt{3}}{\sqrt{2\pi(1-\nu)}} \right)^{\frac{1}{2}} \frac{5-4\nu}{2-\nu} \left( \frac{\bar{n}}{1+e} \right)^{\frac{1}{2}} G^{\frac{1}{2}} P^{\frac{1}{2}} \quad (21)$$

$$\nu_p = \frac{\nu}{2(5-3\nu)} \quad (22)$$

Fig. 2 shows the packing shear modulus versus the initial confining stress. The measured shear modulus from tests on Monterey #0 sand in resonant column device for various confining pressures (5) are shown by symbols in Fig. 2. Monterey #0 is a fairly uniform sand with mean particle diameter of 0.36 mm and the average void ratio of the test samples was 0.676. The measured shear modulus are under a shear strain amplitude  $\leq 10^{-3}\%$  and thus considered to be same as the initial shear modulus. The computed packing shear modulus  $G_p$  from Eq. 21 are plotted on Fig. 2 to compare with the measured data. The coordination number is assumed to be 7.9. The particle properties are as follows:  $G = 5 \times 10^5$  psi,  $\nu = 0.13$ , and  $\phi_\mu = 10^\circ$ . The value of  $G$  used here is about 10 times less than the elastic  $G$  of quartz. This is to account for the fact that the particles in real sand are rough, not perfectly rounded, inelastic and nonlinear and Eq. 21 is intended for perfectly smooth elastic particles. With this value of  $G$ , the predicted results agree reasonably well with the measured data. To show the effect of particle stiffness on the packing shear modulus,  $G_p$  for  $G = 3 \times 10^5$  psi and  $G = 7 \times 10^5$  psi is shown in Fig. 2.

It is noted that the Eq. 21 represents the shear modulus of a packing of perfectly smooth elastic spheres of equal size with isotropic material symmetry. Even though the model is rather idealized, the results obtained are encouraging.

### Anisotropic packings

The stress-strain relationship given by Eq. 15 can be also applied to packings with anisotropic material symmetry. In this section the initial shear moduli for anisotropic packings of equal sized perfectly smooth elastic spheres are discussed.

For anisotropic packing, the contact force varies from contact to contact. Therefore the closed form solutions become complex and numerical solutions are more tractable. In this section numerical results for statistically transverse isotropic packings are presented. The distribution function  $\xi(\gamma, \beta)$  for a transverse isotropic packing is given by

$$\xi(\gamma, \beta) = \frac{1}{4\pi} \left( 1 + \frac{1}{4} a_{20} (3 \cos 2\gamma + 1) \right) \quad (23)$$

Using this distribution function and Eqs. 6 and 8, Eq. 15 can be numerically integrated to obtain the relationship between the incremental strain and incremental stress.

For anisotropic packings, shear moduli are directional dependent. Test results of wave velocities in various directions in a sand samples by Stokoe et al. (14) are used to compare with the computed results. These tests were performed in a large cubical triaxial test apparatus and the test specimen is made of washed mortar sand, a fairly uniform sand with mean particle diameter of 0.46 mm. The measured wave velocities  $v_{mn}$  are used to compute the initial shear moduli  $G_{mn}$  based on the following relationship

$$v_{mn} = \sqrt{\frac{G_{mn}}{\Gamma}} \quad (24)$$

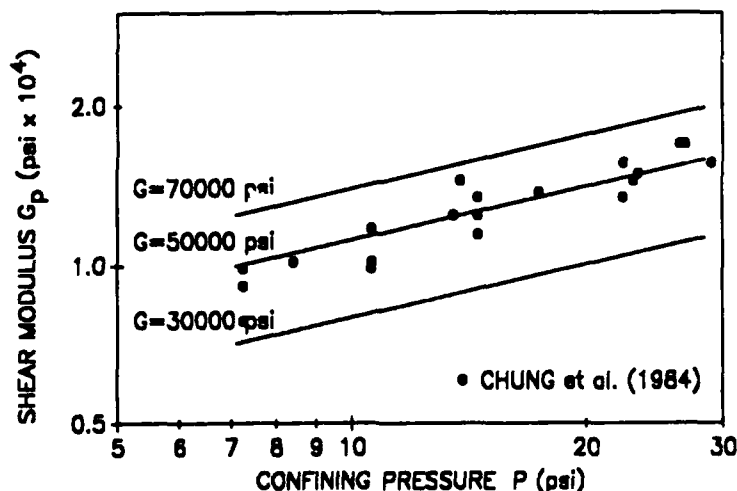


Fig. 2 Comparison of measured and computed results on the packing shear modulus  $G_p$  versus the initial confining stress.

where  $\Gamma$  is the sand density and subscript mn refers to the n direction on the m face, m and n being the cartesian coordinate axes. For example  $G_{mn}$  is shown in Fig. 3. For transverse isotropic packing,  $G_{xy} = G_{yx}$  and  $G_{xz} = G_{zx} = G_{yz} = G_{zy}$ .

The shear moduli obtained from the wave velocities are plotted in Fig. 4, as shown by symbols, against the confining stress for isotropic loading conditions. The measurements show that  $G_{xy} > G_{xz} \approx G_{yz}$ , implying that the test sample is transverse isotropic. This is expected be-

cause The test specimen were produced by air pluviation technique. For comparison, the computed shear moduli are plotted in Fig. 4, as shown by solid lines. The computations are made, assuming that the particle properties are as follows:  $G = 8.5 \times 10^5$  psi,  $\nu = 0.25$  and  $\phi_p = 20^\circ$ . The void ratio of the packing is  $e = 0.68$  and the coordination number is 7.9. The packing of the sand specimen is assumed to be transverse isotropic represented by Eq. 23 with  $a_{20} = -0.33$ . The theoretical computations predict the measured trends reasonably well.

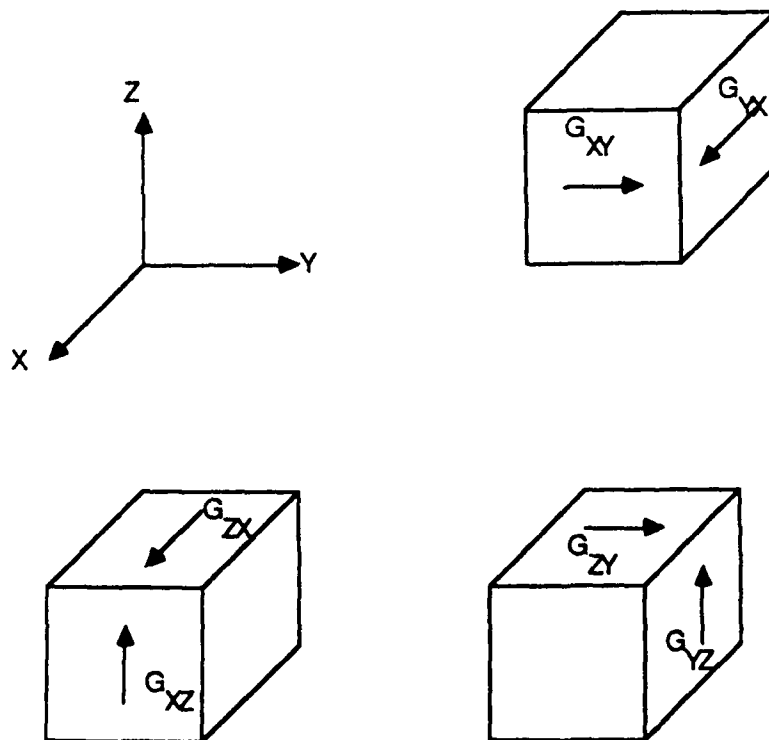


Fig. 3 Sign conventions for the six components of shear moduli for a transverse isotropic packing.

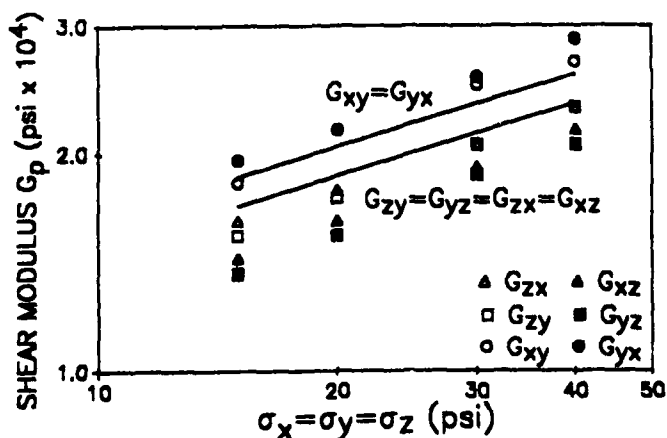


Fig. 4 Comparison of measured and computed results on the packing shear moduli versus the initial confining stress for transverse isotropic packings.

## CONCLUDING REMARKS

Results obtained from a stress-strain relationship considering particle interactions and packing structure are presented. The moduli of sands have been experimentally found to be affected significantly by the void ratio, coordination number, particle properties and the structural anisotropy. These factors are explicitly accounted as parameters in this mathematical model.

The computed initial tangent moduli are compared with measured results. It is encouraging that the theoretical results show same trend as the measured data even though the theory is intended for assemblies of idealized smooth elastic spheres. A good qualitative agreement with the measured data is obtained by selecting a lower value of particle stiffness  $G$  to account for the effect of asperities on the contact stiffness.

## ACKNOWLEDGEMENT

This paper is based on research supported by the Air Force of Scientific Research under Grant No. AFOSR-86-0151 to the University of Massachusetts, monitored by Maj. Steve Boyce

## REFERENCES

1. Batchelor, G.W. and O'Brien, R.W., Thermal or electrical conduction through a granular material, Proceedings of Royal Society London, A355, 1977, 313-333.
2. Bathurst, R.J. and Rothenburg, L., Micromechanical aspects of isotropic granular assemblies with linear contact interactions, Journal of Applied Mechanics, ASME, 1988, 17-23.
3. Chang, C.S., Micromechanical modelling of constitutive relations for granular material, Micromechanics of Granular Materials, Eds. M. Satake and J.T. Jenkins, Elsevier, Amsterdam, 1987, 271-278.
4. Christoffersen, J., Mehrabadi, M.M. and Nemat-Nasser, S., A micromechanical description of granular material behavior, Journal of Applied Mechanics, ASME, 1981, 339-344.
5. Chung, R.M., Yokel, F.Y. and Drnevich, V.P., Evaluation of dynamic properties of sands by resonant column testing, Geotechnical Testing Journal, ASTM, 1984, 60-69.
6. Cundall, P.A. and Strack, O.D.L., A discrete numerical model for granular assemblies, Geotechnique, 1979, 29, 47-65.
7. Hardin, B.O. and Drnevich, V.P., Shear modulus and damping in soils: measurements and parameter effects, Journal of Soil Mechanics and Foundations Engineering, ASCE, 1972, Vol. 98, 603-624.
8. Jenkins, J.T., Volume change in small strain axisymmetric deformations of a granular material, Micromechanics of Granular Materials, Eds. M. Satake and J.T. Jenkins, Elsevier, Amsterdam, 1987, 245-252.
9. Johnson, K.L., Contact Mechanics, Cambridge University Press, London, 1985.
10. Kishino, Y., Statistical consideration on deformation characteristics of granular materials, Proceedings, US-Japan Seminar on Continuum Mechanical and Statistical Approaches in the Mechanics of Granular Materials, Ed. S.C. Cowin and M. Satake, 1978, 114-122.
11. Mindlin, R.D. and Deresiewicz, H., Elastic spheres in contact under varying oblique forces, Journal of Applied Mechanics, ASME, 1953, 327-344.
12. Oda, M., Co-ordination number and its relation to shear strength of granular material, Soils and Found., 1977, Vol. 17, No.2, 29-42.
13. Rothenburg, L. and Selvadurai, A.P.S., Micromechanical definition of the Cauchy stress tensor for particulate media, Mechanics of Structured Media, Ed. A.P.S. Selvadurai, Elsevier, 469-486.
14. Stokoe, K.H., Lee, S.H.H. and Knox, D.P., Shear moduli measurements under true triaxial stresses, Advances in the Art of Testing Soils Under Cyclic Conditions, Ed. V. Khosla, 1985, 166-185.
15. Truesdell, C. and Toupin, R.A., The classical field theories, Handbuch der Physik, Ed. S. Flugge, Vol. III/1, Springer Verlag, Berlin.
16. Walton, K., The effective elastic moduli of a random packing of spheres, Journal of Mechanics and Physics of Solids, 1987, Vol. 35, 213-226.
17. Yanagisawa, E., Influence of void ratio and stress condition on the dynamic shear modulus of granular media, Adv. in the Mechanics and the Flow of Granular Materials, 1983, 947-960.

# A GENERAL STRESS-STRAIN MODEL FOR GRANULAR SOILS

Kingsley Harrop-Williams

The BDM Corp., McLean, VA 22102

## ABSTRACT

A general stress-strain model is derived for granular soils based on the premise that the deformation in these soils is not caused so much by the deformation of individual particles as by the relative movements of the more mobile particles. The model is general and specific relationships are obtained for different loading conditions. For one dimensional and isotropic loading conditions a stress-strain curve concave towards the stress axis is derived, and for triaxial and shear loading conditions the derived stress-strain curve is concave towards the strain axis. In particular soils that show a distinct peak stress are well modeled, and the model reduces to the hyperbolic model for soils exhibiting no distinct peak stress. All cases show excellent fit to experimental data.

## INTRODUCTION

The stress-strain behavior of granular soils is created primarily by individual particle movements to form a denser matrix rather than elastic compression of the particles. As a result the experimental curve is always nonlinear. In general it is concave towards the strain axis under triaxial and shear loading, and concave towards the stress axis in one dimensional and isotropic loading conditions. To adequately predict the settlement under a load one needs to be able to model this nonlinear behavior.

Of primary importance in settlement calculations is the need to model the triaxial compression condition. One simple empirical method proposed by Konder and Zelasko (4) is the widely used hyperbolic model. This model appears to be a natural fit for soils that do not exhibit a distinct peak stress. Another empirical model proposed is a modification of the Ramberg-Osgood model used for dynamic loading for static conditions (2). This is based on fitting a curve to the initial tangent modulus, the modulus of the plastic zone, the yield stress and a

parameter defining the order of the curve. For order one this curve becomes a hyperbola. One other approach suggested is to treat the tangent shear modulus and tangent bulk modulus as variables (5). These are usually taken as linear functions of the octahedral normal and shear stresses.

The difficulty in modelling the nonlinear stress-strain behavior of sand under load has led many investigators to propose numerical curve fitting techniques. One of the most popular of these is the piecewise linear method. Here the nonlinear experimental curve is divided into pieces of linear elastic sections for numerical analysis. Very often these are the incremental Hooke's law or the hypoelastic law (2). Another numerical method is the use of spline functions to fit experimentally observed curves. These are functions that uses the data to provide an analytic curve similar to the graphical process of using a French curve (1). These also require intense numerical procedures, and the data must be presented in a smooth form and not scattered as observed experimentally.

In this paper a general stress-strain model is derived from basic principles. This model is shown to apply to one dimensional, isotropic, triaxial, and shear loading conditions as special cases based on the boundary conditions they impose.

## STRESS AND STRAIN IN GRANULAR SOILS

In the determination of stresses and strains in granular soils any representative element of the soil with volume  $dx dy dz$  must be composed of particles and voids. The element must also consist of enough particles such that the relative movements of the particles as a result of forces on these particles produce strains. This means that in the limit the volume  $dx dy dz$  cannot be made to approach zero but must instead approach some minimal finite volume  $ijh$ . This minimal volume of fixed dimensions  $i$ ,  $j$  and  $h$  in the  $x$ ,  $y$  and  $z$  directions, respectively, is the smallest volume of



granular soil that can be used to define stress and strain. In effect, this volume is analogous to a point in continuous material. The latter having a fixed volume of zero magnitude on a macroscopic scale but at a microscopic level is composed of discrete atoms that enter and leave the point.

Since particles are allowed to enter and leave the minimal element, if  $w$  is the average relative displacement of a particle in the element in the  $z$  direction, then the normal strain in the element in the  $z$  direction is

$$\epsilon_z = w/h \quad (1)$$

For simplicity we introduce a microscopic stiffness coefficient  $k_z$  to represent the average resistance of a particle to movement in the  $z$  direction such that the force on a particle in the minimal element in the  $z$  direction is  $k_z w$ . The magnitude of  $k_z$  depends on the roughness of the particles and the confining pressure. The force in the element in the  $z$  direction is  $F_z = N k_z w$ , where  $N$  is the number of particles in the element. The normal stress in the element in the  $z$  direction is then  $F_z/(ij)$

$$\sigma_z = N k_z w/(ij) \quad (2)$$

In this equation  $N = ijh/[V_p(1+e)]$ , where  $V_p$  is the average volume of a particle and  $e$  is the void ratio. By definition the volumetric strain is related to the void ratio as  $\epsilon_v = (e_0 - e)/(1+e_0)$ , where  $e_0$  is the initial void ratio. Therefore,

$$N = ijh/[V_p(1+e_0)(1-\epsilon_v)] \quad (3)$$

The substitution of equations (1) and (3) into equation (2) and taking the  $z$  direction as the axial direction give the general relationship of axial stress to axial strain as

$$\sigma_a = E_0 \epsilon_a / ((1 - \beta \epsilon_v)) \quad (4)$$

where

$$E_0 = h^2 k_z / [V_p(1+e_0)] \quad (5)$$

and the parameter  $\beta$  was added since the condition  $\epsilon_v = 1$  is unattainable under conventional loads. From equation (4), the derivative of  $\sigma_a$  with respect to  $\epsilon_a$  at  $\epsilon_v = \epsilon_a = 0$  is  $E_0$ . Therefore,  $E_0$  is the initial tangent modulus of the soil.

To look at shear stresses in granular soils consider two minimal elements of soil adjacent to each other but separated by a surface  $dxdy$  in the  $xy$  plane. Let element 1 be at location  $z$  with average particle displacement  $u$  in the  $x$  direction, and element 2 be at location  $z+dz$  with average relative particle displacement  $u+(\partial u/\partial z)dz$  in the  $x$

direction. Also let  $k_x$  represent the average resistance of a particle to movement in the  $x$  direction. Therefore, the force in the  $x$  direction in the lower half of element 1 is  $F_{x1} = N_1 k_x u$ , and the force in the  $x$  direction in the upper half of element 2 is  $F_{x2} = N_2 k_x [u+(\partial u/\partial z)dz]$ . Here  $N_1$  is the number of particles in the lower half of element 1 and  $N_2$  is the number of particles in the upper half of element 2. We assume that  $N$  does not change much with  $z$  as compared with changes in  $u$ , therefore,  $N_1 = N_2 = N/2$ . The shear stress in the  $x$  direction at the interface between the two elements is  $(F_{x1} - F_{x2})/(dxdy)$ , or since  $dxdydz$  approaches  $ijh$  in the limit the shear stress is

$$\tau = [N k_x h / (2ij)] (\partial u / \partial z) \quad (6)$$

#### ONE DIMENSIONAL AND ISOTROPIC COMPRESSION

In one dimensional compression of soils  $\epsilon_v = \epsilon_a$ , and in isotropic compression we have  $\epsilon_v = 3\epsilon_a$ . From equation (4) these two conditions can be represented by the single equation

$$\sigma_a = E_0 \epsilon_a / (1 - \eta \epsilon_a) \quad (7)$$

where  $\eta$  is the reciprocal of the asymptotic strain observed at large stress. Figure (1) shows the excellent fit of equation (7) to data for isotropic loading conditions on two samples of McCormick Ranch sand obtained from reference (2, pg. 193).

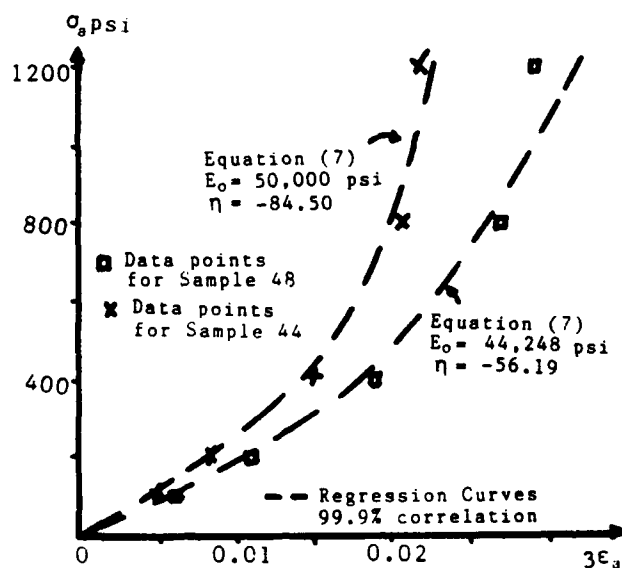


Fig. 1. Stress-Strain in Isotropic Loading  
(1 psi = 6.895 KPa)

One should also note that equation (7) can be written as  $\sigma_a = E_0 (\epsilon_a + \eta \epsilon_a^2 + \dots)$  and by series expansion we have that  $[\exp(2\eta \epsilon_a) - 1] / (2\eta) = \epsilon_a + \eta \epsilon_a^2 + \dots$

Therefore, letting  $\alpha = 2\eta$  and  $A = E_0/\alpha$ , gives the alternate expression

$$\sigma_a = A \exp(\alpha \epsilon_a) - A \quad (8)$$

Equation (8) is the same as that derived by the hypoelastic analysis for these loading conditions (2, pg 139).

### TRIAXIAL COMPRESSION

In triaxial compression of elastic material the radial strain,  $\epsilon_r$ , is proportional to the axial strain, and the proportional constant is the empirical Poisson's ratio. In effect, if  $v_t = -d\epsilon_r/d\epsilon_a$  and  $v_s = -\epsilon_r/\epsilon_a$ , then in elastic material  $v_t = v_s$ . However, in triaxial compression of sands the relationship of radial strain to axial strain is nonlinear (2). To represent this nonlinear condition one can let  $v_s - v_t = D$ , where  $D$  is an empirical constant representing the average difference between  $v_s$  and  $v_t$ . If  $D = 0$  the relationship is linear, and the nonlinearity increases with the magnitude of  $D$ . The definition  $v_s = -\epsilon_r/\epsilon_a$  gives  $dv_s/d\epsilon_a = (\epsilon_r + \epsilon_a v_t)/\epsilon_a^2 = -D/\epsilon_a$ , also since the volumetric strain  $\epsilon_v = \epsilon_a + 2\epsilon_r$  we have  $v_s = (\epsilon_a - \epsilon_v)/(2\epsilon_a)$ , which shows that  $dv_s/d\epsilon_a = -0.5d(\epsilon_v/\epsilon_a)/d\epsilon_a$ . Equating the expressions for  $dv_s/d\epsilon_a$  gives the expression  $d(\epsilon_v/\epsilon_a)/d\epsilon_a = 2D/\epsilon_a$ , which has solution

$$\epsilon_v = B\epsilon_a + 2D\epsilon_a \ln \epsilon_a \quad (9)$$

where  $B$  is an integration constant. It should be noted that  $\ln \epsilon_a$  approaches zero as  $\epsilon_a$  approaches zero.

The relationship of volumetric strain to axial strain under triaxial compression for a medium dense sand at two different confining pressures as obtained from reference (2, pg. 177) is shown in Figure (2a). The regression of equation (9) on the data in this figure is shown as the dashed lines. An excellent fit is observed for each case.

The substitution of equation (9) into equation (4) yields

$$\sigma_a = E_0 \epsilon_a / (1 - 8B\epsilon_a - 28D\epsilon_a \ln \epsilon_a) \quad (10)$$

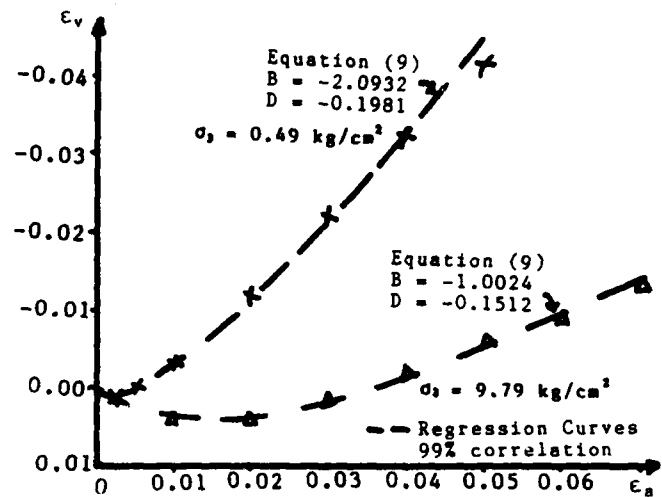
Letting  $\sigma_a = \sigma_p$  and  $\epsilon_a = \epsilon_p$  at maximum stress, we get  $8B = 1/\epsilon_p - E_0/\sigma_p - 28D \ln \epsilon_p$ . Also, setting  $d\sigma_a/d\epsilon_a = 0$  at maximum stress gives  $28D = -1/\epsilon_p$ . The substitution of these into equation (10) gives the relationship

$$\sigma_a = \epsilon_a / [af(\epsilon_a) + b\epsilon_a] \quad (11)$$

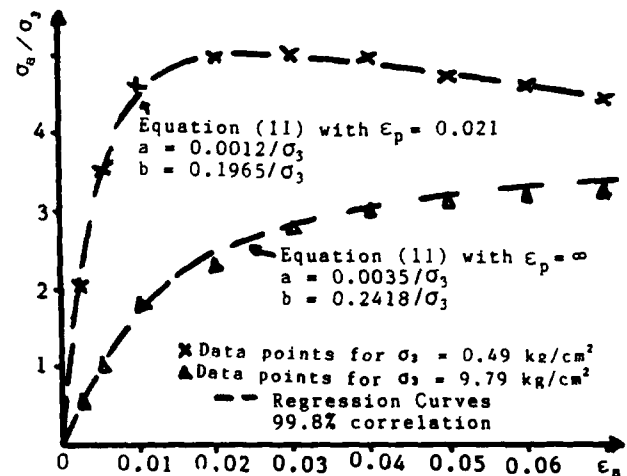
where  $a = 1/E_0$ ,  $b = 1/\sigma_p$ , and

$$f(\epsilon_a) = 1 + (\epsilon_a/\epsilon_p)[\ln(\epsilon_a/\epsilon_p) - 1] \quad (12)$$

In soils with no distinct peak stress such as loose sands and sands under high



(a) Volumetric Versus Axial Strain



(b) Axial Stress-Strain Behavior

Fig. 2. Triaxial Compression

pressure  $\epsilon_p$  approaches infinity. In this case equation (12) gives  $f(\epsilon_a) = 1$ , and equation (11) reduces to the hyperbolic model

$$\sigma_a = \epsilon_a / (a + b\epsilon_a) \quad (13)$$

The excellent fit of equation (11) to the stress-strain responses of a medium dense sand at two different confining pressures is shown in Figure (2b).

### SHEAR LOADING

The shear strain in the element of soil during shear loading is  $\gamma = \partial u / \partial z$ . Therefore, the substitution of equation (3) into equation (6) gives

$$\tau = G_0 \gamma / (1 - \beta \epsilon_v) \quad (14)$$

where

$$G_0 = h^2 k_x / [2V_p (1 + e_0)] \quad (15)$$

and the parameter  $\beta$  was added since the condition  $\epsilon_v = 1$  is unattainable under conventional loads. Evaluating  $d\tau/dY$  at  $Y = \epsilon_v = 0$  shows that  $G_0$  is the initial tangent shear modulus.

In elastic material under shear loading the volumetric strain is proportional to the shear strain. This means that in elastic material  $d\epsilon_v/dY = \epsilon_v/Y$ . In granular soils, however, this linear relation does not hold (6). To represent the nonlinear relationship between  $\epsilon_v$  and  $Y$  we let  $d\epsilon_v/dY - \epsilon_v/Y = C$ , where  $C$  is an empirical constant representing the average difference between the values  $d\epsilon_v/dY$  and  $\epsilon_v/Y$ . This expression says that  $\epsilon_v = Y[(d\epsilon_v/dY) - C]$ . Differentiating both sides of this with respect to  $Y$  gives  $d^2\epsilon_v/dY^2 = C/Y$ , which has solution

$$\epsilon_v = B_2 Y + CY \ln Y \quad (16)$$

where  $B_2$  is an integration constant.

Substituting equation (16) into equation (14) and letting  $\tau = \tau_p$  and  $Y = Y_p$  at peak stress gives the first constant as  $\beta B_2 = 1/Y_p - G_0/\tau_p - \beta C \ln Y_p$ . Further, setting  $d\tau/dY = 0$  at peak stress gives the constant  $\beta C = -1/Y_p$ . The substitution of these into equation (14) gives the expression

$$\tau = Y/[af(Y) + bY] \quad (17)$$

where  $a = 1/G_0$ ,  $b = 1/\tau_p$ , and

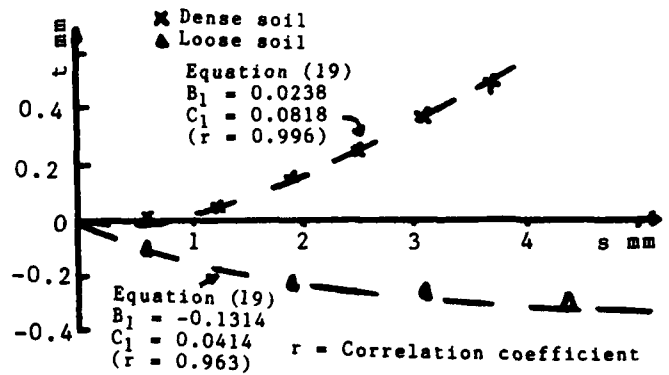
$$f(Y) = 1 + (Y/Y_p)[\ln(Y/Y_p) - 1] \quad (18)$$

For soils with no distinct peak stress we have the condition  $Y_p = \infty$  and equation (18) gives  $f(Y) = 1$ . In this case equation (17) reduces to the hyperbolic model.

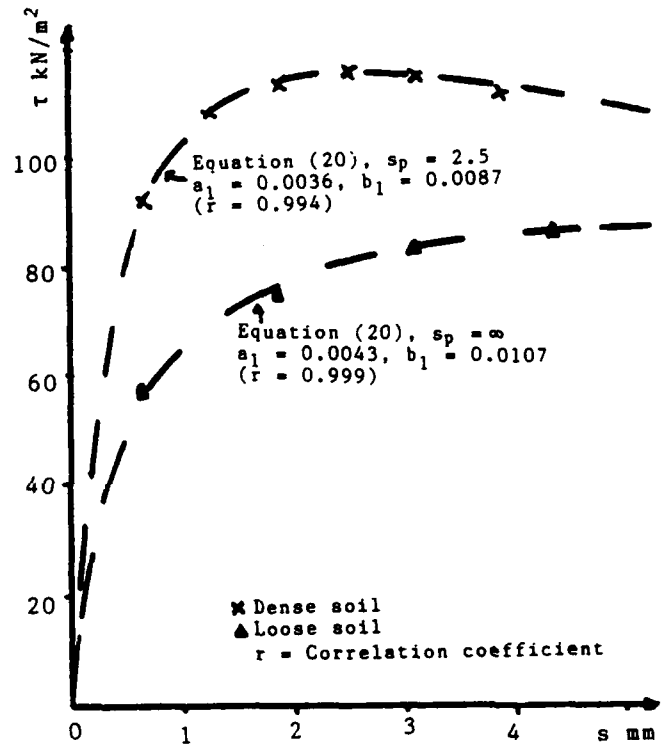
The direct shear experimental data for the change in sample thickness,  $t$ , with respect to shearing displacement,  $s$ , for a sand in a loose and a dense state as presented by Sutton (6, pg. 99), are shown in Figure (3a). The corresponding shear stress versus displacement data for this sand is shown in Figure (3b). The sand was tested under drained conditions and a constant normal stress of  $150 \text{ kN/m}^2$  was applied by the piston in both tests. In the direct shear test the change in sample thickness  $t$  is proportional to the volumetric strain  $\epsilon_v$  and the shearing displacement  $s$  is proportional to the shear strain  $Y$ . Therefore, the relationship of  $t$  to  $s$  is of the same form as equation (16). That is

$$t = B_1 s + C_1 s \ln s \quad (19)$$

where  $B_1$  and  $C_1$  are constants. Also, the relationship of  $\tau$  to  $s$  is of the same form



(a) Change in Sample thickness



(b) Shear Stress Versus Displacement

Fig. 3. Direct Shear loading

as equations (17) and (18), or

$$\tau = s/[a_1 f(s) + b_1 s] \quad (20)$$

and

$$f(s) = 1 + (s/s_p)[\ln(s/s_p) - 1] \quad (21)$$

where  $s_p$  is the displacement at peak stress, and  $a_1$  and  $b_1$  are constants.

The regression of equation (19) on the data of Figure (3a) are shown as the dashed lines of the figure. Also the regression of equation (20) on the data of Figure (3b) are shown as the dashed lines on that figure. In each case the fit is excellent.

## SUMMARY

Based on the assumption that the stress-strain behavior of granular media is controlled by the displacements of individual particles rather than particle compression a general stress-strain model for granular material is derived. This model says that for both axial and shear loading the stress is proportional to  $[\text{strain}/(1-\beta\epsilon_v)]$ , where the proportional constant is the initial modulus of the soil and  $\beta$  is a constant. For one dimensional and isotropic loading conditions the volumetric strain  $\epsilon_v$  is proportional to the axial strain. For triaxial and shear loading conditions nonlinear relationships of  $\epsilon_v$  to the axial strain and  $\epsilon_v$  to the shear strain are developed. It is shown that the model can be used for soils that show distinct peak stresses when under triaxial and shear loading, and that it reduces to the hyperbolic model for soils that shows no distinct peak stress.

## ACKNOWLEDGEMENT

This work was supported by the Air Force Office of Scientific Research, Contract No. F49620-88-C-0019, and is gratefully acknowledged.

## REFERENCES

1. Desai, C.S. (1971). "Nonlinear Analysis Using Spline Functions." J. Soil Mech. & Fdn. Div., ASCE, Vol. 97, No. SM10, pp 1461-1480.
2. Desai, C.S., and Siriwardane H.J. (1984). "Constitutive Laws for Engineering Materials, with Emphasis on Geologic Materials." Prentice-Hall, Englewood Cliffs, N.J., Figs. 8.5 & 8.20.
3. Desai, C.S. and Wu T.H. (1976). "A General Function for Stress-Strain Curves." Proc. 2nd. Int. Conf. on Num. Meth. in Geomech., C.S. Desai editor, Blacksburg, Va.
4. Konder, R.L and Zelasko J.S. (1963). "A Hyperbolic Stress-Strain Formulation for Sands." Proc. Pan-Am. Conf. on Soil Mech. & Fdn. Engrg., 1, Brazil, pp 289-324.
5. Nelson, I. and Barron M.L. (1971) "Application of Variable Moduli Models to Soil Behavior." Int. J. Of Solids Struct., Vol. 7, pp 399-417.
6. Sutton, B. H. C. (1986). "Solving Problems in Soil Mechanics." Longman Scientific & Technical Publishers, Essex, England.

## CONSTITUTIVE MODELLING OF CONCRETE

Dusan Krajcinovic

CEMM Department  
University of Illinois at Chicago  
Chicago, IL 60680, USA

### ABSTRACT

This report is a recapitulation of the highlights of the research performed in the first three years of the AFOSR sponsored research program investigating the micromechanics of concrete. Most of the results pertain to the time-independent processes of the concrete degradation attributed to the externally applied mechanical tractions. Some preliminary results of the chemically-induced deterioration are discussed as well.

### INTRODUCTION

With a present annual consumption estimated at 4.5 billion tons, concrete undoubtedly ranks at the very top of the list of most popular materials. In view of its application in runways and protective structures, concrete is frequently used by the military. The availability of the constituent materials, economy of production, simplicity of manufacturing procedures and a bevy of other desirable properties present a compelling reason for the continuing use of concrete.

As a commonly used material in a variety of different structures, concrete finds itself exposed to a combination of mechanical loads, thermal cycling and chemically aggressive environments. It is, thus, not surprising that concrete is frequently found in various stages of distress requiring costly repairs and ultimately even costlier replacement.

Even at rather modest stress levels the concrete exhibits a decidedly nonlinear dependence between loads and deformations, i.e., stresses and strains. The early, and futile, attempts to modify the venerable plasticity theory to formulate a constitutive model for concrete has since been largely abandoned. Subscribing to the dictum that the character of the nonlinear macrobehavior of a solid is but a reflection of the dominant mode of the irreversible changes of its microstructure spurred renewed interest in the composition of concrete and its influence on the deformation processes. Consequently, micromechanics is lately viewed as a rational framework for the development of the constitutive theories for concrete.

### STRUCTURE OF CONCRETE

Concrete is a complex particulate composite consisting of relatively hard aggregate embedded in a matrix of hardened cement paste (HCP). The HCP itself is a very complex compound in a chemical and morphological sense. Even though both of these aspects play a significant role in the determination of the strength of the inter-particle bonds (van der Waals forces), it is doubtful whether a direct use of the various xerogel models (Wittmann 1983) will ever lead to a practically usable theory. These truly micromechanical models are useful in providing an insight into the phenomena leading to the ultimate demise.

For present purposes, it suffices to consider the so-called mesoscale, i.e., viewing concrete as a composite consisting of hard inclusions (aggregate) embedded within a homogeneous matrix (HCP). The inclusions are, in general, irregular and unequal in size. The matrix also contains a substantial number of crack-like microdefects commonly, but not exclusively, found on the inclusion interface (transition zone). The transition zone, consisting of the plate-like ettringite crystals generously interspersed by voids, is the weak link (strength-limiting phase) of the composite (Kumar Mehta 1986).

It is probably safe to speculate that a majority of cracks are nucleated before the first mechanical loading as a result of thermal gradients (and unequal thermal elongations of constituent phases) and moisture transport (such as shrinkage or bleeding). The exposure to the mechanical and/or thermal stresses during the usage of the structure provides the energy needed to propagate these cracks, rupturing the bonds between the particles near the crack tips and creating new internal surfaces.

The chemically-induced degradation of concrete is a much more complex process. The energy for the damage evolution is provided by complex, and sometimes not well understood, chemical reactions with the substances commonly found in the environment. The analytical simulations of these processes is in its very infancy and

requires further information related to the chemical composition of the HCP and the morphology (size and distribution) of the pore network in the concrete.

Owing to the irregular structure of the concrete, it appears obvious that the required input data (distribution of inclusions, microdefects and pores in terms of their sizes, densities and connectivity) and the theory itself will by necessity have a statistical flavor. The requirements of simplicity and the ultimate objective of applicability in practice limits the considerations to the determination of the expected (average) values of the macrostress and macrostrain fields. The extension of the considerations needed to estimate the higher statistical momenta introduces formidable computational effort of little appeal for practical applications.

#### MICROMECHANICAL MODELLING

The term constitutive modelling refers to the establishment of the expressions relating the kinematic variables of a deformation process (which are commonly measurable) and their conjugate forces. Traditionally, this process was based on the purely macroscopic observations for a given set of tests leading to the so-called phenomenological models. The extension of these models to the 'similar' but non-tested materials and phenomena proved often to be a perilous exercise creating more problems than it was purportedly trying to solve.

Once it was concluded that the nonlinear response is but a macroscopic reflection of a specific micromechanism of the change in microstructure, it became obvious that a purely macroscopic observation will not suffice. A more promising approach, commonly classified as micromechanical, is to focus on the dominant micro mechanism (such as microcrack growth in the case of brittle response) and define patterns of its evolution as a function of the imparted energy and flux retarding energy barriers in its path. The micromechanical modelling inherently involves the determination of the representative volume element (RVE), containing a statistically valid sample of inhomogeneities and defects, which maps on a material point of the macro continuum. The mapping process is commonly referred to as homogenization.

In the case of concrete, a large fraction of the energy is dissipated on the propagation of microcracks. Thus in order to formulate a rational constitutive theory for concrete, it suffices to consider the conditions under which a microcrack will grow and determine the pattern of its growth. The strategy further involves the assumption that the external fields of a particular microcrack weakly depend on the exact position of the adjacent microdefects. The ensuing effective continuum model transforms the original problem of the determination of the stress and strain fields in the original material weakened by a large number of  $N$  cracks within RVE by a juxtaposition of  $N$  simpler problems of a single

crack embedded in an effective continuum (reflecting the presence of the adjacent cracks in a smoothed, or average, sense). This step enables the solution of the problem but at the same time inherently limits the considerations to the case of small to moderate microcrack densities.

This limitation is of little consequence in the case of unconfined specimens and in presence of tensile stresses since the macrofailure commonly occurs at low microcrack densities as a result of a runaway (unstable) propagation of a single crack of preferential geometry. However, in compression of a confined concrete specimen, the crack growth is stable and the ultimate failure (splitting) occurs as a result of the direct interaction of the adjacent (and closely spaced) cracks. Hence in order to predict the onset of failure, it is necessary to know the spacing between the cracks, or the higher statistical momenta of the microcrack distribution.

In summary, micromechanical modelling consist of several phases: analytical description of the dominant micromechanism, transition between the micro- and macroscale (homogenization), determination of the macro fields and prediction of the failure.

#### ESSENTIAL STRUCTURE OF THE THEORY

Applying the described strategy, the constitutive equations mapping the macrostresses on macrostrains in a RVE of a brittle solid can be written as

$$\underline{\epsilon} = (\underline{\mathcal{S}}^0 + \underline{\mathcal{S}}^*): \underline{\sigma} = \underline{\mathcal{S}}: \underline{\sigma} \quad (1)$$

where  $\underline{\mathcal{S}}^0$  is the compliance of the undamaged (virgin) solid while  $\underline{\mathcal{S}}^*(x)$  reflects the influence of all  $N$  microcracks within the RVE. The incremental version of (1) reads

$$d\underline{\epsilon} = \underline{\mathcal{S}}: d\underline{\sigma} + d\underline{\mathcal{S}}^*: \underline{\sigma} \quad (2)$$

The nonlinear component of the strain is, therefore, directly related to the change in the compliance (i.e., nucleation and growth of the microcracks within RVE).

Introducing the complementary (Gibbs) energy

$$\psi = \frac{1}{2} \underline{\sigma}: \underline{\mathcal{S}}: \underline{\sigma} \quad (3)$$

where the energy needed to extend the crack perimeter  $L$  in the direction of its normal by  $\delta a$  is (Rice 1975)

$$d\psi^* = \frac{1}{V} \sum_k \int_{L_k} [(G-2\gamma)\delta a] dL \geq 0 \quad (4)$$

with summation extending over all active cracks in RVE of volume  $V$ . From the second law of thermodynamics (Clausius-Duhem inequality), the change in the complementary energy must be non-negative. In (4)

$$G = \underline{K} : \underline{C} : \underline{K} \quad (5)$$

is the energy release rate (i.e., force driving the crack), while  $2\gamma$  is the surface energy (resisting force). In (5),  $\underline{K}$  is used to denote the stress intensity factors (SIF) arranged into a vector, while  $\underline{C}$  is a second rank tensor defining the properties of the effective medium (including the influence of the adjacent microcracks).

Using equations (3) to (5) it becomes possible, at least in principle, to write the change in compliance whenever the analytical expressions for the tensor  $\underline{C}$  and the SIF's are available. This, unfortunately, is not always the case and is, in fact, restricted to isotropic and transversely isotropic effective continua. Finally, in order to compute the change in the compliance, it is necessary to determine the relation between the change in the crack's size  $a$  (4) and the applied stresses. In order to determine this relation, it is necessary to know the conditions at which a microcrack becomes active as well as the pattern of its growth in function of the microstructure morphology.

In order for a crack to start propagating  $\delta a > 0$ , the energy must be dissipated. Thus from (4) the (Griffith's) condition which must be satisfied for a crack to grow is

$$(G - 2\gamma)_k \geq 0 \quad k = 1, 2, \dots, N \quad (6)$$

where  $G$  is a function of the crack geometry (radius and orientation) and stresses at the crack tip (depending on the externally imparted energy and the crack induced anisotropy). The surface energy (SE) is a random variable with a stepwise distribution dependent on the morphology of the composite at the crack tip. It is commonly accepted that the transition zone has the lowest SE. The HCP has approximately twice as large SE while the aggregates are commonly characterized by superior SE's. The crack will obviously propagate in the direction of lower SE unless this process implies substantial kinking. The hierarchy of toughnesses can be altered using the lightweight aggregate or various modifiers strengthening the transition zone.

Condition (6) represents a curved surface in the stress space enveloping all of stress states for which a particular crack will remain inactive. The inner envelope of  $N$  hypersurfaces (6) represents a surface separating all states which can be reached in a non-dissipative process from those which will involve further damage evolution. This surface obviously plays the role of the yield surface in plasticity.

The surface energy can be drastically reduced in a surface-reactive environment. It was shown (Rice 1978) that the critical SE is a function of the chemical potential and the Gibbs' excessive mass of the adsorbent per unit area. Since the adsorption is a process coupled with the slowly evolving diffusion, the inequality (6) becomes time-dependent forming a function akin to the creep potentials.

## TIME-INDEPENDENT DEFORMATION PROCESSES

The principal objective of the first phase of the AFOSR supported research program was the development of the micromechanical models for the uniaxial tension and compression below the transition point. Since the results of this research were published in the open literature, only a short precis seems to be appropriate for the purpose at hand.

### (a) Uniaxial Tension

In the case of uniaxial tension, a microcrack (attributable, for example, to bleeding) initially occupies a small part of the aggregate - HCP interface (transition zone). Initially the response is purely elastic. At some magnitude of the monotonically increasing external tensile traction, the inequality (6) is satisfied for a crack of preferential geometry (largest radius, surface normal to the tensile axis). At that point this crack increases its surface almost instantaneously until it gets trapped by the higher SE of the HCP at the edge of the aggregate facet. As the external tractions are further increased, more cracks become unstable. Finally, one of the trapped cracks becomes critical (despite the higher SE of the HCP) and starts propagating through the HCP towards the adjacent aggregate. For common volume fractions of the coarse aggregate, this crack cannot be arrested in most cases causing macrofailure.

The governing equations can for this case be derived in closed form (Krajcinovic and Fanella 1986) knowing the volume fraction and distribution of aggregates and initial defects. Despite the fact that the derived stress-strain law does not contain a single fitting parameter, the replication of the experimental data is more than just satisfactory (Fig. 1). The influence of the magnitude of the initial defects and the sieve grading (sizes of the coarse aggregate) are discussed in detail in the original publication.

### (b) Uniaxial Compression

In the case of compression, the analysis is much more delicate and difficult. The cracks first develop in the shear plane and subsequently kink in the direction of the compressive axis (Horii and Nemat-Nasser 1986). In the absence of the lateral tensile stresses, the crack growth is stable and the splitting failure is caused by linking of large cracks. Since the proposed model does not contain an internal variable defining the

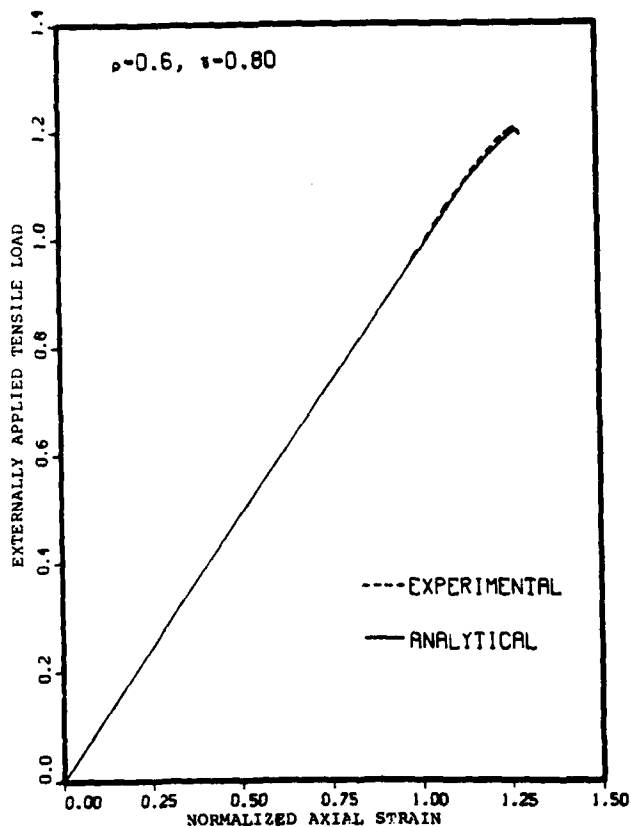


Fig. 1: Stress-strain curve for uniaxial tension.

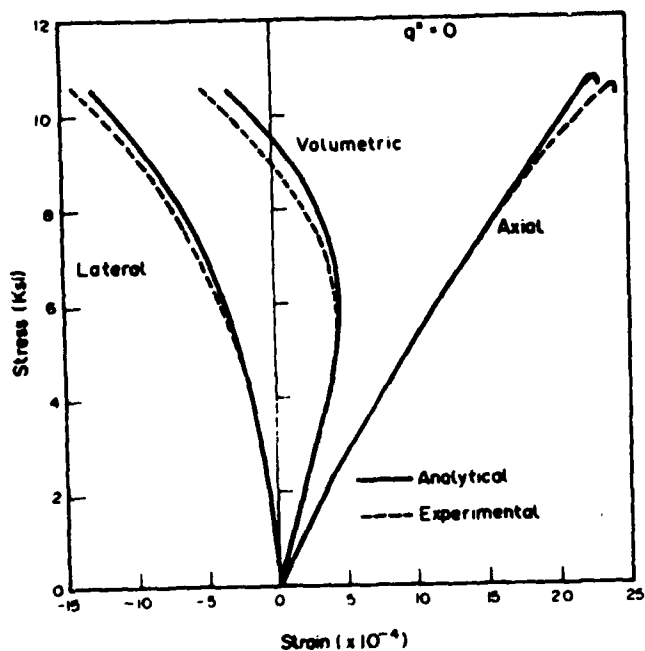


Fig. 2: Stress-strain curve for uniaxial compression.

distance between the cracks, the macrofailure criterion must be imposed extraneously as a function of the crack lengths.

Despite the simplifying assumptions introduced to preserve the simplicity of the model, its accuracy is still remarkable (Fig. 2) (Fanella and Krajcinovic 1988).

The accuracy of these simplified analyses were verified using the self-consistent model (Krajcinovic and Sumarac 1987, Sumarac and Krajcinovic 1987). In most cases when the rupture stress does not exceed the stress at the onset of cracking by a factor of more than three (as is the case in the considered examples), the simplified closed-form analyses prove to be more than sufficiently accurate. Figure 3 summarizes the behavior of concrete showing the loss of stiffness (i.e., the original elastic modulus) in tension and compression (for three different values of the friction coefficient  $\mu$ ) with the increase in damage. The vulnerability of concrete, measured by rapid decrease in stiffness, in tension is quite obvious from Fig. 3.

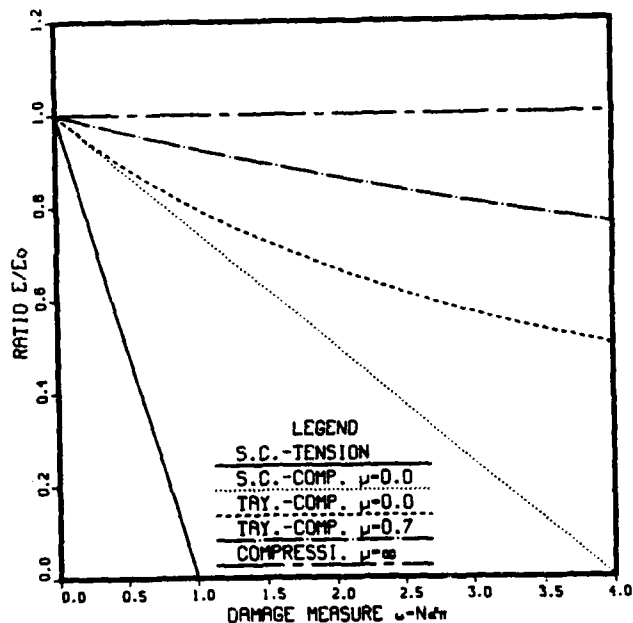


Fig. 3: Deterioration of elastic modulus with damage.

### (c) Phenomenological Modelling

Despite a long list of obvious advantages, pure micromechanical modelling is plagued by some definite limitations. The sheer size of the data-bank containing the necessary information related to the crack density and orientation in each material point (i.e., RVE) for the case of inhomogeneous stress fields will discourage the use of the micromechanical models in practical applications. The complexities associated with further extensions of the theory needed to model the larger crack densities at the incipient localization will almost assuredly render the numerical



computations quite formidable and, perhaps, forbidding as well. Finally, in analyses of various coupled damage-heat transfer-percolation-chemical degradation phenomena, the other governing equations (of diffusion type) are almost always of phenomenological nature.

Consequently, it seems imperative to use the results of the micromechanical models and formulate an appropriate continuum theory on the basis of these considerations. Initial attempts in constructing such a model indicate that in selecting the compliance as the internal variable and a function of the energy release rate as the conjugate thermodynamic force, it becomes possible to prove and derive the damage potential. The subsequent procedure is analogous to those of the conventional plasticity. The first results indicate that the salient trends of the deformation processes can be readily replicated despite a very modest number of readily identifiable material parameters. The stress-strain curves in Fig. 4, computed for the uniaxial compression, plotted for a varying material parameter (related to the aggregate size distribution), present a strong encouragement for the continuation of this effort.

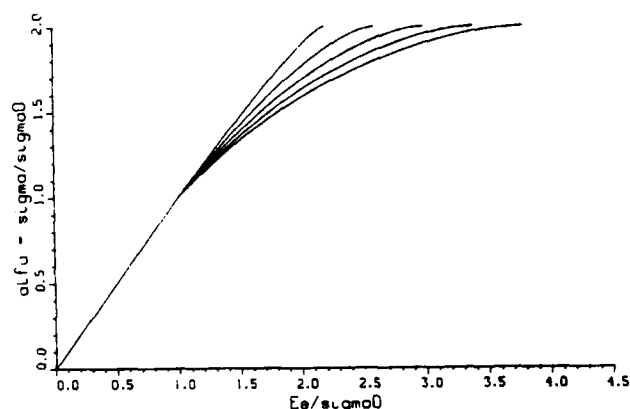


Fig. 4: Stress-strain curves (phenomenological model).

#### TIME-DEPENDENT PROCESSES

The second phase of the AFOSR supported research program is focused on the problem of chemical degradation of concrete in view of its application to the design of the runway rigid pavements. The chemical degradation of concrete is a very common and costly problem which occurs whenever the concrete is exposed to the water-borne aggressive substances commonly found in marshes, groundwaters, effluent waters, etc.

From a mechanical viewpoint, the attention focuses on the following problem. The existing microcracks in concrete are inactive under the given circumstances. The Griffith's criterion (6) can be satisfied only if either  $G$  increases or  $\gamma$  decreases. The former occurs in the case of expansive reaction products (sulphate attack) while the latter case is typical of reactions producing material with toughness inferior to those

of the original matter (cation-exchange reactions and alkali-aggregate reactions).

Consider, for example, the most comprehensively studied and most detrimental case of the HCP exposure to the water borne magnesium sulphate. Since the details of solid-liquid (topochemical) and through-solution chemical reactions are known from the literature (Hansen 1968, Kumar Mehta 1986, etc.), it suffices to discuss the consequences that they have on the stress and strain fields. The dispersion-adsorption of the wetting water bearing the sulphate ions is associated with a reaction during which the affected HCP transforms into gypsum and/or ettringite increasing in volume by almost 20 percent. The process is not only time-dependent but also inhomogeneous. The first aspect is related to the dispersion-adsorption of the fluid through the porous cement. The second aspect is related to the fact that the crystallization of the expansive products can occur only in larger capillaries (Hansen 1968).

Consequently, the wetted (affected) and previously rather homogeneous volume of the HCP transforms into an inhomogeneous material consisting of inhomogeneous (gypsum and/or ettringite) inclusions embedded in the HCP matrix. The inclusions are of inferior toughness and are subjected to large eigenstrains associated with the expansion of the volume during the chemical reaction. These eigenstrains, occurring only in the wetted part of the volume, may cause rather large stresses needed to ensure the compatibility of deformations with the rest of the volume and satisfy the conditions on the boundaries of the specimen.

From the analytical point of view, the chemical degradation of a structure such as a runway slab is a complex phenomenon coupling three distinctly different processes:

- diffusion-adsorption of the water-borne aggressive substance through the porous HCP,
- chemical reaction between the reactive substances, and
- evolution of microcracks in the slab.

These processes are obviously coupled. For example, the crystallization of the expansive product reduces the permeability sealing the largest pores. The volume expansion attributable to the same process causes cracking which, in turn, increases the diffusivity by decreasing the tortuosity of the fluid path.

As a result of the complexities of these processes and the morphologies of the pore network and initial crack-like defects, a pure micromechanical model seems to be somewhat beyond our present reach. However, a micromechanically inspired phenomenological model is not only possible but is expected to be of great utility not only as a precursor of more sophisticated excursions into theory but also as a simple but reliable predictive tool in itself.

Some preliminary results of a basically uncoupled model (assuming the permeability to be constant) for an infinitely extended slab exposed to the water-borne magnesium sulphates were obviously able to capture the salient aspects of the phenomenon. The compressive and tensile stresses in the slab are plotted vs. the time of exposure for various concentrations of the solute in Fig. 5. The compressive stresses in the layer bordering on the exposed (wetted) surface of the slab are largest initially. As the front of the permeating fluid advances through the slab, the compressive stresses steadily decrease while the tensile stresses (on the opposite side of the front) increase monotonically.

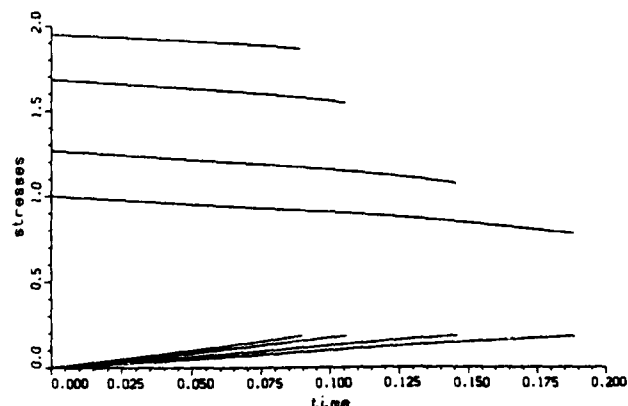


Fig. 5: Maximum compressive (top) and tensile stresses (bottom) for four different concentrations of sulfate.

Thus the failure can occur either as a result of continuous slabbing of the wetted surface (immediately after the contact with the solute has been established) or much later (in terms of months for HCP's of typical porosities) as a result of tensile stresses. The time to tensile failure is plotted as a function of the solute concentrations in Fig. 6. As expected, the solute concentration as the time-to-failure curve has two asymptotes. It will be, of course, of great practical interest to determine the concentrations of solute at which the failure will not occur. The other asymptote has no practical meaning since the failure will occur in compression.

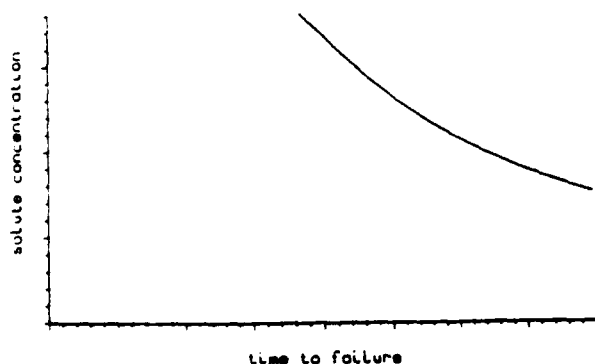


Fig. 6: Time to tensile rupture as a function of solvent concentration.

One of the significant problems encountered even in these preliminary computations is related to the veracity of the available experimental data. For the most part, the experiments consisted of throwing a cement, mortar or concrete block into a pool of sulphate water, leaving it there for a not always specified period of time, and measuring its volume (in not always documented manner) after a sufficient damage has been observed. Since the stresses in the block change as the imbibition front of the wetting fluid advances, it is difficult to ascertain what a global expansion means if it, actually, means anything at all. In the language of mechanics, the degradation process is strongly path dependent and a knowledge of a bulk variable at a single point is of limited utility.

In the case of high concentration of the solute, the failure of the wetted surface may occur early without saturation of the bulk of the block. The stress concentrations are much less emphasized by smaller concentrations and the failure will occur only after a significant part of the volume is permeated. Thus not only the time-to-failure but even the mode of the failure is a function of the solute concentration and the internal stresses (strongly depending on the shape of the specimen and the experiment itself). In other words, a precise calibration of the material parameters and verification of the analytical models will require an experimental program much more in tune with the theoretical developments. In order to be able to measure the influence of the expansion, the stress must be controlled during the experiments and the final volume fraction of ettringite and gypsum inclusions must be ascertained cutting the ruptured specimen.

#### APPLICATION TO RUNWAY PAVEMENTS

The ultimate objective of this research program is to investigate various aspects of the degradation of concrete exposed to mechanical, thermal and chemical influences common to the runway environments. Focusing on the micromechanics of the crack nucleation, growth and their ultimate coalescence into an integrity threatening macro-crack (localization) leads not only to the better insight into these processes but establishes building blocks for a general predictive analytical tool useful in the design of rigid pavements. The need for such a tool was strongly emphasized during the 1987 AFOSR/AFESC Pavement Materials and Systems Workshop which demonstrated that the state-of-art in the design of rigid pavements lags far behind their importance and cost. Based on the outdated empirical reasoning, erroneous perceptions of the underlying physical and chemical phenomena and physically unacceptable modifications of theories originally developed for metals, these design methods are clearly unable to predict the performance of the pavement structures.

The present program will proceed incrementally building gradually more sophisticated models of the concrete slab. The addition of thermal cycling (diurnal and seasonal), dynamic loads, influences of geometry (slab corners, joints,

etc.), reinforcement, etc., will eventually lead to a versatile design tool based on the actual physics and chemistry of the deformation process verifiable by well designed experiments. Such a design tool will allow for a rational selection of the optimum geometry of the structure and concrete mix.

## SUMMARY AND CONCLUSIONS

This report summarizes the work performed during the first three years of the AFOSR sponsored research program on the micromechanics of concrete. In addition to a cursory description of some of the accomplishments, the report also discusses some ongoing research, future directions of the research (as seen from the current vantage point) and needs for the experimental support of theoretical developments.

Most of the already developed models pertain to the time-independent phenomena related to damage evolution attributable to the statically applied external tractions. These results show that a very good accuracy can be achieved through micromechanical modelling without using additional 'fitting' parameters. Some preliminary results of the chemically-induced degradation show a definite ability to predict the salient trends of the phenomena encouraging further developments in the same direction.

Finally, this report is not intended as a comprehensive list of references. A full slate of the important works can be found in the referenced papers by the author.

## ACKNOWLEDGEMENT

The author gratefully acknowledges financial support in the form of the research grant from the Air Force Office of Scientific Research, Directorate of the Aerospace Sciences, Civil Engineering Program to the University of Illinois at Chicago which made this work possible.

## REFERENCES

- Fanella, D. and D. Krajcinovic (1988), A Micromechanical Model for Concrete in Compression, *Eng. Fracture Mech.*, 29, pp. 49-66.
- Hansen, W. C. (1968), The Chemistry of Sulphate-resisting Portland Cements, in 'Performance of Concrete', E. G. Swenson, ed., Univ. of Toronto Press, pp. 18-55.
- Horii, H. and S. Nemat-Nasser (1986), Brittle failure in Compression, *Phil. Trans. Royal Soc. London, A* 319, pp. 337-374.
- Krajcinovic, D. and D. Fanella (1986), A Micromechanical Damage Model for Concrete, *Eng. Fracture Mech.*, 25, pp. 585-596.
- Krajcinovic, D. and D. Sumarac (1987), Micromechanics of the Damage Processes, in 'Continuum Damage Mechanics: Theory and Applications,' D. Krajcinovic and J. Lemaitre, eds., Springer-Verlag, Wien, pp. 135-194.
- Kumar Mehta, P. (1986), *Concrete: Structure, Properties and Materials*, Prentice-Hall, Inc., Englewood Cliffs, NJ.

- Rice, J. R. (1975), Continuum Mechanics and Thermodynamics of Plasticity in Relation to Microscale Deformation Mechanisms, in 'Constitutive Equations in Plasticity,' A. S. Argon, ed., The MIT Press, Cambridge Mass., pp. 23-79.
- Rice, J. R. (1978), Thermodynamics of the Quasi-static Growth of Griffith Cracks, *J. Mech. Phys. Solids*, 26, pp. 61-78.
- Sumarac, D. and D. Krajcinovic (1987), A Self-consistent Model for Microcrack Weakened Solids, *Mech. of Mater.*, 6, pp. 39-52.
- Wittmann, F. H., ed. (1983), *Fracture Mechanics of Concrete*, Elsevier, Amsterdam.

EMPIRICAL STUDY ON THE EFFECTS OF SHOCK LOADS ON AIRCRAFT SHELTER EQUIPMENT COMPONENTS AND  
ASSOCIATED MOUNTING ELEMENTS

Oberstleutnant Hans-Georg Mett, Dipl.-Ing.

Federal Armed Forces Office for Studies and Exercises  
Special Infrastructure Tasks Division  
5060 Bergisch-Gladbach 1, FRG

ABSTRACT

Contact and nearby detonations of conventional weapons apply high-intensity, short-duration shock loads to structures, thus causing effects not only to the structure itself but also, to a considerable degree, to its interior equipment and associated mounting elements.

In support of the study on the effects of conventional weapons on Aircraft Shelter components, the shock response of typical in-shelter equipment and the associated mounting devices was tested.

The result achieved indicate that the customary mounting methods in most cases are inadequate to absorb the shock loading and that inadequately or wrongly mounted equipment represents considerable hazards to in-shelter personnel and materiel.

On the basis of the experimental arrangements and the results achieved, the critical points of the mounting devices used in shelters will be identified and recommendations for practical improvements will be provided.

Finally we will have a look at the forthcoming full scale tests.

1. INTRODUCTION

It has been pointed out repeatedly at several symposia that the problem of shock safety of in-shelter equipment has been inadequately considered, or to say the least, has not been investigated with appropriate consistency.//

It is encouraging to note, therefore, that greater importance is now being attached to the study of stationary and mobile in-shelter equipment, not least because of the fact that weapons effects analysts are approached again and again by representatives of the building trade and the users with specific and detailed questions that can often be answered inadequately only.

Meanwhile, a practical user of this basic information cannot overcome a feeling of uneasiness since it is known that it is extremely difficult to prove the shock tolerance of complex systems by analyses or technical tests due to the dependence on assumptions and models compliant with reality.

The shock tolerance or dynamic load capacity of individual components installed in shelters, however, are only partial aspects of the complex problem area.

Another important aspect is shock safety, which means a specific mechanic quality of the installed equipment as a whole.

A shock-resistant system includes connections, mountings, loads and operating conditions. Secure mounting and arrangement of components as well as isolation, if necessary, are chief aspects of shock safety which serves the protection of employed personnel and the shelter interior as a whole.

The mounting devices which are customary in the building trade are only inadequately tested and approved in terms of dynamic load capacity if they are tested at all; and they are not at all tested for the kind of dynamic load resulting from conventional weapons effects.

With alternatives lacking, the customary mounting devices are all the same predominantly used officially by the construction firms and, regrettably, also unofficially by way of subsequent installation on the part of the respective users.

The Federal Armed Office for Studies and Exercises, Special Infrastructure Tasks Division, has recently become more aware of these problems due to inquiries but also due to own observations made during shelter inspections.

However, the empiric values or engineering approaches available are insufficient to allow for reliable statements regarding individual cases. This is why this Division decided to investigate increasingly the problem area of shock-resistant mounting of in-shelter components, in addition to dealing with computational verifications and the long-term establishment of an empirically supported data bank.

Besides specific tests on a 3rd generation Aircraft Shelter (1:1 scale) it is suggested that any eligible test project should also include the testing of certain equipment components and associated mounting devices - or the mounting device itself only - under realistic conditions, even if the primary test objective serves another purpose.

The following part of this lecture deals with the first tests of this kind and is a presentation of the results so far achieved.

2. TEST PROGRAM

2.1 General

The investigation of structural body components of the 3rd generation Aircraft Shelter comprising

three individual tests offered the opportunity to include tests of the shock-resistant mounting of in-shelter components without noticeably interfering with the primary test program because these tests were carried out under realistic conditions. During the test program, cased charges of approximately 230 kg TNT were detonated against Aircraft Shelter side-wall components, thus representing nearby detonations.

## 2.2 TEST No. 1

### 2.2.1 Test Description (Fig. 1)

The structural test specimen consisted of a fixed reinforced-concrete wall (4m x 4m) with customary Aircraft Shelter reinforcement and wall thickness. A wearing wall was suspended, at the prescribed distance, in front of this wall.

The following equipment was mounted to the back of the main wall (Table 1):

- (1) A 500 Watt interior lamp mounted by means of 1 heavy-duty dowel SL-M 12 N and machine screw M 12.
  - (2) One commercial switch and junction box each, both mounted by means of plastic dowel S6 and wood screws.
  - (3) A power line within a plastic pipe as well as a galvanized steel pipe mounted by means of shaped supports and stirrup clamps.
  - (4) Two cantilevers mounted by means of heavy-duty dowels SL-M 10 N and machine screws M 10. A cable channel mounted to these cantilevers.
  - A 50 kg mass was placed on top of this cable channel.
  - (5) Three acceleration transducers were installed, evenly distributed across the height of the wall. All mounting devices mentioned above are generally used in the shelter. The heavy-duty dowels were force-controlled.
- (Table 2)

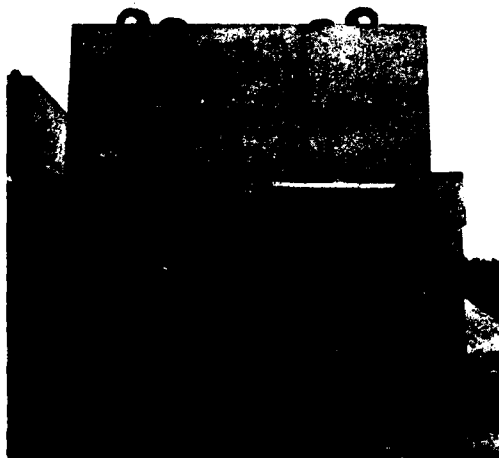


Fig. 1: Setup for TEST 1

## 2.2.2 Results (Table 3 and 4)

- (1) The wall was loaded with positive horizontal peak accelerations between 231 and 2248 g's. The effective duration times of the dominant positive acceleration histories were roughly within the range of 1 to 5 ms.
  - (2) The electrical installation remained fully operative. A plastic duct bed was broken in the lower part of the wall. The flexible power line remained intact.
  - (3) The cable channel was severely warped downward, but remained firmly mounted.
- The 50 kg mass was lying approximately 1.5 m behind the wall. Obviously it had hit the edge of the cable channel first thereby causing the deformation.

## 2.3 TEST No. 2

### 2.3.1 Test Description (Fig. 2)

The structural test specimen consisted of a fixed reinforced-concrete wall (6m x 6m). Supporting beams were concreted to both sides of the wall, for the purpose of simulating the integration of the structural test specimen into a larger structural body.

A shaped scabbing protection was attached to the back of the wall.

The following typical Aircraft Shelter equipment items were mounted to the back of the wall, at different heights:

(Table 1)

- (1) A dummy winch (1000 kg), mounted by means of 4 heavy-duty compound dowels, type UPAT-UKA M 16.
- (2) A fire-extinguisher, 12 kg, mounted by means of 2 heavy-duty dowels SL-M 10 N and machine screws M 10.
- (3) A twin neon light with plastic cover, mounted by means of 2 heavy-duty dowels SL-M 10 N and machine screws M 10.
- (4) A fuse box, approximately 15 kg, mounted by means of 4 heavy-duty dowels SL-M 8 N and machine screws M 8.
- (5) Acceleration transducers were mounted at fuse box, winch mass and fire-extinguisher levels.

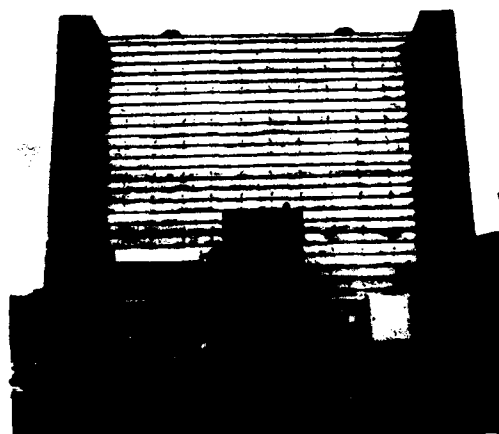


Fig. 2: Setup for TEST 2

### 2.3.2 Results (Table 3 and 4)

(1) The wall was loaded with positive horizontal peak accelerations between 5286 and 12800 g's. The effective duration times of the dominant positive acceleration histories were roughly within the range of 0.16 to 0.45 ms.

(2) The winch mass was torn out of its anchorage, struck the ground for the first time approximately 6 m behind the wall and came to rest at about 8 m.

(3) The fire-extinguisher with its dowels was torn off the wall and, after hitting other obstacles, came to rest, dented and leaking, approximately 10 m behind the wall.

(4) The switch cabinet cover was torn off and flung away. One of the cabinet mounting dowels was torn out of the concrete.

(5) The lamp mounting remained firmly mounted to the wall. The tubular fluorescent lamps and cover were torn out of the seating and destroyed.

### 2.4 TEST No. 3

#### 2.4.1 Test Description (Fig. 3.1 to 3.4)

The structural test specimen consisted of a fixed side-wall segment (6.1m x 5.5m) of the 3rd generation US Aircraft Shelter with specified reinforcement and wall thickness.

The rear scabbing protection consisted of corrugated bolted steel liners.

As in Test No. 2, supporting beams were concreted to both sides of the wall.

The following items of equipment were mounted to the back of the wall or placed on the foundation slab behind it. (Table 1):

(1) A storage rack with 4 dummy rockets amounting to a total mass of 340 kg. The rack was mounted to the wall and the floor by means of 6 heavy-duty dowels SL-M 10 N and machine screws M 10.

Two dummy rockets were tied down to the rack, two were placed on the rack without restraint.

(2) A tool carriage on wheels (1m high) and a tool shelf (2.2 m high) with tools placed on the rack. The tool locations were marked.

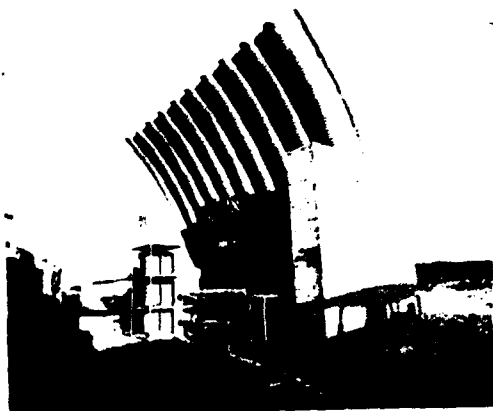


Fig. 3.1: Setup for TEST 3

(3) A dummy winch (1000 kg) mounted to the back of the wall by means of 4 through bolts (20 mm diameter) anchored to the front of the wall by means of steel washers. Four side-loaded rings were inserted into the horizontal channel beams between the back of the wall and the dummy winch and were supported at the back.

(4) A 30 kg steel slab was mounted by means of 4 bent metal straps (100 x 50 x 5 (mm)) and heavy-duty dowels SL-M 8 N.

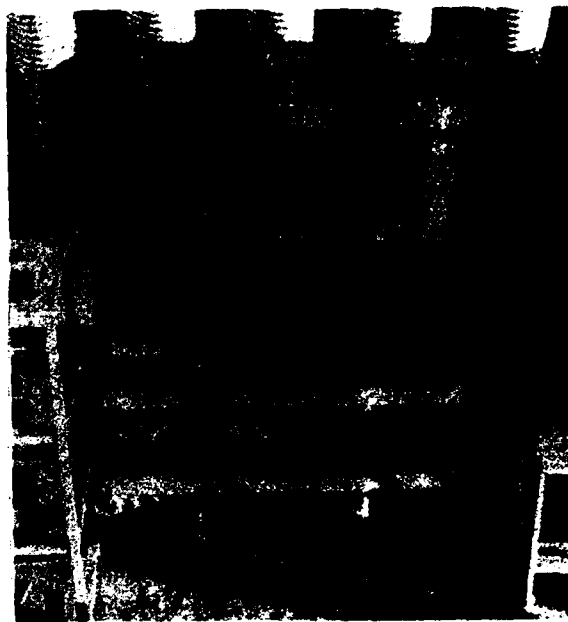


Fig. 3.2: Dummy Winch, Rocket Rack, Tool Shelves

#### 2.4.2 Results (Table 3 and 4)

(1) The wall was loaded with positive horizontal peak accelerations of approximately 2600 g's and the foundation slab with between 200 and approximately 400 g's.

The effective duration times of the dominant positive acceleration histories were roughly within the range of 0.38 to 2.76 ms.

(2) The two unrestrained dummy rockets were thrown off the rack. One of them was lying approximately 1 m in front of the rack. The tied down dummy rockets remained in their positions.

The upper cantilevered part of the rear rack supports were bent, one of the dowel mounts was pulled out, the other one was about to be pulled out. The rack base dowels remained firmly anchored.

(3) The tool shelves were only slightly displaced. The higher one had obviously been hit by one of the dummy rockets and in addition was displaced. The tool items, too, had only slightly moved. Some were lying beside the shelves, on the foundation slab.

(4) The dummy winch was hanging in the 4 mounting bolts which had yielded.

The lower side-loaded rings were compressed by approximately 3 cm, and the bearing points of the channel beam were deformed by approximately 1 cm. The winch mount was no longer safe for operation.

(5) The steel slab was torn off the wall, together with its 4 mounting dowels, and was lying approximately 1 m in front of its original position.



Fig. 3.3: Rocket Rack and Steel Slab after shot



Fig. 3.4: Dummy Winch after shot  
compressed Side-Loaded-Rings/Tubes

### 3. TEST EVALUATION

#### 3.1 Assessment of the Results

(1) The tests have confirmed the known very high, short-duration shock loads resulting from nearby detonations of conventional weapons.

On the basis of the present threat, peak accelerations of up to 15000 g's, with average accelerations between 2000 and 6000 g's are to be expected for exterior walls. Experimental values are given in Tables 3 and 4.

(2) Conventional mounting devices do not provide for shock-safety inside the shelter. As demonstrated by the examples of the dummy winch and the fire-extinguisher in Test No. 2. the integral over the first positive acceleration phase results in a phase final velocity of the wall of approximately  $v_0 = 10.6$  m/s and 12 m/s respectively. A ballistic back calculation on the basis of the known projection distances of the equipment confirmed that the final phase velocity of the wall corresponded to the initial velocity of the equipment.

In neither case a noteworthy restraining effect of the mounting devices could be ascertained. This is not surprising since the used mounts were loadable only with 6 g's in the case of the winch, and with 270 g's in the case of the fire-extinguisher.

The fuse box mounting was designed for approximately 1000 g's and was about to fail, as was demonstrated by the test. The far more elastic structure of the fuse box has probably provided for a greater effect of isolation than the stiff dummy winch or the fire-extinguisher.

(3) Equipment of a lower mass, such as power lines, switches, lamps or receptacles, can be fixed by means of the customary force-controlled mounts. It should be made sure that mounting points are too closely spaced, particularly near duct bends. Force-controlled dowels must not be inserted into narrow concrete ribs, as was done in Test No. 2.

(4) The simple design isolators (Fig. 4) proved to be very effective, both in the case of the winch and the steel slab.

Hazards to personnel and materiel as well as the destruction of the winch were prevented with a high degree of probability.

Regarding the steel slab, the peak acceleration values at the wall were reduced by the metal straps by approximately 25 %. If mounted directly to the wall, the slab would have been flung away at approximately 25 m/s.

Susceptible equipment, however, would not have remained operative in either case.

(5) The mounting points of the rocket rack showed considerable differences in the acceleration history values.

(Tables 3 to 4)

Although the wall and the foundation slab were one unit, the values on the foundation slab were approximately 70 to 90 % lower than those at the wall. This was largely due to the soil damping.

#### 3.2 Recommendations

The results of these first relatively moderate tests lead to the following practical recommendations:

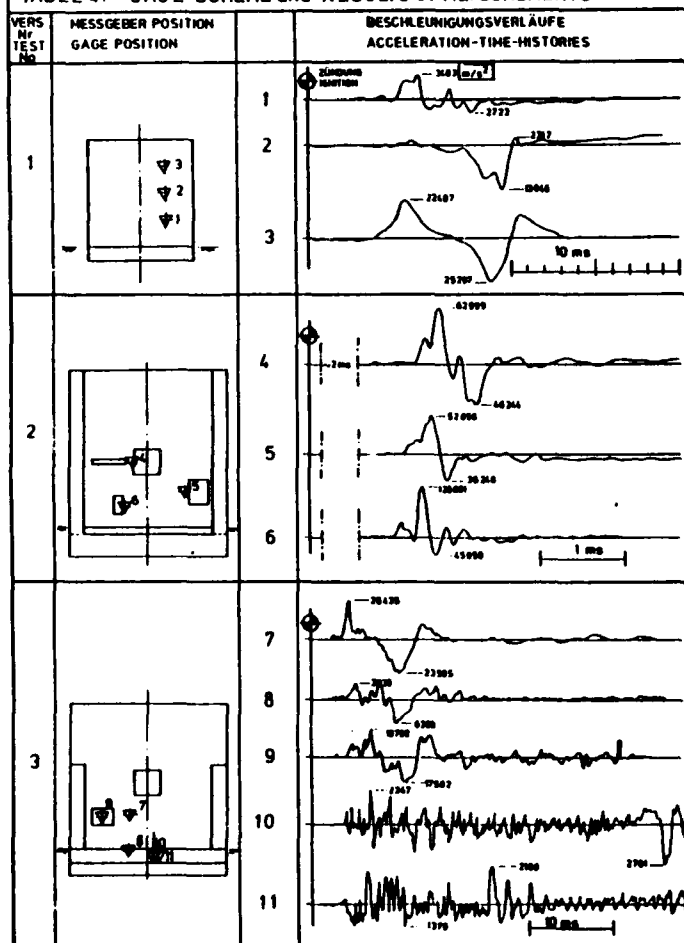
(1) Any shelter directly threatened by conventional weapons should be thoroughly checked for shock-resistant mounting techniques.





| TABLE 1 : INVESTIGATED A/C - SHELTER EQUIPMENT |                            |                                |                         |           |
|--|----------------------------|--------------------------------|-------------------------|-----------|
| TEST No  | GAGE LOCATION from TABLE 4 | EQUIPMENT                      | DIMENSIONS (mm)         | MASS (kg) |
| 1  | 3                          | (1) interior lamp 250/500E     | 310 x 210 x 140         | 2.1       |
|  | 1,2,3                      | (2) circuit line               | 3 x 1.5 mm <sup>2</sup> | -         |
|  | "                          | - steel tube Pg16              | -                       | -         |
|  | "                          | - plastic tube                 | -                       | -         |
|  | "                          | - shaped support 2063F         | 18 x 35                 | -         |
|  | "                          | - clamp 2057                   | -                       | -         |
|  | "                          | - circuit-breaker              | -                       | -         |
|  | "                          | - junction box                 | -                       | -         |
|  | 3                          | (3) 2 x pedestal KTA 400       | L = 400                 | 1.6       |
|  | 2                          | - cable support                | 1550 x 300              | ≈ 25      |
| 2  | 2                          | - concrete block               | 500 x 200 x 200         | 50        |
|  | 4                          | (1) winch (dummy)              | 1100 x 1000 x 500       | 1000      |
|  | 5                          | (2) fuse box                   | 800 x 800 x 300         | ≈ 15      |
|  | 6                          | (3) fire-extinguisher          | -                       | 12        |
| 3  | 4                          | (4) twin-neon-lamp 2 x 40 Watt | 1200 x 200              | ≈ 4       |
|  | 7                          | (1) winch (dummy)              | 1100 x 1000 x 500       | 1000      |
|  | 7,8                        | (2) rocket shelf               | ≈ 1000 x 1000 x 1000    | ≈ 45      |
|  | 10,11                      | - 4 x dummy rockets            | 2000 x d = 140          | 340       |
|  | 9                          | (3) steel plate                | 800 x 600 x 8           | 30        |
|  | 10,11                      | (4) tool carriage              | 1000 x 500 x 1000       | ≈ 30      |
|  | 10,11                      | (5) tool shelf                 | 2200 x 1000 x 800       | ≈ 60      |

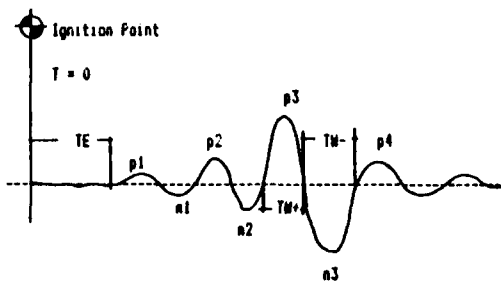
TAFEL 4: MESSGERATANORDNUNG und MESSERGEBNISSE  
TABLE 4: GAGE SCHEME and RESULTS of MEASUREMENTS



| TABLE 2 : EMPLOYED MOUNTINGS               |                   |                 |
|--|-------------------|-----------------|
| Model                                      | Tension Load (kN) | Shear Load (kN) |
| 1. FISCHER - HEAVY LOAD DOWEL, Model: SL-M |                   |                 |
| SL-M 8 N                                   | 16                | 16              |
| SL-M 10 N                                  | 20                | 20              |
| SL-M 12 N                                  | 24.5              | 42              |
| 2. FISCHER - DOWEL, Model: S               |                   |                 |
| S 6  | 3.2               |                 |
| S 8  | 4.5               |                 |
| S 10                                       | 9.3               |                 |
| 3. UPAT - COMPOUND-ANCHOR, Model : UKA-3   |                   |                 |
| UKA-3 M 16                                 | 15                | 15              |

| TABLE 3 : PEAK ACCELERATIONS and ASSIGNED DURATIONS |                     |         |                       |          |          |         |
|---|---------------------|---------|-----------------------|----------|----------|---------|
| TEST No   | GAGE No LOCATION    | TE (ms) | A (m/s <sup>2</sup> ) | TW+ (ms) | TW- (ms) | REMARKS |
|   |                     |         | +(pos) - (neg)        |          |          |         |
| 1   | REAR WALL           |         |                       |          |          |         |
|   | 1 - bottom          | 4.23    | 3483                  | 2722     | 1.48     | 0.93    |
|   | 2 - center          | 4.36    | 2317                  | 13846    | 0.80     | 2.96    |
| 2   | 3 - top             | 2.76    | 22487                 | 25297    | 5.25     | 3.06    |
|   | 4 WINCH (dummy)     | 2.93    | 62999                 | 46244    | 0.39     | 0.36    |
|   | 5 FUSE BOX          | 2.93    | 52856                 | 36248    | 0.45     | 0.23    |
| 3   | 6 FIRE-EXTINGUISHER | 2.79    | 128001                | 45950    | 0.16     | 0.14    |
|   | ROCKET RACK :       |         |                       |          |          |         |
|   | 7 - top/at wall     | 1.82    | 26435                 | 23595    | 2.76     | 4.42    |
|   | 8 - foot/rear       | 1.82    | 3838                  | 6369     | 1.79     | 2.63    |
|   | 10 - foot/front     | 3.57    | 2347                  | 2781     | 0.38     | 1.19    |
|   | 11                  | 3.57    | 2188                  | 1379     | 1.07     | 1.07    |
|   | 9 STEEL PLATE       | 1.82    | 19792                 | 17582    | 1.80     | 2.32    |
|   | 7 WINCH (dummy)     | 1.82    | 26435                 | 23595    | 2.76     | 4.42    |

Legend : A Values of Peak Accelerations  
TE Arrival Time  
TW+ Duration of the relevant positive Peak Acceleration  
TW- Duration of the relevant negative Peak Acceleration  
p.. Maximum positive values  
n.. Maximum negative values



## SMALL-SCALE MODEL TESTING FOR DYNAMICALLY LOADED BURIED STRUCTURES

Hung-Liang Chen,  
Research Associate

Surendra P. Shah and  
Professor

Leon M. Keer  
Professor

Department of Civil Engineering  
Northwestern University, Evanston, IL 60208

### ABSTRACT

An analytical and experimental investigation of the phenomenon of dynamic soil-structure interaction of buried structures was conducted. A shock impulse environment simulated by low velocity impact (free-drop impact system) was developed to generate a well characterized dynamic loading on the free surface. Small-model cylindrical buried structures, constructed of plexiglas and micro reinforced concrete, were then tested under this shock impulse system. Loading relief at the center of the roof of the buried structures was observed. Furthermore, the stiffer structure was observed to experience less soil arching. When a linear-elastic dynamic analysis by the finite element method was conducted, the numerical results were found to have good correlation with the experimental observation of the peak displacement on the buried roof. However, the behavior after the peak response can not be simulated using the current linear-elastic formulation.

### INTRODUCTION

Shallow-buried reinforced concrete (RC) structures can be employed for protective purposes. A series of explosive field tests, generally known as the FOAM HEST (FH) tests, were conducted by Kiger and Getchell in the early 1980's. In the FH tests, 1/4 size shallow-buried box-type RC structures of span-to-thickness ratios ( $L/t$ ) equal to 8.6 and depth-of-burial-to-span ratios ( $D/L$ ) ranging from 0.2-0.5 experienced damage or collapse in shear (FH2), flexure (FH3) and combined shear and flexure (FH4) modes. Data from FH tests indicate that soil-structure interaction in the form of dynamic soil arching can act to significantly reduce the load on the roof of the structure. The importance of accounting for soil arching at depths of burial as shallow as 20% of the clear span with dynamic as well as static loadings was clearly demonstrated.

In this paper, small-scale model tests were conducted to simulate some of the major aspects of the full-scale field observations. The model testing of dynamic soil-structure interaction provided a useful and relatively inexpensive method

of understanding basic aspects related to the complex coupling between soil and structure. It was recognized that the data from field tests were difficult to analyze because the loading conditions on the free surface were difficult to measure. Through small-scale model testing, the generation of an impulse loading on the free surface can be well controlled and the propagation of this impulse loading through the soil and then its action on the buried structure can be traced.

The experiments and analysis for this research were conducted in two phases. During the first phase, the loading set-up was developed and the measured free field responses were verified with an analytical (wave propagation) model. The analysis and experiments with the buried structures constitute the second phase.

### FIRST PHASE RESEARCH

The research of the first phase consisted of the measurement and analysis of plate and soil response under low velocity impact (Fig.1). A free-drop impact system was developed to generate the dynamic loading on the free surface of the plate. The radial strain of the target plate, the longitudinal wave speed and the acceleration of the sand were measured. The measured wave speed data were then used to evaluate the elastic constants of the sand. Based on the Hertzian contact law, momentum balance and measured contact duration, the impact loading function was characterized as a Hanning function for the following analysis.

A time domain analysis based on linear elastodynamics was developed for transient waves on a thin plate resting on an elastic half space. The contact stresses and the normal displacements of the plate were taken as unknown functions. The contact between the plate and the half space was assumed frictionless. The experimental results of the radial strain at the bottom of the target plate and the acceleration of the sand beneath the center of the target plate were compared with the analytical solution. The arrival time, the duration and the magnitude show good correlation between the analysis and experiments. The overall results provide an understanding of the transmission of impact load through the plate, the inter-

action between the plate and the sand, and the propagation of the load into the sand (Chen, et al., 1988).

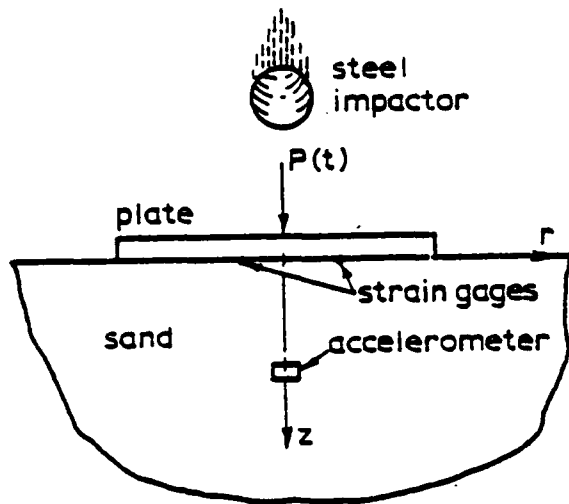


Figure 1 Low Velocity Impact of an Circular Plate Resting on Sand.

## SECOND PHASE RESEARCH

### (a) Experiment

In order to study wave propagation phenomena consistent with field-test observation, a test of an approximately 1/40 scale model cylinder structure (15.24cm x 15.24cm) with 0.635cm thickness and embedded under about 7.6cm thickness of sand was conducted (Fig.2). Low velocity impact system was used to generate the dynamic loading on the free surface. The particular test of a circular aluminum (6061-T51) plate with 30.48cm in diameter and 1.27cm in thickness impacted at its center by a 7.62cm diameter steel (E52100) ball is described in detail here.

One buried structure (Fig.3) was made of Clear Cast Acrylic (Ain Plastic Co.) with Young's modulus and Poisson's ratio equal to 3103 MPa and 0.35 respectively. The response of this structure can be assumed elastic. Thus, analysis can be simplified and some useful phenomenon can be characterized. Micro-concrete and miniature reinforcement developed by Townsend, et al.(1985) were used to construct a model reinforced concrete (RC) circular roof. This RC roof was clamped on a plexiglas hollow-cylinder base (Fig.4). The micro-concrete has properties similar to regular concrete but contains a finer aggregate. It is believed that the interface behavior between the concrete and the soil can be preserved with this microconcrete (Shin, 1987). The miniature reinforcement, 28-gauge black-annealed wire manufactured by Anchor Wire Co. was used. Two wire meshes were constructed with 0.5" (12.7mm) square opening for each RC roof. The reinforced concrete roof was 5/16" (7.9mm) in thickness and 6" (152.4mm) in diameter and was reinforced with the wire meshes on both upper and bottom surfaces (tension and compression). The concrete cover was about 1/32" (0.8mm) on both sides.

### (b) Analysis

The FH test results have been analyzed by several researchers. However, the general problems and uncertainties in the FEM application are:

- (1) The applied loading on the free surface was adopted by the pressure gages measurements. However, out of six gages, usually only two or three sets of records were available and were averaged to get the applied loading which was then assumed uniformly distributed along the free surface. As a result of the reflection from the buried roof the uniform pressure assumption is, in general, not likely to be true.
- (2) The dynamic behavior of sand is not well understood. Typically, the constitutive relationship of sand depends on loading rate, loading magnitude, and loading history (Kiger, 1980). Highly nonlinear, nonhomogeneous stress-strain behavior would have occurred during the field test.
- (3) The boundary conditions of the free surface before and after the explosion were very different.

With the above understanding, as a first order approximation, linear-elastic model for both soil and structures were assumed in the current approach, and the dynamic linear-elastic finite element code, SAP4, was applied. Two-dimensional axisymmetric elements and a direct time integration method were used. This analysis can approximately simulate the physical phenomena of the soil-structure system, and provide an understanding of the loading wave propagating on the buried structure and the corresponding structural response. This program will also form the basis for the future nonlinear analysis.

### (c) Results

#### (1) Plexiglas Buried Structure (Elastic Structure)

The experimental results in comparison with the FEM calculations are shown in Figure 5. In Figure 5(a), the displacement at the center of the roof of the buried structure is plotted. In Figure 5(b), the radial strain at  $r=1.91$ cm from the center of the ceiling is plotted. The calculated response shows good agreement in some of its characteristics with the measured response. There was good agreement between the calculated and the measured arrival time. The peak displacement at the roof center (Fig.5(a)) and the corresponding radial strain (Fig.5(b)) can be predicted by the current linearly elastic analysis with about 75 percent accuracy for both the peak amplitude and the peak arrival. However, the response subsequent to the peak showed poor agreement. The FEM calculation predicted a lower amplitude because of the influence of the tension in the assumed "linear-elastic sand" (after the peak load, the reflection from the bottom of the roof will produce tension), and the interface between soil and structure was assumed continuous and perfect bonded.

The influence of different values of the Poisson's ratio,  $\nu$ , was also studied by assuming the

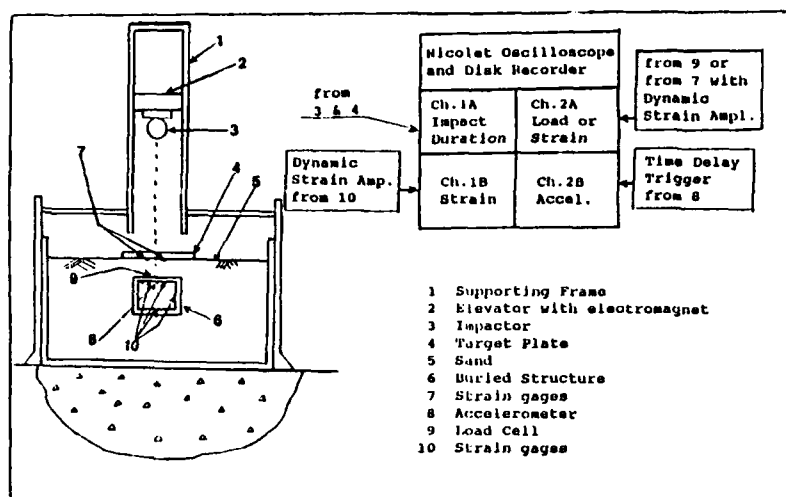


Figure 2 Schematic Drawing of Test Set-Up.

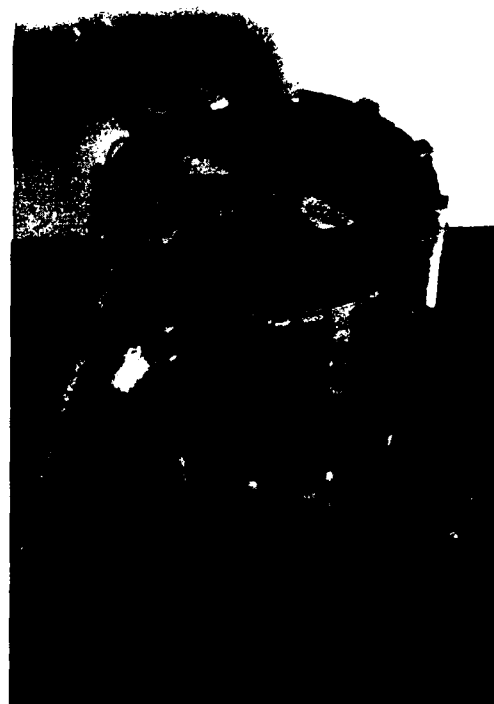


Figure 4 Reinforced Concrete Buried Structure.



Figure 3 Plexiglas Buried Structure.

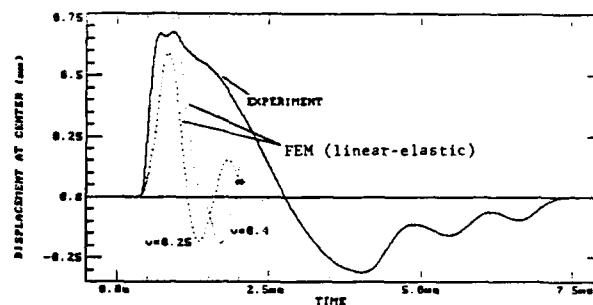


Figure 5a Experiments Compared to Calculations (Displacement at Roof's Center).

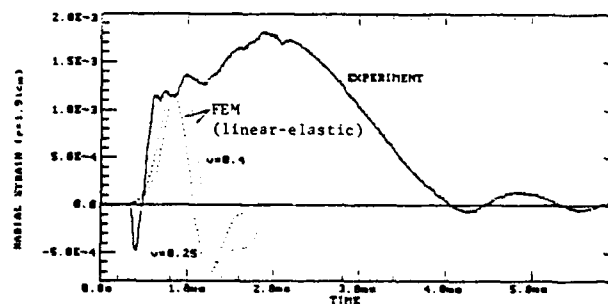


Figure 5b Experiments Compared to Calculation (Radial Strain at  $r=1.91\text{cm}$ ).

longitudinal wave velocity to be equal to the measured wave velocity (263 m/sec). For  $v=0.25$  and  $v=0.4$ , the calculated elastic constants would have about 50% difference. However, by inspecting the calculated response before the peak (Fig. 5), it was found that the dynamic response of the buried structure was not influenced significantly by the material properties of the adjacent soil. This can be understood by knowing that the stiffness of the structure is much larger than the surrounding soil and that there are large differences of the mechanical impedance between the structure and the soil.

#### (11) Reinforced Concrete Buried Structure

##### (1) load and acceleration measurements

The experimental results of the test with the reinforced concrete buried structure are described. In Figure 6, the load measurements of the first hit (solid line), in comparison with the second hit (dotted line) are plotted. It can be seen that the first hit had more oscillations caused by cracking of the concrete. This phenomenon was also seen in the measurements of the radial strain on the buried roof.

The time history of the acceleration on the roof's center during the first hit was measured. Again, high-mode oscillation is observed. The displacement histories shown in Figure 7 were obtained by integrating the acceleration histories. The constant values of displacements for time after 3 msec were not dependable since very little offset of the acceleration signals would result in great difference of displacement after double integration. However, the displacements before the peak were fairly reliable, and the response of second, and third hits were very close, having a peak displacement of about 0.7 mm.

##### (2) failure mode

Flexure failure was observed after completion of ten hits. The load cell became unbonded because of cracking which was radially formed. The picture of the bottom roof (ceiling) is shown in Figure 8. The accelerometer was still bonded at the center ceiling. However, large cracks next to the accelerometer can be seen.

##### (3) comparison between the reinforced concrete roof and plexiglass roof

The dynamic behavior of the buried roof with different rigidity (plexiglas and RC) were compared to obtain better understanding of the arching phenomenon. A test with plexiglas roof mounted on the plexiglas base was conducted. The thickness of the circular plexiglas roof was 1/4 inch. The comparison of the load measurements on the center of the roof between the RC roof and the plexiglas roof is also shown in Figure 6. The response of the plexiglass roof (which behaved elastically) is plotted as a dashed line. It can be seen that the RC roof which has higher stiffness experienced a longer duration and higher loading magnitude than the plexiglass roof. It was concluded that with the same surrounding soil, the stiffer buried structure experienced less soil arching.

##### (4) comparison between experimental and numerical results

The experimental data are compared with the FEM results and plotted in Figure 7. The calculated displacement has reasonable agreement with the measured displacements up to about 0.7 msec. It was noted that the calculated values represent the displacement of an uncracked concrete roof. Therefore, a calculated response lower than the measured displacements was expected; however, the response after 0.7 msec showed poor agreement between the experiments and FEM results. This is due to the linear-elastic assumption of treating sand as a continuum, due to the separation at the interface, and due to nonlinear behavior of the model reinforced concrete structure after cracking.

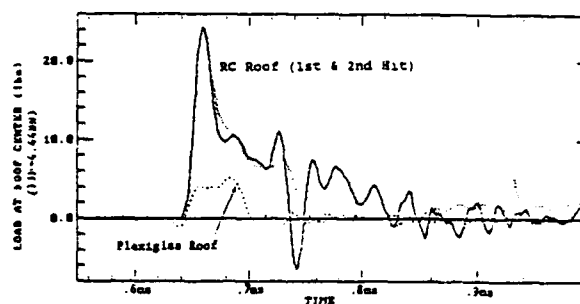


Figure 6 Response with Different Roof's Stiffness.

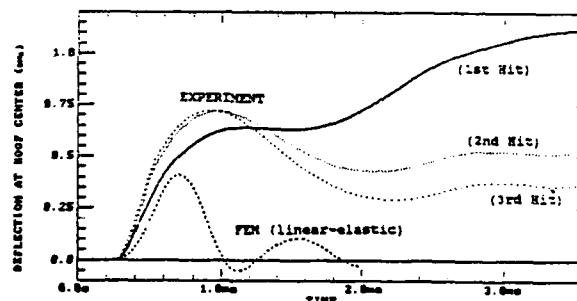


Figure 7 Experiments Compared to Calculations (Displacement at Roof's Center).

#### DISCUSSION OF THE APPLICATION OF THE CURRENT RESEARCH INTO THE FIELD

The practical application of the current research is primarily concerned with answering the following two questions:

1. How can one analyze the buried structures in the field by using the results of the small-scale model developed in this research?
2. Can one calculate the deflection of a buried structure subjected to a general explosion from the results of the current impact-loading technique?

1. As described above, several investigators have conducted the study of dynamic soil-structure interaction by using finite element method. The

difficulties in analyzing the results from field tests include: uncertainties of loading function, soil behavior and interfacial conditions. Hence, the behavior of the buried structure cannot be precisely predicted. This is not only due to the limitations of the numerical methods but also due to the lack of up-to-date experimental technique in the field.

The study herein describes a specific method to approach the above difficulties from both the experimental and analytical point of view, and leads to a better understanding of the physical phenomena of dynamic soil-structure interaction; e.g. the wave reflection, the deflection and the loading release on the buried roof as well as the interfacial conditions. With this understanding, numerical simulation, such as finite element method analysis can be more effectively established. Also, the element formulation, the constitutive relationship and the interfacial conditions of the established finite element method can be checked and modified according to the small-scale experimental models utilizing state-of-the-art modeling techniques.

The application of the developed numerical simulation to the buried structure in the field can be made directly according to the conditions in the field, i.e. the loading, the boundary conditions, the material models, etc. A nonlinear, dynamic finite element method is suggested for this particular study; however, a boundary element method may be suitable for other study with less boundaries. The size effect of the material models used in the finite element calculation needs further investigation.



Figure 8 Failure Mode (Ceiling).

2. An explosive type of loading is expected in the field. As shown in Figure 9,  $E(t, \underline{x})$  represents a typical explosive load distributed on the free surface. If the time history of the explosive loading function can be described as  $E(t)$ , then the loading in the frequency domain,  $E(f)$ , can be obtained from the Fast Fourier Transform (FFT). The results of the current research are due to an impact loading, say  $P(t)$ , and the frequency spectrum of  $P(t)$  is  $P(f)$ .

Assuming that the linear-elastic assumption is appropriate for determining the deflection,  $U_0(t)$ , at the center of the buried roof (As described above, the numerical simulation can predict the deflection of the buried roof with approximately 75% accuracy of the history up to the peak response.), the spectrum of the deflection function can be described as

$$U_0(f) = G(f, 0) * P(f) \quad (1)$$

where,  $G(f, 0)$  is the Green's function of the soil-structure system due to a point force applied at the center of the free surface. By applying the same idea, as shown in Figure 9, the spectrum of the deflection function of the buried structure subjected to explosive loading can be described as

$$U(f) = \int G(f, \underline{x}) * E(f, \underline{x}) d\underline{x} \quad (2)$$

and the deflection history,  $U(t)$ , can be obtained by applying the inverse fast fourier transform of  $U(f)$ , i.e.

$$U(t) = 1/2\pi \int_{-\infty}^{\infty} U(f) e^{-ift} df \quad (3)$$

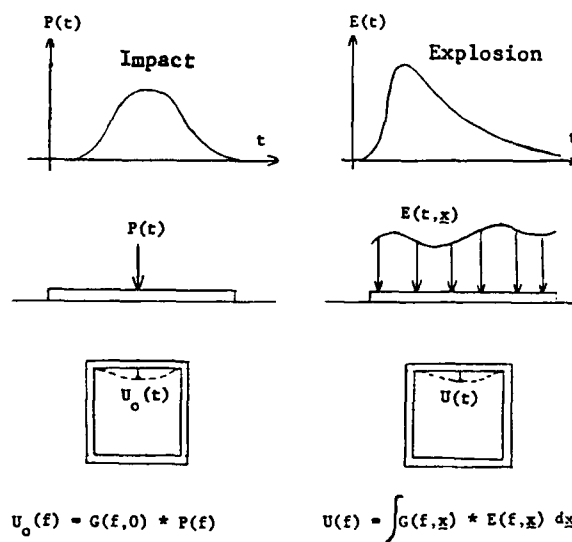


Figure 9 Idealization of Applying Results from Impact to Explosion.

A recent publication in the Journal of Structural Engineering, ASCE, of "Analysis of Underground Protective Structures" by Weidlinger and Hinman in July, 1988 deals with a similar problem to the one in the current study. As shown in Figure 10, a box-shaped reinforced concrete structure located below the ground surface was subjected to an explosive source from three possible positions. The explosion produces a radically expanding compression wave which propagates through the soil and acts on the buried structure. The particular case with the point source exploding on the burster slab is a practical example of the impact-loading study. The use of the concrete burster slab is to protect against penetrating weapons.

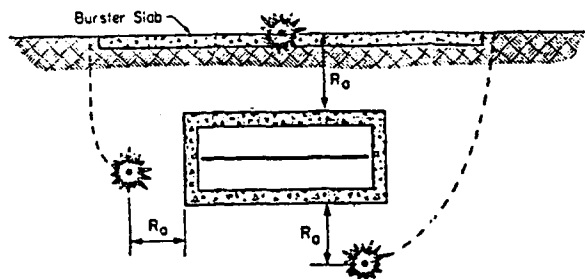


Figure 10 Underground Protective Structure.  
(after Weidlinger and Hinman, 1988)

It is noticed that one of the advantages of the analysis in the current study is that no artificial parameters were used. The experiments and analysis are parallel. The analysis which is simplified under the frame of theoretical development can then be used to explain the physical phenomenon observed from the experiments. Hence, a fundamental understanding is obtainable.

#### SUMMARY AND RESEARCH IN PROGRESS

The problems with large scale field tests such as uncontrollable boundary conditions, unknown soil conditions and unknown dynamic loadings as well as field measurement's difficulties can be eliminated by using the techniques as described in this research. The fundamental physical phenomena of the buried structure interacting with its adjacent soil under dynamic loading can then be well-defined through the test observations as well as through the analysis.

Dynamic, nonlinear finite element approach is being developed to predict the post-peak response of the dynamic behavior of the buried structure. The nonlinearities due to zero tensile capacity in sand and the separation of the soil-structure interface are considered. This approach also includes the ability to take into account of the nonlinear behavior generated by reinforced concrete. For the purposes of direct comparison of the behavior of the model structure to a full scale structure, similitude requirements are introduced. The material properties of the model reinforced concrete are characterized under both static and dynamic loading.

#### ACKNOWLEDGEMENTS

The authors are grateful for support from the Air Force Office of Scientific Research (Grant No. AFOSR-86-0058). They are pleased to acknowledge the Program Manager, Major Steven C. Boyce.

#### REFERENCE

- Al-Mousawi, M.N., "On Experimental Studies of Longitudinal and Flexural Wave Propagations: An Annotated Bibliography," *Applied Mechanics Review*, V. 39, No. 6, 1986.
- Chen, H.L., "Dynamic Response of Embedded Structures", Ph.D. dissertation, Department of Civil Engineering, Northwestern University, 1988.
- Chen, H.L., Lin, W., Keer, L.M. and Shah, S.P., "Low Velocity Impact of an Elastic Plate Resting on Sand," *Journal of Applied Mechanics*, ASME, in press.
- Cunningham, C. H., Townsend, F. C. and Fagundo, F. E., "The Development of Micro-Concrete for Scale Model Testing of Buried Structures," Final Report, ESL-TR-85-49, AFESC, January 1986.
- Ghaboussi, J., Millavec, W. A. and Isenberg, J., "R/C Structures under Impulsive Loading," *Journal of Structural Engineering*, ASCE, Vol. 110, ST3, pp. 505-522, Mar., 1984.
- Gran, J. K., Bruch, J. R. and Colton, J. D., "Scale Modeling of Buried Reinforced Concrete Structures Under Air-Blast Loading," *ACI publication SP73-7*, pp. 125-142, 1982.
- Jackson, J. G., Ehrgott, J. Q. and Rohani, B., "Loading Rate Effects on Compressibility of Sand," Miscellaneous Paper SL-79-24, US Army Engineer Waterways Experiment Station, CE, Vicksburg, MS, November, 1979.
- Kiger, S.A., Getchell, J.V., Slawson, T.R., and Hyde, D.W., "Vulnerability of Shallow-Buried Flat Roof Structures," US Army Engineer Waterways Experiment Station, Technical Report SL-80-7, six parts, 1980-1984.
- Krauthammer, T., Bazeos, N. and Holmquist, T. J., "Modified SDC: Analysis of RC Box-Type Structures," *Journal of Structural Engineering*, ASCE, April 1986.
- Shin, C. J., "Dynamic Soil-Structure Interaction," Ph.D. Thesis, Department of Civil, Environmental, and Architectural Engineering, University of Colorado, Boulder, CO. 1987.
- Slawson, T. R., "Dynamic Shear Failure of Shallow-Buried Flat-Roofed Reinforced Concrete Structures Subjected to Blast Loading," Final Report SL-84-7, US Army Engineer Waterways Experiment Station, Apr., 1984.
- Weidlinger, P. and Hinman, E., "Analysis of Underground Protective Structures," *Journal of Structural Engineering*, ASCE, Vol.114, No.7, July, 1988.
- Windham, J. E., "Finite Element Calculation of Foam HEST 1," Miscellaneous Paper SL-80-1, US Army Engineer Waterways Experiment Station, Vicksburg, MS Apr., 1980.
- Windham, J. E., "Stress Transmission During Foam HEST Tests of Sand-Covered Box Structures: Analysis Using a One-Dimensional Plane Wave Code," US Army Engineer Waterways Experiment Station, Vicksburg, MS, Oct., 1980.

## EXPLOSIVE TESTS ON MODEL CONCRETE BRIDGE ELEMENTS

Brian Hobbs, Alan J Watson and Stuart J Wright

Department of Civil and Structural Engineering  
University of Sheffield, England

### **ABSTRACT**

A model scale investigation of the damage resulting from the detonation of uncased cylindrical high explosive charges in contact with reinforced concrete bridge beams is described. Tests on beams with rectangular and T-shaped cross-sections at scale ratios of 1:10 and 1:4 are reported. Details of the damage generated are presented and a relationship between the extent of damage resulting from vertical charges and the area of contact between the charge and the target is developed. The results of static loading tests on damaged beams are presented and a relationship between residual strength and charge contact area developed. A comparison between results at 1:10 scale and 1:4 scale indicates a high degree of correlation in the geometry of the observed damage.

### **1. BACKGROUND**

The experimental programme described in this paper forms part of an ongoing investigation of the vulnerability of concrete bridge superstructures to damage generated by high explosive weapons. The effect of a weapon on a target may be divided into three components; (i) impact loading, (ii) overall impulsive pressure loading, and (iii) local structural damage in the cross-section. Initial trial calculations were carried out in order to estimate the likely relative importance of these three components in contributing to the total structural damage to typical concrete bridge superstructures and hence their ability to remain standing after an attack. It was concluded that (i) was likely to be negligible, that (ii) was likely to have only a minor influence and that (iii), the local structural damage, was likely to be by far the most significant effect.

A review of existing methods of predicting local structural damage, such as cratering, scabbing, breaching etc,

indicated that there were no procedures directly related to bridge superstructures. The application of general methods for concrete elements such as walls, slabs and beams to typical bridge superstructures yielded very variable results. It was therefore decided that an experimental programme was required to provide a basis for the development of new methods of predicting damage. The vulnerability of a structure depends upon its ability to carry loads in its damaged condition. There appears to be little existing information on the strength of explosively damaged concrete elements and the test programme therefore included load testing of the explosively damaged elements.

### **2. TEST DETAILS**

#### **2.1 Specimens**

There is a very wide range of forms of construction for concrete bridge superstructures. For this initial investigation, however, it was decided that attention should be concentrated on single span, simply supported, reinforced concrete structures. The results presented in this paper relate to the very commonly used beam-and-slab form of construction. This comprises a number of rectangular beams supporting a reinforced concrete slab. In most cases the slab is cast integrally with the beams and acts compositely with them to form a series of T shaped beams. The influence of this composite action has been assessed by testing both isolated rectangular beams and T-section beams.

The design of the beams is based on typical details for a full scale bridge of this form of construction. The initial series of tests was carried out at a nominal scale ratio of 1:10 and this has been followed up by a shorter programme of tests at 1:4 scale. The model beams were designed using linear scaling principles and cross-sectional details are given in Figure 1. The overall lengths of the



beams are 1166mm and 2914mm respectively. They were manufactured using concrete mixes containing rapid hardening portland concrete which gave a compressive cube strength of approximately 40 N/mm<sup>2</sup> at the time of explosive testing (7 days).

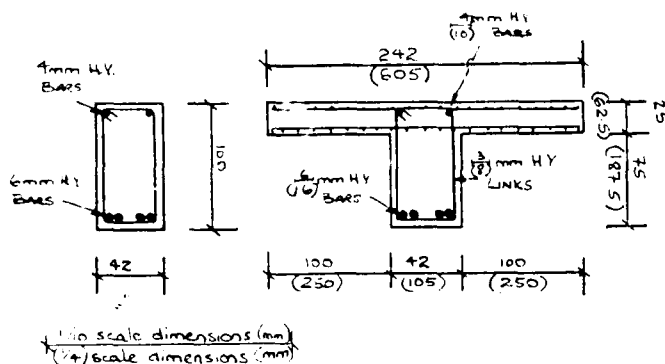


Fig. 1. Beam Details

## 2.2 Explosive Charges

Uncased charges of PE4 plastic explosive have been used. The charges are cylindrical with a truncated conical nose. The dimensions are given in Figure 2. The charge weights were kept constant at 87gm for the 1:10 scale beam tests and 1359gm for the 1:4 scale tests. The variables considered to date are the contact area,  $A_c$ , between the charge and the concrete beam and the orientation of the axis of the charge with respect to the beam surface. The first series of tests at each scale employed vertical charges over the centre line of the beams at the midspan position. The tip diameter was varied between 4mm and 25mm for the 1:10 scale tests and between 10mm and 62.5mm for the 1:4 scale tests.

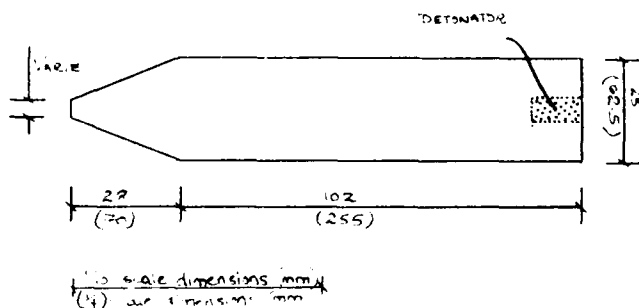


Fig. 2. Charge Dimensions

In the second series of tests at each scale, the charge nose diameter was kept constant at 4mm for 1:10 scale and 10mm for 1:4 scale beams. The nose was positioned on the centre of the beam at midspan and the axis of the charge was inclined at 45°. At 1:10 scale, tests

were carried out both with the inclined charge orientated in the plane of the longitudinal axis of the beam and also at 90° to this plane. The only 1:4 scale test carried out to date had the charge inclined in the plane of the longitudinal axis of the beam.

## 2.3 Test Arrangements

The beams were simply supported on purpose designed bearings with restraint straps to prevent uplift of the ends of the beams during the dynamic flexural response. The arrangement is shown in Figure 3. The transient response of the specimen was monitored using displacement transducers, electrical resistance strain gauges bonded to the main reinforcement at midspan, and high speed cine photography.

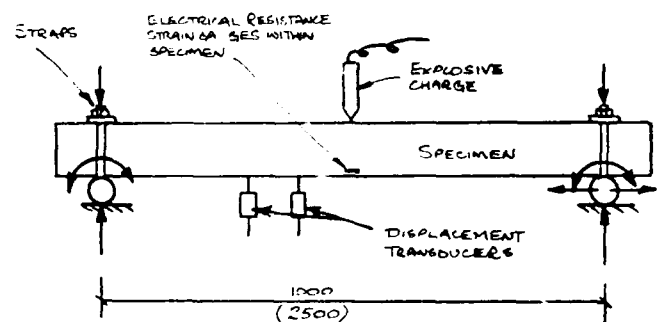


Fig. 3. Test Arrangement

Post-test static loading of the damaged beams was carried out in a servo-hydraulic testing machine under displacement control. This allowed the complete load deflection response, including the post-peak behaviour, to be obtained. This is important so that the energy absorption capacity of the damaged beams can be determined, as well as their maximum load capacity. The beams were supported over the same span as that used in the explosive loading test and two vertical point loads were applied at the third points in the span.

## 3. RESULTS AND DISCUSSION

### 3.1 Vertical Charges on 1:10 Scale Beams

#### 3.1.1. Visible damage

The varying levels of damage resulting from vertical charges with five different contact areas on 1:10 scale rectangular beams are shown in Figure 4. The major influence of charge tip diameter, and hence the contact area  $A_c$ , is clearly demonstrated. The damage to beam B4, with a charge tip diameter of 4mm is relatively minor, but when the tip diameter increases up to 25mm for beam B7 almost the whole midspan cross section of the beam is

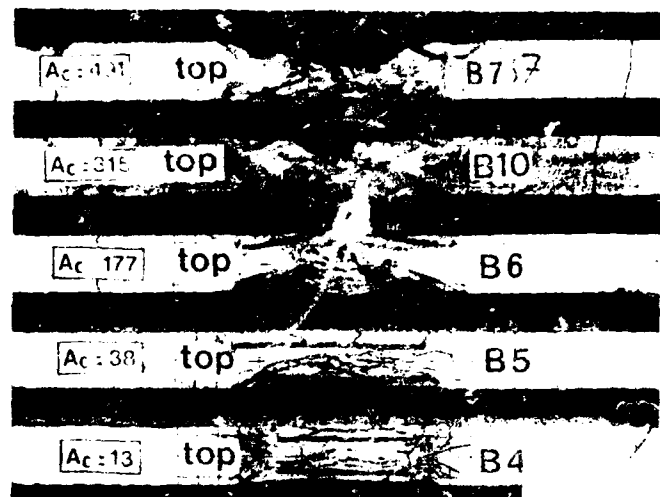
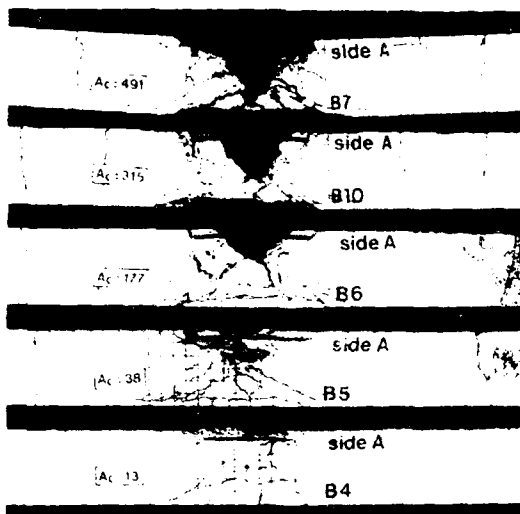


Fig 4. Explosive damage to 1:10 scale rectangular beams with vertical charges having tip diameters of 4mm, 7mm, 15mm and 25mm.

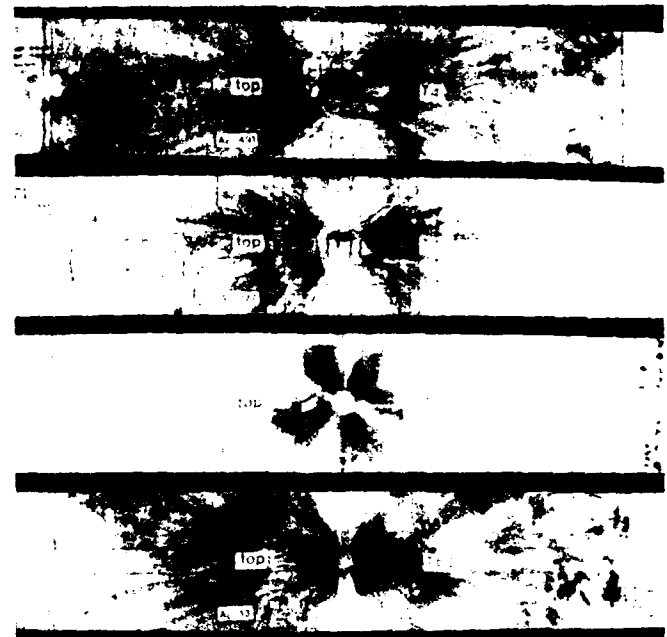
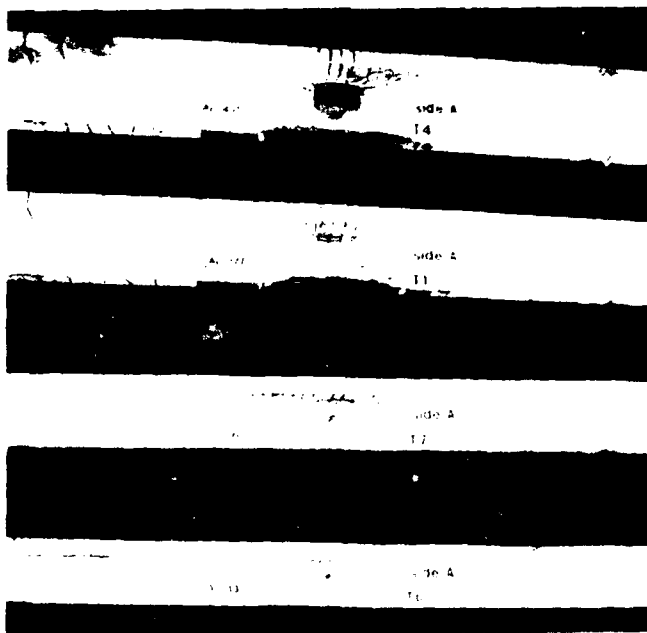


Fig 5. Explosive damage to 1:10 scale T-beams with vertical charges having tip diameters of 4mm, 7mm, 15mm and 25mm.

removed.

Results for T-Beams with four different charge tip diameters are shown in Figure 5. Although the damage to the beam rib itself is similar to that in the equivalent rectangular beams shown in Figure 4, the plan views clearly indicate that the damaged zone is localized around the top of the beam rib and the slab areas each side of the beam are not significantly affected.

The area of cross-section removed at midspan was measured and results for both the rectangular and T beams are plotted in Figure 6. It can be seen that there is an approximately linear relationship between the percentage of the cross-section removed and the charge tip diameter for each type of beam. The steeper slope for the relationship for rectangular beams indicates that a given charge of this configuration is likely to have a significantly greater effect on these

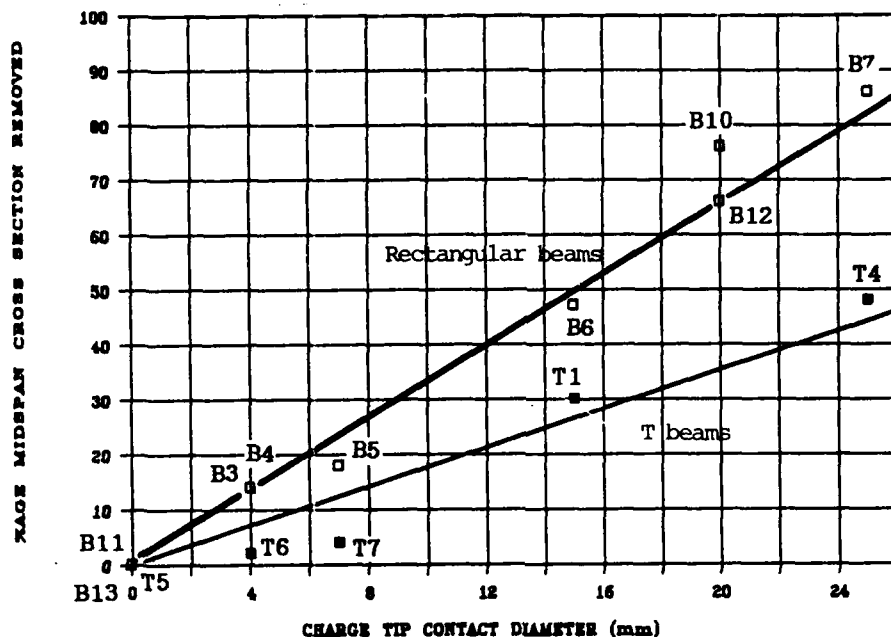


Fig 6. Midspan damage as a function of charge tip diameter for vertical charges on 1:10 scale beams.

beams than on the equivalent T-beams.

### 3.1.2. Residual Strength

Typical results from the post-test static loading of the beams are presented in Figure 7 and are compared with equivalent undamaged beams. These curves clearly demonstrate the far greater structural significance of the damage to the rectangular beam, for which the load carrying capacity is reduced by

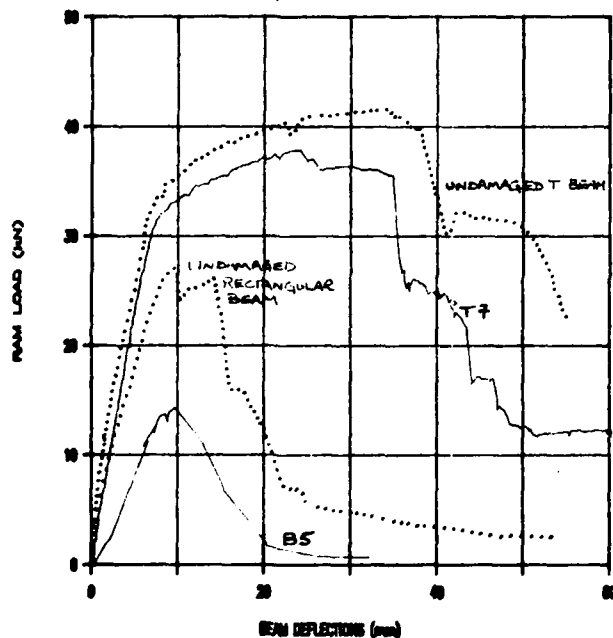


Fig. 7 Load-deflection response for damaged and undamaged beams

approximately 50%, even though the cross-sectional area was reduced by only 18%, compared to the T-Beam, for which the load capacity is reduced by approximately 8% while the cross-sectional area was reduced by approximately 5%.

The ultimate moment of resistance of each damaged midspan section has been calculated from the load test results. The reduction in ultimate moment is plotted against charge tip diameter in Figure 8. The ultimate moment of resistance may be used to calculate the load carrying capacity of the damaged beams for any distribution of applied loading and is therefore a very useful general indicator of residual load capacity. These curves demonstrate even more clearly that a given vertical charge has a much greater effect on the strength of a rectangular beam than on an equivalent T-beam. The difference is particularly pronounced for larger tip diameters. For diameters of 15mm and above, the carrying capacity of the rectangular beams is almost completely destroyed, whereas there is only a 15% reduction in the capacity of the T-beams.

### 3.2 Inclined Charges on 1:10 Scale Beams

The results from the two 45° inclined charges on the rectangular beams are shown in Figure 9. The charge on beam B8 was orientated in the plane of the longitudinal axis of the beam and that on B9 was orientated in a plane at 90° to the axis. The strong influence of charge orientation is apparent. A comparison of these damaged beams with B4, the

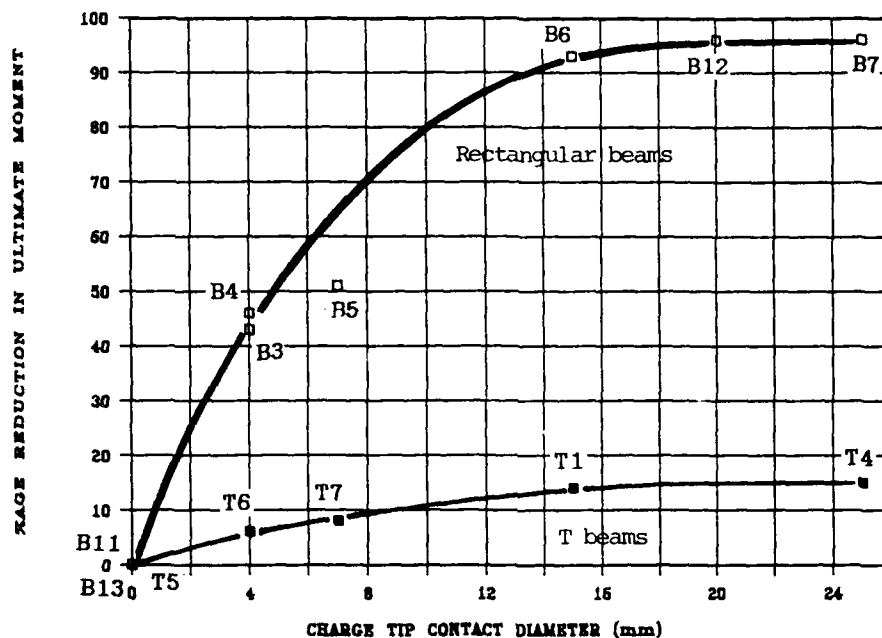


Fig 8. Reduction in ultimate moment of resistance as a function of charge tip diameter for vertical charges on 1:10 scale beams.

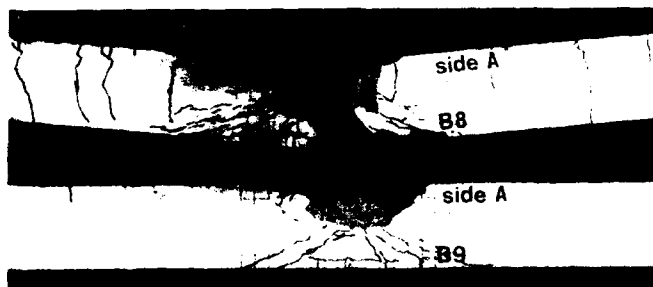


Fig 9. Explosive damage to 1:10 scale rectangular beams with 45° inclined charges.

equivalent beam with a vertical charge shown in Figure 4, shows that the damage from inclined charges, which present a greater area to the beam surface, is much greater than that from a vertical charge with the same tip diameter. The damage to beam B8 is such that the reduction in ultimate moment capacity is almost 100% and therefore no post-test loading has been carried out. Loading results for beam B9 gave a reduction in ultimate moment capacity of 58%, compared with 46% for beam B4.

The equivalent results for T-beams are presented in Figure 10. Again the strong influence of charge orientation is apparent. The concrete in the midspan cross-section of beam T2, with the charge orientated in the plane of the longitudinal beam axis, is completely removed. The damage to T3, however, with the charge orientated at 90°, is confined

primarily to the slab to one side of the beam rib, with little effect on the beam itself or the slab on the other side of the beam. This is reflected in a measured reduction in load capacity of only 37% for beam T3. The nature of the damage resulting from both inclined charge orientations is quite different from that from the equivalent vertical charge on beam T6, for which the reduction in load capacity was only 3%.

### 3.3 Vertical Charges on 1:4 Scale Beams

This series of tests was carried out in order to obtain information of the scaling relationships for explosive damage. Only T-beams have been tested and the damage resulting from tests with three different charge tip diameters is shown in Figure 11. They may be compared with the equivalent 1:10 scale T-beams (T6, T1, T4) in Figure 5. The similarity of the

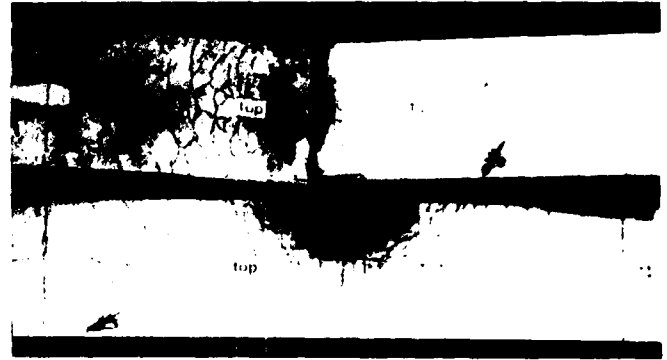
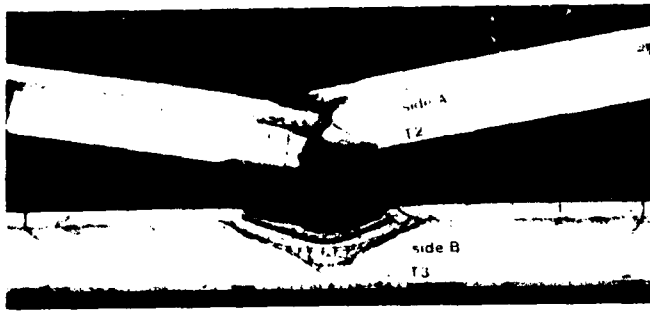


Fig 10. Explosive damage to 1:10 scale T-beams with inclined charges.

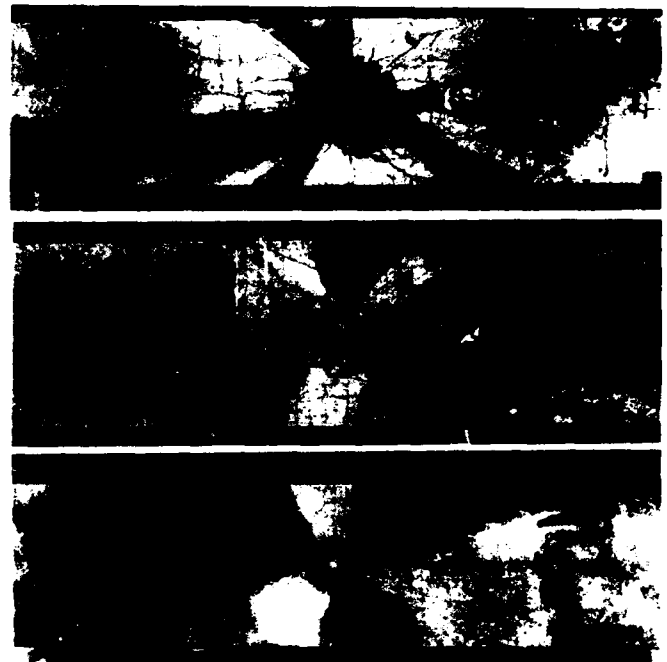
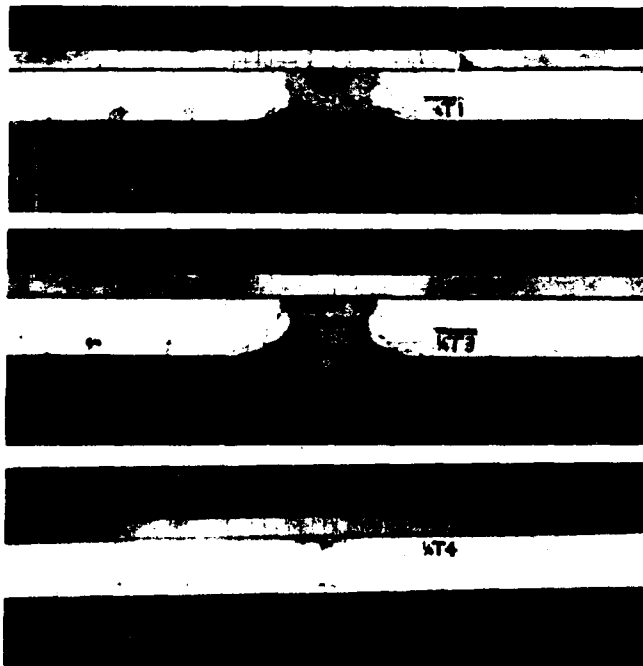


Fig 11. Explosive damage to 1:4 scale T-beams with vertical charges and tip diameters of 10mm, 37.5mm and 62.5mm.

geometry of the damaged zones at the two scales is apparent. Post-test loading of these 1:4 scale beams has yet to be carried out.

#### 3.4 Inclined Charge on 1:4 Scale Beam

A single test with the charge oriented at  $45^\circ$  in the plane of the longitudinal axis of the beam has been completed. The resulting damage is shown in Figure 12. This may be compared with the equivalent 1:10 scale result for beam T2 shown in Figure 10. Again, the similarity of the two results is apparent.

#### 4. CONCLUSIONS

The results from the tests on vertical charges highlight the great influence of the area of contact between the explosive charge and the concrete surface on the damage resulting from a charge of fixed weight and orientation. Over the range of variables covered here, there appears to be an approximately linear relationship between the area of cross-section removed and the diameter of the circle of contact, as shown in Figure 6. The strength of a damaged element is, however, not linearly related to the area of cross-section



Fig 12. Explosive damage to 1:4 scale T-beam with charge inclined at  $45^\circ$  in plane of longitudinal centre line.

removed. The relationship between strength reduction and diameter of the circle of contact appears to be approximately parabolic, as shown in Figure 8.

Whilst the pattern of damage to the beam ribs in T-beam specimens is similar to that in equivalent rectangular beams, the reduction in strength of the beams is only about one fifth of that for the rectangular beams. Since nearly all reinforced concrete beam bridges will effectively comprise a set of parallel T beams, it is clear that full account must be taken of the action of the slab each side of the damage zone in contributing to the residual strength of a damaged beam.

The damage resulting from inclined charges is different in nature and extent from that due to vertical charges, and depends strongly on the orientation of the charge. When the charge is inclined in the plane of the longitudinal axis of the beams, the resulting damage is considerably greater than that from equivalent vertical charges or charges inclined at  $90^\circ$  to this plane. It is also significant that for this charge orientation, the effect on the strength of T-beams is at least as great as that on rectangular beams. This is in marked contrast to the results for vertical charges and is assumed to be related to the increased surface area on which the blast loading can act in a T-beam.

The initial visual comparisons of damage at 1:10 and 1:4 scales indicates that the similarity is great. This gives confidence in the use of model testing for this type of investigation. A more detailed analysis of scale effects will be made once the damaged 1:4 scale beams have been load tested. This investigation has highlighted the importance of a number of parameters in determining the effect of high explosive charges on the strength of model concrete bridge elements. Further work is planned on 1:10 scale multi-web T-beams, to investigate the importance of

transverse load distribution effects, and on slab elements at both 1:10 and 1:4 scale. Tests on full scale T-beam bridges are planned using cased and uncased charges. The results of these further investigations will allow a fuller analysis to be made of scale and casing effects and lead to the development of methods of predicting strength reduction, and hence vulnerability.

##### 5. ACKNOWLEDGEMENTS

The work described in this paper has been carried out under sub-contract to Denver Research Institute as part of a programme of vulnerability studies funded by the Naval Weapons Centre, China Lake. This financial support and the advice and encouragement provided by Larry Ulliyatt and Lou Smith of DRI and Mel Keith of NWC are gratefully acknowledged.

## LABORATORY SIMULATION OF GROUND SHOCK LOADING

F. Y. SORRELL

Department of Mechanical and Aerospace Engineering  
Box 7910, North Carolina State University  
Raleigh, North Carolina 27695-7910

### ABSTRACT

Laboratory test models, which are scaled model wall sections, are constructed of a typical hardened full scale or prototype structure. Structural materials with yield strength and material moduli close to those used in the prototype structure were used in fabrication of the test model. Proper scaling of the test model is addressed, and the models were constructed and dynamically loaded using this scaling. The laboratory technique used to dynamically load the models was a light gas gun facility. The measured load parameters were non-dimensionalized using the scaling criteria, and the results compared to field tests.

### 1. INTRODUCTION

A method is described for laboratory simulation of the ground shock loading from a conventional weapon and resultant failure of hardened (buried) structures. Laboratory testing offers reduced costs and more precisely controlled test conditions, when compared to large scale tests using explosives. In addition, tests conducted in an indoor laboratory can be carried out with less time between individual experiments, and thus a larger number of structural variations can be investigated. This time efficiency when combined with the lower cost/test can provide a larger data base of dynamic loading and failure criteria, which could ultimately lead to improved and innovative structural design. The present approach is to use a light gas gun to dynamically load models of hardened structures.

In practice, laboratory test models, which are scaled model wall sections, were constructed of typical hardened full scale or prototype structures. Structural materials with yield strength and material moduli close to those used in the prototype structures were used in the test model fabrication. Proper scaling of the test models is addressed, and the test models were constructed using this scaling.

Two types of tests were conducted on the models. The first was a series of tests to produce marginal failure, that is, the condition where the test model has just begun to fail is established.

In this case, the model structure is breached, but not destroyed. In the tests, the conditions for marginal failure were defined in terms of the global test parameters. These parameters are the projectile speed and momentum, and the number and type of layers protecting the model (the layers located between projectile impact and the model). By varying the number and type of layers, failure modes from pure spall to predominately bending could be achieved. The failure mode was determined by inspection of models which were recovered after the test, and hence these tests are referred to as recovery tests. Of particular interest was the investigation of the use of different material layers to alter the load verses time history (load profile). This technique was used to tailor the load profile in order to simulate a weapon detonation as well as to investigate the use of such layers for shock mitigation. The recovery test approach was used for an early evaluation of the suitability of the laboratory technique, as it does not require any dynamic load instrumentation.

After initial tests proved encouraging, additional test shots were instrumented to more precisely define the loading on the models. The approach was not to instrument all recovery tests, but to obtain sufficient data that the loading profile could be estimated from the global test parameters. These data were then used to estimate the loading conditions produced in the recovery tests. The estimated load parameters were then non-dimensionalized using the scaling criteria, and the results compared to field tests. The overall results are considered encouraging.

### 2. SCALING CONSIDERATIONS

The loading profile on the prototype structure or the model is defined here by the rise time of the loading, the peak normal stress of the loading, and the decay time of the loading. Consequently, correct scaling of the loading on a model can be determined by the way these three parameters scale.

The scaling of the rise time, which is the time it takes the shock loading to reach the peak stress, is determined by comparing it to the time for the stress loading to be relieved by shock reflections from the back or edges of the structure. In plate or wall structures the quickest stress relief is due to shock reflection

from the back of the plate. Consequently the rise time,  $T_r$ , is non-dimensionalized by the time for an elastic wave to propagate through the wall. The non-dimensional rise time =  $T_r^*$  is:

$$T_r^* = T_r / (C_e)(th) \quad (1)$$

where  $C_e$  is the elastic wave speed, and  $th$  is the wall thickness. Correct scaling requires that  $T_r^*$  in the model test equal  $T_r^*$  expected in the prototype, or:

$$T_{r,m}^* = T_{r,p}^* \quad (2)$$

where the subscript  $m$  is for the model and  $p$  is for the prototype.

The peak stress is non-dimensionalized by the yield stress of the material used in the structure. Therefore, the non-dimensional peak stress =  $P^*$  is:

$$P^* = P_{max} / \sigma_y \quad (3)$$

where  $P_{max}$  is the peak loading stress, and  $\sigma_y$  is the yield stress. Note that the scale model requires that the ratio of yield stress for the concrete to that for the steel be the same as in the prototype, cf. Sabnis et al. (1983), Zia et al. (1981), or Gran et al. (1973). Consequently, either the yield stress of the concrete or steel may be used. Here the compressive yield stress of the concrete was used. Again, correct scaling of the peak stress requires:

$$P_m^* = P_p^* \quad (4)$$

The loading conditions on prototype structures are often characterized by the peak stress and the impulse, e.g., Kiger and Albritton (1980), Abrahamson and Lindberg (1976), and Crawford et al. (1974). The impulse is the integral of the load over time. Eq. (4) gives the scaling of the peak stress, and the rise time is typically very short compared to the overall loading time. Therefore, scaling of the impulse defines scaling of the decay time of the loading. Here the non-dimensional impulse =  $I^*$  is defined as:

$$I^* = \frac{I}{\sigma_y L^2 [\rho/E]^{1/2} L'} \quad (5)$$

where  $I$  = the physical impulse,  $\rho$  = the structure density,  $E$  = the structure modulus of elasticity, and  $L$  the length scale of the structure.  $\sigma_y L^2$  has the dimension of force, and  $[\rho/E]^{1/2} L'$  has the dimension of time. For a plate this time is proportional to the natural frequency in bending if  $L'$  is the length of one side of the plate. If  $L'$  is the thickness of the plate, this time is proportional to the time for an elastic wave to propagate through the structure. For a given wall section the ratio of edge length to thickness is fixed, and thus either may be used. Therefore, this non-dimensionalization should be appropriate

for both bending and spall failures. Correct scaling of the impulse requires:

$$I_m^* = I_p^* \quad (6)$$

Because  $P_{max}$  is set by Eq. (4), this defines the scaling of the loading time. Due to the short rise time, the loading time is largely determined by the decay time. Thus, Eq. (6) in effect defines the scaling of the decay times.

### 3. MODEL DESIGN AND CONSTRUCTION

To provide guidance on model design and to have access to realistic loading profiles, the scale model chosen was of a structural wall that had been tested in prior field experiments. Data were available on wall sections tested in the field with explosive detonation at the U. S. Army Waterways Experiment Station (WES). These wall sections are a 1/3 scale model of a typical hardened command and control center, and the data are reported by Kiger and Albritton (1980) and Baylot et al. (1985). Data on a wall with a length/thickness of 5 and 10 are reported. The present model is a 1/10 scale model of the wall section with a length/thickness = 5. It is, therefore, a 1/10 scale model of a 1/3 scale model; however, the field data are for the 1/3 scale model. A diagram of the test model is shown in Fig. 1. Because of the small scale it was not possible to use as large a number of re-bars as in the field tests. Hence a smaller number of re-bars with larger dia were used. However, the model has the same amount (by area and approximately by volume) of reinforcing steel that was used in the field tests.

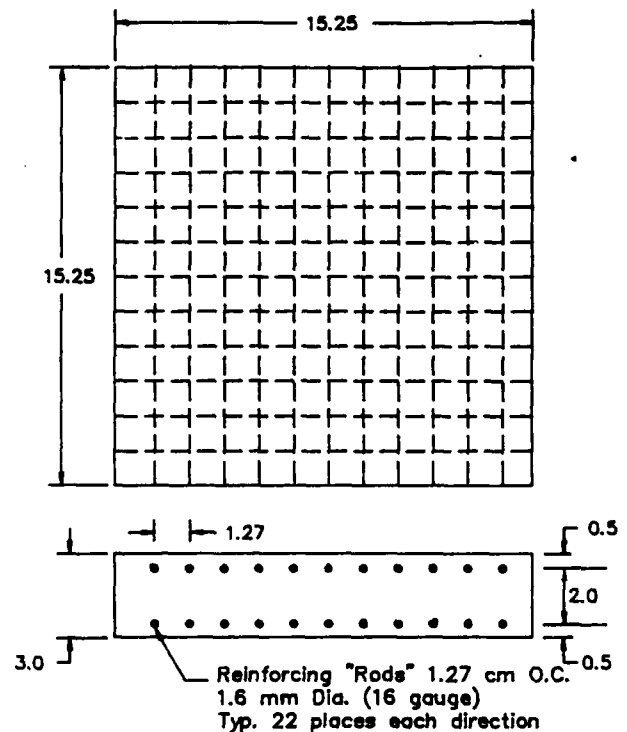


Fig. 1 Diagram of Test Model



The model was constructed using Ultracal 60 brand Gypsum micro-concrete with black steel reinforcing rods. Details on model construction and data on model material properties are given by Sabnis et al. (1983) and Cunningham et al. (1985), who developed the technique and in Sorrell et al. (1987). This technique results in a model with the same ratio of material properties between the concrete and the reinforcing steel as found in prototype structures. Moreover, the micro-concrete has approximately the same yield strength, modulus of elasticity and density as conventional concrete. Consequently,

$$\frac{\sigma_{y,m}}{\sigma_{y,p}} = 1; \quad \frac{E_m}{E_p} = 1; \quad \frac{\rho_m}{\rho_p} = 1 \quad (7)$$

This has the advantage of considerable simplification in the scaling criteria. Eq. (2) becomes:

$$\frac{T_{r,m}}{T_{r,p}} = \frac{(C_{e,m})(th_m)}{(C_{e,p})(th_p)} = \frac{th_m}{th_p} = \frac{1}{S} \quad (8)$$

where  $S$  = the prototype/model length scale ratio. Eq. (3) becomes:

$$\frac{P_{max,m}}{P_{max,p}} = 1 \quad (9)$$

and Eqs. (5) and (6) become:

$$\frac{I_m}{I_p} = \left( \frac{L_m}{L_p} \right) = \frac{1}{S^3} \quad (10)$$

It is assumed that the impulse,  $I$ , is controlled by decay time of the loading. Under this assumption, scaling of the impulse reduces to:

$$\frac{T_{d,m}}{T_{d,p}} = \frac{1}{S} \quad (11)$$

This means that the loading profile on the model should have the same peak stress as that on the prototype, and that the time scale of the loading profile on the model should be reduced by the scale ratio =  $S$ . The technique to produce this loading profile is described in the next section.

#### 4. TEST FACILITY

The technique used to load the test model is a projectile "fired" from a light gas gun. In operation, the breech of the gun is pressurized with helium gas to a pressure that will give the desired projectile speed. The projectile impacts a number of layers that are covering the test model. A diagram of the test setup is shown in Fig. 2. In all cases, a 3.8 cm (1.5") dia projectile was used. Low mass projectiles were fired from a 3.8 cm bore gun. Higher mass (longer projectiles to give longer decay times) were fired from a 15 cm bore gun, with the 3.8 cm impact projectile attached as a sabot on the 15 cm projectile.

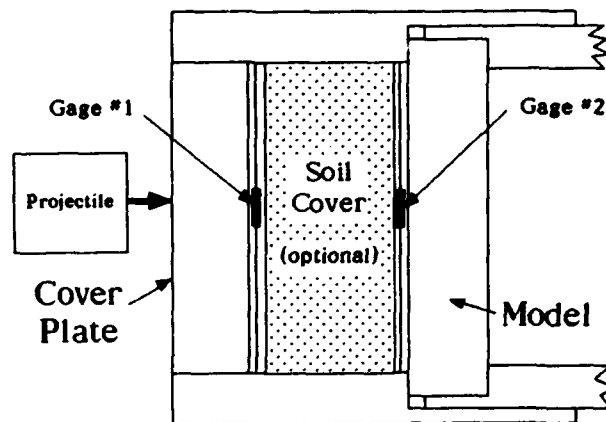


Fig. 2 Diagram of the Test Setup

The peak stress of the loading =  $P_{max}$ , is controlled primarily by the projectile speed and to a lesser degree by the type and thickness of the material layers covering the model. The rise time of the loading =  $T_r$ , is controlled primarily by the type and thickness of the material layers, and the decay time of the loading =  $T_d$ , is controlled primarily by the mass or length of the projectile. There is some interplay between the parameters, and  $T_d$  in particular must be determined experimentally. A description of how the parameters are changed to give the desired loading profile is given by Sorrell et al. (1987).

The loading profile was measured using the normal stress gages located on the cover plate and the model as shown in Fig. 2. Three types of normal stress gages were employed in the tests. These were Manganin and Carbon piezoresistive gages, and Polyvinylidene Fluoride (PVDF) piezoelectric gages. The data from these instrumented tests showed that when the cover layers were either metallic or plastic with known shock Hugoniot,  $P_{max}$  could be accurately calculated from the projectile speed and these Hugoniot. However, when one of the cover materials was porous, such as soil, calculated values for  $P_{max}$  were not accurate. Consequently, in order to estimate  $P_{max}$  when a soil layer was used, a data base on shock attenuation through the soil was developed. This data base was then used to calculate  $P_{max}$ . The data base can be found in Sorrell and Horie (1988). Therefore,  $P_{max}$  was calculated from the shock Hugoniot for metallic and plastic layers, and with soil layers  $P_{max}$  was determined from the shock attenuation data.

$T_r$  was measured experimentally, using gage #2, which is mounted on the model (Fig. 2). When longer rise times were required, a more dispersive cover layer, in this case soil, was used. A thicker soil layer gave longer values of  $T_r$ . In the same manner, the  $T_d$  was also measured by gage #2.  $T_d$  was more closely related to projectile length than to other global parameters, however, no direct empirical relationship to the projectile length was determined. The impulse was directly correlated to the projectile momentum, e.g. projectile speed and mass. For a fixed dia = 3.8 cm the projectile mass is varied by changing the projectile length.

## 5. TEST RESULTS

Test results did not concentrate on a scale reproduction of the WES tests. Rather, it was considered more important to demonstrate that the light gas gun technique could produce loading conditions (loading profiles) over a range parameters reasonably expected during ground shock loading. Loading profiles ranged from very short loading with a peak stress several times the static yield stress to much longer loading with a peak stress lower than the static yield. Conditions to produce marginal failure were determined at these loading conditions. Typically, the short time, large  $P_{max}$  loading produces spall failure, and the longer time, lower  $P_{max}$  loading produces bending failure. Because the results could be put in non-dimensional form, direct comparison with the WES tests is possible. This was done to verify that the laboratory technique is a reasonable reproduction of field tests.

Table 1 lists the test shots that produced marginal failure. Results are given for both models without steel reinforcing and those with scale reinforcing. Marginal failure, that is when the test model was just breached, was achieved in all shots except MO24. Here the model has cracks due to bending on the back (tensile) side. Although the model was not breached, it appeared to have been loaded fairly close to marginal failure. The values for  $P_{max}$  given in Table 1 were calculated as described above. Tests with the prefix M were conducted in the 3.8 cm gun, and the test with prefix 6 was conducted in the 15 cm (6") gun.

TABLE 1

Summary of Recovery Shots  
and Test Parameters

| Shot No | Soil Thick cm | $P_{max}$ MPa | Marginal Failure Mode   |
|---------|---------------|---------------|-------------------------|
| MO18    | 0             | 77            | Spall                   |
| MO19    | 0             | 90            | Spall                   |
| MO22    | 8.6           | 26            | Bending                 |
| MO24    | 8.6           | 64            | See Note <sup>(1)</sup> |
| 6-07    | 11.4          | 50            | Bending                 |

<sup>(1)</sup> Bending cracks on back surface

Loading impulse was estimated by using the projectile momentum. The peak stress,  $P_{max}$ , and the impulse,  $I$ , were non-dimensionalized as previously described. Conditions for marginal failure are plotted against  $p^*$  and  $I^*$  in Fig. 3. Reference to Table 1 shows that low impulse, high  $P_{max}$  condition produces spall failure, and that

marginal failure in bending is produced at lower  $P_{max}$  when the loading has a larger impulse. Conditions to produce marginal failure reported in the WES tests, Kiger and Albritton (1980) and Baylot et al. (1985), were put in non-dimensional form and are also plotted in Fig. 3.

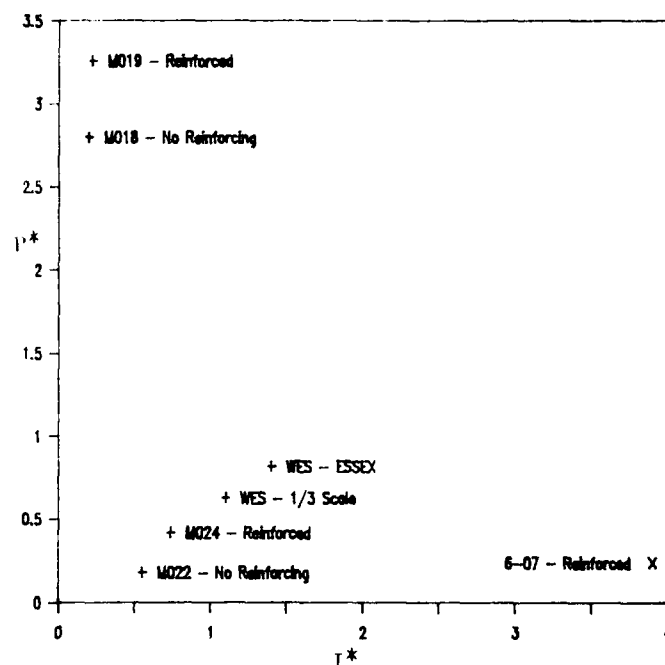


Fig. 3 Plot of Non-dimensional Loading  
Conditions that Produced  
Marginal Failure

As shown in Table 1, the failure mode for all of the test models was either by spalling or bending. In most cases, the wall of a hardened structure is breached by "punch" failure. This occurs when a section of the wall is "punched out" in local shear failure. The reason the test models did not fail in the "punch" mode is presumed to be because the loading was not at the intermediate range of  $p^*$  and  $I^*$  that occurred in the WES field tests. In addition, the clamped mounting of the plate in the test setup may not be a good model of the wall support in the box structures employed in the WES tests. Differences in the failure mechanisms between the two tests is believed to be due to the use of a test model that does not have complete similarity with the prototype. The failure mode of the WES-ESSEX test was in shear, preceded by earlier deterioration in bending. The response in the WES-1/3 scale test was described as flexure/membrane.

## 6. SUMMARY

The light gas gun technique appears well suited to produce the range of loading conditions that occur in ground shock loading. Projectile speed can be varied to give the desired peak stress. The type and thickness of the cover layers can be varied to give the desired rise time of the loading. The projectile mass (or length) can be varied to give the desired loading impulse (or

decay time). Here the desired peak stress was relatively low (100 MPa or 15,000 psi), and low projectile speeds were employed. However, higher speeds are possible, and a peak loading stress of 800 MPa (100,000 psi) can be achieved with relative ease. Possible differences in the dynamic failure mode of the test model when compared to field tests are believed to be due to the lack of complete similarity in the test model, and not because of scaling errors in the loading.

## 7. ACKNOWLEDGEMENT

This work was supported by the Air Force Engineering and Services Center, Tyndall AFB, FL, under Contract FO 8635 85 K 0052.

## 8. REFERENCES

1. Abrahamson, G. R. and Lindberg, H. E. (1976), "Peak Load-Impulse Characterization of Critical Pulse Loads in Structural Dynamics," *Nuc. Eng and Design*, 37 (1), p. 35.
2. Baylot, J. T., Kiger, S. A., Marchand, K. A. and Painter, J. T. (1985), "Response of Buried Structures to Earth-Penetrating Conventional Weapons," AFESC Report ESL-TR-85-09, Tyndall AFB, FL.
3. Crawford, R. E., Higgins, C. J. and Bultman, E. H. (1974), "The Air Force Manual for Design and Analysis of Hardened Structures," AFWL-TR-74-102.
4. Cunningham, C. H., Townsend, F. C., and Fagundo, F. E. (1985), "The Development of Micro-Concrete for Scale Model Testing of Buried Structures," AFESC Report ESL-TR-85-49, Tyndall AFB, FL.
5. Gran, J. K., Bruce, J. R. and Colton, J. D. (1973), "Scale Modeling of Buried Reinforced Concrete Structures Under Air-Blast Loading," ACI SP-73, p. 125.
6. Kiger, S. A. and Albritton, G. E. (1980), "Response of Buried Hardened Box Structures to the Effects of Localized Explosions," U.S. Army Engr. WES TR SL-80-I.
7. Sabnis, G. M., Harris, H. G., White, R. N. and Mirza, M. S. (1983), *Structural Modeling and Experimental Techniques*, Prentice-Hall, Inc., Englewood Cliffs, NJ.
8. Sorrell, F. Y., Horie, Y. and Whitfield, J. K. (1987), "Scaling Problems for Wave Propagation in Layered Systems," AFESC ESL-TR 87-73, Vol. 1.
9. Sorrell, F. Y. and Horie, Y. (1988), "Scaling Problems for Wave Propagation in Layered Systems," AFESC ESL-TR 87-73, Vol. 3.
10. Zia P., White, R. N. and Vanhorn, D. A. (1970), "Principles of Model Analysis," ACI SP 24-2, p 19.

# GRAVITY EFFECTS IN SMALL-SCALE STRUCTURAL MODELING

Tony F. Zahrah and Douglas H. Merkle

Applied Research Associates, Inc., Albuquerque, NM

## ABSTRACT

This study covered the development and application of Froude scaling techniques to design small-scale experiments for dynamically-loaded underground structures. Froude scaling allows true modeling of acceleration without using artificially-induced gravity, i.e., without a centrifuge. While allowing true modeling of gravitational acceleration, Froude scaling requires the use of simulant materials as a substitute for prototype materials. A survey of potential candidates for soil and concrete simulants has been conducted. Full characterization of simulant materials and small-scale experiments on dynamically-loaded buried structures are planned to evaluate the potential benefits of using Froude scaling for the design of small-scale dynamic experiments.

## INTRODUCTION

Experimental research involves exposing both full-scale and small-scale structures to live weapon effects. Small-scale testing is usually more economical than full-scale testing, but is subject to problems with data interpretation caused mainly by violation of similitude criteria, i.e., model distortion. When significant model distortion exists, application of model test data to predict prototype behavior involves extrapolation, which creates uncertainty and decreases confidence in prototype behavior predictions. One of the most troublesome causes of distortion in dynamic tests of model structures is gravity. Gravity causes the shear strength of granular soils to increase with depth, which is important when considering issues related to the effects of conventional weapons such as the strength of buried structures and weapon penetration resistance.

The objective of the current study is to develop concepts and procedures that compensate for gravitational effects without using a centrifuge. The approach is to use Froude scaling which accepts a gravitational scale factor of one.

## SCALING METHODS

The interpretation of test data is simplified if dynamic similitude requirements which account for all the variables governing the response of the structure are developed and adhered to during the experiment. The theory of models is employed to develop the dynamic similitude requirements, or scaling laws, between model and prototype. When all scaling laws are satisfied, the model is said to be a true model, and the results are directly applicable to prototype behavior.

Several approaches can be used to derive the scaling laws which relate prototype and model response (Murphy, 1950; Langhaar, 1951). One approach, described in detail in Zahrah *et al.* (1988), uses the basic concept of dimensional analysis, a set of dimensionally independent base variables and the fundamental scaling law:

The scale factor for any variable is obtained by replacing the variable's dimensions by their scale factors.

Using this approach the scale factors for the factors that influence the response of buried structures are summarized in Table 1, second column. In this table the scale factor for a variable is represented by a lower case letter and is defined as the ratio of its model to prototype values, e.g.,  $l = l_m/l_p$  where  $l$  represents length and the subscripts  $m$  and  $p$  refer to model and prototype, respectively.

Scaling methods differ in the choice of base variables. Two common scaling methods are replica scaling and Froude scaling. In replica scaling the set of base variables consists of length, mass density and stress. Prototype material is used in the experiment. As a result, the mass density and stress scale factors are equal to one, and the scale factors for all other variables can then be expressed in terms of the length scale factor as shown in Table 1, third column.

In Froude scaling the set of base variables consists of length, mass density and acceleration. Since the experiment is performed in a 1-g environment, the acceleration scale factor is equal to one. The scale factors for the other variables can then be expressed in terms of the mass density and length scale factors as shown in Table 1, fourth column.

An examination of the scale factors shows that in replica scaling the acceleration scale factor is equal to the inverse of the length scale factor whereas in Froude scaling it is equal to one. As a result, if gravity effects significantly influence the structure response, Froude scaling should be used to design an experiment in a 1-g environment. While allowing true modeling of gravitational acceleration, Froude scaling places additional constraints on loading conditions and material properties.

## LOADING SIMILITUDE

Replica scaling of an explosive charge simply requires that the charge energy be reduced by the length scale factor cubed ( $l^3$ ). Froude scaling reduces the energy as compared to replica scaling but imposes other requirements. The Froude-scaled loading conditions are:

|                         |                    |
|-------------------------|--------------------|
| Energy                  | $W = \rho l^4$     |
| Energy density (volume) | $W_v = \rho l$     |
| Energy density (mass)   | $W_m = l$          |
| Explosive pressure      | $\sigma = \rho l$  |
| Impulse                 | $i = \rho l^{3/2}$ |

The conditions imposed on the mass and volume energy densities of the explosive require dilution of an explosive charge with an inert mass. The inert mass would be required to have a thermal capacity such that the explosive pressure scale factor would be satisfied. These conditions are not difficult to satisfy.

## MATERIAL SIMILITUDE

When replica scaling is used to design a small-scale experiment, the stress and strain scale factors are equal to one and, as a result, the test articles are generally constructed of the same material as the prototype structure. When Froude scaling is used, the properties of the model material or simulant need to satisfy the following scaling laws:

|                     |                   |
|---------------------|-------------------|
| stress (or modulus) | $\sigma = \rho l$ |
| strain              | $\epsilon = 1$    |
| Poisson's ratio     | $\nu = 1$         |
| friction angle      | $\phi = 1$        |

As a result, simulant materials should be substituted for prototype materials. Since the product of the length and mass density scale factors is usually less than one, the simulant materials need to be weaker than the prototype materials. Although, in principle, one may arbitrarily select the length scale factor, the choice is generally dictated by the properties of the available simulant materials.

## APPLICATION OF FROUDE SCALING

The Air Force is interested in developing concepts for small-scale testing of shallow buried structures subjected to conventional weapon effects. Testing of shallow buried structures show that the soil around the structure has a stiffening effect which tends to limit lateral deflections of the structure. The stiffening effect is due to the development of passive pressures produced by shear stresses in the soil. This phenomenon is generally referred to as soil arching and is responsible for most of the increased structural hardness for buried structures. Gravity causes the shear strength of granular soil to increase with depth. It is thus important to properly simulate gravity effects. The initial objective was then to find simulant materials which can be used to build and field small-scale experiments for buried structures.

A survey of potential simulants for soil and concrete was conducted. The survey concentrated on finding a simulant for granular soil. The material properties of the soil that have most influence in determining the response of a soil-structure system are summarized in Table 2.

The scaling laws for stress and strain imply that there is only a change of scale on the stress axis and no change of scale on the strain axis, and the friction angle of prototype and simulant materials should be

the same. When sufficient information about stress-strain response of candidate simulant materials is unavailable, initial screening can be conducted on the basis of wave speeds. For small-scale experiments with a length scale factor between 1/10 and 1/50, the range of values for the required wave speeds in the soil simulant is summarized in Table 3. Several potential simulants for granular soil have been identified. The four most promising candidates are listed in Table 4. Other potential simulants have been identified and are covered in a report (Zahrah *et al.*, 1988). It became apparent during the survey that the potential simulants are typically used for other applications and, as a result, their engineering properties are not fully known. Full characterization of these potential simulants is necessary before these materials can be used in small-scale experiments.

The material properties which govern the behavior of concrete, the range of values for each property, and the scale factors relating the properties of the prototype and simulant materials are summarized in Table 5. If it is assumed that an experiment is to be conducted at 1/20 scale and that the prototype concrete has 4000 psi unconfined compressive strength, the problem is to design a mix with half the unit weight of regular concrete, a Young's modulus of 100,000 psi and a compressive strength of 100 psi.

A mixture of plaster, celite, sand and water is the most promising concrete simulant (Clough and Niwa, 1982). The ratio of water to plaster is the most important parameter in controlling the mechanical properties of the simulant. The amount of celite used in the mixture can be adjusted to provide good workability and consistency. The addition of sand does not increase the strength of the simulant, but it increases the modulus. Since the ratio of modulus to strength is dimensionless, it should be the same for the simulant and prototype materials. Sand can be used to adjust this ratio to the desired value.

Other candidates for concrete simulant are permalite perlite concrete and vermiculite concrete (Zahrah *et al.*, 1988). These two materials are versatile and, with proper adjustments in the mix proportions, simulant concrete with desired strength and deformation requirements can be obtained.

## CONCLUSIONS

The application of Froude scaling for the design of small-scale experiments on buried structures satisfies all dynamic similitude requirements but requires the

use of simulant materials for which the stress scale factor is equal to the product of the mass density and length scale factors. A survey of potential simulants for soil and concrete has been conducted and candidate simulants have been identified. Future efforts include full characterization of the candidate simulants and conduct of small-scale experiments on buried structures to evaluate the potential benefits of Froude scaling for design of small-scale dynamic experiments.

## ACKNOWLEDGMENTS

The authors express gratitude to the Air Force Engineering and Services Center (HQ AFESC/RD), Tyndall Air Force Base for supporting this program. The HQ AFESC/RD project officer for the initial phase of the program was Capt. Isaac Schantz.

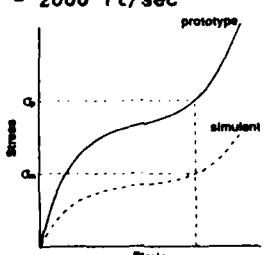
## REFERENCES

- Murphy, G., Similitude in Engineering, Ronald, 1950.
- Langhaar, H.L., Dimensional Analysis and Theory of Models, Wiley, 1951.
- Clough, R.W., and Niwa, A., "Earthquake Simulator Research on Arch Dam Models," Dynamic Modeling of Concrete Structures, ACI, Publication SP-73, 1982
- Zahrah, T.F., Merkle, D.H., and Auld, H.E., "Gravity Effects in Small-Scale Structural Modeling: Use of Froude Scaling Method," prepared for Tyndall Air Force Base, Applied Research Associates, Inc., Albuquerque, NM, April 1988.

**TABLE 1**  
**REPLICA AND FROUDE SCALE FACTORS**

| Variable         | Scale Factor             | Replica Scale Factor | Froude Scale Factor   |
|------------------|--------------------------|----------------------|-----------------------|
| length           | $l$                      | $l$                  | $l$                   |
| mass density     | $\rho$                   | $\rho = 1$           | $\rho$                |
| acceleration     | $a$                      | $a = 1/l$            | $a = 1$               |
| time             | $t = \sqrt{\frac{l}{a}}$ | $t = l$              | $t = \sqrt{l}$        |
| stress (modulus) | $\sigma = \rho a l$      | $\sigma = 1$         | $\sigma = \rho l$     |
| strain           | $\epsilon$               | $\epsilon = 1$       | $\epsilon = 1$        |
| Poisson's ratio  | $\nu$                    | $\nu = 1$            | $\nu = 1$             |
| friction angle   | $\phi$                   | $\phi = 1$           | $\phi = 1$            |
| velocity         | $v = \sqrt{al}$          | $v = 1$              | $v = \sqrt{l}$        |
| impulse          | $i = \rho \sqrt{a l^3}$  | $i = l$              | $i = \rho \sqrt{l^3}$ |
| energy           | $W = \rho a l^4$         | $W = l^3$            | $W = \rho l^4$        |

**TABLE 2**  
**SCREENING OF SIMULANTS FOR GRANULAR MATERIAL**

| Significant Properties   | Requirements and Limitations for Granular Material                                  | Scale Factors for Simulant Materials |
|--|---|--------------------------------------|
| Granular   | Spherical or Angular Shapes<br>(Rough Surface For Friction)                         | -                                    |
| Gradation  | Well Graded<br>(Excellent Shear Strength)   | -                                    |
| Relative Density   | 65 - 100%   | 1                                    |
| Air Voids Content  | 10 - 30%  | 1                                    |
| Dry Unit Weight  | 85 - 115 pcf  | 1                                    |
| Friction Angle   | 27 - 40 degrees   | 1                                    |
| Poisson's Ratio  | 0.2 - 0.35  | 1                                    |
| Wave Speed   |   | $\sqrt{l}$                           |
| Seismic  | 500 - 2500 ft/sec   |                                      |
| Loading  | 400 - 2000 ft/sec   |                                      |
| Stress-Strain Characteristics<br>(relationship needs to hold up to the stress level of interest) |  | $\sigma = \rho l$<br>$\epsilon = 1$  |

**TABLE 3**  
**REQUIRED WAVE SPEEDS FOR SOIL SIMULANTS**

| WAVE TYPE | WAVE SPEED IN PROTOTYPE MATERIAL | LENGTH SCALE | WAVE SPEED IN SIMULANT MATERIAL |
|-----------|----------------------------------|--------------|---------------------------------|
| Seismic   | 500-2500 ft/sec                  | 1/10<br>1/50 | 160-800 ft/sec<br>70-350 ft/sec |
| Loading   | 400-2000 ft/sec                  | 1/10<br>1/50 | 120-650 ft/sec<br>60-300 ft/sec |

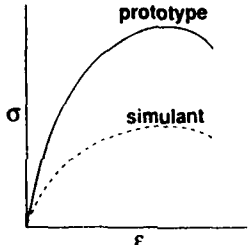
**TABLE 4**  
**SURVEY OF POTENTIAL SIMULANTS FOR GRANULAR MATERIALS**

| PROPERTY             | Q-SELL* | PUMICE | PERLITE** | VERMICULITE*** |
|----------------------|---------|--------|-----------|----------------|
| Size Range           | ✓+      | ✓      | ✓         | ✓              |
| Density              | ✓       | ✓      | ✓         | ✓              |
| Compressive Strength | ✓       | ?      | ✓         | ✓              |
| Loading Wave Speed   | ✓       | ?      | ✓         | ✓              |

- \* Sodium Silicate Micro Spheres/The PQ Corporation
- \*\* Siliceous Volcanic Rock
- \*\*\* Micaceous Mineral
- + property within acceptable range



**TABLE 5**  
**SCREENING OF SIMULANTS FOR CONCRETE**

| Significant Properties          | Requirements and Limitations for Concrete  | Scale Factors for Simulant Materials |
|---------------------------------|--|--------------------------------------|
| Unit Weight                     | 135 - 150 pcf  | $\rho$                               |
| Unconfined Compressive strength | 3000 - 5000 psi  | $\rho l$                             |
| Elastic Modulus                 | $3.0 - 4.0 \times 10^6$ psi  | $\rho l$                             |
| Tensile Strength                | 150 - 500 psi  | $\rho l$                             |
| Poisson's Ratio                 | 0.15 - 0.22  | 1                                    |
| Stress-Strain Characteristics   |  | $\sigma = \rho l$<br>$\epsilon = 1$  |

# CRATERING BY BURIED CHARGES IN WET MEDIA: COMPARISON OF CENTRIFUGE AND FIELD EVENTS\*

Edward S. Gaffney  
Ktech Corporation, 901 Pennsylvania Ave., NE, Albuquerque, NM 87110, USA  
Conrad W. Felice  
Capt., USAF, 485th Civ. Eng. Sq. (USAFE), APO, NY 09188-5000, USA  
and  
R. Scott Steedman  
Engineering Department, Cambridge University, Cambridge, CB2 1PZ, UK

Four small scale (2 gram PETN charges) cratering events are reported. Three of the events were conducted at 60 g, corresponding to a scaled explosive mass of 432 Kg, and one at 1 g. Active measurements were made of total stress in the soil (saturated sand). Apparent crater measurements were also made and data from passive colored sand columns and layers provided information on the extent of the true crater and deformations outside the crater. The high g apparent crater dimensions scale well with other crater data reported for both chemical and nuclear explosions buried near optimum depth of burst in wet soils and soft rocks.

## 1.0 INTRODUCTION

Small-scale explosive events in saturated sand, at ambient and increased acceleration, were conducted as part of an investigation of the effect of buried charges on foundation elements (Ref. 1). The structural aspects of these experiments are reported in a companion paper (Ref. 2). In this paper, we report on the craters and free-field environment from the events and relate those results to data previously reported for explosions near optimum depth of burst in wet geologies.

## 2.0 EXPERIMENTAL DETAILS

### 2.1.0 Test Bed Configuration

The crater data were obtained for 2 gram charges of PETN at a nominal density of 900 kg/m<sup>3</sup> buried at a depth of 74 mm in saturated sand (wet density about 1900 kg/m<sup>3</sup>). Three tests were conducted at 60 g's using the Geotechnical Centrifuge at Cambridge University, UK; the other test was conducted at the same facility at ambient gravity. For the first two events at 60 g, the water table directly above the charge was at a depth of a few centimeters due to the curvature of the equipotential surface in the centrifuge. On the third high g event, the water table above the charge was at the surface and several centimeters of free water stood above the sand surface on either side.

The sand used in the construction of the models was Leighton Buzzard 100/200 supplied by D.J. Ball & Co., Lolworth, England. 100/200 refers to the British Standard sieve sizes through

which the sand should pass/be retained. The nominal grain size was approximately 0.12 mm. The specific gravity of Leighton Buzzard sand is 2.65 and the maximum and minimum void ratios for 100/200 sand are 1.025 (0% relative density) and 0.65 (100% relative density), respectively.

The models were constructed within the circular model chamber in a model preparation room adjacent to the centrifuge loading bay. Starting with an empty chamber, a circular rubber mat was placed in the bottom of the chamber (or tub) to protect the thin steel base from damage. Concrete building blocks approximately 100 mm deep were placed on the rubber mat covering the whole base of the tub as far as possible. Gaps between the blocks and the walls were filled with coarse Leighton Buzzard 14/25 sand (nominal grain size 0.9 mm).

Two steel gantries made from hollow square tube section were fabricated to hold the piles in position, one to hold the two single piles, and one to hold the line of piles. The appropriate gantry was bolted to the stiffening ring with the piles in position leaving a small clearance above the concrete blocks in the base of the tub.

The sand bed was constructed by pouring fine sand from a hopper suspended above the tub. The height of drop was maintained at a constant value by raising the hopper as the pouring progressed. Pouring was interrupted to allow for the placing of transducers. As far as possible transducer leads were taken directly away from the transducer to the wall of the tub and from there up to the wall to the signal conditioning or junction boxes. All transducers placed in the sand bed were oriented such that their sensitive axis was pointed towards the charge in a horizontal plane.

When the sand bed had been raised to shot level, a brass tube was placed and embedded about 10 mm into the sand. Pouring continued around and inside the tube until the bed had been raised to the correct height. The surface was levelled and the model prepared for saturation.

\* Supported by US Air Force Weapons Laboratory, (AFWL/NTESG), Kirtland AFB, NM 87117-6008

To saturate the model, a heavy steel lid was sealed on top of the tub creating a chamber which could be evacuated. A vacuum of up to 29" mercury was pulled on the chamber and water introduced from two points at the base of the tub. The required volume of water was estimated by calculation.

After saturation, the vacuum was released and the model prepared for testing. Junction boxes were bolted to the upper stiffening ring and the transducers connected.

The final task in preparation for flight was placement of the charge. The brass tube, which had been embedded at shot depth, protruded by about 20 mm above the sand surface. The sand inside the tube was removed to the appropriate depth using a spoon, whilst ensuring that the water level inside the tube remained slightly higher than outside.

The charge was placed inside the tube and held in position whilst the hole was backfilled with the excavated sand. Finally, the tube was removed from the sand bed, vibrating it to minimize damage. A section view of a typical test is shown in Figure 1.

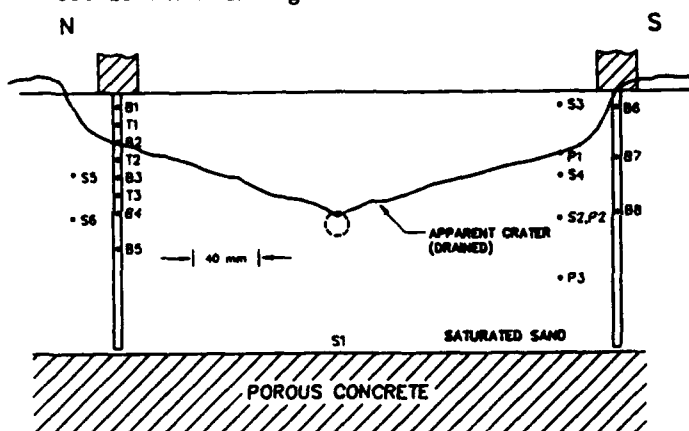


Figure 1. Sectional view of test RSS130 with a pair of isolated piles. Locations of the charge and of the gauges in the free-field and on the piles are shown, as is the apparent crater produced.

The centrifuge was accelerated to 60 g in steps of 20 g. Readings from the pore pressure transducers and strain gauges were taken at each intermediate acceleration level. After the centrifuge reached 60 g, a final series of transducer readings were taken. The firing set, an FS-10 unit which was mounted on the centrifuge arm, was remotely armed, and subsequently triggered, from the control room.

## 2.2.0 Active Instrumentation

Total stress measurements were attempted using gauges of two different designs. The transducers in both designs were biaxially stretched, hysteretically poled polyvinylidene fluoride (PVDF) film 26  $\mu$ m thick manufactured by

Metravib RDS. The PVDF transducers were emplaced in gauges with both probe and flatpack designs. No data were obtained with the single flat pack gauge so it will not be discussed further. The probe design is illustrated in Figure 2. The sensitive area of the PVDF was glued to the end of a short rectangular Lexan post, with the leads going over a rounded bevel and glued to the side. After attachment of a coaxial cable, the post and cable attachment were covered with a 1 mm Lexan sheet and the voids filled with epoxy. For one gauge a ~2000 pF capacitor was placed in parallel with the transducer and potted with it into a single probe.

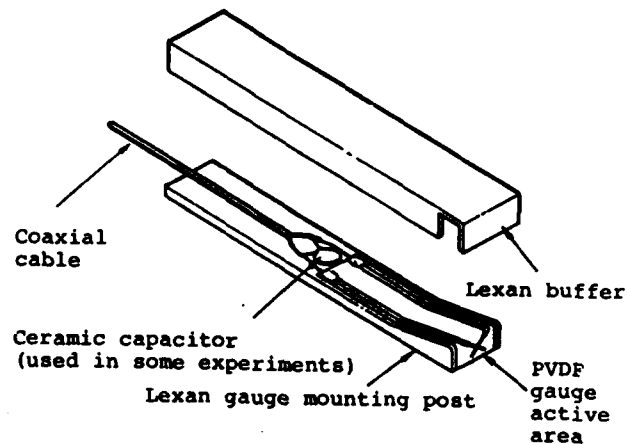


Figure 2. Probe stress gauge design used for most of the total stress measurements in tests RSS130 and RSS131.

All stress gauges were operated in the charge mode. Charge generated by the transducer accumulated on the gauge capacitance (typically 16 pF) and any distributed cable capacitance and on any parallel capacitance. A charge amplifier converted this high impedance signal to one capable of driving a 50  $\Omega$  input impedance recording device. We used PCB 302A charge amplifiers for all our gauges.

## 2.2.1 Calibration

Previous calibration data for these transducers (Ref. 3) have been obtained for stresses above about 200 MPa. We have obtained new data in the range 8 KPa to 800 KPa, illustrated in Figure 3. These data were taken with low amplitude air shocks produced in Ktech's 100 mm shock tube facility. Reflected pressure was measured simultaneously by a PVDF transducer mounted on a plexiglas plug and a PCB model 102A02 pressure gauge. The resulting relation between charge density (Q/A) and pressure ( $\sigma$ ) is  $Q/A = 17.3 \pm 0.7$  pC/N. This linear relation is different than the  $\sigma^{.64}$  dependence found above 200 MPa.

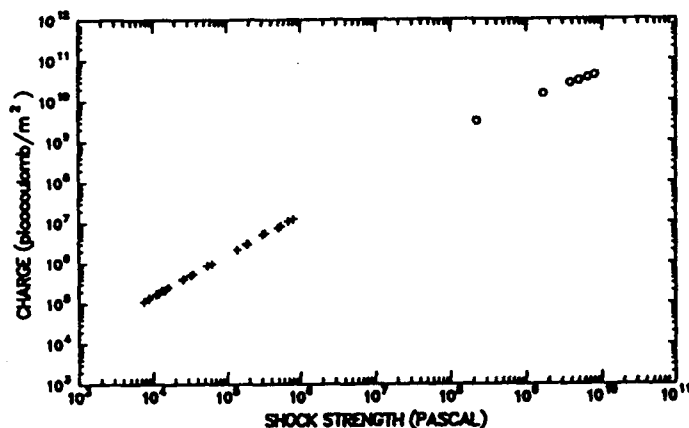


Figure 3. Calibration data for biaxially stretched hysteretically poled PVDF from Metravib RDS. Data from above 100MPa are from Ref. 3; lower data is newly reported.

### 2.3 Passive Measurements

The measurement of the crater profile was made using light-weight plastic rods of known length which were placed, one by one, through a grid of holes in a thick circular plexiglas cover which was mounted over the tub after the test. The plastic rods were lowered gently until they rested on the sand bed vertically below the locating hole in the plexiglas lid. Using a datum depth measurement which had been made into the tub itself, the distance of each individual point from an arbitrary datum could be determined. The measurements thus derived are indicative of the apparent crater.

Horizontal layers of dark blue sand were placed at various levels on all events to determine both true crater dimensions and the extent of deformation around the crater. For the last two events, vertical sand columns were also emplaced at initial ranges of 64, 124, 154, and 184 mm.

## 3.0 RESULTS

### 3.1 Crater Dimensions

For the first two events, the resulting craters were very similar, with radii of about 160 mm, depths of 70 mm, and volumes of  $2.3 \times 10^{-3} \text{ m}^3$ . On the third high g event, where several centimeters of free water stood above the sand surface on either side, the crater was about 145 mm in radius, only 26 mm deep, and had a volume of  $0.93 \times 10^{-3} \text{ m}^3$ . The final event, at 1 g, resulted in a crater 150 mm in radius and 110 mm deep, with a volume of  $3.6 \times 10^{-3} \text{ m}^3$ . Figure 4 shows the crater profiles for each of the high g events.

The horizontal layers and sand columns used on the tests permitted definition of the region of deformation around the craters. The sand column data for test RSS140, the third high g event, are summarized in Figure 5. Each of the columns shows the same general trend of radial displace-

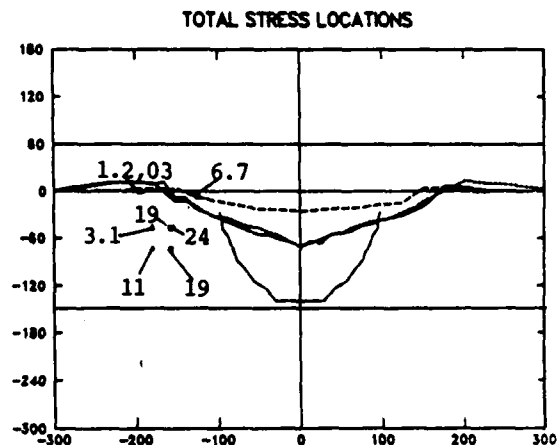


Figure 4. East-west apparent crater profiles for all three 60g shot; true crater profile for shot RSS140; and gauge locations with peak values (in MPa) as indicated. Squares are for RSS130 and Triangles are for RSS131. Dimensions are in mm.

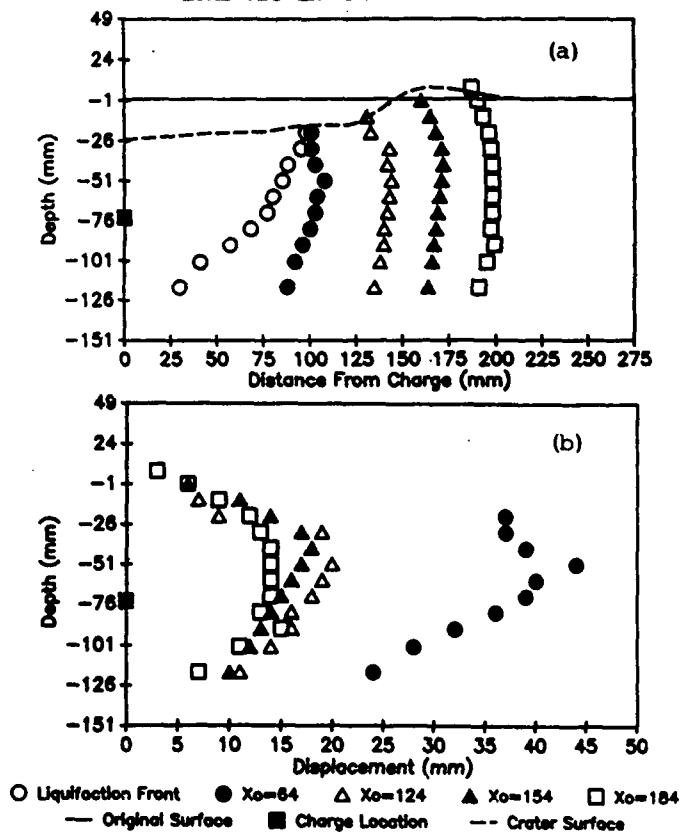


Figure 5. Sand column results from shot RSS140 (60g). (a) Final locations of sand columns and liquefaction front (or true crater) relative to the original surface, the charge location and the final apparent crater.  $X_o$  is the initial horizontal range to the sand columns. (b) Horizontal displacement of sand columns from original horizontal range.

shows the same general trend of radial displacement increasing upward to a maximum followed by decreasing radial displacement approaching the surface. The maximum displacement is between the shot depth and the surface. We speculate that some of the decrease in displacement from there to the surface is an expression of inward slumping or more homogeneous inward flow at late times. The sand column at 124 mm original range shows an abrupt inward lateral discontinuity at about 30 depth which supports this speculation.

There is also a pronounced edge to a central zone of chaotic structure. This bowl shaped region is interpreted to be the maximum extent of blast-induced liquefaction, the limit of the true crater, or both.

### 3.2 Total Stress Measurements

Three typical total stress measurements are shown in Figure 6. We see the passage of the shock as a spike which is limited by the bandwidth of the recorder followed by a much broader stress signal lasting for hundreds of microseconds. Because of the way the gauges are constructed, we consider that this broader stress signal must be due to the dynamic stress of the sand flowing past the relatively massive gauge. The peaks of this broad signal in the total stress measurements are summarized in Table 1. The locations of the measurements relative to the final apparent craters and the true crater in test RSS140 were shown in Figure 4. The similarity of the peak stresses at similar locations in the two events is evident.

Table 1. Total Stress Results

| Shot No. | Gauge No. | Radius (mm) | Depth (mm) | Peak Stress (MPa) |
|----------|-----------|-------------|------------|-------------------|
| RSS130   | TSC3008   | 125         | 7          | 6.7               |
|          | TSC5004   | 158         | 47         | 19                |
|          | TSC6007   | 158         | 74         | 25                |
| RSS131   | TSC1006   | 193         | 0          | 1.4               |
|          | TSC2005   | 193         | 0          | 0.30              |
|          | TSC3004   | 180         | 74         | 11                |
|          | TSC4007   | 180         | 47         | 3.6               |
|          | TSC6008   | 150         | 47         | 24                |

### 4.0 DISCUSSION

#### 4.1 Free-field Stress and Velocity

In the free-field total stress measurements (e.g., (a) and (b) in Figure 4) the initial ground shock arrival at about 100  $\mu$ sec is not resolved by the 20 KHz recording system, but a second broad arrival between about 250 and 700  $\mu$ sec is well recorded. This is tentatively attributed to flow of soil around the stress probes. The duration of the measured free field pulse is probably limited by the length of the gauge and not by the duration of the flow. The actual duration of the crater excavation flow is better indicated by the stress gauges at the end of the beam (e.g., (c) in Figure 4) which show the flow lasting about 4 msec.

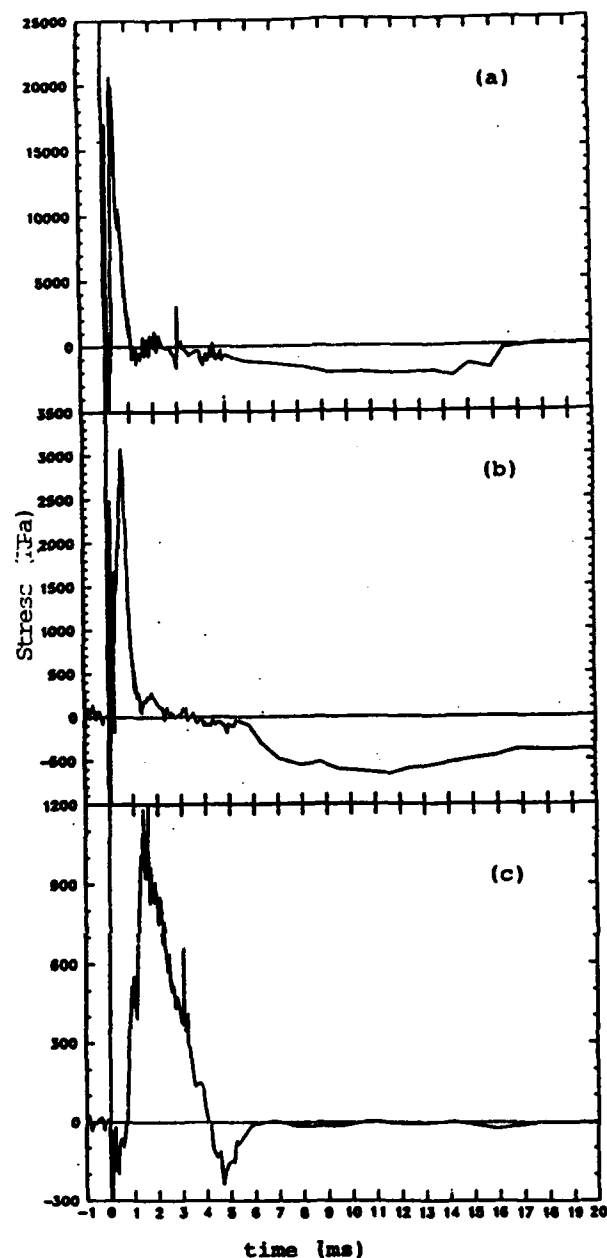


Figure 6. Typical total stress records from pile group test (RSS131). (a) Horizontal stress at 47 mm depth, 150 mm. (b) Horizontal stress at 47 mm depth, 180 mm range. (c) Vertical stress at surface, 193 mm range.

If the "free field" and vertical stress measured in these tests is caused by the flow of the medium around the probes, then we should be able to obtain a rough estimate of the velocity of the crater excavation flow by treating these as

"dynamic pressure" measurements. The dynamic pressure in the flow of a fluid of density  $\rho$  at speed  $c$  is just  $\rho c^2$ . Thus the peak upward velocity of material flowing past gauge TSC1006 would be about

$$c_{\max} = \left( \frac{p_{\max}}{\rho} \right)^{1/2} = \left( \frac{1.4 \times 10^6}{1900} \right)^{1/2} = 27 \text{ m/s}$$

If flow at that velocity lasted for 4 ms the total displacement would be about 100 mm. This is on the order of the displacement required to excavate the craters observed which supports, but certainly does not prove, our interpretation of these records. Proof of our interpretation would probably require a numerical model of the crater growth event with a probe gauge included.

#### 4.2 Apparent Crater Dimensions

The difference between the apparent craters formed in the three 60 g events can probably be attributed to either washing or slumping of the crater rim area into the crater which occurred in RSS140 but not in the two events with slightly lower water tables. The volume of the ejecta in the apparent crater lip for RSS140 is very small. In addition, the sand column data support the occurrence of inward slumping of the crater rim area. However, there are no sand column data from the other two events for comparison.

Data reports for cratering events near optimum depth of burst (say 0.4 to 0.65 m/kg<sup>1/3</sup>) in wet media are not common. We have located fourteen other events which are summarized in Table 2 along with the present results. Because of the

scarcity of data, we have had to combine results from several different media including sand, other soils (although we have not included any events reported for "clay" in the absence of coarser soils), and soft rocks. The explosives used included TNT, ANFO, NM, and nuclear devices. The events come from several series of tests. Two candidate events were excluded because they were unstemmed; comparison with companion stemmed events indicated that lack of stemming lead to craters with volumes reduced by a factor of about 2.

The effect of explosive yield on crater dimensions can be seen in Figure 7. These preliminary results have ignored the differences in medium density and explosive type, lumping all of the events into a single analysis. A more detailed analysis would consider these effects. However, we do not expect that the general trend will be very different.

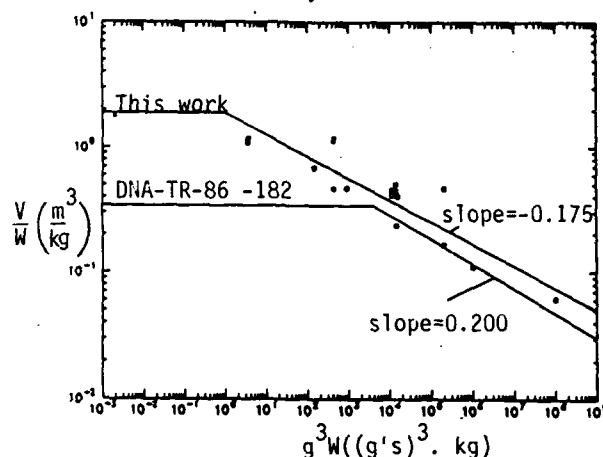


Figure 7. Scaled crater volume vs. scaled yield for explosive craters in wet media at near optimum depth of burst.

TABLE 2. CRATER DATA FOR WET MEDIA WITH  $0.4 < \text{SDOB} < 0.6 \text{ m/kg}^{1/3}$

| Event     | Explosive |                 |                                 |               | DOB<br>(m) | Medium           |                                 | Crater       |               |                             |
|-----------|-----------|-----------------|---------------------------------|---------------|------------|------------------|---------------------------------|--------------|---------------|-----------------------------|
|           | Type      | Mass*<br>(kg)   | Density<br>(kg/m <sup>3</sup> ) | Radius<br>(m) |            | Type             | Density<br>(kg/m <sup>3</sup> ) | Depth<br>(m) | Radius<br>(m) | Volume<br>(m <sup>3</sup> ) |
| RSS130    | PETN      | 0.002           | 900                             | 0.0059        | 0.074      | Sand             | 1920                            | 0.0693       | 0.158         | $2.36 \times 10^{-3}$       |
| RSS131    | PETN      | 0.002           | 900                             | 0.0059        | 0.074      | Sand             | 1910                            | 0.0695       | 0.163         | $2.26 \times 10^{-3}$       |
| RSS140    | PETN      | 0.002           | 900                             | 0.0059        | 0.074      | Sand             | ~1900                           | 0.026        | 0.144         | $0.927 \times 10^{-3}$      |
| RSS141    | PETN      | 0.002           | 900                             | 0.0059        | 0.074      | Sand             | ~1900                           | 0.110        | 0.149         | $3.59 \times 10^{-3}$       |
| UETP111   | TNT       | 3.63            | (1630)                          | 0.0810        | 0.762      | Sand             | --                              | 1.22         | 1.83          | 3.96                        |
| UETP114   | TNT       | 3.63            | (1630)                          | 0.0810        | 0.762      | Sand             | --                              | 1.07         | 1.83          | 4.25                        |
| JJA-3     | TNT       | 4.54            | (1630)                          | 0.0873        | 0.978      | Silt, Clay       | --                              | 0.518        | 1.46          | --                          |
| JJA-5     | TNT       | 4.54            | (1630)                          | 0.0873        | 0.991      | Silt, Clay       | --                              | 0.457        | 1.34          | --                          |
| JJA-7     | TNT       | 4.54            | (1630)                          | 0.873         | 0.978      | Silt, Clay       | --                              | 0.305        | 1.40          | --                          |
| JJA-8     | TNT       | 4.54            | (1630)                          | 0.0873        | 0.954      | Silt, Clay       | --                              | 0.701        | 1.33          | --                          |
| UETP116   | TNT       | 145             | (1630)                          | 0.277         | 2.667      | Sand             | --                              | 2.74         | 5.64          | 99.1                        |
| 12MS      | GMM       | 11250           | 1210                            | 1.304         | 12.0       | Sand, Silt, Clay | ~2000                           | 8.4          | 18.7          | 4680                        |
| 12MPS     | GMM       | 11250           | 1210                            | 1.304         | 12.0       | Sand, Silt, Clay | ~2000                           | 4.1          | 27.6          | 5090                        |
| Hole 2308 | NE        | $2 \times 10^5$ | --                              | --            | 31.4       | Soft Rock        | 1740                            | 21           | 35            | 9400                        |
| Hole 1003 | NE        | $1 \times 10^6$ | --                              | --            | 48.0       | Clay, Shale      | 1800                            | 31           | 53.5          | 11000                       |
| Hole 1004 | NE        | $1 \times 10^8$ | --                              | --            | 200        | Shale            | ~1700                           | 100          | 210           | $6.2 \times 10^6$           |

\* Yield for NE charges

The specific crater volume (V/W) clearly decreases toward higher yields just as it does for craters in dry sand. However, our data and those from events with yields below one ton indicate that the transition from gravity-dominated scaling to strength-dominated scaling occurs at scaled yields of a few kilograms rather than a few tons as suggested by Schmidt et al. (Ref. 4) who did not include any data for yields below about 15 tons in their figure. This difference may be due to our grouping of wet soils and wet soft rocks. The difference between their slope at high yields (0.200) and ours (0.175) is probably not significant.

## 5.0 REFERENCES

1. C.W. Felice, R.S. Steedman and E.S. Gaffney, "Centrifuge models of pile response in a blast and shock environment". Presented at Centrifuge '88: Int. Conf. Geotech. Centrifuge Modelling, Paris, 25-27 April 1988.
2. C.W. Felice, R.S. Steedman and E.S. Gaffney, "Dynamic response of deep foundations". Submitted to Symposium on Interaction of Non-nuclear Munitions with Structures, Tyndall AFB, April 1989.
3. F. Bauer, 1986, "Ferroelectric Properties and Shock Response of a Poled PVF<sub>2</sub> Polymer and of VF<sub>2</sub>/C<sub>2</sub>F<sub>3</sub>H Copolymers". in Y.H. Gupta (ed.) Shock Waves in Condensed Matter, Plenum, New York.
4. R.M. Schmidt et al., 1986, "Gravity Effects in Cratering", DNA-TR-86-182, Defense Nuclear Agency, Washington, DC.